Construction of molecular cathodes and photocathodes for hydrogen evolution

Nicolas Kaeffer

Communauté UNIVERSITÉ Grenoble Alpes

THÈSE

Pour obtenir le grade de

DOCTEUR DE L'UNIVERSITÉ GRENOBLE ALPES

Spécialité : **Chimie inorganique et bio-inorganique**

Arrêté ministériel : 7 août 2006

Présentée par

Nicolas KAEFFER

Thèse dirigée par **Vincent ARTERO**

préparée au sein du **Laboratoire de Chimie et Biologie des Métaux**
dans l'**École Doctorale de Chimie et Sciences du Vivant**

Construction de cathodes et photocathodes moléculaires de production d'hydrogène

Thèse soutenue publiquement le **11 mars 2016**
devant le jury composé de :

Mme Carole DUBOC
Directrice de recherche, Université Grenoble Alpes, Présidente du Jury
M. Christophe COPERET
Professeur, ETH Zürich, Rapporteur
M. Benoît LIMOGES
Directeur de recherche, Université Paris 7, Rapporteur
Mme Elizabeth GIBSON
Lecturer, Newcastle University, Examinatrice
M. Vincent ARTERO
Directeur de recherche, Université Grenoble Alpes, Directeur de Thèse

« A vaincre sans péril, on triomphe sans gloire. »

Le Cid, Corneille.

Remerciements

Qu'il est dur d'inaugurer un manuscrit par la fin, cette fin en soi que sont les remerciements. Il n'en est pas moins dur de trouver un ordre logique, une idée directrice, pour présenter ces remerciements. Je commencerai donc par prendre le cadre du Laboratoire de Chimie et Biologie des Métaux en guise d'introduction. Ce laboratoire fût pour moi, durant ces 3,41 années de thèse, comme une grande famille à la table de laquelle on échange, on apprend, on débat, on rit (accessoirement, travaille-t-on?). Alors bien sûr, comme dans toute grande famille, il y a des différences de points de vue, des désaccords, un cousin d'Amérique avec lequel on est fâché sans plus trop savoir pourquoi, un héritage qu'on convoite... Mais, au LCBM, ce qui prime bien au delà de ces considérations, c'est que l'ouverture d'esprit et l'intelligence de ses membres en font un lieu humain et chaleureux où il fait bon faire de la Science (et pas que!). Je les remercie pour cela, dans leur ensemble.

J'ai pu mettre un premier pied au LCBM grâce au Professeur Marc Fontecave, que je remercie à cette occasion, alors que j'étais en stage de master 2 au sein de son laboratoire du Collège de France. Mettre le second pied au LCBM fût une affaire un peu plus délicate pour le candidat de seconde main que j'étais alors. Mais, fruit d'un repéchâge heureux (d'aucuns diront d'un lobbying intense de ma part), j'ai pu rejoindre ce bateau pour mon aventure de thèse. Comme il est coutume de le faire, je souhaite donc remercier M. Le Directeur du meilleur LCBM, Stéphane Ménage, pour m'avoir accueilli au sein de son Laboratoire et pour avoir, à moi et à mon camarade thésard, insufflé l'art de la confiance en soi. Il n'est par contre pas coutume que, dans un laboratoire, Mme la Directrice partage le sous-sol avec le bas peuple, qu'elle a su supporter pendant presque un an. Technicienne des surfaces biochimiques (sans mauvais jeu de mots), je remercie donc Christine Cavazza pour m'avoir ouvert les yeux sur la grâce de la cristallographie des protéines et, surtout, pour sa bienveillance quotidienne. Il me faut également adresser mes remerciements à mes collègues permanents du bâtiment K'. Je tiens donc à remercier Stéph' Torreli pour un ensemble de choses (non exhaustif) telles que les gaz, la RPE, l'azote liquide, les distil', les complexes de cuivre empruntés à son insu, bref, cette logistique générale dont il raffole tout particulièrement, et aussi pour les affectueux surnoms qu'il a pu me trouver. Je remercie Hamid pour les débats que nous avons pu avoir, ses points de vue toujours nuancés, pour faire couler le café du matin et pour son enthousiasme inaltérable face à notre belle chimie. Mes remerciements vont également à Caro pour ses conseils vestimentaires et sa pharmacie salvatrice, à Sandrine pour ses "Ca va?" mi-malicieux, mi-inquisiteurs, à Nicolas D. pour son aide importante et précieuse à la RMN (arme ô

combien nécessaire au chimiste de synthèse), à Olivier, à Adeline, à Etienne, à Christelle, à Victor et à Christian pour nos échanges quotidiens, ainsi qu'à Nathalie pour son support administratif. Bien sûr, cette vie au laboratoire n'aurait été la même sans un certain nombre de non-permanents (je ne dirai pas "les jeunes" pour ne pas froisser) avec qui j'ai pu partager, de manière plus ou moins directe, mon labeur et bien d'autres choses le long de ces années de thèse. Je remercie pour ce plein de choses, et dans un ordre aléatoire: Lulu (pour nos visions du monde toujours en accord), Mél-Mél (pour le vélo et les *apfel-strudel*), Thibault (stagiaire *pour la Science* et grand consommateur de Canigou®), Stéph', Béa, Charlène, Jean, Marine B., Marine D., Marina, Olbelina, Bianca, Trevor, James, Sukanya, Florian, Reuben, Souvik, Huan, le Pr. Berggren, Eugen, Phanélie, Mahmoud pour les anciens; Johannes, Jessica, Jordan, Jaione, Jordan, Jérôme, (que de "J"!), Alexandre, Sarah, Khemary, Amal pour les "petits" nouveaux!

Au-delà de ces relations au quotidien, ce travail de thèse a été largement enrichi par de nombreuses collaborations, en France comme à l'étranger. Je tiens pour celà à remercier nos collaborateurs pour leur aide, leurs conseils ou encore l'accueil qu'ils m'ont fait au sein de leurs propres groupes. J'adresse donc un grand merci à Colette Lebrun, pour son apport on ne peut plus précieux et salvateur en spectrométrie de masse, à Laure Guétaz pour la microscopie à balayage, au Professeur D. Léonard et à C. Gablin pour la spectrométrie de masse en surface, à Bruno Jousselme, Romain (ses power-rangers) et Tiphaine pour les photocathodes et les CNTs, à E. Martinez pour la spectroscopie XPS, à Jacques Pécaut pour les cristaux, au Professeur Devens Gust, à son équipe (Maxime, Dalvin, Marely,…) et à Dick Co pour les deux mois d'échange passés à *Arizona State University*, à Stéphanie et Frédéric pour le *workshop TCO* et les nombreuses électrodes fournies, à Libby et son équipe (Gareth, Chris) pour le *workshop NiO*, au Professeur B. Dietzek et à Maximilian pour notre première étude sur NiO, et à bien d'autres que j'oublie certainement.

C'est ainsi dans un cadre très riche que ce travail de thèse a pu être mené. Il me semble important d'adresser ici mes remerciements à ceux qui l'ont jugé, évalué et qui ont participé à son amélioration. Je tiens donc à remercier l'ensemble des membres de mon jury de thèse et notamment le Dr. C. Duboc pour avoir accepté de prendre la présidence de ce jury, le Prof. C. Copéret pour avoir apporté son expertise en chimie de surface (et pour m'offrir la possibilité de poursuivre mes travaux scientifiques), le Dr. B. Limoges pour son aide précieuse sur les questions électrochimiques et le Dr. E. Gibson *for sharing her know-how on p-DSS(/PE)C and for a careful proof-reading of my amendable english*.

S'il y eut un cadre extérieur extrêmement riche, ce travail de thèse s'est avant tout développé au sein de l'équipe *SolHyCat*, dernière née du LCBM, sous les auspices de la bienveillante *FVAS*.

Je suis donc reconnaissant à ses membres pour tout ce qu'ils m'ont apporté (beaucoup!) lors de ces dernières années. Mes remerciements vont à Dongyue pour nos nombreux échanges, notamment autour de l'électrochimie des cobaloximes (quelle dévotion!), à Matthieu, véritable amoureux de la Science, rock-star outre-atlantique et soutien alsacien, à Nathan, qui n'aura, j'en suis sûr, aucune difficulté à entretenir ce doux flambeau de l'impertinence et des calembours douteux, à J-F, pour son infinie patience alors qu'il occupait le bureau adjacent au mien lors de la rédaction de ce manuscrit, ainsi qu'aux thésardes intermittentes de la *Fondation* que sont Déborah et Solène pour nous apporter la fraîcheur du dehors, des $[Ni(P_3N_{12})]^{3+}$ et une couleur de cheveux inédite. Il me faut également remercier ceux qui ont su faire preuve d'abnégation pour mener avec moi et de manière conjointe nombre d'études: merci donc à Chris, qui a le courage de reprendre le sujet des photocathodes co-greffées, à Adina, pour des études toujours propres et carrées et pour ses exceptionnels, mais légendaires, coups de chaud et à Julien, maître en chimie organique, colocataire de hotte au plaisir partagé de croiser le fer à propos du rangement de la vaisselle et de la subtilisation des tubes RMN, entraîneur invétéré de mes zygomatiques (et, effet secondaire, détracteur de mon audition) et, enfin, compagnon de *dyecat* devant l'éternel.

Parmi ces compagnons de route, s'en trouve un qui aura partagé ces 3,41 années au LCBM de A à Z avec moi. Il est assez clair que sans nos discussions métaphysiques sur la Science, la Vie, la science dans la vie, la vie de la science, le semi-épluchage des bananes ou l'attribution des places de parking, toujours soutenues par son art du débat et de la précision, toujours exempte de mauvaise foi et de parisianisme forcené, cette longue et parfois rude épreuve qu'est la thèse m'aurait certainement parue plus longue et plus rude (comme cette phrase d'ailleurs, mais bon, ceci n'est pas de l'anglais scientifique). Ensemble, nous fûmes taxés d'exercer de concert notre cynisme le plus malveillant et notre défaitisme le plus exagéré, quand bien même nous nous sommes toujours gardés de penser un traître mot de ce que nous avancions (et vice-versa!). Bref, pour tous ces bonnes choses, pour bien des moments de complicité partagée, mes remerciements les plus forts vont à ce véritable scientifique en devenir qu'est Nico, le plus éminent de mes collègues, et néanmoins ami.

Je tiens aussi à dire un grand merci à Jeni, la force tranquille de cette équipe *SolHyCat*, ô combien bienveillante à notre égard et qui sait assurer une impeccable gestion (logistique mais pas uniquement) de ce groupe parfois ingérable, et ce, toujours avec le sourire!

J'adresse mes remerciements et ma gratitude à Murielle pour son encadrement (officieux, nous ne le dirons pas) extrêmement précieux, notamment en chimie de synthèse, et pour avoir transmis à ses deux Nico pour le prix d'un l'amour du travail propre et bien fait, valeur inestimable dans notre domaine qu'est la recherche scientifique. Elle a su avec flegme prendre soin de ses

turbulents petits, nous offrant même en quelques rares occurrences l'accès au panthéon gustatif que sont ses succulentes mousses au chocolat!

Enfin, je pourrais ici détailler tout un tas d'avantages et d'inconvénients qu'on peut trouver à conduire sa thèse sous la direction de Vincent, mais, pour n'être taxé à nouveau d'impertinence, je me bornerai aux avantages, les inconvénients n'étant que ceux des avantages. Grâce à une (quasi-) omniscience qui est propre à Vincent, j'ai pu à ses côtés enrichir mon savoir (pratique ou théorique) comme jamais auparavant. J'ai éprouvé le plus grand plaisir à mener des études scientifiques sous son encadrement, qui a toujours su trouver le juste équilibre entre directions à suivre, conseils judicieux et liberté d'entreprendre. Mettant également une grande confiance (aveugle?) dans ces étudiants (souvent au-delà de la confiance que ceux-ci ne s'accordent eux-mêmes), il m'a donné l'occasion de prendre part à de nombreux échanges, conférences nationales ou internationales. Ceci m'aura mené vers une autonomie plus large et, j'en suis sûr, préparé pour la poursuite de mon parcours. Je noterai enfin qu'il est chose rare qu'un chimiste de son niveau sache prendre le temps d'inculquer à ses étudiants non seulement un savoir scientifique de haute volée, mais également ses connaissances en Montagne, notamment lors d'ascensions de Chamechaude à peau de phoque. Ainsi, pour ces trois belles années de thèse, et pour tout le reste, j'adresse à Vincent mes remerciements les plus profonds.

C'est donc fort d'une expérience scientifique et humaine intense, et non sans une pointe de mélancolie, que je quitte ce beau navire grenoblois du LCBM. Si cette adolescence de la recherche a agrandi le cercle de ceux que j'estime, il en est qui y sont présents depuis mon plus jeune âge. Je trouve ici l'occasion de les remercier, pour l'ensemble de leurs oeuvres et pour le soutien qu'ils m'ont témoigné lors de mes années de thèse. Je remercie pour cela mes vieux "potes du lycée" (qui me supportent depuis bien trop longtemps), mes amis de prépa, ceux de l'Ecole (pour leur tonne-équivalent-soutien). J'adresse un merci tout particulier à mes meilleurs coloc', Maria et Matthieu, compagnons de cacahuètes, de soirées et de bien plus que ça, et qui ont partagé avec moi les hauts et les bas de la vie de thésards que nous fûmes tous trois.

Mes remerciements vont également à ma famille, qui m'a toujours encouragé dans la poursuite de mes études. Je tiens à remercier profondément mes grands-parents, qui ont une bonne part de responsabilité dans la "réussite" (pour reprendre leurs mots) de leur petis-fils. J'adresse un grand merci à Juju et Caro, pour avoir supporté et pour avoir supporté leur grand-frère depuis tant d'années. Enfin, car ils sont les artisans du bonheur de leurs enfants, cette oeuvre à laquelle ils se dévouent entièrement, et qu'ils ont su me (nous) donner la meilleure éducation qui soit (et le sens du second degré!), je ne pourrai jamais assez remercier mes parents.

Il est des choses qui sont plus parlantes suggérées qu'écrites. A Sophie je dirais simplement: merci, quand même.

Le mot de la fin de ce début m'inspire que les photocathodes moléculaires de production d'hydrogène sont au PV+électrolyse ce que le kiwi est à l'oeuf. Certains diront pas grand-chose mis à part une bonne blague, je dirais qu'elles sont certes moins lisses et plus vertes, mais surtout pleines de pépins!

Table of contents

Table of contents

Abbreviations

APCE: absorbed-photon-to-current conversion efficiency

Asc: ascorbate

BET: Brunauer-Emmett-Teller

bpy: 2,2'-bipyridine

Cat: catalyst

CB: conduction band

CODH: carbon monoxide dehydrogenase

CS: charge separation

Cu-AAC: copper-catalyzed azide-alkyne cycloaddition

CV: cyclic voltammetry

DCM: dichloromethane

DCC: dicyclohexylcarbodiimide

DFT: density functional theory

DHA: dehydroxyascorbic acid

DIPEA: diisopropylethylamine

dist.: distilled

dmg: dimethylglyoxime

DMF: N,N-dimethylformamide

DMSO: dimethylsulfoxide

dpg: diphenylglyoxime

DS: dye-sensitized

DS PEC: dye-sensitized photoelectrochemical cell

DSSC: dye-sensitized solar cell

EA: earth-abundant

E.A.: elemental analysis

EDX: energy dispersive X-ray spectroscopy

equiv.: equivalent

EXAFS: extended X-ray absorption fine structure

Fc: ferrocene

FOWA: foot-of-the-wave analysis

FTO: fluorine-doped tin oxide

Abbreviations

GC: gas chromatography

GCE: glassy carbon electrode

GDL: gas-diffusion layer

h^+: hole

HAsc: ascorbic acid

HATU: 1-[bis(dimethylamino)methylene]-1H-1,2,3-triazolo[4,5-b]pyridinium3-oxidhexa
fluorophosphate

HEC: hydrogen evolution catalyst

HEPES: 2-[4-(2-hydroxyethyl)piperazin-1-yl]ethanesulfonic acid

HER: hydrogen evolution reaction

homog.: homogeneous

HOMO: highest occupied molecular orbital

HOPG: highly oriented pyrolytic graphite

HR-MS: high-resolution mass spectroscopy

ICP: inductively-coupled plasma

IPCE: incident-photon-to-current conversion efficiency

IR: infrared

ISC: intersystem crossing

ITO: indium tin oxide

LH: light harvesting

LHE: light harvesting efficiency

LSV: linear sweep voltammetry

LUMO: lowest unoccupied molecular orbital

MEA: membrane-electrode assembly

MeCN: acetonitrile

MeOH: methanol

MES: 2-(N-morpholino)ethanesulfonic acid

mix.: mixture

MLCT: metal-to-ligand charge transfer

Ms: mesylate

MS: mass spectroscopy

M.W.: micro-wave

MWCNT: multi-walled carbon nanotube

NHE: normal hydrogen electrode

NMR: nuclear magnetic resonance

NP: nanoparticles

OEC: oxygen evolution catalyst

OER: oxygen evolution reaction

ORR: oxygen reduction reaction

PCET: proton-coupled electron transfer

PEC: photoelectrochemical cell

PEM: proton-exchanging membrane

PGE: pyrolytic graphite edge

Ph: phenyl

ppm: parts per million

ppy: 2-phenylpyridine

PS: photosensitizer

PV: photovoltaics

py: pyridine

RHE: reversible hydrogen electrode

ROS: reactive oxygen species

RRDE: rotating ring-disk electrode

R.T.: room temperature

SC: semiconductor

SEA: sacrificial electron acceptor

SED: sacrificial electron donor

SEM: scanning electron microscopy

*t*Boc: *tert*-butyloxycarbonyl

TCO: transparent conducting oxide

TEA: triethylamine

TEOA: triethanolamine

TFA: trifluoroacetic acid

TMS: trimethylsilane

TMSBr: trimethylsilyl bromide

TOF: turnover frequency

TOF_0: intrinsic turnover frequency

TOF_{max}: maximum turnover frequency

ToF-SIMS: time-of-flight secondary ionization mass spectroscopy

Abbreviations

TON: turnover number

TON_{lim}: maximum turnover number

UV: ultraviolet

VB: valence band

V_{OC}: open-circuit voltage

WS: water splitting

XANES: X-ray absorption near-edge structure

XPS: X-ray photoelectron spectroscopy

XRD: X-ray diffraction

Constants

c: speed of light in vacuum ($3.00 \cdot 10^8$ m·s^{-1})

h: Planck constant ($6.63 \cdot 10^{-34}$ J·s)

e: elementary charge ($1.602 \cdot 10^{-19}$ C)

F: Faraday constant (96485 C·mol^{-1})

R: ideal gas constant (8.314 J·K^{-1}·mol^{-1})

14

Preamble

Hydrogen is the simplest chemical element. It is also the most abundant in the Universe, being 75% of its known mass, and thus represents 9 atoms out of 10.[1] Furthermore, the nucleic forms of hydrogen ^{1}H and deuterium ^{2}D are the first two steps in primordial nucleosynthesis, the fusion process that occurred just after the Big Bang and generated the light elements.[2] As the main component of our Sun, hydrogen fuels the nuclear reactions in its core, through proton-proton chain or carbon-nitrogen-oxygen cycle, releasing radiation, subsequently absorbed and reemitted to yield the ultraviolet, visible and infrared light that finally feed our Earth.[3] On Earth, hydrogen is the 3rd most abundant element, although it does not exist in the atomic state[4] and only as traces (4 ppm) as its diatomic form,[4b] the dihydrogen molecule (H_2). This molecule, gaseous under atmospheric pressure and temperature conditions, often borrows the name of its atomic component - hydrogen. Nonetheless, the element hydrogen is one of the main components of organic backbones and of water, both being essential for the life on our planet. Water also gave it its name. Back in 1766, Cavendish demonstrated that hydrogen, he called "inflammable air", gives water through combustion with dioxygen (O_2). Lavoisier reinvestigated the demonstration in 1783 and first reversed it to split water into dihydrogen. He subsequently burned the obtained gas with dioxygen, observing the formation of water.[5] This experiment is part of the founding settlements of modern chemistry that are recorded in his "Traité élémentaire de Chimie"[6] published in 1789. In the co-authored book "Méthode de Nomenclature Chimique"[7] he proposed a new nomenclature to name chemical compounds, which is still in use today, and gave the greek-based etymological name to this "inflammable air": hydrogen - that creates water. This exothermic reaction between H_2 and O_2 provides an energy of 286 kJ per mole of H_2. Knowing that hydrogen has the lowest molecular mass (2.016 g·mol^{-1}), it hence features the highest mass energetic density for chemicals in which energy is stored, that is to say fuels.

Speaking about energy, whether hydrogen is under the deuterium and tritium forms for controlled nuclear fusion (ITER project[8]), as an additive in combustion engines[9] or as a fuel in fuel cells,[9] it has drawn mankind's attention on the key role it could play for the resolution of current energetic issues. Indeed, humanity should turn to a sustainable energy pattern to face the future shortage in fossil fuels and to step down global warming. A striking fact is that solar light can provide the earth with 10^4 times more energy than mankind needs. Yet, the sun, as wind, hydraulic or other natural sources, dispenses energy in an intermittent way. While we know how to harvest the energy of solar radiation and transform it into electricity through photovoltaic

technology, the central point and the biggest bottleneck is now to solve large scale storage. Splitting water into dihydrogen and dioxygen, in a process called electrolysis, or photoelectrolysis for the case in which the reaction is directly driven by light, gives an opportunity to store energy as electronic energy in the H-H bond. Obtained from water through the action of sunlight, hydrogen is one of the so-called *Solar Fuels*. Plus, this energetic vector reconstitutes the energy stored by simple recombination with O_2, in devices like fuel cells that generate electricity and discharge a single and clean exhaust gas, water. Utilizing hydrogen atoms in water and sunlight primarily originating from hydrogen fusion in the sun, this virtuous cycle is all about hydrogen.

Already in 1875, Jules Vernes prophetically proposed in "L'île mystérieuse" the idea to use hydrogen as a fuel. It is thus highly surprising that a technology relying on hydrogen as a solar fuel is not broadly available today. There are indeed two "but"s.

First, in water splitting (WS), the conversion of protons in water to H_2, called hydrogen evolution reaction (HER) and of water to O_2, called oxygen evolution reaction (OER), not only face thermodynamic barriers but also kinetic ones. For instance, to proceed at a significant rate, the multielectronic reduction of proton to hydrogen requires a supplementary amount of energy than what is strictly stored in the H-H bond. This value is known as *overpotential*. Such a loss of energy can be limited by the use of chemical entities called catalysts that lower the overpotential and make the reaction faster. As an example, in the alkaline electrolysis of water, the catalyst is made of a nickel-based material. Though being mature and relatively low cost,[4b] this technology exploits operating units whose limited flexibility could not match an intermittent use. Alternatively, the proton-exchanging membrane (PEM) devices, which realize water splitting under rather acidic conditions, are more adaptable hence more prone to rely on intermittent sources of energy. However, these devices require the utilization of catalysts based on platinum or other noble metals.[4b] Such noble metals are very rare, e.g. with a crustal abundance in the ppb range for Pt[10] (*ca* 10^{-9} less than silicium), and so extremely expensive (about 30 000 € per kilogram for Pt[11]). A major challenge is to find alternative compounds based on earth abundant (EA) elements and able to catalyze HER, or OER, with a good efficiency.

Second, to effectively use sunlight as the source of energy, the light harvesting process should be coupled with the catalytic process of water splitting. Whatever the design of the corresponding operating device, it has to comply with technical specifications. First, such a device should rely on cheap, available elements, to conform to a large-scale utilization as above-mentioned concerning catalysts. Also, a technology-ready device must feature a good net efficiency and a positive global energy balance, which are only possible if stability is sustained on the long term. Today, none of the different approaches studied has yet lead to prototypes meeting all these requirements. In this

view, the PEM technology might be extrapolated so as to design photoelectrochemical cells (PEC) able to realize a light-driven water splitting. This concept still depends on the development of new catalysts for such PEC devices. Of course, the design should also allow the catalyst to be directly combined with a light harvesting unit.

To achieve solutions to these two issues, researchers are taking their inspiration from nature.

First, acknowledging that proton reduction is catalyzed in nature through enzymes which rely on the use of earth abundant metals only, scientists have followed this track to develop cheap catalysts for HER. The hydrogenase enzymes interconvert protons to hydrogen at thermodynamic equilibrium (*i.e.* with no loss of energy).[12] The core of their active site, where the reaction takes place, is constructed around iron and/or nickel atoms and also features a chemical entity, named the proton relay, able to take the proton very close to the metal actually performing catalysis. Chemists have derived such a strategy to create *bio-inspired* molecular catalysts. These species generally involve one or several non-noble metal center(s) surrounded by a chelating ligand, which can feature a proton relay function. Many studies have been reported on the development of these bio-inspired catalysts for the last 20 years.[12] This approach harnesses the versatility and the precision of inorganic and organic synthesis to create molecules of controlled shape. Among them, one of the most stable and active noble-metal free molecular catalysts for hydrogen evolution has been developed in our laboratory. This catalyst consists of cobalt, a relatively abundant element (20-30 ppm), which is the metallic center surrounded by an equatorial tetradentate diimine-dioxime ligand N_2,N_2-propanediylbis(2,3-butanedione 2-imine 3-oxime), abbreviated as **(DOH)$_2$pn**, and two axial ligands X: **[Co(DO)(DOH)pnX$_2$]** (X = Cl, Br).[13] This catalyst has been chosen to conduct the studies reported in the present manuscript.

Second, on the point of joining water-splitting catalysis with light harvesting, nature could once again be our source of inspiration through the photosynthetic process. In photosynthesis, solar light is harvested by two photosystems (photosystem I and photosystem II), in which the light energy creates charge separation (an electron is dissociated from its positive and oxidant equivalent, a hole). The holes are directed to the nearby oxygen-evolving cluster where they serve as oxidizing equivalents for the OER reaction in which water is oxidized into dioxygen. The electrons are shuttled to the Calvin cycle, in which CO_2 fixation to carbohydrates occurs. In that place, some particular organisms, as cyanobacteria or green algae, use these electrons for the reduction of protons to hydrogen catalyzed by hydrogenases.[12] By coupling light harvesting with catalysis, photosynthesis efficiently generates solar fuels in the form of carbohydrates or hydrogen. Mimicking the overall process, chemists target to associate water splitting or CO_2 fixation catalysis with light harvesting, providing the basis for the so-called *artificial*

photosynthesis field.[14] Indeed, by reproducing the primary processes at stake in photosystems chemists have created new molecular photoactive entities able to harvest sunlight efficiently. Their incorporation into device has lead to dye-sensitized solar cells (DSSCs), able to generate electricity upon exposure to sunlight. To go one step further in artificial photosynthesis, they now seek to directly add into these devices catalytic species for water splitting, so as to build dye-sensitized photoelectrochemical cells (DS PECs).

This is the approach giving the frame of the present work. More specifically, the holy grail of our studies is to couple a hydrogen-evolving cathode, photoactive or not, with a photoanode catalyzing OER, into an overall light-driven water splitting DS PEC, a tandem cell.

Our group had expertise with the design of cathodes for proton reduction based on the **[Co(DO)(DOH)pnX$_2$]** catalyst,[15] yet not being photoactive. To go from the dark side to the bright side, the idea is now to include this catalyst within a dye-sensitized molecular photocathode for hydrogen evolution. This idea was set as the main goal of the present thesis.

Thus, this work aims at constructing molecular cathodes and photocathodes for hydrogen evolution and possibly realizing their integrations in tandem cell devices. In this PhD dissertation, the project will be derived in 3 different axes.

- First, we will explore the influence of operating conditions in water on the HER reaction catalyzed by **[Co(DO)(DOH)pnX$_2$]** in solution or supported onto carbon nanotubes. We will report on the activity of the catalyst in the presence of residual O$_2$ in the media. Also, we will discuss the real nature of the catalytic entity in acidic aqueous electrolyte. Then, we will depict our first attempts to integrate our molecular cathode materials in a tandem cell device.

- In a second part, we will describe our efforts to create cathode materials made of **[Co(DO)(DOH)pnX$_2$]** immobilized onto transparent conducting oxides (TCOs). Proposed synthetic pathways to derivatize **[Co(DO)(DOH)pnX$_2$]** with anchoring groups for covalently binding to TCO surfaces, immobilization procedures and electrode characterizations will be detailed.

- Finally, taking elements from the first two points, we will report on the construction of molecular photocathodes for hydrogen evolution based on the immobilization of **[Co(DO)(DOH)pnX$_2$]** onto nickel oxide (NiO), a *p*-type TCO. As a preliminary step, a benchmarking study of different NiO electrode sources for their use in *p*-type DSSCs will be presented. Then, the construction of a NiO-based photocathodes relying on a dye-catalyst co-grafting strategy will be described, along with structural characterizations and photoelectrocatalytic activity for hydrogen evolution. Last, but not least, the synthetis and characterization of a covalent dye-catalyst dyad that can be attached onto NiO will be shown.
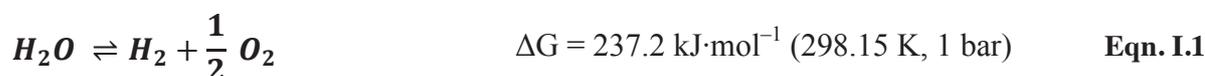
References

1.   Stwertka, A., *A Guide To The Elements*. Second ed.; Oxford University Press Inc.: 2002.

2.   (a) Alpher, R. A.; Bethe, H.; Gamow, G. *Phys. Rev.* **1948,** *73* (7), 803-804; (b) Steigman, G. *Ann. Rev. Nucl. Part. Sci.* **2007,** *57,* 463-491; (c) Weiss, A. Equilibrium and Change: The physics behind Big Bang Nucleosynthesis *Einstein Online* [Online], 2006, p. 1017. http://www.einstein-online.info/spotlights/BBN_phys/?set_language=en; (d) Weiss, A. Big Bang Nucleosynthesis: Cooking up the first light elements *Einstein Online* [Online], 2006, p. 1018. http://www.einstein-online.info/spotlights/BBN.

3.   (a) Bethe, H. A. *Phys. Rev.* **1939,** *55,* 434-456; (b) Eddy, J. A., *A New Sun: The Solar Results from Skylab*. NASA: 1979.

4.   (a) Miessler, G. L.; Tarr, D. A., *Inorganic Chemistry*. Third ed.; 2004; (b) Grimes, A. C.; Varghese, O. K.; Ranjan, S., *Light, Water, Hydrogen: The Solar Generation of Hydrogen by Water Photoelectrolysis*. Springer: 2008.

5.   The Chemical Revolution. In *An International Historic Chemical Landmark*, ACS; ASIF; SFC, Eds. Paris, 1999.

6.   Lavoisier, A.-L., *Traité élémentaire de Chimie, présenté dans un ordre nouveau et d'après les découvertes modernes*. Cuchet: 1789.

7.   Morveau, L. B. G. d.; Hassenfratz, J.-H.; Fourcroy, A.-F.; Lavoisier, A.-L.; Adet, P.-A.; Bertholet, C. L., *Méthode de nomenclature chimique*. Cuchet: 1787.

8.   www.iter.org/proj.

9.   Schlapbach, L.; Züttel, A. *Nature* **2001,** *414,* 353-358.

10.   (a) Cotton, F. A.; Wilkinson, G.; Gaus, P. L., *Basic Inorganic Chemistry*. Third ed.; Wiley: 1995; (b) Zou, X.; Zhang, Y. *Chem. Soc. Rev.* **2015,** *44* (15), 5148-80.

11.   Loferski, P. J., Platinum-Group Metals. U.S. Geological Survey: 2015.

12.   Lubitz, W.; Ogata, H.; Rudiger, O.; Reijerse, E. *Chem. Rev.* **2014,** *114* (8), 4081-148.

13.   Jacques, P. A.; Artero, V.; Pecaut, J.; Fontecave, M. *Proc. Natl. Acad. Sci. USA* **2009,** *106* (49), 20627-32.

14.   (a) Gust, D.; Moore, T. A.; Moore, A. L. *Faraday Discuss.* **2012,** *155,* 9-26; (b) Faunce, T.; Styring, S.; Wasielewski, M. R.; Brudvig, G. W.; Rutherford, A. W.; Messinger, J.; Lee, A. F.; Hill, C. L.; deGroot, H.; Fontecave, M.; MacFarlane, D. R.; Hankamer, B.; Nocera, D. G.; Tiede, D. M.; Dau, H.; Hillier, W.; Wang, L.; Amal, R. *Energy Environ. Sci.* **2013,** *6* (4), 1074.

15.   Andreiadis, E. S.; Jacques, P. A.; Tran, P. D.; Leyris, A.; Chavarot-Kerlidou, M.; Jousselme, B.; Matheron, M.; Pecaut, J.; Palacin, S.; Fontecave, M.; Artero, V. *Nat. Chem.* **2013,** *5* (1), 48-53.
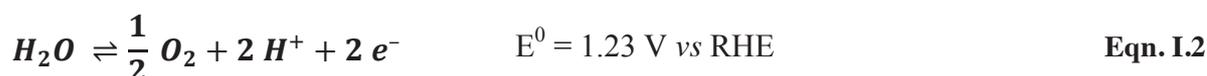
Chapter I

Introduction

A sustainable self-sufficient energy supply is possible if sunlight is used to generate an environmental-innocent fuel.[1] For instance, sunlight can serve to electrolyze water, a resource highly abundant on the earth, through a process called water-splitting (Eqn. I.1). Water-splitting generates dioxygen and, more important, dihydrogen. Hydrogen formed in that way is indeed foreseen as a very promising energetic vector since its oxidation in a fuel cell efficiently reconstitutes the energy stored.[2]

$$H_2O \; \rightleftharpoons H_2 + \frac{1}{2} \, O_2 \qquad \qquad \Delta G = 237.2 \text{ kJ·mol}^{-1} \text{ (298.15 K, 1 bar)} \qquad \textbf{Eqn. I.1}$$

In standard conditions, Gibb's free energy variation for water splitting is positive (237.2 kJ·mol^{-1}) and thus the reaction does not occur spontaneously. Translated in terms more appropriate for electrolysis reaction, the net reversible electronic work of this reaction is $V_{WS}^0 = 1.23$ V.

In natural systems, as for the sake of simplicity, water splitting might be decomposed into two half reactions: water oxidation (Eqn. I.2) and proton reduction (Eqn. I.3).

$$H_2O \; \rightleftharpoons \frac{1}{2} \, O_2 + 2 \, H^+ + 2 \, e^- \qquad E^0 = 1.23 \text{ V } vs \text{ RHE} \qquad \textbf{Eqn. I.2}$$

$$2 \, H^+ + 2 \, e^- \; \rightleftharpoons H_2 \qquad E^0 = 0 \text{ V } vs \text{ RHE} \qquad \textbf{Eqn. I.3}$$

By definition, the equilibrium potential of the reversible hydrogen evolution is 0 V *versus* the Reversible Hydrogen Electrode (RHE) at 25°C and 1 bar and, hence, the one for OER is 1.23 V *vs* RHE. To electrolyze water into hydrogen and oxygen, a theoretical voltage of 1.23 V should then be applied between two electrodes dipped in water. HER takes place at the *cathodic part* and OER at the *anodic part*. But these reactions only occur at significant rates if a voltage larger than 1.23 V is applied, due to the overpotentials. Catalysts may thus be introduced at both parts to limit the overpotentials.

Also, coupling these WS electrocatalytic systems with light harvesting (LH) units permits to harness the energy of sunlight. Photons from sunlight are in the UV-visible range, mainly between 300 and 1000 nm, which is in terms of energy between 4.13 and 1.24 eV. As a consequence, they

have enough energy to realize photoelectrocatalytic water splitting, provided that overpotentials of the catalytic systems are not too high.

The present bibliographic introduction will focus on the part concerning hydrogen evolution, both for electro- and photoelectrocatalytic processes, but similar concepts are true for oxygen evolution. We will first describe catalysts and especially earth-abundant molecular catalysts for hydrogen evolution. In particular, we will report on state-of-the-art systems for which catalysts have been immobilized onto an electrode material. Finally, we will describe more precisely the **[Co(DO)(DOH)pnX$_2$]** catalyst used in our studies.

In the second part, we will introduce the construction of dye-sensitized photocathodes for hydrogen evolution, with an emphasis on their building components. Then, examples of such photocathodes reported in the literature will be extensively described with final conclusion on the DS PEC tandem cells realizing overall water splitting.

1. Molecular catalysis for hydrogen evolution

Here, we will focus here on earth-abundant molecular electrocatalysts for HER. Firstly, basic definitions and metrics are given which apply to the study of the hydrogen evolution catalysts (HECs). Then, an overview of efficient families of EA molecular catalysts is depicted, with a greater emphasis on the **[Co^{III}(DO)(DOH)pnL$_2$]** used in this work. Finally, we will present the strategies used to attach molecular HECs onto surface, and more precisely describe the molecular cathode based on **[Co^{III}(DO)(DOH)pnL$_2$]** further used in the manuscript.

Although there is a cornucopia of solid-state electrocatalytic systems for proton reduction,[3] some of them being among the most efficient ones,[4] we intentionally discard them of this introduction as being out of the scope of this work. Unless otherwise noted, we will refer implicitly to molecular catalysts when quoting catalysts.

1.1. Metrics for the benchmarking of molecular hydrogen evolution catalysts

The development of a hydrogen evolution catalyst (HEC) should be accompanied by a rigorous assessment of its performance for proton reduction.[5] In that goal and prior to go further in the detailed literature on molecular HECs, a brief introduction to the key parameters describing the efficiency of such a catalyst is proposed. These parameters are generally related to concepts proper to electrochemical techniques, as cyclic voltammetry (CV) or chronoamperometry (CA), which are particularly suited for assaying HER activity. We note that similar concepts are used for solid-state catalysts. Not an extensive description, this section is rather a short-list of the most used and relevant parameters.

1.1.1. General definitions

We first give here definitions regarding basic concepts of electrochemistry related to HER catalysis.

1.1.1.1. Equilibrium potential

The equilibrium of the interconversion of protons into hydrogen is defined in Eqn. I.3. Given a solvent, the proton source with its associated pK$_a$, the apparent standard potential for this reaction is $E_{H^+/H_2}^{0,app}$. This potential might be determined from the standard potential of the H$^+$/H$_2$ couple E_{H^+/H_2}^0 in the considered solvent using the following equation:

$$E_{H^+/H_2}^{0,app} = E_{H^+/H_2}^0 - \frac{RT}{2\mathcal{F}} \cdot pK_a \qquad\qquad \textbf{Eqn. I.4}$$

where R is the perfect gas constant, T the absolute temperature and $\mathcal{F}$ the Faraday constant.

In the case of non-aqueous solvents, the concentration in protons impacts the actual value of the apparent equilibrium potential E_{H^+/H_2}^{app} and the homoconjugation of the acid/base couple has to be considered.[6] For some organic solvents, as acetonitrile (MeCN), N,N-dimethylformamide (DMF) or dimethylsulfoxide (DMSO), the values of E_{H^+/H_2}^0 and pK$_a$s are tabulated, though subjected to caution use due to experimental errors ($\pm$ 50 mV) and debates concerning practical methods for their determination.[6]

If solvent is water, the case is simple, since we have by definition E_{H^+/H_2}^0 = 0 V vs the Normal Hydrogen Electrode (NHE) and thus, from the Nernst equation, the reversible potential for hydrogen evolution at a given pH is:

$$E_{H^+/H_2}^{0,app,H_2O} = -\frac{RT}{2\mathcal{F}} \cdot pH \approx -0.059 \cdot pH \qquad \text{V } vs \text{ NHE} \qquad \text{at 25°C, 1 bar.} \qquad \textbf{Eqn. I.5}$$

In water, for commodity, we will commonly refer our potentials against the Reversible Hydrogen Electrode, which directly accounts the pH effect:

$$E_{H^+/H_2}^{0,app,H_2O} = 0 \qquad\qquad \text{V } vs \text{ RHE} \qquad \text{at 25°C, 1 bar.} \qquad \textbf{Eqn. I.6}$$

Finally, the overpotential η is defined as the difference between the apparent equilibrium potential $E_{H^+/H_2}^{0,ap}$ and the potential E at which the reaction is examined:[7]

$$\eta = E_{H^+/H_2}^{0,app} - E \qquad\qquad \textbf{Eqn. I.7}$$

1.1.1.2. Rate constant

H$^+$ reduction to H$_2$ is a 2-electron, 2-proton process. Homolytic or heterolytic pathways are possible. In the case of a homolytic one, the formation of one molecule of H$_2$ involves two molecules of catalyst. In the case of a heterolytic one, only one molecule of catalyst is involved. The global reaction catalyzed by a catalyst (cat), which undergoes reduction to its catalytically active form from E_{cat}, is written in a general way as follows:
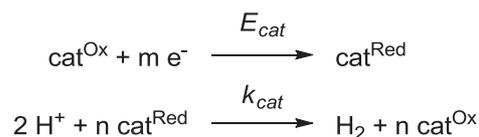
$$cat^{Ox} + m\ e^- \xrightarrow{E_{cat}} cat^{Red}$$

$$2\ H^+ + n\ cat^{Red} \xrightarrow{k_{cat}} H_2 + n\ cat^{Ox}$$

Figure I.1. Overall catalytic scheme for HER (n = 2, m = 1 for a homolytic pathway; n = 1, m = 2, for a heterolytic pathway). cat^{Ox}, respectively cat^{Red}, are the oxidized, respectively reduced, forms of the catalytic species cat.

The overall rate constant for hydrogen evolution k_{cat} thus reflects kinetics of the whole reaction. This constant is linked to the reaction rate v through the following relation:

$$\boldsymbol{v = k_{cat} \cdot [H^+]^p \cdot [cat]^q}$$ **Eqn. I.8**

The mechanism of hydrogen evolution gathers electron transfer (E) and chemical (C) steps at the catalyst. For instance, heterolytic pathways could proceed through EECC, ECEC or ECCE mechanisms. k_{cat} includes rate constants of each E and C steps involved in the catalytic process. Hence, its determination generally requires the elucidation of the whole catalytic pathway.[7] However, at given catalyst concentrations, k_{cat} is linked to an observed rate constant k_{obs} as:

$$\boldsymbol{k_{obs} = k_{cat} \cdot [H^+]^p}$$ **Eqn. I.9**

This relation allows a straightforward determination of k_{cat} in some particular occurrences, like ECCE or ECEC limited by a kinetic determining step and for which p = 1.

1.1.2. Kinetic metrics of the catalytic process

The catalytic process is correlated to kinetic values that give information about how fast the catalyst turns over and hence how fast hydrogen is produced.

1.1.2.1. Apparent rate constant: k_{cat}

When a HEC is submitted to cyclovoltammetric analysis in the presence of a proton source, additional waves might build up. Especially, a high current wave can develop at potentials more cathodic than RHE. This wave often corresponds to the reduction of protons by the catalyst and is thus called a *catalytic wave*.

In the ideal case, a regime where the current is only limited by the diffusion of the species at the electrode is attained. This regime is known as *pure kinetic* conditions. The CV then depicts a *canonical S-shaped wave* that reaches a plateau. The plateau current i_{pl} is independent of the scan rate and is correlated to the apparent rate constant as follows:[8]

$$i_{pl} = 2\mathcal{F}S \cdot [cat]_b \cdot \sqrt{D_{cat}} \cdot \sqrt{k_{cat}[H^+]_b}$$ **Eqn. I.10**

where S is the surface of the electrode, $[cat]_b$ and $[H^+]_b$ are the concentrations of the catalyst and of the proton or acid, respectively, in the bulk of the solution, D_{cat} is the diffusion coefficient of the catalyst.

This allows for the determination of k_{cat}, which indicates how fast the catalytic process is.

In non-ideal cases, in which the catalyst deactivates or is inhibited by products or in which the substrate is consumed, the current does not reach a plateau. Instead, a peak-shaped wave is displayed and associated with a peak current i_p. The equation Eqn. I.10 is sometime incorrectly used here, replacing i_{pl} by i_p, to access an under-estimated approximated value of k_{cat}.[9]

1.1.2.2. Turnover frequency: TOF

The turnover frequency (TOF) is the number of catalytic cycles achieved by one catalyst molecule per unit of time.[10] The value of TOF is directly linked to the apparent rate constant of the reaction for hydrogen evolution: the highest the k_{cat}, the highest the TOF.[10-11] In other words, at a given potential, the catalyst displaying the highest TOF is the one turning over the fastest.

TOFs should be calculated taking into account the number of molecules which effectively partake to catalysis. For a catalyst in solution, the pool of molecules in the reaction-diffusion layer at the vicinity of the electrode has to be considered.[12]

Values of TOF can be readily accessed when canonical CVs, thus k_{cat}, are available. A methodology has been reported in the case where side-phenomena make CVs non-canonical.[12] This strategy is built on the foot-of-the-wave (FOWA) analysis of catalytic CVs.

For chronoamperometric measurements (electrolysis) in a steady-state regime, catalysis is limited by charge transport and is hence submitted to dependence on geometric parameters, as electrode or cell architectures. Also, TOF calculations are in this case based on the overall amount of catalyst in the whole electrochemical cell. For these reasons, this practice which is used in a large majority of the literature misestimates values of TOFs for HECs. More, such practice artificially disadvantages molecular catalysts toward material-based catalysts.[12]

1.1.3. Overpotential for hydrogen evolution

The overpotential required for proton reduction to occur due to an HEC, often implicitly (but misleadingly) named as *overpotential* in the context of hydrogen evolution, is a key, but discussed, notion. *Overpotential requirement* would be a more relevant alternative denomination.

But whatsoever the name, the definition is indeed very subjective and several propositions have been made regarding the determination of its value.[13]

We will first briefly describe common methodologies, whether they refer to non-ideal cases or they are broadly used in the literature.

Nonetheless, in the ideal case of an elucidated mechanism, a relationship directly relates the overpotential (the applied electrode potential) η and the TOF, allowing for a straightforward benchmarking of HER catalysts. This methodology, which has been recently reported,[10-11] bypasses other methodologies used to determine overpotential requirement for hydrogen evolution. Though it proposes an objective benchmarking of catalysts, this method is also the more demanding one, since it relies on the knowledge of the whole catalytic mechanism.

1.1.3.1. Potential of the catalytic peak current: E_p

With CVs displaying a peak-shape behavior at the catalytic process, the potential corresponding to the peak maximum E_p can be straightforwardly found. Here, the overpotential may be obtained as:

$$\boldsymbol{\eta} = \boldsymbol{E_p} - \boldsymbol{E_{H^+/H_2}^{0,app}}$$
<div align="right">Eqn. I.11</div>

However, the E_p potential varies with the concentration of protons, which does not permit to define a single value for the catalyst.

1.1.3.2. Onset potential: E_{onset}

The onset potential for hydrogen evolution E_{onset} is often taken as the potential at which the catalytic current starts to rise. Its definition relies on experimenters' eyes and thus is intrinsically subjective. However, when potential sweep electrocatalysis of HER is coupled to a quantitative method for analysis of the produced gas, as with rotating ring-disk electrode (RRDE) or in-line gas chromatography (GC), an experimental potential at which hydrogen starts to be evolved might be determined (an example is given later, in Figure I.25, left).[14] This determination is possibly dependent on the scan rate and/or the time resolution of the analytic technique. Despite this point, monitoring of the H_2 production is an insightful way to benchmark catalysts in regard to their experimentally observed overpotential requirement for proton reduction.

1.1.3.3. Half catalytic wave potential: $E_{cat/2}$

$E_{cat/2}$ is defined as the potential corresponding to half the current of the catalytic wave, or plateau i_{cat} (Figure I.2). This current can be defined easily in the case of a canonical catalytic S-shape CV, leading to an accurate value of $E_{cat/2}$. Hence, the overpotential might be determined as:

$$\boldsymbol{\eta = E_{cat/2} - E_{H^+/H_2}^{0,app}} \hspace{4cm} \textbf{Eqn. I.12}$$

If the CV moves away from this canonical behavior, determining $E_{cat/2}$ might be subjected to the experimenters' judgment. Suggestions have been made to provide guidance on this determination.[15]

The comparison of $E_{cat/2}$ for two catalysts gives an idea of the catalyst having the smallest overpotential for hydrogen evolution.
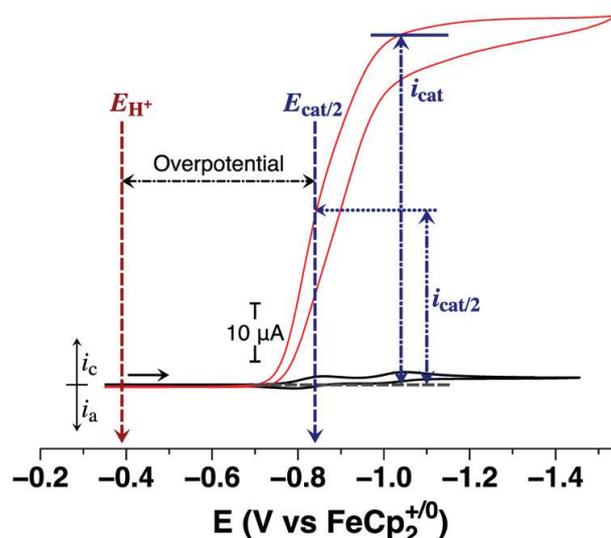

Figure I.2. Half catalytic wave overpotential determination exemplified with $[\textbf{Ni(P}_2^{\textbf{Ph}}\textbf{N}_2^{\textbf{Ph}}\textbf{)}_2\textbf{(BF}_4\textbf{)}_2]$ (see text later) in the absence (black line) or presence (red line) of acid.[15] Reproduced with permission from ref[15], copyright 2014 American Chemical Society.

Here, the performance of the catalyst can be given by the determination of the ($E_{cat/2}$, i_{cat}) couple. But the catalyst is even better described through its highest TOF TOF_{max} and its overpotential requirement η. These two values are in fact intrinsically linked and they can be correlated as shown in the next paragraph.

1.1.3.4. Catalytic Tafel plots: log(TOF) vs η

The *catalytic Tafel plots* have been recently described as an equivalent for molecular homogeneous catalysts to the Tafel plots valid for heterogeneous catalysts.[10-11]

To obtain these plots, the relation linking the TOF to the overpotential has been established as:

$$TOF = \frac{TOF_{max}}{1 + exp\left[\frac{\mathcal{F}}{RT}\left(E_{H^+/H_2}^{0,app} - E_{1/2}\right)\right] \cdot exp\left(-\frac{\mathcal{F}}{RT} \cdot \eta\right)}$$

Eqn. I.13

where $E_{1/2}$ is a potential related to a specific electrochemical step in the catalytic pathway and TOF_{max} is the maximum turnover frequency artificially taken at $[H^+] = 1$ M and defined as:

$$TOF_{max} = k_{cat}[H^+]^p = k_{cat}$$

Eqn. I.14

TOF_{max} and $E_{1/2}$ are both functions of the different rate constants. To determine these constants, the mechanism should be known or assumed. This step is thus a necessary condition to access the catalytic Tafel plot giving $log(TOF)$ as a function of η (Figure I.3).

Of note, extrapolated at zero overpotential these graphs also give at TOF_0 constant, called intrinsic turnover frequency for the considered catalyst.[12]
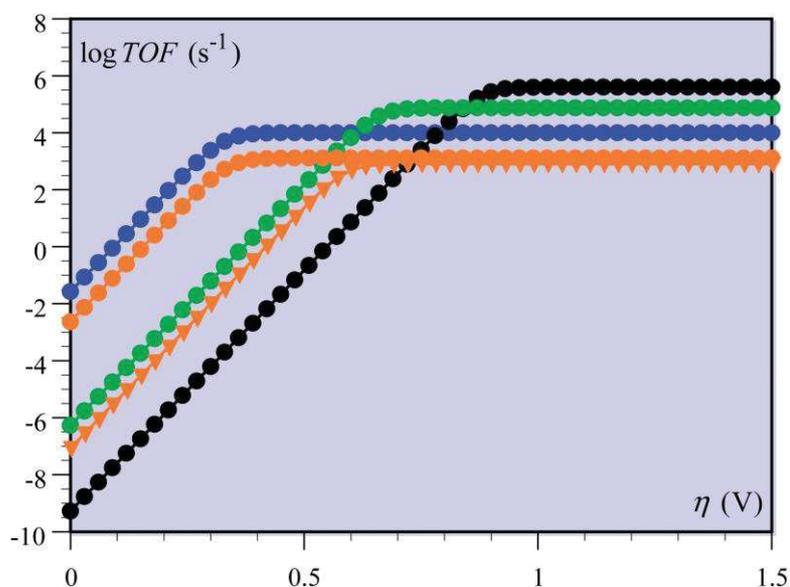
Figure I.3. Catalytic Tafel plots for molecular HECs under various conditions,[10] among others **[Fe(TPP)Cl]** (black), **[Ni(P$_2$^{Ph}N^{Ph})$_2$]$^{2+}$** (green) and **[Co(dmgH)$_2$PyCl]** (blue), quoted later in the text. Reproduced with permission from ref[10], copyright 2014 Royal Society of Chemistry.

Generally, a catalytic Tafel plot allows for a direct comparison of the performance of catalysts. The line corresponding to the catalyst able to best lower the overpotential for HER while turning over at the highest rate will lay in the upper left corner. Its bad boy equivalent will lay in the bottom right part.

1.1.4. Stability

An HER catalyst might be deactivated by several processes.[12] For instance, it can undergo inhibition by the product. Otherwise, it might degrade to form another species. Either this species

is not active for hydrogen evolution, which will *in fine* terminate catalysis, or the new species might also be an HER catalyst and simply modify the apparent rate constant of catalysis. *En passant*, we note that the degradation of a molecular catalyst might lead to other molecular species or to heterogeneous entities.

To test the robustness of the catalyst, several parameters can be examined, which are presented here.

1.1.4.1. Faradaic efficiency: η_F

Most widely, chronoamperometry is used to assess the stability of a catalyst. A steady current *a priori* implies that the catalyst is stable inasmuch the depletion in substrate concentration is not susbstantial. An important point is to ensure that the observed current is directed toward catalysis producing hydrogen and not toward electrochemically driven degradation pathways. In that aim, qualitative and quantitative analysis of the media and of the reaction products (H_2 here), e.g. with the help of GC or a hydrogen sensor, are required.

The comparison of the charge Q_{tot} passed into the cell during an electrochemical experiment and the total amount of hydrogen produced $n_{tot}^{H_2}$ gives the faradaic efficiency (η_F) or yield:

$$\eta_F = \frac{n_{tot}^{H_2}}{|2 \cdot \mathcal{F} \cdot Q_{tot}|}$$

Eqn. I.15

The faradaic efficiency thus directly relates to the ratio of electrons passed in the cell which served for HER catalysis, regardless the amount of catalyst. This faradaic yield then gives an indication of the stability of the operating catalyst. The highest it is (ideally 100%) the most stable the catalyst is.

We note here that if the experimental setup allows for the time-resolved determination of hydrogen production rate $v^{H_2}(t)$, an instantaneous faradaic yield $\eta_F(t)$ might be calculated, through:

$$\eta_F(t) = \frac{v^{H_2}(t)}{|2 \cdot \mathcal{F} \cdot i(t)|}$$

Eqn. I.16

where *i(t)* is the current flowing at the electrode.

1.1.4.2. Turnover number: TON

The time-extensive value total turnover number (TON) refers to the total number of catalytic turnovers realized by a single catalyst before its deactivation.[10]

It has been proposed very recently[5] to extract from the electrolysis data a maximum turnover number TON_{lim}, which reflects the maximum of catalytic cycles a catalyst is able to perform before deactivation. Interestingly, it directly links the global rate constant for catalysis k_{cat} to the rate constant of the deactivation process k_{deact} by the relation:

$$TON_{lim} = \frac{k_{cat}}{k_{deact}}$$

<div align="right">**Eqn. I.17**</div>

This intrinsic value for a catalyst is thus a view of the competition between the catalytic process steps and the deactivation processes. The highest the TON_{lim} is, the longest the catalyst catalyzes hydrogen evolution.

1.1.5. Device-related specifications

Along with metrics related to intrinsic parameters of the catalyst, it is also necessary to benchmark the activity of a given catalyst under *real* conditions corresponding to operation within a WS device.

1.1.5.1. Tolerance toward oxygen

In such a device, water is split into H_2 and O_2 in the cathodic and anodic compartments, respectively. Whatever the construction type, a certain amount of both gases will likely diffuse in the opposite compartment. Especially, at the cathode, small concentrations of O_2 might then be present.

It is thus important that the HEC can reduce protons in the presence of oxygen.[16] The thermodynamic potentials of the oxygen reduction reactions (ORRs) yielding reactive oxygen species (ROS), as hydrogen peroxide or superoxide, are more positive than the one for the H^+/H_2 couple. Except if O_2 is preferentially reduced by 4 e^- into H_2O, ROS production can hence occur at the cathode which is poised at a potential reductive enough to reduce protons.

In the case where the presence of O_2 inhibits the catalyst, by irreversible binding or by oxidative destruction due to ROS formation, the hydrogen evolution is hindered. As a note, this issue is particularly well known for hydrogenases, most of them being deactivated by O_2.[17]

To overcome the O_2-sensitivity, two solutions arise. The first one is that the catalyst is designed to partake to ORRs without being deactivated in the process. Although the apparent rate and the faradaic yield for hydrogen evolution decreases because of this side-reduction, there is ideally no irreversible destruction of the catalyst. In the other option, the catalyst is, by synthetic

construction, selective for proton reduction over O_2 reduction. If this construction is done successfully, the presence of O_2 has no apparent impact on hydrogen production.

The optimal oxygen-tolerant catalyst would selectively reduce protons under oxygenic conditions, without suffering from deactivation due to O_2. If shielding strategies exist to protect catalysts from the presence of O_2,[18] it is clear that an intrinsically O_2-tolerant catalyst offers a noticeable advantage for the use in WS devices.

1.1.5.2. Operation in water

The broad majority of studies on HEC are performed in organic solvents, permitting the use of selected proton sources. Of course, the solvent of choice for a viable *water* splitting device is water. It is thus important that the catalyst assessed in organic solvents also displays catalytic activity and extended stability in water. If the catalyst is prone to hydrolysis by water, it will then decompose to form a species which might or not be active for hydrogen evolution. On this, several controversies have been reported in the literature for molecular HECs that degrade under turnover and form heterogeneous species, active for hydrogen evolution.[19] This point is misleading on the exact nature of the catalytic species.

Thus, the retention of the structure of the catalyst under turnover conditions in aqueous media is an asset towards its integration in device.

Moreover, we note here that if the catalyst in not directly water soluble, this issue might be advantageously bypassed through its immobilization onto an electrode. This approach indeed constitutes an important step forward in regard to the integration of catalysts in device. This point will be discussed later on.

1.2. Earth-abundant molecular electrocatalysts for hydrogen evolution

After having set the relevant parameters for their evaluation, we will give a short overview of some families of molecular catalysts for hydrogen evolution present in the literature. There are hundreds of molecular catalysts that have been reported so far.[17] A comprehensive description of this literature would not only be a lengthy review but also irrelevant in the frame of this work. Instead, we will focus on earth-abundant only molecular catalysts. Even tighter, we will give major characteristics with restriction to the families of compounds featuring the highest efficiencies with regard to the above-mentioned metrics. To this, additional interest will be drawn toward the designs integrating these catalysts onto electrode surfaces, in line with the project developed in the current manuscript.

But first, it should be noted that the development of these hydrogen-evolving catalysts, whether they are bio-mimetic, bio-inspired, or not, has broadly exploited the essential concepts lying at the active site of hydrogenase enzymes. Thus, these general concepts will be introduced in a short foreword.

1.2.1. Bio-inspiration: Concepts borrowed to nature

Hydrogenases are enzymes which catalyze the interconversion of protons into hydrogen at the thermodynamic equilibrium potential. The first crystallographic structures have been reported during the late 90's.[17] Among other structural characteristics, the hydrogenases have very specific active sites, whose nature usually defines the group in which they are classified. This active site features two iron atoms for [FeFe] hydrogenases and one iron, one nickel for [NiFe] hydrogenases. The composition of the active sites is a key factor for the activity of these enzymes.

For the sake of simplicity, we will consider the case study of [FeFe] hydrogenases, but similar concepts apply in [NiFe] hydrogenases.

The typical active site of the majority of [FeFe] hydrogenases is made of 2 iron atoms, bearing CN^- and CO ligands, and that are linked through an azadithiolate (adt^{2-}) bridge (Figure I.4, left).[20]

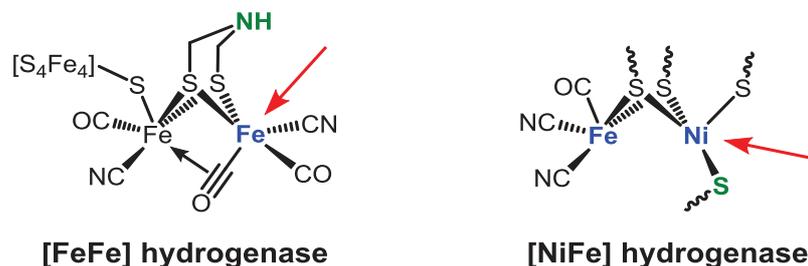
[FeFe] hydrogenase   **[NiFe] hydrogenase**

Figure I.4. Active sites of [FeFe] (left) and [NiFe] (right) hydrogenases. Blue symbols indicate metal atoms that participate in metal-hydride bond formation; green symbols indicate pendent bases; red arrows indicate open coordination sites.

The reduction of proton is a 2-electron, 2-proton process. Hydrogen evolution occurs through the heterolytic coupling of an hydride bond to an iron atom with a proton. This process is permitted thanks to, at least, three important features of the active site. First, the redox cycling necessary for HER catalysis occurs on one of the Fe atom. This atom displays redox properties appropriately tuned by the other metal site. Second, an open coordination site is also available on this Fe atom. A proton can be captured at this coordination site and stabilized in the form of an iron-hydride bond. Third, a proton is believed to be taken very close to this hydride through the nearby amino base on the adt^{2-} bridge.[17] The presence of this nearby amino base is thought to facilitate the step of heterolytic formation of the H-H bond between the hydride and a proton (Figure I.5, right).
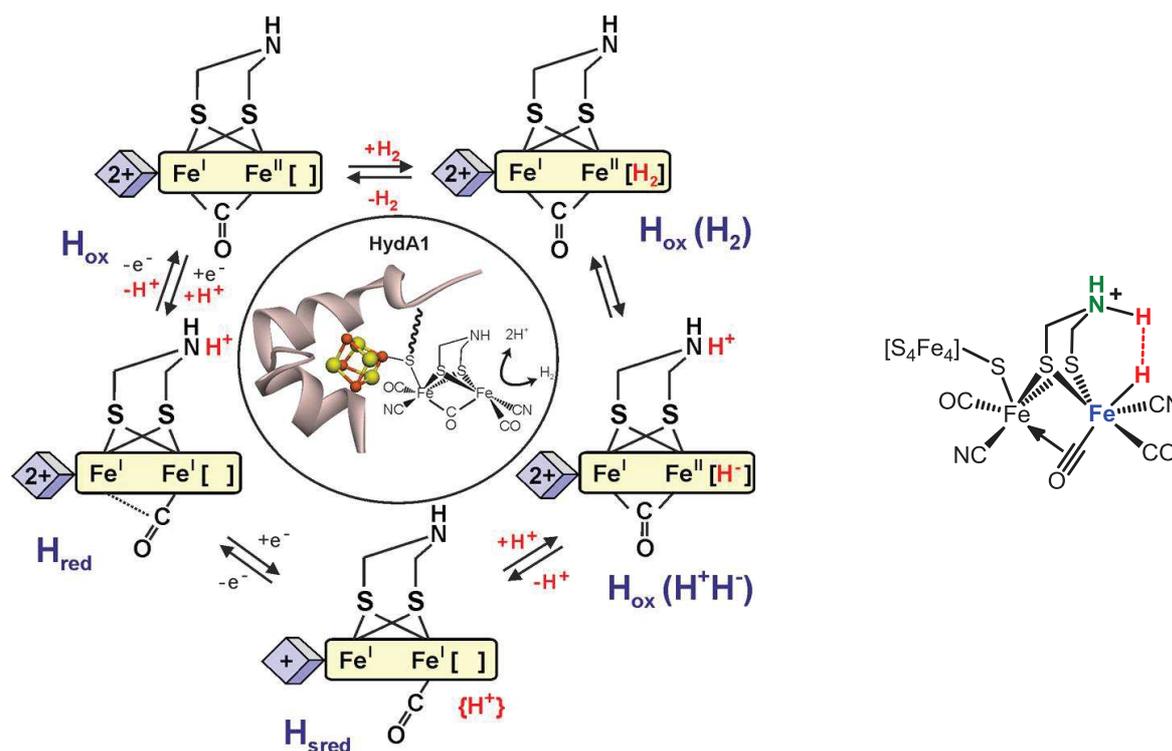
Figure I.5. Proposed catalytic mechanism for H_2 evolution and uptake at a [FeFe] hydrogenase active site[17] (left) and putative intermediate during proton reduction by [FeFe] hydrogenase showing importance of the proximate basic group (right). Reproduced and adapted with permission from ref[17], copyright 2014 American Chemical Society.

These features have been widely utilized to design molecular bio-inspired HEC. Basically, they are:

- A metallic center which can be reduced or oxidized at moderate potentials. They are usually *d*-block transition metals in their usual oxidation states.

- A coordination site which is vacant for the formation of metal-hydride bond, or which becomes vacant after the exchange of a labile ligand. Such sites are often formed by reductive elimination of a ligand.

- A proximal basic group which is able to capture and deliver protons at the vicinity of the reactive center. This group is often called a *proton relay*. Ideally, the hydride acceptor ability of the metal and the proton acceptor ability of the base should be in good energetic matching to stick to reversibility.[17, 21] Also, the vicinity of the proton attached at the proton relay facilitates proton-coupled electron transfer (PCET) steps that participate in decreasing the energy of intermediate states.

1.2.2. A rapid tour through the most efficient HECs

Bio-mimetic and bio-inspired HECs have been widely studied the last two decades. Biomimetic catalysts tend to faithfully reproduce the structures of the active site of hydrogenases,

and rely on Fe and or Ni centers. Although they provide very insightful details for the understanding of mechanisms at stake for HER, they usually suffer from very poor stability.[22] Bio-inspired complexes only keep the essential ideas and may prove much more efficient.

Bio-inspired or not, only selected classes of effective catalysts are presented here. For the majority of the families described below, one of their representative examples has been subjected to rational benchmarking through the catalytic Tafel plot given in ref[10] and presented in Figure I.3.

1.2.2.1. Porphyrin-based catalysts

Porphyrinic metal transition complexes have been one of the early examples of molecular catalysts for hydrogen evolution,[23] even prior to the structural determination of hydrogenases. They usually involve metallic centers as Fe,[23c, 24] Co[23a, 23b, 25] or Ni[26] surrounded by a symmetrical or derivatized porphyrinic ring.

Savéant and co-workers namely reported a symmetric iron porphyrin **[Fe(TPP)Cl]** (Figure I.6, left) able to reduce protons at high TOF$_{max}$ (in the 10^6 s^{-1} range, Figure I.3).[23c] However, this type of catalysts commonly displays high overpotential requirements, e.g. **[Fe(TPP)Cl]** reaches TOF$_{max}$ at a 900 mV overpotential. Besides, they show remarkable long-term stabilities joined with near unity faradaic efficiencies for HER. This point is quite noteworthy in the case of the **[Fe(TPP)Cl]** complex, since most of the molecular HECs involving an iron center (the most abundant transition metal on the earth) usually suffer from poor stability.[27] Similar iron porphyrins modified with hydrophilic groups have shown activity in neutral aqueous media, while retaining a steady activity over hours.[25c]

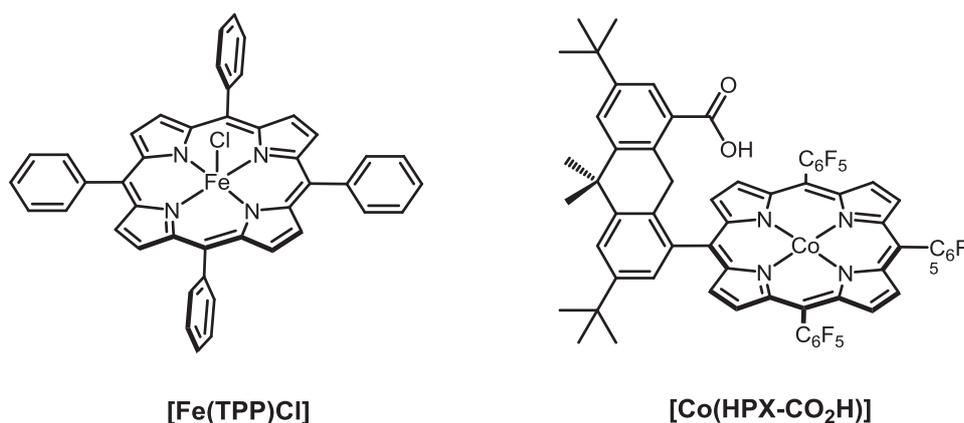**[Fe(TPP)Cl]**   **[Co(HPX-CO$_2$H)]**

Figure I.6. Selected examples of porphyrin-based catalysts.

Another major interest is that these porphyrinic complexes provide a relevant backbone for the mechanistic studies. Nocera and co-workers have produced a series of so-called *hangman* porphyrins featuring pendent acido-basic groups. The acido-basic group can be a sulfonic[24] or a

carboxylic[24-25, 26] acid (**[Co(HPX-CO₂H)]**; Figure I.6, right) or an amine[24] and is located just upon the metallic center. Elegant studies show that the presence of this proximate proton relay facilitates PCET reactions. This feature participates in decreasing the overpotential for hydrogen evolution and increasing the TOF.[24-25, 26] Of note, a related striking achievement has been reached by Savéant and co-workers through incorporation of H-donating groups in the FeTTP backbone, but regarding the reduction of CO_2 to CO.[28]

1.2.2.2. Nickel bisdiphosphine complexes: "Dubois' catalysts"

These catalysts are based on a nickel metallic center coordinated to two diphosphine ligands in a square planar geometry. Both ligands bear one or two pendent amino groups, referring to the **[Ni(P₂ᴿN₂ᴿ')₂]ⁿ⁺** or to the **[Ni(P₂ᴿNᴿ')₂]ⁿ⁺** type, respectively. These catalysts have been widely studied during the last 10 years, with major, not to say exclusive, contributions from the group of D. Dubois. This is the reason why this class of catalysts is commonly nicknamed "Dubois' catalysts".[21a]

R = Ph, R' = Ph, L = none, n = 2 **[Ni(P₂ᴾʰN₂ᴾʰ)₂]²⁺**

R = Ph, R' = Ph

[Ni(P₂ᴾʰNᴾʰ)₂]²⁺

[Ni(P₂ᶜʸN₂ᴬʳᵍ)₂]⁷⁺

L = H⁺, n = 7

Figure I.7. Selected examples of nickel DuBois' catalysts.

These complexes are the class example of bio-inspired catalysts since the presence of a proton relay under the form of pendent amines in close contact with the metal center was shown to enhance the rate of H_2 activation.[21] They prove very efficient for hydrogen evolution, with TOFs estimated in the range of 10^2 to 10^3 s^{-1} for the **[Ni(P₂ᴿN₂ᴿ')₂]ⁿ⁺** series.[29] As expected, the variation of the basicity of the amino group, *i.e.* its ability to deliver protons, has a direct impact on catalytic

turnover. Roughly, the TOF increases as the acidity of the protonated amine increases, although other effects interfere in this trend.[29]

Of note, switching from two amino dangling groups per ligand for the $[Ni(P_2^{Ph}N_2^{Ph})_2]^{2+}$ complex to only one for the $[Ni(P_2^{Ph}N^{Ph})_2]^{2+}$ complex improves the TOF for HER by two orders of magnitude.[30] This result has been attributed to the inactive conformation of protonated forms of the diamino-diphosphine $P_2^{Ph}N_2^{Ph}$ ligand.[29] However, the overpotential requirement of this complex is larger than for other series of catalysts.[10]

The $[Ni(P_2^{R}N_2^{R'})_2]^{n+}$ series was initially shown to perform HER catalysis from fully organic or mixed organic aqueous media.[21, 29] Recent developments have led to $[Ni(P_2^{R}N_2^{R'})_2]^{n+}$ incorporating ligands with hydrophilic groups, as carboxylic acids[31] or arginine-derivatives,[32] that render the whole complex water-soluble. Nearly reversible hydrogen evolution and uptake has been observed in fully aqueous acidic media with $[Ni(P_2^{Cy}N_2^{Arg})_2]^{7+}$, though at elevated temperatures.[32a] Maximal TOFs have been reported in the range of 10^2 s^{-1} for pHs between 0 and 1, but the activity dramatically decreases as soon as the pH exceeds 2.

The $[Ni(P_2^{R}N_2^{R'})_2]^{n+}$ have also been utilized for immobilization onto electrodes, yielding very efficient catalytic materials.[33] This point will be further expanded later.

1.2.2.3. Earth-abundant metal polypyridinic catalysts

This class of catalysts is characterized by an EA transition metal coordinated to a ligand that displays several pyridinic moieties. While parent $[Co(bpy)_n]^{2+}$ (n = 1, 2, 3) complexes had already been studied in the early 80's by Sutin and co-workers for photocatalytic hydrogen evolution,[34] this series of polypyridinic complexes has been reinvestigated for HER only very recently. Initiated by the studies of J. Long, C. Chang and co-workers from 2010, the development of these catalysts has been raising interest of the WS community up.[35]

The structures are usually constructed around a Co[36] or Mo[35a, 37] metallic center. The diverse polypyridinic ligands mainly feature derivatized pyridine,[36g] bipyridine[36c-e] or phenantroline[36f] moieties. These moieties chelate the metallic center through several aromatic nitrogen and let one or two available coordination sites on the metal. A strong σ-donor ability and a metal-to-ligand π-back bonding are provided by the pyridinic ligands. This property tends to stabilize the low oxidation levels of the metallic center, which are key states for catalytic hydrogen evolution. In addition, the aromatic nature of these pyridinic moieties makes them very stable toward hydrogenation that is thought to occur on some non aromatic imine or oxime based ligands.[38]

Interestingly, neutral polypyridinic ligands generally yield charged complexes (+1 or most commonly +2). With an appropriate choice of the counter-anion(s), most of them are water-

soluble complexes. Although this point is not restricted to polypyridinic-based catalysts, it has often been invoked as a figure of merit for this family.[36g] Namely, water solubility allows them to evolve hydrogen from aqueous media.

For instance, **[Mo(PY5Me$_2$)O]$^{2+}$** (Figure I.8, left) has been shown to produce hydrogen from a fully aqueous solution at neutral pH, with TOFs in the range of 10^1 s^{-1}.[35a] Extensive electrolysis (72h) at unity faradaic efficiency revealed that the catalyst is preserved over time, which validates the use of a polypyridinic ligand backbone. As a counterpart, the overpotential requirements for hydrogen evolution stay quite large, probably due to the stabilization of low redox level on the metal (onset overpotential at 520 mV for **[Mo(PY5Me$_2$)O]$^{2+}$** at pH 7).

	R = H	**[Co(PY5Me$_2$)H$_2$O]$^{2+}$**	
[Mo(PY5Me$_2$)O]$^{2+}$	R = CF$_3$	**[Co(CF$_3$PY5Me$_2$)H$_2$O]$^{2+}$**	**[Co(ppq)Cl$_2$]**
	R = NMe$_2$	**[Co(NMe$_2$PY5Me$_2$)H$_2$O]$^{2+}$**	
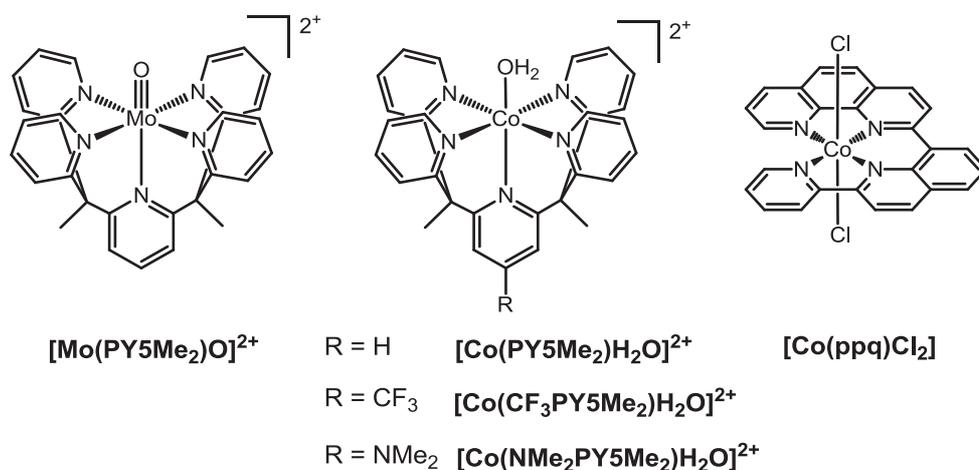
Figure I.8. Selected examples of polypyridine-based catalysts.

Redox properties might be modulated by introduction of electron-donating or withdrawing groups[36b] (**[Co(RPY5Me$_2$)H$_2$O]$^{2+}$** series, Figure I.8, middle) or by changing the denticity of the ligand (4 or 5-coordinated metal).[36a, 36g] Namely, redox-active ligands, like phenanthroline[36f] (**[Co(ppq)Cl$_2$]**, Figure I.8, right), have been introduced to act as electron reservoirs. This design may favor ligand-centered processes at potentials less cathodic than the ones required to reach the low oxidation states of the metal that are usually necessary for proton reduction.

The presence of a nearby pendent base has been proved to directly improve the efficiency of molecular HECs.[21] It is hence surprising to note that, to the best of our knowledge, no polypyridinic type catalyst has been developed to date with integration of a pendent base at the ligand. However, the development of this class of catalysts being relatively new, it is likely that future studies will soon provide original designs as well as more insightful mechanistic details.

1.2.2.4. Bisglyoximato cobalt complexes

These catalysts are made of a cobalt center bearing two glyoximato-type equatorial ligands and two other *trans* axial ligands and usually referred to as *cobaloximes*. If the first occurrence of

these complexes dates back from the beginning of the twentieth century,[39] their use as catalysts for proton reduction was only stated much later by Lehn in 1983[40] and further by Espenson in 1986.[41] Following simultaneous reports of the group of J. C. Peters[42] and ours[43] in 2005 on the electrocatalytic activity of these complexes for HER, extensive studies have appeared during the last 10 years.[44] These catalysts indeed show very high efficiency together with low overpotential requirements. This compromise is well illustrated by the **[Co(dmgH)₂PyCl]** on the comparative Tafel plot in Figure I.3.

Usually synthetized as Co^{II} or Co^{III} complexes, the positive charge is partially compensated by deprotonation of one oxime moiety on each ligand. This deprotonation allows the formation of two hydrogen-bonded O-H··O bridges yielding a pseudo-macrocyclic tetradentate ligand. Alternatively, the bridging hydrogen atoms might be replaced by difluoroboryl groups upon treatment with $BF_3 \cdot Et_2O$.[44a]

[Co(dmgH)₂LL']   **[Co(dmgBF₂)₂L₂]**   **[Co(dpgBF₂)₂L₂]**

L = Cl⁻   L = solvent (MeCN, H₂O)

L' =   **[Co(dmgH)₂PyCl]**

L' =   **[Co(dmgH)₂Py$_{NMe2}$Cl]**

L' =   **[Co(dmgH)₂Py$_{CONHtBu}$Cl]**

Figure I.9. Selected examples of cobaloximes.

Interestingly, the R substituents on the glyoxime ligands, noted as **dRgH₂**, permit to tune the redox properties of the complex. For instance, a more electron-withdrawing group diminishes the driving force for reduction on the metal center. But on the other side, this shift decreases the basicity of the catalyst and disfavors the protonation steps. As a result, the catalytic activity of the complex is decreased and hydrogen may be evolved with strong acids only.[44b] Such opposite

effect was observed namely by switching from methyl moieties on the dimethylglyoxime ligand (**dmgH$_2$**) to more electron-withdrawing phenyl moieties on the diphenylglyoxime ligand (**dpgH$_2$**) (**[Co(dmgBF$_2$)$_2$]$^{2+}$** and **[Co(dpgBF$_2$)$_2$]$^{2+}$**, Figure I.9 middle and right, respectively).[9b, 42] This change shifts the potential of the Co$^{II/I}$ wave *ca* 300 mV more positive, but the activity for hydrogen evolution is lowered and only possible with highly acidic proton sources. Similar opposite effects have been noticed also going from H-bridged cobaloximes to BF$_2$-annulated ones.[43, 44b] As a consequence, it was concluded that tuning the equatorial ligands was not relevant to improve the catalytic properties of cobaloximes. In a broad manner, this dual behavior might be extended to other families of proton reduction catalysts.[45]

However, in the case of cobaloximes this statement is not true for the axial ligands. On this, a series of cobaloximes bearing a pyridine derivative on one axial position have been studied.[43] During catalytic cycle, the pyridinic axial ligand is believed to stay coordinated to the cobalt at the CV timescale, while the formation of a Co^{III}-hydride bond in *trans* is postulated. Variations of the substituent in the *para* position of the axial pyridine have direct influence on the subsequent protonation of the hydride yielding H$_2$ (**[Co(dmgH)$_2$PyCl]**, **[Co(dmgH)$_2$Py$_{NMe2}$Cl]**, **[Co(dmgH)$_2$Py$_{CONHtBu}$Cl]**, Figure I.9, left). More electron-donating groups (NMe$_2$ > H > CONH*t*Bu) increase the basicity of the postulated hydride, thus favoring the final step and improving the catalytic activity.[46]

This interpretation relies on the formation of H$_2$ through an ECEC heterolytic mechanism. Discrimination of such a mechanism has been subject of several contradictory reports.[9b, 44a, 47] Theoretical computations have now led to the consensus that this pathway should occur through a Co^{III}-H hydride further reduced to Co^{II}-H.[48] Yet, to date, the intermediate hydridocobaloxime Co^{III}-H species could not be isolated.[49] It should be pointed out that such a Co^{III}-H is putatively highly reactive or could exist as a tautomer.[50] Hence, the direct observation of the Co^{III}-H may be extremely challenging, which does not discard this hydride as a possible *intermediate* in hydrogen evolution catalyzed by cobaloximes. Current investigations in our laboratory are dedicated to shed more light on mechanisms for HER catalyzed by related cobaloximes.[51]

This task is also being complicated by the relative low stability of the cobaloximes. Indeed, the H-bridged forms are prone to undergo hydrolysis of the bridge under acidic conditions with concomitant decoordination of one equatorial ligand.[41, 45] The stability of the complex is improved with BF$_2$-annulated species.[42] For instance, in media more acidic than pH 5, H-bridged cobaloximes are not stable whereas BF$_2$-annulated ones are for several hours.[47]

However, the nature of the true active entity has been recently questioned in several reports.[52] Actually, in specific acidic conditions the equatorial ligand was shown to be subjected to electroreductive hydrolysis of the imine and hydrogenolysis of the oxime bonds.[38, 53]

In an attempt to overcome the low stability of this set of complexes, our group developed some years ago a second generation of catalysts borrowing main features to cobaloximes.[54] These catalysts are constructed around a diimine-dioxime tetradentate ligand, which ensures a higher stability of the complex while permitting to conserve activity for hydrogen evolution.

This new generation of cobalt diimine-dioxime catalysts will be the point of the third part of the present introduction.

1.3. Cobalt diimine-dioxime catalysts

Cobalt diimine-dioxime catalysts lay at the core of the work developed in this manuscript. This section is dedicated to their description in this scope. Main features described here have been developed in a recent account by the group, which is added as an appendix of the manuscript (Paper I).[55] First, a short historical background will be drawn. Then, we will turn to the synthesis of the complexes and the related characterizations. A third part will concern the mechanism for HER catalyzed by these complexes. Finally, their utilization in homogeneous light-driven systems for proton reduction will be reported.

1.3.1. Once upon a time…

The adventure of the cobalt diimine-dioxime complexes sprang up with the elucidation of the structure of vitamin B_{12} in the 50's. Vitamin B_{12}, or cobalamin, was simultaneously isolated for the first time by Folker and by Smith in 1948.[56] Crowfoot-Hodgkin issued in 1955 a first crystallographic structure,[57] work for which, among others, she was awarded the 1964 Nobel Prize for Chemistry. The structure revealed a cobalt complex in a hexagonal geometry (Figure I.10, left). The central cobalt atom is 4-coordinated through the aromatic nitrogen atoms of an equatorial corrin ring. This multisubstituted corrin namely bears an arm whose terminal benzimidazole acts as axial ligand for the Co center. A cyanide was first believed to be the second axial ligand. But Barker demonstrated in 1958 that the cyanide ligand was an isolation artifact and that the second axial ligand in the biologically active form of this enzymatic co-factor was instead an adenine nucleoside.[58] A new crystallographic study by Crowfoot-Hodgkin surprisingly showed that this axial ligand was bound to the cobalt through a metal-carbon σ bond.[59] This work

therefore contained the first evidence of a native organometallic compound within a biologic environment.[56]

The unusual organo-cobalt structure was particularly interesting for chemists. Under its active super-reduced form B_{12s} the cobalt is at the formal +1 oxidation state and was demonstrated as being a powerful nucleophile.[56] For instance, oxidative additions of various organic moieties on this reduced center result in Co^{III} organo-metallic compounds. The particular reactivity of the B_{12s} state is central for the biological activity of this enzymatic cofactor.[60]

Similarly, in the presence of protons this super-reduced state was believed to produce a Co^{III} hydride.[56, 61] In the course of this step, the shift from an oxidation state of +1 to +3 translates in the gift of 2 electrons to the substrate. This 2-electron stoichiometry is indeed particularly relevant for catalytic proton reduction. More emphasis will be given on these points later.

In order to facilitate the study of the quite unique chemistry related to vitamin B_{12}, several groups, among which the ones of Costa and Schrauzer,[62] developed in the 60's cobalt complexes that structurally mimic vitamin B_{12} organo-metallic center. With backbones much simpler compared to the enzymatic co-factor, cobaloximes (Figure I.10, top right) represented a first generation of bio-mimetic vitamin B_{12} models. But cobaloximes feature a di-charged coordination sphere whereas in vitamin B_{12} the corrin equatorial ligand is a mono-charged anion. Hence, to get closer to the structure of the metallic site in vitamin B_{12}, Costa and co-workers synthetized a new set of mimics.[62c] In this series, the two glyoximato ligands of cobaloximes have been fused into one single, mono-charged, tetradentate moiety, by introduction of a propyl bridge: cobalt diimine-dioxime complexes were born (Figure I.10, bottom right).
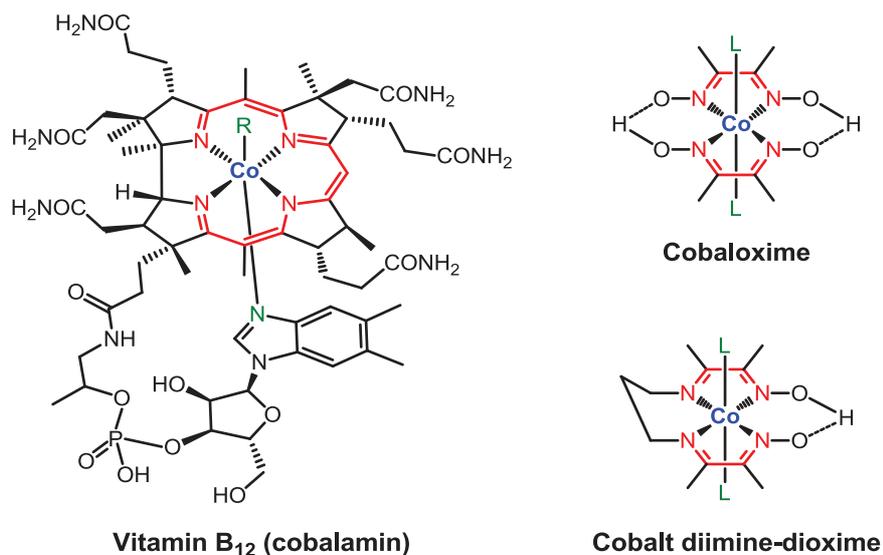
Figure I.10. Vitamin B_{12} (R = H_2O, CN^-, CH_3, adenosyl,...), cobaloximes and cobalt diimine-dioxime complexes.

In the 80's, the groups of Sutin[34a, 63] and Lehn[40, 64] demonstrated the possibility to use cobalt complexes as catalysts for light driven hydrogen evolution. These reports paved the way to extensive studies during the first decade of this millenium on the utilization of cobalt-based species, among which are cobaloximes, in the frame of artificial photosynthesis.[42-44] As said above, the relatively low stability of cobaloximes has lead our laboratory to report from 2009 on the development of cobalt diimine-dioxime complexes as a new generation of catalysts for proton reduction.[54]

1.3.2. Synthesis

The general structure of the ligand is N^2-$N^{2'}$-*alkyl*diylbis(butan-2-imine-3-oxime), abbreviated as **(DOH)$_2$R**, where R indicates the nature of the bridging *alkyl* group. We will focus in the present manuscript on propyl-bridged diimine-dioxime, written as **(DOH)$_2$pn**, and their analogues derivatized on this bridge.

1.3.2.1. Synthesis of [Co(DO)(DOH)pnL$_n$]

The synthesis of the simple **(DOH)$_2$pn** ligand was first described by Uhlig and Friedrich[65] in 1966 and repeated by Costa and co-workers.[62c] The synthesis is a one step Schiff base condensation of 1,3-diaminopropane onto 2,3-butadione monoxime yielding the expected N^2-$N^{2'}$-propanediylbis(butan-2-imine-3-oxime) **(DOH)$_2$pn**. This procedure although gives low yields and was further improved by Marzilli and co-workers,[66] inspired from a work of Finke and co-workers[67] and performing the reaction with a dean-stark apparatus (Figure I.11, top).

Metallation is usually achieved by addition of a cobalt divalent salt (CoCl$_2$, CoBr$_2$) while bubbling air into the solution (Figure I.11, middle). These smoothly oxidizing conditions allow the formation of the Co^{III} species **[Co^{III}(DO)(DOH)pnL$_2$]**. The obtained complex adopts an octahedral configuration, with four equatorial positions occupied by nitrogen atoms of the diimine-dioxime moiety and two *trans* axial ligands L. Meanwhile, deprotonation occurs on one oxime of the **(DOH)$_2$pn**, yielding a −1 charged **(DO)(DOH)pn$^-$** ligand. Favored by the formation of an O-H··O hydrogen bridge, this deprotonation provides the overall neutrality of the **[Co^{III}(DO)(DOH)pnL$_2$]** complex. The presence of a hydrogen bond between oximato oxygen atoms is confirmed by a highly unshielded nuclear magnetic resonance (NMR) shift at *ca* 19 ppm. The exchangeable proton is replaced by a difluoroboryl group through reaction with BF$_3$·Et$_2$O, to give the **[Co^{III}((DO)$_2$BF$_2$)pn)L$_2$]** complex (Figure I.11, bottom).[54]

The replacement of the halogen L ligands by water, for instance by precipitation of Br$^-$ into AgBr after addition of AgNO$_3$, leads to the di-charged bisaquo **[Co^{III}(DO)(DOH)pn(H$_2$O)$_2$]$^{2+}$**

complex.[68] Alternatively, aquation also slowly occurs by dissolution of **[Co^{III}(DO)(DOH)pnL$_2$]** in water.
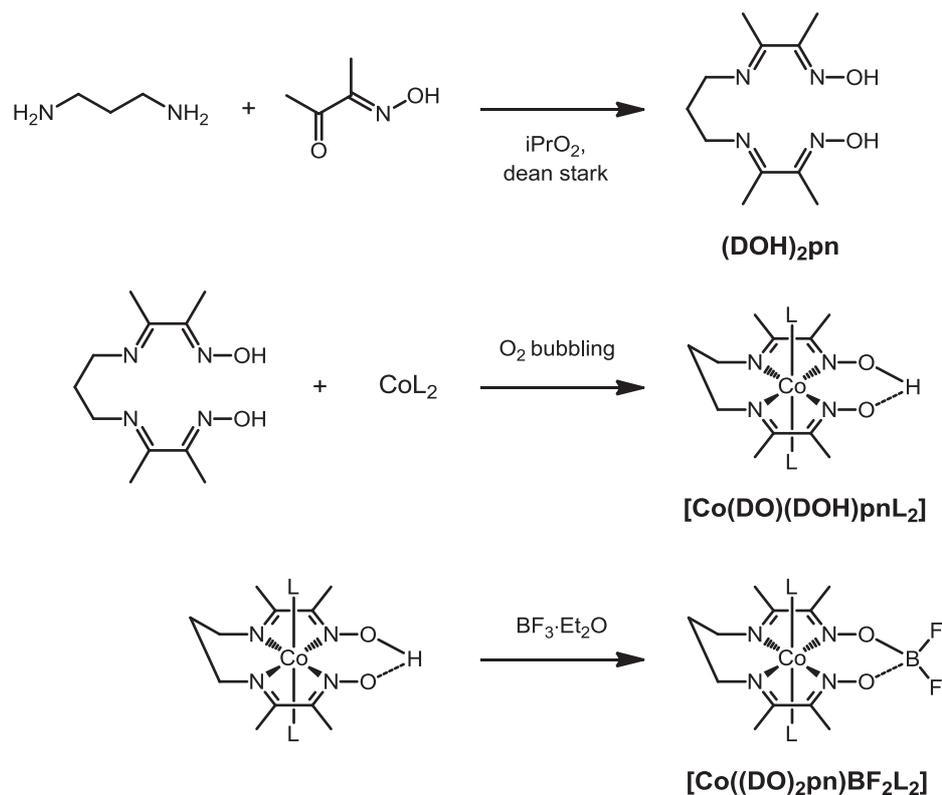
Figure I.11. Synthesis scheme of ligand **(DOH)$_2$pn**, **[Co(DO)(DOH)pnL$_2$]** and **[Co((DO$_2$)BF$_2$)pnL$_2$]** complexes (L = Cl$^-$, Br$^-$).

Coordination of a phosphine ligand is known to stabilize low oxidation states at the metal. Hence, an axial phosphine ligand, e.g. triphenylphosphine PPh$_3$, can be introduced at the Co^I state obtained by chemical (NaBH$_4$) or photochemical reduction of the Co^{III} complex and generates the **[Co^I(DO)(DOH)pnPPh$_3$]** species.[54, 69]

1.3.2.2. Synthesis of bridge-derivatized [Co(DO)(DOH)pnLn]complexes

In the frame of studies related to understanding and mimicking the activity of cobalamin, derivatization of **[Co^{III}(DO)(DOH)pnL$_2$]** has been investigated. In the natural co-factor, one of the axial ligands, the benzimidazole one, is covalently linked to the equatorial corrin. To stick closer to this structure, Marzilli and co-workers synthetized a diimine-dioxime ligand whose propane bridge bears a pendent arm decorated with a pyridine which comes as an axial ligand of the cobalt.[70]

The development of **[Co^{III}(DO)(DOH)pnL$_2$]** immobilized electrodes for their integration in PEC devices has lead our group and others to consider the derivatization of the bridge as an

opportunity to introduce anchoring groups.[14, 71] The two main synthetic pathways followed until now are described here.

1.3.2.2.1. Synthesis of azido derivative

This pathway is based on a strategy developed by our group to use *click*-chemistry reactions, and in particular the Huisgen azide-alkyne cycloaddition (AAC),[72] to covalently attach the catalyst onto surface.[14]
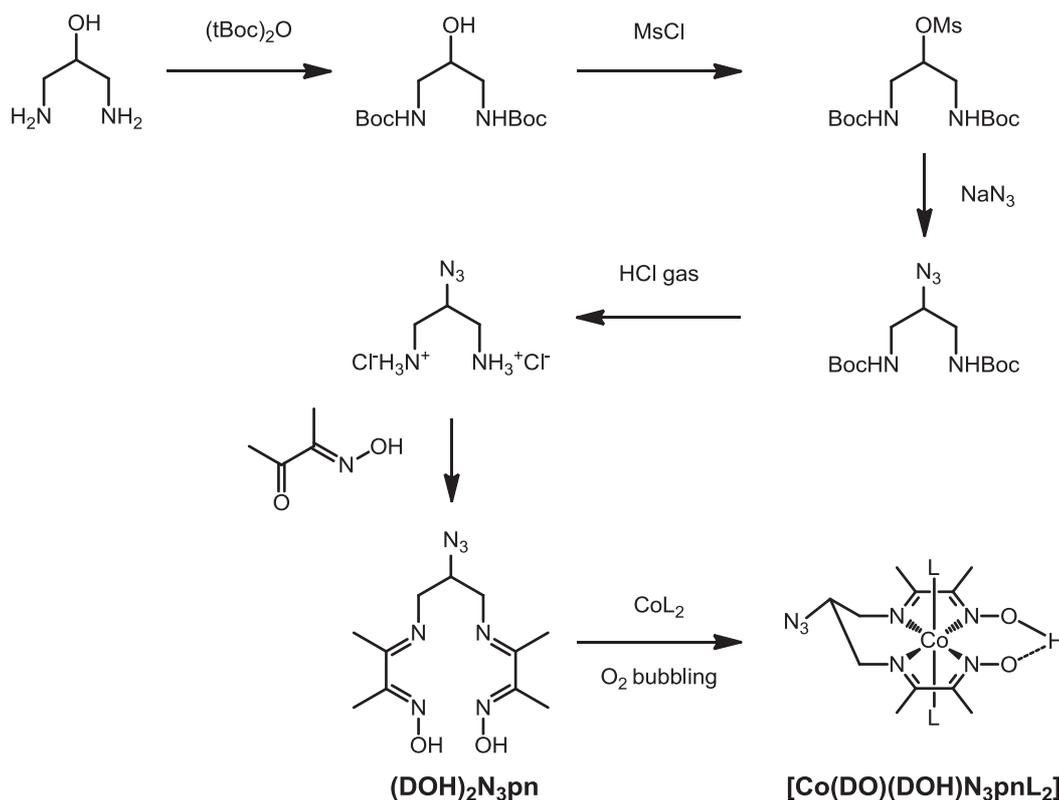
Figure I.12. Synthesis scheme of the **(DOH)$_2$N$_3$pn** ligand and of the **[Co(DO)(DOH)N$_3$pnL$_2$]** complex (L = Cl$^-$, Br$^-$). *t*Boc: *tert*-butyloxycarbonyl; Ms: mesylate.

The bridge is first derivatized starting from the commercially available 2-hydroxy-1,3-diaminopropane and following a procedure from the literature (Figure I.12).[73] After *t*Boc protection of the amine functions, the hydroxyl group is activated by conversion into mesylate. A nucleophilic substitution yields the azide intermediate. Amines are deprotected under acidic conditions and converted to imines by a the Schiff base condensation with 2,3-butadione monoxime. The obtained N^2,N$^{2'}$-2-azidopropanediylbis(butan-2-imine-3-oxime) ligand, noted as **(DOH)$_2$N$_3$pn**, is metallated as described above to give the azido-derivatized complex **[Co^{III}(DO)(DOH)N$_3$pnL$_2$]**. The presence of the azide group will give access to the toolbox of AAC.

1.3.2.2.2. Malonic-like synthesis

This synthetic pathway has been proposed by Reisner and co-workers and involves the functionalization by benzylic groups on the propyl bridge (Figure I.13).[71, 74]

A first condensation between 4-bromobenzaldehyde and malononitrile, followed by reduction with NaBH$_4$, gives the mono-substituted bridge. This platform is further substituted with a second 4-bromobenzyl group under smoothly basic conditions. A Pd-catalyzed cross-coupling reaction then replaces the aromatic bromine by phosphonate esters, before borane reduces nitrile functions into amine ones. At this stage, 2,3-butadione monoxime is condensed in the presence of cobalt bromide to directly yield the expected complex bearing phosphonate esters. The selective deprotection of these esters with trimethylsilyl bromide (TMSBr) affords the complex functionalized with phosphonic acids as putative anchoring groups.
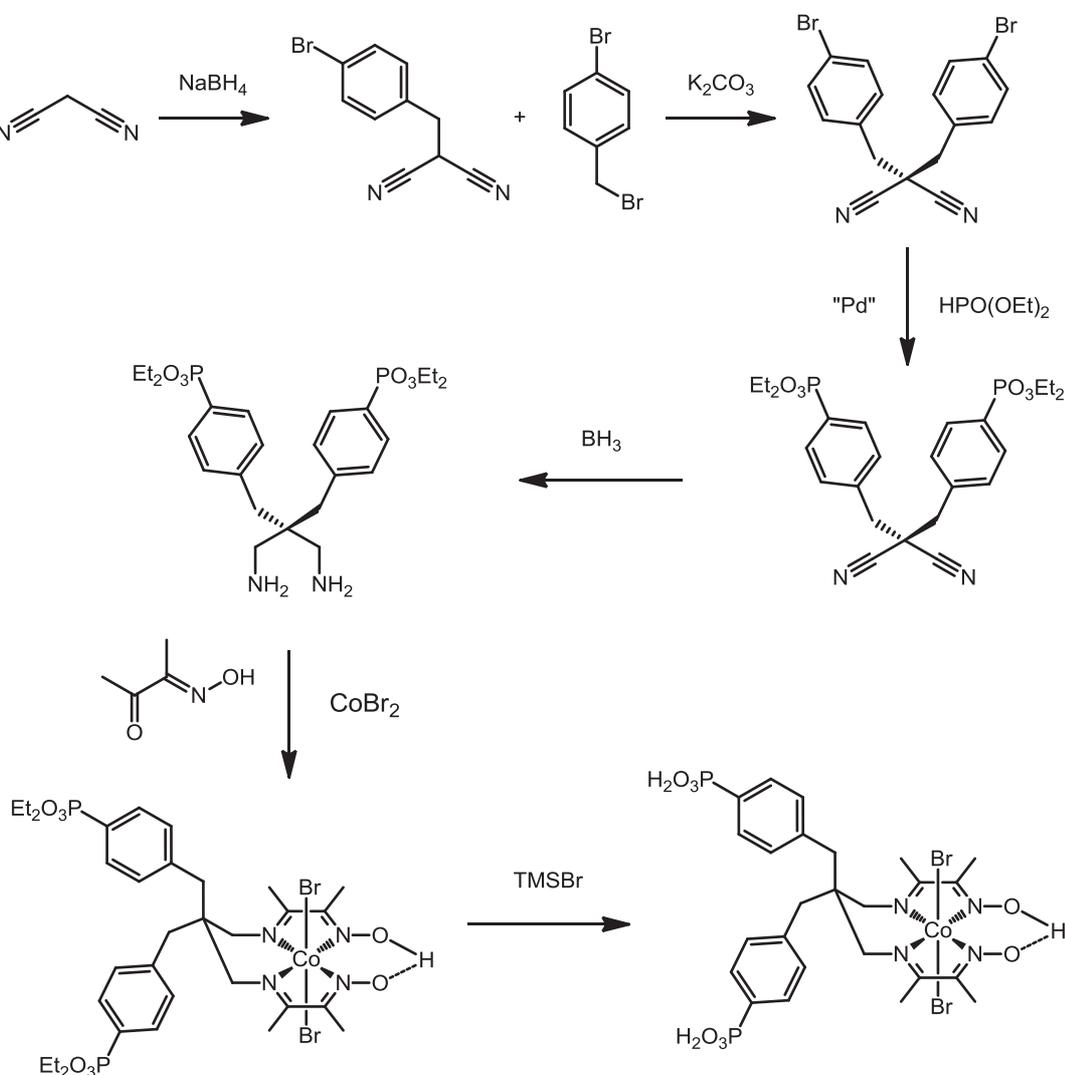
Figure I.13. Synthesis scheme of the benzylphosphonic-functionalized **[Co^{III}(DO)(DOH)pnL$_2$]** complex. TMSBr: trimethylsilyl bromide.

A similar synthetic pathway has been used to produce a heterosubstituted complex bearing a phosphonic acid grafting moiety and a pendent pyridine as Co axial ligand.[71a, 74b]

1.3.3. Hydrogen evolution: performance and mechanistic issues

Hydrogen evolution catalyzed by **[Co^{III}(DO)(DOH)pnL$_2$]** has been assessed by electro- and photochemical measurements. We will first discuss here electrocatalytic studies, which namely allow drawing a mechanistic scheme of HER catalyzed by this complex. The proposed mechanism is further supported by DFT studies.

1.3.3.1. Electrocatalytic behaviour

The voltammogram of **[Co^{III}(DO)(DOH)pnBr$_2$]** in acetonitrile displays two monoelectronic redox waves at –0.57 and –1.11 V *vs* Fc$^{+/0}$ attributed to the Co$^{III/II}$ and Co$^{II/I}$ processes, respectively (Figure I.14, top).[54] While the Co$^{II/I}$ process shows a reversible behavior, the process assigned to Co^{III} to Co^{II} reduction is only partially reversible. This observation might be explained by the loss of the two bromide axial ligands upon reduction from the Co^{III} to the Co^{II} level. X-ray absorption spectro-electrochemical measurements confirm this hypothesis.[75]

Upon addition of acid in the electrolyte, the development of a catalytic wave is observed, growing in intensity with increasing acid concentrations. This wave raises at potentials anodic compared to the Co$^{II/I}$ couple. The extent of the anodic shift also depends on the strength of the acid used: the higher the pKa, the larger the shift of the catalytic wave. By contrast, the difluoroboryl-annulated complex **[Co^{III}((DO)$_2$BF$_2$)pnBr$_2$]** reveals a catalytic wave that develops sumperimposed on the Co$^{II/I}$ couple (Figure I.14, bottom). In both cases, near unity faradaic efficiencies and TONs in the 10s range are reported for hydrogen evolution during 3-hour extensive electrolysis at the potentials matching the respective catalytic waves. These observations clearly point out the role of the O-H··O bridge, which is likely protonated during the catalytic cycle, in proton reduction realized by **[Co^{III}(DO)(DOH)pnBr$_2$]**,

The catalytic performances have been assessed in a wide range of organic acidic conditions. With acid pK$_a$s from 7.6 to 12.6 the overpotential ($E_{cat/2}$) remains within a 220-290 mV window, taking into account the homoconjugation of the acid.[6, 55] Based on the overall pool of catalyst in the electrolyte solutions, extensive electrolyses give TOFs comparable to cobaloximes in similar conditions.[54] However, a benchmarking through a catalytic Tafel plot would be valuable for the cobalt diimine-dioxime catalysts.
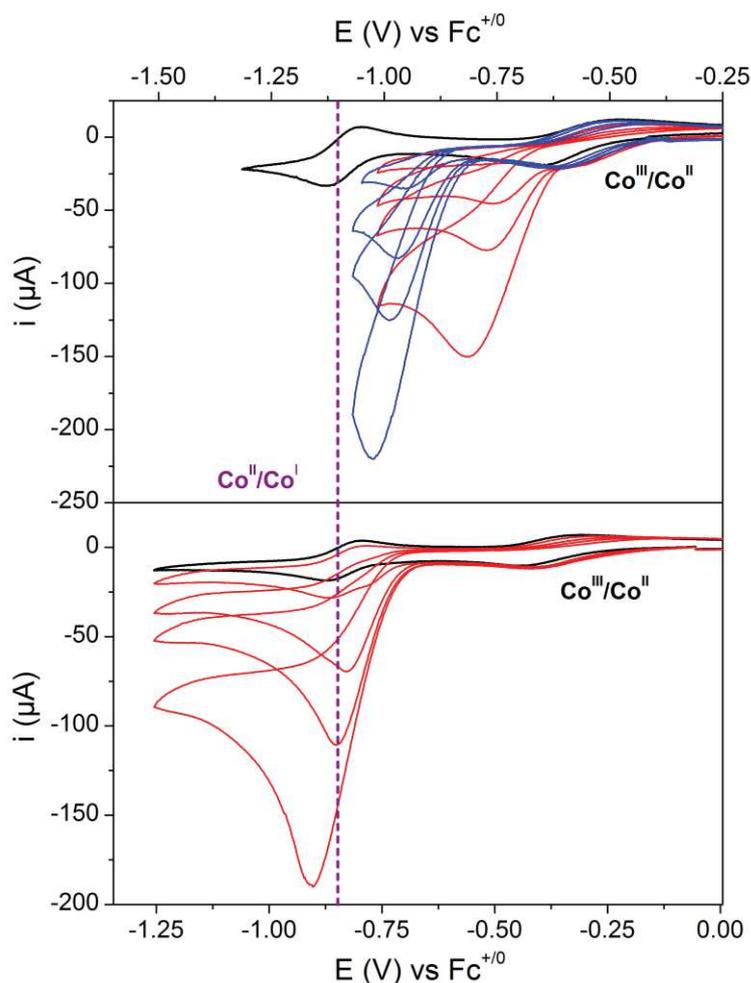
Figure I.14. Cyclic voltamogramms of **[Co^{III}(DO)(DOH)pnBr$_2$]** (top) and **[Co^{III}((DO)$_2$BF$_2$)pnBr$_2$]** (bottom) recorded in CH$_3$CN (0.1 M nBu$_4$BF$_4$) at a glassy carbon electrode with a scan rate of 100 mV·s^{-1} in the absence of acid (black lines), in the presence of p-cyanoanilinium (red lines; 1, 3, 5, and 10 equiv.) or cyanoanilium (blue lines; 1, 3, 5 and 10 equiv.) tetrafluoroborate. Note the shifted horizontal scales used to center graphs on the Co$^{II/I}$ waves.

Peters and co-workers reported on the activity of the complex **[Co^{III}(DO)(DOH)pn(H$_2$O)$_2$]$^{2+}$** in fully aqueous media.[68] In a phosphate buffer at pH 2.2, an overpotential (E$_{onset}$) around 260 mV was observed for a wave the authors assigned to hydrogen evolution by the above-mentioned complex. Changing the buffer, thus the pH of the solution, they also showed an effect of the acidity of the media on the potential of this wave. Decreasing the pH translates in a positive shift of this wave, suggesting a PCET process. However, we will provide later in this manuscript a distinct interpretation of these results.

1.3.3.2. Theoretical studies

DFT calculations have been performed by collaborators of the group, Field and co-workers, to further elucidate the possible pathways for hydrogen evolution.[76] By computing energies and related potentials of all plausible intermediates using B3LYP and BP86 functionals, a logical

mechanistic path has been tentatively proposed. Calculated potentials are in good agreement, within methodological errors, with the ones experimentally measured.

The proposed mechanism is presented in Figure I.15. This mechanism starts from a $Co^{II}L$ complex obtained from the reduction of the $Co^{III}L$ complex, where L is the **(DO)(DOH)pn⁻** ligand for the ongoing paragraph. Solvent axial ligands, which might be present after loss of halide ligands at the $Co^{II}L$ state, are omitted here for the sake of clarity. The one-electron reduction to $Co^{I}L$ occurs with a concomitant protonation of the O-H··O bridge to yield the $Co^{I}LH$ in a PCET process. Depending on the acid strength and based on the moderate shift of the $Co^{III/II}$ wave recorded in the presence of acid (Figure I.14), it is however likely that a certain ratio of the complex is already protonated at the Co^{II} state ($Co^{II}LH$). Nonetheless, the potential computed for the $Co^{II}L/Co^{I}LH$ couple is found more positive than the one for $Co^{II}L/Co^{I}L$, also in line with calculations performed by Hammes-Schiffer and co-workers.[77] These calculations giving a more positive $Co^{II}L/Co^{I}LH$ potential provide explanation for the anodic shift observed in CV upon addition of an acid.
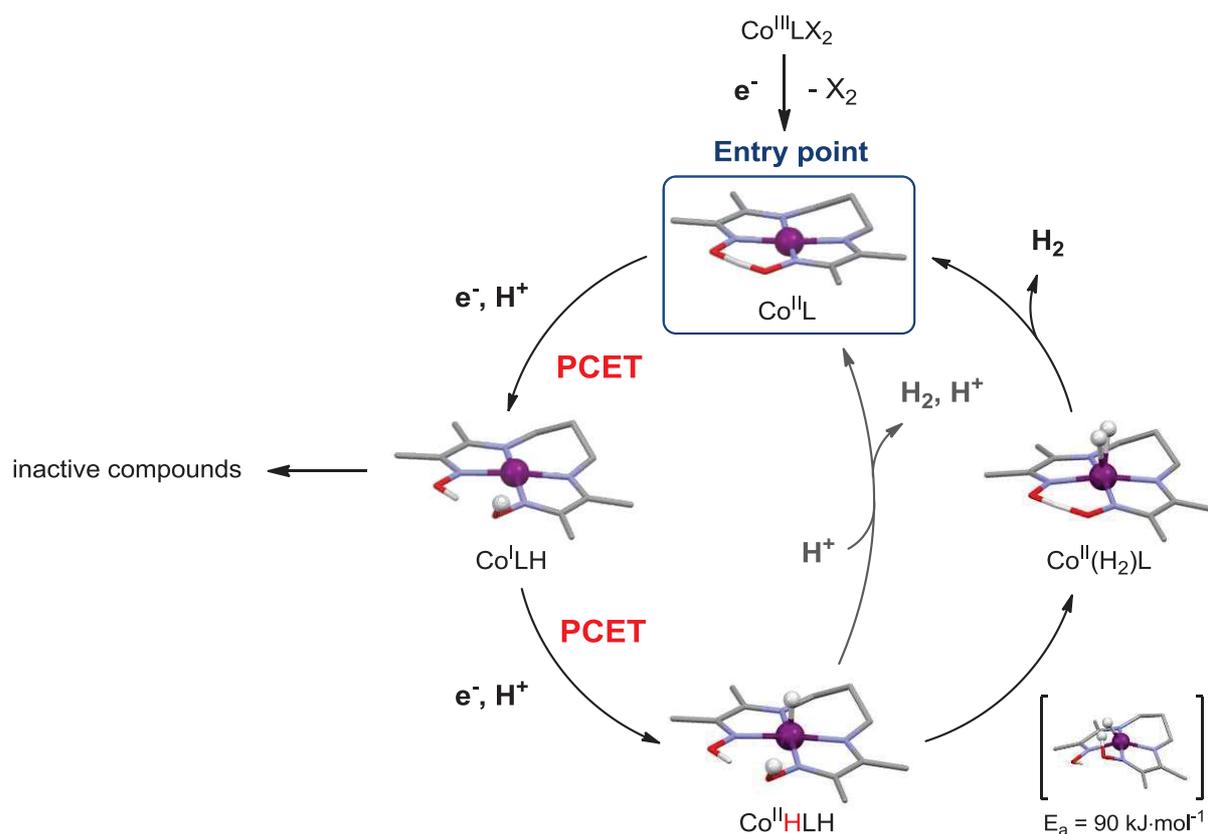
Figure I.15. Proposed pathways for hydrogen evolution catalyzed by **[Co^{III}(DO)(DOH)pnX₂]**. Structures shown have been optimized by DFT and solvent axial ligands have been omitted for clarity.

A second PCET step, *i.e.* the formation of the $Co^{III}HLH$ hydride and a further reduction, leads to the Co^{II}-hydride species $Co^{II}HLH$. The computational values for this PCET step give the

Co^{I}LH/Co^{II}HLH couple at a potential even more anodic than the Co^{II}L/Co^{I}LH couple. This comparison evidences the possibility for the catalytic cycle to develop on the Co^{II}L/Co^{I}LH wave, consistently with the shape observed in CV.

Finally, hydrogen evolution occurs *via* protonation of the Co^{II} hydride, releasing H$_2$ and the possibly deprotonated initial Co^{II}L complex. Intramolecular protonation is believed to occur at the active site of hydrogenases during the formation of the H-H bond. A similar process might be at stake here, involving an oximato proton, the activation energy found around 90 kJ·mol^{-1} being in good line with other reports concerning enzymes or HER catalysts.[55]

1.3.3.3. Discussion

The mechanism proposed here involving two PCET processes exemplifies the role of the O-H··O bridge as a proximal proton relay. Protonation at the bridge indeed facilitates the reduction processes at the metal center and makes the electrocatalytic potentials to adapt to varying acidic conditions. This feature is very reminiscent to hydrogenase active sites or the bio-inspired DuBois' nickel bisdiphosphine as illustrated in Figure I.16.[17]

[Co(DO)(DOH)pnL$_2$]   **[FeFe] hydrogenase**   **[Ni(8P$_2$^{R}N$^{R'}$)$_2$]$^{2+}$**
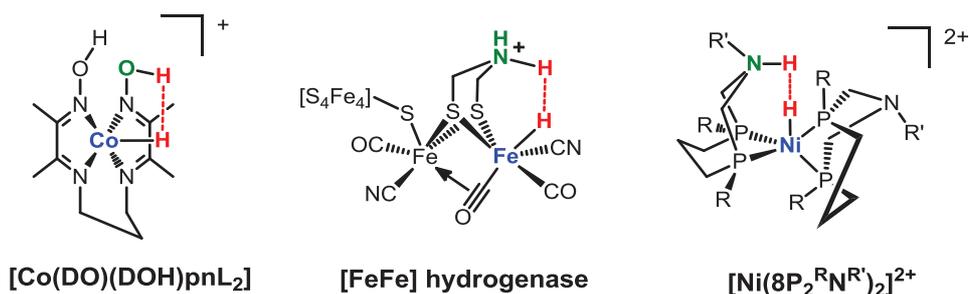
Figure I.16. Proposed intermediate H$_2$ formation steps for HER catalyzed by **[Co(DO)(DOH)pn]** (left), [FeFe] hydrogenase (middle) and **[Ni(8P$_2$^{R}N$^{R'}$)$_2$]$^{2+}$** (right). R = cyclohexyl, R' = 4-bromophenyl.[78]

Of note, in the case of **[Co^{III}(DO)(DOH)pnBr$_2$]**, the electron density on the O-H··O bridge might be correlated with the one on the metallic Co center, as a result of conjugation of the imine-oxime moiety. Thus, increasing electron density at the metal upon reduction possibly renders the oximato oxygen more electron rich, hence more basic. This increased basicity would favor protonation of the O-H··O bridge. But the protonated bridge would then withdraw electron density from the cobalt center. This behavior could lead to two antagonist effects, similar to the ones discussed earlier for the tuning of equatorial ligands of cobaloximes. On the one hand, an electron poorer Co center is easier to reduce, lowering down the overpotential requirement in the presence of an acid. On the other hand, the loss of electron density decreases the basicity of the Co hydride, slowing down the formation of the H-H bond. Determining catalytic Tafel plots of the **[Co^{III}(DO)(DOH)pnBr$_2$]** under different acid conditions would deliver insightful information to

decipher the extent of both effects on catalysis. To conclude, one might also notice that this electronic coupling does not occur, at least through bonds, at the [FeFe] hydrogenase active site (not [NiFe]) nor with Dubois' nickel bisdiphosphine catalysts.

1.3.4. Light-driven homogeneous catalysis

Toward a possible use to produce hydrogen as a *solar* fuel, **[Co^{III}(DO)(DOH)pnL$_2$]** have been assayed in different homogeneous photocatalytic systems. These systems usually rely on a photosensitizer (PS), a sacrificial electron donor (SED) and a source of protons. Several conditions have been reported so far in the literature, with PS made of Ir- or Re-based compounds. Alberto and co-workers have shown that the **[Co^{III}(DO)(DOH)pnBr$_2$]** operates both in an organic solvent (DMF here) as well as in fully aqueous media.[79]

In fully aqueous systems, the SED is usually present in high concentrations (0.5 to 1 M) and thus also acts as a buffer through its acido-basic behavior. Changing from triethanolamine (TEOA; HTEOA$^+$/TEOA pK_a 7.8) to ascorbic acid (H$_2$Asc; H$_2$Asc/HAsc$^-$ pK_a 4.1) allows switching from mildly alkaline (pH 7-9) to mildly acid operating media (pH 2-5). Studies conducted under otherwise similar conditions and involving **[Re(bpy)py(CO)$_3$]$^+$** as a PS evidence that the observed TONs for H$_2$ production reach optimal values at a pH close to the pK_a of the SED couples.[79a, 79b] This phenomenon namely arises from the necessity of keeping high the concentration of the SED basic form, which is the reductive quencher for the excited PS in the photocatalytic cycle. However, the most acidic conditions with H$_2$Asc/HAsc$^-$ display TONs one order of magnitude higher than alkaline ones and up to 90 per catalyst unit after 30 h of irradition.[79b] This observation tends to demonstrate that **[Co^{III}(DO)(DOH)pnBr$_2$]** has an improved activity in rather acidic media (ideally between pH 2 to 5).

Of note, **[Co^{III}(DO)(DOH)pnBr$_2$]** also displays enhanced long-term stability compared to cobaloxime equivalents under similar conditions.[79a] This is in good agreement with the electrocatalytic behavior and is a rationale of the tetradentate consolidated ligand design. Yet, under conditions purposely optimized for an other cobalt polyimine catalyst, **[Co^{III}(DO)(DOH)pnBr$_2$]** gives comparatively a quite moderate activity.[80]

However, benchmarking catalysts through their photocatalytic activity might be tedious. For two catalysts, optimal photocatalytic conditions could actually be quite different. This point probably reflects the numerous pathways that can be followed during catalytic cycles and that depend on a wide set of parameters as the media, PS, SED and pH. For instance, our group was able to improve the performance of **[Co^{III}(DO)(DOH)pnL$_2$]** in homogeneous light-driven systems through the utilization of an Ir-cyclometalated PS, operating in an equivolumic mixture of

water and acetonitrile, though.[69] With TEA as SED, the **[Co^{III}(DO)(DOH)pnBr$_2$]** lead to 300 TONs after 3 hours of irradiation before deactivation (Figure I.18, left). Noteworthy, the **[Co^{III}((DO)$_2$BF$_2$)pnBr$_2$]** complex only reaches 50 TONs under the same conditions, which further supports the importance of the O-H··O bridge for catalytic activity.
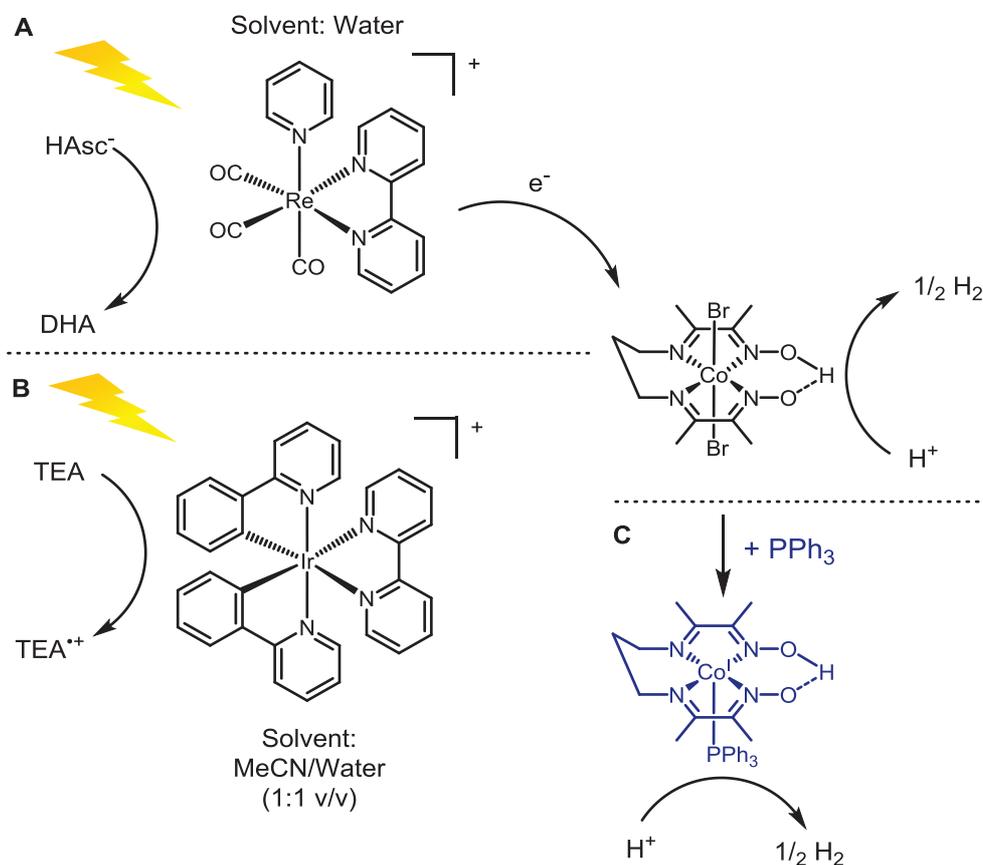

Figure I.17. Examples of photocatalytic systems used with **[Co^{III}(DO)(DOH)pnBr$_2$]**. (A) SED: H$_2$Asc/HAsc$^-$ 1 M; PS: **[Re(bpy)py(CO)$_3$]$^+$** 30 μM; catalyst 500 μM; solvent: water.[79c] (B) SED: HTEA$^+$/TEA 10% vol; PS: **[Ir(ppy)$_2$(bpy)]$^+$** 100 μM; catalyst 100 μM; solvent: water/MeCN (1:1 v/v).[69] (C) Identical to (B) with 2 equiv. PPh$_3$ (200μM) added. DHA: dehydroxyascorbic acid.

One step further, the addition of triphenylphosphine (PPh$_3$) in the mixture results in a 2-fold increase in TONs realized by **[Co^{III}(DO)(DOH)pnBr$_2$]** with prolonged activity (up to 700 TONs in 10 h of irradiation; Figure I.18, left). Phosphine ligands are actually known to stabilize low oxidation states of cobalt complexes. For instance, this fact is illustrated by a 280 mV anodic shift of the Co$^{II/I}$ wave in the presence of PPh$_3$. The UV-visible monitoring of the early phases of photocatalysis shows noticeable differences in the spectroscopic signature with or without PPh$_3$ (Figure I.18, right).
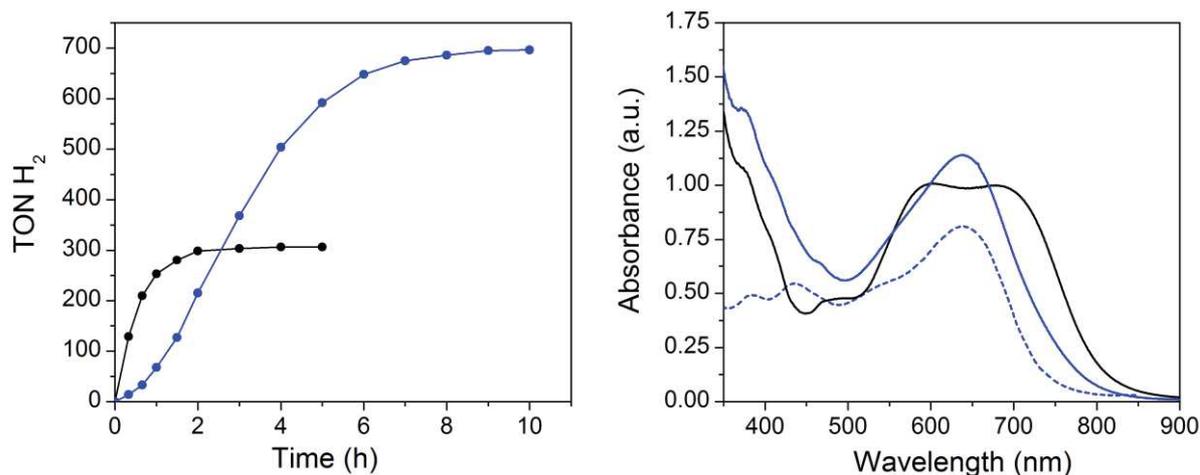
Figure I.18. TONs in H_2 *vs* time for photocatalytic systems comprising **[Co^{III}(DO)(DOH)pnBr$_2$]** 100 μM, **[Ir(ppy)$_2$(bpy)]$^+$** 100 μM, HTEA$^+$/TEA 10% vol. without (black dots) and with PPh$_3$ (blue dots) 200μM in a MeCN/water 1:1 (v/v) mixture (left); UV-visible spectra of the same mixture after 60 s of irradiation without PPh$_3$ (black line) or after 70 s of irradiation with PPh$_3$ (blue line) 100μM and of the synthetized **[Co^I(DO)(DOH)pnPPh$_3$]** 100 μM (blue dashed line) (right).

With PPh$_3$ added, the appearance of a band centered at 638 nm indicates the formation of **[Co^I(DO)(DOH)pnPPh$_3$]**. A different UV signature is observed in the absence of PPh$_3$, with two bands at 602 and 678 nm. Similar bands are also found for many cobaloximes putatively reduced at the Co^I state.[50-51] These observations prove that PPh$_3$, which is coordinated in the axial position in the Co^I state, directly imparts the resting state of catalysis. Hence, tuning the axial ligand provides an opportunity to enhance the catalytic activity, both for light-driven and electrochemical systems. While **[Co^{III}(DO)(DOH)pnBr$_2$]** is quite versatile for homogeneous photocatalysis regarding experimental parameters and is namely able to operate in water, this opportunity opens a window to further extend the conditions for light-driven HER.

1.4. Immobilized electrodes for HER

To facilitate the integration in device the immobilization of HER catalysts at the surface of conducting electrodes is highly desirable. Staying consistent with the main idea of this work, we will focus exclusively on electrode assemblies and not on heterogeneous systems where HECs could be attached onto dispersed nanoparticles (NP), although similar anchoring approaches might be exploited. As a start, some general considerations about the immobilization of molecular proton reduction catalysts onto electrode will be set. Then, strategies used to attach molecular HECs onto surfaces will be described and briefly exemplified with relevant supported EA molecular catalysts for proton reduction. Finally, as a prelude of the first studies developed in the present manuscript, more emphasis will be given on the construction of **[Co^{III}(DO)(DOH)pnL$_2$]**-based cathodes through diazonium electro-reduction.

1.4.1. General considerations

Homogeneous systems contain a large pool of molecules not directly involved in electrocatalysis, because not in the reaction-diffusion layer. This pool represents a fresh feedstock of intact HECs which limits any apparent loss of activity through deactivation during an extensive cycling. The same is not true for immobilized electrodes. In that case, all the catalysts attached to the electrode surface ideally partake to HER, *i.e.* either turnover or deactivate. As such, the performance of an anchored HEC is a good reflect of its efficiency and robustness. It should be pointed out that the strategy undertaken for surface immobilization is also of major importance. Interfacial layers generally required to graft HEC at an electrode can indeed generate electron or proton-diffusion resistances.[23b, 81] This phenomenon hence hinders the observed catalytic activity. But the presence of such interfacial connections displays two interesting features. First, under the form of a mesoporous material, the interfacial layer increases the density of catalytic entities per surface area and accordingly the activity.[33b] Second, this layer can also act as a third coordination sphere for HECs grafted on it, for instance by buffering the local environment or providing a nearby proton relay.[82]

Besides, the attachment of the catalysts at a surface advantageously allows the use of water as a solvent for electrolysis, even if the native catalyst is not water-soluble. Aqueous operating conditions are indeed one of the first requirements for a viable WS device. The possible utilization of supported catalysts intrinsically not soluble in water has been reported at many occurrences.[33a, 33b, 83]

1.4.2. Strategies for HEC attachment onto electrodes

Direct deposition onto a conductive electrode substrate is widely used with heterogeneous catalysts that can be electrodeposited, sputtered or thermally sintered, to name a few techniques.[4, 84] By contrast, the immobilization of a molecular HEC is more challenging. The procedure should not alter the coordination sphere finely tuned for the catalysis of proton reduction and the synthesis of which is usually demanding. At the same time, the deposition process has to ensure a strong binding of the molecules at the surface. Thus, anchoring molecular HECs onto electrodes is generally not as straightforward as for material-based HECs and may require several steps.

Several strategies for the immobilization of molecular HEC onto electrodes have been exploited. These strategies rely either on physi- or chemi-sorption[85] and are shortly depicted here.

1.4.2.1. Entrapment into a polymeric layer

This approach simply consists in the physical incorporation of the catalytic moiety into a polymeric matrix. The matrix is further casted onto an electrode to create a top-lying film containing HECs. These films are usually obtained from polyvinyl and/or hydrophilic polystyrene derivatives or Nafion®, deposited on carbonaceous electrodes.
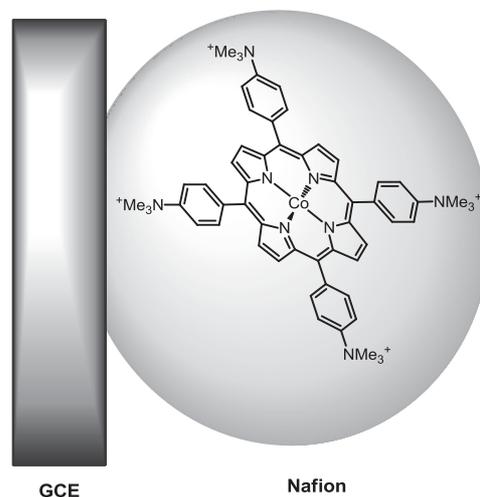

Figure I.19. Example of a charged Co-porphyrin entrapped into Nafion® deposited onto GCE.

This strategy was implemented already in 1985 by Spiro and co-workers to introduce charged Co porphyrin derivatives into Nafion® films (Figure I.19).[23b] Steady catalytic activity for HER is observed for 90 min although at low TOFs (10^{-3} s^{-1} range). Similar strategies were used by others,[81] for instance to entrap Co porphyrins in amphiphilic co-polymers,[81b] accessing higher activities (10^2 s^{-1}) but with seemingly large overpotential requirements. In such an approach, the moderate activity is believed to result from a slow electron transfer within the matrix.

1.4.2.2. Attachment with coordinating moieties

Integrating HER catalysts onto electrodes might also be realized through coordination chemistry. This strategy generally involves a chelating group present on the catalyst and a metallic atom at the surface. Broadly used to graft molecules onto transparent conducting oxides (TCO) in the frame of developing DS PEC,[86] this approach is a central point of the present work. We will here only briefly exemplify it but more extensive discussion will be found in the second part of the introduction.

The examples presented are namely based on HECs decorated with carboxylic or phosphonic acid groups that permit attachment onto TCOs. For instance, cobaloximes derivatives bearing a carboxylic acid were grafted to planar fluorine-doped tin oxide (FTO) as a TCO, likely through the chelation of Sn by carboxylic groups.[87] The surface assembly displays a catalyst loading in the

range of a monolayer. However, leach off of the catalyst is observed in the presence of tosic acid, making the electrode unsuitable for proton reduction catalysis.
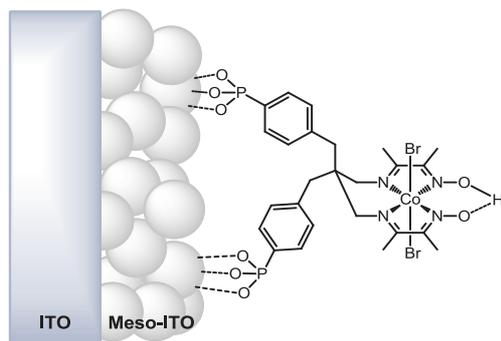

Figure I.20. Benzylphosphonic-functionalized **[Co^{III}(DO)(DOH)pnBr$_2$]** derivative anchored to a meso-ITO electrode through coordination by phosphonate groups.

A similar strategy was followed by Reisner and co-workers to immobilize phosphonic acid derivatives of **[Co^{III}(DO)(DOH)pnL$_2$]** (as the one described in Figure I.20) onto mesoporous indium-tin oxide (meso-ITO) (Figure I.20) or SnO$_2$-coated electrodes.[71, 74] The 3D-templated architectures of the mesoporous layers afford large catalyst loadings in the range of 10^{-7} to 10^{-8} mol·cm^{-2}.[71] The supported catalysts are redox cycled in neutral aqueous media and the subsequent retainment of their electrochemical, UV-visible and X-ray photoelectron spectroscopy (XPS) signatures suggest that the grafted assemblies are stable. However, catalytic activity is only reported with an excess amount of catalyst present in the electrolyte solution and no clear evidence of HER catalysis due to the immobilized complexes is presented.[71b] These limitations might originate from a poor stability of the supporting electrodes or anchors upon sustained cathodic polarization.

1.4.2.3. Immobilization through Π stacking

This approach relies on the immobilization of the catalyst through π-π interactions with the supporting layer. Such immobilization is allowed by the presence of an extended aromatic moiety in the structure of the catalyst. This aromatic part is either located in the first coordination sphere or on a purpose-placed anchoring group. Due to the nature of the interaction, electronic conduction at the interface is generally well retained. Also, while π systems commonly display hydrophobic properties, the operation of the immobilized electrode in aqueous media does not lead to the peel off of the catalyst in solution. More, immobilization procedures are quite straightforward, since π stacking occurs spontaneously between the HEC and the supporting electrode.

Recent examples of these systems include Co bis-aryldithiolate catalysts[88] or covalent frameworks[89] (Figure I.21, left) immobilized onto highly ordered pyrolytic graphite (HOPG) or graphene layered on conducting glass electrodes.[88-89] Here, π stacking takes place between the aryl moiety on the ligand and the π-conjugated surface. These assemblies evolve hydrogen from rather acidic aqueous electrolyte with activities maintained over hours. Notable catalytic performances reveal TOFs estimated in the range of 10^3 s^{-1} with proton reduction shifted 370 mV more cathodic than a platinum electrode[88] or current density reaching 10 mA·cm^{-2} at 340 mV overpotential.[89] While a monolayer deposition might logically be expected for this type of immobilized electrodes, with a theoretical maximal surface density around 10^{-10} mol·cm^{-2}, much higher catalyst loadings (until 10^{-6} mol·cm^{-2}) have surprisingly been reported,[89] indicative of multiple layers.
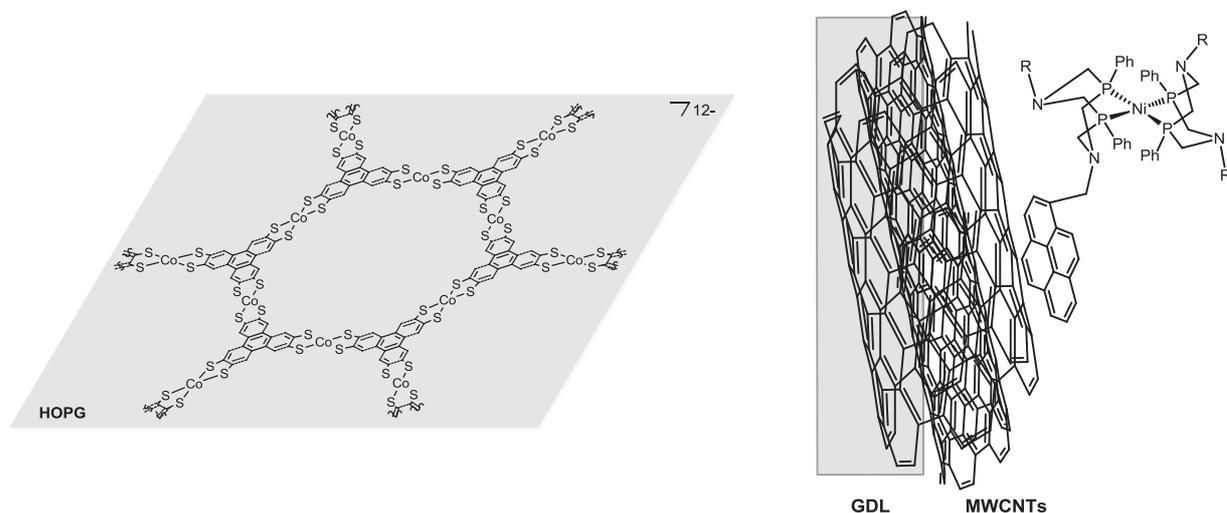
Figure I.21. Cobalt bis-aryldithiolate framework deposited on HOPG (left) and pyrene derivatives of a DuBois' nickel bisdiphosphine immobilized onto MWCNTs (right). R = pyren-1-methylene; GDL: gas diffusion layer; MWCNTs: multi-walled carbon nanotubes.

Meanwhile, intentional increase of the catalyst loading per surface area was achieved by our group. Multiwall carbon nanotubes (MWCNTs) were deposited onto a gas and electron-conducting sheet (GDL; gas diffusion layer), resulting in a forest of interconnected nanotubes. This procedure hence enhances the porosity of the GDL electrode while retaining electronic conductivity. Pyrene-decorated DuBois' nickel bisdiphospine are immobilized onto the electrode support (Figure I.21, right) which is further assembled with a Nafion membrane. The membrane-electrode assembly (MEA) cathodic material catalyzes proton reduction from an aqueous H_2SO_4 0.5 M solution at potentials merged with the thermodynamic one.[33b] Electrocatalytic activity is sustained over hours as an evidence of the stability of the π-π interactions approach. Interestingly, increasing the amount of deposited MWCNTs, increases the grafting density in actives sites up to

the 10^{-8} mol·cm^{-2} range. The activity for HER linearly follows this raise, providing a path to improve performance of such MEAs.

1.4.2.4. Covalent attachment through an electropolymerized film

Interfacial coatings might be obtained by electrochemically assisted polymerization or immobilization of films at a surface of an electrode. These films display pendent reactive moieties purposely designed to achieve covalent coupling with the molecular backbones of HECs. The functionalized electrodes generally preserve the electronic conduction properties.

Pickett and co-workers tackled this strategy by electropolymerizing pyrrole monomers bearing activated ester groups onto a glassy carbon electrode (GCE).[90] Di-iron biomimetic complexes of hydrogenase active sites decorated with an hydroxyl moiety were then covalently bound through transesterification. The supported complex (Figure I.22, left) shows an electrochemical behavior consistent with its homogeneous equivalent. A catalytic peak tentatively assigned to proton reduction is observed at 120 mV more positive than the unmodified electrode, but still lying at large overpotential values.
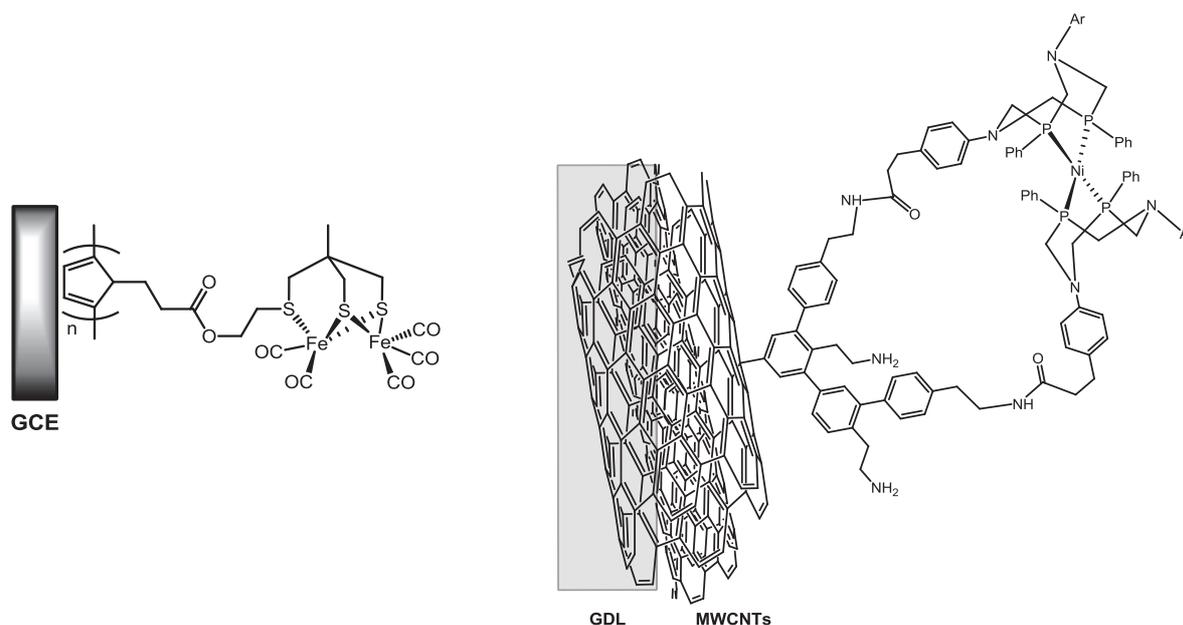
Figure I.22. Di-iron biomimetic catalyst immobilized onto GCE through a polypyrrole film (left) and derivative of a DuBois' nickel bisdiphosphine complex covalently grafted onto MWCNTs (right). Ar = Ph(CH$_2$)$_2$COOPht.

Diazonium salt electroreduction[91] has been set as a popular and efficient way to anchor diverse HECs onto electrodes.[14, 33a, 33c, 83a, 85, 92] For instance, an amino-decorated diazobenzene salt generates an oligomeric layer covalently bound to the electrode surface, possibly carbonaceous. Dangling amino moieties provide an opportunity to create amide bonds with activated esters placed onto molecular HECs. Among others, this strategy was implemented by our group for

alternative functionalization of the GDL/MWCNT assembly described above. A phtalimide moiety introduced on a DuBois' nickel catalyst allows its covalent linkage to the supporting material upon amide formation yielding a stable grafting with a surface density in the range of 10^{-9} mol·cm^{-2}.[33a] Mounted in MEA, the electrode (Figure I.22, right) depicts impressive catalytic performance as the reversible catalysis of proton reduction from a 0.5 M H$_2$SO$_4$ aqueous media. Proton reduction catalysis attains current density of 4 mA·cm^{-2} at 300 mV overpotential. At the same potential, a 10-hour electrolysis reveals steady currents and hydrogen evolution with a near unity faradaic efficiency accompanied with TOFs in the 10^1 s^{-1} range.

This work therefore evidences a straightforward way to strongly anchor molecular catalysts at the surface of a mesoporous electrode designed for MEA while maintaining a high and stable catalytic activity.

1.4.3. Cobalt diimine-dioxime engineered electrodes

Taking advantage of such a path to anchor molecular catalysts onto high surface area electrodes, our group constructed a new cathodic material by the introduction of **[Co^{III}(DO)(DOH)pnCl$_2$]**.[14]

1.4.3.1. Electrode preparation

The supporting material was elaborated first by filtration of a solution containing MWCNTs and Nafion® onto a GDL. The electroreduction of 4-(2-aminoethyl)-benzene diazonium at the mesoporous substrate creates an oligomeric film functionalized with pendent amino groups, yielding the **GDL/MWCNT-amino** electrode (Figure I.23). Meanwhile, the **[Co^{III}(DO)(DOH)N$_3$pnCl$_2$]** azido derivative was coupled to a cyclooctyne ring containing a phtalimide ester moiety (Figure I.23) to afford the **[Co^{III}(DO)(DOH)pnC$_8$PhtCl$_2$]** intermediate.

This procedure is inspired from a methodology developed by Bertozzi and co-workers[93] and bypasses the use of copper-catalyzed conditions that would, in our case, lead to the substitution of copper for cobalt in the **[Co^{III}(DO)(DOH)N$_3$pnCl$_2$]** complex. The copper-free azide-alkyne cycloaddition (Cu-free AAC) occurs spontaneously as a consequence of steric strains on the cyclooctine ring. The activated ester moiety in **[Co^{III}(DO)(DOH)pnC$_8$PhtCl$_2$]** was reacted with the amino-tethered **GDL/MWCNT-amino** electrode under mild basic conditions to form an amide bond (Figure I.23). The procedure yielded the **GDL/MWCNT-Co** electrode where the **[Co^{III}(DO)(DOH)pnCl$_2$]** derivative is covalently linked to the surface of the substrate.
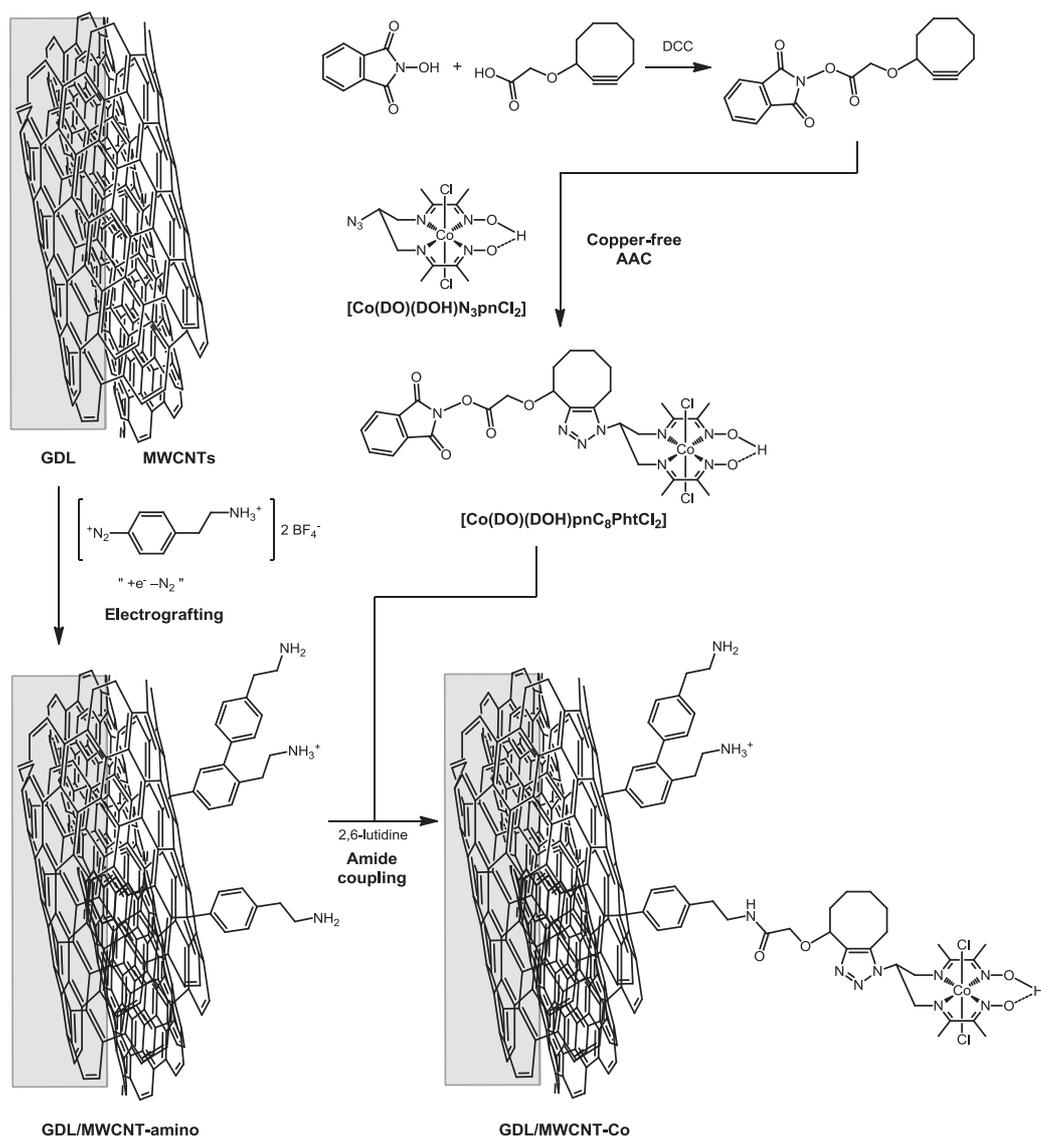
Figure I.23. Synthetic routes for the preparation of the **GDL/MWCNT-Co** electrode. DCC: dicyclohexylcarbodiimide.

1.4.3.2. Electrode characterization

Once functionalized, the electrode was subjected to analysis by electrochemical and spectroscopic methods. Cyclic voltammetry (Figure I.24, left) in MeCN (0.1 M nBu$_4$NBF$_4$) reveals a reversible wave at −1.08 V *vs* Fc$^{+/0}$. This wave is attributed to the Co$^{II/I}$ couple by comparison to the homogeneous **[Co^{III}(DO)(DOH)pnCl$_2$]** species.[54] The Co$^{III/II}$ wave is neither reversible nor well-defined, likely a consequence of the decoordination of the axial chloride ligands upon reduction to Co^{II}. CV also shows a strong background, arising from non-faradaic currents attributed to the mesoporous nature of the **GDL/MWCNT** substrate (Figure I.24, left).
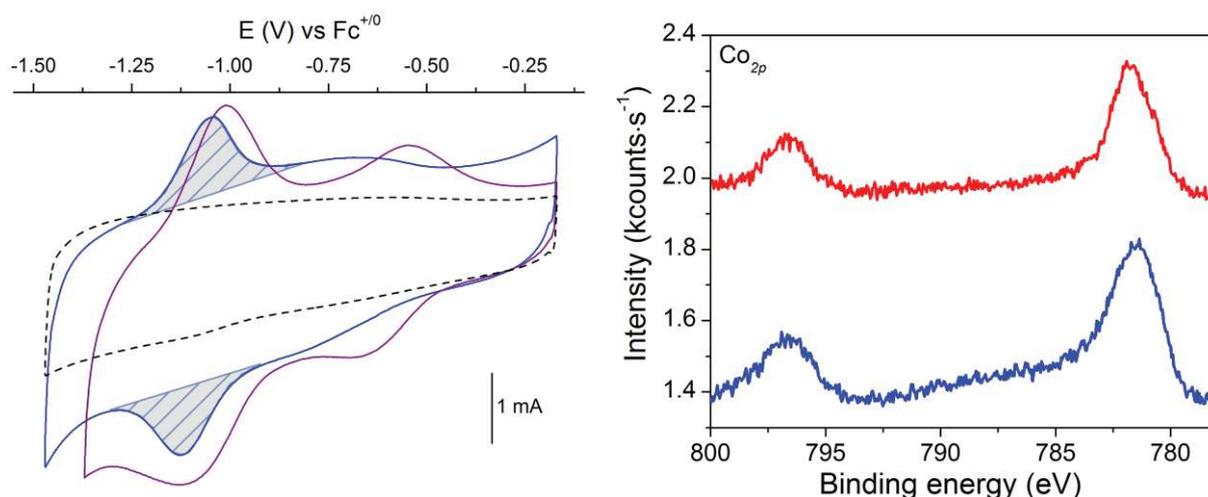
Figure I.24. Cyclic voltamogramms of **[Co^{III}(DO)(DOH)pnCl$_2$]** recorded in MeCN (0.1 M nBu$_4$BF$_4$) at a **GDL/MWCNT** electrode (purple line), of a **GDL/MWCNT-Co** electrode (blue line) and of a control **GDL/MWCNT** electrode (dashed black line) recorded in MeCN (0.1 M Et$_4$NCl) at 100 mV.s^{-1} (left); XPS Co$_{2p}$ core levels of a **GDL/MWCNT-Co** electrode prior (blue line) and after (red line) electrolysis at –0.59 V vs RHE in acetate buffer (0.1M) at pH 4.5 (right).

The intensity of the peak currents related to the Co$^{II/I}$ wave linearly increases with the scan rate. This observation is indicative of a non-diffusive behavior that evidences the immobilization of the cobalt catalyst onto the electrode substrate. Integration of the wave allows to estimate a grafting density around 4.5 10^{-9} mol·cm^{-2}.

At binding energies corresponding to the Co $2p$ levels, the XP spectrum of the functionalized electrode (Figure I.24, right) features two peaks. These peaks are centered at 781.7 and 796.6 eV, shifted by 14.9 eV of spin orbit split, and in a respective 2:1 ratio. The signals are thus attributed to the Co $2p_{3/2}$ and $2p_{1/2}$ core levels, respectively. These Co $2p$ levels display a signature in good agreement with the one of the free **[Co^{III}(DO)(DOH)pnCl$_2$]**. The absence of nearby satellites evidences that the immobilized complex remains in the Co^{III} state when anchored.

1.4.3.3. Electrocatalytic performance

Catalytic activity of the electrode was assessed in fully aqueous media. In a pH 4.5 acetate buffer, the cathodic polarization curve reveals an increase in current which is distinctive from the **GDL/MWCNT** control electrode. The electrochemical setup is equipped with a continuous sampling of the headspace that permits time-resolved GC analysis. Hydrogen evolution was thus detected from ca 350 mV overpotential (E_{onset}) for the **GDL/MWCNT-Co** electrode (Figure I.25, left).

A current density of 1 mA·cm^{-2} is reached by equilibrating the electrode at –0.6 V vs RHE (Figure I.25, right). This current is stable over hours and related to hydrogen evolution in unity faradaic efficiency. During a 7-hour extensive electrolysis the catalyst is found to turn about

55000 times over, with TOFs accordingly in the range 10^1 s^{-1}. It is of note that the supported catalyst performs TONs orders of magnitude higher than in homogeneous solution.[54] This observation reveals the enhancement in stability provided by the immobilization of the catalyst. Also, XPS analysis at the Co *2p* core levels after catalytic turnover (Figure I.24, right) is consistent with the one of the fresh sample. Namely, no lower binding energy peaks characteristic of metallic Co could be detected. This result further supports the preservation of the grafted catalyst upon activity.

Whereas the **[Co^{III}(DO)(DOH)pnCl$_2$]** complex has been reported to decompose at cathodic potentials when it is free in aqueous solution,[94] the stability of the grafted complex is therefore questioning. It is proposed that deactivation in solution may result from intermolecular pathways involving radical attacks on ligands or slow electron delivery, none of which is likely to occur at the decorated electrode. Indeed, the tethered molecular complexes are spatially far from each other on the surface, disfavoring the intermolecular deactivation. Furthermore, the attachment approach implemented here permits a fast electron transfer from the electrode to the catalytic entities, which possibly decreases the lifetime of intermediate reduced species prone to decomposition.
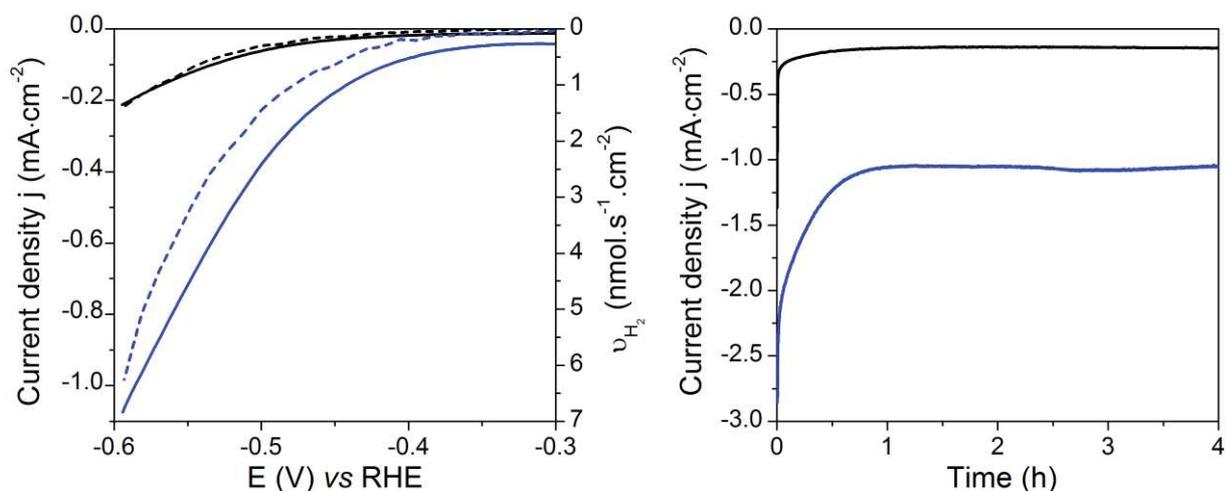

Figure I.25. Current densities (solid lines) and H$_2$ evolution rates as measured by in-line continuous GC setup (dashed lines) recorded during linear cathodic sweeps on a **GDL/MWCNT-Co** electrode (blue lines) and on a control **GDL/MWCNT** electrode (black lines) at 0.05 mV·s^{-1} in acetate buffer (0.1M) at pH 4.5 (left); chronoamperometric measurements on a **GDL/MWCNT-Co** electrode (blue line) and on a control **GDL/MWCNT** electrode (black line) poised at –0.59 V *vs* RHE in acetate buffer (0.1M) at pH 4.5 (right).

This strategy thus proved fruitful to integrate a molecular catalyst on a mesoporous conducting substrates. The engineered cathode steadily evolves hydrogen at low overpotentials from mildly acidic aqueous media. On the basis of these results, the **GDL/MWCNT-Co** electrode will be our starting material to address further issues related to the integration of molecular (photo)cathodes in a device.

2. Molecular engineered photocathodes for hydrogen evolution

It has been demonstrated that molecular catalysts could be integrated into electrocatalytic materials for HER. But to build a light-driven electrode, a photoactive entity has to be introduced in the system. On irradiation, the photoactive entity uses photon energy to provide electrons to the catalyst at a potential suitable for achieving HER. This construction, which permits proton reduction through light irradiation, is called a photocathode for hydrogen evolution. As a central point of the current manuscript, our focus will be directed to photocathodes relying on molecular species for both catalysis and photoactivity. These constructions are usually referred to as dye-sensitized (DS) photocathodes.

The second part of this introduction is dedicated to describing such systems. As proposed for molecular catalysts, the most common metrics used for benchmarking photocathodes will be given. Then, working principles at stake in a DS photocathode will be presented. Following this, the architecture investigated in the present manuscript will be depicted, with particular emphasis on the individual components. Finally, state-of-the-art examples of DS photocathodes are shown to illustrate the approach and to highlight current challenges in the field.

2.1. Figures of merit for photocathodes

The important parameters related to catalysts (activity, stability, operating conditions) and described above in the introduction still apply for molecular photocathodes, but are also extended to the light-harvesting unit. Here, we present a short selection of figures of merit for the evaluation of photocathodes. We note that these figures account for any type of photocathodes, including DS photocathodes.

2.1.1. Photopotential and photocurrent

Overall WS PECs are usually unbiased two-electrode setups.[95] This architecture is required for the final operating device but introduces several device-related issues. In particular, the geometry of the cell or the placement of the electrodes results in undesired additional ohmic and diffusional effects. For this reason, the evaluation of photocathodes is often performed in standard 3-electrode electrochemical cells.[96] This type of setup bypasses such cell-related experimental issues.

In these setups, the linear voltammograms of photocathode could be recorded in the absence (dark or non photoactive electrode with an identical catalyst) or in the presence (light) of

simulated sunlight irradiation (Figure I.26). Under irradiation, as a result of the energetic income of light, the electrons are delivered at the cathode at a given current, which is called a *photocurrent*, and a given potential, which is called a *photopotential*. The most anodic potential at which the two voltammograms dissociate one from each other is called the onset photopotential E_{onset}^{photo}. Under irradiation, when potentials are scanned downward from E_{onset}^{photo}, the current density increases before reaching, in the ideal case, a plateau. This plateau corresponds to the saturating photocurrent J_{sat}^{photo}.
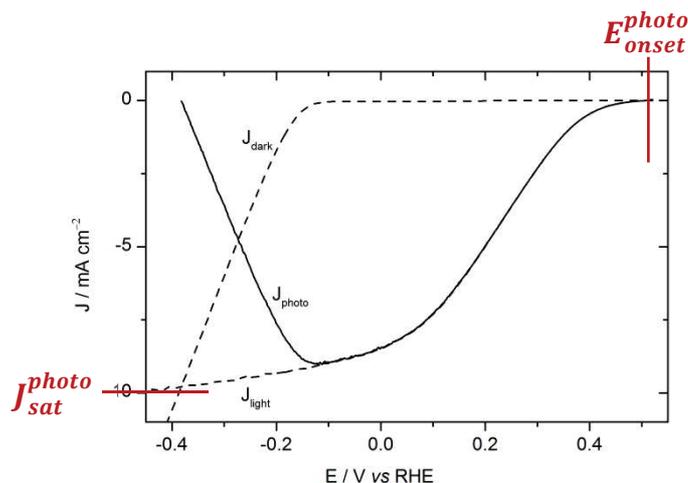
Figure I.26. Linear voltammograms of an ITO\PEDOT:PSS\P3HT:PCBM\LiF\Al\Ti\MoS$_3$ photocathode under irradiation (dashed line, J_{light}) and an ITO\MoS$_3$ cathode in the absence of light (dashed line, J_{dark}) recorded at 50 mV·s^{-1} in H$_2$SO$_4$ 0.5 M.[97] The relative photocurrent J_{photo} is plotted as a function of E^{RHE}. Reproduced and adapted with permission from ref[97], copyright 2015 American Chemical Society.

To be relevant in the context of saving energy through solar fuels, E_{onset}^{photo} has to be positive from the thermodynamic potential of hydrogen evolution.

On the other hand, the saturating photocurrent density is a picture of the global kinetics ruling the electron flow at the photocathode. Namely, these kinetic limitations reflect the competition between productive (catalysis) and unproductive (charge recombination) pathways at the interface. An increased saturating photocurrent is indicative of higher photoelectrocatalytic rates.

2.1.2. Light transformation: LHE, IPCE and APCE

2.1.2.1. Light harvesting efficiency: LHE

The behavior of a photocathode under solar illumination is directly related to its LH/CS properties. These properties can be assessed primary through the determination of the light harvesting efficiency (LHE), by a straightforward transformation of the absorption spectra of the photocathode, as follows:[98]

$$LHE(\lambda) = 1 - 10^{-A(\lambda)}$$ **Eqn. I.18**

where $A(\lambda)$ is the absorbance of the photocathode at a given wavelength λ.

The overall $LHE(\lambda)$ spectrum shows the wavelength intervals at which the incoming irradiation is the most absorbed by the photocathode. To further assess how efficient the conversion of absorbed light into electronic energy is, additional parameters are used.

2.1.2.2. Incident photon-to-current efficiency: IPCE

The incident photon-to-current conversion efficiency (IPCE) indicates the ratio of photons which are converted into electrons at the photocathode. For reasons evoked earlier, practical measurements are performed in a 3-electrode setup poising the photocathode at an applied potential E_{app}. The determination of $IPCE(\lambda)$ is found as:[98]

$$IPCE(\lambda) = \frac{\phi_{E_{app}}^{electrons}(\lambda)}{\phi_{inc}^{photons}(\lambda)} = \frac{\left|J_{E_{app}}(\lambda)\right| \cdot hc}{P_{inc}(\lambda) \cdot \lambda \cdot e} \approx 1240 \cdot \frac{\left|J_{E_{app}}(\lambda)\right|}{P_{inc}(\lambda) \cdot \lambda}$$ **Eqn. I.19**

where $\phi_{E_{app}}^{electrons}(\lambda)$ and $\phi_{inc}^{photons}(\lambda)$ are respectively the fluxes of electrons generated at the applied potential E_{app} by the photocathode and of incident photons, $J_{E_{app}}(\lambda)$ is the current density at the applied potential E_{app} and $P_{inc}(\lambda)$ is the incoming light power density, at the wavelength λ; h is the Planck constant, c is the celerity of the light and e is the elementary charge of the electron.

This definition is however irrespective of the absorbtivity.

2.1.2.3. Absorbed photon-to-current efficiency: APCE

Another metrics takes into account the harvested photons only. This parameter is logically called the *absorbed* photon-to-current conversion efficiency (APCE) and determined as follows:[98]

$$APCE(\lambda) = \frac{IPCE(\lambda)}{LHE(\lambda)}$$ **Eqn. I.20**

A photocathode securing high spectral values of IPCE and APCE is expected to raise high yields for the processes of light harvesting and charge separation.

The IPCE reflects the global performance of the photocathode. Instead, the normalization with the LHE, yielding the APCE, focuses only on the efficiency of the processes once the incident photons have been captured.[98] Especially, in the case of a DS photocathode, the IPCE roughly adopts the shape of the absorption spectrum of the sensitizing dye. This feature is by contrast

flattened on the APCE spectrum, which smoothes the wavelength dependency of the photon-to-current efficiency.

Although these parameters are important figures of merit for a photocathode, they do not include the catalytic process eventually producing the expected solar fuel, hydrogen.

2.1.3. From light to fuel: STH, power saved.

Generation of hydrogen through light-driven HER catalysis is at the core of our approach. Hence, we give here important figures of merit to evaluate the conversion of the solar energy into chemical one.

2.1.3.1. Solar-to-hydrogen efficiency: STH

This metric gives the ratio between energy stored in the hydrogen bond and the incoming light energy. Such a definition is used for 2-electrode setups performing overall WS at an operating current J_{op} under (simulated) solar light and is expressed as this:[96, 99]

$$STH = \frac{|J_{op}| \cdot V_{WS}^0}{P_{inc}^{tot}} \cdot \eta_F = 1.23 \cdot \frac{|J_{op}|}{P_{inc}^{tot}} \cdot \eta_F \qquad \text{Eqn. I.21}$$

where P_{inc}^{tot} is the light total incident power.

We note that this figure of merit gathers information linked to the photocurrent generation in the cell (J_{op}) but also to the holding of a catalytic process (η_F). This metric hence describes the global efficiency of the light-driven HER catalysis. On this, the faradaic efficiency η_F is sometime assumed to be unity, especially when the immobilized electrode is known to operate in dark conditions with 100% efficiency.[98] The calculation of the STH efficiency is then directly derived from the current establishing in the irradiated cell. However, this approximation might induce falsely positive biases in the assessment of the effective light-driven H_2 evolution.

Such a definition only applies for a 2-electrode device. Again, ways to consistently rank photocathodes have been developed for 3-electrode configurations.

2.1.3.2. Ratiometric power saved relative to an ideal electrode

To bypass the use of STH, strategies rely on the determination of the power saved using a photoactive electrode as compared to a dark electrode. Several definitions have been proposed for such metrics. Among others, a simple and natural concept is to refer to an ideal non-polarizable electrode for hydrogen evolution *i.e.* the Reversible Hydrogen Electrode (RHE).
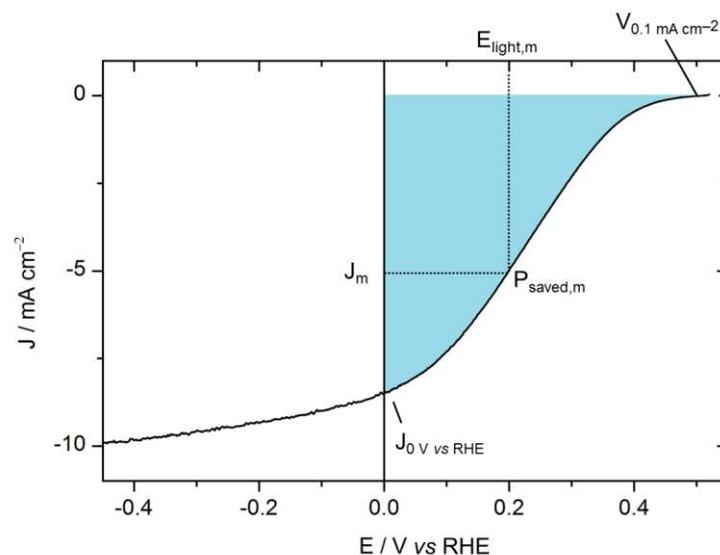
Figure I.27. Linear voltammogram of an ITO\PEDOT:PSS\P3HT:PCBM\LiF\Al\Ti\MoS$_3$ photocathode under irradiation (black line) recorded at 50 mV·s^{-1} in H$_2$SO$_4$ 0.5 M.[97] $E_{light,m}$, J_m and $P_{saved,m}$ respectively corresponds to E_{max}^{RHE}, $J_{light}(E_{max}^{RHE})$ and P_{max}^{RHE} in the text. Reproduced and adapted with permission from ref[97], copyright 2015 American Chemical Society.

First, the power curve should be derived from the linear sweep votammogramm recorded under illumination (Figure I.27, see legend for the equivalence between symbols in the text and on the plot). In that aim, $P(E^{RHE}) = \left| E^{RHE} \cdot J_{light}(E^{RHE}) \right|$ is plotted as a function of E^{RHE}, where E^{RHE} is the potential *versus* RHE, and $J_{light}(E^{RHE})$ is the current density under illumination at the E^{RHE} potential. This curve displays a maximum point of coordinates $(E_{max}^{RHE}; P_{max}^{RHE})$ for positive values of E^{RHE}, with a corresponding current density $J_{light}(E_{max}^{RHE})$. The ratiometric power saved *versus* RHE Φ_{saved}^{RHE} then relates to this maximum power point and is given by the following equation:[96-97]

$$\Phi_{saved}^{RHE} = \frac{\left| J_{light}(E_{max}^{RHE}) \right| \cdot E_{max}^{RHE}}{P_{inc}^{tot}} \cdot \eta_F \qquad \qquad \textbf{Eqn. I.22}$$

This metric compares the performance of a photocathode to the one of an ideal dark electrode. Hence, this figure of merit reflects the *absolute* power saved by using the photocathode at its maximal efficiency.

2.1.3.3. Ratiometric power saved relative to an identical non photoactive electrode

It is also interesting to measure the impact of the electrode photoactivity on the extent of the power saved. The comparison to a non-photoactive electrode bearing the same catalyst and assessed under identical but dark conditions has been proposed.
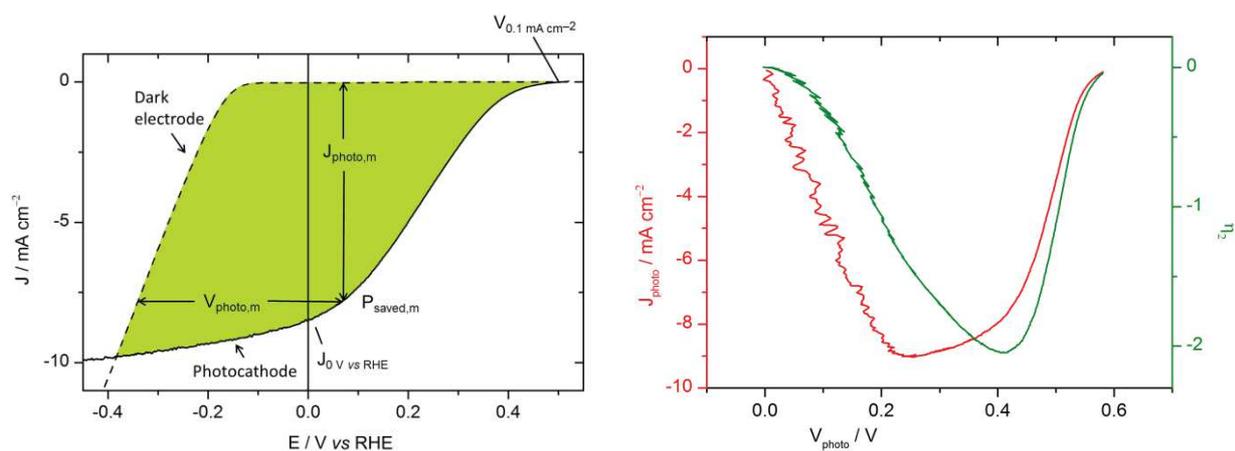
Figure I.28. Linear voltammograms of an ITO\PEDOT:PSS\P3HT:PCBM\LiF\Al\Ti\MoS$_3$ photocathode under irradiation (black line) and an ITO\MoS$_3$ cathode in the absence of light (dashed black line) recorded at 50 mV·s^{-1} in H$_2$SO$_4$ 0.5 M (left) and relative photocurrent density (red line, left scale) and power (green line, right scale) as a function of the photovoltage (right).[97] $V_{photo,m}$, $J_{photo,m}$ and $P_{saved,m}$ respectively corresponds to $\boldsymbol{V_{photo,max}}$, $\boldsymbol{J_{photo}(V_{photo,max})}$ and $\boldsymbol{P(V_{photo,max})}$ in the text. Reproduced and adapted with permission from ref[97], copyright 2015 American Chemical Society.

The maximum power point has also to be calculated. Here, the treatment is based on the voltamogramms recorded under irradiation for the photocathode and in the dark for its non photoactive component (Figure I.28, left; see legend for the equivalence between symbols in the text and on the plot). First, the substraction of these voltamogramms gives the relative photocurrent curve $J_{photo}(E^{RHE}) = \left| J_{light}(E^{RHE}) - J_{dark}(E^{RHE}) \right|$, where $J_{dark}(E^{RHE})$ is the current density in the dark for the non photoactive electrode at the E^{RHE} potential. Similarly, to every photocurrent density J value corresponds a value of the $V_{photo}(J)$ photovoltage. This photovoltage is actually defined as $V_{photo}(J) = \left| E_{light}^{RHE}(J) - E_{dark}^{RHE}(J) \right|$ where $E_{light}^{RHE}(J)$ and $E_{dark}^{RHE}(J)$ are the potentials *versus* RHE at the current density J respectively in the presence of light for the photocathode and in the absence of light for its non photoactive counterpart. Analytic treatments of the thusly obtained data gives the $J_{photo}(V_{photo})$ relative photocurrent density-photovoltage curve and the $P(V_{photo}) = V_{photo} \cdot J_{photo}(V_{photo})$ power curve (Figure I.28, right). The power takes a maximal value $P(V_{photo,max})$ at $V_{photo,max}$. The Φ_{saved}^{NPAC} ratiometric power saved relative to the non photoactive electrode with the identical catalyst and tested in similar but dark conditions is then defined as:[97, 99b]

$$\Phi_{saved}^{NPAC} = \frac{\left| J_{photo}(V_{photo,max}) \right| \cdot V_{photo,max}}{P_{inc}^{tot}} \cdot \eta_F \qquad \textbf{Eqn. I.23}$$

Such a definition is actually independent of the overpotential of the dark catalyst. This figure of merit is indicative of the added value in terms of power saved that is attributed to the introduction of a photoactive moiety on the electrode.

In both cases, the faradaic efficiency η_F might be assumed as unity, although, as said earlier, its determination provides stronger data in terms of effective power saved into fuel. If Φ_{saved}^{NPAC} gives crucial information on the income of the light on the energy stored, the absolute aim is to optimize Φ_{saved}^{RHE}.

Until now, these power saved metrics have mainly been applied to photoelectrodes relying on material-made components for light-harvesting and/or catalysis. Indeed, only few examples of DS photocathodes have been published to date.[85] All the more, the moderate performance of the reported examples make the measurement of power saved efficiencies quite tedious. Yet, the recent interest in this type of photocathodes will possibly result in improved performance permitting the benchmarking of their power-saved efficiencies.

2.2. Molecular photocathodes for hydrogen evolution

This last section is dedicated to the description of DS photocathodes. Firstly, the background for the construction of DS photocathodes for HER will be presented. Then, possible components envisioned for the construction targeted in the current work will be described. An overview of molecular-based photocathodes will be given in a last step. A more precise description of the few reported examples of DS photocathodes, including their integration in overall WS cells, closes the introduction.

2.2.1. General features in DS photocathodes

The following part aims at laying the fundamentals operating principles in a DS photocathode, within the general concepts. Details will be discussed later, along with the description of the components used.

2.2.1.1. Requirements

H_2-evolving DS photocathodes have to gather a catalytic species able to perform HER as well as a dye responsible for light harvesting (LH) and charge separation (CS). To create an electrode material possibly integrated into a device, the immobilization of these two chemicals on the same surface is required.

About half the photons striking the Earth are in the visible range (between *ca* 400-800 nm). To harvest this photonic energy the dye should be engineered for adsorption in the visible range.

Also, the electrode material should not stop such photons and thus it has to be transparent at visible wavelengths.

In addition, the conductive supporting electrode has to favor electronic injection from the surface to the LH/CS entity, as needed for the photoinduced reduction of protons. Such a character is usually found in materials displaying an electronic structure in bands, e.g. semi-conductors (SC). A class of materials securing the whole set of requirements (visible transparency, semi-conducting properties) are the transparent semi-conducting oxides,[100] which are often referred to as transparent *conducting* oxides (TCOs), for the sake of simplicity. Logically, TCOs are used to act as supporting electrodes at the top of which could be immobilized both LH/CS and catalytic moieties. The nature of the material also drives the possible ways to attach these molecules onto the surface.

In a following part, we will describe more extensively the anchoring groups available for grafting molecules onto these surfaces.

2.2.1.2. Operation principle

The approach developed in DS photocathodes is based on a multiplicity of concomitant processes at the material/dye-catalyst/solution interface (Figure I.29).[86, 101] First, the absorption of a photon leads to an excited state of the dye (shown as 1 in Figure I.29). More precisely, the energy of an electron of the dye is raised from the highest occupied molecular orbital (HOMO) to the lowest unoccupied molecular orbital (LUMO). Then, the HOMO of the dye is regenerated by electronic injection from the conducting band of the TCO (2). This reduction of the excited dye creates a positive equivalent, a hole (h^+), in the TCO. Replenishing this hole actually generates a photocurrent, a main characteristic for photocathodes, as discussed above. Meanwhile, the electron on the LUMO of the dye is used to reduce the nearby HEC (3). If the whole process (1-2-3) is repeated twice, the catalyst accumulates two reducing equivalents and can hence turn over to evolve H_2 from 2 H^+. The interface is continuously fueled in electrons at the E_{app} potential applied by an external electric generator or a photoanode. Electronic shuttling to the interface is ensured through the conducting band of the TCO.

Besides, unproductive processes counter act this H_2-evolving pathway. Among them, the recombination of an electron on the LUMO with a hole located in the TCO conducting band (4) is a major issue. As well, similar electron-hole recombinations are possible from the reduced catalyst to the conducting band (5) or to the excited dye (6).
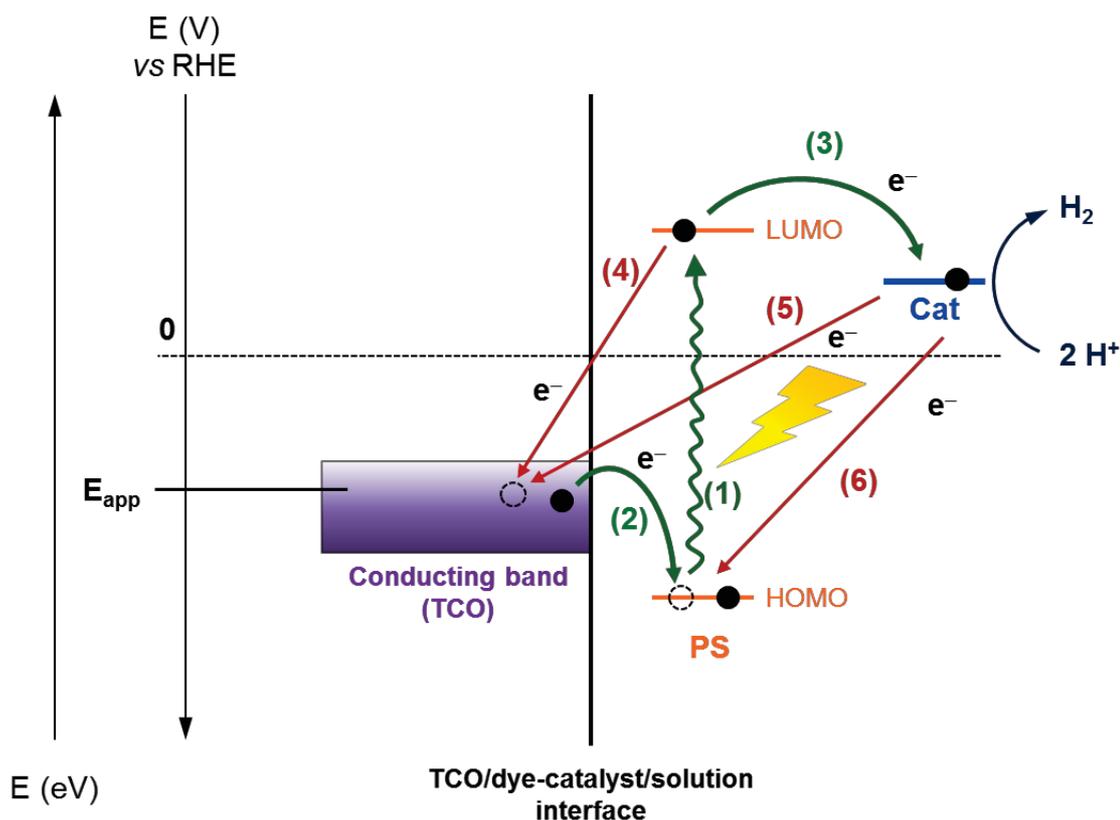
Figure I.29. Schematic representation of processes involved in the light-driven HER by a DS photocathode. Plain dots: electrons; empty dots: holes; *PS*: photosensitizer; *Cat*: catalyst; E_{app}: applied potential.

In a general manner, the kinetic competition between productive and unproductive processes governs the global performance of the DS photocathode.

2.2.1.3. Background

To build DS photocathodes for HER, inspiration has been found with photoelectrodes for DSSCs and for water oxidation. In both cases, the properties of semiconducting transparent materials decorated with a dye are utilized either to generate electricity or to achieve electrocatalytic reactions.

2.2.1.3.1. Band theory

To better understand the role of these materials, they have to be examined under the light of the band theory in SCs. Roughly, this theory describes the electronic structure of SCs with two bands: a valence band (VB) at lower energies and a conduction band (CB) at higher energies, separated one from each other by a band gap, in which the density of states is in theory nil.

n-type SCs have their valence band completely filled with electrons whereas the conduction band is only partially filled. Hence, the Fermi level (E_F) of the SC is just downward from the

conduction band. In *n*-type SCs, the electronic conduction is realized by electrons in the conduction band, which are the majority charge carriers. These charge carriers are negative, that gives the "*n*" in "*n*-type" SCs.

On the contrary, for a *p*-type SC, the conduction band is empty while the valence band contains some electronic vacancies, the holes. The Fermi level is then located just upward from the valence band. The holes in the VB, which are the majority charge carriers ("*p*" for positive), are responsible for the electronic conduction within the material.

2.2.1.3.2. A transversal inspiration

In DSSCs, the photoelectrode is made of a dye adsorbed at the surface of a transparent SC. Upon irradiation, the excited state of the dye can give or take an electron from the SC and be regenerated by a redox shuttle in solution. The overall process creates a photocurrent. Classical DSSCs, or Grätzel cells, are known as *n*-type DSSCs, since the support of the photoelectrode is a *n*-type SC (usually TiO_2).[102] In this case, the excited dye injects an electron in the CB of TiO_2 and oxidizes a redox shuttle. Their counterpart constructed with *p*-type SCs are called *inverse* DSSCs, as the electronic flux is found to occur in the inverse way. Their development emerged in the early 2000's,[103] with the global aim to construct tandem DSSCs coupling *n* and *p*-type photoelectrodes to overpass limits of efficiency of classical Grätzel cells.[103-104]

In DS PECs, the final electron or hole acceptor at the photoelectrode is not a redox shuttle, but a chemical to be irreversibly oxidized or reduced. To create DS photoanodes for OER, at which water is oxidized into oxygen, the architecture of the photoelectrode has logically been derivatized from that featured in well-established *n*-type DSSCs. Similarly, the inspiration can be taken from *p*-DSSCs to create DS photocathodes for HER.

Also, the translation from photoanodes in *n*-DSSCs to oxygen-evolving DS photoanodes faced several challenges, among which shifting from organic to aqueous electrolyte or co-anchoring a catalyst. The same challenges apply to go from DS photocathodes in *p*-DSSC to DS photocathodes for HER. The knowledge brought by the anodic part should thus facilitate the design of such photocathodes. Still, only few examples of DS photocathodes for HER have been reported to date,[85-86, 105] compared to DS photoanodes for OER.[106] These photocathodes present strong similarities, borrowed from *p*-DSSCs, as far as the supporting SC, the dye or the strategy for surface anchoring are concerned.[85-86, 105]

The following paragraphs aim at overviewing the materials available to build DS photocathodes for hydrogen evolution.

2.2.2. Constructing photocathodes for hydrogen evolution

In this part, we will focus on the TCO, the PS and the way to attach molecular entities at the surface. Only few molecular catalysts have been used to create DS photocathodes for HER, they will be shown within the architectures described in the last section.

2.2.2.1. Transparent conducting oxides

2.2.2.1.1. General considerations

As exemplified in Figure I.29, a major and necessary feature of a TCO relevant for the construction of a DS photocathode is the presence of a band that can deliver electrons at an energy higher than the HOMO level of the dye.[85-86, 105] Translated in the band theory of SCs, this point means that the SC should display a Fermi level located upward from the HOMO level of the dye.

With Fermi levels located in this suitable region, wide band gap *p*-type SCs have been a matter of choice first for application in inverse DSSCs then for application in H$_2$-evolving DS photocathodes.[101, 107] Their partially filled VB permits electronic conduction by holes within the material. Moreover, holes formed upon photoexcitation of a grafted dye might be injected into the VB, securing their collection and transport. This phenomenon constitutes a fundamental prerequisite for such photoelectrodes. In the case of DS photocathodes, we note that the value of the onset photopotential (E_{onset}^{photo}) is generally close to the top edge of the VB.

Nickel oxide (NiO) is a wide band gap *p*-type SC with a Fermi level adapted to the required electron injection properties. Moreover, NiO is also *quasi*-transparent. For these reasons, it has been chosen as the *p*-type transparent material in the large majority of the studies on inverse DSSCs.[101, 107] NiO is now logically utilized for the construction of proton or CO$_2$ reduction DS photocathodes. Only punctual investigations on alternative p-type TCOs, such as mixed metal-copper delafossites, have been reported to date in the field of inverse DSSCs.[108]

As a note, recent studies also showed that a degenerated *n*-type SC (ITO) with quasi-metallic properties might be used in inverse DSSC schemes,[109] provided the energy matching between the CB of the SC and the HOMO level of the dye is well controlled.[109b]

2.2.2.1.2. Nickel oxide films for DS photocathodes

With the knowledge brought by *p*-type DSSCs, all DS photocathodes for hydrogen evolution reported so far are based on NiO as the TCO layer.[79, 99] NiO is usually prepared as a nanostructured film.[110] A wide variety of preparations exists starting from a molecular Ni precursor or from preformed NiO nanoparticles. The nanostructuration is obtained after a high temperature annealing process (solvothermal, sol-gel, etc.), typically between 300-500°C.[110] The

nanotemplated NiO offers high surface areas (in the 10^1 m^2·g^{-1} range) which are desired for improving dye and/or catalyst loading.[110] NiO films are usually deposited on a back contact substrate made of a conductive glass layer, commonly FTO or ITO.

The nanostructured film displays interconnected crystallites of NiO in the NaCl centered face cubic structure with octahedral geometries for both Ni and O atoms. Actually, these crystallites are overstoichiometric in O^{2-} ions, resulting in Ni^{2+} vacancies. To keep the charge balance, the non-stoichiometry leads to the creation of Ni^{3+} sites that represent the introduction of holes in the valence band (Figure I.30).[111] Despite this non-stoichiometry and for the sake of clarity, we will use the generic term NiO in the current manuscript, whereas the true structure is more accurately described as NiO_x where x represents the stoichiometry of oxygen in the structure. The $Ni^{III/II}$ mixed valence is believed to be the origin of p-type character as well as the greyish coloration of nanocrystalline NiO films.[111-112] NiO presents a wide band gap of ca 4 eV.[111] The VB was originally reported as being about 0.54 V vs NHE at pH 7.[103, 112] A more recent study gives a flat-band potential, that corresponds to the bulk material away from any surface band bending, at about 0.30 V and a top edge of the VB at 0.37 V both vs NHE at pH 7.[113] Despite the discrepancy in such values, both may be suitable for hole injection from an interfacial dye.

The intrinsic conductivity (by holes) of bulk NiO is 2 to 3 orders of magnitude lower than the conductivity of the n-type benchmark counterpart TiO$_2$.[101, 113] The blame has been put on this moderate conductivity to rationalize poor performances of NiO p-DSSC compared to n-DSSC.[101, 107, 114] This low conduction is accompanied with a short hole diffusion length (few μm).[110] Added to this the intrinsic light absorption on NiO that prevents a part of the incident photons to reach the dyes, the optimal film thickness for NiO photoelectrodes is reported around 2 μm.[110] This value is much thinner than state-of-the-art TiO$_2$ Grätzel cells. The resulting less intense dye loading also accounts for the low performance of the NiO-based photoelectrodes.[101]

But nanostructured NiO films also present defects due to their preparation.[110-111] These defects are namely localized specific surface sites (typically surface Ni^{3+}).[101, 110, 115] Hole hopping through these surface states is proposed to take part to conduction in a substantial way.[101, 110, 113, 116] Recent reports gave some pieces of answer about this phenomenon,[114, 115c] and the possibility to reach high currents with NiO electrodes has been stated.[114] Such results further question the reason for the limitations on photocurrents observed in NiO p-DSSCs.
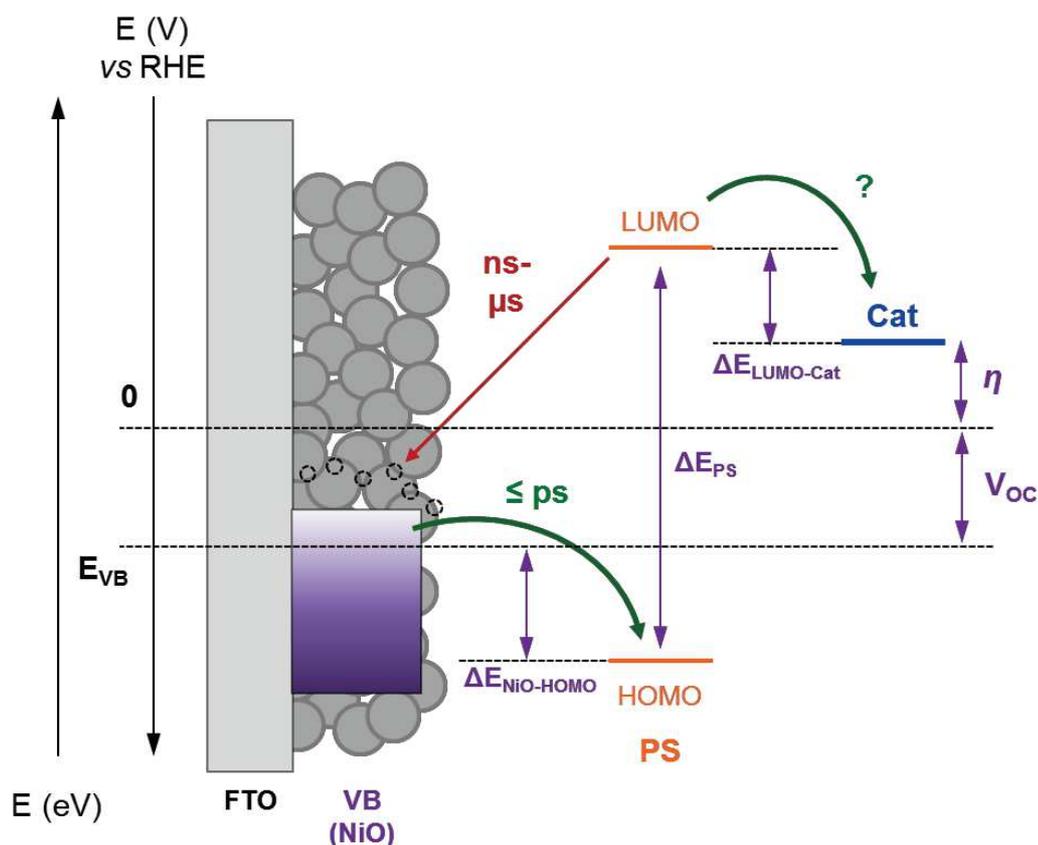
Figure I.30. Simplified view of kinetic and thermodynamic parameters involved in charge transfers at the NiO/PS/catalyst interface. E_{VB}: VB top edge potential; V_{OC}: open-circuit voltage; ΔE_{PS}: PS electronic band gap; $\Delta E_{NiO\text{-}HOMO}$: driving force for electronic transfer between the NiO VB and the excited PS HOMO; $\Delta E_{LUMO\text{-}Cat}$: driving force for electronic transfer between the reduced PS LUMO and the catalyst. Empty dots: surface holes. Other abbreviations as defined above.

Overall, the possibility of mixed valence sites in the bulk and at the surface explains a peculiar native redox signature of NiO as well as its electrochromic properties.[111] The surface confined oxidation or reduction processes are namely coupled with ion exchanges, especially in the case of aqueous electrolytes.[110, 115a] This process typically leads to two broad waves around 0.5 and 0.9 V *vs* NHE at pH 7, assigned in an oversimplified view to the oxidations of Ni^{II} to Ni^{III} then Ni^{IV} (waves I and II in Figure I.31, left, respectively) coupled with proton losses at the surface (Figure I.31, right).[110, 115a] We will come back later in the current manuscript on electrochemistry at the NiO/electrolyte interface.

Despite its temperamental chemistry which renders it preparation-dependent and the multiple questions around its conductivity, NiO has been used in the first place to build *p*-DSSCs and DS photocathodes, for practical and synthetic reasons.[101, 110] In this project, NiO will serve as the supporting TCO for the construction of DS photocathodes.
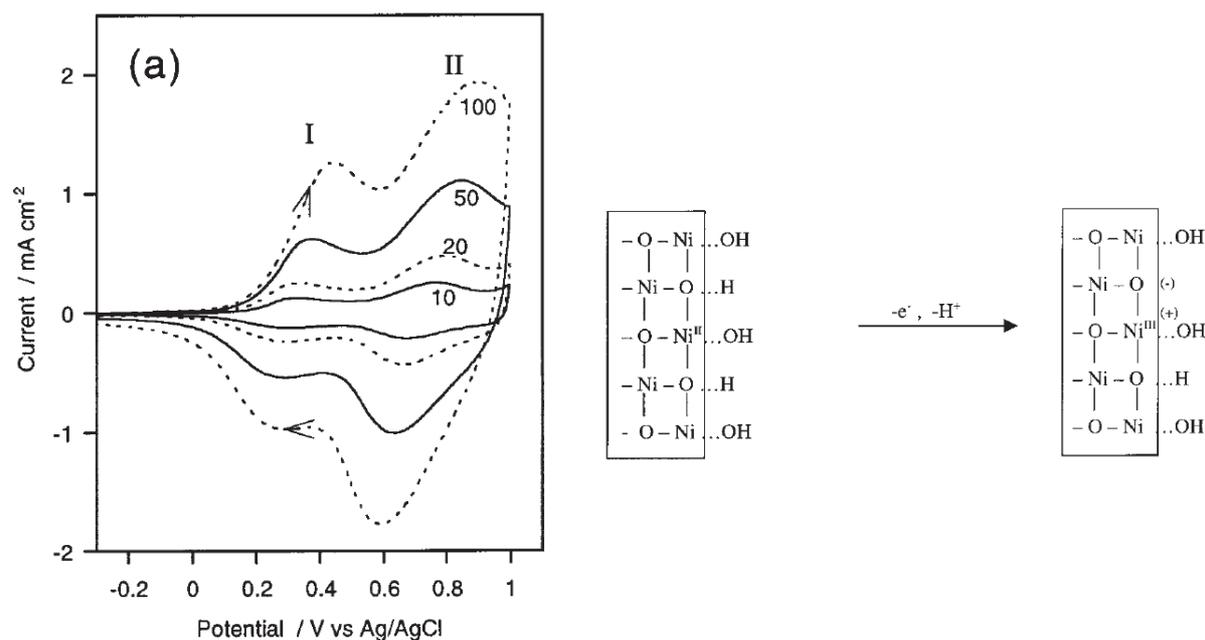
Figure I.31. CVs at a nanostructured NiO film recorded in aqueous 0.2 M KCl, 0.01 M potassium phosphate buffer at pH 6.8 at different scan rates indicated on the graph (left) and proposed proton-coupled electron transfer for oxidation at wave I (right). Reproduced and adapted with permission from ref[115a], copyright 2001 American Chemical Society.

2.2.2.2. Photosensitizers

To harvest a maximum of solar photons, the dyes for use in DS photocathodes have to present a broad absorption, particularly in the visible region. Also, the optimal film thickness of NiO is about 2 μm, as said above, which limits the amount of dyes possibly loaded per geometric surface area.[110] Photosensitizers with high molar extinction coefficients are thus good candidates for use in NiO-based photoelectrodes.

Energetically speaking, to enable hole injection from the excited dye into the VB, a first requirement is that the HOMO level of the dye should match the VB levels, but should not be upward. As well, the LUMO level should locate higher than the potential of the H^+/H_2 couple. Especially, the LUMO has to realize electronic injection into the catalytic state of the considered HEC. This assumption implies that the LUMO level is separated from RHE with more than the overpotential requirement of the HEC.[86, 105] These specifications are usually met by the synthetic tuning of Ru(bpy)$_3$-like photosensitizers or purely organic dyes.[85-86, 105]

Along with these energetic considerations the charge transfer kinetics has to be examined. Especially, the hole injection from the excited dye to the NiO VB should be faster than the relaxation of the dye. This process might be facilitated by an intimate coupling between the HOMO of the dye and the VB of the SC. Such a coupling would rely on the hybridization of these orbitals, which is directly related to the electronic properties of the anchoring group linking the

dye to the surface. Carboxylic acid is widely utilized in *n*-DSSCs as an electron-rich attachment moiety prone to ease electronic injection in TiO$_2$ CB.[101, 102b] Despite this behavior that might not be adapted to hole injection in NiO,[117] the large majority of reported NiO *p*-DSSCs and H$_2$-evolving DS photocathodes are based on carboxylate anchoring groups. Still, hole injection in the VB is commonly found to occur quite fast, in the pico- to subpicosecond time scale (Figure I.30).[101 118]

Yet, the major bottleneck is that the charge recombination between the reduced dye and the holes in the VB is also quick, falling in the nanosecond range (Figure I.30).[118b, 118c] Such a fast recombination is likely a central phenomenon that limits the performance of dye-sensitized NiO photoelectrodes. The rapide nature of this unproductive process has been tentatively ascribed to the presumed hole conduction by surface states. Surface holes would actually act as nearby sites available for the recombination of energetic electrons on the reduced dyes.[101, 115b, 115c, 118c]
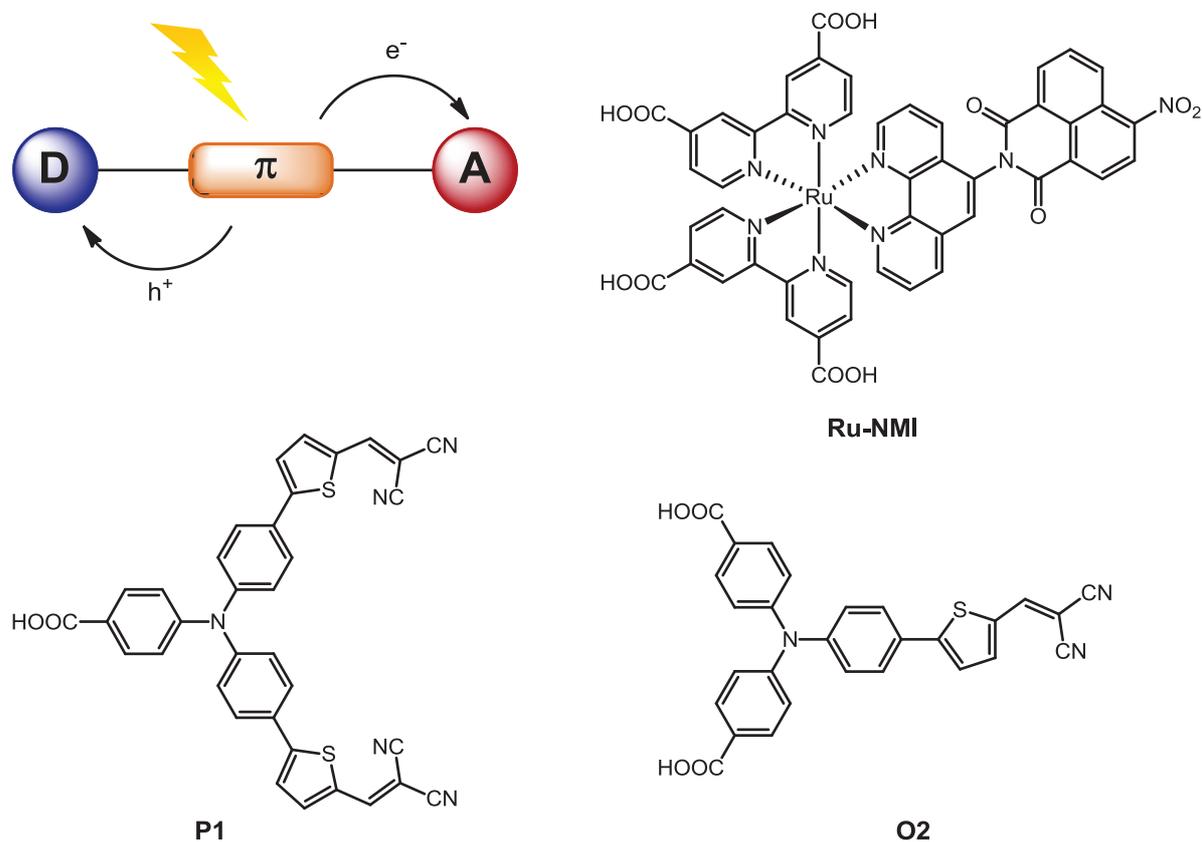
Figure I.32. Working principle (top left) and selected examples of "push-pull" dyes or Ru(bpy)$_3$-like (**Ru-NMI**) either organic (**P1**, **O2**) ones. A: electron acceptor moiety; D: electron donor moiety; π: π-conjugated part.

To hinder this recombination, "push-pull" photosensitizers have been used, borrowed to the field of *n*-DSSCs.[102b] These PSs gather on the same molecule an electron donor moiety and an electron acceptor one, situated at the opposite ends. Under irradiation, they experience a substantial spatial charge separation, the electron density being pushed from the donor moiety far

on the acceptor moiety pulling it (Figure I.32, top left). Moreover, the electron donor part is bearing the anchoring groups to surface, which promotes fast hole injection. Thus, the electronic density of the reduced dye is farer away from surface, which is important since the recombination rate is decreasing with distance[119] in an exponential manner if tunneling is considered.[101] The application of such a strategy to either Ru bipyridine-like[120] or, more commonly, fully organic dyes[121] (Figure I.32) proved fruitful to construct *p*-DS photocathodes integrated in DSSCs and DS PECs. Pulling the electron acceptor farer away from the surface while ensuring a good orthogonality between the HOMO and LUMO levels,[122] as exemplified in Figure I.33, resulted in long-lived charge separated states ranging in the microsecond scale.[122a, 122d] Such dyes lead to photocathodes utilized in the top record *p*-DSSCs[122d] and for light-driven hydrogen evolution.[123]

n = 1,2,3

TPA-nT-PMI
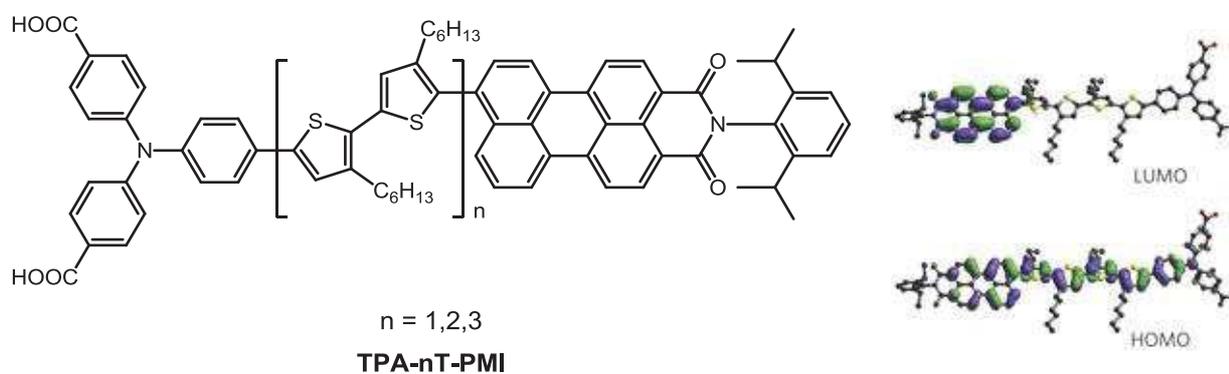
Figure I.33. Push-pull organic photosensitizer bearing a secondary perylene-monoimide electron acceptor (left) as illustrated by the electron-density distribution on the LUMO level (right). Reproduced and adapted with permission from ref[122d], copyright 2010 Nature Publishing Group.

Such noble–metal free organic push-pull dyes also present higher molar extinction coefficient compared to Ru(bpy)$_3$-like ones.[102b] All together, these properties make the organic dyes particularly interesting platforms for the development of DS photocathodes for HER. The synthetic chemistry at stake opens rooms for tuning the electronic properties, for further derivatization and for introducing adequate grafting moieties.

2.2.2.3. Anchoring groups

2.2.2.3.1. General considerations

Multiple strategies could be envisioned to attach dyes and catalysts at the surface of TCOs, like NiO. The majority of the approaches described above for the immobilization on non-photoactive materials extend to DS photocathodes, with the exception of π-stacking interactions, requiring a π-conjugated surface absent in TCOs. Especially, the condensation between metal-bound hydroxyl groups that are present at the TCO surfaces and a specific anchoring moiety on the molecular entity (dye/catalyst) has proved particularly well suited for attachment on TCOs.[124] Such a

pathway has been applied to a large number of metal oxide surfaces. But the formation of the grafted (mono)layer as well as its hydrolytic stability logically experiences a dependence with the nature of the TCO surface.[124] In a general way, the surface concentration of available hydroxyl groups might be increased by various means (etching, plasma or ozone-treatment, etc.) to favor the anchoring and the stability of the molecular layer. As well, post-grafting procedures, as improved condensation through thermal curing or deposition of protecting atomic layers, generally result in stronger attachments.[124]

2.2.2.3.2. A variety of possible anchoring groups

A wide panel of grafting groups[124] exists, which are either based on reactive carbon-carbon (alkene[125] or alkyne[126]) or carbon-heteroatom (halogenide[127] or hydroxyl[128]) bonds or on multidentate moieties (silanes, carboxylic or phosphonic acids, etc.).[124]

On the one hand, the reactive carbon-carbon and carbon-heteroatom precursor groups are known to yield stable surface layers onto TCOs in aqueous solutions.[124] Such layers are usually prepared by UV-induced radical pathways for carbon-carbon moieties, or condensated through thermal Williamson-like ether formation for the carbon-heteroatom ones. Both processes are preferentially realized from a neat solution of the pure molecular entity, which thus needs to be liquid. Yet, the large majority of dyes and catalysts are solids under atmospheric conditions and would not suffer harsh thermal or UV-induced activations. For these reasons, such grafting strategies that proved fruitful elsewhere might not be applied easily to our construction of DS photocathodes.

On the other hand, a large number of anchoring groups that display multidentate properties, such as silanes, carboxylates, phosphonates, cathecolates, hydroxamates or acetylacetonates,[124] have been screened for the covalent attachment onto TCOs. Among them, silanes, carboxylates and phosphonates are the most utilized anchoring groups in the directly related fields of *n*-DSSCs,[102b, 124, 129] and DS photoanodes for OER.[130] As a consequence, their properties regarding grafting, electronic coupling and stability onto TiO_2 have been extensively studied. As such, these groups constitute a benchmark for the development of *p*-DSSCs and DS photocathodes although their anchoring onto NiO surfaces has been much scarcely investigated. Silane, carboxylate and phosphonate bindings are briefly presented here, with a short highlight on the last two ones.

Indeed, silanes rapidly form covalent linkages ideally yielding a self-assembled monolayer (SAM) onto the TCO substrate and are thus harnessed in quite diverse areas.[124, 131] But silanes are quite prone to self-aggregation, the process of which is favored by high water and/or silane precursor concentrations. As a consequence, the binding is much dependent of the immobilization

procedure and often leads to multi-layers. This issue is partially solved by the use of silatrane groups that foster ideal cross-linked monolayers.[132] Yet, the immobilization with silanes is also deeply hampered by a well known hydrolytic instability, even in mildly aqueous solutions.[124] This main drawback prevents them to be widely utilized in DS photoelectrodes for WS.

2.2.2.3.3. Carboxylate binding

Interlinkages involving carboxylic acids have been broadly harnessed onto TCOs, especially for the attachment of dyes at the surface of TiO_2 in DSSCs.[102b, 129] Carboxylic acids are found to generate different binding modes (Figure I.34, left) as commonly evidenced through infrared (IR) or XPS.[124, 133] Electrostatic or H-bonded architectures, also called outer-sphere adsorption complexes, reveal particularly weak. But thermal conditions might promote the formation of more stable inner-sphere adsorption complexes (Figure I.34, right). Whether the adsorption involves a mono- or bi-dentate bridging is also believed to influence the strength for attachment.
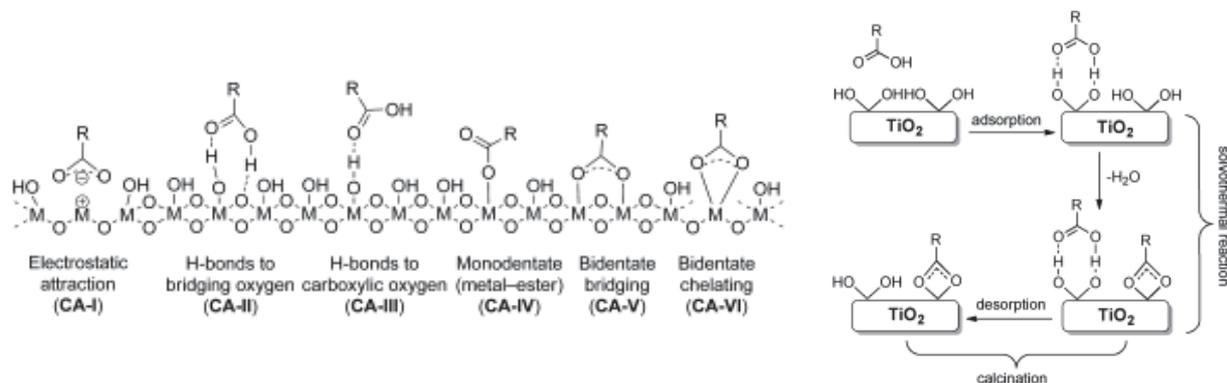
Figure I.34. Possible binding modes for interactions with carboxylate at the surface of TCOs (left) and solvothermal condensation of physiadorbed to chemiadsorbed carboxylate onto TiO_2 (right). Reproduced and adapted with permission from ref[124], copyright 2014 John Wiley & Sons, Inc.

Nonetheless, the carboxylate linkages are well known to be prone to facile hydrolysis.[132b, 134] This point is particularly noteworthy in the context of water splitting where the aqueous media, likely acidic at the photocathode, could accelerate the desorption. To bypass this weakness, dyes displaying several carboxylic acid groups have been designed and successfully integrated into NiO based p-DS photocathodes.[122d, 123, 135] For instance, Ru trisbipyridine-like derivatives bearing two carboxylic acids proved to display a high affinity for the attachment to NiO surface compared to other grafting moieties.[135] Along with this strategy, a rather easy synthetic chemistry and simple attachment procedures also render the carboxylic acid derivatives an interesting option for grafting dyes/catalysts onto NiO.

2.2.2.3.4. Phosphonate binding

The anchoring through phosphonate binding is known to display good hydrolytic stability.[124, 136] Such layers might be obtained from phosphonic acids, rather insoluble in organic solvents, or alternatively from phosphonate ester derivatives. Various media can hence be used for their immobilization. This feature permits an appropriate choice of solvent, eventually driving the formation of highly packed monolayers. [124, 136a]
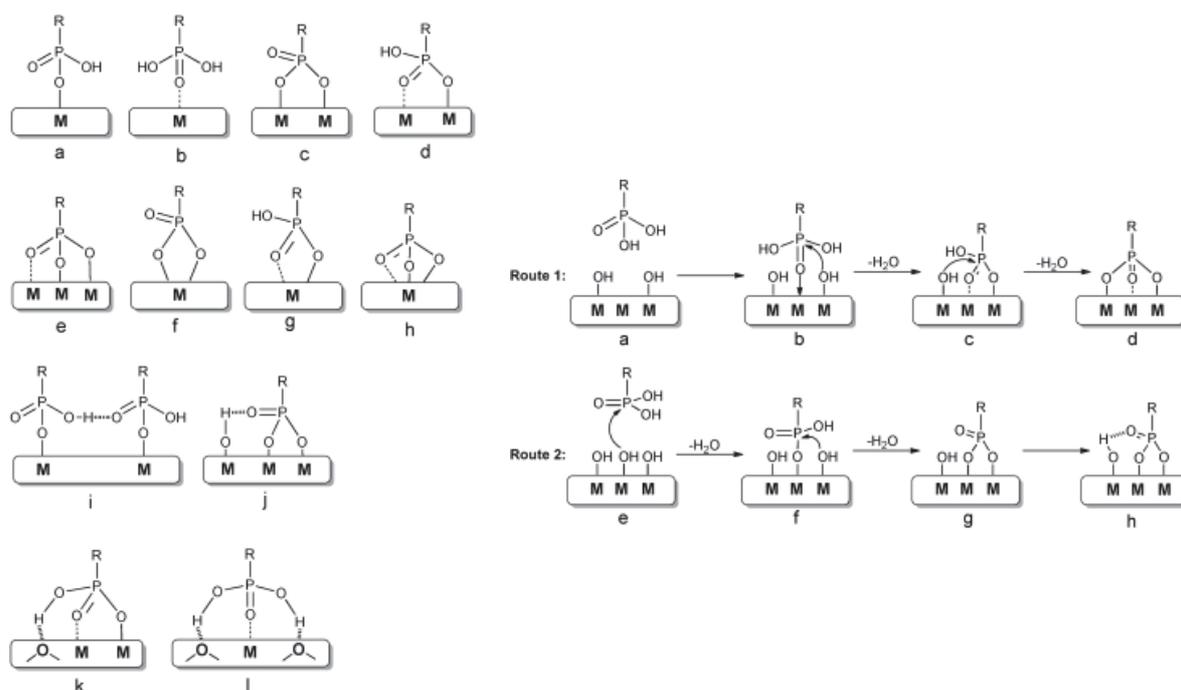

Figure I.35. Possible binding modes of phosphonates at a TCO surface (left) and mechanisms of condensation for the formation of phosphonate anchored monolayers with a Lewis acidic (route 1) or weakly Lewis acidic (route 2) TCO metal (right). Reproduced and adapted with permission from ref[124], copyright 2014 John Wiley & Sons, Inc.

Other reaction parameters such as temperature, pH or ionic strength also affect chemisorption of the phosphonate groups.[136b] Indeed, as for carboxylate, phosphonate anchored moieties display mono-, bi-, or tridentate binding modes that might involve hydrogen bonds (Figure I.35, left). In a general manner, a mild thermal annealing subsequent to sensitization improves the grafting by the condensation to covalent P-O-M bonds (M being the metal of the TCO).[124, 136b] For example, time-of-flight secondary ionization mass spectroscopy (ToF-SIMS) permitted to evidence through the surface mass spectrometric analysis such covalent P-O-Ti bonds onto a TiO_2-like surface.[137] The formation of these covalent linkages occurs with different mechanisms depending on the Lewis acidity of the media (Figure I.35, right), but is generally fostered by high oxidation levels of the metal M.[124]

Being quite resistant to hydrolysis and practically simple, the attachment through phosphonate groups has been widely implemented to anchor photosensitizers and/or catalysts onto TCOs (as

TiO$_2$, ITO or FTO) which results in OER photoanodes able to steadily operate in aqueous media.[86, 130] While they also showed advantageous properties for the integration of dyes in NiO-based *p*-type DSSCs,[135] phosphonic acids provide a promising anchor to construct DS photocathodes for HER.

2.2.2.4. Challenges

Although the main constituent possibly utilized to build a H$_2$ evolving DS photocathode are known, several challenges actually underlay the architecture.

A first constraint arises from the kinetics imparted by the rate of processes related to multielectronic catalysis at the HEC (underlined by a question mark in Figure I.30). For instance, holes are known to be injected very fast into NiO. But a slow electron transfer to catalyst and/or slow HER catalysis would by contrast favor recombination.

The second challenge is correlated with the use of water as a solvent of choice that might lead to interfacial charging effects at the surface in a pH dependent fashion. Specifically, the Fermi level of the SC tends to align with the equilibrium potential of the species in solution, yielding a so-called *band-bending* phenomenon. Usually neglected for nanoparticulate films, a recent report pointed out that such an effect might bend bands to the extent of 800 mV in the case of NiO films, as a result of the low dielectric constant of this material.[113] If observed, such an important band bending would have a major impact of the interfacial transfers at NiO surface.

Finally, the third constraint is also related with water as a solvent, which, through pH effects might ease the desorption of anchored dye and/or catalysts.

We will now introduce the few successful examples of effective DS photocathodes for HER.

2.2.3. State-of-the-art examples of dye-sensitized photocathodes for hydrogen evolution

A wide range of inorganic photocathodes based on solid-state EA materials for both light-harvesting and catalysis have been described and can operate HER from various aqueous conditions.[85, 138] Besides, much fewer examples harnessing molecular components have been reported until now. Hybrid architectures have emerged, coupling the use of a molecular catalyst along with material-based photosensitizers, like intrinsic solid-state inorganic SCs or, more recently, organic ones.[85] Especially, some hybrid structures constructed onto solid-state SCs proved that efficient molecular catalysts can be successfully implemented in light-driven HER electrodes.[85, 139] A comprehensive description of these systems is out of the scope of the current introduction and has been the object of a recent review published by the group, added as an

appendix of the manuscript (Paper II).[85] But a relevant example of such systems has been presented by G. Moore and co-workers in a work where the authors chemisorbed a cobaloxime catalyst within a polymeric matrix grafted on an intrinsically photoactive (100) p-GaP (Figure I.36, left). The resulting photoelectrode proved to evolve hydrogen quite steadily from neutral aqueous media and with onset photovoltage as high as 760 mV vs RHE. The presence of the supported cobaloxime was clearly demonstrated to largely promote HER catalysis. The study, among others,[139d, 139e] points out the beneficial income provided by molecular catalysts for proton reduction once coupled with LH parts.

This knowledge participates in the design of photocathodes gathering molecular components for both light-harvesting and hydrogen evolution catalysis. These architectures have emerged recently and are presented here along with their integration into tandem cells for overall WS, when realized.

2.2.3.1. Proofs of concept

To gain insight into the influence of aqueous conditions for p-type photoelectrodes, our team in collaboration with others first investigated the light-driven electronic injection from dye-sensitized TCOs towards a sacrificial electron acceptor (SEA) in solution.[109a, 140] Especially, during this work we contributed to the construction of photocathodes by sensitization of NiO with a push-pull organic dye (Figure I.36, right). This study has been recently published and is added as an appendix of the manuscript (Paper III),[140] but we summarize here the main insights it contains.

The photoelectrode obtained after sensitization with the organic dye displays a *quasi*-homogeneous distribution of the dye on the surface, as evidenced from a resonance Raman mapping. Under irradiation, a cathodic photocurrent establishes in the presence of the $[Co(NH_3)_5Cl]Cl_2$ SEA in solution. At an applied potential of ca 0.47 V vs RHE, the photocurrent stabilizes around -200 $\mu A \cdot cm^{-2}$, byword of sustained light-driven electron injection towards the SEA (Figure I.36, right). Of important note, these steady photocurrents are observed in an aqueous pH 4.5 acetate buffer, which has been reported as an interesting media for HER catalyzed by supported **[Co^{III}(DO)(DOH)pnL₂]**.[55] This observation is encouraging towards the application of such a photocathode for HER. Also of note, the photocurrent density does not increase linearly as a function of the NiO thickness but nearly saturates for electrodes made of two layers of the nano-templated NiO films (about 500-600 nm). This point might be explained by the limited diffusion of SEA within the film but also echoes with the rather thin optimal thickness for NiO-based DSSCs (around 2 μm) due to the moderate hole transport properties.[101]

Figure I.36. Hybrid inorganic SC-cobaloxime photocathode for HER (left)[139b, 139c, 141] and a push-pull organic dye attached to NiO in a *p*-type photocathode approach (right).[140]

Further on, Odobel, Collomb and co-workers used electrodes prepared by the sensitization of NiO with a Ru(bpy)₃ analogue PS to perform the photoelectroreduction of various molecular HECs under non-aqueous conditions (acetonitrile solvent).[142] Namely, cathodic photocurrents are observed for the light-driven reduction of $[Rh^{III}(bpy)Cl_2]^+$-like complexes into $[Rh^{I}(bpy)_2]^+$-like precatalysts. In the presence of a weak acid, a Rh^{III}-hydride intermediate is formed but the driving force is not sufficient enough to enable photoelectrocatalytic hydrogen evolution. The utilization of a stronger acid results in an almost total loss of the photocurrent. The authors tentatively assigned this loss to the variations in the NiO flat-band potential as a function of acid concentration, which hinder electron injection at high acid concentration.

If here the reduced catalyst in solution was not proven to catalytically generate hydrogen, the group of Sun gave in 2012 the first proof for this concept by simply drop casting a cobaloxime at the surface of a **P1**-sensitized NiO electrode.[143] Submitted to light irradiation, the electrode evolves hydrogen at –0.4 V *vs* Ag/AgCl from neutral (pH 7) aqueous media, as monitored by H_2 detection through a Clark electrode. Photocurrents fall in the −5 to −20 μA·cm^{-2} range, yet experiencing a rapid decay (within minutes). This decay was explained by the leach of the physiadsorbed, thus weakly bound, catalyst from the surface.

2.2.3.2. Towards fully immobilized photocathodes

To further warrant sustained performance, it appeared that the immobilization of both dye and catalyst at the surface was required. Two strategies might be envisioned in this aim.

The first one consists in anchoring in parallel the dye and the catalyst at the surface, in the so-called *co-grafting* strategy (Figure I.37, top left). A main advantage of such a strategy is the easy screening of different dye/catalyst couples at the surface that does not need challenging synthetic chemistry. Also, the light-harvesting and the multielectronic catalytic processes are spatially decoupled one from each other. This point is particularly interesting if the kinetics of these processes are not in good correlation. Noteworthy, this approach was broadly harnessed in the

field of OER photoanodes to couple Ru(bpy)$_3$-based PS and molecular oxygen-evolving catalysts (OECs) at the surface of TCOs.[130]

The second strategy relies on a supramolecular or covalent linkage of the dye and the catalyst within the same molecular entity (Figure I.37, bottom left). Although more synthetically challenging, this means proved fruitful in the past to create supramolecular assemblies between a dye and an HEC, such as cobaloximes. Developed by our group[144] and others,[145] these systems showed electron injection from the dye into the catalyst. The supramolecular assemblies can lead to improved light-driven hydrogen evolution as compared to the bimolecular analogues.[144] Attached on a surface, such assemblies should also give directionality to the electron transfer from the surface to the catalyst through the excited state of the PS.

Both strategies have been explored, but only limited occurrences are reported in the literature to date.

Figure I.37. Co-anchoring strategy principle (top left) and example (top right) and supramolecular or covalent strategy principle (bottom left) and example (bottom right) to create DS photocathodes for HER.

The *co-grafting* approach was set up by Hammarström and co-workers to immobilize a coumarin organic dye and a Fe-based molecular HEC at a NiO electrode (Figure I.37, top right).[146] The surface attachment is ensured through carboxylate anchoring groups and assessed by UV-visible spectroscopy and resonance Raman data. The authors performed transient absorption measurements on the thusly created electrode, which lead them to propose a mechanism for

electron transfer at the surface, summarized here. Upon laser excitation of the dye, a dye$^-$/NiO$^+$ pair is formed within the femtosecond time range, as expected by the fast hole injection on NiO. A large driving force (*ca* 500 mV) enables electron hopping from the reduced dye to the catalyst. This electron hopping is found to occur under the time resolution of the setup used. The recombination of the electron on the reduced catalyst with a hole in NiO is observed within the microsecond time scale. This slow recombination time contrasts with the one observed from the reduced dye in the absence of co-attached catalyst (picosecond range). Hence, the measurements demonstrate a rather long lifetime for a reduced catalyst at the surface of NiO. This mono-reduced catalyst species thus lives long enough to possibly expect a second reduction process permitting HER catalysis to proceed, prior to recombination. Although the study is not directed toward H$_2$ production and detection, this result is therefore encouraging for the construction of co-grafted electrodes.

Alternatively, the strategy based on supramolecular assembly was explored by Wu and co-workers. The authors first attached a Ru(bpy)$_3$-based PS with push-pull properties onto NiO. A pendent pyridine on the PS serves to axially coordinate the Co center of a cobaloxime creating a supramolecular assembly (Figure I.37, bottom right)[147] as supported by the measurement of the related association constant. Inductively-coupled plasma (ICP) mass spectroscopy (MS) realized after dissolution of the film showed that only 1 cobalt atom is present for 10 ruthenium ones. Nonetheless, photocurrents are observed in neutral aqueous media, starting from *ca* 0.42 V *vs* RHE and saturating at about -8 µA·cm^{-2}. A two-fold increase in photocurrents is observed when NiO is coated through atomic layer deposition (ALD) of alumina before the dye-catalyst entity is anchored. This layer is indeed expected to diminish the charge recombination at the interface. The ALD-protected electrode also shows sustained photocurrents over time (2.5 h) that equilibrates around -10 µA·cm^{-2} at an applied potential of 0.1 V *vs* NHE. Subsequent hydrogen evolution is observed with a 68% faradaic efficiency, as detected by GC analysis. The observation of steady photocurrents is in line with the noteworthy stable surface attachment of the PS through a carboxylic acid moiety. The stability of the anchoring is shown by the insignificant desorption of the PS upon prolonged immersion in the buffer used for photoelectrocatalytic experiments. Of note, the sustained hydrogen production through pyridine bound cobaloximes is rather unexpected given that such an axial ligand can possibly decoordinate during extensive catalytic HER cycling. This study thus set a first landmark for immobilized dye-catalyst supramolecular assemblies actually realizing light-driven hydrogen evolution, but also opens a room to improve the coupling between the two entities, for instance through the introduction of a covalent link.

2.2.3.3. DS photocathodes for HER integrated in tandem devices

While it has been proven that photocathodes only based on molecular components can efficiently proceed HER, recent works joined such photocathodes with OER photoanodes for the construction of tandem cells able to perform overall light-driven WS.

A first example was provided by the groups of Mozer, Bäuerle, Bach and co-workers using the NiO-based photocathode described above for *p*-DSSCs (Figure I.33).[122d] Operated in neutral aqueous media, the electrode yields photocurrents in the range −2 to −4 µA·cm^{-2} at 0 V *vs* Ag/AgCl that reveal steady over 4 hours and generate hydrogen with unity faradaic efficiencies.[123] Upon light excitation, the reduced forms of the push-pull organic dye is proposed to be responsible for hydrogen evolution, given its large cathodic potential (−1.3 V *vs* RHE at pH 7). In good agreement, IPCE measurements unambiguously relate the observed photocurrents to light absorption by the attached PS. But to the best of our knowledge, no mechanism for the direct proton reduction catalysis on organic dye has been reported yet. Nonetheless, the rather good stability of the photoelectrode is strongly supported by experiments of desorption of the dye performed in different aqueous media (deionized water, 1 M HCl and 1 M NaOH). Whatever the pH, the PS was shown to bind to surface over months (213 days) without significant leach off in the dark. When light is shined on the samples, degradation is observed, that is more pronounced in acidic media, albeit on quite long times (120 hours). Such data speak in favor of a strong attachment of the organic dye onto NiO and give a ground to the anchoring through multiple carboxylate moieties.

The prolonged performance of the photocathode was harnessed to construct a tandem cell by the introduction of an OER BiVO$_4$ photoanode. The two electrodes display photocurrents in overlapping potential ranges, which indicates a possible concerted work in a tandem device. Indeed, under light irradiation the 2-electrode device establishes a current around 2-4 µA·cm^{-2} in a steady fashion over 12 hours. This current is further correlated to hydrogen evolution at the photocathode in *ca* 80% faradaic efficiency. But O$_2$ formation at the photoanode could not be evidenced, likely arising from the sensitivity limit of the GC setup used here. In this case, both electrodes are enlighted by two parallel light beams which does not reflect real conditions envisioned for such a setup. But the utilization of an organic PS, at the photocathode here, permits to further imagine the design of dyes absorbing in complimentary regions of the solar spectra for the DS photocathode and -anode. Such complementarity would make possible the use of these electrodes in a tandem device where both are crossed one after each other by the same raylight.

This strategy has been very recently brought further by Sun and co-workers, capitalizing on previous works on tandem devices.[148] A tandem cell was constructed based on a photocathode and a photoanode both integrating organic dyes and molecular catalysts for HER and OER, respectively (Figure I.38).[149] Under illumination, the co-grafted cobaloxime/**P1** NiO-based photocathode was evidenced to develop cathodic photocurrents about -35 $\mu A \cdot cm^{-2}$ at -0.2 V *vs* Ag/AgCl in phosphate buffer at pH 7. This photocurrent slowly decays to *ca* -20 $\mu A \cdot cm^{-2}$ after 90 min but results in H_2 generation, as detected by GC, in a 68% faradaic yield. In the absence of a co-anchored HER catalyst, the observed photocurrent is much less intense (*ca* 4 $\mu A \cdot cm^{-2}$). This observation represents an interesting proof of concept for the co-immobilization strategy. As well, sustained photocurrents tend to demonstrate that the phosphonate linkage used to supramolecularly attach the cobaloxime at the NiO does not leach off over time, even in a neutral phosphate buffer. The sustained photocurrents are also noticeable since the H-bridged cobaloximes can undergo deactivation or decoordination over extensive turnover from the pyridine ligand ensuring the surface grafting.
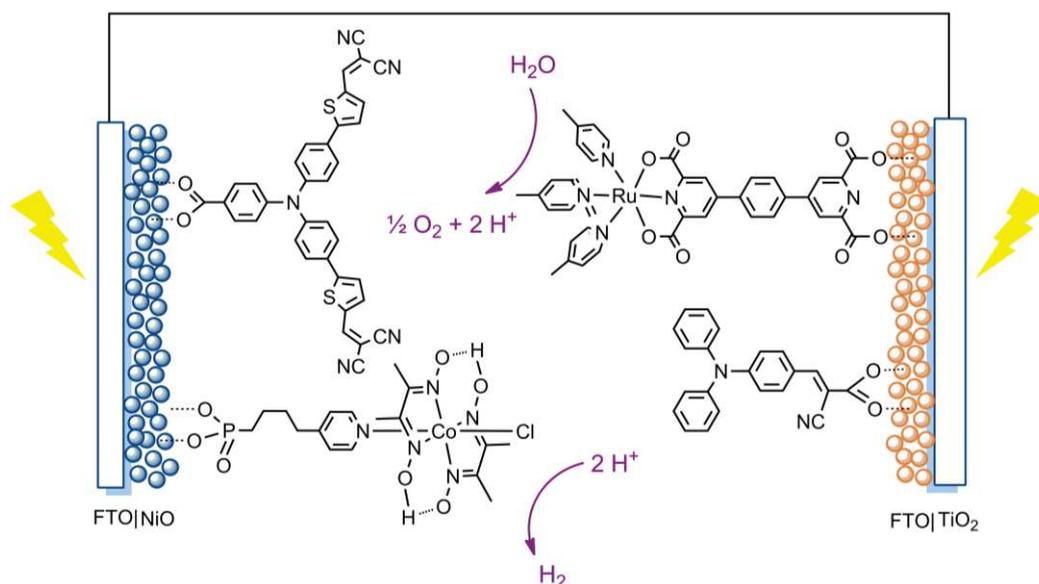
Figure I.38. Tandem cell device based on fully molecular photocathodes and photoanodes.[149]

The TiO$_2$-based photoanode constructed in the same work also displays stable activity with photocurrents equilibrating about 200 $\mu A \cdot cm^{-2}$ at 0 V *vs* Ag/AgCl in an identical buffer. The authors thus built a tandem device gathering the two photoelectrodes. Irradiation from the photocathode side proves here particularly interesting. This electrode is actually less absorbing and permits a higher light intensity to reach the photoanode that overall drives the device. Further investigations were however realized with illumination from both sides, thus securing higher photocurrents. The two electrodes being mounted as the working and the auxiliary electrodes, an

unbiased light-driven experiment yields photocurrents in the 75-50 $\mu A \cdot cm^{-2}$ range over 10 minutes. The less performing electrode, which is the photocathode, was shown to develop -35 $\mu A \cdot cm^{-2}$ poised at -0.2 V *vs* Ag/AgCl in a 3-electrode classical setup. Therefore, this electrode is expected to limit the current at similar values in the tandem device, by contrast to the observation. The authors postulate that the good adjustment of both electrodes assists the charge flow in the tandem device and permitsto reach higher currents.

Nonetheless, extending light irradiation further stabilizes the photocurrent to values about 15-20 $\mu A \cdot cm^{-2}$, while displaying hydrogen evolution in a 55% faradaic efficiency. These measurements allow the determination of a STH efficiency for the tandem device, reported at 0.05%. The activity of the tandem device is possibly favored through the use of organic dyes displaying UV-visible absorption maxima slightly shifted (*ca* 50 nm). This point is further supported by the IPCE spectrum of the complete device which overlaps regions corresponding to both dyes, although it also displays a large band at wavelengths inferior to 400 nm and possibly assigned to the absorption of NiO.

Overall, the study reported here gives insightful details to drive the construction of molecular photocathodes for HER that can be implemented in full WS devices.

3. Lessons from the state-of-the-art

During the last 25 years, many hydrogen evolution catalysts relying only on EA metals have been developed. Benchmarking studies are still ongoing to shortlist the higher performing and most appropriate ones for integration in WS devices. However, some of these catalysts displaying noteworthy features have already been immobilized onto functional HER electrodes. The attachment of $[Ni(P_2^{Ph}N_2^{Ph})_2]^{2+}$ onto CNTs represents the class example of bio-inspired electrodes for hydrogen evolution and uptake in rather acidic aqueous media. Similar constructions with $[Co^{III}(DO)(DOH)pnL_2]$ anchored to a **GDL/MWCNT** assembly also successfully achieve proton reduction at a milder pH value, *a priori* more adapted to the use in PEC devices.

As such, the current work takes this last construction, mastered in the laboratory, as a starting point. In Chapter II, the investigations will be directed to the assessment of figures of merit related to the use of such $[Co^{III}(DO)(DOH)pnL_2]$-based electrodes in devices. On this, the behavior of the catalyst under acidic media and O_2-tolerance at the immobilized cathode will be studied. Further on, the attempts to implement this **GDL/MWCNT-Co** electrode within a tandem cell are reported.

In the same vein, $[Co^{III}(DO)(DOH)pnL_2]$ have also been attached onto mesoporous templated TCOs resulting in high surface coverage. In Chapter III, this point will be set as a first step toward the construction of photocathodes. Studies involving new derivatization paths for the catalyst, followed by its anchoring onto TCOs are presented in a second part.

Building *p*-type molecular photocathodes for hydrogen evolution and which rely on $[Co^{III}(DO)(DOH)pnL_2]$ will constitute the last part of the work and be presented in Chapter IV.

The co-grafting strategy was shown to lead to effective photocathodes. Of particular interest, its modularity will be harnessed to join dyes with a catalyst derivative onto NiO, a benchmark material for DS photocathodes. In that aim, push-pull organic dyes have been identified as good candidates for the design of dye-sensitized photocathodes, both regarding LH/CS and stability properties. Hence, an organic dye will be broadly put at stake here, keeping in mind the Ru(bpy)$_3$-like PSs reference. In addition, we will specifically investigate around species bearing anchoring groups as phosphonate or carboxylate for attachment onto surfaces, as they were successfully used in effective HER photocathodes.

Last, but not least, the elegant supramolecular approach that was developed in the group earlier on will be extended to the construction of covalent dye-catalyst dyads for surface immobilization. Facing with challenges in molecular synthesis, recent advances in this direction will be briefly described in the final part.

References

1.	Faunce, T.; Styring, S.; Wasielewski, M. R.; Brudvig, G. W.; Rutherford, A. W.; Messinger, J.; Lee, A. F.; Hill, C. L.; deGroot, H.; Fontecave, M.; MacFarlane, D. R.; Hankamer, B.; Nocera, D. G.; Tiede, D. M.; Dau, H.; Hillier, W.; Wang, L.; Amal, R. *Energy Environ. Sci.* **2013,** *6* (4), 1074.
2.	Lewis, N. S.; Nocera, D. G. *Proc. Natl. Acad. Sci. USA* **2006,** *103* (43), 15729-15735.
3.	(a) Du, P.; Eisenberg, R. *Energy Environ. Sci.* **2012,** *5* (3), 6012-6021; (b) Faber, M. S.; Jin, S. *Energy Environ. Sci.* **2014,** *7* (11), 3519-3542; (c) McKone, J. R.; Marinescu, S. C.; Brunschwig, B. S.; Winkler, J. R.; Gray, H. B. *Chem. Sci.* **2014,** *5* (3), 865-878; (d) Thoi, V. S.; Sun, Y.; Long, J. R.; Chang, C. J. *Chem. Soc. Rev.* **2013,** *42* (6), 2388-2400; (e) Zeng, M.; Li, Y. *J. Mater. Chem. A* **2015,** *3* (29), 14942-14962.
4.	McCrory, C. C.; Jung, S.; Ferrer, I. M.; Chatman, S. M.; Peters, J. C.; Jaramillo, T. F. *J. Am. Chem. Soc.* **2015,** *137* (13), 4347-57.
5.	Costentin, C.; Passard, G.; Savéant, J.-M. *J. Am. Chem. Soc.* **2015,** *137* (16), 5461-5467.
6.	Fourmond, V.; Jacques, P. A.; Fontecave, M.; Artero, V. *Inorg. Chem.* **2010,** *49* (22), 10338-47.
7.	Bard, A. J.; Faulkner, L. R., *Electrochemical methods: fundamentals and applications*. Second ed.; Wiley: 2001.
8.	Savéant, J.-M. *Chem. Rev.* **2008,** *108* (7), 2348-2378.
9.	(a) Sampson, M. D.; Kubiak, C. P. *Inorg. Chem.* **2015,** *54* (14), 6674-6; (b) Hu, X.; Brunschwig, B. S.; Peters, J. C. *J. Am. Chem. Soc.* **2007,** *129* (29), 8988-8998.
10.	Artero, V.; Saveant, J. M. *Energy Environ. Sci.* **2014,** *7* (11), 3808-3814.
11.	Costentin, C.; Savéant, J.-M. *ChemElectroChem* **2014,** *1* (7), 1226-1236.
12.	Costentin, C.; Drouet, S.; Robert, M.; Saveant, J. M. *J. Am. Chem. Soc.* **2012,** *134* (27), 11235-42.
13.	Rountree, E. S.; McCarthy, B. D.; Eisenhart, T. T.; Dempsey, J. L. *Inorg. Chem.* **2014,** *53* (19), 9983-10002.
14.	Andreiadis, E. S.; Jacques, P. A.; Tran, P. D.; Leyris, A.; Chavarot-Kerlidou, M.; Jousselme, B.; Matheron, M.; Pecaut, J.; Palacin, S.; Fontecave, M.; Artero, V. *Nat. Chem.* **2013,** *5* (1), 48-53.
15.	Appel, A. M.; Helm, M. L. *ACS Cat.* **2014,** *4* (2), 630-633.
16.	Wakerley, D. W.; Reisner, E. *Energy Environ. Sci.* **2015,** *8* (8), 2283-2295.
17.	Lubitz, W.; Ogata, H.; Rudiger, O.; Reijerse, E. *Chem. Rev.* **2014,** *114* (8), 4081-148.
18.	Plumere, N.; Rudiger, O.; Oughli, A. A.; Williams, R.; Vivekananthan, J.; Poller, S.; Schuhmann, W.; Lubitz, W. *Nat. Chem.* **2014,** *6* (9), 822-7.
19.	Artero, V.; Fontecave, M. *Chem. Soc. Rev.* **2013,** *42* (6), 2338-2356.
20.	Berggren, G.; Adamska, A.; Lambertz, C.; Simmons, T. R.; Esselborn, J.; Atta, M.; Gambarelli, S.; Mouesca, J. M.; Reijerse, E.; Lubitz, W.; Happe, T.; Artero, V.; Fontecave, M. *Nature* **2013,** *499* (7456), 66-9.
21.	(a) Rakowski Dubois, M.; Dubois, D. L. *Acc. Chem. Res.* **2009,** *42* (12), 1974-1982; (b) Rakowski DuBois, M.; DuBois, D. L. *Chem. Soc. Rev.* **2009,** *38* (1), 62-72.
22.	Simmons, T. R.; Berggren, G.; Bacchi, M.; Fontecave, M.; Artero, V. *Coord. Chem. Rev.* **2014,** *270-271*, 127-150.
23.	(a) Kellett, R. M.; Spiro, T. G. *Inorg. Chem.* **1985,** *24* (15), 2373-2377; (b) Kellett, R. M.; Spiro, T. G. *Inorg. Chem.* **1985,** *24* (15), 2378-2382; (c) Bhugun, I.; Lexa, D.; Savéant, J.-M. *J. Am. Chem. Soc.* **1996,** *118* (16), 3982-3983.
24.	Graham, D. J.; Nocera, D. G. *Organometallics* **2014,** *33* (18), 4994-5001.
25.	(a) Lee, C. H.; Dogutan, D. K.; Nocera, D. G. *J. Am. Chem. Soc.* **2011,** *133* (23), 8775-7; (b) Roubelakis, M. M.; Bediako, D. K.; Dogutan, D. K.; Nocera, D. G. *Energy Environ. Sci.* **2012,** *5* (7), 7737-7740; (c) Beyene, B. B.; Mane, S. B.; Hung, C.-H. *Chem. Commun.* **2015,** *51* (81), 15067-15070.
26.	Bediako, D. K.; Solis, B. H.; Dogutan, D. K.; Roubelakis, M. M.; Maher, A. G.; Lee, C. H.; Chambers, M. B.; Hammes-Schiffer, S.; Nocera, D. G. *Proc. Natl. Acad. Sci. USA* **2014,** *111* (42), 15001-6.
27.	Simmons, T. R.; Artero, V. *Angew. Chem. Int. Ed.* **2013,** *52* (24), 6143-5.
28.	Costentin, C.; Drouet, S.; Robert, M.; Savéant, J.-M. *Science* **2012,** *338* (6103), 90-94.
29.	Kilgore, U. J.; Roberts, J. A.; Pool, D. H.; Appel, A. M.; Stewart, M. P.; DuBois, M. R.; Dougherty, W. G.; Kassel, W. S.; Bullock, R. M.; DuBois, D. L. *J. Am. Chem. Soc.* **2011,** *133* (15), 5861-72.
30.	Helm, M. L.; Stewart, M. P.; Bullock, R. M.; DuBois, M. R.; DuBois, D. L. *Science* **2011,** *333* (6044), 863-866.
31.	Dutta, A.; Lense, S.; Hou, J.; Engelhard, M. H.; Roberts, J. A.; Shaw, W. J. *J. Am. Chem. Soc.* **2013,** *135* (49), 18490-6.
32.	(a) Dutta, A.; DuBois, D. L.; Roberts, J. A. S.; Shaw, W. J. *Proc. Natl. Acad. Sci. USA* **2014,** *111* (46), 16286-16291; (b) Dutta, A.; Roberts, J. A.; Shaw, W. J. *Angew. Chem. Int. Ed.* **2014,** *53* (25), 6487-91.
33.	(a) Le Goff, A.; Artero, V.; Jousselme, B.; Tran, P. D.; Guillet, N.; Metaye, R.; Fihri, A.; Palacin, S.; Fontecave, M. *Science* **2009,** *326* (5958), 1384-7; (b) Tran, P. D.; Le Goff, A.; Heidkamp, J.; Jousselme, B.; Guillet,

N.; Palacin, S.; Dau, H.; Fontecave, M.; Artero, V. *Angew. Chem. Int. Ed.* **2011,** *50* (6), 1371-4; (c) Rodriguez-Macia, P.; Dutta, A.; Lubitz, W.; Shaw, W. J.; Rudiger, O. *Angew. Chem. Int. Ed.* **2015.**

34. (a) Krishnan, C. V.; Sutin, N. *J. Am. Chem. Soc.* **1981,** *103* (8), 2141-2142; (b) Richard Keene, F.; Creutz, C.; Sutin, N. *Coord. Chem. Rev.* **1985,** *64,* 247-260.

35. (a) Karunadasa, H. I.; Chang, C. J.; Long, J. R. *Nature* **2010,** *464* (7293), 1329-33; (b) Bigi, J. P.; Hanna, T. E.; Harman, W. H.; Chang, A.; Chang, C. J. *Chem. Commun.* **2010,** *46* (6), 958-60.

36. (a) Queyriaux, N.; Jane, R. T.; Massin, J.; Artero, V.; Chavarot-Kerlidou, M. *Coord. Chem. Rev.* **2015,** *304–305,* 3-19; (b) Sun, Y.; Bigi, J. P.; Piro, N. A.; Tang, M. L.; Long, J. R.; Chang, C. J. *J. Am. Chem. Soc.* **2011,** *133* (24), 9212-5; (c) Guttentag, M.; Rodenberg, A.; Bachmann, C.; Senn, A.; Hamm, P.; Alberto, R. *Dalton. Trans.* **2013,** *42* (2), 334-7; (d) Rodenberg, A.; Orazietti, M.; Probst, B.; Bachmann, C.; Alberto, R.; Baldridge, K. K.; Hamm, P. *Inorg. Chem.* **2015,** *54* (2), 646-57; (e) Singh, W. M.; Baine, T.; Kudo, S.; Tian, S.; Ma, X. A.; Zhou, H.; DeYonker, N. J.; Pham, T. C.; Bollinger, J. C.; Baker, D. L.; Yan, B.; Webster, C. E.; Zhao, X. *Angew. Chem. Int. Ed.* **2012,** *51* (24), 5941-4; (f) Tong, L.; Zong, R.; Thummel, R. P. *J. Am. Chem. Soc.* **2014,** *136* (13), 4881-4; (g) Zee, D. Z.; Chantarojsiri, T.; Long, J. R.; Chang, C. J. *Acc. Chem. Res.* **2015,** *48* (7), 2027-36.

37. Karunadasa, H. I.; Montalvo, E.; Sun, Y.; Majda, M.; Long, J. R.; Chang, C. J. *Science* **2012,** *335* (6069), 698-702.

38. (a) Anxolabehere-Mallart, E.; Costentin, C.; Fournier, M.; Nowak, S.; Robert, M.; Saveant, J. M. *J. Am. Chem. Soc.* **2012,** *134* (14), 6104-7; (b) Anxolabéhère-Mallart, E.; Costentin, C.; Fournier, M.; Robert, M. *J. Phys. Chem. C* **2014,** *118* (25), 13377-13381.

39. (a) Tchugaeff, L. *Z. Anorg. Allg. Chem.* **1905,** *46* (1), 144-169; (b) Tschugaeff, L. *Ber. Deutsch. Chem. Ges.* **1907,** *40* (3), 3498-3504; (c) Tschugaeff, L. *Ber. Deutsch. Chem. Ges.* **1906,** *39* (3), 2692-2702.

40. Hawecker, J.; Lehn, J.-M.; Ziessel, R. *Nouv. J. Chim.* **1983,** *7* (5), 271-277.

41. Connolly, P.; Espenson, J. H. *Inorg. Chem.* **1986,** *25* (16), 2684-2688.

42. Hu, X.; Cossairt, B. M.; Brunschwig, B. S.; Lewis, N. S.; Peters, J. C. *Chem. Commun.* **2005,** (37), 4723-4725.

43. Razavet, M.; Artero, V.; Fontecave, M. *Inorg. Chem.* **2005,** *44* (13), 4786-4795.

44. (a) Dempsey, J. L.; Brunschwig, B. S.; Winkler, J. R.; Gray, H. B. *Acc. Chem. Res.* **2009,** *42* (12), 1995-2004; (b) Artero, V.; Chavarot-Kerlidou, M.; Fontecave, M. *Angew. Chem. Int. Ed.* **2011,** *50* (32), 7238-66.

45. Artero, V.; Fontecave, M. *Coord. Chem. Rev.* **2005,** *249* (15–16), 1518-1535.

46. Wakerley, D. W.; Reisner, E. *PCCP* **2014,** *16* (12), 5739-46.

47. Baffert, C.; Artero, V.; Fontecave, M. *Inorg. Chem.* **2007,** *46* (5), 1817-1824.

48. (a) Muckerman, J. T.; Fujita, E. *Chem. Commun.* **2011,** *47* (46), 12456-8; (b) Solis, B. H.; Hammes-Schiffer, S. *Inorg. Chem.* **2011,** *50* (21), 11252-62; (c) Solis, B. H.; Hammes-Schiffer, S. *J. Am. Chem. Soc.* **2011,** *133* (47), 19036-9.

49. Lacy, D. C.; Roberts, G. M.; Peters, J. C. *J. Am. Chem. Soc.* **2015,** *137* (14), 4860-4.

50. Estes, D. P.; Grills, D. C.; Norton, J. R. *J. Am. Chem. Soc.* **2014,** *136* (50), 17362-5.

51. (a) Smolentsev, G.; Cecconi, B.; Guda, A.; Chavarot-Kerlidou, M.; van Bokhoven, J. A.; Nachtegaal, M.; Artero, V. *Chem. Eur. J.* **2015,** n/a-n/a; (b) Bhattacharjee, A.; Chavarot-Kerlidou, M.; Dempsey, J. L.; Gray, H. B.; Fujita, E.; Muckerman, J. T.; Fontecave, M.; Artero, V.; Arantes, G. M.; Field, M. J. *ChemPhysChem* **2014,** *15* (14), 2951-8; (c) Bhattacharjee, A.; Chavarot-Kerlidou, M.; Andreiadis, E. S.; Fontecave, M.; Field, M. J.; Artero, V. *Inorg. Chem.* **2012,** *51* (13), 7087-93.

52. Artero, V.; Fontecave, M. *Chem. Soc. Rev.* **2013,** *42* (6), 2338-56.

53. El Ghachtouli, S.; Fournier, M.; Cherdo, S.; Guillot, R.; Charlot, M.-F.; Anxolabéhère-Mallart, E.; Robert, M.; Aukauloo, A. *J. Phys. Chem. C* **2013,** *117* (33), 17073-17077.

54. Jacques, P. A.; Artero, V.; Pecaut, J.; Fontecave, M. *Proc. Natl. Acad. Sci. USA* **2009,** *106* (49), 20627-32.

55. Kaeffer, N.; Chavarot-Kerlidou, M.; Artero, V. *Acc. Chem. Res.* **2015,** *48* (5), 1286-95.

56. Abeles, R. H.; Dolphin, D. *Acc. Chem. Res.* **1976,** *9* (3), 114-120.

57. (a) Brink, C.; Hodgkin, D. C.; Lindsey, J.; Pickworth, J.; Robertson, J. H.; White, J. G. *Nature* **1954,** *174* (4443), 1169-1171; (b) Hodgkin, D. C.; Pickworth, J.; Robertson, J. H.; Trueblood, K. N.; Prosen, R. J.; White, J. G. *Nature* **1955,** *176* (4477), 325-328; (c) Hodgkin, D. C.; Kamper, J.; Mackay, M.; Pickworth, J.; Trueblood, K. N.; White, J. G. *Nature* **1956,** *178* (4524), 64-66.

58. Barker, H. A.; Weissbach, H.; Smyth, R. D. *Proc. Natl. Acad. Sci. USA* **1958,** *44* (11), 1093-1097.

59. Lenhert, P. G.; Hodgkin, D. C. *Nature* **1961,** *192* (4806), 937-938.

60. Giedyk, M.; Goliszewska, K.; Gryko, D. *Chem. Soc. Rev.* **2015,** *44* (11), 3391-404.

61. Schrauzer, G. N.; Holland, R. J. *J. Am. Chem. Soc.* **1971,** *93* (6), 1505-1506.

62. (a) Schrauzer, G. N.; Kohnle, J. *Chem. Ber.* **1964,** *97* (11), 3056-3064; (b) Schrauzer, G. N. *Acc. Chem. Res.* **1968,** *1* (4), 97-103; (c) Costa, G.; Mestroni, G.; De Savorgnani, E. *Inorg. Chim. Acta* **1969,** *3* (2), 323-328.

63. Brown, G. M.; Brunschwig, B. S.; Creutz, C.; Endicott, J. F.; Sutin, N. *J. Am. Chem. Soc.* **1979,** *101* (5), 1298-1300.

64.   (a) Lehn, J.-M.; Kirch, M.; Sauvage, J.-P. *Helv. Chim. Acta* **1979,** *62* (4), 1345-1384; (b) Lehn, J.-M.; Ziessel, R. *Proc. Natl. Acad. Sci. USA* **1982,** *79* (2), 701-704.

65.   Uhlig, E.; Friedrich, M. *Z. Anorg. Allg. Chem.* **1966,** *343* (5-6), 299-307.

66.   (a) Marzilli, L. G.; Gerli, A.; Calafat, A. M. *Inorg. Chem.* **1992,** *31* (22), 4617-4627; (b) Parker, W. O.; Bresciani-Pahor, N.; Zangrando, E.; Randaccio, L.; Marzilli, L. G. *Inorg. Chem.* **1985,** *24* (23), 3908-3913.

67.   Finke, R. G.; Smith, B. L.; McKenna, W. A.; Christian, P. A. *Inorg. Chem.* **1981,** *20* (3), 687-693.

68.   McCrory, C. C.; Uyeda, C.; Peters, J. C. *J. Am. Chem. Soc.* **2012,** *134* (6), 3164-70.

69.   Zhang, P.; Jacques, P. A.; Chavarot-Kerlidou, M.; Wang, M.; Sun, L.; Fontecave, M.; Artero, V. *Inorg. Chem.* **2012,** *51* (4), 2115-20.

70.   Gerli, A.; Sabat, M.; Marzilli, L. G. *J. Am. Chem. Soc.* **1992,** *114* (17), 6711-6718.

71.   (a) Willkomm, J.; Muresan, N. M.; Reisner, E. *Chem. Sci.* **2015,** *6* (5), 2727-2736; (b) Muresan, N. M.; Willkomm, J.; Mersch, D.; Vaynzof, Y.; Reisner, E. *Angew. Chem. Int. Ed.* **2012,** *51* (51), 12749-53.

72.   Kolb, H. C.; Finn, M. G.; Sharpless, K. B. *Angew. Chem. Int. Ed.* **2001,** *40* (11), 2004-2021.

73.   Ramalingam, K.; Raju, N.; Nanjappan, P.; Nowotnik, D. P. *Tetrahedron* **1995,** *51* (10), 2875-2894.

74.   (a) Scherer, M. R.; Muresan, N. M.; Steiner, U.; Reisner, E. *Chem. Commun.* **2013,** *49* (89), 10453-5; (b) Reynal, A.; Willkomm, J.; Muresan, N. M.; Lakadamyali, F.; Planells, M.; Reisner, E.; Durrant, J. R. *Chem. Commun.* **2014,** *50* (84), 12768-71.

75.   Giorgetti, M.; Berrettoni, M.; Ascone, I.; Zamponi, S.; Seeber, R.; Marassi, R. *Electrochim. Acta* **2000,** *45* (27), 4475-4482.

76.   Bhattacharjee, A.; Andreiadis, E. S.; Chavarot-Kerlidou, M.; Fontecave, M.; Field, M. J.; Artero, V. *Chem. Eur. J.* **2013,** *19* (45), 15166-74.

77.   Solis, B. H.; Yu, Y.; Hammes-Schiffer, S. *Inorg. Chem.* **2013,** *52* (12), 6994-9.

78.   Wiese, S.; Kilgore, U. J.; Ho, M.-H.; Raugei, S.; DuBois, D. L.; Bullock, R. M.; Helm, M. L. *ACS Cat.* **2013,** *3* (11), 2527-2535.

79.   (a) Probst, B.; Guttentag, M.; Rodenberg, A.; Hamm, P.; Alberto, R. *Inorg. Chem.* **2011,** *50* (8), 3404-12; (b) Guttentag, M.; Rodenberg, A.; Kopelent, R.; Probst, B.; Buchwalder, C.; Brandstätter, M.; Hamm, P.; Alberto, R. *Eur. J. Inorg. Chem.* **2012,** *2012* (1), 59-64; (c) Oberholzer, M.; Probst, B.; Bernasconi, D.; Spingler, B.; Alberto, R. *Eur. J. Inorg. Chem.* **2014,** *2014* (19), 3002-3009.

80.   Varma, S.; Castillo, C. E.; Stoll, T.; Fortage, J.; Blackman, A. G.; Molton, F.; Deronzier, A.; Collomb, M. N. *PCCP* **2013,** *15* (40), 17544-52.

81.   (a) Abe, T.; Taguchi, F.; Imaya, H.; Zhao, F.; Zhang, J.; Kaneko, M. *Polymers for Advanced Technologies* **1998,** *9* (9), 559-562; (b) Zhao, F.; Zhang, J.; Abe, T.; Wöhrle, D.; Kaneko, M. *J. Mol. Catal. A: Chem.* **1999,** *145* (1–2), 245-256.

82.   Mueller-Westerhoff, U. T.; Nazzal, A. *J. Am. Chem. Soc.* **1984,** *106* (18), 5381-5382.

83.   (a) Vijaikanth, V.; Capon, J.-F.; Gloaguen, F.; Schollhammer, P.; Talarmin, J. *Electrochem. Commun.* **2005,** *7* (4), 427-430; (b) Tran, P. D.; Artero, V.; Fontecave, M. *Energy Environ. Sci.* **2010,** *3* (6), 727.

84.   (a) Kibsgaard, J.; Tsai, C.; Chan, K.; Benck, J. D.; Nørskov, J. K.; Abild-Pedersen, F.; Jaramillo, T. F. *Energy Environ. Sci.* **2015**; (b) Zou, X.; Zhang, Y. *Chem. Soc. Rev.* **2015,** *44* (15), 5148-80.

85.   Queyriaux, N.; Kaeffer, N.; Morozan, A.; Chavarot-Kerlidou, M.; Artero, V. *J. Photochem. Photobiol., C* **2015,** *25*, 90-105.

86.   Yu, Z.; Li, F.; Sun, L. *Energy Environ. Sci.* **2015,** *8* (3), 760-775.

87.   Berben, L. A.; Peters, J. C. *Chem. Commun.* **2010,** *46* (3), 398-400.

88.   Eady, S. C.; Peczonczyk, S. L.; Maldonado, S.; Lehnert, N. *Chem. Commun.* **2014,** *50* (59), 8065-8.

89.   Clough, A. J.; Yoo, J. W.; Mecklenburg, M. H.; Marinescu, S. C. *J. Am. Chem. Soc.* **2015,** *137* (1), 118-21.

90.   Ibrahim, S. K.; Liu, X.; Tard, C.; Pickett, C. J. *Chem. Commun.* **2007,** (15), 1535-1537.

91.   Pinson, J.; Podvorica, F. *Chem. Soc. Rev.* **2005,** *34* (5), 429-39.

92.   Elgrishi, N.; Griveau, S.; Chambers, M. B.; Bedioui, F.; Fontecave, M. *Chem. Commun.* **2015,** *51* (14), 2995-8.

93.   Jewett, J. C.; Bertozzi, C. R. *Chem. Soc. Rev.* **2010,** *39* (4), 1272.

94.   Cobo, S.; Heidkamp, J.; Jacques, P. A.; Fize, J.; Fourmond, V.; Guetaz, L.; Jousselme, B.; Ivanova, V.; Dau, H.; Palacin, S.; Fontecave, M.; Artero, V. *Nat. Mater.* **2012,** *11* (9), 802-7.

95.   Ager, J. W.; Shaner, M. R.; Walczak, K. A.; Sharp, I. D.; Ardo, S. *Energy Environ. Sci.* **2015,** *8* (10), 2811-2824.

96.   Coridan, R. H.; Nielander, A. C.; Francis, S. A.; McDowell, M. T.; Dix, V.; Chatman, S. M.; Lewis, N. S. *Energy Environ. Sci.* **2015,** *8* (10), 2886-2901.

97.   Bourgeteau, T.; Tondelier, D.; Geffroy, B.; Brisse, R.; Cornut, R.; Artero, V.; Jousselme, B. *ACS Appl. Mater. Interf.* **2015,** *7* (30), 16395-403.

98.   Shi, X.; Cai, L.; Ma, M.; Zheng, X.; Park, J. H. *ChemSusChem* **2015,** *8* (19), 3192-3203.

99. (a) Walter, M. G.; Warren, E. L.; McKone, J. R.; Boettcher, S. W.; Mi, Q.; Santori, E. A.; Lewis, N. S. *Chem. Rev.* **2010,** *110* (11), 6446-6473; (b) Dotan, H.; Mathews, N.; Hisatomi, T.; Gratzel, M.; Rothschild, A. *J. Phys. Chem. Lett.* **2014,** *5* (19), 3330-4.

100. (a) Edwards, P. P.; Porch, A.; Jones, M. O.; Morgan, D. V.; Perks, R. M. *Dalton Trans.* **2004,** (19), 2995-3002; (b) Tadatsugu, M. *Semicond. Sci. Technol.* **2005,** *20* (4), S35; (c) Gu, D.; Schuth, F. *Chem. Soc. Rev.* **2014,** *43* (1), 313-44.

101. Odobel, F.; Pellegrin, Y. *J. Phys. Chem. Lett.* **2013,** *4* (15), 2551-2564.

102. (a) O'Regan, B.; Gratzel, M. *Nature* **1991,** *353* (6346), 737-740; (b) Hagfeldt, A.; Boschloo, G.; Sun, L.; Kloo, L.; Pettersson, H. *Chem. Rev.* **2010,** *110* (11), 6595-6663.

103. He, J.; Lindström, H.; Hagfeldt, A.; Lindquist, S.-E. *J. Phys. Chem. B* **1999,** *103* (42), 8940-8943.

104. He, J.; Lindström, H.; Hagfeldt, A.; Lindquist, S.-E. *Sol. Energy Mater. Sol. Cells* **2000,** *62* (3), 265-273.

105. Tian, H. *ChemSusChem* **2015,** *8* (22), 3746-3759.

106. Ashford, D. L.; Gish, M. K.; Vannucci, A. K.; Brennaman, M. K.; Templeton, J. L.; Papanikolas, J. M.; Meyer, T. J. *Chem. Rev.* **2015,** *115* (23), 13006-49.

107. Odobel, F.; Pellegrin, Y.; Gibson, E. A.; Hagfeldt, A.; Smeigh, A. L.; Hammarström, L. *Coord. Chem. Rev.* **2012,** *256* (21-22), 2414-2423.

108. (a) Kawazoe, H.; Yasukawa, M.; Hyodo, H.; Kurita, M.; Yanagi, H.; Hosono, H. *Nature* **1997,** *389* (6654), 939-942; (b) Nattestad, A.; Zhang, X.; Bach, U.; Cheng, Y.-B. *J. Photon. Ener.* **2011,** *1* (1), 011103; (c) Renaud, A.; Chavillon, B.; Le Pleux, L.; Pellegrin, Y.; Blart, E.; Boujtita, M.; Pauporté, T.; Cario, L.; Jobic, S.; Odobel, F. *J. Mater. Chem.* **2012,** *22* (29), 14353.

109. (a) Hamd, W.; Chavarot-Kerlidou, M.; Fize, J.; Muller, G.; Leyris, A.; Matheron, M.; Courtin, E.; Fontecave, M.; Sanchez, C.; Artero, V.; Laberty-Robert, C. *J. Mater. Chem. A* **2013,** *1* (28); (b) Huang, Z.; He, M.; Yu, M.; Click, K.; Beauchamp, D.; Wu, Y. *Angew. Chem. Int. Ed.* **2015,** *54* (23), 6857-61.

110. Dini, D.; Halpin, Y.; Vos, J. G.; Gibson, E. A. *Coord. Chem. Rev.* **2015,** *304-305*, 179-201.

111. Niklasson, G. A.; Granqvist, C. G. *J. Mater. Chem.* **2007,** *17* (2), 127-156.

112. Tench, D. M.; Yeager, E. *J. Electrochem. Soc.* **1973,** *120* (2), 164-171.

113. Natu, G.; Hasin, P.; Huang, Z.; Ji, Z.; He, M.; Wu, Y. *ACS Appl. Mater. Interf.* **2012,** *4* (11), 5922-9.

114. D'Amario, L.; Boschloo, G.; Hagfeldt, A.; Hammarström, L. *J. Phys. Chem. C* **2014,** *118* (34), 19556-19564.

115. (a) Boschloo, G.; Hagfeldt, A. *J. Phys. Chem. B* **2001,** *105* (15), 3039-3044; (b) Liu, Q.; Wei, L.; Yuan, S.; Ren, X.; Zhao, Y.; Wang, Z.; Zhang, M.; Shi, L.; Li, D.; Li, A. *RSC Adv.* **2015,** *5* (88), 71778-71784; (c) Huang, Z.; Natu, G.; Ji, Z.; He, M.; Yu, M.; Wu, Y. *J. Phys. Chem. C* **2012,** *116* (50), 26239-26246.

116. Zhu, H.; Hagfeldt, A.; Boschloo, G. *J. Phys. Chem. C* **2007,** *111* (47), 17455-17458.

117. Munoz-Garcia, A. B.; Pavone, M. *PCCP* **2015,** *17* (18), 12238-46.

118. (a) Morandeira, A.; Boschloo, G.; Hagfeldt, A.; Hammarström, L. *J. Phys. Chem. B* **2005,** *109* (41), 19403-19410; (b) Qin, P.; Wiberg, J.; Gibson, E. A.; Linder, M.; Li, L.; Brinck, T.; Hagfeldt, A.; Albinsson, B.; Sun, L. *J. Phys. Chem. C* **2010,** *114* (10), 4738-4748; (c) Smeigh, A. L.; Le Pleux, L.; Fortage, J.; Pellegrin, Y.; Blart, E.; Odobel, F.; Hammarstrom, L. *Chem. Commun.* **2012,** *48* (5), 678-80; (d) Brautigam, M.; Kubel, J.; Schulz, M.; Vos, J. G.; Dietzek, B. *PCCP* **2015,** *17* (12), 7823-30.

119. Ji, Z.; Natu, G.; Huang, Z.; Kokhan, O.; Zhang, X.; Wu, Y. *J. Phys. Chem. C* **2012,** *116* (32), 16854-16863.

120. (a) Ji, Z.; Wu, Y. *J. Phys. Chem. C* **2013,** *117* (36), 18315-18324; (b) Freys, J. C.; Gardner, J. M.; D'Amario, L.; Brown, A. M.; Hammarstrom, L. *Dalton. Trans.* **2012,** *41* (42), 13105-11; (c) Gennari, M.; Legalite, F.; Zhang, L.; Pellegrin, Y.; Blart, E.; Fortage, J.; Brown, A. M.; Deronzier, A.; Collomb, M. N.; Boujtita, M.; Jacquemin, D.; Hammarstrom, L.; Odobel, F. *J. Phys. Chem. Lett.* **2014,** *5* (13), 2254-8.

121. (a) Qin, P.; Zhu, H.; Edvinsson, T.; Boschloo, G.; Hagfeldt, A.; Sun, L. *J. Am. Chem. Soc.* **2008,** *130* (27), 8570-8571; (b) Ji, Z.; Natu, G.; Huang, Z.; Wu, Y. *Energy Environ. Sci.* **2011,** *4* (8), 2818.

122. (a) Le Pleux, L.; Smeigh, A. L.; Gibson, E.; Pellegrin, Y.; Blart, E.; Boschloo, G.; Hagfeldt, A.; Hammarström, L.; Odobel, F. *Energy Environ. Sci.* **2011,** *4* (6), 2075; (b) Powar, S.; Wu, Q.; Weidelener, M.; Nattestad, A.; Hu, Z.; Mishra, A.; Bäuerle, P.; Spiccia, L.; Cheng, Y.-B.; Bach, U. *Energy Environ. Sci.* **2012,** *5* (10), 8896; (c) Weidelener, M.; Mishra, A.; Nattestad, A.; Powar, S.; Mozer, A. J.; Mena-Osteritz, E.; Cheng, Y.-B.; Bach, U.; Bäuerle, P. *J. Mater. Chem.* **2012,** *22* (15), 7366; (d) Nattestad, A.; Mozer, A. J.; Fischer, M. K.; Cheng, Y. B.; Mishra, A.; Bauerle, P.; Bach, U. *Nat. Mater.* **2010,** *9* (1), 31-5.

123. Tong, L.; Iwase, A.; Nattestad, A.; Bach, U.; Weidelener, M.; Götz, G.; Mishra, A.; Bäuerle, P.; Amal, R.; Wallace, G. G.; Mozer, A. J. *Energy Environ. Sci.* **2012,** *5* (11), 9472.

124. Pujari, S. P.; Scheres, L.; Marcelis, A. T.; Zuilhof, H. *Angew. Chem. Int. Ed.* **2014,** *53* (25), 6322-56.

125. (a) Wang, X.; Landis, E. C.; Franking, R.; Hamers, R. J. *Acc. Chem. Res.* **2010,** *43* (9), 1205-1215; (b) Franking, R. A.; Landis, E. C.; Hamers, R. J. *Langmuir* **2009,** *25* (18), 10676-84.

126. Pujari, S. P.; Li, Y.; Regeling, R.; Zuilhof, H. *Langmuir* **2013,** *29* (33), 10405-15.

127. (a) English, C. R.; Bishop, L. M.; Chen, J.; Hamers, R. J. *Langmuir* **2012,** *28* (17), 6866-76; (b) Chen, J.; Franking, R.; Ruther, R. E.; Tan, Y.; He, X.; Hogendoorn, S. R.; Hamers, R. J. *Langmuir* **2011,** *27* (11), 6879-89.

128. Paoprasert, P.; Kandala, S.; Sweat, D. P.; Ruther, R.; Gopalan, P. *J. Mater. Chem.* **2012,** *22* (3), 1046-1053.

129.   Zhang, L.; Cole, J. M. *ACS Appl. Mater. Interf.* **2015,** *7* (6), 3427-55.

130.   Swierk, J. R.; Mallouk, T. E. *Chem. Soc. Rev.* **2013,** *42* (6), 2357-87.

131.   Haensch, C.; Hoeppener, S.; Schubert, U. S. *Chem. Soc. Rev.* **2010,** *39* (6), 2323-2334.

132.   (a) Brennan, B. J.; Keirstead, A. E.; Liddell, P. A.; Vail, S. A.; Moore, T. A.; Moore, A. L.; Gust, D. *Nanotechnology* **2009,** *20* (50), 505203; (b) Brennan, B. J.; Llansola Portoles, M. J.; Liddell, P. A.; Moore, T. A.; Moore, A. L.; Gust, D. *PCCP* **2013,** *15* (39), 16605-14.

133.   Guan, X.-h.; Chen, G.-h.; Shang, C. *J. Environm. Sci.* **2007,** *19* (4), 438-443.

134.   Martini, L. A.; Moore, G. F.; Milot, R. L.; Cai, L. Z.; Sheehan, S. W.; Schmuttenmaer, C. A.; Brudvig, G. W.; Crabtree, R. H. *J. Phys. Chem. C* **2013,** *117* (28), 14526-14533.

135.   Pellegrin, Y.; Le Pleux, L.; Blart, E.; Renaud, A.; Chavillon, B.; Szuwarski, N.; Boujtita, M.; Cario, L.; Jobic, S.; Jacquemin, D.; Odobel, F. *J. Photochem. Photobiol., A* **2011,** *219* (2-3), 235-242.

136.   (a) Queffelec, C.; Petit, M.; Janvier, P.; Knight, D. A.; Bujoli, B. *Chem. Rev.* **2012,** *112* (7), 3777-807; (b) Guerrero, G.; Alauzun, J. G.; Granier, M.; Laurencin, D.; Mutin, P. H. *Dalton. Trans.* **2013,** *42* (35), 12569-85.

137.   Adden, N.; Gamble, L. J.; Castner, D. G.; Hoffmann, A.; Gross, G.; Menzel, H. *Langmuir* **2006,** *22* (19), 8197-8204.

138.   Morales-Guio, C. G.; Hu, X. *Acc. Chem. Res.* **2014,** *47* (8), 2671-81.

139.   (a) Cedeno, D.; Krawicz, A.; Doak, P.; Yu, M.; Neaton, J. B.; Moore, G. F. *J. Phys. Chem. Lett.* **2014,** *5* (18), 3222-6; (b) Krawicz, A.; Cedeno, D.; Moore, G. F. *PCCP* **2014,** *16* (30), 15818-24; (c) Krawicz, A.; Yang, J.; Anzenberg, E.; Yano, J.; Sharp, I. D.; Moore, G. F. *J. Am. Chem. Soc.* **2013,** *135* (32), 11861-8; (d) Seo, J.; Pekarek, R. T.; Rose, M. J. *Chem. Commun.* **2015,** *51* (68), 13264-7; (e) Kumar, B.; Beyler, M.; Kubiak, C. P.; Ott, S. *Chem. Eur. J.* **2012,** *18* (5), 1295-8.

140.   Massin, J.; Brautigam, M.; Kaeffer, N.; Queyriaux, N.; Field, M. J.; Schacher, F. H.; Popp, J.; Chavarot-Kerlidou, M.; Dietzek, B.; Artero, V. *Interface Focus* **2015,** *5* (3), 20140083.

141.   Cedeno, D.; Krawicz, A.; Moore, G. F. *Interface Focus* **2015,** *5* (3).

142.   Castillo, C. E.; Gennari, M.; Stoll, T.; Fortage, J.; Deronzier, A.; Collomb, M. N.; Sandroni, M.; Légalité, F.; Blart, E.; Pellegrin, Y.; Delacote, C.; Boujtita, M.; Odobel, F.; Rannou, P.; Sadki, S. *J. Phys. Chem. C* **2015,** *119* (11), 5806-5818.

143.   Li, L.; Duan, L.; Wen, F.; Li, C.; Wang, M.; Hagfeldt, A.; Sun, L. *Chem. Commun.* **2012,** *48* (7), 988-90.

144.   Fihri, A.; Artero, V.; Razavet, M.; Baffert, C.; Leibl, W.; Fontecave, M. *Angew. Chem. Int. Ed.* **2008,** *47* (3), 564-7.

145.   Veldkamp, B. S.; Han, W.-S.; Dyar, S. M.; Eaton, S. W.; Ratner, M. A.; Wasielewski, M. R. *Energy Environ. Sci.* **2013,** *6* (6), 1917.

146.   Gardner, J. M.; Beyler, M.; Karnahl, M.; Tschierlei, S.; Ott, S.; Hammarstrom, L. *J. Am. Chem. Soc.* **2012,** *134* (47), 19322-5.

147.   Ji, Z.; He, M.; Huang, Z.; Ozkan, U.; Wu, Y. *J. Am. Chem. Soc.* **2013,** *135* (32), 11696-9.

148.   Fan, K.; Li, F.; Wang, L.; Daniel, Q.; Gabrielsson, E.; Sun, L. *PCCP* **2014,** *16* (46), 25234-40.

149.   Li, F.; Fan, K.; Xu, B.; Gabrielsson, E.; Daniel, Q.; Li, L.; Sun, L. *J. Am. Chem. Soc.* **2015,** *137* (28), 9153-9.

Chapter II

From catalytic behaviour in aqueous media to device integration

This chapter deals with the catalytic performance of the **[Co^{III}(DO)(DOH)pnL₂]** HER catalyst in aqueous media, towards possible integration in a device.

First, the activity of the catalyst, either in homogeneous phase or immobilized onto the **GDL/MWCNT-Co** electrode is investigated with regard to the pH. A recent report emphasized an improved activity of the catalyst in aqueous acidic media.[1] Taking this report into account, our study shed light on the origin of the catalysis at low pH.

Second, the activity of the **GDL/MWCNT-Co** electrode is investigated again but in the presence of oxygen in the aqueous electrolyte. This point is particularly important if the cathodic material is to be implemented in a tandem cell where oxygen, produced at the anodic part, might reach the cathode.

To conclude this piece of work, we report on the implementation of the **GDL/MWCNT-Co** cathode within a tandem cell. These investigations were conducted in collaboration with the group of A. Moore, T. Moore and D. Gust at *Arizona State University* and supported by the *Solar Fuels Institute* (*SOFI*). Attempts to realize light-driven overall WS in this device are presented. Some important conclusions are drawn that give noteworthy details for the next studies.

1. About the activity of cobalt diimine-dioxime catalyst in acidic aqueous media

To achieve the reductive side of water splitting, hydrogen evolution catalysts are *in fine* to be used in water. Thus, aqueous conditions are highly desirable to benchmark the catalytic performance, like TOFs, overpotential requirements or stability.

Back in 2012, our group reported a study dedicated to assessing the performance of **[Co^III(DO)(DOH)pnL₂]** in water, since precedent electrochemical investigations had been conducted only in organic solvents. With that aim, electrochemical studies of HER catalyzed by **[Co^III(DO)(DOH)pnL₂]** were performed in the well-known phosphate buffer (KPi) at pH 7.[2] These neutral conditions are particularly relevant for overall WS.

Under such conditions, a cathodic scanning of **[Co^III(DO)(DOH)pnCl₂]** results in a hydrogen-evolving catalytic wave from *ca* −0.9 V *vs* Ag/AgCl. However, the HER activity was accompanied with the deposition of a composite film. A similar coating can also be obtained by the use of simple cobalt metallic salts (e.g. $Co(NO_3)\cdot 6H_2O$). The deposit was characterized through different techniques as energy dispersive X-ray spectroscopy (EDX), XPS, X-ray absorption near-edge structure (XANES) and extended X-ray absorption fine structure (EXAFS). The coating was evidenced to be a nano-particulate material made of a metallic cobalt core surrounded by cobalt-oxo/hydroxo/phosphate layers. This material is active for proton reduction catalysis in cobalt-free media with an onset potential of *ca* 50 mV *vs* RHE as detected by an in-line GC setup. Of note, nitrogen is not found within the film when **[Co^III(DO)(DOH)pnCl₂]** is the starting material. This observation indicates the complex is split during aqueous cathodic scanning, likely joined with the decomposition of the ligand. Therefore, a major conclusion of this work is that the HER activity of **[Co^III(DO)(DOH)pnCl₂]** in its molecular form is quite unlikely under homogeneous neutral aqueous conditions. Actually, the ambiguity in the nature of the catalytic species, either as homogeneous molecules or as heterogeneous and nanoparticulate materials arising from the decomposition of a molecular pre-catalyst, is well known in catalysis. This issue has been reviewed at several occurrences, especially in the context of WS.[3]

On the other hand, Peters and co-workers recently reported about proton reduction catalyzed by molecular cobalt-based HECs, including **[Co^III(DO)(DOH)pn(H₂O)₂]^2+**, in aqueous acidic media. Their study points out the good activity for hydrogen evolution of the molecular complex at pH 2.2, conditions under which the complex was found to be stable. With the light shed by the studies in our group[2] and others,[4] the stability of the complex is rather unexpected in aqueous and/or

acidic media. This point led us to re-investigate the conditions used by Peters and co-workers, to gain more insights in the electrochemical behavior of the catalyst in acidic aqueous media.

Poised at negative potentials in a pH 2.2 buffer, we could demonstrate that the molecular complex actually degrades. This degradation leads to the deposition of Co-based nanoparticles on the electrode surface, which are the true HER catalyst. However, the detection of the deposited material is tedious and cannot be performed by classical rinse-test experiments.

Our findings are developed and formatted here in the structure of an article that was recently published and to which the reader is referred to. Notations and references are inserted in this article independently from the whole manuscript.

ACS Catalysis

The Dark Side of Molecular Catalysis: Diimine−Dioxime Cobalt Complexes Are Not the Actual Hydrogen Evolution Electrocatalyst in Acidic Aqueous Solutions

Nicolas Kaeffer,[†,‡,§] Adina Morozan,[†,‡,§] Jennifer Fize,[†,‡,§] Eugenie Martinez,[†,‖] Laure Guetaz,[†,⊥] and Vincent Artero*,[†,‡,§]

[†]Université Grenoble Alpes, Grenoble 38000 France

[‡]Laboratoire de Chimie et Biologie des Métaux, CNRS UMR 5249, 17 rue des Martyrs, Grenoble CEDEX F-38054, France

[§]Commissariat à l'énergie atomique et aux énergies alternatives (CEA), Direction de la Recherche Fondamentale, Grenoble 38000, France

[‖]Commissariat à l'énergie atomique et aux énergies alternatives (CEA); Laboratoire d'Electronique et de Technologies de l'Information (LETI), MINATEC Campus, Grenoble 38054, France

[⊥]Commissariat à l'énergie atomique et aux énergies alternatives (CEA); Institut Laboratoire d'Innovation pour les Technologies des Energies Nouvelles et les Nanomatériaux (LITEN), Grenoble 38000, France

Ⓢ *Supporting Information*

ABSTRACT: The perspective of integrating molecular catalysts for hydrogen evolution into operating devices requires the benchmarking of their activity preferentially in aqueous media. Within a series of cobalt complexes assessed in that way, cobalt diimine−dioxime derivatives were shown to be the most active catalysts with onset overpotential for proton reduction as low as 260 mV in phosphate buffer (pH = 2.2) (McCrory et al. *J. Am. Chem. Soc.* **2012**, *134*, 3164−3170). Combining a set of analytical techniques (electrochemistry, gas chromatography, SEM, and XPS), we demonstrate here that the electrochemical wave previously assigned to H₂ evolution catalyzed by the molecular complex actually corresponds to low levels of catalytic hydrogen production (≤27% faradaic yield). Instead, we assign this wave to the reductive degradation of the molecular complex and to the formation of a nanoparticulate deposit at the electrode. Actually, this coating is responsible for the high faradaic yields for hydrogen evolution observed at more cathodic potentials. The catalytic nanoparticulate material is metastable and readily redissolves, so that rinse-test experiments were insufficient here to rule out the formation of solid-state materials. This point accounts for the previous misidentification of the active species in H₂ evolution mediated by a cobalt diimine−dioxime complex in aqueous phosphate buffer (pH = 2.2). Our finding, exemplified on a cobalt complex, may be extended to other molecular systems and suggests that the routine use of rinse-test experiments may not be sufficient to ascertain the molecular nature of active water-splitting catalytic species.

KEYWORDS: *cobalt, nanoparticle, cobaloximes, diimine−dioxime complexes, solar fuels, electrocatalysis, rotating ring disk electrode*
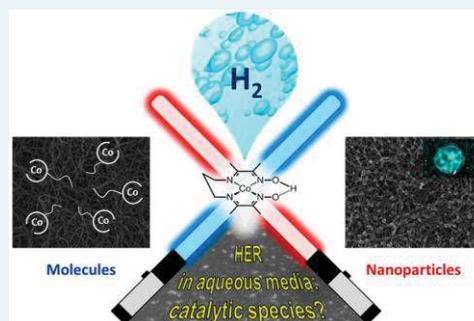
■ INTRODUCTION

The rise of a post-oil economy requires that economically viable and sustainable solutions are developed for massive energy storage.[1] Hydrogen technologies are appealing in this context because of the high energetic content of the H−H bond. In addition, a circular economy can be derived from a combination of water electrolysis, hydrogen storage and fuel cell technologies. However, these technologies significantly rely on the use of noble metal catalysts such as platinum and cannot be extended at the terawatt scale because of scarcity and cost.[2] The search for alternative noble metal-free catalysts for the hydrogen evolution reaction (HER) is the focus of intense research programs. Molecular chemistry allows the design of highly tunable catalytic systems based on earth-abundant

metallic centers such as Co, Ni, Fe, or Mo.[3−8] Over the last 10 years, efficient HER catalysts have been reported, the performances of which have been demonstrated in solution based on photo- or electrochemical measurements. The challenge is now shifting toward their integration into technologically relevant devices such as tandem photoelectrochemical cells. Yet, a major prerequisite step, that has been underestimated so far, consists in the evaluation of molecular catalysts under realistic conditions (i.e., in aqueous media). Indeed, most of the electrocatalytic and photocatalytic studies
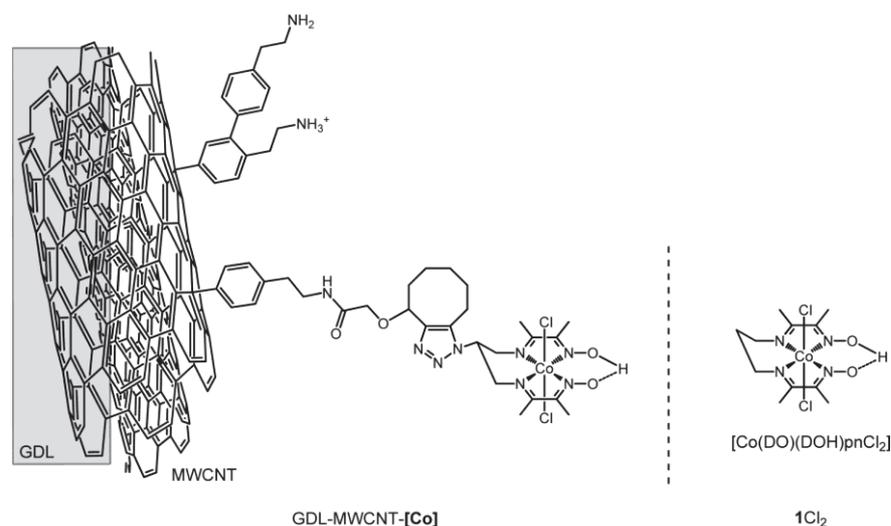
Figure 1. Structure of $[Co(DO)(DOH)pnCl_2]$ ($1Cl_2$) and representation of the GDL/MWCNT-[**Co**] electrode.

on such molecular complexes are typically carried out in nonaqueous solvents, and methodologies have been reported to benchmark the performances of HER catalysts under such conditions.[9,10] By contrast, only few benchmarking methodologies have been reported in fully aqueous media.[11,12]

Targeting the implementation in devices, our group recently reported on the covalent attachment of the cobalt diimine–dioxime HER catalyst $[Co(DO)(DOH)pnCl_2]$ ($1Cl_2$, Figure 1) to multiwalled carbon nanotubes (MWCNTs) deposited onto a gas diffusion layer (GDL).[13] The obtained hybrid electrocatalytic material, GDL/MWCNT-[**Co**], sustainably evolves hydrogen from an aqueous acetate buffer (pH = 4.5) while retaining the structure of the molecular catalyst. The onset overpotential for H_2 evolution catalysis was determined to be ~350 mV (this value corresponded to the minimum overpotential for which H_2 was detected using gas chromatography). On the other hand, a study by Peters and co-workers systematically assessed the performances of this complex, along with other Co macrocycles, for electrocatalytic proton reduction in a wide range of acidic to neutral aqueous buffers using rotating disk electrode (RDE) and chronocoulometric measurements.[11] The authors especially pointed out an aqueous phosphate buffer at pH = 2.2 in which the diaquo derivative $1(H_2O)_2^{2+}$ evolves hydrogen with high faradaic yields (>80%) and at low overpotential values (260 mV at the onset of the catalytic wave and 380 mV at the midwave). Under these conditions, the formation of catalytically active nanoparticles, something we refer to as the Dark Side in the title of this article, via the reductive decomposition of $1(H_2O)_2^{2+}$ was ruled out through rinse-test procedures. Rinsing is usually used by electrochemists to remove soluble components that are only weakly physisorbed to the electrode surface. In that case, the rinsed electrodes did not display any significant catalytic activity for hydrogen evolution, indicating that this activity is not related to the coating of the electrode surface with an insoluble, strongly attached species formed through decomposition of the molecular species introduced. Later on, a study by Anxolabéhère-Mallart and co-workers performed in nonaqueous media on similar cobalt glyoximato complexes indicated that the catalyst may be cobalt nanoparticles and not the introduced molecular catalyst.[14] We also demonstrated that such a

degradative process readily occurs in neutral phosphate buffer (KPi, pH = 7) from $1Cl_2$ with formation of a nanoparticulate material (H_2−CoCat), active for the HER.[15] Of note, solvation and displacement of chloride ligands by solvent molecules is known to occur in this series of complexes for cobalt oxidation states below II,[16] so that using $1(H_2O)_2^{2+}$ or $1Cl_2$ as starting material should not make any difference. In fact, interrogating the nature of the true active species is major in molecular catalysis in general and water splitting in particular. An elucidation in this regard is not easy because low amounts of synthetic impurities, adventitious metallic traces or degradation products are potential effective catalytic entities.[14,17−19] Reaching a solid conclusion generally requires the combination of several analytic techniques (electrochemistry, microscopy, spectroscopy....) and to develop specific experimental protocols.

Herein, we differentiate molecular catalysis, the process involved on decorated electrodes from its Dark Side (i.e., heterogeneous catalysis originating from degradation products). While the molecular complex turnsover in aqueous media and retains its molecular structure once grafted on MWCNTs,[13] we present a set of data gained with multiple techniques demonstrating that $1Cl_2$ actually decomposes in acidic aqueous solution under reductive conditions and forms a solid-state HER active material, in contrast with the conclusions of the previous study.[11] In particular, a clarification was possible through electrochemical investigations directly coupled to the detection of hydrogen and combined with a careful analysis of the electrode materials after use. We further evidence that the *in situ* generated active nanoparticles are not stable enough for facile identification. Our results therefore question the value of basic rinse-test measurements, routinely provided as the only control experiment to exclude water-splitting activity by strongly adsorbed and insoluble solid-state entities formed through decomposition of molecular catalysts.[17] This report finally proposes methodological pieces of advice to fully address this important issue regarding the benchmarking of the performance of molecular electrocatalysts.

■ EXPERIMENTAL SECTION

Materials and Reagents. Synthetic starting materials purchased from Sigma-Aldrich, sodium perchlorate (Prolabo),

potassium dihydrogenophosphate (Acros), phosphoric acid and acetic acid (Fischer), all in the highest purity available, were used as received, unless otherwise stated. Acetonitrile and dichloromethane were distilled over CaH_2. Nafion 117 solution (5 wt % in a mixture of lower aliphatic alcohols and water) was purchased from Sigma-Aldrich. UP-NC7000WT (purity >90%) multiwalled carbon nanotubes (MWCNTs) were obtained from Nanocyl. The gas diffusion layer (GDL) substrate (CARBEL CL-P-02360) was purchased from GORE Fuel Cell Technologies.

The cobalt diimine−dioxime complex $[Co(DO)(DOH)$-$pnCl_2]$ (labeled $\mathbf{1}Cl_2$) and the dichloro cobalt complex of a diimine−dioxime ligand bearing an activated ester group, $[Co(DO)(DOH)C_8\text{-}pnCl_2]$ (labeled $[\mathbf{Co}]$) were synthesized as previously described.[13] (4-Aminoethyl)benzene diazonium tetrafluoroborate was prepared according to literature procedures.[20] The GDL/MWCNT and GDL/MWCNT-$[\mathbf{Co}]$ cathodes were made following procedures described in a previous study.[13]

Electrochemical Measurements. Electrochemical analysis was performed using a BioLogic SP300 bipotentiostat and a typical three-electrode setup. A titanium wire was used as the auxiliary electrode and a Ag/AgCl, KCl (3 M) (denoted below Ag/AgCl) as the reference electrode. The potential of the reference electrode was calibrated after each experiment either with hydroxymethylferrocene (redox couple noted as $Fc_{CH2OH}^{+/0}$) directly in the electrochemical cell or with the $[Fe(CN)_6]^{3-}/[Fe(CN)_6]^{4-}$ couple in an external electrochemical setup. Calibrations against the $[Fe(CN)_6]^{3-}/[Fe(CN)_6]^{4-}$ couple were performed with a glassy carbon electrode (0.07 cm^2) and a platinum wire as working and auxiliary electrodes, respectively, in 0.5 M potassium phosphate buffer (pH = 7). The potential of the $[Fe(CN)_6]^{3-}/[Fe(CN)_6]^{4-}$ couple is denoted below as $E_{Fe(III)/Fe(II)}$, and the conversion of potentials against the Reversible Hydrogen Electrode (RHE) potential is thus realized using the following equation: $E_{vs\,RHE} = E_{vs\,Ag/AgCl} - E_{Fe(III)/Fe(II)} + E_{Fe(III)/Fe(II)\,vs\,NHE} + 0.059 \times pH$, where $E_{Fe(III)/Fe(II)\,vs\,NHE} = 0.446$ V refers to the tabulated value of $E_{Fe(III)/Fe(II)}$ against the Normal Hydrogen Electrode (NHE) potential.[21] This calibration procedure allowed us to reference the $Fc_{CH2OH}^{+/0}$ couple at 0.395 V vs NHE under our working conditions, slightly lower than reported elsewhere under different conditions (0.435 V vs NHE).[22] The potentials calibrated against the $Fc_{CH2OH}^{+/0}$ couple were corrected with the value we determined. We used both GDL/MWCNT-modified electrodes described above and glassy carbon disks (Origalys, 1.1 cm^2) as the working electrodes.

The electrolyte used was an aqueous potassium phosphate buffer (0.1 M, pH = 2.2) with 0.1 M $NaClO_4$.

Electrochemical Measurements Coupled to Gas Chromatography for H_2-Evolution Rate Determination. Chronoamperometry (CA) and linear sweep voltammetry (LSV) measurements were carried out in a two-compartment three-electrode electrochemical cell. The working and reference electrodes were placed in the same compartment filled with the electrolyte loaded with $\mathbf{1}Cl_2$ when specified. The counter electrode was placed in a second compartment of the cell filled with the unloaded electrolytic solution. The GDL/MWCNT-modified electrodes were stored in closed falcon tubes under N_2 and glassy carbon disks in an O_2/H_2O-free glovebox before surface analysis.

In the in-line gas chromatography (GC) configuration, the compartment of the working electrode is continuously flushed by N_2 carrier gas, whose rate is fixed through a Bronkhorst EL Flow Select mass flowmeter at 5 mL·min^{-1}. The output gas is analyzed with a PerkinElmer Clarus 500 gas chromatograph equipped with a porapack Q 80/100 column (6′ 1/8″) thermostated at 40 °C and a TCD detector thermostated at 100 °C. The GC is mounted in the so-called *continuous flow* mode in which the carrier gas stream fills an injection loop of 100 μL in the GC. The content of the injection loop is fed every 2 min into the GC setup, where gases (H_2 and O_2) are separated and the area under the peaks computed. Control calibrations were performed via chronopotentiometric experiments at cathodic currents of −1 mA or −150 μA, in which a platinum mesh was used as the working electrode to evolve hydrogen from a 0.1 M H_2SO_4 solution (pH = 1). In these control experiments, the faradaic yields are assumed to be unitary, which allows the determination of calibration constants for large or small currents including all experimental biases of the continuous flow setup. These values were then used to relate the area under the H_2 peak given by the in-line GC to the experimentally observed production rate of H_2 in the electrochemical cell (η_{obs}).

The expected production rate for H_2 derived from the current i passed in the cell, assuming a unitary faradaic yield, is calculated following the formula: $\eta_{curr} = i/(2 \times F)$ where F is the Faraday constant ($F = 96485$ C·mol^{-1}). The η_{obs}/η_{curr} ratio then gives the instantaneous faradaic yield of the electrode for H_2-evolution. Note that a lag-time exists between the measurement of the current and the detection of H_2 in the GC, which corresponds to a slight shift in the reconstructed figures. This shift depends on the scan rate and on the gas flow and can be corrected.[23] In this study, we decided to show raw data because they avoid overlapping between current and GC traces. We only corrected this shift in Figure S1, which displays two measurements carried out at different scan rates. The correction was made after calibration with measurements made at the same scan rates and current ranges, but using Pt electrodes for which a unity faradaic yield is attested in aqueous solutions.

Rotating Ring-Disk Electrode (RRDE) Measurements. A Pine RRDE with a glassy carbon disk (0.196 cm^2) and a Pt ring (0.110 cm^2) was used as working electrode. RRDEs were polished on a MD-Nap (Struers) polishing pad with 1 μm DP diamond paste (Struers) and DP-blue lubricant (Struers), then rinsed with ethanol and dried in the air. RRDE experiments were carried out in a single-compartment electrochemical cell under a continuous bubbling of nitrogen. The RRDE curves were recorded at 10 mV·s^{-1}, with a rotation speed of 1000 rpm. The potential of the Pt ring was set at 0.30 V vs Ag/AgCl. Current collection efficiency has been measured to 18−20% using the one-electron $[Fe(CN)_6]^{3\text{-}/4\text{-}}$ redox couple. Calibration of H_2 production rates was realized by using the same setup, while replacing the glassy carbon disk of the RRDE by a Pt disk. A series of controlled current electrolysis at the Pt disk was recorded with simultaneous monitoring of the ring current. The calibration curve for H_2 production rate measured by the RRDE setup was drawn assuming the faradaic yield for H_2 evolution at the Pt disk equal to unity.

Scanning Electron Microscopy. Scanning electron microscopy (SEM) images showing the electrode morphology were recorded with a field emission gun scanning electron microscope (FEG-SEM) Zeiss-Leo 1530 operating at 10 kV
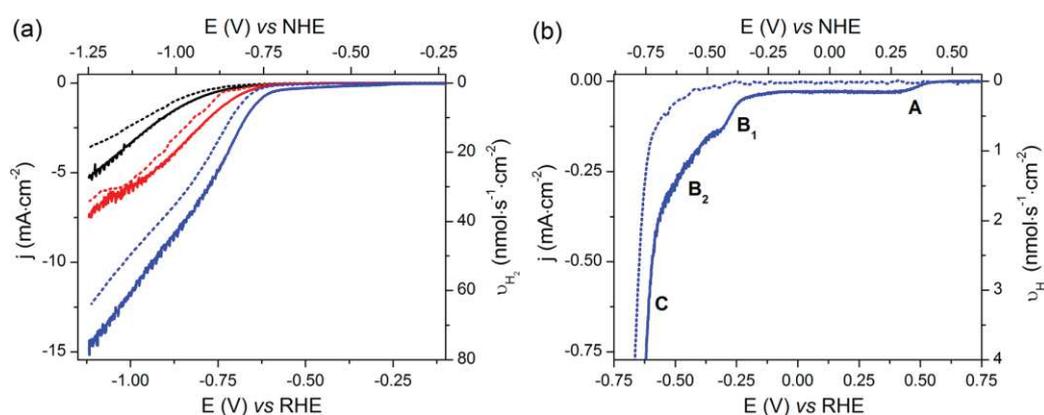
Figure 2. (a) LSV curves (plain lines) and H_2 evolution rates as measured by the in-line GC setup (dotted lines) for: GDL/MWCNT (black line), GDL/MWCNT-[**Co**] (red line) and GDL/MWCNT with **1**Cl$_2$ 0.3 mM in solution (blue line). Electrolyte: aqueous phosphate buffer (pH = 2.2); scan rate: 0.1 mV·s^{-1}. (b) Magnification of the low-current-density region for the LSV of GDL/MWCNT with **1**Cl$_2$ 0.3 mM in solution (aqueous phosphate buffer pH = 2.2; 0.1 mV·s^{-1}). Scales have been correlated so that superimposition of plain and dotted lines indicate a unity instantaneous faradaic efficiency. The letters relate to electrochemical events mentioned in the text. H_2 evolution rates at low current densities are compared in Figure S2.

and equipped with an energy dispersive X-ray detector (Bruker SDD EDX detector). The EDX analyses were performed using a SEM acceleration voltage of 15 kV.

X-ray Photoemission Spectroscopy (XPS). The analyses were performed with a VersaProbe II spectrometer from Physical Electronics using a high-resolution monochromatic Al Kα line X-ray source at 1486.7 eV. Fixed analyzer pass energy of 23 eV was used for core level scans leading to an overall energy resolution of 0.6 eV. Survey spectra were captured at pass energy of 117 eV. The photoelectron takeoff angle was 45°, which provided an integrated sampling depth of approximately 5 nm. All spectra were referenced against an internal signal, typically by adjusting the C 1s level peak at a binding energy of 284.8 eV.

■ **RESULTS**

H_2 Evolution by the Immobilized Catalyst. We previously described the covalent anchoring of **1**Cl$_2$ on MWCNTs deposited onto a GDL. The immobilized catalyst mediates H_2 evolution from quite low overpotential values (ca. 350 mV) in 0.1 M aqueous acetate buffer (pH = 4.5), as depicted on Figure S1.[13,24,25] As a remark, the overpotential is taken here as the potential at which the gas chromatography (GC) setup detected H_2 and hence relates to the effectively experienced onset potential for the HER, although certainly dependent on the sensitivity of the setup. This value is also comparable to the one determined for the same homogeneous catalyst in acetonitrile electrolyte.[26,27] To check whether more acidic conditions can be beneficial for the catalytic activity, we switched to a phosphate buffer (pH = 2.2) similar to that used by Peters and co-workers[11] to benchmark the performances of macrocyclic cobalt complexes. The linear sweep voltammetry (LSV) at the GDL/MWCNT-[**Co**] material was recorded using the same in-line GC setup. The current onsets from ca. −0.51 V vs RHE (Figure 2a and S1, plain red lines) with the concomitant H_2 production evidenced by GC measurements (dotted red lines). Actually, the onset overpotential is more than 200 mV cathodically shifted compared to the one measured through a RDE technique for **1**(H$_2$O)$_2$$^{2+}$ in the same buffer (−0.26 V vs RHE), as reported by Peters and co-

workers (corresponding to midwave overpotential of 380 mV).[11] Besides, the shape of the electrocatalytic process in the LSV of the GDL/MWCNT-[**Co**] material is not as Nernstian as the one reported for homogeneous **1**(H$_2$O)$_2$$^{2+}$.[11,13] We took these observations as first indications that the active species are not the same in both cases.

H_2 Evolution by the Homogeneous Catalyst. For comparison, the LSV at the GDL/MWCNT electrode with **1**Cl$_2$ (0.3 mM) in aqueous phosphate buffer (pH = 2.2) was also recorded (Figure 2a, blue lines). In this case, the current density and hydrogen evolution rate significantly differ from those measured at the GDL/MWCNT-[**Co**] material. A first reduction event (noted as **A** in Figure 2b) is observed at +0.49 V vs RHE, and the current density reaches a plateau around −0.03 mA·cm^{-2} attributed to the reduction of **1**Cl$_2$ from the Co^{III} to the Co^{II} state. Such a process was previously described by Peters and co-workers from similar measurements at a glassy carbon-RDE but otherwise the same conditions.[11] We note that all axial chloride ligands in **1**Cl$_2$ are likely replaced by water molecules in redox states below Co^{II}.[16] A second reduction phenomenon (noted as **B$_1$** in Figure 2b) is observed starting from ca. − 0.20 V vs RHE. This wave reaches an inflection point at a current density of −0.14 mA·cm^{-2} and a potential of −0.33 V vs RHE. At this point, a third reductive event (noted as **B$_2$**) overlays with **B$_1$**. Finally, the current sharply increases (process **C**) reaching 10 mA·cm^{-2} at −0.93 V vs RHE. In-line GC measurements do not evidence H_2 evolution concomitant to the first two events, but only starting from ca. − 0.40 V vs RHE (onset of wave **B$_2$**). While the potential of wave **B$_1$** is identical to the one of the catalytic wave reported by Peters and co-workers,[11] our observations indicate that this process does not correspond to H_2 evolution. Instead, this process might be involved in the formation of active species, evolving H_2 at more cathodic potentials (event **C**).

Characterization of Electrode Surfaces. Cathodically scanned GDL/MWCNT electrodes were analyzed by field electron gun-scanning electron microscopy (FEG-SEM) and X-ray photoelectron spectroscopy (XPS). At the GDL/MWCNT electrode measured with dissolved **1**Cl$_2$ in solution, the presence of nanoparticles (ca. 50 nm diameter) deposited on the surface of nanotubes was revealed (Figure 3a). No similar

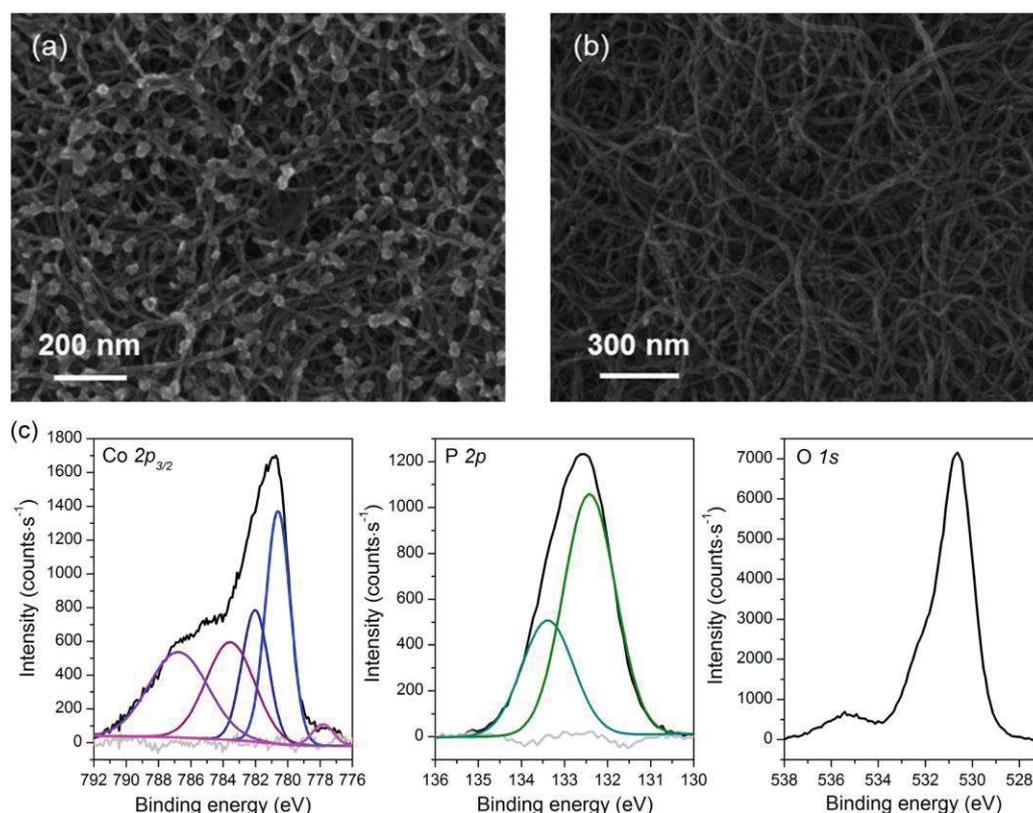**Figure 3.** SEM images for: (a) GDL/MWCNT electrode with **1**Cl$_2$ (0.3 mM) in aqueous phosphate buffer (0.1 M, pH = 2.2) and (b) GDL/MWCNT-[**Co**] electrode in aqueous phosphate buffer (0.1 M, pH = 2.2); both micrographs were taken after LSV measurement until −1.20 V vs RHE at a scan rate of 0.1 mV·s^{-1}; (c) XPS Co 2p$_{3/2}$, P 2p decomposed core regions and O 1s core region of the electrode from (a). Metallic cobalt displays a single 2p$_{3/2}$ signal at 777.8−778.5 eV binding energy.[28]

deposit was detected at the surface of the GDL/MWCNT-[**Co**] cathode after catalytic assay (Figure 3b). XPS analysis of the nanoparticulate material shows the presence of Co, P, and O atoms in a 1:1.2:6.7 ratio (Figure 3c), and the absence of nitrogen. A broad signal for the 2p$_{3/2}$ core level of Co$_{2p}$ is observed with several contributions (at 780.6, 782.1, 783.6, and 786.8 eV) accounting for Co^{II} species,[15] whereas the minor contribution at 777.8 eV corresponds to metallic cobalt (pink trace in Figure 3c).[28] The P$_{2p}$ core region, which is centered at 132.5 eV, exhibits 2 peaks at 132.4 and 133.4 eV in a 2:1 ratio, attributed to 2p$_{3/2}$ and 2p$_{1/2}$ electronic levels, respectively. The spectrum is quite comparable to that of the previously described H$_2$−CoCat material which forms from **1**Cl$_2$ under reductive conditions in aqueous phosphate buffer (pH = 7).[15]

Catalytic Activity of the Nanoparticulate Deposit. A nanoparticulate cobalt deposit on a GDL/MWCNT electrode was obtained by the cathodic sweep of **1**Cl$_2$ (0.3 mM) in phosphate buffer (pH = 2.2). At the end of the scan, the electrode was quickly disconnected and dried under N$_2$. The as-prepared electrode was then immediately scanned in fresh phosphate buffer electrolyte (pH = 2.2) starting from −0.22 V vs RHE (Figure 4). Simultaneous GC-monitoring reveals H$_2$ evolution catalysis starting from −0.40 V vs RHE, similarly to GDL/MWCNT measured in the presence of **1**Cl$_2$. This clearly indicates that the Co-based nanoparticulate material formed during the first cathodic scan is the true active species for H$_2$ evolution. After this second run, XPS analysis of the electrode
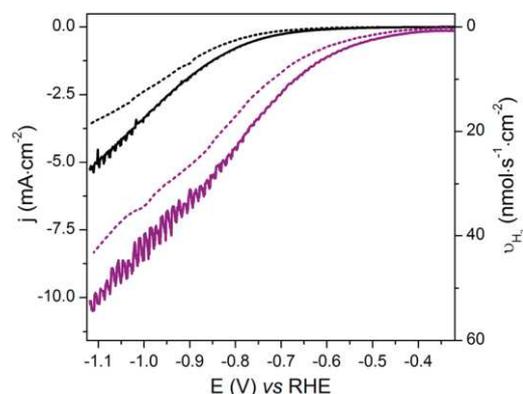
Figure 4. LSV curves (plain lines, scan rate: 0.1 mV·s^{-1}) and H$_2$ production rates measured by the in-line GC setup (dashed lines) at GDL/MWCNT electrodes in aqueous phosphate buffer (0.1 M, pH = 2.2): pristine electrode (black lines) and electrode decorated with the cobalt-based deposit (purple lines).

surface revealed a similar composition but with a slightly higher amount of Co^0 evidenced at a binding energy of 777 eV (Figure S3).

Rotating Ring-Disk Electrode Experiments on Glassy Carbon Electrodes. To directly link previous data with those gained by Peters and co-workers,[11] we performed additional electrochemical experiments at a RRDE with a glassy carbon
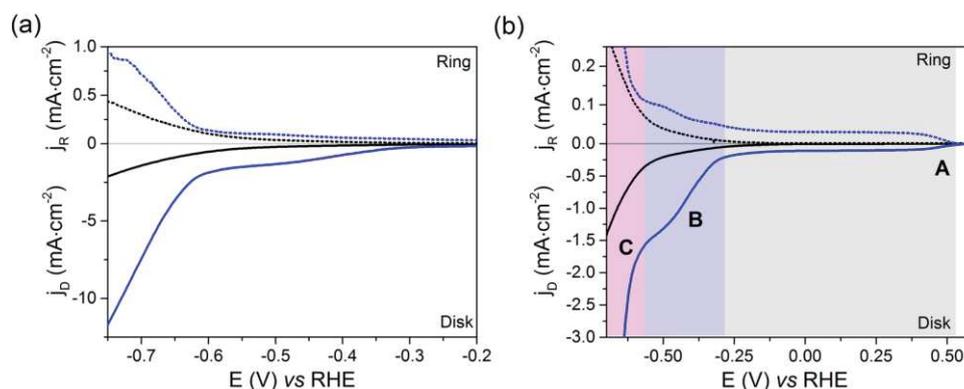
Figure 5. (a) RRDE measurements in aqueous phosphate buffer (0.1 M, pH = 2.2) in the absence (black lines) or in the presence of **1**Cl₂ 0.3 mM (blue lines); (b) Magnification of the low current density regions of RRDE curves shown in (a). The letters indicate successive electrochemical events (see text). The Pt ring electrode was polarized at 0.60 V vs RHE; rotation speed: 1000 rpm; scan rate: 10 mV·s⁻¹.
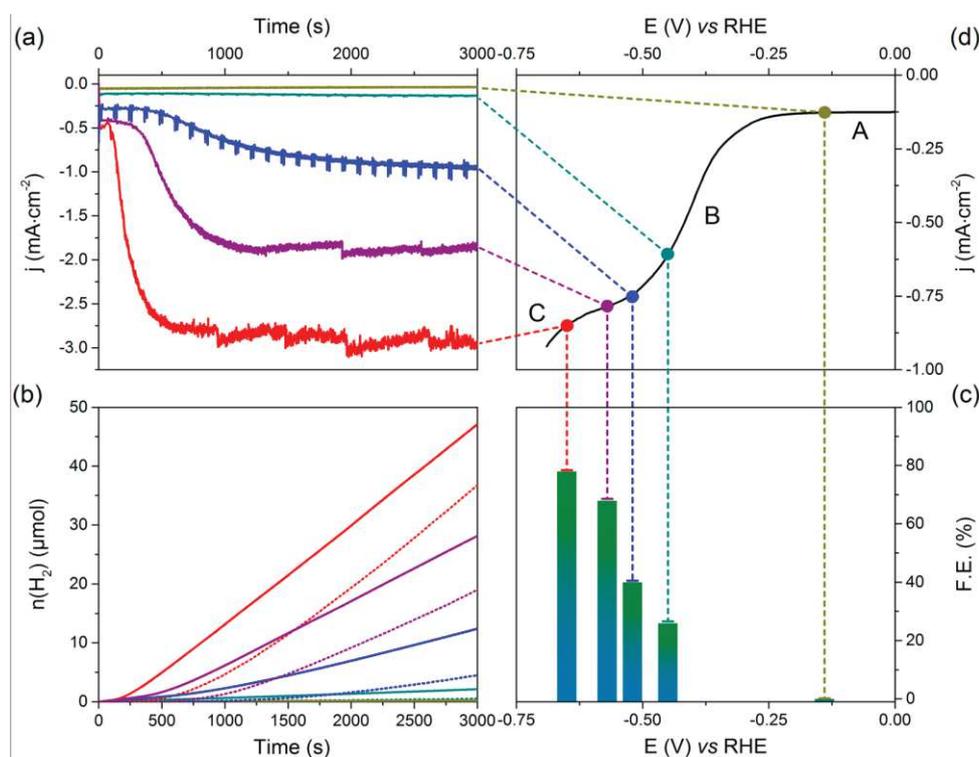
Figure 6. Chronoamperometric measurements at −0.14 V (yellow lines), −0.45 V (cyan lines), −0.52 V (blue lines), −0.57 V (purple lines), and −0.65 V (red lines) V vs RHE at a glassy carbon electrode in aqueous phosphate buffer (0.1 M, pH = 2.2) with **1**Cl₂ 0.3 mM: (a) current density vs time (b) amount of hydrogen produced assuming an unity faradaic efficiency (plain lines) and as observed by the in-line GC setup (dashed lines); (c) faradaic efficiencies. (d) LSV (10 mV·s⁻¹) at the same electrode under identical conditions showing the applied potentials for the chronoamperometric measurements. Charge passed after 3000 s: 145, 411, 2394, 3930, and 9094 mC at −0.14, −0.45, −0.52, −0.57, and −0.65 V vs RHE, respectively.

disk and a Pt ring. In such RRDE experiments, the species reduced at the disk reach the Pt ring poised at 0.30 V vs Ag/AgCl (i.e., 0.60 V vs RHE) where they get reoxidized. The ring potential was selected so as to reoxidize both reduced cobalt complexes and H₂. With the proper calibration, the ring current then relates to the amount of reduced species formed at the disk.

Figure 5a displays RRDE LSV curves recorded in phosphate buffer (pH = 2.2) with **1**Cl₂ (0.3 mM). The magnification of

the low currents region (Figure 5b) highlights the early events at both the disk and the ring electrodes. The disk potential was swept downward from 0.80 V vs RHE. A first reduction process ($E_{1/2}$ = +0.48 V vs RHE, wave **A**) yields a current density plateau around −0.11 mA·cm⁻² (Figure 5b, gray area) corresponding to the reduction of Co^III to Co^II. The reverse process occurs at the ring and gives a positive current. At −0.28 V vs RHE, a second wave (**B**) is observed with a concomitant increase in oxidation current at the ring (Figure 5b, blue area).
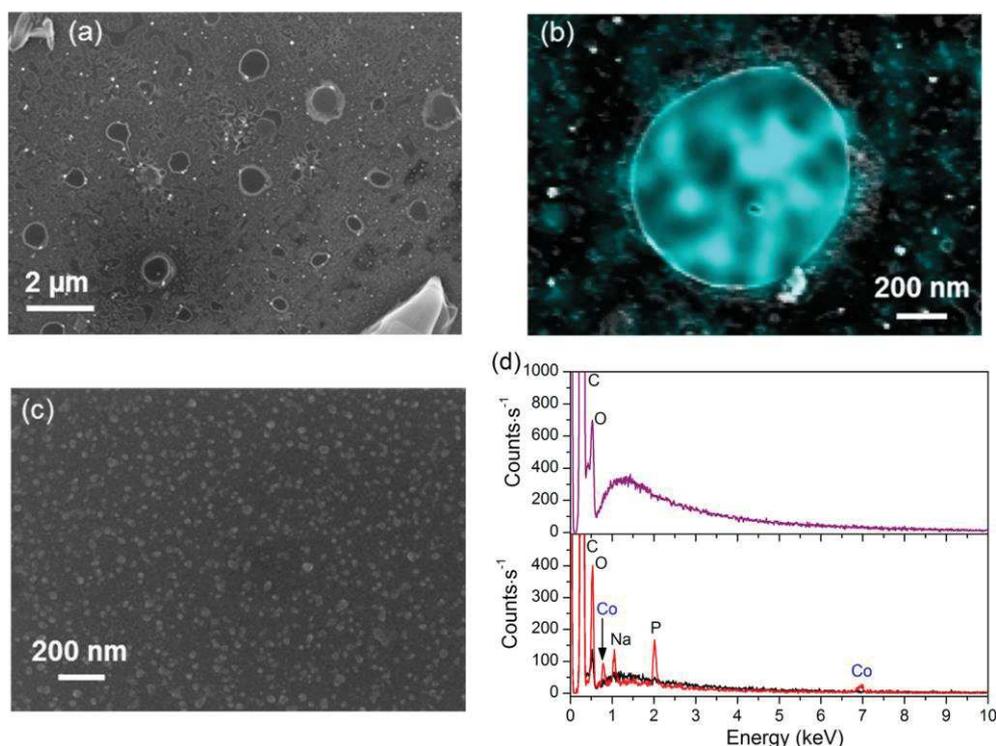
Figure 7. (a) SEM image and (b) Co ($K_{\alpha 1}$ line) elemental mapping of a glassy carbon electrode equilibrated at −0.57 V vs RHE for 1 h in aqueous phosphate buffer (0.1 M, pH = 2.2) with **1**Cl₂ 0.3 mM; (c) SEM image of the electrode prepared in a similar manner than (a) after rinsing with distilled water (See Figure S8 for a micrograph recorded at larger scale); (d) EDX spectra for: top) the surface of electrode shown in (c) (purple line); bottom) Co-containing particles (red line) and the background surface (black line) recorded on the electrode from (a).

The potential window of this wave actually corresponds to processes B_1 and B_2 described above for GDL/MWCNT electrodes. The two processes are not resolved at the disk but distinguishable at the ring. The corresponding ring current is of the same magnitude than observed for the reoxidation of Co^{II}, pointing out limited (if any) H_2 evolution catalysis. Current collection efficiency at the ring is similar for wave **A** and at the beginning of wave **B** (potentials corresponding to process B_1) and the measured values (22%) indicate that all species reduced at the disk are reoxidized at the ring. Therefore, the B_1 wave yields a reduced soluble compound. However, the current collection efficiency drops to 7% when measured at wave B_2, in line with formation of an insoluble species confined at the disk and not diffusion to the ring. The half-wave potentials (+0.48 V and −0.37 V vs RHE, respectively) and the relative magnitudes (1:6) of waves **A** and **B** are in good adequacy with the RDE electrochemistry of $1(H_2O)_2^{2+}$ reported by Peters and co-workers in Figure 4 of ref 11. Scanning toward more negative potentials, however, reveals a steep raise in current (wave **C**) from −0.56 V vs RHE with synchronous increase in anodic current at the ring (Figure 5b, magenta area), likely due to H_2 evolution catalysis. Data gained from RRDE experiments therefore parallel those measured on GDL/MWCNT electrodes and reproduce previously reported results.[11]

Preparative Electrolysis Experiments. Using a non-rotating glassy carbon plate ($S = 1.1$ cm²) as electrode, the same features (waves **A**, **B**, and **C**, Figure 6d and Figure S4) can be observed from the LSV curve recorded in phosphate buffer (pH = 2.2) with dissolved **1**Cl₂ (0.3 mM). Bulk electrolysis experiments were performed on such fresh electrodes for 1 h at

five distinct potentials (−0.14, −0.45, −0.52, −0.57, and −0.65 (±0.01) V vs RHE) corresponding to the top of wave **A**, the course of wave **B**, the onset (two measures) and the course of wave **C**, respectively. At the end of each electrolysis experiment, the electrode was disconnected before the potential could reequilibrate to the open-circuit value, taken out of the cell under a stream of N_2, dried under N_2 and transferred, with limited exposure to air, to the FEG-SEM instrument where their surface morphology was analyzed.

No hydrogen is evolved upon equilibration on wave **A** (−0.14 V vs RHE) and limited current density values are measured (Figure 6a), in agreement with a noncatalytic current. The analysis at the surface of the electrode shows ∼10 nm range particulate singularities (Figure S5) that were attributed to the roughness of the glassy carbon surface by comparison with a pristine glassy carbon electrode (Figure S6).

The electrolysis experiment realized on wave **B** (at −0.45 V vs RHE) evidences a very slow increase of the current during the chronoamperometric measurement (Figure 6a). Hydrogen is produced after the first 5 min but with a 27% faradaic yield measured at the end of the 1 h run (Figure 6b,c). Importantly, SEM images of the as-used electrode (Figure S7) do not show noticeable nanoparticulate deposits.

These first two experiments contrast with those carried out at the onset or in the course of wave **C**. The electrode then undergoes an induction period of ∼5 min at ca. −0.4 mA·cm⁻² during which no hydrogen is produced (Figure 6a,b). The current then increases and reaches a plateau of −1.0, − 1.8, and −2.8 mA·cm⁻² at −0.52, −0.57, and −0.65 V vs RHE, respectively. Hydrogen is evolved with faradaic yields of 40, 70,

and 80%, respectively. SEM images reveal the presence of deposits with various shapes at the surface of the electrode equilibrated at −0.57 V vs RHE (Figure 7a). EDX analysis allows discriminating the nature of these deposits. Large units of several tens of microns were found to consist of supporting electrolyte ions and do not contain cobalt species. Smaller round-shaped particles (500 nm to 1 μm) are also observed, the elemental mapping of which reveals the incorporation of significant amounts of cobalt (Figure 7b), as well as oxygen, phosphorus, and sodium (Figure S9). The EDX spectrum of such an entity is shown on Figure 7d (spectrum shown in red) and displays characteristic signatures of the Co K and L lines respectively at 6.9 and 0.8 keV. Electrodes equilibrated at −0.65 V vs RHE (Figure 6a–d) show larger areas with similar composition likely arising from the coalescence of such round-shaped area (Figure S10). For comparison, EDX analysis of the background glassy carbon surface does not show significant peaks in these regions (Figure 7d, spectrum shown in black).

As a control experiment, we examined the surface of electrodes dipped for 1 h in aqueous phosphate buffer (0.1 M, pH = 2.2) with $\mathbf{1}Cl_2$ 0.3 mM and further dried without any rinsing step. Figures S11 and S12 clearly show that the surface is not affected by such a process and that the cobalt particles observed above do not simply result from drops of the $\mathbf{1}Cl_2$ solution after drying. No cobalt can be evidenced using EDX and XPS analysis.

Rinse-Test Experiments. A glassy carbon electrode was equilibrated at −0.57 vs RHE in 0.3 mM $\mathbf{1}Cl_2$ phosphate buffer (pH = 2.2) and similarly disconnected at the end of 1 h experiment before reequilibration of the potential to the open-circuit value. The electrode was then rinsed by dipping for 10 s in distilled water and analyzed by SEM and EDX. A SEM image representative of the global surface morphology is shown in Figure 7c and S8, which is similar to that of a pristine glassy carbon electrode (Figure S6). EDX analysis on this surface (Figure 7d, purple line) does not reveal the presence of significant amounts of cobalt at the surface of the electrode, nor K, P, Cl, or Na from the electrolyte. These data directly show that such cobalt-based nanoparticles are readily eliminated during the quick rinsing of the electrode.

Accordingly, the rinsed electrode shows quite low activity when it is further subjected to electrolysis at −0.57 V vs RHE in a cobalt-free phosphate buffer electrolyte (pH = 2.2) (Figure S13). Figure S14 even shows that without rinsing, the activity of the deposit in a pristine electrolyte is extremely reduced, indicating that such Co-based nanoparticles are not stable (and/or not firmly adsorbed at the surface of the electrode) in the absence of applied cathodic potential.

We finally performed the same rinse-test experiment on the GDL/MWCNT electrode coated with cobalt nanoparticles. After rinsing for a few seconds in water, the SEM image (Figure S15) of the electrode still shows some Co-based nanoparticles, but their size is significantly reduced and their shape is also modified with only the core of the particles remaining. This confirms that these nanoparticles rapidly corrode in neutral water at open circuit.

■ DISCUSSION

Cobaloximes[29] and cobalt diimine−dioxime complexes[25] have been highlighted among the most efficient molecular cobalt catalysts for H_2 evolution in terms of turnover frequency/overpotential relationship based on data gained in nonaqueous and aqueous media, respectively.[9,11,12] Such compounds also

proved valuable for the construction of molecular-engineered electrode[13,24] and photoelectrode[30−34] materials for H_2 evolution. In particular, our group reported on the covalent immobilization of the $\mathbf{1}Cl_2$ diimine−dioxime cobalt complex at the surface of multiwalled carbon nanotubes (MWCNTs). The obtained material, GDL/MWCNT-[**Co**], steadily evolves hydrogen in fully aqueous media (pH = 4.5) and with overpotential values as low as 350 mV. In that context, a study by Peters and co-workers[11,12] drew our attention because it showed that a similar diimine−dioxime complex $\mathbf{1}(H_2O)_2^{2+}$ displays record efficiencies among other cobalt tetraazamacrocyclic complexes in aqueous phosphate buffer (pH = 2.2). Indeed, the RDE voltammogram recorded for $\mathbf{1}(H_2O)_2^{2+}$ under such conditions displays an irreversible reduction wave with an onset of −0.63 V vs SCE (−0.26 V vs RHE; half-wave at −0.38 V vs RHE) and plateauing at a current value 7-fold that of the monoelectronic Co^{III}/Co^{II} wave. This wave was assigned to catalytic H_2 evolution mediated by the molecular complex. The authors supported this assignment with a 2 h electrolysis carried out at −0.56 V vs RHE, corresponding to H_2 evolution with 80% faradaic efficiency.

We have therefore been quite disappointed not to observe the same behavior for GDL/MWCNT-[**Co**] when we assessed this material under similar conditions. LSV curve (Figure 2a and S1) indeed displays higher current density values associated with H_2 evolution in more acidic conditions (pH = 2.2), but the onset potential for catalysis, as determined by the GC-coupled electrochemical setup, is similar to that at pH = 4.5. This translates to 140 mV higher onset overpotential in the more acidic media, as a consequence of the dependence of the H^+/H_2 equilibrium potential with pH. Such a behavior is at contrast with previous observations made in acetonitrile, where the potential of the electrochemical wave was shown to adapt to the acid−base conditions, indicating that the rate of catalysis was determined by a proton-coupled electron transfer step. Yet, a 60 mV per pH unit shift of the catalytic wave was actually reported by Peters and co-workers for the complex in aqueous solutions.[11] This point led us to clarify the solution electro-assisted catalytic behavior of $\mathbf{1}Cl_2$ at a pristine GDL/MWCNT electrode (Figure 2a,b). Of note, X-ray absorption studies previously demonstrated that chloride ligands in $\mathbf{1}Cl_2$ are displaced from the cobalt center in redox states below Co^{III}.[16]

Data collected during the LSV measurement at a static GDL/MWCNT electrode compare well with those measured with rotating glassy carbon disk electrodes. They are also in quite good agreement with the report from Peters and co-workers.[11] We complement such studies with bulk electrolysis experiments coupled with in-line quantification of H_2 evolution through gas chromatography. A first reductive plateau (process **A** in Figures 2 and 5) is observed from +0.49 V vs RHE downward. It is accompanied by an orange coloration of the solution and attributed to the reduction of Co^{III} to Co^{II} in $\mathbf{1}Cl_2$ as previously reported.[11] At ca. −0.20 V vs RHE, a second reductive event **B** takes place, which can be resolved in two distinct processes $\mathbf{B_1}$ and $\mathbf{B_2}$ when scanning the potential at a very low rate on static electrodes. No H_2 could be detected for the $\mathbf{B_1}$ process through the GC-coupled electrochemical setup (Figure 2b). H_2 evolution actually onsets at a potential corresponding to the $\mathbf{B_2}$ process (Figure 2b) but occurs with limited efficiency (Figure 5). A steady-state measurement on this event (Figure 6, cyan lines) gives a poor faradaic efficiency (27%), which further evidences that this event is not mainly ruled by proton reduction catalysis. When potentials are scanned more negative,

a last electrochemical wave **C** is evidenced, corresponding to the effective and catalytic production of hydrogen.

These novel results raise two main issues. First, event **B$_1$** (onset at −0.26 V vs RHE; half-wave at −0.38 V vs RHE) assigned to catalytic H$_2$ evolution in ref 11 should be reassigned because it is obviously not the dominating process. Second, the nature of the active species responsible for H$_2$ evolution in processes **B$_2$** and **C** should be clarified.

The potential at which wave **B** develops might correspond to the formation of a Co^I form of **1Cl$_2$**. However, the current at the top of wave **B** is found between 6 (Figure 5 and S16) and 7 times that of a monoelectronic wave.[11] This value is close to the 8 e$^-$ stoichiometry required for the hydrogenation of the 4 C═N bonds (1 e$^-$ and 1 H$^+$ each) and the hydrogenolysis of the 2 N−O bonds (2 e$^-$ and 2 H$^+$ each). Therefore, multielectronic reduction of the diimine−dioxime ligand in **1Cl$_2$** likely occurs, as previously established by Anxolabéhère-Mallart and co-workers[14,35,36] for similar glyoximato cobalt complexes in acidic nonaqueous media. As this process couples electron transfer(s) to proton transfer(s),[35,37] such an assignment also rationalizes the pH dependence of the wave, observed by Peters and co-workers.[11] Nevertheless, we cannot completely rule out the activity of the molecular catalyst for proton reduction on wave **B**. But the modest current densities, the low faradaic efficiencies and the limited electron-delivery rates strongly support that this wave is mainly dominated by degradation of the complex. Current collection efficiencies measured during RRDE experiments show that soluble reduced species (Co^I complex and cobalt complexes with diimine−dioxime ligand at various reduction stages) are formed at the beginning of wave **B** (process **B$_1$**). These molecular species with degraded ligands are then further transformed into nanoparticulate systems active for hydrogen evolution. We note that the above conclusions likely apply for all the macrocyclic cobalt complexes investigated in ref 11.

Hydrogen is in fact produced, but at more cathodic potentials (process **C** with an onset of −0.57 V vs RHE or −0.93 V vs SCE, Figure 5). We remark that this potential corresponds to the one used in ref 11 to carry out bulk electrolysis experiments and evidence catalytic H$_2$ evolution. To interrogate the nature of the catalytic species, we recorded the time course of such electrolysis experiments on stationary electrodes (Figure 6, purple and red lines). An induction period is clearly observed with low initial current (−0.5 mA·cm^{-2}) followed by a 6-fold increase to reach a steady state at −2.0 to −3.0 mA·cm^{-2}. A parallel monitoring of the hydrogen produced shows that proton reduction does not quantitatively occur during the induction period, but only once the current is established at higher values. Such an induction phase confirms that **1Cl$_2$** is not the true catalytic species but actually a precatalyst, which is activated under these reductive conditions.[17] It is actually well-known that Co and Ni-based nanoparticles can be reductively formed from molecular complexes under organic[14,35−41] or aqueous[15,41] HER conditions. To investigate this hypothesis, we intentionally scanned our high surface area GDL/MWCNT electrode with **1Cl$_2$** in phosphate buffer (pH = 2.2) to more negative potentials, from wave **B** to wave **C**. A complete loss of the color in solution, as also reported by Peters and co-workers,[11] tends to indicate that all **1Cl$_2$** initially in solution is decomposed. At the end of the LSV measurement, the electrode was rapidly disconnected and dried under nitrogen. SEM images revealed nanoparticles (ca. 50 nm in diameter) homogeneously dispersed at the surface of

MWCNTs (Figure 3a). Similar cobalt-based deposits are also observed at the surface of flat glassy carbon electrodes treated under similar conditions (Figure 7a,b,d). XPS and EDX analysis of the material further confirms the presence of cobalt in these particles along with phosphorus and oxygen (Figure 3c, 7b,d). The composition of these Co-based particles is similar to the HER catalytic H$_2$−CoCat metastable material, which is deposited at cathodic potentials from **1Cl$_2$** or Co^{II} aqueous salts in phosphate buffer (pH = 7[15] or 1.6[42]). When such activated electrodes are measured in **1Cl$_2$**-free solutions starting from relatively cathodic potentials, hydrogen is evolved with quantitative faradaic yield (Figure 4). After such a measurement, XPS analysis of the GDL/MWCNT electrode coated with Co-based particles confirmed that the nature of the particles is not significantly altered during electrocatalytic assay (Figure S3), yet with the appearance of a small metallic cobalt contribution. Collectively, these data evidence that **1Cl$_2$** yields Co-based particles at the surface of the electrode when potentials are set more negative than wave **B** and that such deposits are the catalytic species responsible for hydrogen evolution. We assign both the induction phase observed during bulk electrolysis experiments and the process **B$_2$** observed during LSV experiments to the formation of the Co-based particles from **1Cl$_2$**. The latter conclusion is supported by the low value of the current collection efficiency measured during RRDE experiments at the potential of this process.

We however note that the formation of such catalytically active solid-state materials at the surface of the electrode was ruled out in the initial study by Peters and co-workers on the basis of rinse tests carefully carried out.[11] In that study, a 64 cm^2 plate was first poised for 2 h at −0.93 V vs SCE (−0.56 V vs RHE) in a **1(H$_2$O)$_2$** loaded electrolyte at pH = 2.2. The electrolysis delivered about 50.3 C of charge with H$_2$ evolution occurring at 80% faradaic efficiency. The electrode was then rinsed with water and submitted to a second electrolysis experiment under identical but **1(H$_2$O)$_2$$^{2+}$**-free conditions. The rinsed electrode passed only 3.4 C of charges, a value similar to a freshly polished control electrode (4.2 C). The authors therefore concluded that no deposited material was responsible for hydrogen evolution catalysis. Reproducing that protocol, we subjected a glassy carbon electrode with freshly deposited Co-based nanoparticles to a rinse test with water. SEM and EDX analysis revealed that, if the electrode is rinsed (even quickly) in distilled water, the film readily dissolves or deadsorbs and yields a pristine electrode surface (Figure 7c,d). The electrode consequently loses almost all its HER activity (Figure S10). The same happens if the electrode is not rinsed but let to equilibrate in electrolyte (Figure S11). These behaviors can be related to the metastability of the film depicted under similar conditions in the study by Symes and co-workers.[42] Such a metastability corresponds to the dissolution and formation of soluble Co^{II} ions as seen on MWCNT electrodes, although we cannot exclude that desorption of some particles and formation of a "homogenous" nanoparticle solution occur.[42] As a consequence, we show that the rinse-test performed by Peters and co-workers in their study is a false-positive for what concerns the deposition and the activity of cobalt-containing nanoparticles.[11] Our finding further clarifies this point and demonstrates that the catalytic activity in aqueous media is not due to a molecular cobalt complex but to metastable Co-based nanoparticles formed via the reductive degradation of the diimine−dioxime ligand.

CONCLUSION

Molecular approaches allow for a fine-tuning of the catalytic properties through ligand design. However, it is important to verify that the active species retains its molecular structure upon turnover. This is even more important for benchmarking studies that aim at selecting the best molecular platforms for further technological implementation. We revisit here a previous study dealing with H_2 evolution catalysis mediated by diimine−dioxime cobalt complexes in acidic aqueous solution. Combining a series of analytical techniques, we were able to consistently reinterpret electrochemical data. We conclude that the multielectron wave initially assigned to catalytic H_2 evolution is in fact associated with ligand degradation while the active species for H_2 evolution consists of Co-based nanoparticles formed on the electrode surface. Beyond this specific conclusion, this study is informative at four more general levels regarding stability of molecular catalysts, benchmarking approaches and methodologies to distinguish homogeneous from heterogeneous catalysis as detailed below:

1. It appears quite clear that molecular complexes in general, and cobalt diimine−dioxime complexes in particular, act as molecular catalysts when assessed for catalytic H_2 evolution in nonaqueous conditions in the presence of mild acids as proton sources.[27] However, the use of harsher hydrolytic conditions, either as strong and concentrated acids[14,35−41,43] or as aqueous[15,41] electrolyte, very often results in the deposition of a metal-based nanoparticulate film at the surface of the electrodes. In some cases, and especially in the case of Ni and Co complexes, this films displays catalytic activity for H_2 evolution. It stays, however, true that both homogeneous and heterogeneous catalytic processes may run in parallel under certain conditions and that the electrode itself introduces nucleation sites which are, for example, absent under pure photochemical conditions.[40,44,45] In particular, coating of the electrode surface is not favored under dynamic conditions associated with fast scan rate of the potential scale. On the other hand, we should also consider that such deposits might be appealing, especially if the nanostructuration or the nature of the materials can be controlled by the initial ligand.[46−49]

2. According to the first point, the community should resist to the temptation to only or systematically perform benchmarking studies under technologically relevant, that is, strongly acidic or alkaline aqueous conditions, typically used for solid-state inorganic materials.[50] Instead, comparison based on electrochemical measurements performed under conditions where the catalysts has been shown to be stable should be preferred, as for example the "catalytic Tafel plot" methodology developed by Savéant and co-workers.[9,51−53] Of course, extreme conditions are likely to boost the performances of the catalyst, and they should be tested if it can be demonstrated in parallel that the molecular nature of the catalyst is preserved. We point that previous studies and this work have demonstrated that molecular catalysts, including cobalt diimine−dioxime complexes, can sustain H_2 evolution catalysis under acidic aqueous conditions when they are immobilized onto electrode surfaces. In such a configuration, the catalysts retain their molecular nature even after extensive cycling.[13,54,55]

3. In the initial study,[11] bulk electrolysis experiments and H_2 quantification have been carried out at a potential significantly more negative than the one of the wave under consideration. This led to the misidentification of the catalytic species. It is therefore highly recommended to perform the bulk electrolysis experiments at more representative potentials, even if this will be at the expense of the catalytic current.

4. Rinse tests are usually used in electro-assisted catalysis to rule out that an insoluble, strongly attached species formed through decomposition of the molecular species mediates the catalytic reaction. Indeed, weakly physisorbed molecular species are eliminated during rinsing while solid state coatings will not. From the study at hand, it seems clear that a single basic measurement, such as the rinse test experiment described here, is not sufficient to rule out the formation of deposits at the surface of the electrode. Such rinse test experiments is in that way comparable to the mercury test often used to exclude the formation of metallic nanoparticles during photocatalytic experiments.[17] These two protocols prove very efficient and are conclusive when noble metal compounds are concerned because both their related elemental nanoparticles and metal oxides are very stable. This is obviously not always the case with earth-abundant metals. We disclose here a clear example where the deposit is metastable and readily desorbs or redissolves if not maintained in its potential-pH stability domain.[15,56] We finally note that rinse-tests can also be inefficient to identify cases where nanoparticles simply deadsorb to form a "homogenous" nanoparticle solution that is then responsible for the catalysis.[57,58] In that case, analysis of the surface of the electrode should be paralleled with analysis of the electrolyte, for example using dynamic light scattering techniques.[17]

We hope that identifying the Achille's heel of HER catalysts operated in aqueous solutions will help to develop more resilient ligand backbones, for instance, integrating pyridinic rather than iminic moieties.[59] This statement and above recommendations find equivalents in water oxidation catalysis, the other side of water splitting.[17−19,45] Coupled to systematic studies to decipher the true origin of catalysis, as the one developed here, we believe that this approach will provide the field with smart design as well as correct assessment of the performances of molecular catalysts for water-splitting in aqueous media.

ASSOCIATED CONTENT

S **Supporting Information**

The Supporting Information is available free of charge on the ACS Publications website at DOI: 10.1021/acscatal.6b00378.

Additional linear scan voltammograms, RRDE measurements, XPS analysis and SEM images coupled with EDX analysis (PDF)

AUTHOR INFORMATION

Corresponding Author

*E-mail: vincent.artero@cea.fr.

Notes

The authors declare no competing financial interest.

REFERENCES

(1) McKone, J. R.; Lewis, N. S.; Gray, H. B. *Chem. Mater.* **2014**, *26*, 407−414.
(2) Armaroli, N.; Balzani, V. *ChemSusChem* **2011**, *4*, 21−36.
(3) Simmons, T. R.; Berggren, G.; Bacchi, M.; Fontecave, M.; Artero, V. *Coord. Chem. Rev.* **2014**, *270−271*, 127−150.
(4) McKone, J. R.; Marinescu, S. C.; Brunschwig, B. S.; Winkler, J. R.; Gray, H. B. *Chem. Sci.* **2014**, *5*, 865−878.
(5) Tran, P. D.; Artero, V.; Fontecave, M. *Energy Environ. Sci.* **2010**, *3*, 727−747.
(6) Barton, B. E.; Olsen, M. T.; Rauchfuss, T. B. *Curr. Opin. Biotechnol.* **2010**, *21*, 292−297.
(7) Shaw, W. J.; Helm, M. L.; DuBois, D. L. *Biochim. Biophys. Acta, Bioenerg.* **2013**, *1827*, 1123−1139.
(8) Tard, C.; Pickett, C. J. *Chem. Rev.* **2009**, *109*, 2245−2274.
(9) Artero, V.; Saveant, J.-M. *Energy Environ. Sci.* **2014**, *7*, 3808−3814.
(10) Appel, A. M.; Helm, M. L. *ACS Catal.* **2014**, *4*, 630−633.
(11) McCrory, C. C. L.; Uyeda, C.; Peters, J. C. *J. Am. Chem. Soc.* **2012**, *134*, 3164−3170.
(12) Roy, S.; Bacchi, M.; Berggren, G.; Artero, V. *ChemSusChem* **2015**, *8*, 3632−3638.
(13) Andreiadis, E. S.; Jacques, P. A.; Tran, P. D.; Leyris, A.; Chavarot-Kerlidou, M.; Jousselme, B.; Matheron, M.; Pecaut, J.; Palacin, S.; Fontecave, M.; Artero, V. *Nat. Chem.* **2013**, *5*, 48−53.
(14) Anxolabéhère-Mallart, E.; Costentin, C.; Fournier, M.; Nowak, S.; Robert, M.; Savéant, J. M. *J. Am. Chem. Soc.* **2012**, *134*, 6104−6107.
(15) Cobo, S.; Heidkamp, J.; Jacques, P.-A.; Fize, J.; Fourmond, V.; Guetaz, L.; Jousselme, B.; Ivanova, V.; Dau, H.; Palacin, S.; Fontecave, M.; Artero, V. *Nat. Mater.* **2012**, *11*, 802−807.
(16) Giorgetti, M.; Berrettoni, M.; Ascone, I.; Zamponi, S.; Seeber, R.; Marassi, R. *Electrochim. Acta* **2000**, *45*, 4475−4482.
(17) Artero, V.; Fontecave, M. *Chem. Soc. Rev.* **2013**, *42*, 2338−2356.
(18) Ullman, A. M.; Liu, Y.; Huynh, M.; Bediako, D. K.; Wang, H.; Anderson, B. L.; Powers, D. C.; Breen, J. J.; Abruña, H. D.; Nocera, D. G. *J. Am. Chem. Soc.* **2014**, *136*, 17681−17688.
(19) Roger, I.; Symes, M. D. *J. Am. Chem. Soc.* **2015**, *137*, 13980−13988.
(20) Griveau, S.; Mercier, D.; Vautrin-Ul, C.; Chaussé, A. *Electrochem. Commun.* **2007**, *9*, 2768−2773.
(21) O'Reilly, J. E. *Biochim. Biophys. Acta, Bioenerg.* **1973**, *292*, 509−515.
(22) Durand, F.; Limoges, B.; Mano, N.; Mavré, F.; Miranda-Castro, R.; Savéant, J.-M. *J. Am. Chem. Soc.* **2011**, *133*, 12801−12809.
(23) Hernández, S.; Bensaid, S.; Armandi, M.; Sacco, A.; Chiodoni, A.; Bonelli, B.; Garrone, E.; Pirri, C. F.; Saracco, G. *Chem. Eng. J.* **2014**, *238*, 17−26.
(24) Kaeffer, N.; Morozan, A.; Artero, V. *J. Phys. Chem. B* **2015**, *119*, 13707−13.
(25) Kaeffer, N.; Chavarot-Kerlidou, M.; Artero, V. *Acc. Chem. Res.* **2015**, *48*, 1286−1295.
(26) Fourmond, V.; Jacques, P. A.; Fontecave, M.; Artero, V. *Inorg. Chem.* **2010**, *49*, 10338−10347.
(27) Jacques, P.-A.; Artero, V.; Pécaut, J.; Fontecave, M. *Proc. Natl. Acad. Sci. U. S. A.* **2009**, *106*, 20627−20632.
(28) *Photoelectron Spectroscopy: Principles and Applications*; Hüfner, S., Ed.; Springer: Berlin Heidelberg, 1996.
(29) Dempsey, J. L.; Brunschwig, B. S.; Winkler, J. R.; Gray, H. B. *Acc. Chem. Res.* **2009**, *42*, 1995−2004.
(30) Ji, Z.; He, M.; Huang, Z.; Ozkan, U.; Wu, Y. *J. Am. Chem. Soc.* **2013**, *135*, 11696−11699.
(31) Yu, Z.; Li, F.; Sun, L. *Energy Environ. Sci.* **2015**, *8*, 760−775.
(32) Li, F.; Fan, K.; Xu, B.; Gabrielsson, E.; Daniel, Q.; Li, L.; Sun, L. *J. Am. Chem. Soc.* **2015**, *137*, 9153−9159.
(33) Fan, K.; Li, F.; Wang, L.; Daniel, Q.; Gabrielsson, E.; Sun, L. *Phys. Chem. Chem. Phys.* **2014**, *16*, 25234−25240.
(34) Gu, J.; Yan, Y.; Young, J. L.; Steirer, K. X.; Neale, N. R.; Turner, J. A. *Nat. Mater.* **2016**, *15*, 456.
(35) Anxolabéhère-Mallart, E.; Costentin, C.; Fournier, M.; Robert, M. *J. Phys. Chem. C* **2014**, *118*, 13377−13381.
(36) El Ghachtouli, S.; Fournier, M.; Cherdo, S.; Guillot, R.; Charlot, M.-F.; Anxolabéhère-Mallart, E.; Robert, M.; Aukauloo, A. *J. Phys. Chem. C* **2013**, *117*, 17073−17077.
(37) McCarthy, B. D.; Donley, C. L.; Dempsey, J. L. *Chem. Sci.* **2015**, *6*, 2827−2834.
(38) Ghachtouli, S. E.; Guillot, R.; Brisset, F.; Aukauloo, A. *ChemSusChem* **2013**, *6*, 2226−2230.
(39) Cherdo, S.; Ghachtouli, S. E.; Sircoglou, M.; Brisset, F.; Orio, M.; Aukauloo, A. *Chem. Commun.* **2014**, *50*, 13514−13516.
(40) Chen, L.; Chen, G.; Leung, C.-F.; Yiu, S.-M.; Ko, C.-C.; Anxolabéhère-Mallart, E.; Robert, M.; Lau, T.-C. *ACS Catal.* **2015**, *5*, 356−364.
(41) Basu, D.; Mazumder, S.; Shi, X.; Staples, R. J.; Schlegel, H. B.; Verani, C. N. *Angew. Chem., Int. Ed.* **2015**, *54*, 7139−7143.
(42) Bloor, L. G.; Molina, P. I.; Symes, M. D.; Cronin, L. *J. Am. Chem. Soc.* **2014**, *136*, 3304−3311.
(43) Berben, L. A.; Peters, J. C. *Chem. Commun.* **2010**, *46*, 398−400.
(44) Stracke, J. J.; Finke, R. G. *J. Am. Chem. Soc.* **2011**, *133*, 14872−14875.
(45) Stracke, J. J.; Finke, R. G. *ACS Catal.* **2013**, *3*, 1209−1219.
(46) Yamada, Y.; Miyahigashi, T.; Kotani, H.; Ohkubo, K.; Fukuzumi, S. *Energy Environ. Sci.* **2012**, *5*, 6111−6118.
(47) Hong, D.; Jung, J.; Park, J.; Yamada, Y.; Suenobu, T.; Lee, Y.-M.; Nam, W.; Fukuzumi, S. *Energy Environ. Sci.* **2012**, *5*, 7606−7616.
(48) Shevchenko, D.; Anderlund, M. F.; Thapper, A.; Styring, S. *Energy Environ. Sci.* **2011**, *4*, 1284−1287.
(49) Huan, T. N.; Andreiadis, E. S.; Heidkamp, J.; Simon, P.; Derat, E.; Cobo, S.; Royal, G.; Bergmann, A.; Strasser, P.; Dau, H.; Artero, V.; Fontecave, M. *J. Mater. Chem. A* **2015**, *3*, 3901−3907.
(50) McCrory, C. C. L.; Jung, S.; Ferrer, I. M.; Chatman, S. M.; Peters, J. C.; Jaramillo, T. F. *J. Am. Chem. Soc.* **2015**, *137*, 4347−4357.
(51) Costentin, C.; Savéant, J.-M. *ChemElectroChem* **2014**, *1*, 1226−1236.
(52) Costentin, C.; Dridi, H.; Savéant, J.-M. *J. Am. Chem. Soc.* **2014**, *136*, 13727−13734.
(53) Costentin, C.; Drouet, S.; Robert, M.; Savéant, J.-M. *J. Am. Chem. Soc.* **2012**, *134*, 11235−11242.
(54) Tran, P. D.; Le Goff, A.; Heidkamp, J.; Jousselme, B.; Guillet, N.; Palacin, S.; Dau, H.; Fontecave, M.; Artero, V. *Angew. Chem., Int. Ed.* **2011**, *50*, 1371−1374.
(55) Le Goff, A.; Artero, V.; Jousselme, B.; Tran, P. D.; Guillet, N.; Metaye, R.; Fihri, A.; Palacin, S.; Fontecave, M. *Science* **2009**, *326*, 1384−1387.
(56) Kanan, M. W.; Surendranath, Y.; Nocera, D. G. *Chem. Soc. Rev.* **2009**, *38*, 109−114.
(57) Nakagawa, T.; Bjorge, N. S.; Murray, R. W. *J. Am. Chem. Soc.* **2009**, *131*, 15578−15579.
(58) Gambardella, A. A.; Bjorge, N. S.; Alspaugh, V. K.; Murray, R. W. *J. Phys. Chem. C* **2011**, *115*, 21659−21665.
(59) Queyriaux, N.; Jane, R. T.; Massin, J.; Artero, V.; Chavarot-Kerlidou, M. *Coord. Chem. Rev.* **2015**, *304−305*, 3−19.

Supporting Information

The Dark Side of Molecular Catalysis: Diimine-Dioxime Cobalt Complexes are not the Actual Hydrogen Evolution Electrocatalyst in Acidic Aqueous Solutions

Nicolas Kaeffer,[1,2,3] Adina Morozan, [1,2,3] Jennifer Fize, [1,2,3] Eugenie Martinez,[1,4] Laure Guetaz,[1,5] and Vincent Artero*[1,2,3]

[1]Université Grenoble Alpes, Grenoble 38000 France

[2] Laboratoire de Chimie et Biologie des Métaux, CNRS UMR 5249, 17 rue des Martyrs, F-38054 Grenoble cedex France

[3]Commissariat à l'énergie atomique et aux énergies alternatives (CEA), Direction de la Recherche Fondamentale, Grenoble 38000, France

[4]Commissariat à l'énergie atomique et aux énergies alternatives (CEA) ; Laboratoire d'Electronique et de Technologies de l'Information (LETI), MINATEC Campus Grenoble 38000, France

[5]Commissariat à l'énergie atomique et aux énergies alternatives (CEA) ; Institut Laboratoire d'Innovation pour les Technologies des Energies Nouvelles et les Nanomatériaux (LITEN), Grenoble 38000, France

*to whom correspondence should be addressed. E-mail address: vincent.artero@cea.fr
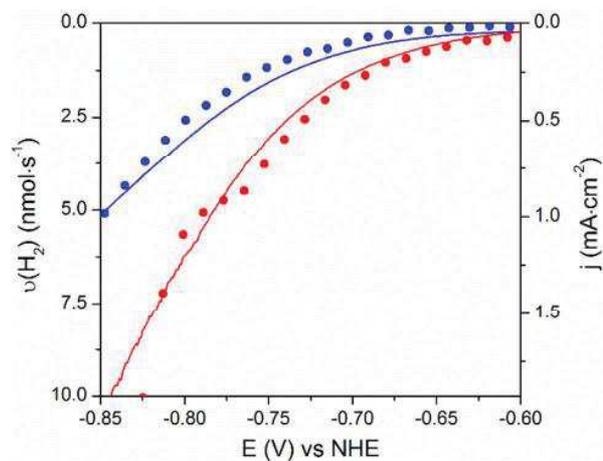
Figure S1. Current densities (plain lines) and hydrogen evolution rates (compensated for different scan rates, see the experimental section) as measured by the in-line GC setup (dots) during LSVs at GDL/MWCNT-**[Co]** electrodes recorded in aqueous phosphate buffer (0.1 M, pH = 2.2) at a scan rate of 0.1 mV·s^{-1} (red) and in aqueous acetate buffer (0.1 M, pH = 4.5) at a scan rate of 0.05 mV·s^{-1} (blue).
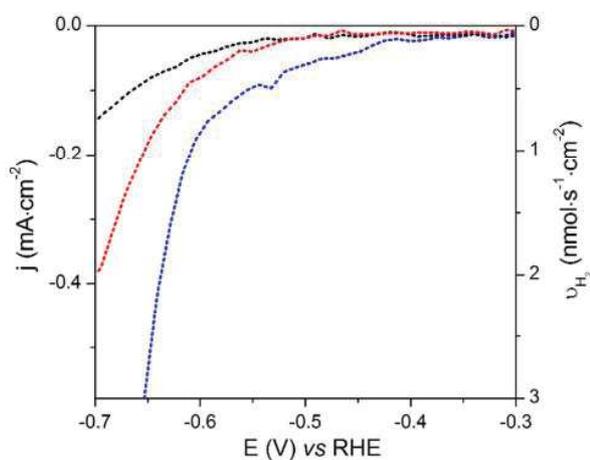
Figure S2. Magnification of the H_2 evolution rates as measured by the in-line GC setup for: GDL/MWCNT (black line), GDL/MWCNT-**[Co]** (red line) and GDL/MWCNT with **1**Cl$_2$ 0.3 mM in solution (blue line). Electrolyte: aqueous phosphate buffer (pH = 2.2); scan rate: 0.1 mV·s^{-1}.

2
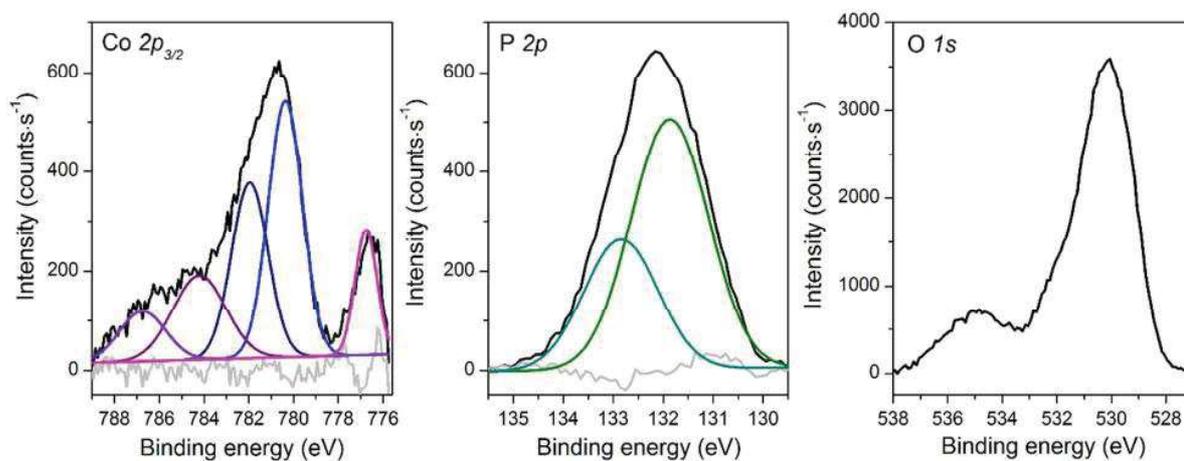
Figure S3. XPS Co *2p₃/₂*, P *2p* decomposed core regions and O *1s* core region of a GDL/MWCNT electrode decorated with the cobalt-based deposit after LSV in pristine aqueous phosphate buffer (0.1 M, pH = 2.2) (see **Figure 4**, purple lines).
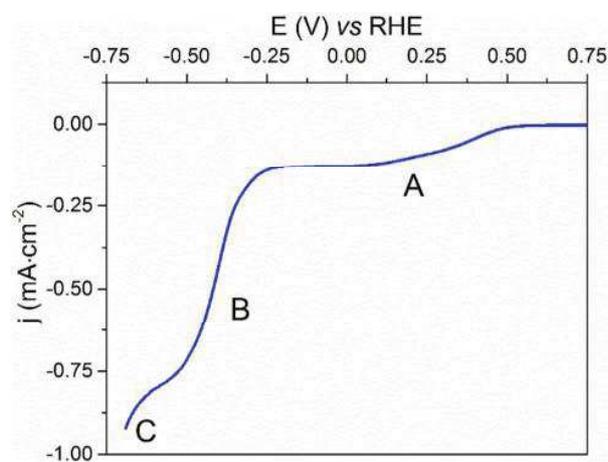
Figure S4. LSV at a static glassy carbon electrode in aqueous phosphate buffer (0.1 M, pH 2.2) with **1**Cl₂ 0.3 mM. Scan rate: 10 mV·s⁻¹.
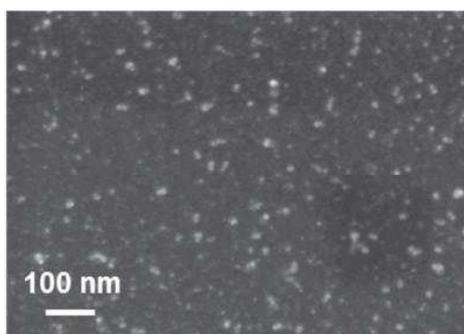
Figure S5. SEM image of glassy carbon electrode equilibrated at – 0.14 V vs RHE for one hour in aqueous phosphate buffer (0.1 M, pH = 2.2) with **1**Cl$_2$ 0.3 mM. The composition of the white particles seen here is similar to the electrolyte and do not contain cobalt.
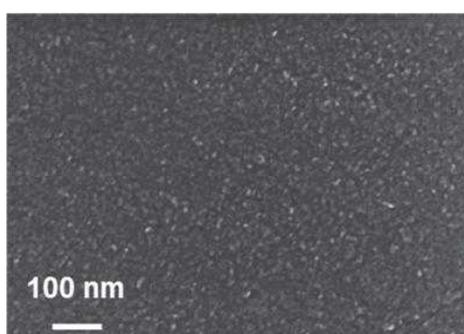
Figure S6. SEM image of a pristine glassy carbon electrode.
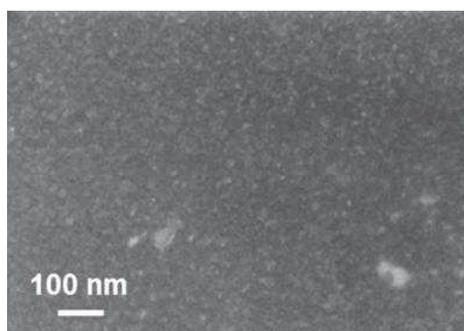
Figure S7. SEM image of glassy carbon electrode equilibrated at –0.45 V vs RHE for one hour in aqueous phosphate buffer (0.1 M, pH = 2.2) with **1**Cl$_2$ 0.3 mM. The composition of the white particles seen here is similar to the electrolyte and do not contain cobalt.

4
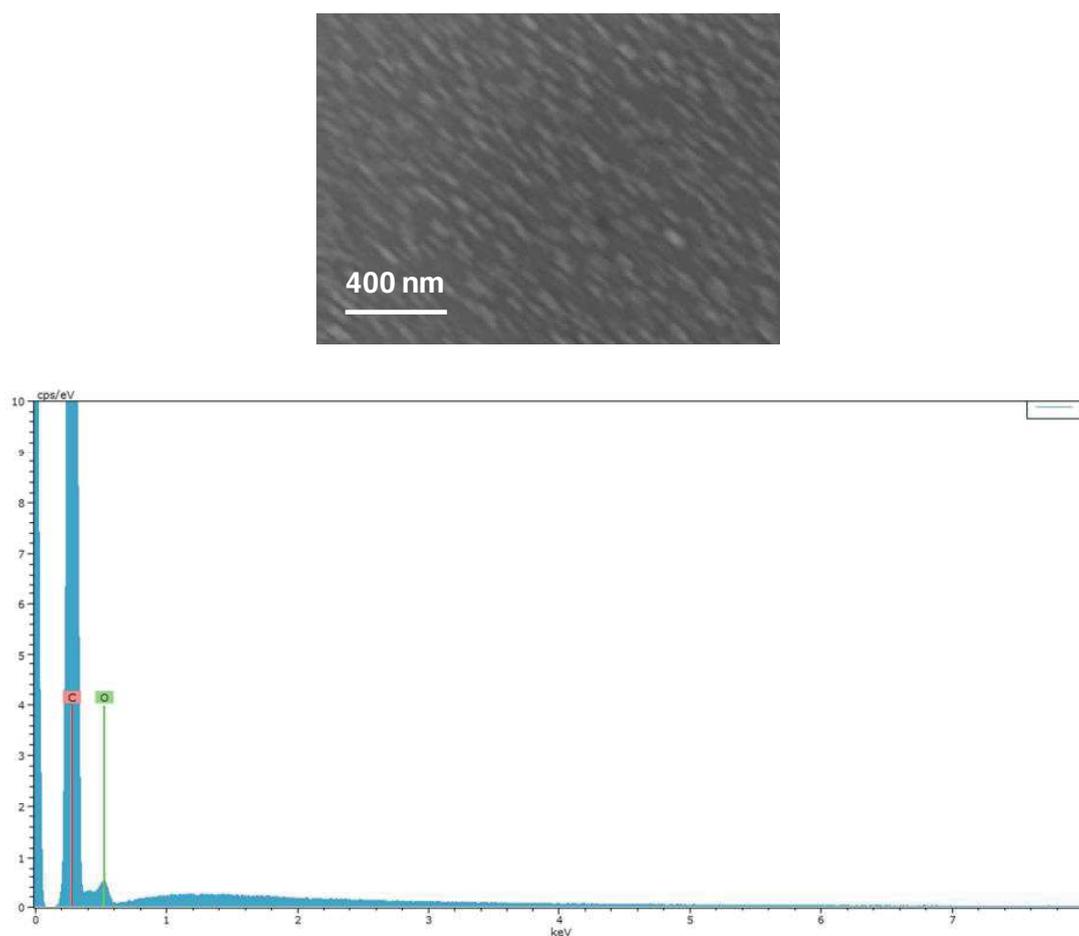
Figure S8. SEM image: amplification of Fig. 7c (glassy carbon electrode equilibrated at –0.57 V vs RHE for 1 hour in aqueous phosphate buffer (0.1 M, pH = 2.2) with **1**Cl$_2$ 0.3 mM after rinsing with distilled water); EDX spectra of the same electrode

5
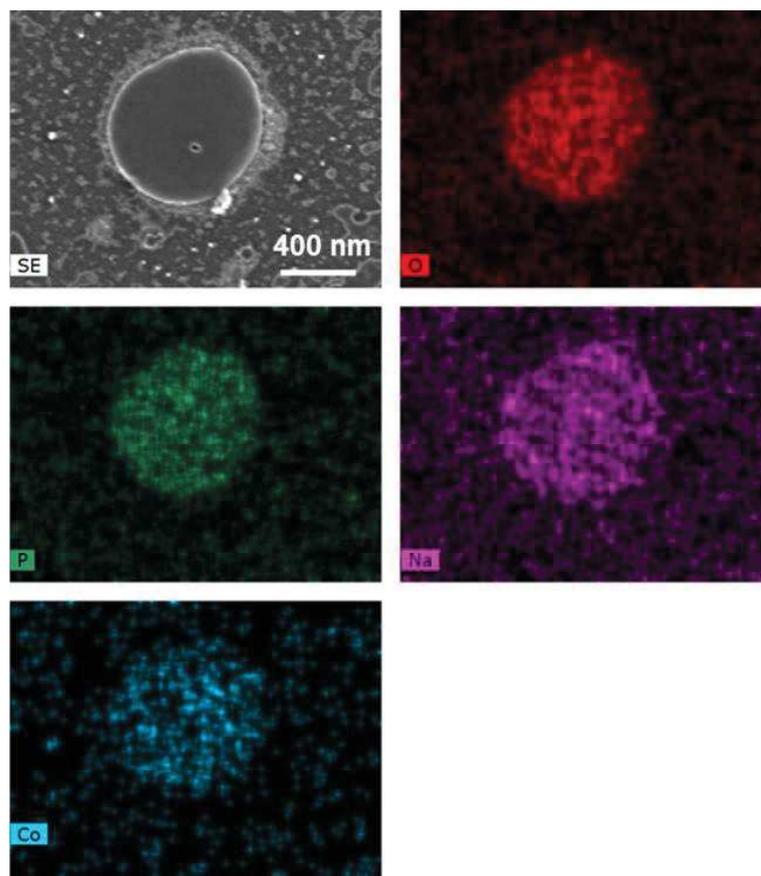
Figure S9. SEM image and EDX elemental mapping at a glassy carbon electrode equilibrated at –0.57 V vs RHE for one hour in aqueous phosphate buffer (0.1 M, pH = 2.2) with **1**Cl$_2$ 0.3 mM
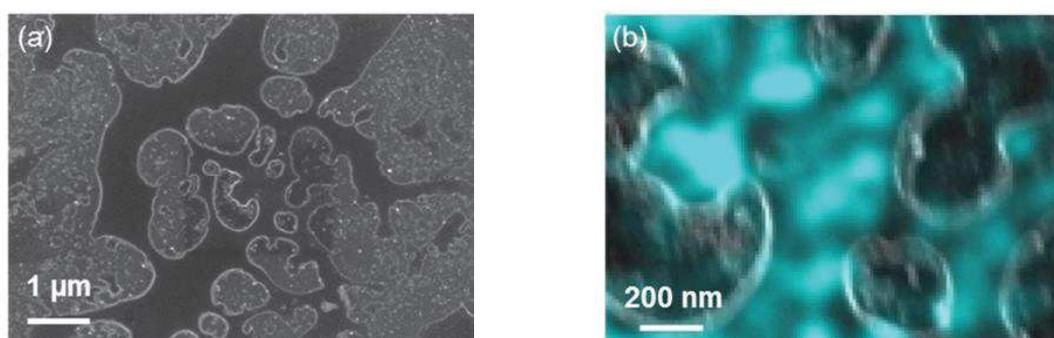
Figure S10. (a) SEM image and **(b)** EDX elemental mapping for Co (Kα_1 line) of a glassy carbon electrode equilibrated at –0.65 V vs RHE for one hour in aqueous phosphate buffer (0.1 M, pH = 2.2) with **1**Cl$_2$ 0.3 mM.

6
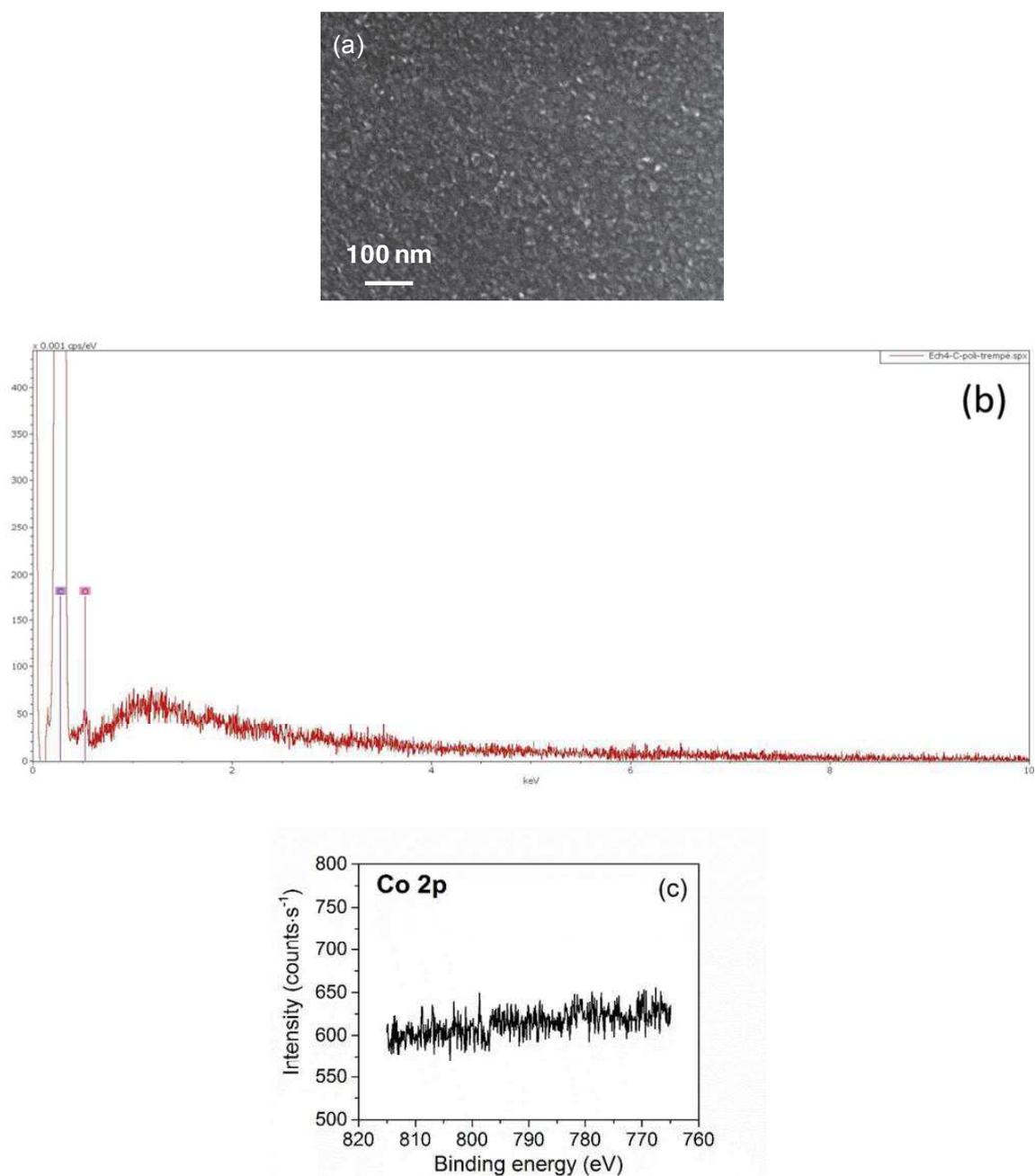
Figure S11. SEM image (a), EDX (b) and XPS spectra (c) of glassy carbon electrode dipped for 1 h in a solution of **1**Cl$_2$ (0.3 mM) in aqueous phosphate buffer (0.1 M, pH = 2.2) and dried in the air without prior rinsing.
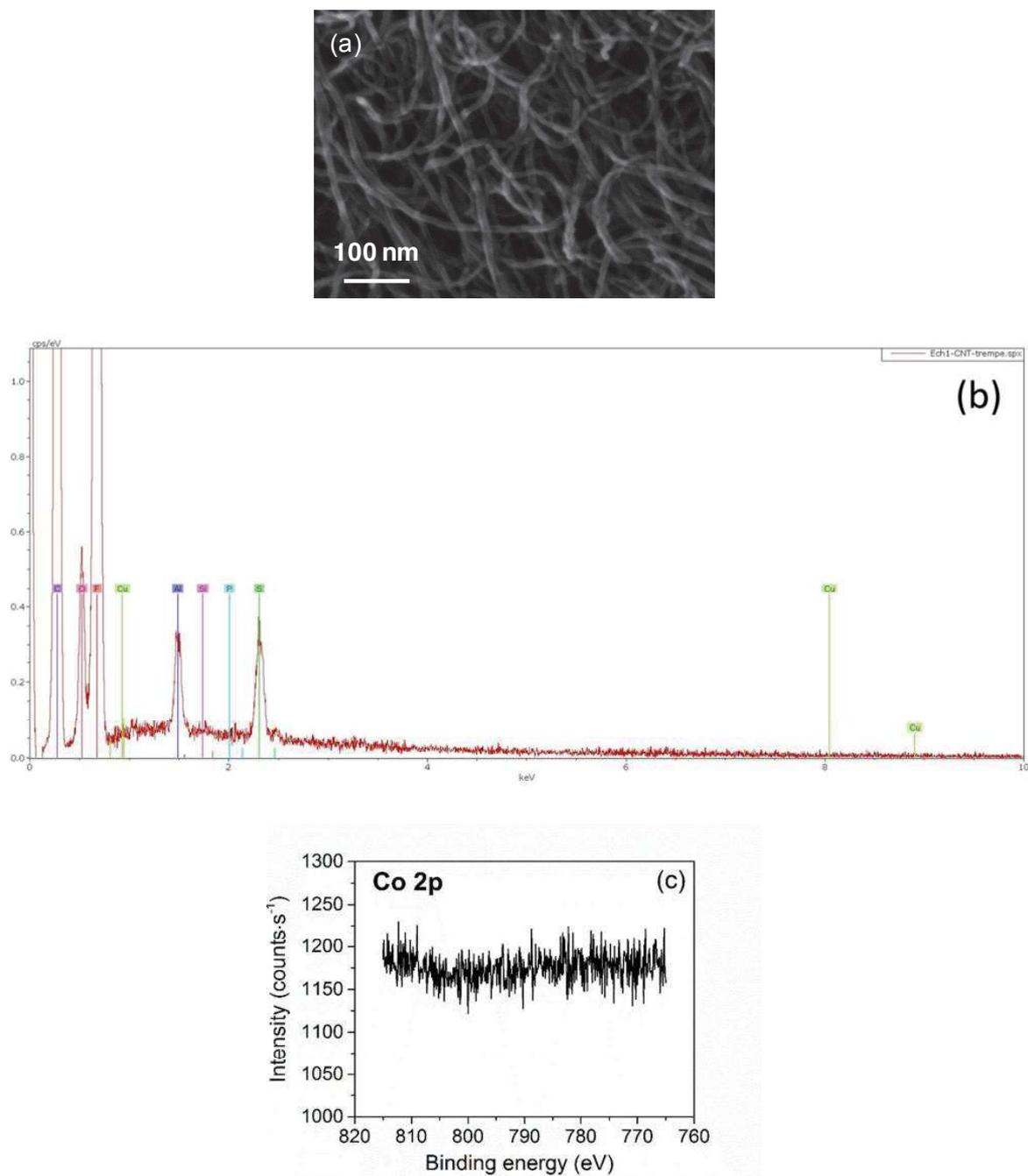
Figure S12. SEM image (a), EDX (b) and XPS spectra (c) of glassy carbon/MWCNT electrode dipped for 1 h in a solution of **1**Cl$_2$ (0.3 mM) in aqueous phosphate buffer (0.1 M, pH = 2.2) and dried in the air without prior rinsing.

8
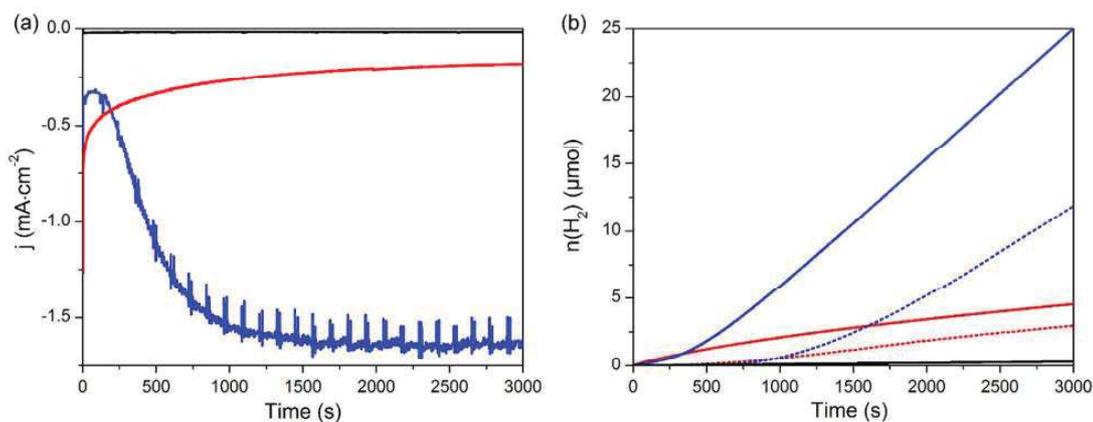
Figure S13. Chronoamperometric measurements at –0.57 V vs RHE at a glassy carbon electrode in aqueous phosphate buffer (0.1 M, pH = 2.2) with **1**Cl$_2$ 0.3 mM (blue lines), at the same electrode after rinsing with distilled water (red lines) and at a blank glassy carbon electrode (black lines) in pristine aqueous phosphate buffer (0.1 M, pH = 2.2): **(a)** current density versus time; **(b)** amount of hydrogen produced assuming an unity faradaic efficiency (plain lines) and as observed by the in-line GC setup (dashed lines).
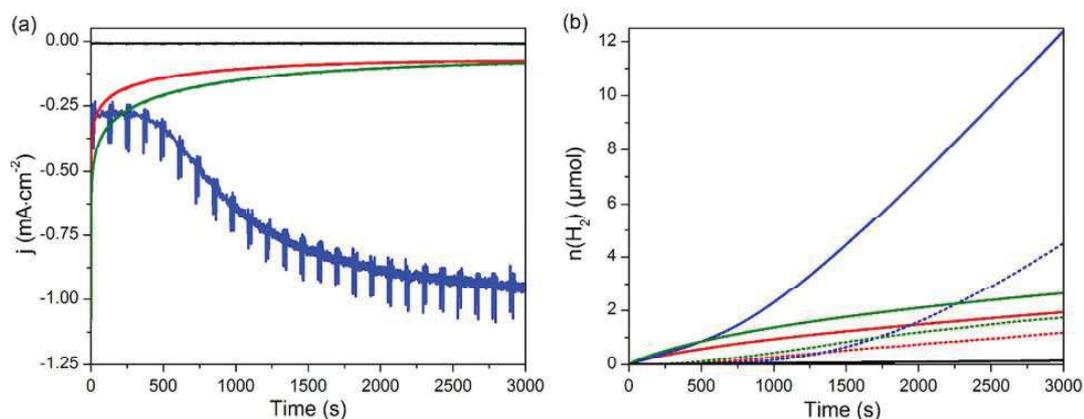
Figure S14. Chronoamperometric measurements at –0.52 V vs RHE at a glassy carbon electrode in aqueous phosphate buffer (0.1 M, pH = 2.2) with **1**Cl$_2$ 0.3 mM (blue lines), at the same electrode after rinsing with distilled water (red lines), at an identically prepared electrode but without rinsing (green lines) and at a blank glassy carbon electrode (black lines) in pristine aqueous phosphate buffer (0.1 M, pH = 2.2): **(a)** current density versus time; **(b)** amount of hydrogen produced assuming an unity faradaic

9

efficiency (plain lines) and as observed by the in-line GC setup (dashed lines).
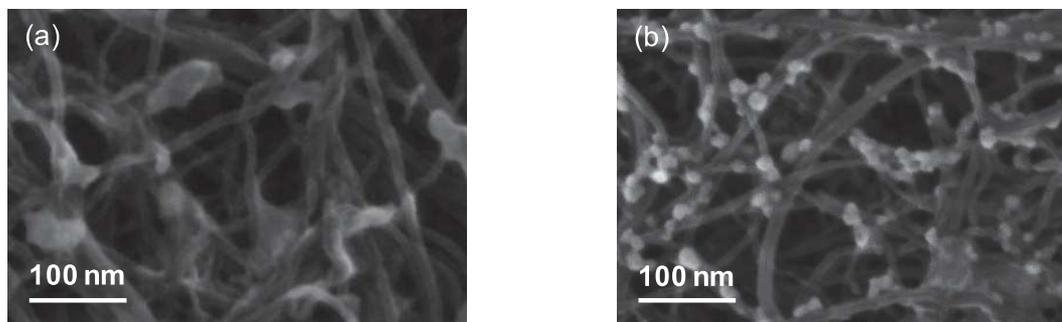
Figure S15. SEM images for: (a) GDL/MWCNT electrode with **1**Cl$_2$ (0.3 mM) in aqueous phosphate buffer (0.1 M, pH = 2.2) after electrolysis at −1.20 V vs RHE for 1h and (b) the same electrode washed for 10 s in water at open circuit potential.
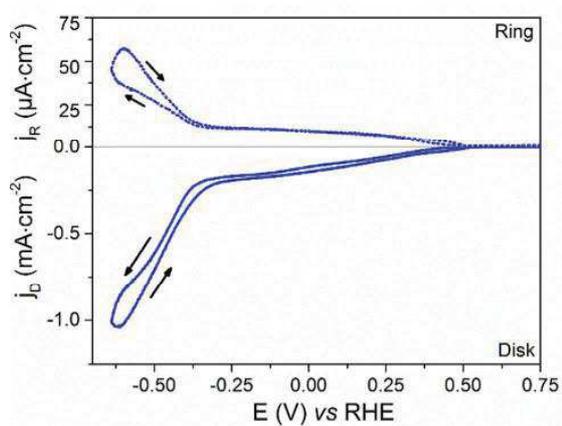
Figure S16. RRDE CV measurements in aqueous phosphate buffer (0.1 M, pH = 2.2) with **1**Cl$_2$ 0.3 mM. The Pt ring electrode was polarized at 0.60 V vs RHE; rotation speed: 1000 rpm; scan rate: 10 mV·s^{-1}.

10

2. Oxygen-tolerance at the immobilized cobalt diimine-dioxime catalyst

To achieve the reductive side of water splitting, hydrogen evolution catalysts are *in fine* to be used in combination with oxygen evolution catalysis. As such, any proton reduction catalyst operating in a device might come in contact with oxygen. The question that follows is whether the catalyst retains its structure and related activity for HER in the presence of O_2 or not. Tolerance to oxygen has hence been identified as another figure of merits for a catalyst.[5] This issue has been tackled in several reports for bulk homogeneous conditions,[5a, 6] but never for molecular HECs attached onto an electrode substrate. And catalyst-immobilized electrodes for hydrogen evolution are especially relevant for the implementation in an overall WS device. We therefore decided to address the issue of oxygen tolerance of the grafted cobalt diimine-dioxime complex and conducted this study on a material similar to the **GDL/MWCNT-Co** one.

We found that the attached **[Co^{III}(DO)(DOH)pnCl₂]** complex catalyzes the reduction of O_2 dissolved in aqueous media with an onset potential of 0.55 V *vs* RHE. The monitoring of the reduced species *via* a rotating ring-disk electrode setup showed that 2- and 4-electron processes are concomitantly occurring at the decorated electrode, yielding water and hydrogen peroxide in 3:1 proportions.

The material is also competent for hydrogen evolution, displaying an overpotential of *ca* 350 mV. Interestingly, the catalytic current attributed to proton reduction in potential sweep experiments is not altered by the presence of oxygenic concentrations in the electrolyte. This finding supports that the grafted **[Co^{III}(DO)(DOH)pnCl₂]** is tolerant to oxygen for the catalysis of hydrogen evolution under transient conditions, which mimics that at stake at early stages of operation of a PEC device.

This work is fully developed below, under the form of an article published by our group in 2015, presenting our findings about O_2-tolerance at the immobilized electrode.[7] Notations and references are inserted in this article independently from the whole manuscript.

Oxygen Tolerance of a Molecular Engineered Cathode for Hydrogen Evolution Based on a Cobalt Diimine−Dioxime Catalyst

Nicolas Kaeffer, Adina Morozan, and Vincent Artero*

Laboratoire de Chimie et Biologie des Métaux, Univ. Grenoble Alpes, CNRS, CEA, 17 rue des Martyrs, 38000, Grenoble, France

ABSTRACT: We report here that a bioinspired cobalt diimine−dioxime molecular catalyst for hydrogen evolution immobilized onto carbon nanotube electrodes proves tolerant toward oxygen. The cobalt complex catalyzes O_2 reduction with an onset potential of +0.55 V vs RHE. In this process, a mixture of water and hydrogen peroxide is produced in a 3:1 ratio. Our study evidences that such side-reductions have little impact on effectiveness of proton reduction by the grafted molecular catalyst which still displays good activity for H_2 evolution in the presence of O_2. The presence of O_2 in the media is not detrimental toward H_2 evolution under the conditions used, which simulate turn-on conditions of a water-splitting device.
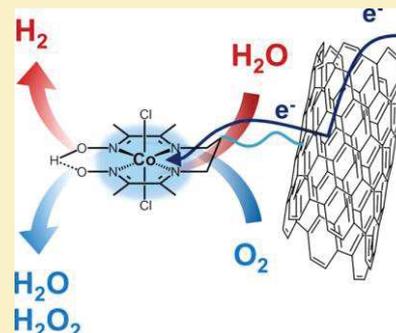
INTRODUCTION

Hydrogen is one of the cleanest and most efficient energy carriers so far.[1] In addition, sustainable hydrogen production through water splitting technologies appears as a promising pathway for large-scale growth in carbon-free energy.[2,3] However, such processes always require catalysts to increase the reaction rate and lower the overpotential of the hydrogen evolution reaction (HER). Platinum-group metals are the most active electrocatalysts for HER, but their large scale utilization is restricted by their limited supply and the cost issue.[4] The development of nonprecious alternative catalysts is thus a key scientific challenge. Nature provides examples of such catalysts in the form of hydrogenases having iron- and nickel-based active sites for fast and reversible interconversion of protons into hydrogen.[5] The resolution of the tridimensional structure of their active site and further insights into their catalytic mechanism allowed synthetic chemists to develop a series of molecular bioinspired HER electrocatalysts composed of inexpensive, earth-abundant elements.[6−8] These compounds have recently been subjected to the benchmarking of their catalytic performances.[9] However, while good activity and robustness are the primary figures of merit for assessing their possible implementation in technological devices, HER catalytic materials should also exhibit a certain tolerance to oxidative conditions. Specifically, these catalysts have to prove resistant to degradation by molecular oxygen either penetrating into the device during turn-off phases or produced *in situ* as a result of water splitting. This concern is reminiscent from hydrogenases, the most active of which are extremely oxygen sensitive and susceptible to inactivation by even traces of oxygen,[5] even if some of them exhibit good tolerance to atmospheric oxygen thanks to a specific iron−sulfur cluster.[10−13] Similarly, O_2 inhibition has been identified as a main barrier in producing viable molecular proton reduction catalysts.[14] However, there

has been very little progress in the development of transition-metal-based H_2-generating molecular catalysts that operate in the presence of O_2. To the best of our knowledge, all known examples shown to be functional under air are based on cobalt, including cobaloximes,[15,16] a cobalt−corrole catalyst,[17] a cobalt−microperoxidase,[18] and cobalt diimine−dioxime complexes.[19] Significant progress has been made in our laboratory during the last 10 years regarding the development of highly active molecular catalysts for HER[6,20−30] and their integration within electrocatalytic nanomaterials[24,31,32] based on carbon nanotubes (CNTs).[14e,15] The morphology and electrical conductivity of CNTs make them ideal supports to promote the electrocatalytic activity of the molecular complexes.[33] In particular, we recently reported on an efficient cathode active for HER from aqueous solution and based on a cobalt diimine−dioxime complex[30] immobilized on amino-functionalized multiwall carbon nanotubes (MWCNTs).[34] Here we report on the behavior of this H_2-evolving cathode material in the presence of oxygen.

EXPERIMENTAL SECTION

Materials. Solvents, starting materials, and supporting electrolyte salt (tetrabutylammonium tetrafluoroborate, $^nBu_4NBF_4$) were purchased in the highest purity from Sigma-Aldrich and used as received, unless otherwise stated. 2,6-Lutidine was purchased from Lancaster. Acetonitrile and dichloromethane were distilled on CaH_2. Nafion 117 solution (5 wt % in a mixture of lower aliphatic alcohols and water,
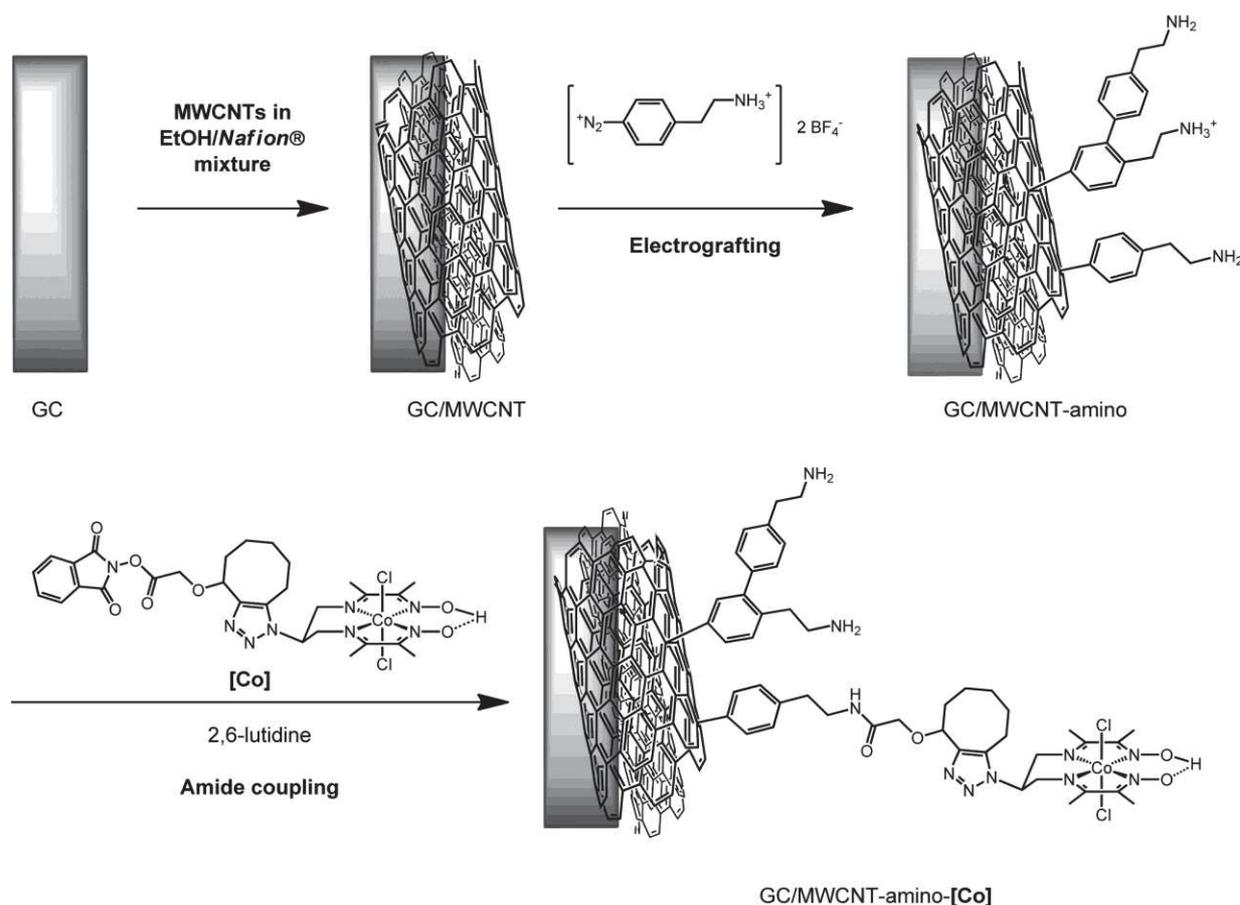
Figure 1. Synthetic approach used to construct the GC/MWCNT-amino-[Co] electrode.

Sigma-Aldrich) was used. Oxygen gas (Air Products ultrapur quality) was of 99.995% purity. UP-NC7000WT (purity >90%) multiwall carbon nanotubes (MWCNTs) were obtained from Nanocyl (Belgium). The dichloro cobalt complex of a diimine−dioxime ligand bearing an activated ester group, [Co(DO)-(DOH)C_8-pnCl$_2$] (labeled [Co]) was prepared as previously described.[34] (4-Aminoethyl)benzene diazonium tetrafluoroborate was prepared according to literature procedures.[35]

Preparation of the GC/MWCNT Electrode. The glassy carbon (GC) disk (0.196 cm^2) of the rotating ring-disk electrode (RRDE, Pt ring, Pine Instruments) was polished on an MD-Nap polishing pad (Struers) with 1 μm synthetic diamond suspension (Struers, DP-Suspension M) and lubricant (Struers, DP-Lubricant Blue) and then was rinsed with ethanol and dried in the air. The MWCNTs (2 mg) were dispersed in a mixture of ethanol (200 μL) and 5 wt % Nafion solution (20 μL) under sonication (30 min). A GC/MWCNT electrode was obtained by dropping 100 μL of the MWCNT suspension onto the GC disk and drying in the air.

Functionalization of the GC/MWCNT Electrode with [Co]. The method is adapted from the procedure described in the literature.[34] The GC/MWCNT working electrode was used in a three-electrode electrochemical cell setup connected to a potensiostat (SP-300 Bio-Logic) and a MSR rotator (Pine Instruments). The counter electrode and reference electrode were a Ti wire and a Ag/AgCl/3 M KCl electrode (abbreviated as Ag/AgCl), respectively.

(4-Aminoethyl)benzene diazonium tetrafluoroborate (10 mg, 31 μmol) was dissolved in acetonitrile (25 mL) together with ^{n}Bu$_4$NBF$_4$ (0.1 M). The solution was degassed with argon prior to use. The functionalization of the GC/MWCNT electrode was performed using cyclic voltammetry through the recording of three scans between −1.0 and +0.5 V vs Ag/AgCl. The amino-functionalized GC/MWCNT electrode (GC/MWCNT-amino) was then rinsed by rotation of the electrode dipped in a pristine MeCN solution at 200 rpm for a few minutes and subsequently dried under a flow of argon. The GC/MWCNT-amino electrode was dipped into a solution of [Co] (3.7 mg, 5 μmol) in distilled dichloromethane (5 mL) added with 2,6-lutidine (5 μL). The reaction was held overnight under an argon atmosphere with continuous rotation of the electrode at 200 rpm. The resulting GC/MWCNT-amino-[Co] electrode was then rinsed with dichloromethane and dried under a flow of argon.

Electrochemical Measurements. Electrochemical analysis was performed using a BioLogic SP300 bipotentiostat. The electrochemical experiments were carried out in three-electrode electrochemical cells under a nitrogen atmosphere using the modified GC/Pt RRDE described above as the working electrode. A titanium wire was used as the auxiliary electrode. The Ag/AgCl reference electrodes were independently calibrated with 5 mM [Fe(CN)$_6$]$^{4-}$. The [Fe(CN)$_6$]$^{3-}$/[Fe(CN)$_6$]$^{4-}$ couple (E^0 = 0.20 V vs Ag/AgCl in phosphate

B

buffer at pH 7) has then been used for the standardization of the measurements.[36]

The electrolyte used was either an aqueous acetate buffer (0.1 M, pH 4.5) or acetonitrile with $^{n}Bu_4NBF_4$ (0.1 M) as supporting electrolyte. Voltammograms were recorded by scanning the disk potential between −0.6 and +0.7 V vs Ag/AgCl at 10 mV·s^{-1} in N_2- and O_2-saturated electrolytes. RRDE measurements were conducted at 10 mV·s^{-1}, with a rotation speed of 1500 rpm in an O_2-saturated electrolyte; the potential of the Pt ring was set at +1.1 V vs Ag/AgCl. The HER polarization curves were measured at a scan rate of 10 mV·s^{-1} in both N_2- and O_2-saturated electrolytes.

■ RESULTS

In order to have a better control on oxygen amounts, the molecular engineered cathode for hydrogen evolution based on a cobalt diimine−dioxime catalyst was constructed onto a glassy carbon (GC) electrode instead of the previously used porous gas diffusion layer (GDL). This design indeed allows a straightforward degassing of the electrolyte solution and avoids entrapment of O_2 in the porous electrode substrate. The cathode was prepared according to Figure 1, following the method previously described.[34] MWCNTs were suspended in an ethanol/Nafion mixture and drop casted onto the GC electrode. Subsequent surface functionalization by amino groups was performed through the electroreduction of (4-aminoethyl)benzene diazonium tetrafluoroborate using cyclic voltammetry.[32,37] The dichloro cobalt complex of a diimine−dioxime ligand bearing an activated ester group, $[Co(DO)(DOH)C_8\text{-}pnCl_2]$ (hereafter labeled $[Co]$), was covalently grafted at the surface of MWCNTs through amide coupling between the activated ester moiety in $[Co]$ and an amine function at the surface of MWCNTs.

The resulting GC/MWCNT-amino-$[Co]$ electrode was characterized by cyclic voltammetry in acetonitrile. The grafting of $[Co]$ is evidenced by the observation of two quasi-reversible systems at −0.11 and −0.67 V vs Ag/AgCl (Figure 2), respectively, assigned to the Co(III)/Co(II) and the Co(II)/Co(I) couples of $[Co]$ by analogy with previous studies.[34] The integration of the wave assigned to the Co(II)/Co(I) couple allows a catalyst loading of ca. 1.1×10^{-8} mol·cm^{-2} to be determined.
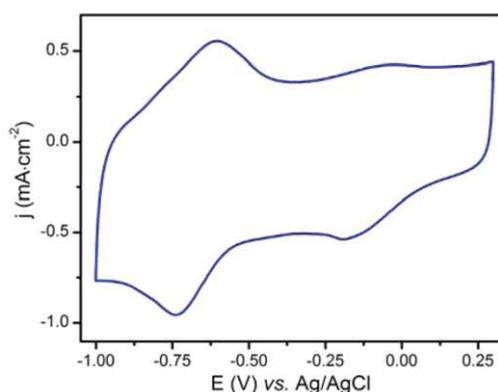
Figure 2. Cyclic voltammogram of a GC/MWCNT-amino-$[Co]$ cathode recorded in acetonitrile solution of $^{n}Bu_4NBF_4$ (0.1 M) at 20 mV·s^{-1}.

We then investigated the behavior of the GC/MWCNT-amino-$[Co]$ cathode in the presence of oxygen. All following electrochemical studies were performed in a 0.1 M aqueous acetate buffer (pH 4.5) electrolyte which was shown to provide optimal conditions for proton reduction.[34] Cyclic voltammograms recorded at the GC/MWCNT-amino-$[Co]$ cathode or GC/MWCNT-amino electrodes in N_2-saturated media do not display any noticeable electrochemical features (Figure 3).
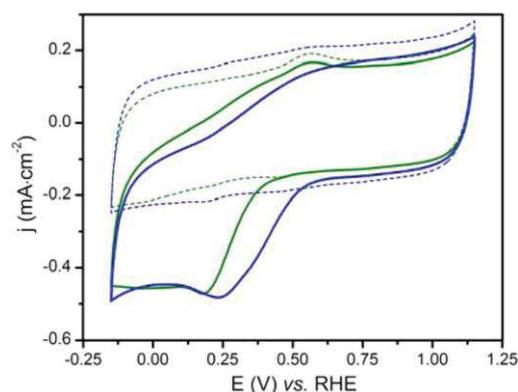
Figure 3. Cyclic voltammograms recorded at GC/MWCNT-amino (green lines) and GC/MWCNT-amino-$[Co]$ (blue lines) electrodes in O_2-saturated (plain lines) or N_2-saturated (dashed lines) aqueous acetate buffer electrolytes (0.1 M, pH 4.5) at a scan rate of 10 mV·s^{-1}.

However, when the solution is saturated with oxygen, a reduction wave appears for both electrodes and is assigned to a catalytic oxygen reduction reaction (ORR). This wave shifts by 170 mV to more positive potentials for the GC/MWCNT-amino-$[Co]$ cathode compared to the GC/MWCNT-amino electrode used as a control (Figure 3). This observation suggests that the grafted cobalt complex plays an active role in the ORR process.

To gain more insights into the ORR process, we then used the rotating ring-disk electrode (RRDE) technique which allows quantification of the relative amounts of H_2O_2 and H_2O resulting from the two-electron (eq 1) and four-electron (eq 3) reductions of O_2, respectively.

$$O_2 + 2H^+ + 2e^- \rightarrow H_2O_2 \tag{1}$$

$$H_2O_2 + 2e^- + 2H^+ \rightarrow H_2O \tag{2}$$

$$O_2 + 4H^+ + 4e^- \rightarrow 2H_2O \tag{3}$$

Indeed, in such an experiment, H_2O_2 produced at the rotating disk electrode is ejected radially and oxidatively detected at the Pt ring maintained at a potential of 1.1 V vs Ag/AgCl (1.55 V vs RHE). The current measured at the ring thus directly relates to the amount of H_2O_2 produced at the disk during ORR. The number of electrons (n) transferred to O_2 during ORR and the relative amount of hydrogen peroxide (% H_2O_2) produced can be determined using the following equations

$$n = (4I_d)/[I_d + (I_r/N)] \tag{4}$$

$$\% \ H_2O_2 = [(4 - n)/2] \times 100 \tag{5}$$

where I_d is the faradic current at the disk and I_r the faradic current at the ring (S_{ring} = 0.110 cm^2). The value of the
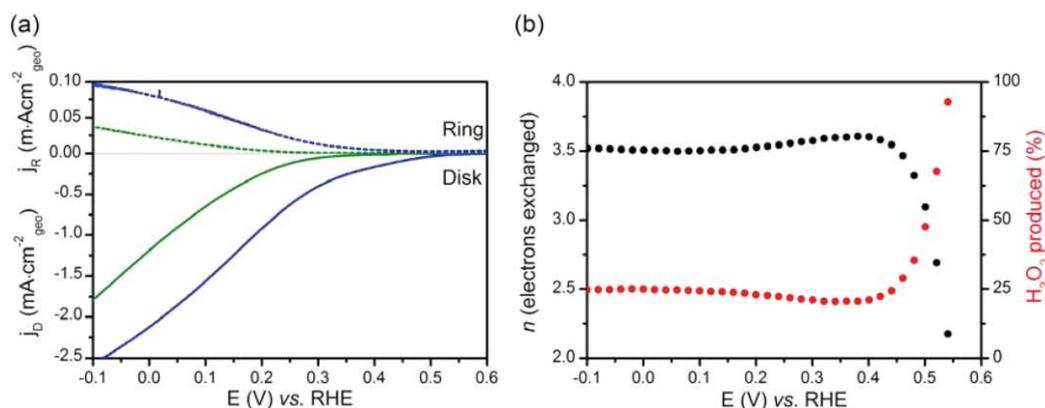
Figure 4. (a) RRDE measurements at GC/MWCNT-amino (green lines) and GC/MWCNT-amino-[Co] (blue lines) electrodes with disk and ring currents shown as plain lines and dashed lines, respectively (E_{ring} = 1.55 V vs RHE, 1500 rpm, scan rate: 10 mV·s^{-1}). (b) The potential dependence of n (black dots, left scale) and of the ratio of H_2O_2 produced (red dots, right scale).

collection efficiency of the rotating ring disk electrode was measured as $N = 0.27$ using the one-electron $[Fe(CN)_6]^{3-/4-}$ redox couple, according to the manufacturer's instructions.

The RRDE curves for GC/MWCNT-amino and GC/MWCNT-amino-[Co] electrodes are shown in Figure 4a, and the potential dependence of n is shown in Figure 4b. The reduction of O_2 on the GC/MWCNT-amino-[Co] electrode commences at +0.55 V vs RHE, while the reduction wave on the GC/MWCNT-amino electrode starts at +0.40 V vs RHE, reproducing the behavior observed on CVs (Figure 3). The reduction current continuously increases with increasing cathodic potential. No current plateau is observed, as expected for ORR reaction only controlled by O_2 diffusion. The observation of positive ring currents indicates production of hydrogen peroxide at the disk. The calculated number of electrons involved in ORR on the GC/MWCNT-amino-[Co] electrode was found at ca. 3.5 (Figure 4b), and the ORR is essentially assigned to a combined O_2 reduction via 2e$^-$ and 4e$^-$ reduction pathways with ca. 25% H_2O_2 production.

The GC/MWCNT-amino-[Co] cathode catalyzes HER at more negative potentials than ORR. Figure 5 shows the corresponding polarization curve measured in acetate buffer in

the absence of dissolved oxygen and provides a comparison with the GC/MWCNT-amino material.[38] A 150 mV positive shift of the polarization curve is observed upon covalent grafting of the [Co] complex, as previously reported.[34] The GC/MWCNT-amino-[Co] cathode produces H_2 from an onset potential of −0.35 V vs RHE and reaches a current density of 1 mA·cm^{-2} at ca. −0.55 V vs RHE.

To further determine if the presence of dissolved oxygen impacts the HER activity of the GC/MWCNT-amino-[Co] cathode, we studied its behavior toward proton reduction in an O_2-saturated electrolyte. As shown in Figure 6, a first reductive
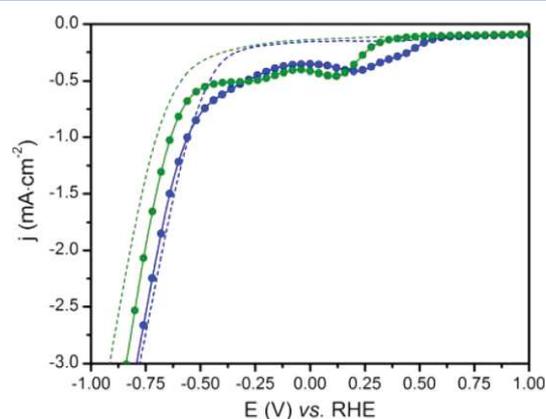
Figure 6. Linear sweep voltammograms of GC/MWCNT-amino (green lines) and GC/MWCNT-amino-[Co] (blue lines) electrodes in O_2-saturated (plain line) or N_2-saturated (dashed lines) aqueous acetate buffer electrolytes (0.1 M, pH 4.5) at 10 mV·s^{-1} scan rate.

Figure 5. Linear sweep voltammograms for GC/MWCNT-amino (green line) and GC/MWCNT-amino-[Co] (blue line) electrodes recorded in N_2-saturated aqueous acetate buffer electrolyte (0.1 M, pH 4.5) at 10 mV·s^{-1} scan rate.

event starting from +0.55 V vs RHE is observed, assigned to ORR by comparison with RRDE experiments (Figure 4). While shifting potential downward, a catalytic current raises from ∼ −0.35 V vs RHE. This current overlaps very well with the one observed in the absence of oxygen (Figure 5) and assigned to H_2 evolution. The GC/MWCNT-amino electrode behaves differently with ORR taking place at more negative potentials and the catalytic proton reduction polarization curve shifted 80 mV more cathodic than for GC/MWCNT-amino-[Co].

■ DISCUSSION

Current efforts to integrate the MWCNT-amino-[Co] H$_2$-evolving cathode[34] within a complete photoelectrochemical (PEC) water-splitting cell lead us to investigate the impact of residual O$_2$ on the HER. As we were manipulating our material under atmospheric conditions before experiments, we noticed that a reductive side-reaction occurred during cathodic polarization. This event, found at more positive potentials than proton reduction, was assigned to the reduction of residual oxygen. Actually, oxygen can be present in the cathodic compartment for, at least, two reasons. It can first be trapped inside the porous gas diffusion layer (GDL) used as an electrode support,[34] as a consequence of atmospheric handling of the cathode material. Alternatively, O$_2$ can diffuse from the anodic part where it is produced as a result of water oxidation. The impact of O$_2$ on catalytic proton reduction activity hence appears as a general issue when dealing with integration of HER cathodes within full PEC devices. In the present study, we report on the impact of O$_2$ on the production of H$_2$ with a MWCNT-amino-[Co] cathode deposited on a compact glassy carbon (GC) electrode support, thus allowing for an easy and complete purge of the cell when needed. The GC/MWCNT-amino-[Co] architecture was successfully designed by the covalent approach previously developed in our group (Figure 1).[34] The catalyst loading, estimated around 1.1 × 10^{-8} mol·cm^{-2}, is in good agreement with the one previously determined for the GDL/MWCNT-amino-[Co] cathode (4.5 × 10^{-9} mol·cm^{-2}). It follows that changing the electrode substrate from GDL to GC does not influence further surface functionalization and grafting of the cobalt diimine−dioxime complex.

As shown in Figure 2, the presence of [Co] on the amino-functionalized MWCNTs has a direct impact onto the ORR, with a 150 mV anodic shift of the reduction wave. This observation supports an active role of the immobilized [Co] complex for catalyzing O$_2$ reduction. Cobalt complexes are known to be ORR catalysts and have been intensively studied in that context.[39,40] In particular, Shamsipur et al. made similar observations with a cobalt diimine−dioxime complex [Co(DO)(DOH)pnCl$_2$], adsorbed onto the surface of a preanodized GC electrode and dipped into a 0.1 M aqueous acetate buffer solution at pH 4.[19] In line with this report, we also observe that catalytic ORR reaction develops at a potential corresponding to the Co(III)/Co(II) couple of the immobilized cobalt complex (Figure 2). Of note, [Co] sites are not equally distributed within the bulk of the MWCNT film but rather in a thin enveloping coating.[37] This explains why we do not see any effect of the nanostructure of the MWCNT film to limit O$_2$ diffusion, as it has been found by Armstrong and co-workers for a hydrogenase-based 3D electrode based on compact porous carbon material.[41]

ORR is a multielectronic process. Hence, its mechanism is quite complicated and involves many intermediates, primarily depending on the nature of the electrode material, catalyst, and/or electrolyte. Two pathways are possible in acidic media:[42] (i) one is a 2e$^-$ mechanism generating the intermediate hydrogen peroxide, H$_2$O$_2$ (eq 1), with further reduction (eq 2) or its dismutation; (ii) the other is a 4e$^-$ mechanism directly producing H$_2$O (eq 3), an ideal pathway, since it avoids the formation of reactive oxygen species (ROS). RRDE measurements showed that 3.5 electrons on average are involved in O$_2$ reduction at the GC/MWCNT-amino-[Co] electrode over a wide range of potentials (−0.1 to +0.4 V vs RHE). This is an indication of mixed 2e$^-$ and 4e$^-$ processes with a predominantly 4e$^-$ transfer pathway and ca. 25% H$_2$O$_2$ production. A likely mechanism for ORR involves first coordination of O$_2$ to a Co(II) species, generating a Co(III)-superoxo intermediate,[43] immediately reduced at the electrode to give a Co(II)-peroxo/hydroperoxo species[44−46] from which the two pathways diverge.

Generation of H$_2$O$_2$ at the vicinity of the electrode surface may damage the structure of the cobalt-based molecular catalyst. To address this issue, we then investigated the HER properties of the GC/MWCNT-amino-[Co] electrode both under N$_2$-degassed and O$_2$-saturated conditions. Under deaerated conditions, H$_2$ evolution is observed from an onset overpotential of 350 mV, consistent with a catalytic cycle involving the Co(II)/Co(I) couple of the grafted [Co] complex.[47] The overpotential corresponding to a current density of 1 mA·cm^{-2} is 550 mV for the GC/MWCNT-amino-[Co] electrode. Such a value is comparable with that (580 mV) measured for the same material deposited onto GDL[34] if the variation in [Co] loading is taken into consideration. This point demonstrates the ability of the GC/MWCNT-amino-[Co] cathode to evolve hydrogen at low overpotential. Within the accuracy of the measurement, the HER activity of the [Co]-based cathode is unaffected by the presence of O$_2$, as far as both the overpotential corresponding to a current density of 1 mA·cm^{-2} and the onset overpotential are concerned. The only notable difference is the reduction process observed at potentials below 0.55 V vs RHE assigned to ORR. Of note, on the control GC/MWCNT-amino electrode, the catalytic wave attributed to HER appears as superimposed onto the catalytic plateau ORR current, indicating that O$_2$ and H$^+$ reduction processes can occur simultaneously at the electrode surface. Such a phenomenon is not observed on the GC/MWCNT-amino-[Co] cathode. By contrast, the HER polarization curves recorded in the presence of O$_2$ are superimposed with that measured in its absence, which speaks for both processes competing for the same [Co] catalytic sites. It is possible that HER and ORR take place in geographically distinct regions. The [Co] sites exposed at the surface of the film may achieve ORR preventing access of O$_2$ to the bulk of the MWCNT-amino-[Co] film where only H$_2$ evolution takes place. This dual behavior would mirror the mechanism at play in a recently reported enzymatic hydrogel.[48,49] However, we found it unlikely because of the relatively low thickness of the polyphenylene film deposited at the external surface of the MWCNT film during functionalization.[37] Anyhow, our data show that the [Co] sites are O$_2$-tolerant HER catalysts, since they are able to achieve H$_2$ evolution in the presence of O$_2$. A similar conclusion was previously reached by Reisner's group on a parent [Co(dmgH)$_2$]-type (dmgH$_2$ = dimethylglyoxime) catalyst when 21% O$_2$ was introduced in the headspace of the electrochemical cell.[15] We note that the conditions used in our experiments are quite harsh and do not directly reflect more realistic O$_2$ concentration in electrolyte when a 21% O$_2$ in air atmosphere is used as headspace. Still, we postulate that the conditions used to obtain the data shown in Figure 6 simulate in first approximation the events at stake just after turning on a PEC device. Back to the results previously described in ref 34 (Figure 4b and c), it is obvious that the deviation of faradic yield from unity mainly occurs at the start of the controlled potential coulometry experiment, which we assigned to reduction of traces of O$_2$ trapped within the film with 495 ± 25 turnovers achieved with the experiment.

Several reasons might be invoked to support the high O_2 tolerance of the HER catalyzed by grafted [Co] complexes. A reason for the disconnection between H^+ and O_2 reduction processes could first arise from the fact that ORR develops at potentials corresponding to the Co(III)/Co(II) couple of the grafted complex while HER involves its Co(II)/Co(I) couple. Then, the solubility of O_2 in aqueous solutions is quite low (0.27 mmol·L^{-1}) compared to the proton concentration. It is thus not surprising that proton binding takes over O_2 activation at potentials where Co(I) is formed. However, should oxygen bind to a grafted Co(I) complex, it would directly generate the same Co(III)-peroxo/hydroperoxo intermediate as discussed above. From this species, H_2O_2 shall evolve before degradation could occur through intramolecular attack[50] on nearby unsaturated imino positions of the diimine–dioxime ligand. In any case, formation of H_2O_2, even as a minor product of ORR, might be an issue for long-term operation if it accumulates in the electrolyte. Solutions to overcome long-term degradation may include the use of catalysts such as catalase mimics for H_2O_2 dismutation into O_2 and H_2O. Another strategy has been recently developed by Plumeré and co-workers. The catalyst, an O_2-sensitive hydrogenase, was integrated into a methyl-viologen containing hydrogel. In the reduced state formed under catalytic H^+/H_2 conditions, this redox mediator reduces O_2 at the extremity of the catalytic layer in contact with the electrolyte and thus prevents degradation of buried hydrogenase enzymes.[48] It would be very interesting to extend such a strategy, by which an immobilized HER catalyst is shielded from undesired ORR, to synthetic molecular systems such as our MWCNT-amino-[Co] electrode.

CONCLUSION

We report here on O_2 tolerance of an inexpensive cobalt diimine–dioxime catalyst covalently grafted on carbon nanotubes which evolves H_2. Electrochemical studies demonstrate good selectivity for electrocatalytic reduction of protons over oxygen under O_2-saturated conditions. Oxygen is mainly reduced to water through a $4e^-$ process, but significant amounts of H_2O_2 are formed anyway, which may cause long-term degradation of such a cathode material integrated in a PEC device. To overcome this issue, alternative O_2 protection strategies are required.

AUTHOR INFORMATION

Corresponding Author
*E-mail: vincent.artero@cea.fr. Phone: +33 4 38 78 91 06.

Notes
The authors declare no competing financial interest.

ACKNOWLEDGMENTS

REFERENCES

(1) Armaroli, N.; Balzani, V. The Hydrogen Issue. *ChemSusChem* **2011**, *4*, 21–36.
(2) Lewis, N. S.; Nocera, D. G. Powering the planet: Chemical Challenges in Solar Energy Utilization. *Proc. Natl. Acad. Sci. U.S.A.* **2006**, *103*, 15729–15735.
(3) Thapper, A.; Styring, S.; Saracco, G.; Rutherford, A. W.; Robert, B.; Magnuson, A.; Lubitz, W.; Llobet, A.; Kurz, P.; Holzwarth, A.; et al. Artificial Photosynthesis for Solar Fuels — an Evolving Research Field within AMPEA, a Joint Programme of the European Energy Research Alliance. *Green* **2013**, *3*, 43–57.
(4) Vesborg, P. C. K.; Jaramillo, T. F. Addressing the Terawatt Challenge: Scalability in the Supply of Chemical Elements for Renewable Energy. *RSC Adv.* **2012**, *2*, 7933–7947.
(5) Lubitz, W.; Ogata, H.; Rüdiger, O.; Reijerse, E. Hydrogenases. *Chem. Rev.* **2014**, *114*, 4081–4148.
(6) Artero, V.; Chavarot-Kerlidou, M.; Fontecave, M. Splitting Water with Cobalt. *Angew. Chem., Int. Ed.* **2011**, *50*, 7238–7266.
(7) Du, P. W.; Eisenberg, R. Catalysts Made of Earth-Abundant Elements (Co, Ni, Fe) for Water Splitting: Recent Progress and Future Challenges. *Energy Environ. Sci.* **2012**, *5*, 6012–6021.
(8) Thoi, V. S.; Sun, Y. J.; Long, J. R.; Chang, C. J. Complexes of Earth-Abundant Metals for Catalytic Electrochemical Hydrogen Generation under Aqueous Conditions. *Chem. Soc. Rev.* **2013**, *42*, 2388–2400.
(9) Artero, V.; Saveant, J.-M. Toward the Rational Benchmarking of Homogeneous H2-Evolving Catalysts. *Energy Environ. Sci.* **2014**, *7*, 3808–3814.
(10) Goris, T.; Wait, A. F.; Saggu, M.; Fritsch, J.; Heidary, N.; Stein, M.; Zebger, I.; Lendzian, F.; Armstrong, F. A.; Friedrich, B.; et al. A Unique Iron-Sulfur Cluster is Crucial for Oxygen Tolerance of a [NiFe]-Hydrogenase. *Nat. Chem. Biol.* **2011**, *7*, 310–318.
(11) Fritsch, J.; Scheerer, P.; Frielingsdorf, S.; Kroschinsky, S.; Friedrich, B.; Lenz, O.; Spahn, C. M. T. The Crystal Structure of an Oxygen-Tolerant Hydrogenase Uncovers a Novel Iron-Sulphur Centre. *Nature* **2011**, *479*, 249–252.
(12) Wulff, P.; Day, C. C.; Sargent, F.; Armstrong, F. A. How Oxygen Reacts with Oxygen-Tolerant Respiratory [NiFe]-Hydrogenases. *Proc. Natl. Acad. Sci. U.S.A.* **2014**, *111*, 6606–6611.
(13) Pandelia, M. E.; Lubitz, W.; Nitschke, W. Evolution and Diversification of Group 1 [NiFe] Hydrogenases. Is there a Phylogenetic Marker for O_2-Tolerance? *Biochim. Biophys. Acta, Bioenerg.* **2012**, *1817*, 1565–1575.
(14) Losse, S.; Vos, J. G.; Rau, S. Catalytic Hydrogen production at Cobalt Centres. *Coord. Chem. Rev.* **2010**, *254*, 2492–2504.
(15) Lakadamyali, F.; Kato, M.; Muresan, N. M.; Reisner, E. Selective Reduction of Aqueous Protons to Hydrogen with a Synthetic Cobaloxime Catalyst in the Presence of Atmospheric Oxygen. *Angew. Chem., Int. Ed.* **2012**, *51*, 9381–9384.
(16) Wakerley, D. W.; Gross, M. A.; Reisner, E. Proton Reduction by Molecular Catalysts in Water under Demanding Atmospheres. *Chem. Commun.* **2014**, *50*, 15995–15998.
(17) Mondal, B.; Sengupta, K.; Rana, A.; Mahammed, A.; Botoshansky, M.; Dey, S. G.; Gross, Z.; Dey, A. Cobalt Corrole Catalyst for Efficient Hydrogen Evolution Reaction from H_2O under Ambient Conditions: Reactivity, Spectroscopy, and Density Functional Theory Calculations. *Inorg. Chem.* **2013**, *52*, 3381–3387.
(18) Kleingardner, J. G.; Kandemir, B.; Bren, K. L. Hydrogen Evolution from Neutral Water under Aerobic Conditions Catalyzed by Cobalt Microperoxidase-11. *J. Am. Chem. Soc.* **2014**, *136*, 4–7.
(19) Shamsipur, M.; Salimi, A.; Haddadzadeh, H.; Mousavi, M. F. Electrocatalytic Activity of Cobaloxime Complexes Adsorbed on Glassy Carbon Electrodes Toward the Reduction of Dioxygen. *J. Electroanal. Chem.* **2001**, *517*, 37–44.
(20) Kaeffer, N.; Chavarot-Kerlidou, M.; Artero, V. Hydrogen Evolution Catalyzed by Cobalt Diimine-Dioxime Complexes. *Acc. Chem. Res.* **2015**, DOI: 10.1021/acs.accounts.5b00058.
(21) Fontecave, M.; Artero, V. Bioinspired Catalysis at the Crossroads Between Biology and Chemistry: A Remarkable Example of an Electrocatalytic Material Mimicking Hydrogenases. *C. R. Chim.* **2011**, *14*, 362–371.
(22) Caserta, G.; Roy, S.; Atta, M.; Artero, V.; Fontecave, M. Artificial Hydrogenases: Bbiohybrid and Supramolecular Systems for Catalytic Hydrogen Production or Uptake. *Curr. Opin. Chem. Biol.* **2015**, *25*, 36–47.

(23) Simmons, T. R.; Berggren, G.; Bacchi, M.; Fontecave, M.; Artero, V. Mimicking Hydrogenases: From Biomimetics to Artificial Enzymes. *Coord. Chem. Rev.* **2014**, *270−271*, 127−150.

(24) Chenevier, P.; Mugherli, L.; Darbe, S.; Darchy, L.; DiManno, S.; Tran, P. D.; Valentino, F.; Iannello, M.; Volbeda, A.; Cavazza, C.; Artero, V. Hydrogenase Enzymes: Application in Biofuel Cells and Inspiration for the Design of Noble-Metal Free Catalysts for H_2 Oxidation. *C. R. Chim.* **2013**, *16*, 491−516.

(25) Canaguier, S.; Fourmond, V.; Perotto, C. U.; Fize, J.; Pecaut, J.; Fontecave, M.; Field, M. J.; Artero, V. Catalytic Hydrogen Production by a Ni-Ru Mimic of NiFe Hydrogenases Involves a Proton-Coupled Electron Transfer Step. *Chem. Commun.* **2013**, *49*, 5004−5006.

(26) Fourmond, V.; Canaguier, S.; Golly, B.; Field, M. J.; Fontecave, M.; Artero, V. A Nickel-Manganese Catalyst as a Biomimic of the Active Site of NiFe Hydrogenases: a Combined Electrocatalytical and DFT Mechanistic Study. *Energy Environ. Sci.* **2011**, *4*, 2417−2427.

(27) Canaguier, S.; Fontecave, M.; Artero, V. Cp*(−)-Ruthenium-Nickel-Based H_2-Evolving Electrocatalysts as Bio-inspired Models of NiFe Hydrogenases. *Eur. J. Inorg. Chem.* **2011**, 1094−1099.

(28) Vaccaro, L.; Artero, V.; Canaguier, S.; Fontecave, M.; Field, M. J. Mechanism of Hydrogen Evolution Catalyzed by NiFe Hydrogenases: Insights from a Ni-Ru Model Compound. *Dalton Trans.* **2010**, *39*, 3043−3049.

(29) Bacchi, M.; Berggren, G.; Niklas, J.; Veinberg, E.; Mara, M. W.; Shelby, M. L.; Poluektov, O. G.; Chen, L. X.; Tiede, D. M.; Cavazza, C.; et al. Cobaloxime-Based Artificial Hydrogenases. *Inorg. Chem.* **2014**, *53*, 8071−8082.

(30) Jacques, P.-A.; Artero, V.; Pécaut, J.; Fontecave, M. Cobalt and Nickel Diimine-Dioxime Complexes as Molecular Electrocatalysts for Hydrogen Evolution with Low Overvoltages. *Proc. Natl. Acad. Sci. U.S.A.* **2009**, *106*, 20627−20632.

(31) Tran, P. D.; Le Goff, A.; Heidkamp, J.; Jousselme, B.; Guillet, N.; Palacin, S.; Dau, H.; Fontecave, M.; Artero, V. Noncovalent Modification of Carbon Nanotubes with Pyrene-Functionalized Nickel Complexes: Carbon Monoxide Tolerant Catalysts for Hydrogen Evolution and Uptake. *Angew. Chem., Int. Ed.* **2011**, *50*, 1371−1374.

(32) Le Goff, A.; Artero, V.; Jousselme, B.; Tran, P. D.; Guillet, N.; Metaye, R.; Fihri, A.; Palacin, S.; Fontecave, M. From Hydrogenases to Noble Metal-Free Catalytic Nanomaterials for H_2 Production and Uptake. *Science* **2009**, *326*, 1384−1387.

(33) Tasis, D.; Tagmatarchis, N.; Bianco, A.; Prato, M. Chemistry of Carbon Nanotubes. *Chem. Rev.* **2006**, *106*, 1105−1136.

(34) Andreiadis, E. S.; Jacques, P.-A.; Tran, P. D.; Leyris, A.; Chavarot-Kerlidou, M.; Jousselme, B.; Matheron, M.; Pécaut, J.; Palacin, S.; Fontecave, M.; Artero, V. Molecular Engineering of a Cobalt-based Electrocatalytic Nano-Material for H_2 Evolution under Fully Aqueous Conditions. *Nat. Chem.* **2013**, *5*, 48−53.

(35) Griveau, S.; Mercier, D.; Vautrin-Ul, C.; Chaussé, A. Electrochemical Grafting by Reduction of 4-Amino-Ethylbenzenedia-zonium Salt: Application to the Immobilization of (Bio)Molecules. *Electrochem. Commun.* **2007**, *9*, 2768−2773.

(36) O'Reilly, J. E. Oxidation-Reduction Potential of Ferro-Ferricyanide System in Buffer Solutions. *Biochim. Biophys. Acta* **1973**, *292*, 509−515.

(37) Le Goff, A.; Moggia, F.; Debou, N.; Jegou, P.; Artero, V.; Fontecave, M.; Jousselme, B.; Palacin, S. Facile and Tunable Functionalization of Carbon Nanotube Electrodes with Ferrocene by Covalent Coupling and pi-Stacking Interactions and their Relevance to Glucose Bio-Sensing. *J. Electroanal. Chem.* **2010**, *641*, 57−63.

(38) Decoration with amino functions as a result of the electro-grafting process has very little effect on HER properties

(39) Morozan, A.; Jousselme, B.; Palacin, S. Low-Platinum and Platinum-Free Catalysts for the Oxygen Reduction Reaction at Fuel Cell Cathodes. *Energy Environ. Sci.* **2011**, *4*, 1238−1254.

(40) Shao, M. *Electrocatalysis in Fuel Cells: A Non- and Low- Platinum Approach*; Springer-Verlag: London, 2013.

(41) Xu, L.; Armstrong, F. A. Pushing the Limits for Enzyme-Based Membrane-Less Hydrogen Fuel Cells - Achieving Useful Power and Stability. *RSC Adv.* **2015**, *5*, 3649−3656.

(42) Yeager, E. Electrocatalysts for O_2 Reduction. *Electrochim. Acta* **1984**, *29*, 1527−1537.

(43) Blacquiere, J. M.; Pegis, M. L.; Raugei, S.; Kaminsky, W.; Forget, A.; Cook, S. A.; Taguchi, T.; Mayer, J. M. Synthesis and Reactivity of Tripodal Complexes Containing Pendant Bases. *Inorg. Chem.* **2014**, *53*, 9242−9253.

(44) Cho, J.; Sarangi, R.; Kang, H. Y.; Lee, J. Y.; Kubo, M.; Ogura, T.; Solomon, E. I.; Nam, W. Synthesis, Structural, and Spectroscopic Characterization and Reactivities of Mononuclear Cobalt(III)−Peroxo Complexes. *J. Am. Chem. Soc.* **2010**, *132*, 16977−16986.

(45) The formation of μ-peroxo-bis dimer chelates (Schrauzer, G. N.; Lee, P. L. *J. Am. Chem. Soc.* **1970**, *92*, 1551−1557) is not favored in the case of immobilized catalysts spatially distant from each other.

(46) Shi, C.; Steiger, B.; Yuasa, M.; Anson, F. C. Electroreduction of O_2 to H_2O at Unusually Positive Potentials Catalyzed by the Simplest of the Cobalt Porphyrins. *Inorg. Chem.* **1997**, *36*, 4294−4295.

(47) The potential of the Co(II)/Co(I) couple of [Co] was determined as −1.1 V vs Fc$^+$/Fc in CH_3CN.[30,34] This corresponds to −0.57 V vs NHE[51] and thus −0.30 V vs RHE.

(48) Plumeré, N.; Rüdiger, O.; Oughli, A. A.; Williams, R.; Vivekananthan, J.; Pöller, S.; Schuhmann, W.; Lubitz, W. A Redox Hydrogel Protects Hydrogenase from High-Potential Deactivation and Oxygen Damage. *Nat. Chem.* **2014**, *6*, 822−827.

(49) Fourmond, V.; Stapf, S.; Li, H.; Buesen, D.; Birrell, J.; Rüdiger, O.; Lubitz, W.; Schuhmann, W.; Plumeré, N.; Léger, C. Mechanism of Protection of Catalysts Supported in Redox Hydrogel Films. *J. Am. Chem. Soc.* **2015**, *137*, 5494−5505.

(50) Kunishita, A.; Kubo, M.; Sugimoto, H.; Ogura, T.; Sato, K.; Takui, T.; Itoh, S. Mononuclear Copper(II)−Superoxo Complexes that Mimic the Structure and Reactivity of the Active Centers of PHM and DβM. *J. Am. Chem. Soc.* **2009**, *131*, 2788−2789.

(51) Massin, J.; Bräutigam, M.; Kaeffer, N.; Queyriaux, N.; Field, M. J.; Schacher, F. H.; Popp, J.; Chavarot-Kerlidou, M.; Dietzek, B.; Artero, V. Dye-Sensitized PS-b-P2VP-Templated Nickel Oxide Films for Photoelectrochemical Applications. *Interface Focus* **2015**, *5*, 20140083.

G

3. Integration of the hybrid cobalt diimine-dioxime cathode into a tandem device

3.1. Introduction

To achieve the reductive side of water splitting, hydrogen evolution catalysts are *in fine* to be used within an overall water splitting cell.

3.1.1. Tandem cells

Overall water splitting cells are designed to perform unbiased light-driven water splitting. To this end, an OER anode is associated with a HER cathode, one of which should at least be a photoactive electrode. In theory, a cell based on a single SC photoelectrode could furnish a photovoltage high enough to exceed the 1.23 V required to split water into H_2 and O_2.[8] Yet, such devices only reach low solar-to-fuels efficiencies, namely due to their limited absorption in the visible range. Architectures including several photoelectrodes able to harvest visible light, named as *tandem cell*, have hence been explored. These devices can gather an OER photoanode and a HER photocathode, but additional photovoltaic (PV) units might also be included.[8b, 9] An ion-exchanging membrane is usually integrated between the anodic and the cathodic parts to separate the gases. The presence of this membrane, but also of multiple interfaces, generates ohmic losses, which increase the actual overpotential requirement for overall WS.[10]

The state-of-the-art systems reported in the literature rely *quasi*-exclusively on material-based photoelectrocatalytic components. A first example of an OER photoanode|HER photocathode tandem cell made only of molecular components has been very recently given by the group of Sun (Chapter I.2.2.3.3).[11] But the observed STH efficiency (0.05 %) in this seminal work is still far below the ones of state-of-the-art systems that can reach more than 10 % if a PV unit is integrated.[12] Thus, tandem cells relying on molecular components either for light-harvesting or catalysis require further developments to gain new understanding. In the current part, our aim is to construct a prototype of such a molecular-based tandem cell that would operate overall WS.

This work first requires the selection of possible components for the construction of the cell. Especially, a statement of the literature is that molecular oxygen-evolving photoanodes have been more successfully established to date than their hydrogen-evolving counterparts. An attractive approach to build a tandem device hence consists in coupling such a molecular-based photoanode with photovoltaic units and a non-photoactive dark cathode. DSSCs are known to be PV units of choice for application in tandem cells since they gather an easy tuning of their absorption in the

visible range and a limited photovoltage dependence to light intensity.[8b] Of note, DSSCs have been coupled with non-noble metal-oxide photoanodes absorbing in a complementary region of the visible range to build tandem devices realizing unassisted WS.[8b, 13] We thus decided to fashion our device on the photoanode|DSSC|HER cathode pattern. While Pt is ubiquitously used to realize proton reduction in reported examples of such tandem cells, we believe that its substitution for an earth-abundant efficient cathodic material would represent another step to secure a relatively low cost.

3.1.2. Presentation of the collaborative work

The study has been launched through a collaboration with the group of A. Moore, T. Moore and D. Gust at the *Center for Bio-Inspired Solar Fuel Production* in the *Chemistry and Biochemistry Department* of *Arizona State University* (Tempe, AZ, USA). Travel and hosting support was brought by the *Solar Fuels Institute* (*SOFI*, www.solar-fuels.org), an international consortium uniting private companies and academic institutions for *"the development of an efficient and cost-effective system that uses sunlight to produce a liquid fuel"*.

The study initiated here addresses the construction of an OER photoanode|DSSC|HER cathode tandem cell relying on an OER photoanode and a DSSC developed by the team at *ASU* and the **GDL/MWCNT-Co** HER cathode prepared in our laboratory. A view of the integrated components is given in Figure II.1.

The construction of the photoanode and the DSSC recalls precedent results of the team at *ASU* and their co-workers.[14] A short summary of important features of these electrodes is given here, an extensive description falling out of the scope of this manuscript.

The photoanode is assembled onto nanostructured TiO_2, the *n*-type supporting TCO. The electrode is photosensitized with the **ZnP** zinc porphyrin, since porphyrinic systems were shown to yield highly efficient *n*-type DS photoelectrodes.[15] Iridium oxide (**IrO$_x$**) NPs are co-immobilized on the TCO to act as OEC entities, knowing that they are efficient catalysts for water oxidation displaying limited overpotential requirements.[16] An additional benzimidazole-phenol (**BIP**) moiety[14b, 17] mimics a tyrosine-histidine couple within photosystem II that plays a crucial role in hindering charge recombinations thanks to an intermolecular PCET process.[18] Interestingly, this moiety was shown to enhance photocurrents for water oxidation in functional photoanodes[14c] and was hence further implemented in the design of new photoanodes.
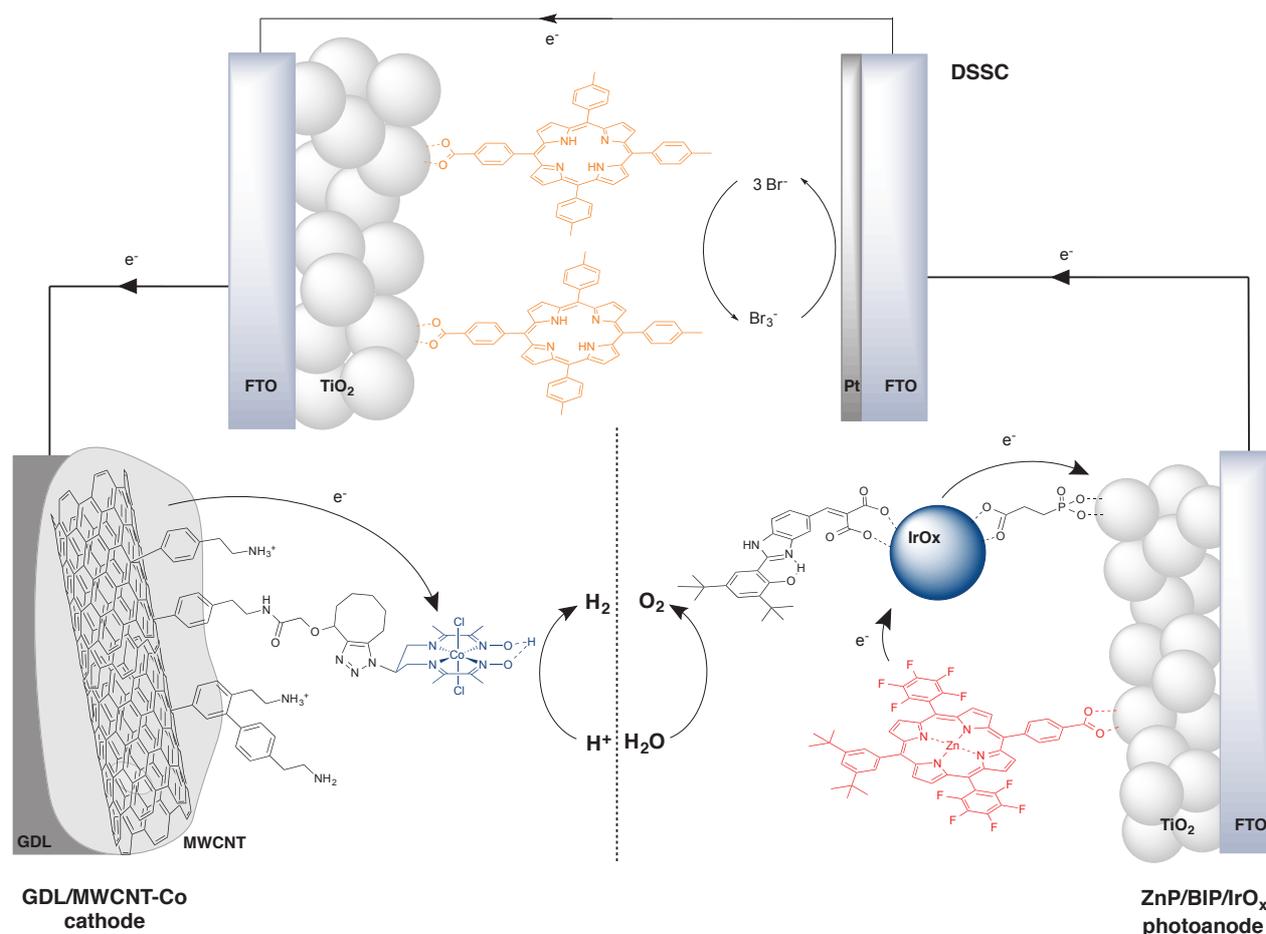
Figure II.1. Global scheme of the envisioned tandem cell gathering the **GDL/MWCNT-Co** HER cathode, the **TMP** DSSC and the **ZnP/BIP/IrO$_x$** OER photoanode.

The DSSC also relies on a porphyrinic dye (**TMP**), but a metal-free one. The utilization of porphyrins as PSs does not only give access to top record performance in DSSCs,[15] but also permits to find orthogonal absorption ranges between the DSSC and the OER photoanode[8b, 13] by simple derivatization and/or metalation. The Br^{3-}/Br$^-$ redox shuttle was used to increase the V_{OC}.[19]

Experimental part

Device construction

The prototypes were constructed using two plastic UV cuvettes as the two electrode compartments. The cuvettes were cut at the desired shape with at least one hole in each to host the electrodes, one to insert a membrane (anion-exchanging membrane) between the two compartments and one to introduce the sensors. The as-prepared cuvettes were glued together with epoxy glue and to a supporting *Plexiglas* plate. A secondary plate which is screwed to the first one is used to stack the setup with the electrodes inside. Pseudo-reference electrodes were introduced as plain Ag wires and PTFE tubes serve as gas in- and outlet. All tight junctions of the cell were ensured with silicone sheets or 2-component latex glues.

Photoelectrochemical experiments

The photoanodes and DSSCs were prepared by the collaborators at *ASU* with modification of previous procedures.[14] The **GDL/MWCNT-Co** was prepared according procedures developed in Grenoble.[20]

Linear sweep voltammograms were recorded with CH Instruments 650C or 760D electrochemical workstations. In the 3-electrode configuration a Pt wire served as the counter-electrode and a Ag wire as a pseudo-reference electrode. In the 2-electrode configuration, the reference electrode terminal was plugged within the counter-electrode terminal.

Light irradiation was provided by a Xe lamp equipped with a 400 nm UV filter, an AM 1.5 filter and a water IR filter. The experiments were run at an incident light power density of 100 mW·cm^{-2}.

Oxygen and hydrogen detections were performed by Unisense OX-N and H2-N in-needle micro-Clark probes poised at −800 and 800 mV, respectively, and driven by a 4-channel Unisense micrometer monometer unit. The probes were priorly calibrated by exposing them to saturating and nil concentrations of O_2 and H_2, respectively, in the same buffers than used for further photoelectrocatalysis.

Photoelectrochemical experiments were performed either in the lab-built tandem device or in electrochemical glass cells consisting of two compartments separated by the anion-exchanging membrane.

When DSSCs were used in the setup, they were placed behind the tandem cell so that the light beam first reachs the photoanode and then the DSSCs.

3.2. Results and discussion

The project was practically begun by a 2-month visit at *ASU* in Fall 2013. The results presented below were mainly obtained during this period, in an income shared with M. Fournier, post-doctoral fellow in the team of D. Gust.

3.2.1. Device design

The starting point of this project was to build a tandem cell prototype in which light-driven experiments can be performed. This prototype is depicted in Figure II.2.
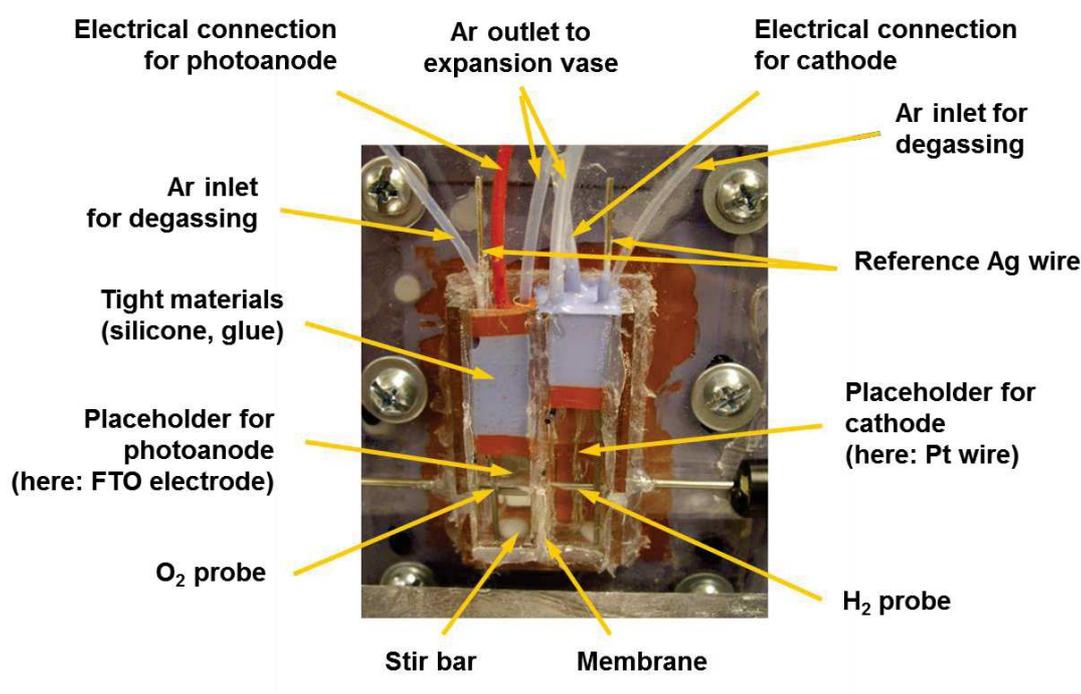
Figure II.2. Scheme of a first prototype of the device with important components shown through yellow arrows.

The cell is constructed to host the OER photoanode and the HER cathode, while the DSSC is to be included externally. The stacked architecture of the device allows a facile change of the electrodes to screen several operating conditions. The two catalytic electrodes are plunged in the same supporting electrolyte. These electrodes are thus separated by an anion-exchanging membrane for the separation of gases. The limited volumes of solution and headspace (typically 1-1.5 mL and 0.5-1.5 mL, respectively) are intended to improve the accuracy for the quantitative measurements of the evolved gases. To detect and quantify these gases, an O_2-sensor and an H_2-sensor (Clark micro-probes) are positioned in the anodic and cathodic compartments, respectively. The vigorous stirring of the electrolyte in each part restrains diffusion-controlled processes and increases the time-resolution of the gas detection. A series of electrical connections are also set.

These connections serve to plug the working electrode and the Ag pseudo-reference electrode introduced at both sides. The PTFE in- and outlet permit to degas the anodic and cathodic parts with a stream of Ar. Degassing the operating cell is indeed crucial to remove any residual O_2 either from the photoanode part that would bias the detection of evolved O_2 or from the cathode part that would lead to undesired O_2 reduction (see 0). For these reasons, the whole cell is sealed with oxygen-tight materials, such as silicon-based glue and plates.

Once built, the setup was used to test different configurations and to run overall WS experiments.

3.2.2. Light-driven experiments

Several conditions for the device have been screened, in terms of number and positioning of the DSSCs but also in terms of choice of the buffer. Only a selected panel of relevant results is shown here.

3.2.2.1. Hybrid cathode associated with DSSC

A first goal was to demonstrate that light harvested by the DSSC provides an energetic income able to ease proton reduction at the cathode. For this, a simplified system was used (Figure II.3), which included the **GDL/MWCNT-Co** cathode, a Pt wire as anode and a **TMP** DSSC for irradiated experiments.
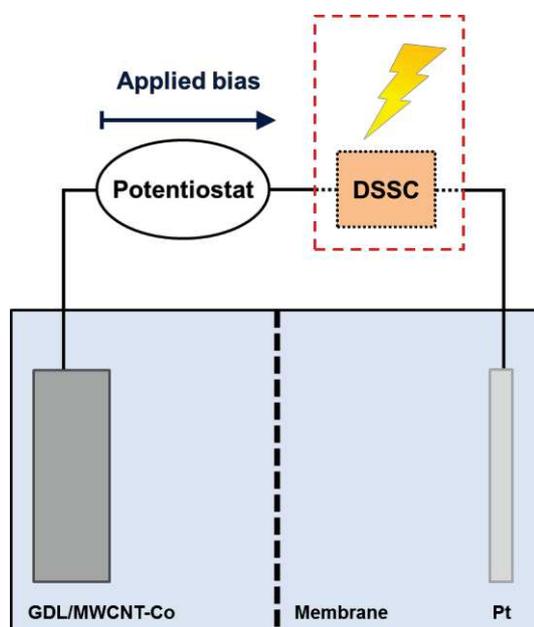
Figure II.3. Simplified scheme of the 2-electrode configuration without or with (red dashed line) a DSSC connected in series in the circuit and irradiated during the measurements.

The linear sweep voltammogram is registered in a 2-electrode configuration. This configuration permits to display the global overvoltage (V_{tot}) for water-splitting, taking into account all ohmic losses (η_{cell}) from the setup and given as:

$$V_{tot} = V^0_{WS} + \eta_c + \eta_a + \eta_{cell}$$ **Eqn. II.1**

where η_c and η_d represent the cathodic overpotential for HER and the anodic overpotential for OER, respectively.

The LSV in the dark displays global voltages about 1.6 V at onset and 1.9 V at −100 µA·cm^{-2}, these current values being normalized by the surface of the cathode (Figure II.4, left). The onset value is consistent with V^0_{WS} **=** 1.23 V to which is added the proton reduction overpotential of the **GDL/MWCNT-Co** cathode (*ca* 350 mV). The overpotential of the Pt anode and the ohmic losses are considered to be quite low at low currents.
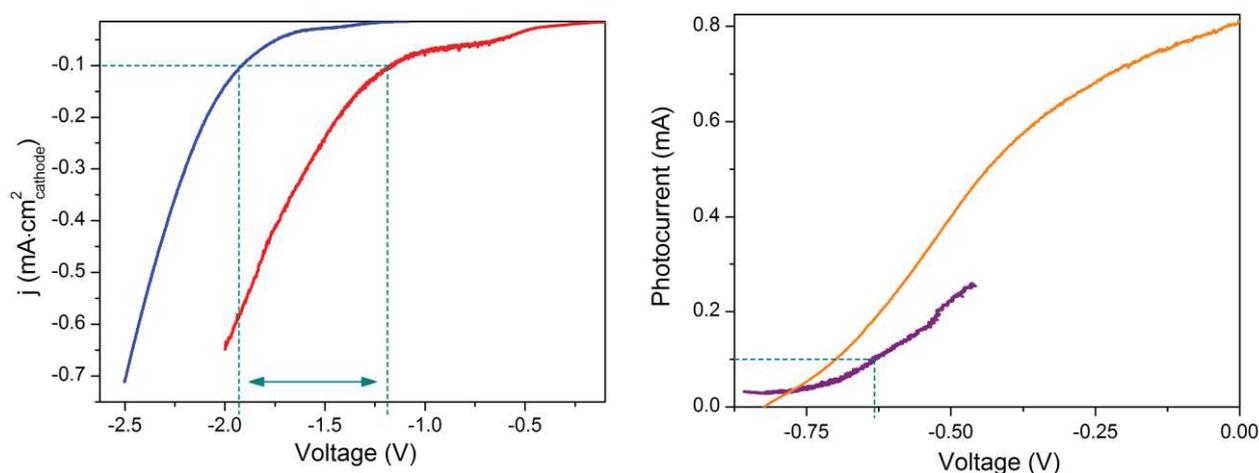
Figure II.4. Linear sweep voltammograms of the **GDL/MWCNT-Co** cathode|Pt anode device in a 2-electrode configuration in the absence (blue line) and in the presence (red line) of an irradiated **TMP** DSSC in the circuit and recorded in a pH 5 MES/HEPES/NaClO$_4$ 0.1 M each buffer at a scan rate of 0.5 mV·s^{-1} (left); *i-V* characteristics of the DSSC extracted from the in-device LSVs (purple line) and for the unloaded DSSC recorded at a scan rate of 10 mV·s^{-1} (orange line) (right). Cyan lines indicate the way to extract the graph on the right from the one on the left for the **GDL/MWCNT-Co** cathode|Pt anode device.

Interestingly, when the DSSC is added to the circuit and light is on, the voltammogram is shifted anodically. The global voltage at −100 µA·cm^{-2} is now of *ca* 1.2 V (Figure II.4, left). This figure is inferior to the thermodynamic requirement for WS. The light income being transformed at the DSSC hence provides a photovoltage for this reaction.

By subtraction of the currents in the absence from the ones in the presence of light, a photocurrent-voltage characteristic is accessed for the in-device DSSC (Figure II.4, right). The photocurrent-voltage behaviors depicted on Figure II.4, right, show that the onset photovoltage furnished by the solar cell when integrated in the device (around 0.78 V) is in good line with the

open-circuit photovoltage of the unloaded cell (around 0.82 V). These curves also feature similar shapes although a deviation is observed at higher current densities, with the in-device DSSC delivering less current than expected. The LSV of the full device is recorded at scan rate much lower than the one of the unloaded DSSC (0.1 *vs* 10 mV·s^{-1}), making the irradiation time quite longer. Thus, a progressive light-induced degradation of the DSSC during the in-device measurement can explain the observed partial loss in photocurrent.

Yet, the results suggest that the **TMP** DSSC can act as a current-voltage supplier to split water. These results also represent a first demonstration of the PV+electrolysis approach[10] based on molecular components for LH and proton reduction. Such findings are thus encouraging towards the construction of a self-sufficient WS tandem cell.

3.2.2.2. Self-sufficient light-driven O$_2$ evolution

To get closer to a self-sufficient device for water splitting, further incorporation of a second photoactive entity has to be considered. Indeed, as shown above, the maximum photovoltage provided by a single DSSC is not high enough to drive the overall WS reaction that requires 1.23 V. To overcome that point, the **ZnP/BIP/IrO$_x$** OER photoanode can be introduced in the device. However, the system was studied in a simplified view first, in which the cathode was replaced by a Pt wire and a single-part cell was used.

The LSV of the **ZnP/BIP/IrO$_x$** photoanode recorded in this model cell in a 2-electrode configuration is presented in Figure II.5. Under light irradiation, an anodic photocurrent develops and raises a plateau at about 17 µA·cm^{-2} before a marked increase in current is observed starting from *ca* 1.1 V. This photocurrent is ascribed to water oxidation.
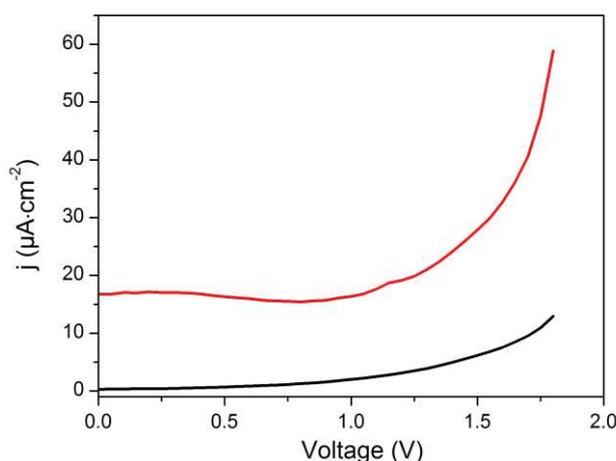
Figure II.5. Linear sweep voltammograms of the **ZnP/BIP/IrO$_x$** photoanode|Pt cathode device in a 2-electrode configuration in the dark (black line) and under illumination (red line) recorded in a pH 7 phosphate buffer 50 mM at a scan rate of 5 mV·s^{-1}.

To reach improved current in the device, a potential higher than that of onset of the sharp increase in photocurrent (*ca* 1.1 V) should be applied. Given the value of this onset, a single DSSC of V_{OC} around 0.82 V is not expected to comply with that condition. Hence, in the tandem device, 2 DSSCs were introduced in series, so that their photovoltages are added. Such a device consisted in a **ZnP/BIP/IrO$_x$** photoanode, 2 **TMP** DSSCs and a Pt cathode, all components being wired in series (Figure II.6, left). The irradiated device generates a photocurrent of 10 µA, with concomitant oxygen evolution, as observed through the O$_2$-sensor (Figure II.5, right, red line). Moreover, oxygen is produced with a faradaic efficiency close to unity for the duration of the experiment (Figure II.5, right, blue line).
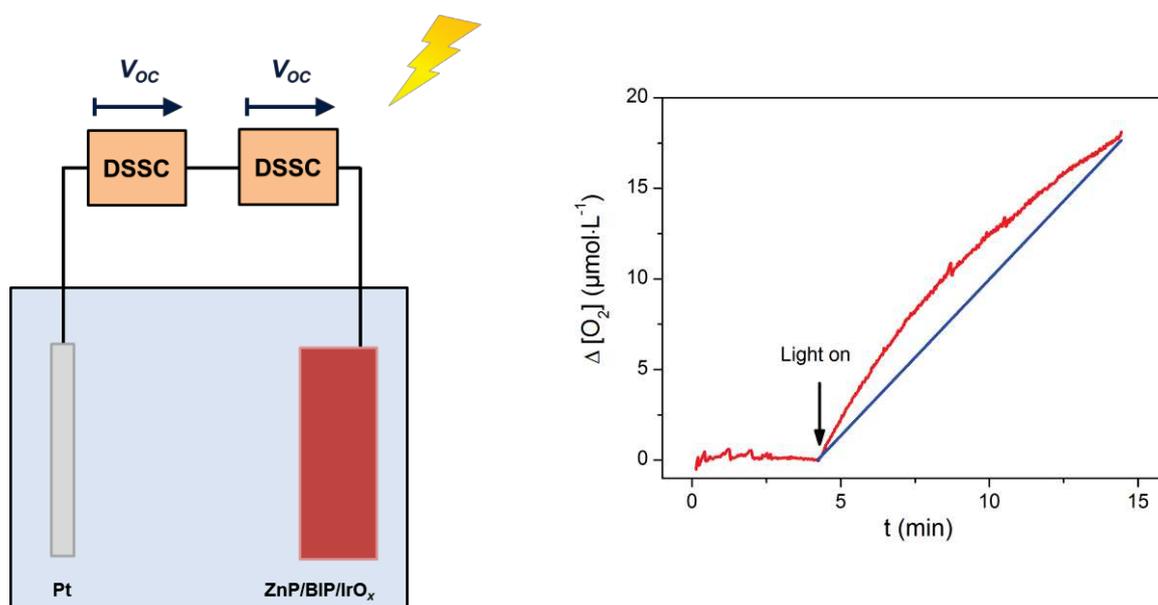
Figure II.6. Simplified scheme of the **ZnP/BIP/IrO$_x$** photoanode|2 **TMP** DSSCs|Pt cathode device used for light-driven overall water-splitting (left) and O$_2$-evolution as monitored through an O$_2$ Clark micro-sensor (red line) and as expected assuming a unity faradaic efficiency from the steady 10 µA current establishing in this device (blue line) operated in a pH 7 phosphate buffer 50 mM (right).

Enthusiastic about these results, we envisaged the further step that consisted in substituting the **GDL/MWCNT-Co** for Pt at the cathode device. First, we simulated the photocurrent-voltage response of the 2-electrode setup **ZnP/BIP/IrO$_x$** photoanode|**GDL/MWCNT-Co** cathode. In that aim, the overpotential requirement for the **GDL/MWCNT-Co** cathode (approx. 350 mV; see Chapter II.1) is artificially implemented into the photocurrent-voltage curve of the **ZnP/BIP/IrO$_x$** photoanode|Pt cathode device shown in Figure II.5 (red line). We could estimate from the intersection of this curve with the photocurrent-voltage characteristics of 2 **TMP** DSSCs in series, the expected J_{Op} operating current and V_{Op} voltage of the complete device (Figure II.7). The values for the operating voltage and current were found at *ca* 1.49 V and 18.5 µA·cm^{-2}. As a note, these calculations only give an approximation of the operating conditions, a more precise

estimation would require further investigations. In any case, as the slope of the current-voltage curve of the 2 DSSCs is nearly vertical nearby the intersection (Figure II.7, inset), a drift in J_{Op} is more likely expected than a drift in V_{Op}.
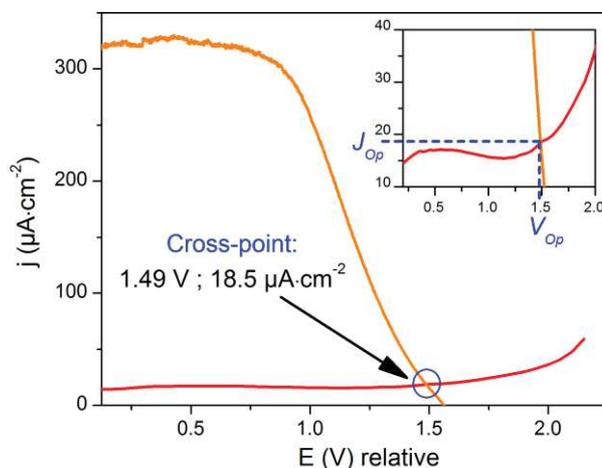
Figure II.7. Cross-graph between the LSV of the irradiated **ZnP/BIP/IrO$_x$** photoanode artificially implemented with a 350 mV additional voltage (red line) and of the current-voltage curve of 2 **TMP** DSSCs mounted in series (orange line) with a magnification of the crossing zone (inset) showing the expected current and voltage in the irradiated tandem cell.

When the overall **ZnP/BIP/IrO$_x$** photoanode|2 **TMP** DSSCs|**GDL/MWCNT-Co** cathode device is irradiated, the current establishing into the cell is at 6 µA. This current is actually lower than the value obtained from the estimated cross-graph. Despite this current, no hydrogen production was observed at the cathode, which would be the final warrant of the cell design.

Our investigations then focused on the reason why a current develops, which does not yield HER catalysis at the cathode. We therefore measured the potential at the cathode in the irradiated tandem cell against a silver wire pseudo-reference. The operating cathodic potential was found more positive than the potential required to reduce proton at this **GDL/MWCNT-Co** cathode. We thus suspected a side-reaction turning over at lower overpotential at the cathode, like O$_2$ reduction. To confirm this hypothesis, we recorded a LSV at a non-degassed cathode.

This LSV (Figure II.8, left) displays a marked event peaking at $ca - 0.75$ V vs Ag$^{+/0}$, thus at a potential positive from the catalytic hydrogen evolution. As well, if a small constant current is applied at the undegassed electrode, the potential establishes at this event (around –0.6 V vs Ag$^{+/0}$) before reaching more negative values (Figure II.8, right). These results relate well with the process of O$_2$ reduction that was evidenced at the **GCE/MWCNT-Co** cathode (see 0). Hence, we postulated that during operation of the full tandem device, in which low currents develop (10 µA range), the cathode equilibrates on the ORR reaction, which hinders any hydrogen evolution occurring at larger overpotentials.
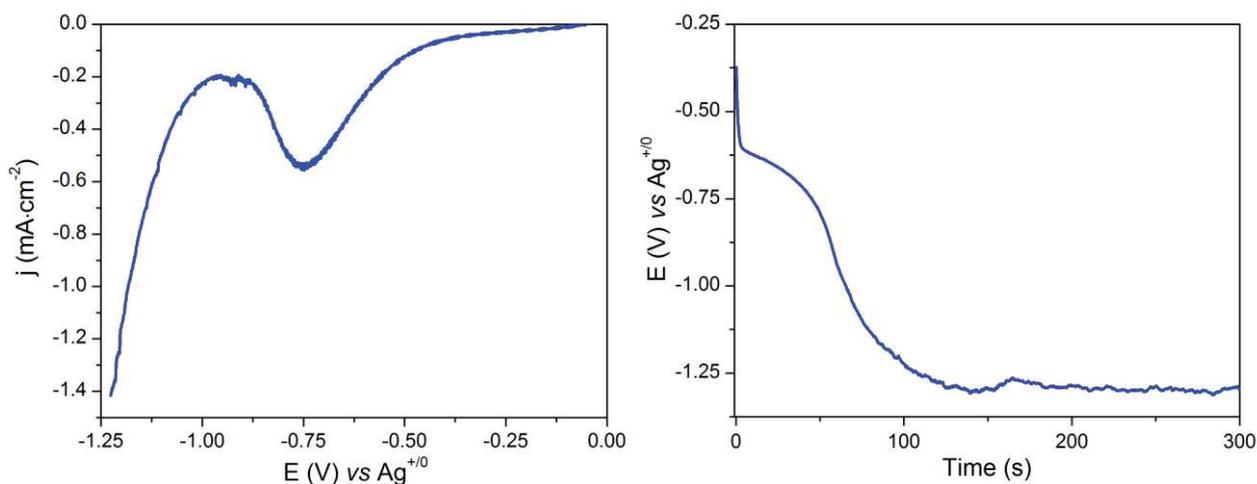
Figure II.8. LSV recorded at an undegassed **GDL/MWCNT-Co** cathode in 0.1 M phosphate buffer at pH 4.7 with a scan rate of 10 mV·s^{-1} (left) and potential *versus* time during a chronopotentiometric measurement at −100 μA at an undegassed **GDL/MWCNT-Co** cathode in 0.1 M NaClO$_4$ aqueous electrolyte at pH 4.9 (right).

Although the cell was degassed with Ar before operation, air could actually be trapped within the GDL membrane that can hardly be removed, due to the geometry of the lab-built device. Thus, this geometry should be further engineered in future works.

3.3. Conclusion and perspectives

This project was a premise to the construction of a tandem cell for overall WS. The first milestone we reached was the design of a prototype that can host the electrodes for WS as well as certain materials to assess their performance once integrated. We then analyzed sequentially the behavior of the **GDL/MWCNT-Co** cathode and the **ZnP/BIP/IrO$_x$** photoanode when coupled with the **TMP** DSSCs used to supply the additional voltage necessary for proton reduction or water oxidation, respectively. These prior analyses made us conclude that in a first approach 2 DSSCs should be introduced in the device to generate enough photovoltage. In particular, the **ZnP/BIP/IrOx** photoanode|2 **TMP** DSSCs|Pt cathode setup evidences self-sufficient WS under light irradiation, producing oxygen with unity faradaic yield.

Finally, the full device implemented with the **GDL/MWCNT-Co** cathode generated a photovoltage under unbiased conditions. Yet, the current does not lead to hydrogen evolution at the cathode. The reason for this observation has been identified as the side-reduction of residual oxygen. As low currents flow into the light-driven cell, the time to pass enough charge to reduce the total amount of O$_2$ trapped at the cathode can be quite long. Although this material was demonstrated to be O$_2$-tolerant,[7] the presence of limited oxygenic concentrations still represents a main concern for the operation of the tandem device. To tackle this issue, following prototypes

were constructed at *ASU* on alternative architectures that should permit a better degassing of the cathodic material.

More fundamental considerations to improve the setup rely on the introduction of a photoactive entity directly within the cathode. Especially, a setup gathering a hydrogen-evolving DS photocathode coupled with the oxygen-evolving photoanode can possibly achieve WS without the need of external DSSCs. This approach is the one that was recently shown fruitful by the group of Sun (see Chapter I.2.2.3.3).[11] Current developments in our group concerning HER photocathodes, including the ones presented in the following chapters, let us envision the construction of tandem devices based on molecular systems with fully covalent immobilization.

Conclusions and outlook

In this chapter we investigated the properties of the **[Co$^{\text{III}}$(DO)(DOH)pnL$_2$]** catalyst in the frame of its integration in device.

First, we could demonstrate that the homogeneous catalyst poised at potentials low enough to perform proton reduction is transformed into Co-based nanoparticles which are the effective HER catalyst. This phenomenon was previously observed at pH 7 and we could further establish that it also occurs at pH 2.2. We therefore posit that this degradation takes place in aqueous solutions whatsoever the pH. Overall, these observations raise the interesting questions of the nature of the deactivation pathways but also of the detection of the degradation products possibly catalyzing HER.

By contrast, the molecular catalyst remains intact and active for proton reduction, namely at pH 4.5, once grafted onto **GDL/MWCNT** electrodes. The molecular-engineered cathode displays low overpotential for HER and sustained activity in aqueous media. These encouraging features further drove our work to device-related studies.

In this view, the **GCE/MWCNT-Co** cathode was shown to operate HER in the presence of high concentrations of oxygen, which does not significantly impact the overpotential for proton reduction. The relative tolerance toward oxygen of the **GCE/MWCNT-Co** assembly is particularly appealing for an immobilized architecture that has to operate in a tandem cell.

Introducing such a cathodic material actually represents a main bottleneck to reach a platinum free self-sufficient WS tandem cell. Indeed, the **ZnP/BIP/IrO$_x$** photoanode|2 **TMP** DSSCs|Pt cathode device was demonstrated to evolve oxygen in unity faradaic yields under unbiased irradiated conditions. But the **GDL/MWCNT-Co** cathode integrated in the tandem cell preferentially realizes the reduction of residual amounts of oxygen over proton at low currents.

Further studies will focus to improve the design of this tandem device to facilitate O$_2$-free conditions at the HER cathode. But the ideal solution to the O$_2$ issue is to develop efficient O$_2$-tolerant photocathodes generating high photocurrents that would quickly reduce oxygen without deactivation and further equilibrate on hydrogen evolution. The immobilized **[Co$^{\text{III}}$(DO)(DOH)pnL$_2$]** complex was demonstrated to display tolerance to O$_2$ while operating in aqueous media. Therefore, we will now dedicate our work to the construction of photocathodes integrating the **[Co$^{\text{III}}$(DO)(DOH)pnL$_2$]** catalyst. More especially, we will attempt to associate photosensitizers along with the catalyst to perform both LH/CS and hydrogen evolution catalysis. Such DS photocathodes would then represent candidates of choice for implementation in an overall WS tandem device.

References

1.   McCrory, C. C.; Uyeda, C.; Peters, J. C. *J. Am. Chem. Soc.* **2012,** *134* (6), 3164-70.
2.   Cobo, S.; Heidkamp, J.; Jacques, P. A.; Fize, J.; Fourmond, V.; Guetaz, L.; Jousselme, B.; Ivanova, V.; Dau, H.; Palacin, S.; Fontecave, M.; Artero, V. *Nat. Mater.* **2012,** *11* (9), 802-7.
3.   Artero, V.; Fontecave, M. *Chem. Soc. Rev.* **2013,** *42* (6), 2338-2356.
4.   (a) Anxolabéhère-Mallart, E.; Costentin, C.; Fournier, M.; Robert, M. *J. Phys. Chem. C* **2014,** *118* (25), 13377-13381; (b) El Ghachtouli, S.; Fournier, M.; Cherdo, S.; Guillot, R.; Charlot, M.-F.; Anxolabéhère-Mallart, E.; Robert, M.; Aukauloo, A. *J. Phys. Chem. C* **2013,** *117* (33), 17073-17077; (c) Anxolabehere-Mallart, E.; Costentin, C.; Fournier, M.; Nowak, S.; Robert, M.; Saveant, J. M. *J. Am. Chem. Soc.* **2012,** *134* (14), 6104-7; (d) Ghachtouli, S. E.; Guillot, R.; Brisset, F.; Aukauloo, A. *ChemSusChem* **2013,** *6* (12), 2226-30.
5.   (a) Wakerley, D. W.; Reisner, E. *Energy Environ. Sci.* **2015,** *8* (8), 2283-2295; (b) Osterloh, F. E. *J. Phys. Chem. Lett.* **2014,** *5* (15), 2510-2511.
6.   (a) Wakerley, D. W.; Gross, M. A.; Reisner, E. *Chem. Commun.* **2014,** *50* (100), 15995-8; (b) Lakadamyali, F.; Kato, M.; Muresan, N. M.; Reisner, E. *Angew. Chem. Int. Ed.* **2012,** *51* (37), 9381-4.
7.   Kaeffer, N.; Morozan, A.; Artero, V. *J. Phys. Chem. B* **2015,** *119* (43), 13707-13713.
8.   (a) Linic, S.; Christopher, P.; Ingram, D. B. *Nat. Mater.* **2011,** *10* (12), 911-21; (b) Prévot, M. S.; Sivula, K. *J. Phys. Chem. C* **2013,** *117* (35), 17879-17893.
9.   Gratzel, M. *Nature* **2001,** *414* (6861), 338-344.
10.   Jacobsson, T. J.; Fjällström, V.; Edoff, M.; Edvinsson, T. *Energy Environ. Sci.* **2014,** *7* (7), 2056.
11.   Li, F.; Fan, K.; Xu, B.; Gabrielsson, E.; Daniel, Q.; Li, L.; Sun, L. *J. Am. Chem. Soc.* **2015,** *137* (28), 9153-9.
12.   Ager, J. W.; Shaner, M. R.; Walczak, K. A.; Sharp, I. D.; Ardo, S. *Energy Environ. Sci.* **2015,** *8* (10), 2811-2824.
13.   (a) Brillet, J.; Yum, J.-H.; Cornuz, M.; Hisatomi, T.; Solarska, R.; Augustynski, J.; Graetzel, M.; Sivula, K. *Nature Photon.* **2012,** *6* (12), 824-828; (b) Brillet, J.; Cornuz, M.; Formal, F. L.; Yum, J.-H.; Grätzel, M.; Sivula, K. *J. Mater. Res.* **2011,** *25* (01), 17-24.
14.   (a) Youngblood, W. J.; Lee, S.-H. A.; Kobayashi, Y.; Hernandez-Pagan, E. A.; Hoertz, P. G.; Moore, T. A.; Moore, A. L.; Gust, D.; Mallouk, T. E. *J. Am. Chem. Soc.* **2009,** *131* (3), 926-927; (b) Zhao, Y.; Swierk, J. R.; Megiatto, J. D., Jr.; Sherman, B.; Youngblood, W. J.; Qin, D.; Lentz, D. M.; Moore, A. L.; Moore, T. A.; Gust, D.; Mallouk, T. E. *Proc. Natl. Acad. Sci. USA* **2012,** *109* (39), 15612-6; (c) Megiatto, J. D., Jr.; Antoniuk-Pablant, A.; Sherman, B. D.; Kodis, G.; Gervaldo, M.; Moore, T. A.; Moore, A. L.; Gust, D. *Proc. Natl. Acad. Sci. USA* **2012,** *109* (39), 15578-83.
15.   Mathew, S.; Yella, A.; Gao, P.; Humphry-Baker, R.; Curchod, B. F.; Ashari-Astani, N.; Tavernelli, I.; Rothlisberger, U.; Nazeeruddin, M. K.; Gratzel, M. *Nat. Chem.* **2014,** *6* (3), 242-7.
16.   McCrory, C. C.; Jung, S.; Peters, J. C.; Jaramillo, T. F. *J. Am. Chem. Soc.* **2013,** *135* (45), 16977-87.
17.   Megiatto, J. D., Jr.; Mendez-Hernandez, D. D.; Tejeda-Ferrari, M. E.; Teillout, A. L.; Llansola-Portoles, M. J.; Kodis, G.; Poluektov, O. G.; Rajh, T.; Mujica, V.; Groy, T. L.; Gust, D.; Moore, T. A.; Moore, A. L. *Nat. Chem.* **2014,** *6* (5), 423-8.
18.   Hammarström, L.; Styring, S. *Energy Environ. Sci.* **2011,** *4* (7), 2379.
19.   Wang, Z.-S.; Sayama, K.; Sugihara, H. *J. Phys. Chem. B* **2005,** *109* (47), 22449-22455.
20.   Andreiadis, E. S.; Jacques, P. A.; Tran, P. D.; Leyris, A.; Chavarot-Kerlidou, M.; Jousselme, B.; Matheron, M.; Pecaut, J.; Palacin, S.; Fontecave, M.; Artero, V. *Nat. Chem.* **2013,** *5* (1), 48-53.

Chapter III

Attaching cobalt diimine-dioxime complexes onto transparent conducting oxides

In the perspective of developing versatile molecular photocathodes, the most straightforward path was to harness the *co-grafting* strategy described in introduction. While previous works of the group realized the attachment of **[Co^{III}(DO)(DOH)pnL₂]** onto dark electrodes,[1] the underlying requirement is then to shift to transparent conducting electrodes.

This chapter, as a preamble to Chapter IV, is focused on the development of architectures with the molecular complex grafted at the surface of TCOs and the subsequent characterizations of these hybrid electrodes.

First, the two strategies envisioned for the attachment onto TCOs are quickly presented. Some preliminary results are depicted, which drove us to focus more specifically our investigations on one of these strategies.

This strategy is then developed in more details in the rest of the chapter. To start, the syntheses of new derivatives of **[Co^{III}(DO)(DOH)pnL₂]** bearing TCO-purposed anchoring moieties is shown.

The immobilization of these new derivatives onto TiO_2, as a benchmark TCO, is described. Characterizations of these hybrid electrodes, mainly by electrochemical means, is presented in parallel.

In a final part, the attachment of a new **[Co^{III}(DO)(DOH)pnL₂]** derivative onto NiO, the *p*-type TCO chosen for the construction of DS photocathodes, was set up. The results of electrochemical and spectroscopic investigations conducted with these architectures is discussed more broadly.

1. Strategies envisioned for the attachment on transparent conducting oxides

Our approach is based on the utilization of anchoring moieties to graft the **[Co^{III}(DO)(DOH)pnL$_2$]** complex onto TCOs. Among them, the attachment through phosphonate or carboxylate binding groups has shown encouraging results when set in application into DS-photoelectrodes.[2] To immobilize a catalyst *via* an anchoring moiety at the surface of a TCO, two strategies might be envisioned.

1.1. Description

A first strategy, named here as *sequential functionalization*, (Strategy A, Figure III.1) consists to priorly grafting a species displaying a pendent reactive group. Then, the catalyst decorated with a complementary moiety is coupled by reaction with the reactive group which is already attached onto surface.

The major interests for following this approach are the less demanding molecular synthetic steps and the versatility of the reactive moieties involved in coupling the catalytic motif with the surface anchor. On the other side, the reaction on the surface is likely to be less controlled than its equivalent under homogenous conditions for which classical purification methods, such as flash chromatography, are available. Also, the correct characterization of the surface-anchored species requires advanced analysis techniques as XPS, TOF-SIMS or surface-related NMR. This characterization should in theory be repeated at each step, which renders the process practically long. Meanwhile, we note that electrochemistry also provides insightful characterizations of the electrode from a structural and, more importantly here, from a functional point of view.

The second strategy (Strategy B, Figure III.1) is to first build the entire molecular entity that contains both the deprotected anchoring group(s) and the catalytic motif, but often associated with solubility issues. Then, this molecule is readily attached at the surface of the TCO to yield the expected desired architecture. Such a strategy will be quoted in the present manuscript as *full entity functionalization*.

This pathway is synthetically more challenging, since it requires the preparation of molecules displaying both the catalytic motif and the surface anchoring groups. But this point also facilitates the precise characterization of the molecular entity prior to grafting through classical molecular analyses like NMR, mass spectroscopy (MS) or elemental analysis (E.A.). Once the synthesis is

completed, the immobilization onto electrode is obtained in one step, thus in a straightforward fashion.

This section briefly describes preliminary results based on the sequential functionalization strategy for immobilizing **[Co^{III}(DO)(DOH)pnL₂]** at the surface of TCOs. This strategy revealed unfruitful in the first place, the reason why we further focused our investigations on the full entity functionalization strategy. This second pathway will constitute the main core of this chapter.

Strategy A
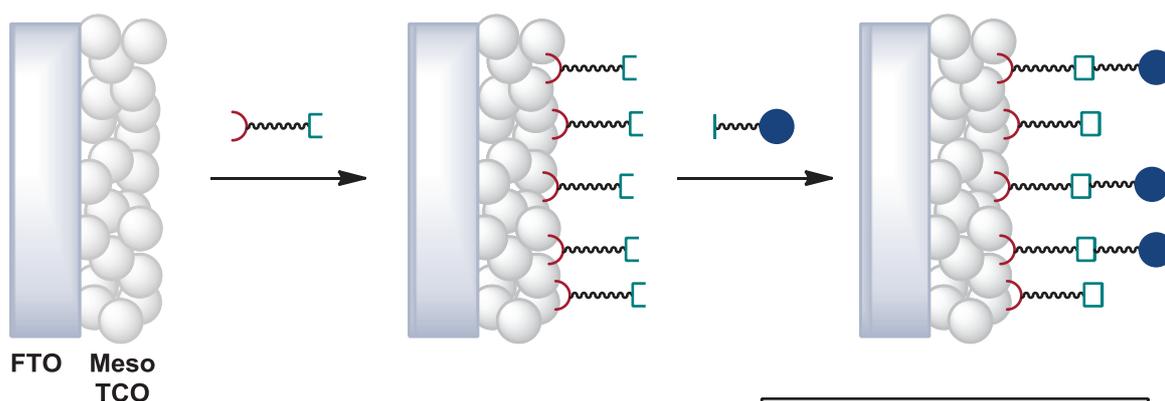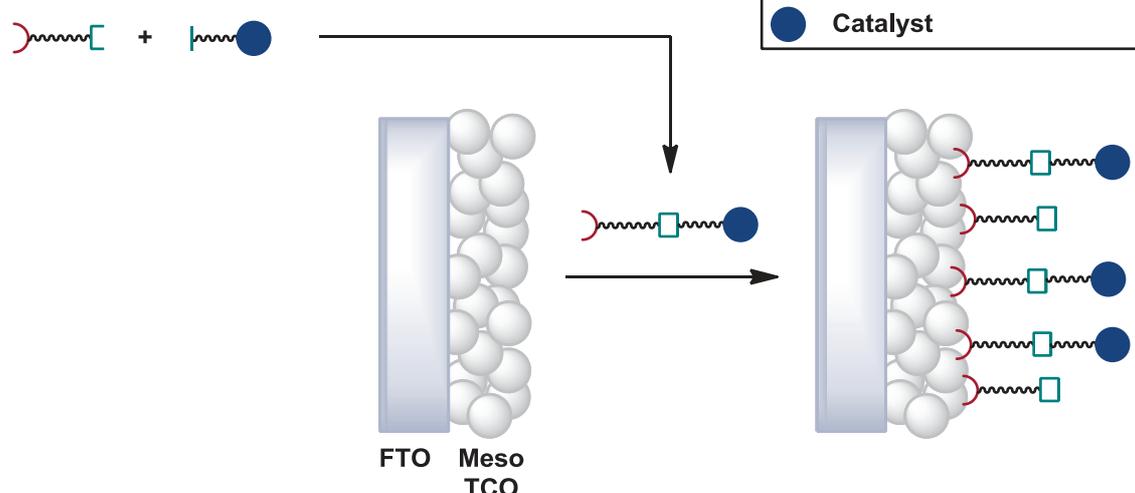
Figure III.1. Strategies envisioned for the attachment of HECs onto TCO surfaces.

1.2. Sequential grafting strategy: preliminary results

This sequential functionalization strategy has been widely used to immobilize efficient molecular HECs onto various substrates.[1, 3] In particular, the construction of the **GDL/MWCNT-Co** hybrid material (see Chapter I.1.4.3) relies on this approach. In this case, amino groups were attached to MWCNTs through the reduction of 4-(2-aminoethyl)-benzene diazonium salts. Then, this moiety was reacted with the phtalimide activated ester group on the catalyst derivative

[Co^{III}(DO)(DOH)pnC$_8$PhtCl$_2$] to yield a covalent amide bond. We logically followed this strategy for our first assays to attach the HEC onto TCOs. Whereas diazonium salt reduction was previously used for the grafting onto carbonaceous electrode substrates, alternative anchoring groups for the attachment onto TCOs, as phosphonate or carboxylate bindings, are to be considered here.

To exploit the **[Co^{III}(DO)(DOH)pnC$_8$PhtCl$_2$]** activated ester derivative priorly developed by the group, we investigated the possibility to react it with surface-anchored amino groups. We used model surface and surface attachment linkers to validate this strategy.

The electrodes were constructed onto planar FTO surfaces, since FTO displays a quasi-metallic behavior[4] that would facilitate the electrochemical characterization of the decorated substrates. The commercial 2-aminoethylphosphonic acid **PC$_2$NH$_2$** (Figure III.2) was employed for the attachment of reactive amino groups onto surface, through binding of the terminal phosphonate moiety. A short spacer chain (2 carbon atoms) was selected in this first example to ensure facile electron transfer from the electrode to the Co centers.

For the first immobilization step, water was used as a solvent to dissolve the **PC$_2$NH$_2$** product. The expected **FTO-PC$_2$NH$_2$** surfaces are further reacted with **[Co^{III}(DO)(DOH)pnC$_8$PhtCl$_2$]** under dry conditions in the presence of 2,6-lutidine as a base (Figure III.2), following the procedure developed for the construction of the **GDL/MWCNT-Co** electrodes.[1a]
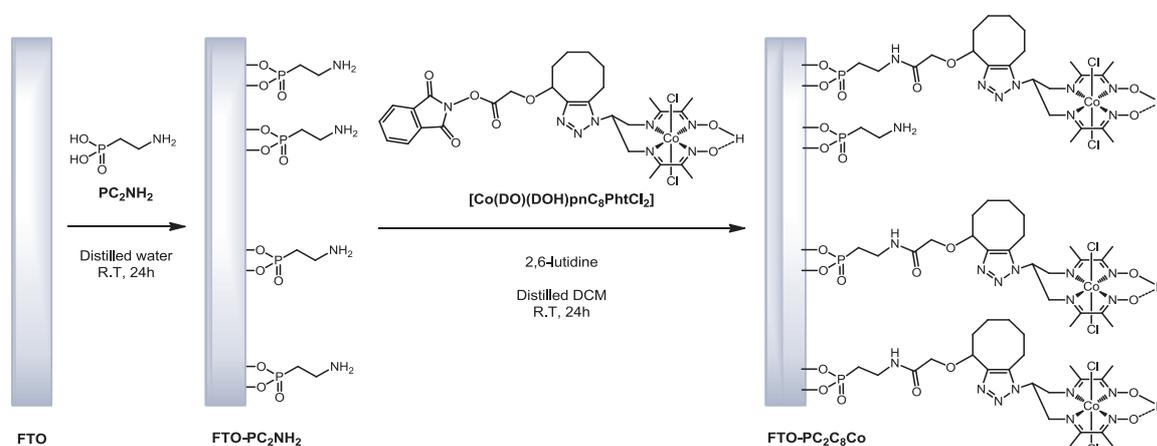
Figure III.2. Sequential functionalization pathway towards the construction of the **FTO-PC$_2$C$_8$Co** electrodes.

At each step, the electrodes were characterized through electrochemical means. As an example, the corresponding cyclic voltammograms (CVs) are shown in Figure III.3. A wave is observed at *ca* −0.50 V *vs* Ag/AgCl at the targeted **FTO-PC$_2$NH$_2$** electrode.
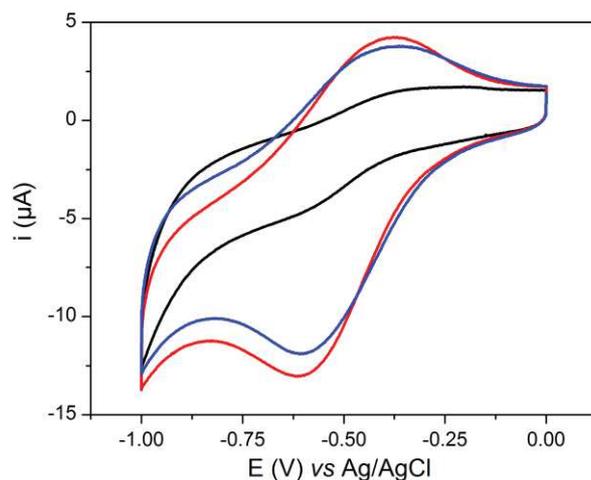
Figure III.3. CVs recorded at a blank FTO (black line), the expected **FTO-PC₂NH₂** (red line) and the expected **FTO-PC₂C₈Co** (blue line) electrodes in a 0.1 M NaCl aqueous electrolyte at a scan rate of $100 \ mV \cdot s^{-1}$.

The intensity of the peak of this wave depends linearly on the scan rate (not shown). This behavior indicates a non-diffusional electrochemical event.[5] The integration of the electrochemical waves leads to surface densities around 1-2 10^{-10} mol·cm^{-2} of electroactive sites, in the range of a monolayer. However, the question of the origin of such an electrochemical event is not answered. Indeed, no species obviously reducible at this moderately cathodic potential is introduced at the **FTO-PC₂NH₂** electrode. We tentatively postulate that this behavior results from the interaction between a FTO surface Sn^{IV} site and one or several dangling NH₂ group(s), the coordination of which would facilitate the reduction of Sn^{IV} to Sn^{II}.

Upon addition of the **[Co^{III}(DO)(DOH)pnC₈PhtCl₂]** derivative, a *quasi*-identical electrochemical feature is seen. At the same time, the electrochemical signature of the **[Co^{III}(DO)(DOH)pnCl₂]** complex is not present. These observations lead us to conclude that the amide bond formation that should yield the **FTO-PC₂C₈Co** electrode does not occur under these conditions. This point is also in line with the unavailability of the pendent NH₂ groups in the hypothesis where they are bound to surface.

These primary results, as well as other similar attempts on different TCOs (TiO₂, ITO), showed that the sequential functionalization pathway based on an amide coupling is not as straightforward as expected for the preparation of **[Co^{III}(DO)(DOH)pnL₂]**-decorated TCO electrodes. For this reason, our investigations were afterwards directed toward the full entity functionalization strategy.

2. Attachment onto benchmark TCOs by full entity functionalization

A better control of the molecules attached onto surfaces is expected through the full entity functionalization strategy. The synthesis of new derivatives of the **[Co^{III}(DO)(DOH)pnL$_2$]** complex directly bearing TCO-purposed anchoring moieties is described first. In a second part, their immobilization onto a benchmark TCO is depicted. The obtained electrodes are characterized by electrochemical and, when available, spectroscopic means.

2.1. Synthesis

We synthetized a series of three derivatives of **[Co^{III}(DO)(DOH)pnL$_2$]**. One derivative is functionalized by a carboxylic acid group and the other two carry a phosphonic acid group.

2.1.1. Carboxylic acid-functionalized derivative

A carboxylic acid derivative was inspired by the activated ester **[Co^{III}(DO)(DOH)pnC$_8$PhtCl$_2$]** used in previous studies.[1] The **C$_8$COOH** cyclooctyne (Figure III.4) was commercially synthetized following a procedure from the literature.[6] The Cu-free Huisgen cycloaddition with the azido-functionalized **[Co^{III}(DO)(DOH)N$_3$pnCl$_2$]** complex readily gives the **Co$_{COOH}$** acid carboxylic derivative in good yields (Figure III.4).
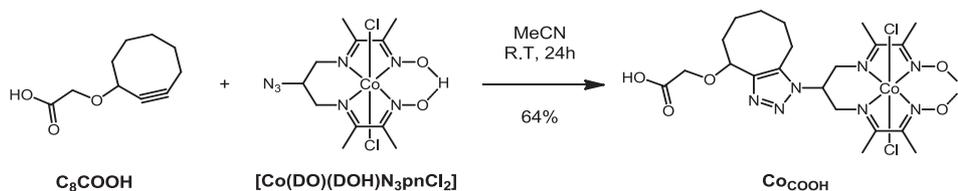
Figure III.4. Synthetic pathway to the **Co$_{COOH}$** acid carboxylic derivative. R.T.: room temperature.

The ^{1}H NMR spectrum recorded after acetone washing displays a single-defined series of peaks that indicates a single regioisomer is obtained. This isomer is likely the *exo* isomer represented on Figure III.4, as a consequence of steric constraints. A peak at 12.59 ppm, the integration of which corresponds to 0.9 proton, is attributed to the proton of the carboxylic acid. This observation indicates that the carboxylic acid is protonated and does not bind to the Co center, which further supports the presence of the single *exo* isomer. The carboxylic acid moiety will be exploited later to attach this **[Co^{III}(DO)(DOH)pnL$_2$]** derivative onto TCO.

2.1.2. Phosphonic acid-functionalized derivatives

In a second approach, we investigated phosphonic acid binding groups for the immobilization of **[Co^{III}(DO)(DOH)pnL$_2$]** variants. The constructions were designed to drive the electron transfer from the surface to the catalyst, upon excitation of a supported photosensitizer. Thus, long spacer chains were introduced to locate the Co catalytic centers on the top of the PS layer. These spacers were also utilized as a way to functionalize the backbone with the phosphonate moieties. To simplify the synthesis, diethyl ester phosphonates served as masked phosphonic acids and were deprotected at the last step.

2.1.2.1. Cyclooctyne-based pathway

This first entity was also constructed on the platform developed above for Cu-free cycloaddition. The **P$_{Et}$C$_{12}$NH$_2$** commercial C$_{12}$ alkyl chain (Figure III.5) bearing a diethyl ester phosphonate and an amine at opposite ends was selected as linker. An amide bond is formed upon reaction of the terminal amine with the carboxylic acid of **C$_8$COOH** in the presence of the 1-[bis(dimethylamino)methylene]-1H-1,2,3-triazolo[4,5-b]pyridinium 3-oxid hexafluorophosphate (HATU) coupling reagent. The **P$_{Et}$C$_{12}$C$_8$** product was obtained as an oil, from which traces of the DMSO solvent used for the amide coupling could not be completely excluded, even after repeated extractions or flash silica column purification.
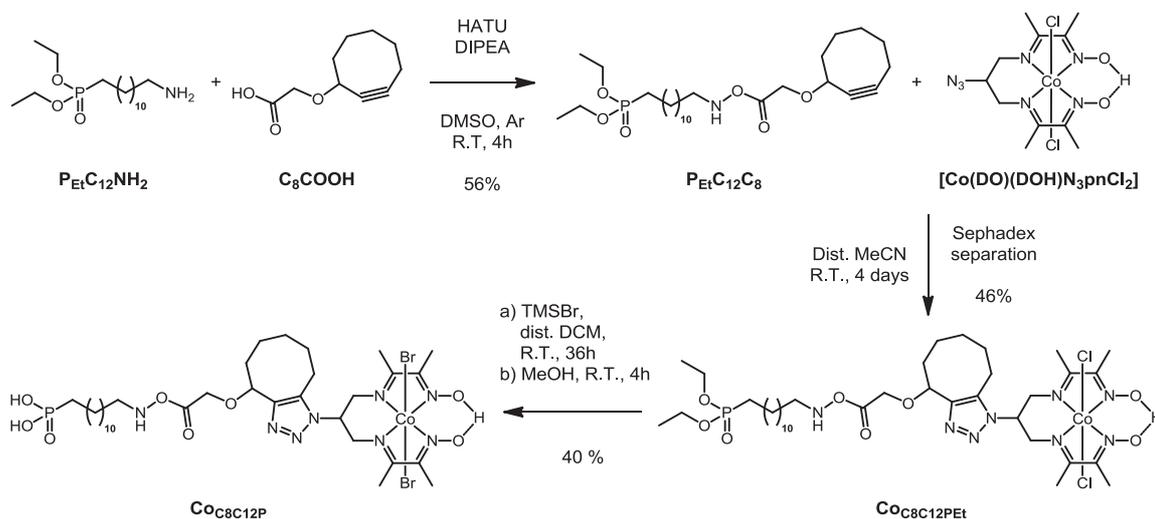
Figure III.5. Synthetic pathway to the **Co$_{C8C12P}$** phosphonic acid derivative. DIPEA: N,N-diisopropylethylamine; dist.: distilled; DCM: dichloromethane; MeOH: methanol.

This intermediate was then reacted with **[Co^{III}(DO)(DOH)N$_3$pnCl$_2$]** in a Huisgen cycloaddition to afford the **Co$_{C8C12PEt}$** ester phosphonate derivative. This product was purified by elution through a size exclusion chromatography on Sephadex gel. MS analysis of the selected

fraction evidences the formation of the expected $Co_{C8C12PEt}$. However, two series of peaks were observed in the ^1H NMR spectrum, which likely indicates the presence of the two regio-isomers of the clicked compound. The diethyl ester phosphonates were converted into phosphonic acids through a deprotection assisted by TMSBr. This last steps yielded the bi-deprotected phosphonic acid Co_{C8C12P} but in the presence of mono-deprotected and protected analogues. Mass spectroscopy analysis in the negative mode also reveals that the ancillary chloride ligands have been mainly exchanged for bromide ligands due to the utilization of TMSBr.

The mixture of products was used without further purification to validate in the first place the proof of concept for the attachment of **[Co^{III}(DO)(DOH)pnL$_2$]** phosphonic acid derivatives onto benchmark TCOs.

2.1.2.2. Copper-catalyzed pathway

A strained cyclooctyne ring, initially developed by Bertozzi,[7] has been exploited until now to couple **[Co^{III}(DO)(DOH)N$_3$pnL$_2$]** with functionalization moieties through a Cu-free Huisgen [3+2] cycloaddition. This strategy was applied to avoid the substitution of Co for Cu in the diimine-dioxime ligand, which is observed when classical Cu-catalyzed conditions involving unactivated alkynes are employed for the cycloaddition. However, the cyclooctyne ring is quite strained and can thus possibly result in side-reactions. For instance, such degradative pathways were observed when $P_{Et}C_{12}C_8$ was directly deprotected with TMSBr. Also, the non-catalyzed Huisgen [3+2] cycloaddition is less regioselective than the Cu-catalyzed one.[8] These reasons prompted us to re-investigate the synthetic strategy through the classical copper-catalyzed azide-alkyne cycloaddition (CuAAC).[9]

The synthetic route was started from the **[Cu^{II}(DO)(DOH)N$_3$pn]ClO$_4$** Cu-metallated complex (Figure III.6). This complex was reacted by CuAAC with the commercial $P_{Et}C_9CC$ linker (Figure III.6) featuring both a terminal diethyl ester phosphonate and a terminal alkyne moieties. The click reaction is catalyzed through a mixture of CuSO$_4$ and sodium ascorbate (NaAsc) which yields *in situ* the Cu^I catalytic species.[9b] Since the Cu^{II} center prohibits correct identification on the ^1H NMR spectra, the coupled product is characterized by MS which confirms the formation of Cu_{C11Pet} (Figure III.6).

This intermediate is directly involved in the next step where Co^{III} is substituted for Cu^{II}. Prior attempts in the group relied on the removal of Cu^{II} from the **(DO)(DOH)pn$^-$** coordination sphere with chelating agents as EDTA or thiocyanates. To date, they proved unfruitful. Hence, the possibility to insert in one-pot Co^{III} in the place of Cu^{II} was envisioned. Mimicking the Co^{III} metalation process of the **(DOH)$_2$pn** ligand,[1a, 10] the substitution was performed by adding an

excess amount of a cobalt salt ($CoCl_2$ or $CoBr_2$, for instance) while bubbling air into the reaction media. Air bubbling was intended to oxidize the inserted Co^{II} to the Co^{III} state which has a higher affinity for the negatively charged tetradentate **(DO)(DOH)pn$^-$** ligand. Such an oxidation step was not performed in the previous attempts of the group. This oxidation likely pushes the reaction toward the full incorporation of Co into the **(DO)(DOH)pn$^-$** ligand.
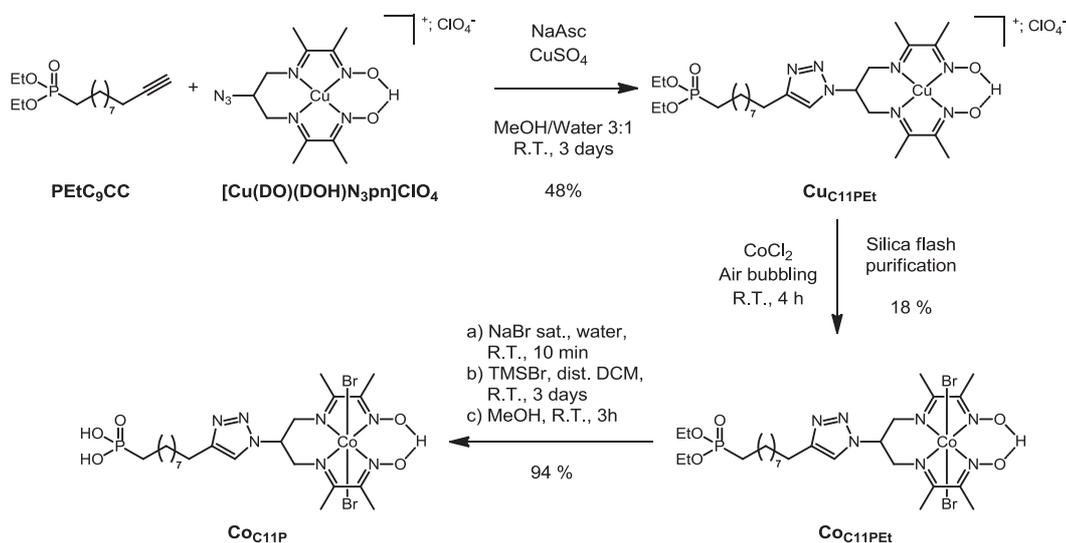
Figure III.6. Synthetic pathway to the **Co$_{C11P}$** phosphonic acid derivative. Sat.: saturated.

The crude mixture is further purified by silica flash chromatography using a mixed organic/aqueous eluant. Under these conditions, the chloride ancillary ligands are displaced for aquo ligands. The reprecipitation of the selected fractions with a NaBr-saturated aqueous solution yields the expected **Co$_{C11PEt}$** derivative displaying bromide axial ligands. Finally, the diethyl ester phosphonate is converted to the di-deprotected phosphonic acid with TMSBr. This reaction proceeds in good yields and gives the expected **Co$_{C11P}$** derivative that contains only Br$^-$ axial ligands.

Without additional treatment, **Co$_{C11P}$** will be immobilized onto TCOs through the free phosphonic acid group.

2.2. Characterization of the new derivatives supported onto benchmark TiO$_2$

The derivatives synthetized above were assessed in regard to their attachment onto TCO surfaces.

2.2.1. TCO considered

To facilitate comparison, we first selected supporting materials with well-known characteristics and electrochemical behavior. As well, mesostructured films are interesting candidates, since they present high surface areas thus possibly high surface loadings. This property renders the characterization of the pool of grafted species more straightforward. Different TCOs were envisioned for this preliminary study, as FTO, ITO and TiO$_2$, but the only one at our disposal to gather good transparency, well-known electrochemical signatures and a mechanically resistant mesostructuration was TiO$_2$.

Indeed, TiO$_2$ is the benchmark TCO implemented in the large majority of *n*-type DSSCs. This *n*-type SC has a CB located downward from NHE, although the exact positions of its Fermi and conduction band levels are matters of debate.[11] Actually, these levels can slightly vary depending on the structure of the TiO$_2$ used and on the assessment techniques and conditions. Of note, due to the protonation of the surface species, the potentials of the band edges show a Nernstian behavior.[11a, 12] Electronic conductivity might still be expected at potentials more cathodic than 0 V *vs* NHE. In practice, many examples report possible electrochemical scanning of redox couples in the negative potential window at TiO$_2$ electrodes.[13] This point is relevant here since the **[Co^{III}(DO)(DOH)pnL$_2$]** derivatives are expected to have an electrochemical signature at potentials negative to NHE.[10, 14] We thus started our investigations onto *n*-type mesoporous TiO$_2$ as the benchmark TCO.

2.2.2. Immobilization onto TiO$_2$

Mesoporous TiO$_2$ layers are routinely produced at the industrial scale by the *Solaronix* company, partner of this work in the frame of the *ArtipHyction* European project. The electrodes used in our study are prepared by one or two steps of screen-printing of a paste containing preformed TiO$_2$ nanoparticles at the top of a FTO layer deposited onto glass. The films are further sintered in our laboratory in Grenoble, by burning them in a flat furnace at 450 °C. SEM photographs of the thusly prepared electrodes are shown Figure III.7. The TiO$_2$ mesoporous layers

used in this study are about 600 nm for singly screen-printed electrodes and 1.2 µm thick for doubly screen-printed ones.
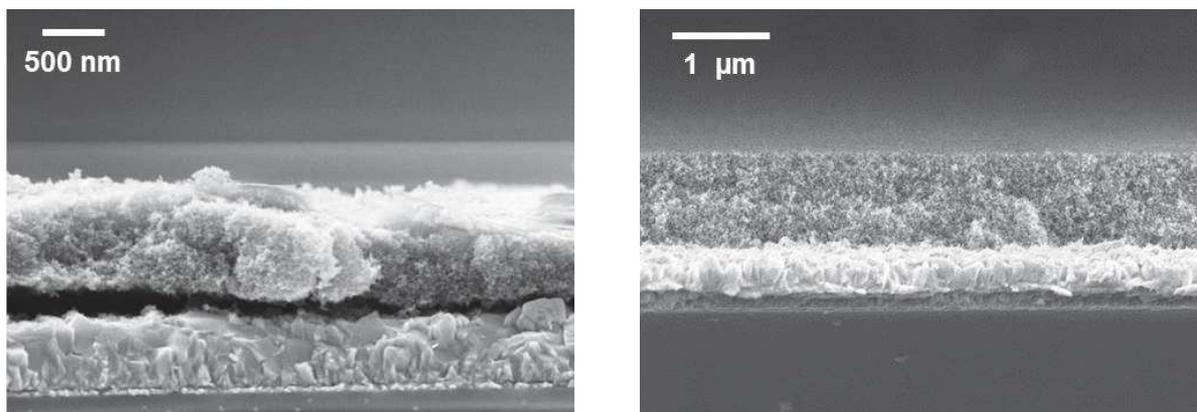
Figure III.7. SEM photographs at the perpendicular (left) or with a tilt angle (right) of a singly screen-printed Glass/FTO/mesoTiO$_2$ electrode.

The graftings were performed in methanolic solutions at 0.5 mM of the **Co$_{C8C12P}$**, **Co$_{C11P}$** or **Co$_{COOH}$** compounds. The substrates were dipped in the solution just after sintering, when still warm (*ca* 90°C), and sensitized for 24h. At the end of the immobilization process, the electrodes were rinsed with MeOH to remove any physisorbed catalyst from the surface.

2.2.3. Characterization of the electrodes

To test the TiO$_2$ hybrid electrode constructions at the laboratory scale, electrochemical investigations were conducted. These investigations aim at the detection of the attached **[Co^{III}(DO)(DOH)pnL$_2$]** derivatives onto TiO$_2$ surfaces. **[Co(DO)(DOH)pnBr$_2$]** has two reduction waves at –0.57 and –1.11 V *vs* Fc$^{+/0}$ for Co$^{III/II}$ and Co$^{II/I}$ events.[10, 14] Thus, its derivatives are expected to display electrochemical waves at similar potentials, which are likely accessible onto TiO$_2$ electrodes, especially for the Co$^{II/I}$ event.

2.2.3.1. *TiO$_2$-Co$_{COOH}$ electrodes*

The immobilization of **Co$_{COOH}$** onto TiO$_2$ electrodes is performed as described above and is schematically represented in Figure III.8.
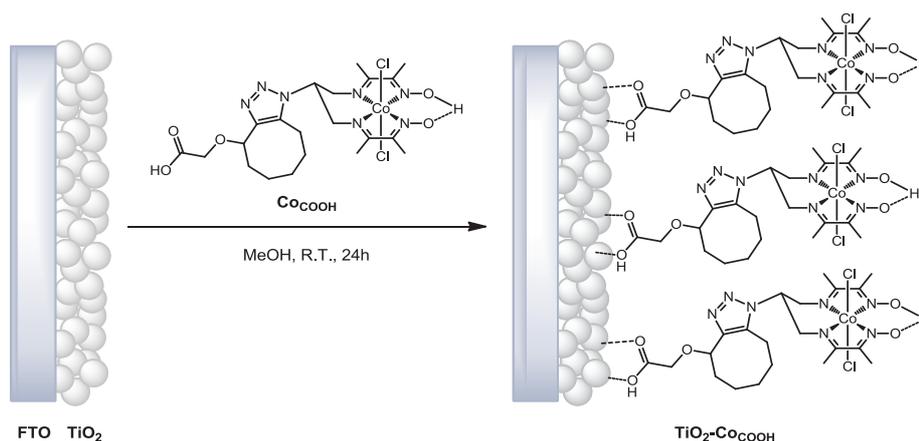
Figure III.8. Preparation of the **TiO$_2$-Co$_{COOH}$** electrodes (doubly screen-printed substrate).

The cyclic voltammogram of the corresponding **TiO$_2$-Co$_{COOH}$** electrode in neutral aqueous media is shown in Figure III.9. At positive potentials, a flat background is observed, as expected in this region corresponding to the band gap of TiO$_2$. Scanning potentials downward, the CV displays an irreversible cathodic peak at *ca* −0.25 V *vs* NHE. A second feature appears at more negative potentials. This feature is observed close to the return potential, with a raise in reduction currents and a small bump at −0.56 V *vs* NHE in the reoxidation current.
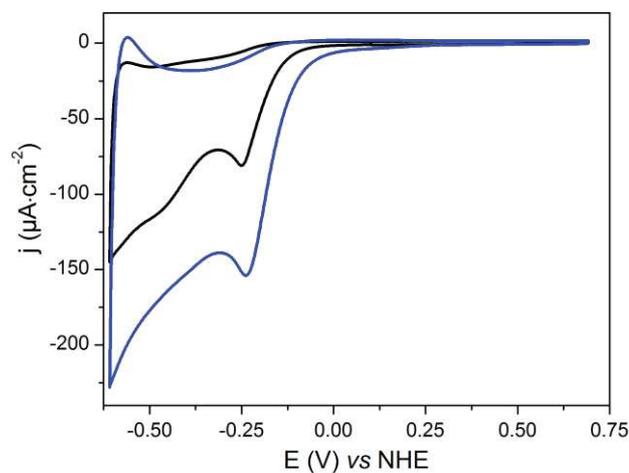
Figure III.9. CVs of a pristine **TiO$_2$** (black line) and a **TiO$_2$-Co$_{COOH}$** (blue line) electrodes recorded in NaCl 0.1M aqueous electrolyte at a scan rate of 100 mV·s^{-1}.

These two signatures are also present at the blank TiO$_2$ electrode (Figure III.9). Thus, these events are not correlated to the presence of **Co$_{COOH}$** at the surface but rather to intrinsic properties of the TiO$_2$ electrode.

The peak at −0.25 V *vs* NHE is actually ascribed to the presence of mono-energetic states in the intra-band gap region.[11a, 12c, 15] These states, which are believed to be localized at grain boundaries,[11c, 16] act as electron traps. The observed peak is due to the capacitive electron charging of such trap states.

At more negative potentials, electrons are enough energetic to fill the states corresponding to the CB of TiO$_2$ that yields the feature observed nearby the return potential. The CB is partially charged during the forward scan, which explains the raise in cathodic current, and discharged during the backward scan, which explains the bump in reoxidation current.[12a] Overall, these processes are more precisely described by mixed resistive and capacitive behaviors within the film and at the film/electrolyte interface.[12a] A complete description of these two phenomena falls out of the scope of this manuscript, but relevant models can be found in the literature.[11c, 12a, 13a, 13c]

Nevertheless, the CVs show that the **Co$_{COOH}$** derivative is not significantly present at the surface of the electrode, when dipped in a neutral aqueous media. This result is in agreement with the poor stability of carboxylate binding onto TiO$_2$ under aqueous conditions,[17] which has been shown to readily desorb from TiO$_2$ at neutral pH.[17c]

For this reason, we further switched our investigations to derivatives bearing phosphonic acid moieties for the grafting onto TiO$_2$.

2.2.3.2. TiO$_2$-Co$_{C12C8P}$ electrodes

The following work was conducted with the **Co$_{C12C8P}$** derivative. The immobilization is performed identically to the previous case, as shown in Figure III.10.
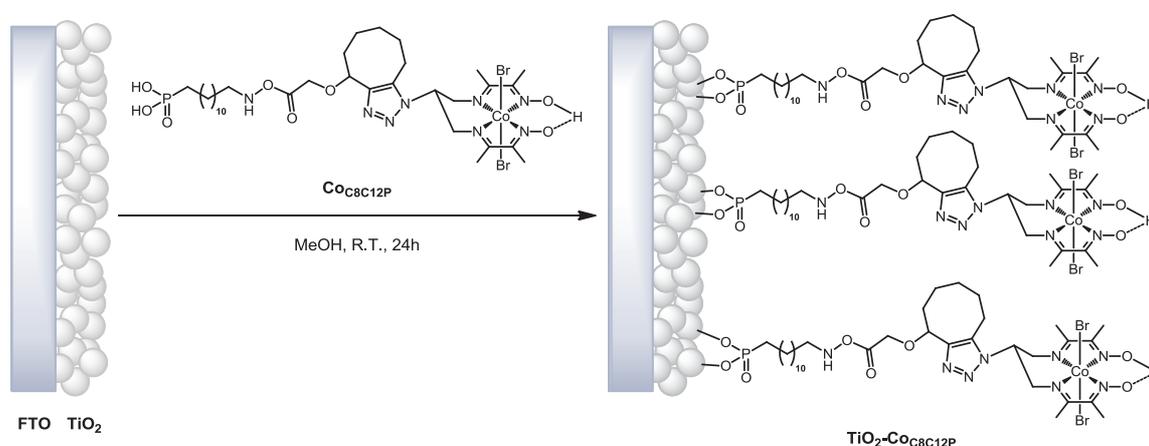
Figure III.10. Preparation of the **TiO$_2$-Co$_{C8C12P}$** electrodes (doubly screen-printed substrate).

The CV of the **TiO$_2$-Co$_{C12C8P}$** electrode shows a broad, partially reversible wave centered at −0.40 V *vs* NHE (Figure III.11, left). The blank **TiO$_2$** electrode does not display a similar feature at this potential. This wave is thus attributed to the Co$^{II/I}$ couple of the **Co$_{C12C8P}$** derivatives attached onto the surface. The Co$^{II/I}$ potential of the grafted complex is anodically shifted compared to the **GDL/MWCNT-Co** immobilized one (−1.08 V *vs* Fc$^{+/0}$ *i.e.* −0.54 V *vs* NHE). While the reduction wave is well defined, the broad reoxidation wave indicates a slow process. This observation is more striking when the scan rate is increased to higher values (Figure III.11,

right). The peak-to-peak potentials difference becomes more marked, and the peak currents difference points a sluggish reoxidation system. Similar behavior has been observed on TiO_2 electrodes decorated with redox probes for the cathodic window.[13a, 13c]
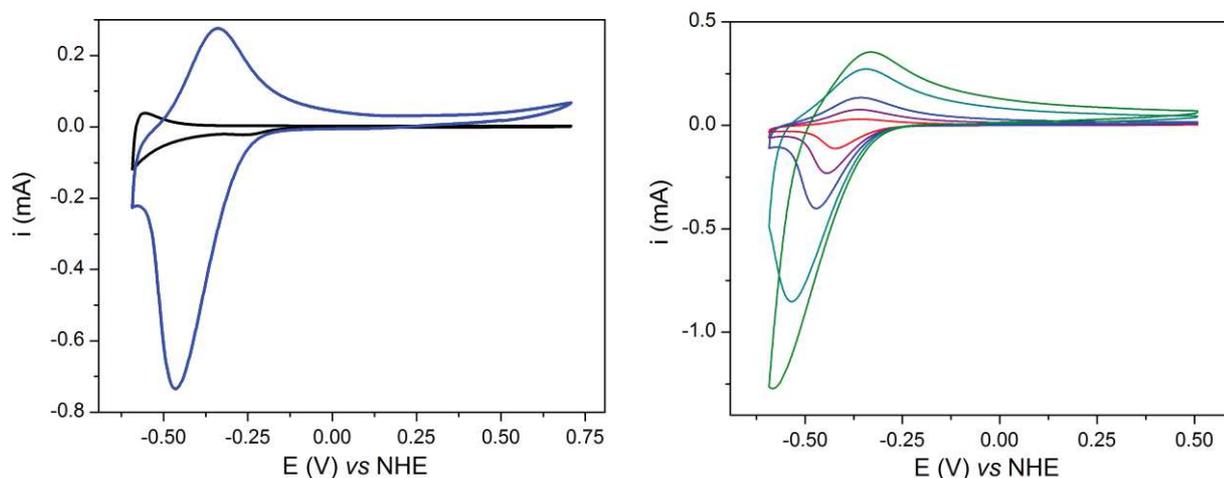
Figure III.11. CVs of a pristine **TiO₂** (black line) and a **TiO₂-Co$_{C12C8P}$** (blue line) electrodes recorded at a scan rate of 100 mV·s⁻¹ (left) and of a **TiO₂-Co$_{C12C8P}$** electrode recorded at 10 (red line), 50 (purple line), 100 (blue line), 250 (cyan line) and 500 (green line) mV·s⁻¹ in NaCl 0.1 M aqueous electrolyte (right).

However, the signature of the complex is lost upon repeated cycling, possibly caused by detachment of the **Co$_{C8C12P}$**. The incomplete hydrolysis of ester phosphonates (see Chapter III.2.1.2.1) might result in a weaker surface binding. Thus, we decided to directly pursue our investigations with the **Co$_{C11P}$** derivative.

2.2.3.3. *TiO₂-Co$_{C11P}$ electrodes*

The **Co$_{C11P}$** derivative could be anchored onto TiO₂ in the same manner than the **Co$_{C12C8P}$** one (Figure III.12).
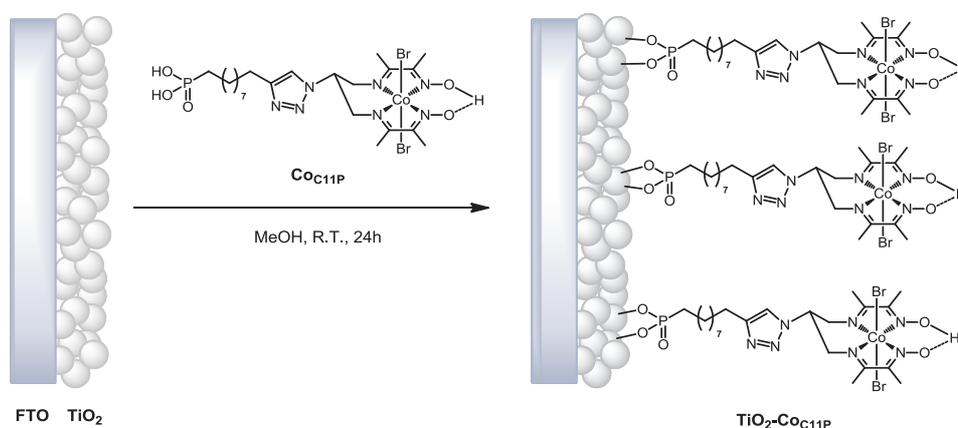
Figure III.12. Preparation of the **TiO₂-Co$_{C11P}$** electrodes (singly screen-printed substrate).

A wave at –0.38 V *vs* NHE is seen on the CV of the **TiO₂-Co_{C11P}** electrode recorded in NaCl 0.1 M aqueous electrolyte (Figure III.13, left). The shape of the wave is similar to the one observed at the **TiO₂-Co_{C12C8P}** electrode, with a sharp reductive peak and a broad reoxidation one. The linear dependence of peak currents as a function of the scan rate (Figure III.13, left, inset) is indicative of an event which is not controlled by diffusion. Thus, we ascribed this wave to the Co$^{II/I}$ couple of **Co_{C11P}** moieties immobilized on the surface of TiO₂.

A small ill-defined wave is also present at *ca* 0.25 V *vs* NHE. This event is in a region where the conduction through TiO₂ is forbidden. Hence, this wave can possibly be assigned to **Co_{C11P}** derivatives directly attached at the FTO surface. The low resolution and the potential of the wave suggest that this signature is that of the Co$^{III/II}$ couple.

The signature of the **Co_{C11P}** complex is also observed when CV is recorded in organic electrolyte (Figure III.13, right). The reduction wave is still peak-shaped, whereas the oxidation process almost splits into two distinct waves (ca –1.17 and –0.96 V *vs* Fc$^{+/0}$). The reason for this split is not fully understood but we tentatively propose that it arises from different conformations of the molecule on the surface.
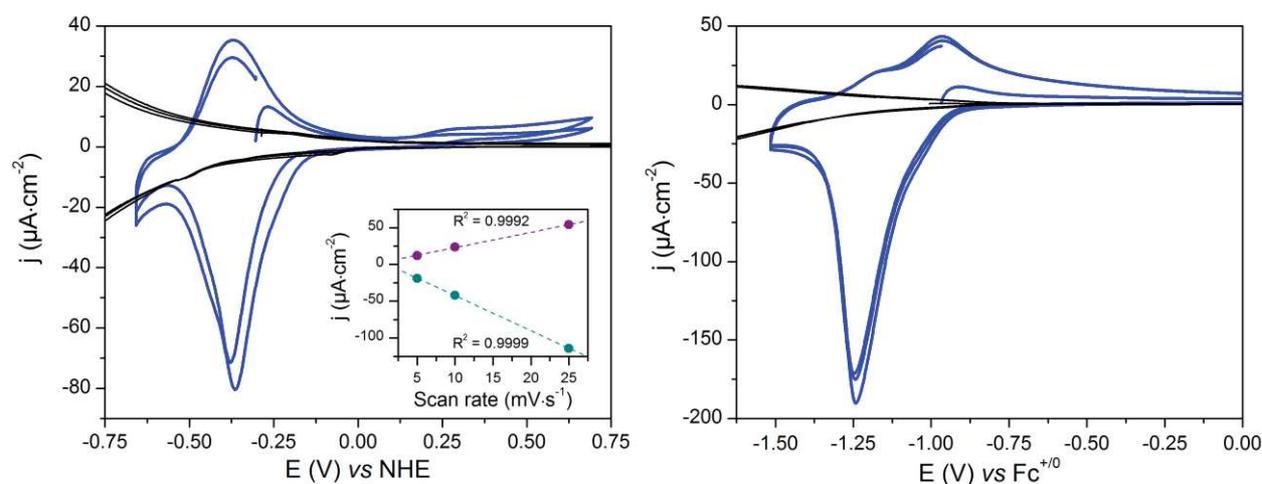
Figure III.13. CVs of a pristine **TiO₂** (black lines) and a **TiO₂-Co_{C11P}** (blue lines) electrodes recorded in (left) NaCl 0.1 M aqueous electrolyte at a scan rate of 10 mV·s⁻¹, with (inset) anodic (purple) and cathodic (cyan) peak currents (dots) and associated linear fits (dotted lines) as a function of the scan rate and (right) in *n*Bu₄NBF₄ 0.1 M dist. MeCN electrolyte at a scan rate of 10 mV·s⁻¹.

Providing a stable anchoring for the **Co_{C11P}**, the **TiO₂-Co_{C11P}** electrodes served as a starting point for the construction of molecular photocathode architectures in which the **Co_{C11P}** derivative will be translated onto a different TCO. The electrode was analyzed by XPS to get additional characterizations of the attached catalyst. Indeed, XPS usually probes the structure at the very surface of the screened samples (*ca* 0-10 nm) and can detect over the ppm range.

The XP survey spectrum of the **TiO₂-Co_C11P** electrode is shown in Figure III.14. The intense couple of peaks at around 457 and 463 eV is attributed to the *2p* core levels of Ti atoms and the sharp peak at around 529 eV is assigned to the *1s* core level of O atoms. These signatures account in majority for the TiO₂ supporting matrix.
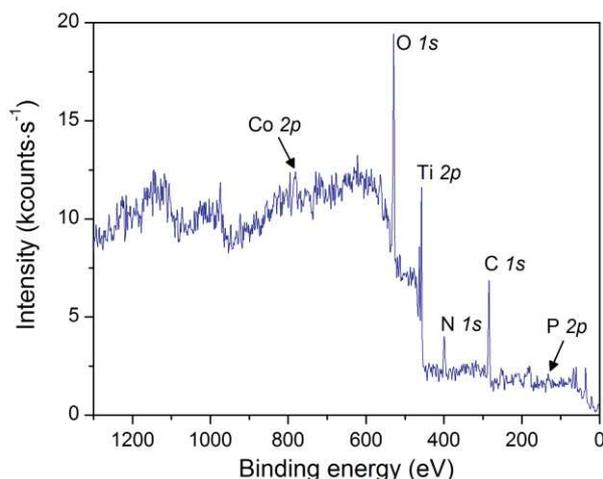
Figure III.14. XP survey spectra of the **TiO₂-Co_C11P** electrode.

Among others, less prominent peaks are found on the spectra and attributed to the P *2p*, C *1s*, N *1s* and Co *2p* levels. To get more precise information on the signature of the attached **Co_C11P** compound, XPS analyses were performed at the Co *2p₃/₂*, N *1s* and P *2p* levels (Figure III.15).

The Co *2p₃/₂* levels (Figure III.15, left) displays a major contribution at 781.1 eV, that is in good agreement with the reported signature of Co^{III} in the **[Co(DO)(DOH)pnL₂]** coordination sphere.[1a, 18] The contributions at higher energies (at *ca* 782.4, 785.1, 788.1 eV) possibly indicate the presence of the Co^{II} complex[18] or an alternative coordination sphere by substitution of the ancillary Br⁻ ligands.
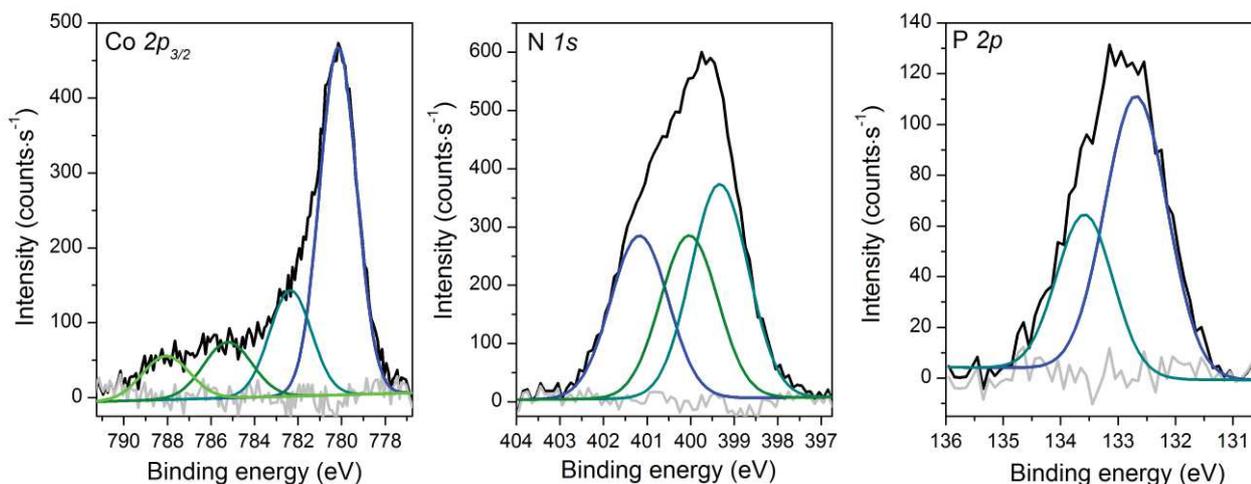
Figure III.15. XPS analyses of a **TiO₂-Co_C11P** electrode at the Co *2p₃/₂* (left), N *1s* (middle) and P *2p* (right) core levels. Black lines: baseline corrected spectra; blue, cyan, olive and green lines: fitted deconvolutions; gray lines: residual backgrounds.

The N *1s* peak (Figure III.15, middle) can be deconvoluted into three main contributions, at 399.2, 400.0 and 401.1 eV. The peaks of similar area at 400.0, respectively 401.1 eV, can tentatively be attributed to the two imino, respectively two oximato, nitrogen atoms in the **[Co^{III}(DO)(DOH)pnL$_2$]** coordination sphere.[18] The third peak at 399.2 eV is likely the signal of the N atoms at the triazole ring. These interpretations are also in good agreement with the relative areas of the peaks expected at a 3:2:2 ratio and found around a 2.6:2:2 ratio (399.2, 400.0 and 401.1 eV).

At the P *2p* core levels (Figure III.15, right), the deconvolution shows two peaks centered at 132.7 and 133.6 eV. The area ratio of 2:1 (132.7, 133.6 eV) and the splitting energy of 0.9 eV both evidence that these contributions relate to the 2p$_{3/2}$ and 2p$_{1/2}$ levels at a single P environment.

The comparison of the areas of the peaks at these three core levels yields an atomic ratio for P, Co and N of 1:1.5:7.1. Although a fair estimation at this accuracy is subject to caution, this value is in good line with the atomic formula of the **Co$_{C11P}$** derivative, for which a theoretical ratio of 1:1:7 is expected.

Overall, the electrochemical and XPS data evidences that the **Co$_{C11P}$** complex is present onto TiO$_2$, with the molecular structure likely retained upon grafting. While we could characterize the **Co$_{C11P}$** derivative attached at the surface of TiO$_2$, a *n*-type TCO, our point was now to translate our investigations at the surface of a *p*-type TCO. As such, we investigated the grafting of **Co$_{C11P}$** onto nickel oxide electrodes.

3. Immobilization of a cobalt diimine-dioxime phosphonic acid derivative onto nickel oxide

Acid phosphonic grafting moieties have been rarely utilized for the construction of molecular-based photocathodes onto NiO. Particularly, these anchors were assessed for the attachment of Ru(bpy)$_3$-based dyes applied in the frame of *p*-DSSCs.[19] The NiO surface coverage with the phosphonic acid grafting groups is found comparable to that observed with carboxylic acid anchors classically used in such architectures, although their binding constant is an order of magnitude down.[19] A very recent work by Sun and co-workers interestingly includes a phosphonate linker to attach a cobaloxime derivative at the surface of NiO.[20] This work was more broadly highlighted in the introduction of this manuscript but the main relevant features are recalled here. Under light irradiation, the DS photocathode obtained through co-grafting of an organic PS with the cobaloxime onto NiO evolves hydrogen from fully aqueous neutral media. This electrode constitutes the best performing one among the very few reported examples of H$_2$-evolving molecular DS photocathodes. Although some characterizations are provided in this work, there is to date no comprehensive description of a supported HER catalyst at the surface of nickel oxide. In this part, we aim at providing more detailed characterization of the **[Co^{III}(DO)(DOH)pnBr$_2$]** derivative **Co$_{C11P}$** attached onto NiO.

3.1. The nickel oxide substrate

The NiO substrate used in the present work has been included in a benchmarking study. In this study, different NiO preparations were assessed regarding various structural and functional specifications. We took part to the workshop organized under the *COST PERSPECT-H$_2$O* umbrella and hosted at the *University of Nottingham* in the group of E. Gibson, for the purpose of this benchmarking. We present here characterization of the NiO electrodes utilized throughout our studies. Additional data will be commented in Chapter IV, but for more detailed information the reader is referred to the article recently published on this study, added as an appendix of this manuscript (Paper IV).

3.1.1. Preparation

The NiO electrodes used in this work were purchased from a Swedish company, *Dyenamo*. The electrodes are prepared in the *Dyenamo* laboratory by screen-printing of a paste containing pre-formed NiO nanoparticles onto FTO-coated glass. Different widths of the NiO layer might be

obtained by repeating the screen-printing process. We use doubly printed substrates in this section. The as-printed NiO plates are further sintered in our laboratory at 450°C.

3.1.2. Structural characterization

SEM measurements of the sintered NiO electrodes (Figure III.16) show a nanostructured film. The width of the doubly printed mesoporous layer is around 1.7-1.8 μm.
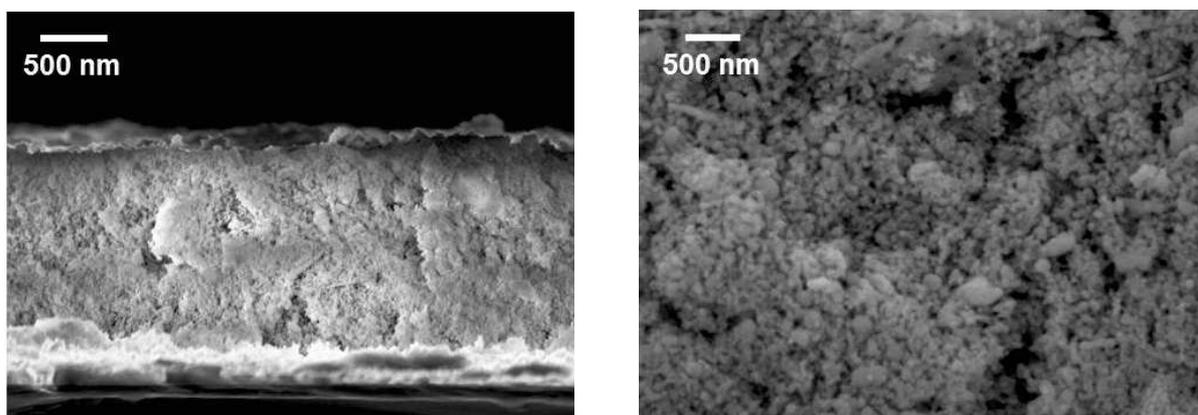
Figure III.16. SEM photographs at the edge (left) and zoomed at the edge (right) of a doubly screen-printed Glass/FTO/mesoNiO electrode purchased from *Dyenamo* and sintered at 450°C.

This value falls in the range of the optimal film thickness reported for NiO *p*-photoelectrodes (*ca* 2 μm).[21] The film is composed of a compact layer of interconnected crystallites. The X-ray diffraction (XRD) analysis of the material permits to estimate through the Scherrer equation a mean crystallite size about 15.4 nm. Brunauer-Emmett-Teller (BET) isotherm measurements by Kr adsorption give a film porosity around 71 $m^2 \cdot g^{-1}$. This value is comparatively high for a nanostructured NiO film[21a] and might provide a large surface loading.
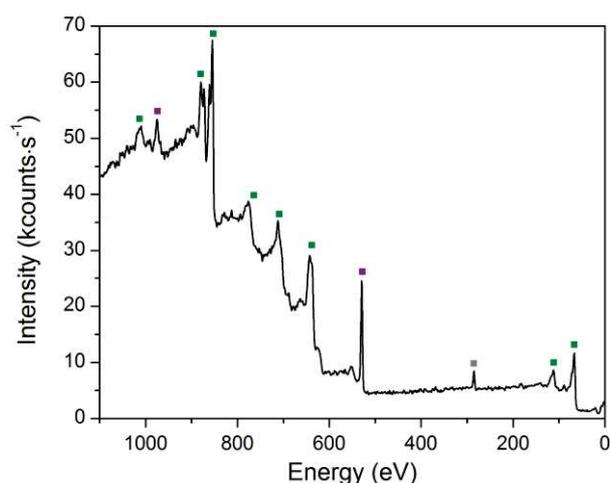
Figure III.17. XPS analysis of a doubly screen-printed Glass/FTO/mesoNiO electrode purchased from *Dyenamo* and sintered at 450°C. Green dots: Ni levels; purple dots: O levels; gray dot: C *1s* core level.

The XP survey spectrum of the electrode is shown in Figure III.17. The core levels of Ni and of O represent the majority of the features displayed on the spectrum. A peak at 285 eV matches the *1s* core level of carbon. The presence of carbon is either adventitious (from an external contaminant) and/or residual from the preparation of NiO.

3.2. A phosphonate-linked cobalt diimine-dioxime complex at the surface of NiO

Inspired by the immobilization of **Co$_{C11P}$** onto TiO$_2$, we sought for attachment of the derivative onto NiO. A similar procedure is followed as for the grafting of the derivative onto TiO$_2$, the electrodes being dipped in a **Co$_{C11P}$** 0.5 mM methanolic solution (Figure III.18) just after sintering at 450°C, while still hot (*ca* 90°C). The NiO plates sensitized on longer times than TiO$_2$ ones (typically 66 h).
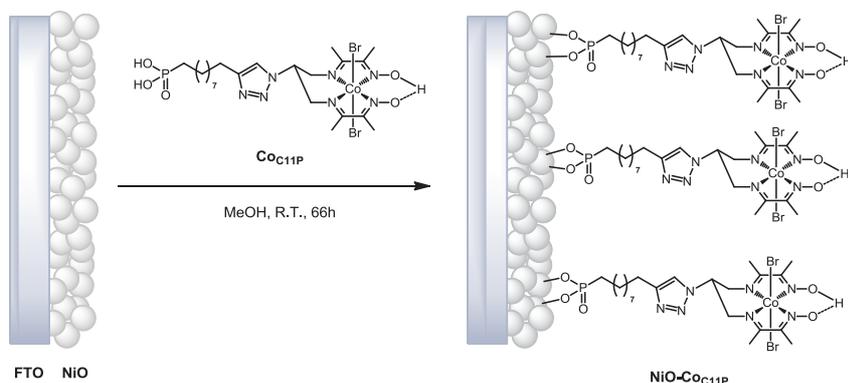
Figure III.18 Preparation of the **NiO-Co$_{C11P}$** electrodes.

3.2.1. Electrode characterization

The hybrid **NiO-Co$_{C11P}$** electrodes were analyzed by XPS, surface mass spectroscopy, electrochemistry and UV-visible spectroelectrochemistry.

3.2.1.1. XPS analysis

The XP survey analysis of the decorated electrode (Figure III.19, top left) displays the features characteristic of the NiO substrate, as observed for the pristine one. In addition, the comparison with the signature of **TiO$_2$-Co$_{C11P}$** electrodes permits to the identification of peaks attributed to the **[Co^{III}(DO)(DOH)pnBr$_2$]** derivative grafted onto the surface.
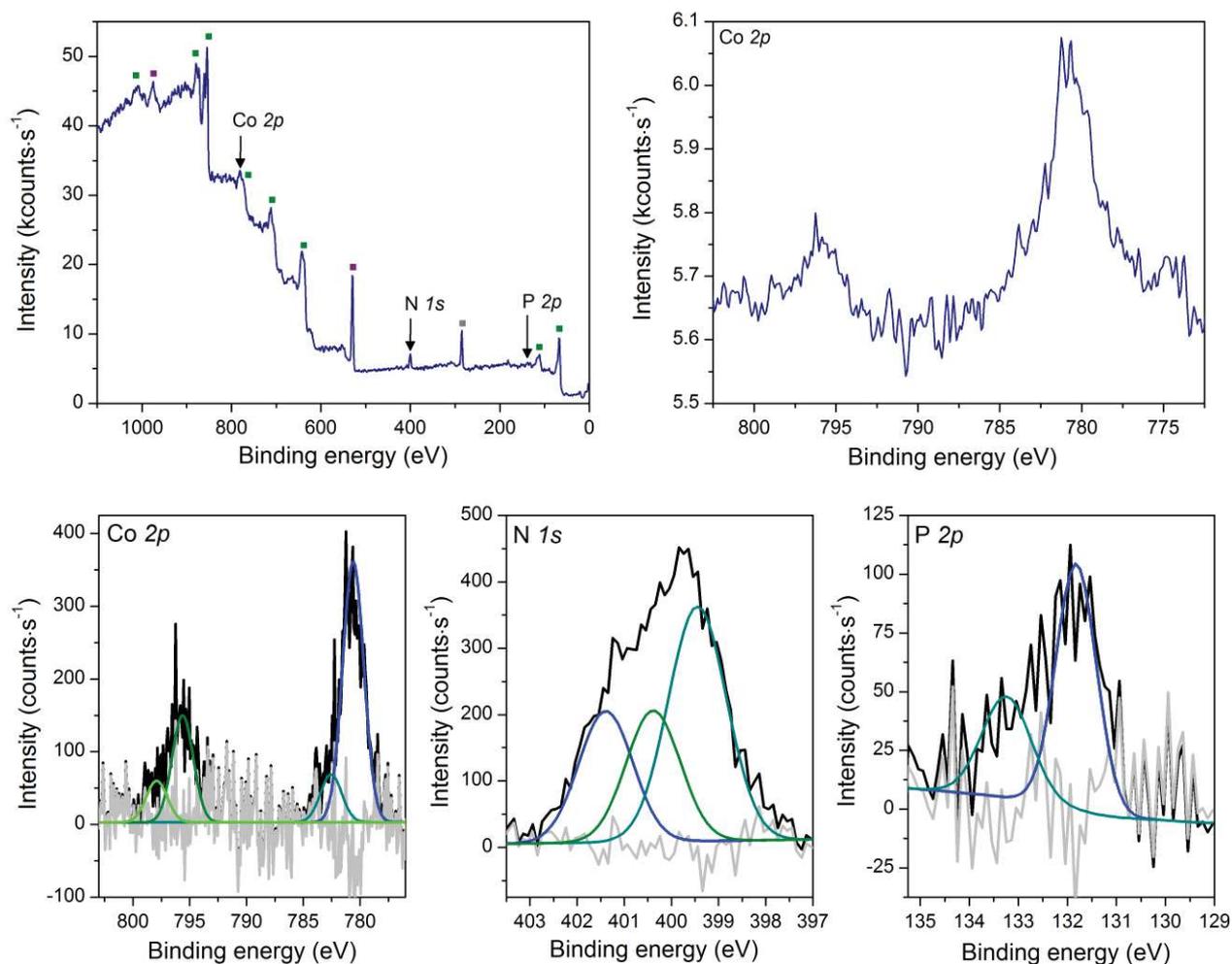
Figure III.19. XPS analysis of a **NiO-Co$_{C11P}$** electrode at the survey mode (top left), the Co *2p* core levels (top right) and the baseline corrected Co *2p* (bottom left), N *1s* (bottom middle) and P *2p* (bottom right) core levels. Green dots: Ni levels; purple dots: O levels; gray dot: C *1s* core level. Black lines: baseline corrected spectra; blue, cyan, olive and green lines: fitted deconvolutions; gray lines: residual backgrounds.

Especially, in the region of the Co *2p* core levels, two peaks are observed (Figure III.19, top right). These peaks are located on the top of a broad and intense signal at 765-790 eV (Figure III.19, top left) already present on the pristine NiO spectrum (Figure III.17) and likely assigned to a Auger line of Ni.[22] A polynomial background was used to tentatively subtract the contribution of the Ni Auger line from the signatures observed in the Co *2p* region. This treatment results in two peaks with a better defined shape (Figure III.19, bottom left), centered at 780.8 and 795.6 eV and separated by 14.8 eV of spin-orbit split. The signature is thus attributed to the Co *2p$_{3/2}$* and Co *2p$_{1/2}$* core levels, respectively, of the **[Co^{III}(DO)(DOH)pnBr$_2$]** derivatized complex. These features are in good agreement with the ones observed for the Co *2p* levels on both the **TiO$_2$-Co$_{C11P}$** (Figure III.15, left) and the **GDL/MWCNT-Co** electrodes.[1a]

A signal at 400 eV on the survey spectrum (Figure III.19, top left) is a clear indication of the presence of nitrogen at the surface of the grafted sample. The peak recorded at the N *1s* level (Figure III.19, bottom middle) can be expressed in a set of three contributions at 399.4, 400.3 and 401.4 eV. Such contributions are very similar to the ones found at the **TiO₂-Co$_{C11P}$** electrodes (Figure III.15, middle). This peak is also attributed to the three sets of chemically inequivalent N atoms in **Co$_{C11P}$**.

The signal ascribed to the P *2p* levels barely builds up from the survey spectrum (Figure III.19, top left). The low response is likely due to its low molecularity in the compound. But repeated scans in the P *2p* region evidence a peak centered at 131.8 eV (Figure III.19, bottom right). This peak is assigned to the signature of phosphonate anchoring groups. The signal observed on **NiO-Co$_{C11P}$** is slightly shifted to lower binding energies compared to the one on **TiO₂-Co$_{C11P}$** (131.8 *vs* 132.7 eV). The change in the surface (TiO₂ *vs* NiO) to which the phosphonate group is expected to bind provides a possible explanation for this shift.

Overall, the XPS analysis is well correlated with a surface of NiO decorated with **Co$_{C11P}$**.

3.2.1.2. Surface mass spectroscopy

The **NiO-Co$_{C11P}$** electrodes were further analyzed by ToF-SIMS, in the frame of a collaboration with the team of D. Leonard at the *Institut des Sciences Analytiques* in Villeurbanne. The ToF-SIMS technique permits the detection and analysis through mass spectroscopy of molecular compounds attached to a surface, by ionization at the top of this surface (within few tens of Å). The detection takes the charge of molecular fragments into account and the analysis is realized in m/z spectra. Noteworthy, this technique has been previously used to evidence the covalent attachment of model acid phosphonic derivatives at TiO₂-like surfaces, based on fragmentations at the binding phosphonate groups.[23]

For the **NiO-Co$_{C11P}$** electrode, the spectrum obtained in the positive mode is shown in Figure III.20. Different fragments are proposed for the interpretation that have been summarized in Figure III.21.

A first set of peaks is located around m/z = 650 (Figure III.20, top). This set can be attributed to a **[Co^{III}$_{C11P}$ – PO₃H₂⁻]⁺** compound, which features an isotopic pattern with a major contribution at 650.07 g·mol⁻¹ and secondary ones at 648.07 and 652.07 g·mol⁻¹ (Figure III.21, left track). By the subsequent loss of a bromide joined with the reduction to the Co^{II} state or with a deprotonation, the two **[Co^{II}$_{C11P}$ – PO₃H₂⁻]⁺** and **[Co^{III}$_{C11P}$ – PO₃H₂⁻ – Br⁻ – H⁺]⁺** intermediates are formed, of exact masses 569.15 and 568.15 g·mol⁻¹, respectively. We note that the in-source reduction of Co^{III} to Co^{II} is often seen under positive MS conditions for the

[Co^{III}(DO)(DOH)pnL₂]-like complexes. These masses correctly account for the peaks at m/z = 568 and 569 in the broad motif around m/z = 571 (Figure III.20, middle).

Very interestingly, the peak at m/z = 627 (Figure III.20, top) can be ascribed to a **[Co^{II}₍C11P₎ + Ni²⁺ – 2H⁺ – 2Br⁻]⁺** species having an exact mass of 627.13 g·mol⁻¹ (Figure III.21, top right). This fragment thus corresponds at **Co₍C11P₎** moieties displaying a doubly unprotonated phosphonate group that bind Ni^{II} *via* two P-O-Ni ester bonds. Such covalent links likely provide a stable attachment to the NiO surface.

The observation of these first fragments support that a part of the **Co₍C11P₎** moieties are strongly anchored on the NiO surface through phosphonate binding.

Besides, the motif at m/z = 650 (Figure III.20, top) also partially correlates with a **[Co^{III}₍C11P₎ – Br⁻]⁺** compound that displays two major isotopes at 650.13 and 652.12 g·mol⁻¹ in similar intensities (Figure III.21, right track). This fragment can further lose a second Br⁻ ligand accompanied either by the loss of a proton or, more likely, by the reduction of the Co^{III} center to Co^{II}. This path leads to three possible fragments of formulae **[Co^{III}₍C11P₎ – 2Br⁻ –H⁺]⁺** or **[Co^{II}₍C11P₎ – 2Br⁻]⁺** with respective exact masses of 570.20 and 571.21 g·mol⁻¹ (Figure III.21, right track). The signatures of such compounds are represented in the broad motif observed around m/z = 571 (Figure III.20, middle).

This second fragmentation pathway is likely indicative of **Co₍C11P₎** molecules anchored to NiO through H-bonding of phosphonic acid groups or possibly through physisorption.

The series of peaks observed on this spectrum cannot be completely described by a single fragmentation pathway. This point thus suggests that several anchoring modes cohabitate at the surface of NiO.

Of note, both fragmentation pathways described above further lead to the **[Co^{II}₍C11P₎ – PO₃H₂⁻ – 2Br⁻ – H⁺]⁺** intermediate, the isotopic pattern of which (major isotope at 489.23 g·mol⁻¹, Figure III.21, bottom) matches the peak observed at m/z = 489 (Figure III.20, bottom). This intermediate is additionally split in a series of compounds by the stepwise losses of CH₂ fragments (14.02 g·mol⁻¹), well correlated with the sets of peaks in the −14 series (475/461/447/433/419/405, Figure III.21, bottom).
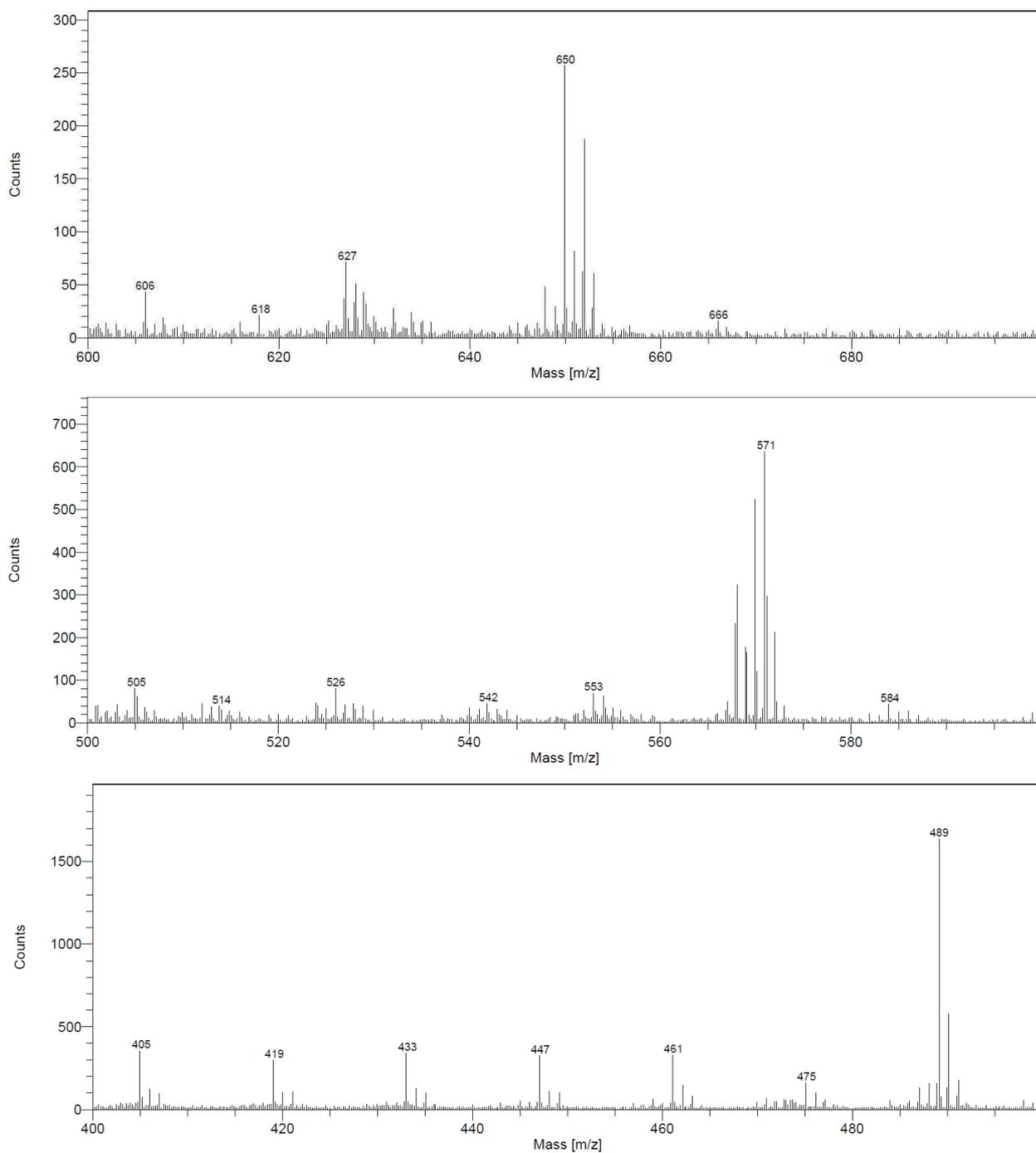
Figure III.20. ToF-SIMS analysis at the surface of a **NiO-Co$_{C11P}$** electrode, recorded in the positive mode at m/z between 700-600 (top), 600-500 (middle), 500-400 (bottom).
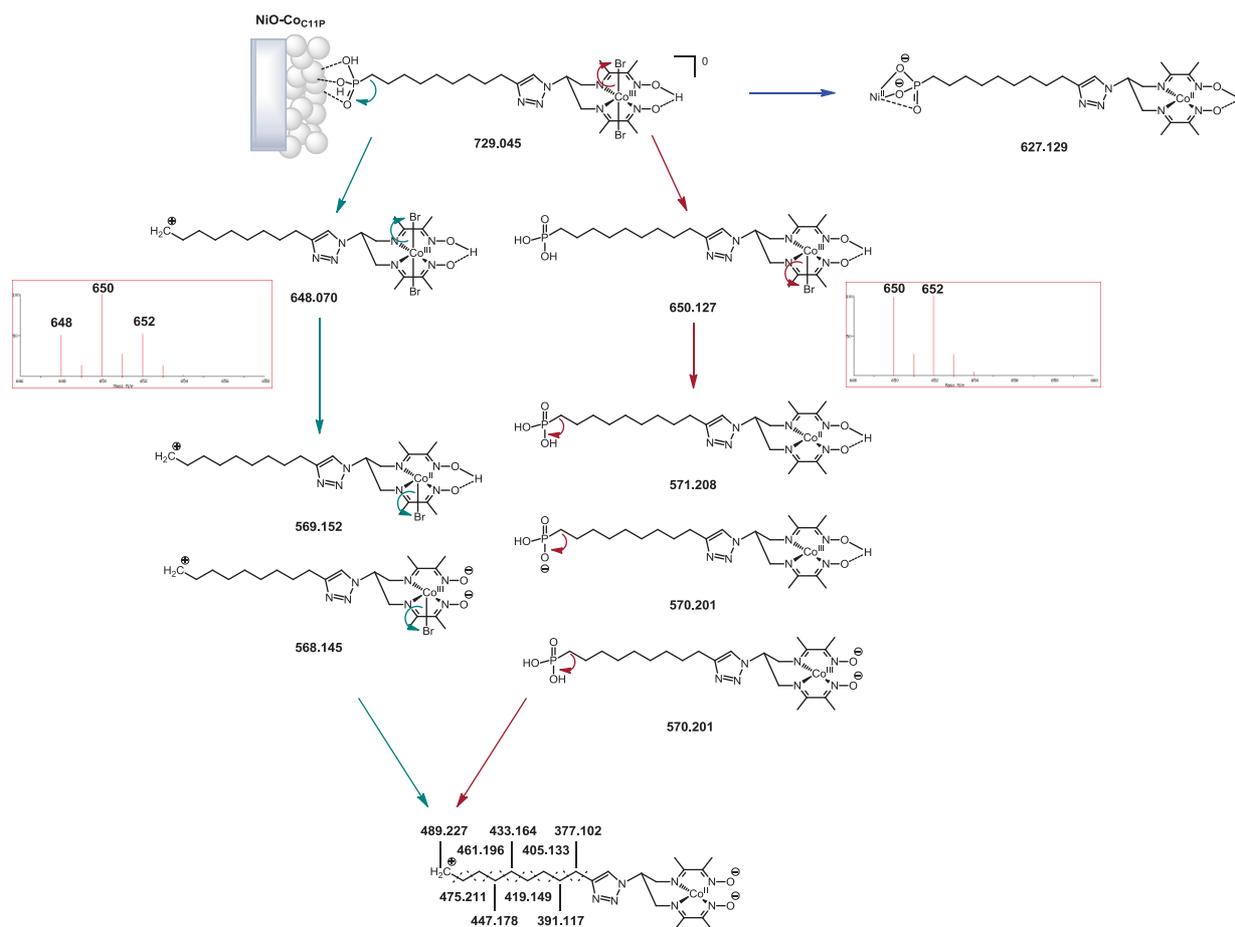
Figure III.21. Proposed fragments for the attribution of peaks on the ToF-SIMS positive mode analysis at a **NiO-Co$_{C11P}$** electrode. Figures indicate the exact mass of considered compounds; for the sake of clarity the charges of the compounds have been omitted and, unless otherwise noted, are all equal to +1.

Consequently, this ToF-SIMS analysis evidences that the covalent grafting of **Co$_{C11P}$** onto NiO *via* ester phosphonate linkages is achieved for a part of the immobilized species. As well, the observation of the complex retaining its molecular structure once grafted lead us to conclude that the grafting procedure does not alter the nature of the catalyst. We then aimed at characterizing the electrode from a more functional point of view.

3.2.1.3. Electrochemistry

The cyclic voltammetry recorded at a pristine NiO electrode and at a **NiO-Co$_{C11P}$** electrode is shown in Figure III.22, left. A broad wave at around 0.3 V vs NHE is observed for the pristine electrode. This wave is attributed to a surface-confined Ni$^{III/II}$ redox event likely coupled with the exchange of a proton, as described in the introduction (see Chapter I.2.2.2.1.2). This feature is also present at the decorated electrode, but with a shape slightly modified possibly upon immobilization of the catalyst at the surface.
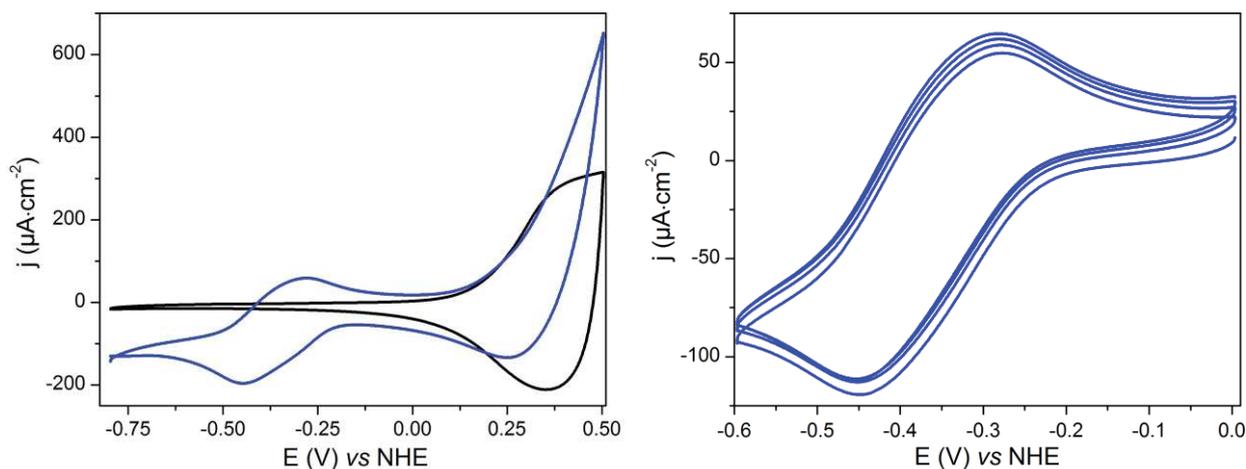
Figure III.22. CVs recorded at a pristine NiO electrode (black line) and at a **NiO-Co$_{C11P}$** electrode (blue line) (left) and successive scans in the cathodic region at a **NiO-Co$_{C11P}$** electrode (right) with a scan rate of 100 mV·s^{-1} in a NaCl 0.1 M aqueous electrolyte.

A reversible wave at -0.37 V *vs* NHE is observed on the **NiO-Co$_{C11P}$** electrode. The potential of the wave is in good agreement with the one observed on **TiO$_2$-Co$_{C11P}$** electrodes and this wave is tentatively attributed to the Co$^{II/I}$ couple.

However, the valence band of NiO is usually reported as being positive to NHE at neutral pH (0.3-0.5 V *vs* NHE at pH 7), though the exact value is discussed.[24] At the potential of the observed wave, downward from NHE, the NiO layer is thus not expected to be conductive. The presence of this redox event is hence questioning. To get stronger information on the event associated with this wave, we submitted the electrode to further electrochemical analysis.

First, the electrode was scanned repeatedly around the potential of the considered wave (Figure III.22, right). No major modification of the wave is observed upon cycling. The stability of this wave points to a surface-immobilized redox species. The cyclic voltammograms of the electrode were also recorded at multiple scan rates (Figure III.23, left) between 10 and 100 mV·s^{-1}. The intensity of the square cathodic peak is plotted as a function of the scan rate (Figure III.23, right) and the experimental data are well fitted with a linear function. This result supports an electrochemical event that implies electron hopping throughout Co centers, associated with an apparent diffusion coefficient of 4.4 10^{-8} cm^2·s^{-1}. For further information on that point, the reader is referred to the Addendum to Chapter III.3.2.1 given as an appendix of this manuscript.

Collectively, these points all suggest that the electrochemical signature is likely the one of the Co$^{II/I}$ couple of **Co$_{C11P}$** grafted onto the NiO electrode.
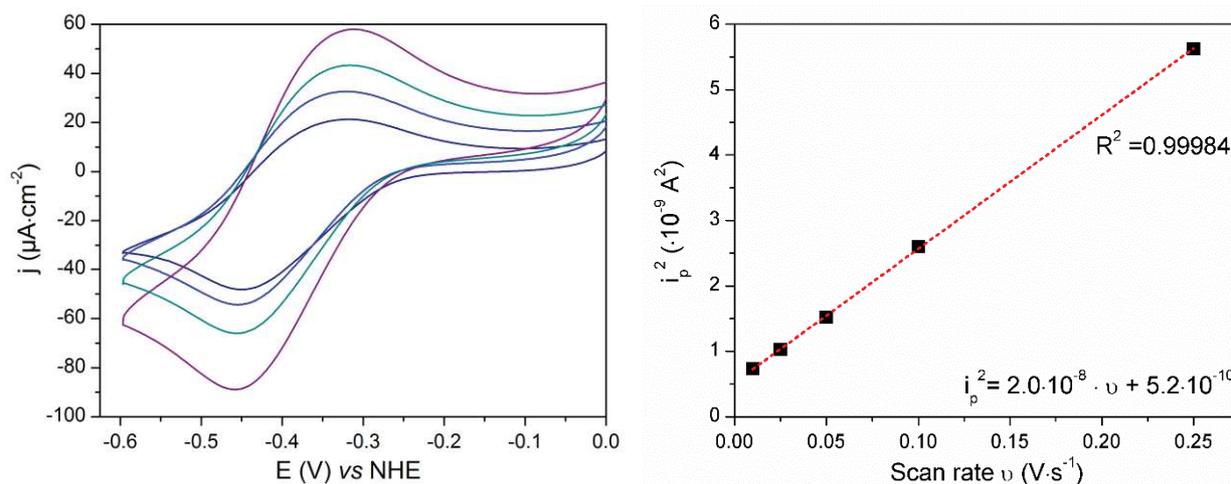
Figure III.23. CVs recorded at a **NiO-Co$_{C11P}$** electrode in a NaCl 0.1 M aqueous electrolyte, with scan rates of 10 (navy line), 25 (blue line), 50 (cyan line) and 100 (purple line) mV·s^{-1} (left) and the corresponding plot of square *baseline-corrected* peak current as a function of the scan rate (dots) with associated linear fit (dashed lines) (right).

3.2.1.4. Spectroelectrochemistry

The Co^I state of **[Co^I(DO)(DOH)pn]** is known to display a characteristic UV-visible signature, with a broad, bicephalous, signal between 500 and 800 nm,[25] as described in the introduction (see Chapter I.1.3.4). This signature can be utilized to get additional evidence of the putative Co$^{II/I}$ redox event through UV-visible spectroelectrochemistry. UV-visible spectra were recorded at the **NiO-Co$_{C11P}$** electrode poised first at a potential more anodic (–0.24 V *vs* NHE) and then at a potential more cathodic (–0.84 V *vs* NHE) compared to the wave ascribed to the Co$^{II/I}$ couple, as shown in Figure III.24.
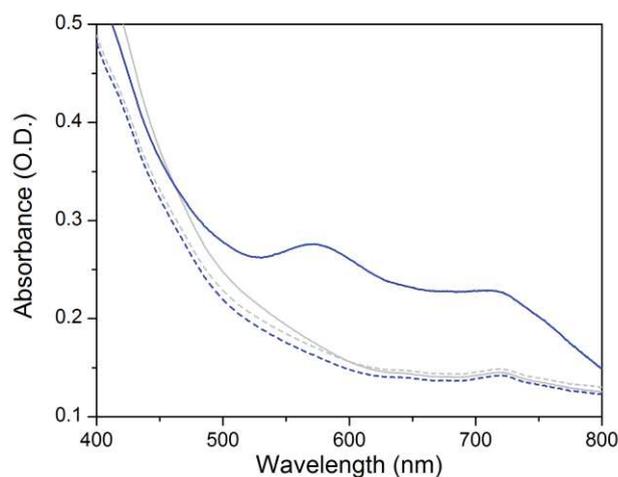
Figure III.24. UV-visible spectra of a **NiO-Co$_{C11P}$** electrode (blue lines) and of a pristine NiO electrode (gray lines) poised at –0.24 V *vs* NHE (dotted lines) then at –0.84 V *vs* NHE (plain lines) in a NaCl 0.1 M aqueous electrolyte.

A marked change is observed upon cathodic equilibration of the **NiO-Co$_{C11P}$** electrode. A large band featuring two maxima (*ca* 573 and 708 nm) appears when the electrode is equilibrated at potentials downward from the assumed Co$^{II/I}$ wave. Of note, no similar signature is found with the blank electrode, although NiO is slightly electrochromic in the potential window considered. This observation thus relates the specific spectroscopic signal to the presence of **Co$_{C11P}$** at the surface of the electrode.
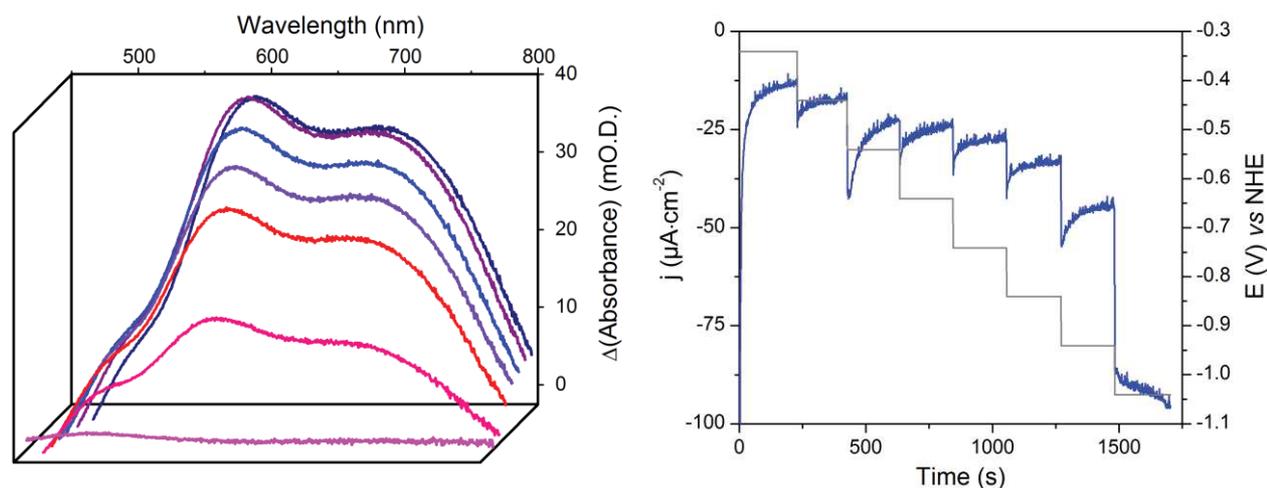
Figure III.25. Differential UV-visible spectra of a **NiO-Co$_{C11P}$** electrode poised in a NaCl 0.1 M aqueous electrolyte at –0.44 (magenta line), –0.54 (pink line), –0.64 (red line), –0.74 (violet line), –0.84 (blue line), –0.94 (purple line) and –1.04 (navy line) V *vs* NHE, with subtraction of the spectrum of the same electrode poised at –0.34 V *vs* NHE under identical conditions (left); corresponding current densities (blue line, left scale) at the different potentials (gray line, right scale) applied to the **NiO-Co$_{C11P}$** electrode in a NaCl 0.1M aqueous electrolyte during the acquisition of the UV-visible spectra shown on the graph on left (right).

More, if potentials are cathodically swept along the wave, the growth of the visible signature between 500 and 800 nm is clearly monitored on the difference spectra depicted in Figure III.25, left. The signal of the reduced electrode shows two merged bands with maxima at 592 nm and 687 nm. The maxima are slightly shifted compared to the raw UV spectra (Figure III.24), likely because the spectrum of the non-reduced electrode has been subtracted. Overall, this signature is in very good agreement with the one of the **[Co^I(DO)(DOH)pn]** complex.[4] The establishment of such signal upon cathodization is imparted to the pool of supported **Co$_{C11P}$** complex which is stepwise reduced from the Co^{II} state to the Co^I state. We therefore attribute the wave monitored at –0.37 V *vs* NHE at the **NiO-Co$_{C11P}$** electrode to the Co$^{II/I}$ couple of the **Co$_{C11P}$** species immobilized at the surface of NiO. The visible signature at the reduced electrode allowed us to estimate the surface coverage in **Co$_{C11P}$** around 4.5 nmol·cm^{-2}. Further details about this estimate are to be found in the Addendum to Chapter III.3.2.1, appendix of this manuscript.

Interestingly, we note that the background equilibrium current density increases as potential is decreased (Figure III.25, right). This phenomenon can be indicative of a catalytic process occurring at the electrode, possibly H_2 evolution. To gain more insight in this view, we performed a series of electrocatalytic experiments with the **NiO-Co$_{C11P}$** electrode.

3.2.2. Electrocatalytic behavior

The chronoamperometric analyses were performed in a two-compartment cell with a H_2 Clark micro-sensor introduced in the electrolyte at the cathodic compartment for tracking any hydrogen production by the immobilized cathode. This compartment was vigorously stirred to homogenize the concentration of H_2 in solution and to facilitate its detection.

3.2.2.1. Activity in neutral media

The experiments were performed in the same *quasi*-neutral NaCl 0.1 M aqueous electrolyte (pH ~ 6.4) and the electrode was poised at a potential of –0.55 V *vs* RHE (–0.93 V *vs* NHE), downward from the Co$^{II/I}$ wave. A cathodic current is observed, which undergoes an initial decay to stabilize around –10 $\mu A \cdot cm^{-2}$ after 100 s (Figure III.26, left). The steady current density is inferior under these conditions to the one expected from previous spectroelectrochemical measurements (between –30 and –40 $\mu A \cdot cm^{-2}$ from Figure III.25, right). After 5 min of electrolysis *ca* 4.5 mC of charges are passed, which should yield about 23 nmol of H_2 if the faradaic efficiency for HER is unity (Figure III.26, right). However, the Clark sensor shows that no hydrogen is produced during the chronoamperometric experiment (Figure III.26, right).
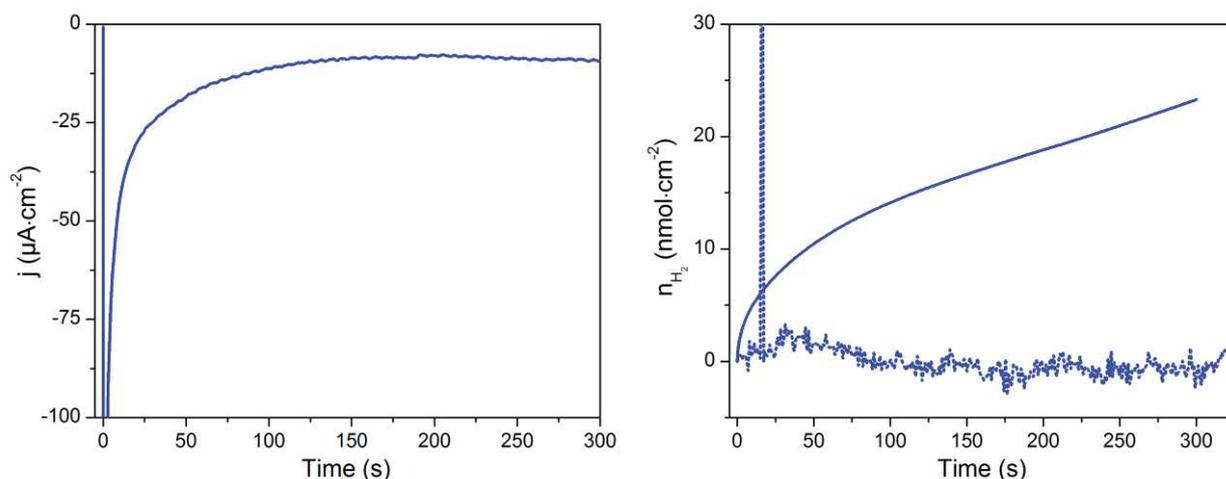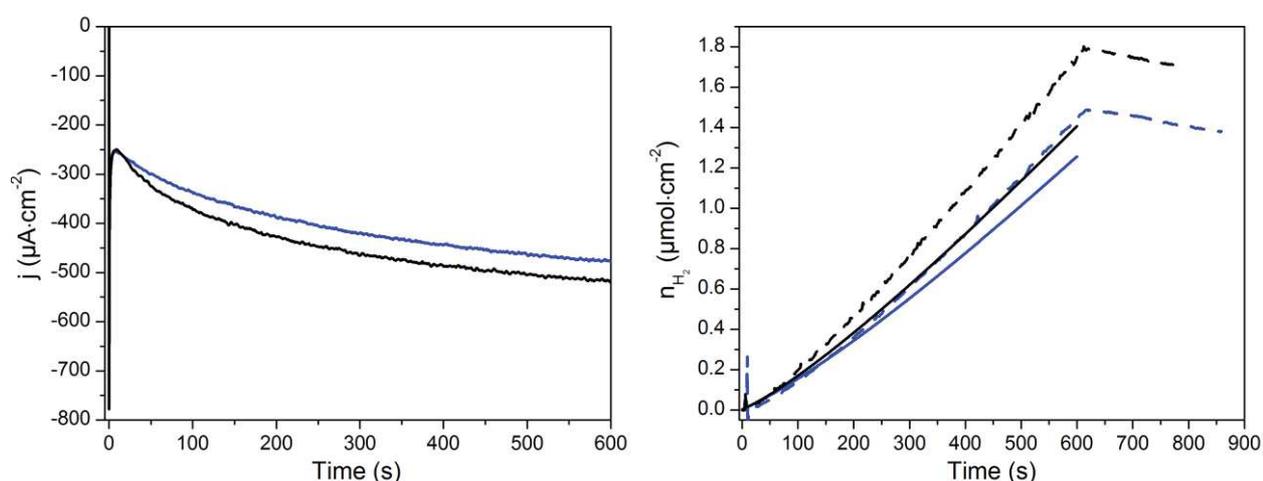

Figure III.26. Current density (left), H_2 produced assuming a unity faradaic efficiency from charges passed (plain line) and as observed with a H_2 Clark micro-sensor (dotted line) (right) during a 300 s electrolysis at –0.55 V *vs* RHE of a **NiO-Co$_{C11P}$** electrode in a NaCl 0.1 M aqueous electrolyte.

These observations indicate that the low current observed at such potential is not catalytic for hydrogen production and is thus ascribed to a side-reduction. Such process might be a capacitive charging of the electrode or the reduction of residual oxygen trapped in pores within the NiO film and that was not removed even after the thorough degassing.

To foster hydrogen evolution catalysis by the hybrid electrode, the potential was poised at a more negative value. At –0.75 V *vs* RHE (–1.13 V *vs* NHE), a cathodic current builds up, starting from –250 $\mu A \cdot cm^{-2}$ and continuously increasing to reach –450 $\mu A \cdot cm^{-2}$ at the end of the chronoamperometric measurement (Figure III.27, left). During the same time, hydrogen is produced in quantitative faradaic yields, as monitored by the Clark probe (Figure III.27, right). However, the current densities, charges passed and hydrogen production are nearly identical to that observed at a control pristine NiO electrode (Figure III.27).
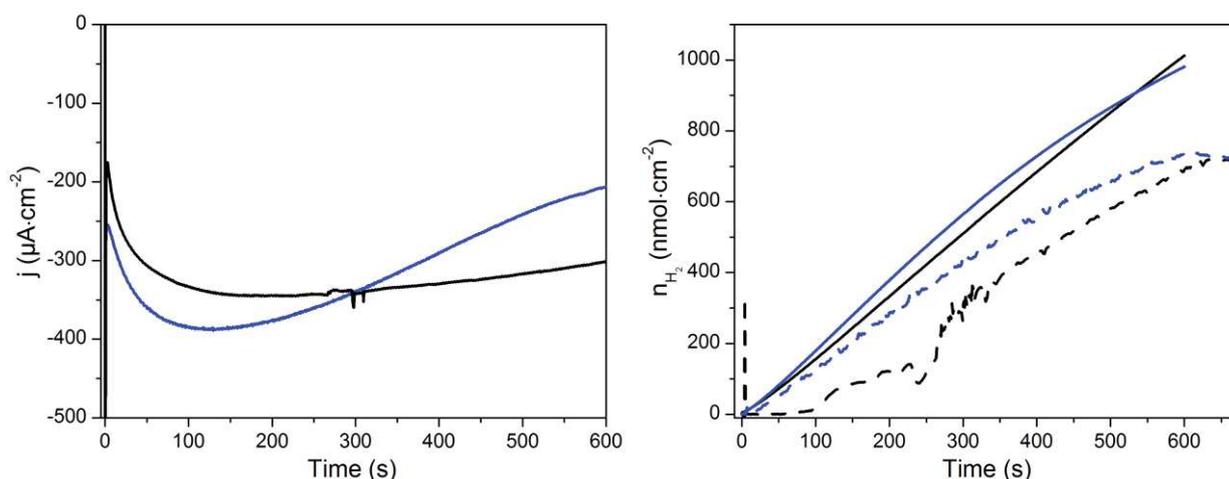

Figure III.27. Current densities (left), H_2 produced assuming a unity faradaic efficiency from charges passed (plain lines) and as observed with a H_2 Clark micro-sensor (dotted lines) (right) during a 600 s electrolysis at –0.75 V *vs* RHE of a pristine NiO (black lines) and of a **NiO-Co$_{C11P}$** (blue lines) electrodes in a NaCl 0.1 M aqueous electrolyte.

This observation shows that the NiO substrate has an intrinsic activity for the electroreduction of proton. That result is in line with reports from the literature in which related Ni alloys surfaces have been utilized as electrocatalysts for HER.[26] Hence, the electrocatalysis of H_2 production observed at the **NiO-Co$_{C11P}$** electrode is likely attributed to this intrinsic activity of the NiO support at such a cathodic potential.[26]

Yet, these experiments were conducted in a non-buffered aqueous media, in which the pH has increased at the cathodic part after the electrolysis, as a result of the consumption of the protons and the slow ionic exchange with the anodic part. To avoid such a pH shift and rule out subsequent undesired effects, we performed the same set of electrolyses but in a TEOA 0.1 M

aqueous buffer at pH 7 (not shown). Similar trends in the electrocatalytic behaviors of **NiO-Co$_{C11P}$** and pristine NiO were seen.

We could thus conclude that in neutral media the **NiO-Co$_{C11P}$** electrode does not catalyze hydrogen evolution at moderate overpotential (–0.55 V *vs* RHE) where Co^I is formed, while catalysis is directly performed by the supporting NiO substrate at more negative potential (–0.75 V *vs* RHE). These conclusions are also in line with the poor activity for HER observed for the supported complex at **GDL/MWCNT-Co** in aqueous buffer at pH 7.[1a]

3.2.2.2. Activity in mildly acidic media

By contrast, the immobilized catalyst has been shown to display improved performance for proton reduction in an acetate 0.1 M aqueous buffer at pH 4.5.[1a] We therefore shifted our investigations to this electrolyte.

Under these conditions, the **NiO-Co$_{C11P}$** set at –0.55 V *vs* RHE (–0.82 V *vs* NHE), develops a cathodic current that first grows from –250 to –380 µA·cm^{-2} at 100 s and then decreases to reach –200 µA·cm^{-2} after 10 min (Figure III.28, left). Concomitant hydrogen evolution is observed in good faradaic efficiency (*ca* 75 %, Figure III.28, right). The current density at the control pristine NiO electrode also grows in a first phase to reach –345 µA·cm^{-2} after 160 s, but undergoes a much less marked decay giving a value of −300 µA·cm^{-2} at the end of the electrolysis (Figure III.28, left). Hydrogen is produced in similar faradaic yields (*ca* 68%, Figure III.28, right).

Figure III.28. Current densities (left), H$_2$ produced assuming a unity faradaic efficiency from charges passed (plain lines) and as observed with a H$_2$ Clark micro-sensor (dotted lines) (right) during a 600 s electrolysis at –0.55 V *vs* RHE of a pristine NiO (black lines) and of a **NiO-Co$_{C11P}$** (blue lines) electrodes in an acetate 0.1 M aqueous buffer at pH 4.5.

The comparison of the activities for HER between **NiO-Co$_{C11P}$** and the blank NiO substrate tends to demonstrate that the hydrogen evolution is mainly driven by the NiO surface in acetate buffer at pH 4.5 as already observed in neutral media. This point is quite intriguing since the

anchored **[Co^{III}(DO)(DOH)pnL$_2$]** catalyst is known to display high turnover at such a pH.[1a] However, the grafted electrode features higher catalytic currents than the pristine one at the beginning of the electrolysis (Figure III.28, left). This improved activity is tentatively ascribed to the electrode-bound **Co$_{C11P}$** catalytic moieties. The important current decrease in the second phase observed at **NiO-Co$_{C11P}$** (Figure III.28, left) then suggests a deactivation of the electrode. We propose that this deactivation occurs through a leach off of the **Co$_{C11P}$** derivatives from the surface. The displacement of **Co$_{C11P}$** might originate from the competitive surface binding of the electrolytic acetate ions and/or from the modification of the surface states due to the intrinsic activity for HER of the NiO material (Figure III.28, right).

To gain insight in that direction, we recorded the CV of a pristine NiO electrode after chronoamperometric experiments in an acetate buffer at pH 4.5 (Figure III.29, top). At negative potentials, a broad event is displayed with a large reduction wave peaking at –0.43 V *vs* RHE and a large reoxidation one at –0.07 V *vs* RHE. Such event is likely the signature of a desorption-adsorption phenomenon involving Ni at the +II to 0 states. This observation corroborates the modification of the NiO surface upon electrolysis under cathodic conditions.
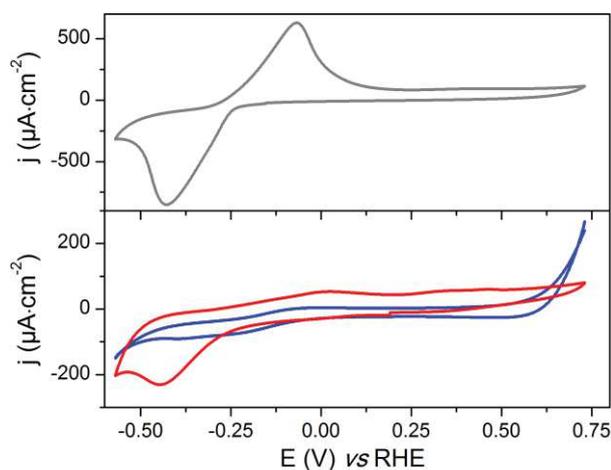
Figure III.29. CVs at a pristine NiO electrode after electrolyses in an acetate 0.1 M aqueous buffer at pH 4.5 (gray line) and at a **NiO-Co$_{C11P}$** electrode before (blue line) and after (red line) electrolyses in an acetate 0.1 M aqueous buffer at pH 4.5, recorded in the same buffer at a scan rate of 100 mV·s^{-1}.

At the **NiO-Co$_{C11P}$** electrode, a small irreversible wave is observed around –0.20 V *vs* RHE before performing the chronoamperometric measurements (Figure III.29, bottom, blue line), which is attributed to the catalysis of proton reduction by **Co$_{C11P}$**. This feature disappears after reductive electrolyses in acetate buffer at pH 4.5, while at the same time the desorption-adsorption event seen at the pristine electrode appears, although to a lesser extent (Figure III.29, bottom, red line). Overall, such observations point to a leach off of the **Co$_{C11P}$**, very likely arising from a modification of the surface states under reductive conditions at pH 4.5.

Collectively, these studies show that grafting **Co_{C11P}** at the NiO surface does not result in improved electrocatalytic activity for hydrogen evolution. On the one hand, the catalyst is not active enough in neutral media. On the other hand, the intrinsic activity of NiO at cathodic applied potentials participates in the undesired peel off of the bound **Co_{C11P}** species. For these reasons, we focused our next investigations on photoelectrocatalysis that does not necessitate highly reductive conditions, since the required energetic income will be provided by the light.

3.3. Discussion

From the XPS, ToF-SIMS and (spectro)electrochemical data, we could demonstrate that the **Co_{C11P}** complex is immobilized at the surface of NiO. The exact binding mode is not yet fully deciphered. However, the fragments observed in surface mass spectroscopy indicate that a pool of molecules at the **NiO-Co_{C11P}** electrode are grafted through strong Ni-O-P links.

Importantly, the attachment is stable enough in neutral aqueous electrolyte to allow for electrochemical investigations of the interface. The redox event observed at −0.37 V *vs* NHE on the **NiO-Co_{C11P}** electrode is indeed attributed to the Co^{II/I} wave of the immobilized complex, as shown from the spectroelectrochemical experiments. This result suggests that, under the conditions used (NaCl 0.1 M aqueous electrolyte, pH ~ 6.4), the NiO decorated electrode *does* feature conductivity at this cathodic potential. Such an observation is questioning, since bulk NiO is not conductive at the potential of this wave, located in the band-gap energies. Actually, the insulating properties of NiO at negative potentials under similar aqueous conditions is well supported by a recent work of Armstrong and co-workers. In that study, the authors adsorb a film of CO dehydrogenase enzymes (CODH) at the top of NiO and pyrolytic graphite edge (PGE) electrodes.[13d] The decorated conductive PGE electrode reversibly catalyzes the interconversion of CO_2 to CO at the thermodynamic equilibrium of the CO_2/CO couple ($E^{0,app}_{CO_2/CO}$ = −0.46 V *vs* NHE) in an aqueous buffer at pH 6, which translates in a bidirectional catalytic current at that potential. At contrast, such a catalytic current is not observed on the hybridized *p*-type NiO electrodes. The authors conclude that the loss in activity on NiO arises from the *p*-type nature of this SC.

Several hypotheses might be drawn to explain the conductivity in the negative potential window that is observed with the **NiO-Co_{C11P}** electrodes. First, the attachment of **Co_{C11P}** directly at the surface of the supporting FTO layer is possible. Since FTO is a *quasi*-metallic oxide, it would allow accessing the cathodic potential necessary to reduce Co^{II} to Co^{I}. However, redox centers deposited at the surface of the planar FTO substrate would represent a monolayer, or less. The surface loading observed at the **NiO-Co_{C11P}** electrode is in the 10^{-9} mol·cm^{-2} range, which

means at least one order of magnitude higher than a monolayer (10^{-10} mol·cm^{-2} range). We thus postulate that the Co$^{II/I}$ wave is not mainly associated with the redox behavior of **Co$_{C11P}$** molecules attached at the FTO substrate, although this process might coexist to a certain extent. This point further implies that the electron conductivity is occurring throughout the NiO mesoporous structure.

A possible explanation is that electrons are conducted through the film by the Co centers themselves, in a process called *electron hopping*.[27] This phenomenon implies that an electron is transfered from the FTO back electrode and hops along redox active Co centers anchored to NiO. Such behavior has been observed on *n*-type (TiO$_2$) or insulating (ZrO$_2$, Al$_2$O$_3$) mesoporous films[28] or metal organic frameworks (MOFs)[29] deposited onto conductive glass and to which redox probes are attached. To the best of our knowledge, this behavior has not been reported yet at the surface of NiO. This process requires a dense packing of the electron hopping centers,[28] which is possibly accessed in the case of the **NiO-Co$_{C11P}$** electrode. The long alkyl arm of **Co$_{C11P}$** might allow the redox centers to move around. This additional degree of freedom could ease the electron hopping process. We demonstrated here that this phenomenon, associated with an apparent diffusion coefficient of 4.4 10^{-8} cm^2·s^{-1}, is likely the one responsible for the electronic condutivity at the surface of **NiO-Co$_{C11P}$** electrodes (see also Addendum to Chapter III.3.2.1 in appendix for more details).

At the opposite, because of their larger dynamic radius, the CODH enzymes adsorbed onto a NiO film[13d] do not easily percolate to attach at the conductive glass supporting electrode. Thus, the first electron transfer from the conducting support is not permitted. As well, a dense packing of enzymes within the mesoporous film, permitting electronic communication between each other, is likely not attained. For these reasons, the electron-hopping process can be ruled out at the enzyme-decorated NiO electrode, accordingly reported inactive at cathodic potentials,[13d] whereas this process is possible for **NiO-Co$_{C11P}$** electrodes.

Although the hypothesis of electron-hopping would suit the observations, we also want to suggest some pieces of thought about alternative interpretations. Indeed, the true nature of effective charge transport mechanisms in NiO is not fully understood to date and is quite discussed in the literature.[24, 30]

It was also recently proposed that NiO displays a substantial density of trap states at the top of the VB (until around –0.25 V *vs* NHE).[30b, 31] Such states have been correlated with an important current conduction in the cathodic region (to *ca* –0.65 V *vs* NHE) at NiO electrodes, but in non-aqueous electrolyte with the I$_3^-$/I$^-$ redox shuttle.[30b] This point also tentatively provides an answer

to our observations of the $Co^{II/I}$ process onto NiO electrodes, though the associated wave is actually quite downward from the VB of NiO.

Alternatively, surface states have been proposed to play a role in the conduction of NiO.[24, 32] Especially, *hole hopping* (under the form of *polaron hopping*)[24] could be partially responsible for the conductivity. Such conductivity would occur through holes present as Ni^{III} species located at the material/electrolyte interface.[32] In our case, the attachment of a molecular compound by a phosphonate anchor might affect such surfaces sites. In particular, Ni^{III} are possibly preferential electrophilic sites for the condensation of phosphonic acids. Thus, grafting **Co$_{C11P}$** at the surface of NiO could impede a partial filling of the surface hole-conducting states. This filling would result in a positive shift (in energy) of the Fermi level, rendering the SC material more conductive at higher energies *i.e.* at cathodic potentials.

Such interpretations are given here more about raising additional tracks for understanding than a strict correlation of data. It stays however true that the conductivity of NiO is not well understood. Namely, electrochemical investigations of surface anchored species on NiO are clearly lacking. This point is even sharper given that electrochemical studies at the surface of NiO are usually conducted in organic media or at anodic potentials.

At contrast, our investigations have been conducted both in the cathodic window and in aqueous media. These conditions add the pH of the solution as an important parameter. First, as it was concluded from the electrocatalytic experiments conducted at **NiO-Co$_{C11P}$**, varying the pH can affect the binding of molecules at the surface. Such feature is quite noticeable since the anchoring groups commonly used to attach molecules onto NiO are usually acido-basic moieties (as carboxylic or phosphonic acids). Besides, the pH, which can be seen as a specific ionic strength in aqueous electrolytes, participates in the *band bending* phenomenon at the NiO/electrolyte interface. Whereas this phenomenon is usually negligible with other nanoparticulate TCOs, such as TiO_2, the bending of the valence band has been observed to impact the charge transfer at NiO electrodes in contact with either aqueous or organic electrolytes.[24, 33]

Overall, this piece of work presents the first insights regarding the electrochemical signature in the negative potentials window of a HER catalyst immobilized onto *p*-type NiO. Further studies giving an improved understanding of the conduction of NiO in the cathodic region, in particular in the case of aqueous electrolytes, would be much valuable for shedding more light on the results obtained here.

Conclusion

The investigations we have performed at the surface of different TCOs lead us to harness the immobilization of the **Co$_{C11P}$** phosphonate derivative of **[Co^{III}(DO)(DOH)pnBr$_2$]** onto NiO electrodes. The **Co$_{C11P}$** was shown to attach in a covalent way at the NiO surface, likely through several binding modes. The attachment of the molecular complex was evidenced by electrochemical investigations, conducted in *quasi*-neutral aqueous media. The **NiO-Co$_{C11P}$** electrode displays a redox wave at –0.37 V *vs* NHE assigned to the Co$^{II/I}$ couple. The reasons for the observation of such a cathodic event onto *p*-type NiO are not fully understood. Yet, we could clearly demonstrate by spectroelectrochemical means that the species observed downward from this wave is actually the complex at the Co^{I} state. In acidic media, HER catalysis is expected to occur at potentials slightly anodically shifted from this Co$^{II/I}$ wave. Thus, reaching the Co^{I} state at the surface of the **NiO-Co$_{C11P}$** electrode is encouraging for possible use of this electrode in the catalysis of proton reduction. However, the hybrid electrode was demonstrated to suffer from instability under the reductive conditions used for electrocatalyzing hydrogen evolution in mildly acidic aqueous media.

As a consequence, we will now seek to co-graft a PS onto NiO electrodes decorated with **Co$_{C11P}$** so as to construct DS photocathodes that could turn over for hydrogen evolution at innocent potentials.

Experimental part

Reagents and materials

Solvents, starting materials and supporting electrolyte salts were purchased from Sigma-Aldrich and used without further purification, unless otherwise stated. **(DOH)$_2$pnN$_3$** and **C$_8$COOH** were commercially synthetized by Oribase Pharma according to procedures from the literature.[1a] **P$_{Et}$C$_9$CC** and **P$_{Et}$C$_{12}$NH$_2$** were purchased from Sikemia. **[Co(DO)(DOH)pnN$_3$]Cl$_2$** was obtained following reported procedures.[1a] Dry dichloromethane and dry acetonitrile were obtained by distillation on CaH$_2$ and kept under Ar. Fresh MeCN was directly loaded onto activated 3 Å molecular sieve to get *quasi*-dry MeCN, kept under Ar. Unless otherwise noted, all reactions in solution were performed at room temperature under atmospheric conditions

Synthesis

Characterization

NMR spectra were recorded at 298 K in 5 mm o.d. tubes on a Bruker 300 spectrometer equipped with a QNP probehead operating at 300.0 MHz for ^{1}H, 75.5 MHz for ^{13}C and 121.5 MHz for [31]P. Chemical shifts reported in ppm are given relative to TMS. ^{1}H and ^{13}C NMR spectra were referenced internally to the residual solvent resonance. ^{31}P NMR spectra were calibrated against an internal H$_3$PO$_4$ 85% tip or an external 85% H$_3$PO$_4$ reference.

Mass spectra were acquired on a Thermo Scientific LXQ mass spectrometer equipped with an electrospray source, at the *Service de Chimie Inorganique et Bioinorganique* of the *CEA-Grenoble/CNRS* (Grenoble, FRANCE).

High resolution mass spectra were recorded at the *Institut de Chimie Organique et Analytique* of the *Université d'Orléans/CNRS* (Orléans, FRANCE).

Elemental analyses were performed at the *Plateforme d'Analyses pour la Chimie* of the *Université de Strasbourg/CNRS* (Strasbourg, FRANCE).

Procedures

Carboxylic acid derivative: Co$_{COOH}$

Complex **[Co(DO)(DOH)pnN$_3$]Cl$_2$** (163 mg, 0.40 mmol, 1 equiv.) and **C$_8$COOH** (72 mg, 0.40 mmol, 1 equiv.) were dissolved in 9 mL MeCN. The mixture was stirred for 60 h, yielding a pale green precipitate. The reaction mixture was evaporated to dryness, dissolved in CHCl$_3$ and

filtered. The filtered solid was kept apart. The filtrate was evaporated, then dissolved in acetone and evaporated. The solid was taken again in a minimal portion of CHCl₃ and filtered. The filtered solid was joined with the first fraction to give 55 mg (0.093 mmol, 24 %) of the expected complex **Co$_{COOH}$**.

Co$_{COOH}$
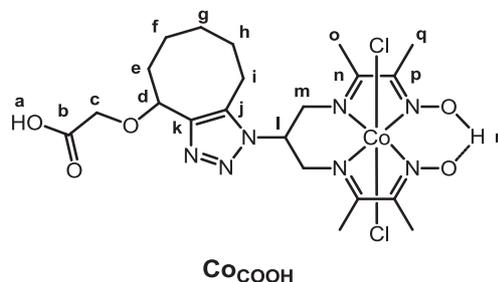
^{1}H NMR (DMSO-d$_6$, 300 MHz): δ (ppm) 19.26 (s, 1H, H$_r$), 12.59 (broad s, 1H, H$_a$), 5.34 (m, 1H, H$_l$), 4.97 (m, 1H, H$_d$), 4.59–4.39 (m, 4H, H$_{m,m'}$), 4.01 (m, 2H, H$_{c,c'}$), 3.02–2.86 (m, 1H, H$_i$), 2.76–2.59 (m, 7H, H$_{o,o'}$ + H$_{i'}$), 2.53 (s, 6H, H$_q$), 2.13–1.99 (m, 1H, H$_e$), 1.94–1.75 (m, 2H, H$_{e'}$ + H$_h$), 1.72–1.43 (m, 4H, H$_{h'}$ + H$_{f,f'}$ + H$_g$) 1.30-1.09 (m, 1H, H$_{g'}$).

^{13}C NMR (DMSO-d$_6$, 75 MHz): δ (ppm) 176.6 (C$_{n,n'/p,p'}$), 171.4 (C$_b$), 155.6 (C$_{n,n'/p,p'}$), 155.5 (C$_{n,n'/p,p'}$), 142.4 (C$_j$), 134.4 (C$_k$), 73.3 (C$_d$), 64.9 (C$_c$), 54.5(C$_{m,m'}$), 54.3 (C$_{m,m'}$), 53.5 (C$_l$), 34.2 (C$_e$), 25.3 (C$_g$), 25.0 (C$_h$), 20.4 (C$_f$), 19.9 (C$_i$), 17.5 (C$_{o,o'}$), 17.5 (C$_{o,o'}$), 13.0 (C$_{q,q'}$), 13.0 (C$_{q,q'}$).

MS (ESI+): m/z calcd for C$_{21}$H$_{32}$ClCoN$_7$O$_5$ 556.1; found 556.1 [M–Cl⁻]⁺.

MS (ESI–): m/z calcd for C$_{21}$H$_{31}$Cl$_2$CoN$_7$O$_5$ 590.1; found 589.8 [M–H⁺]⁻.

HR-MS (ESI+): m/z calcd for C$_{21}$H$_{32}$ClCoN$_7$O$_5$ 556.1480; found 556.1481 [M–Cl⁻]⁺.

E.A.: calcd for C$_{21}$H$_{32}$ClCoN$_7$O$_5$ + 0.25 CHCl₃: C, 41.02; H, 5.22; N, 15.76; found: C, 40.92; H, 5.31; N, 15.88.

Phosphonic acid derivative: **Co$_{C12C8P}$**

P$_{Et}$C$_{12}$C$_8$

300 mg of **C$_8$COOH** (1.65 mmol, 1 equiv.) and 288 µL **DIPEA** (1.65 mmol, 1 equiv.) were dissolved in 4 mL of Ar-degassed DMSO. The mixture was stirred for 5 min **HATU** (687 mg, 1.82 mmol, 1.1 equiv) was added to the mixture, which was further stirred for one hour. The solution turned from yellow to redish orange. In a separate flask **P$_{Et}$C$_{12}$NH$_2$** (529 mg, 1.65 mmol, 1 equiv.) and **DIPEA** were introduced in 4 mL of Ar-purged DMSO. The mixture was stirred for 15 min and added to the previous reaction medium. This mixture was stirred for 4 hours under a

small Ar overpressure. Then, the reaction mixture was diluted into 20 mL of distilled water. This phase was extracted 3 times with 20 mL DCM. The resembled organic phases were washed by three 20 mL portions of 0.1 M HCl aqueous solution, dried with NaCl-saturated aqueous solution, then over $MgSO_4$, filtered and condensed as an yellowish oil further dried under vacuum. To remove undesired traces of DMSO, the oil was diluted in 10 mL of distilled water. This phase was extracted twice with 10 mL diethylether. The organic phase was washed with distilled water, dried with NaCl sat., over $MgSO_4$, filtered and evaporated and dried under high vacuum to yield $P_{Et}C_{12}C_8$ as a *quasi*-transparent oil (447 mg, 56 % yield).
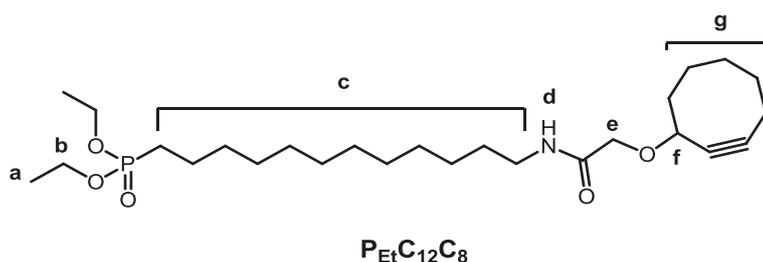
$P_{Et}C_{12}C_8$

^{1}H NMR (CD$_2$Cl$_2$, 300 MHz): δ (ppm) 6.48 (m, 1H, H$_d$), 4.27-4.19 (m, 1H, H$_f$), 4.10-3.95 (m, 4H, H$_b$), 3.98-3.78 (m, 2H, H$_e$), 3.27-3.18 (m, 2H, H$_c$), 2.27-2.07 (m, 3H, H$_g$), 2.03-1.43 (m, 13H, H$_c$+H$_g$), 1.40-1.25 (m, 22H, H$_a$ + H$_c$).
Residual DMSO at 2.75 ppm (*ca* 0.15 equiv.)

$Co_{C8C12PEt}$

In an Ar-purged Schlenk, $P_{Et}C_{12}C_8$ (425 mg, 0.88 mmol, 1.1 equiv.) was dissolved in 10 mL of dist. MeCN. This solution was transferred to another Schlenk purged by three Ar/vacuum cycles and in which **[Co(DO)(DOH)pnN$_3$Cl$_2$]** (329 mg, 0.80 mmol, 1 equiv.) had been loaded. The Schlenk was sealed under Ar and the reaction media stirred for 4 days. The reaction mixture was evaporated as a green powder and dried under vacuum. This crude was purified portion-wise (*ca* 100 mg) by elution with acetone/DCM 1:1 through a size exclusion chromatography on Sephadex LH20 gel. The selected fractions gave the expected **Co$_{C8C12PEt}$** product (55 mg, 46 % partial yield).
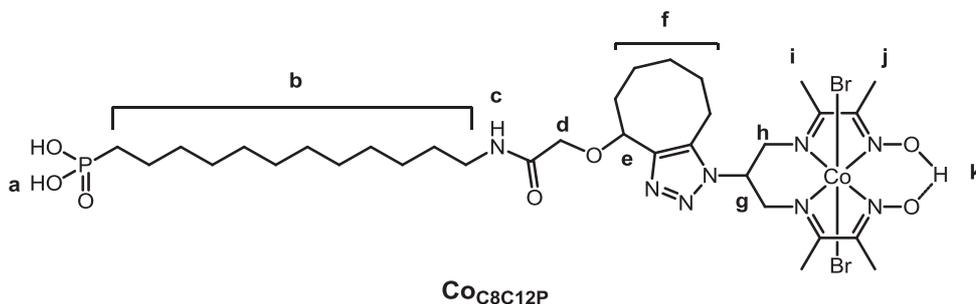

$Co_{C8C12PEt}$
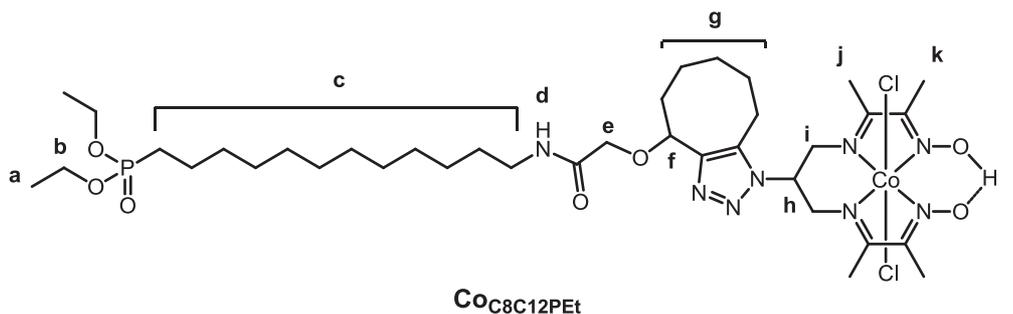
¹H NMR (CD$_2$Cl$_2$, 300 MHz): δ (ppm) 19.28 (s, 1H, H$_l$), 6.48 (m, 1H, H$_d$), 5.98-5.67 (m, 1H, H$_h$) 4.93-4.59 (m, 3H, H$_i$+H$_f$), 4.45-4.24 (m, 2H, H$_{i'}$), 4.15-3.79 (m, 6H, H$_e$ + H$_b$), 3.33-3.22 (m, 1H, H$_g$), 3.20-2.88 (m, 2H, H$_c$), 2.84-2.68 (m, 1H, H$_g$), 2.27-2.08 (m, 1H, H$_g$), 2.07-1.93 (m, 1H, H$_g$), 2.60 (s, 12H, H$_j$+H$_k$), 1.88-1.44 (m, 8H, H$_{c+g}$), 1.45-1.15 (m, 24H, H$_a$ + H$_c$).

³¹P NMR (CD$_2$Cl$_2$, 121 MHz)**:** δ (ppm) 32.73

MS (ESI+): *m/z* calcd for C$_{34}$H$_{66}$ClCoN$_8$O$_7$P 859.4; found 859.3 [M–Cl⁻]⁺.

Co$_{C8C12P}$

Co$_{C8C12PEt}$ (55 mg, 0.06 mmol, 1 equiv.) was dissolved in 5 mL Ar-purged DCM. In a separate flask, a solution of **TMSBr** (48 µL, 0.37 mmol, 6 equiv.) in 1.5 mL Ar-purged DCM was prepared. This solution was added dropwise to the previous one. The reaction media was stirred for 26 h, then the solvent was evaporated. The product was dissolved in 4 mL MeOH and the media stirred for 7h. The reaction being incomplete, the solvent was evaporated and dried under high vacuum to leave a solid. The solid was taken in DCM, the solution introduced in a Schlenk and the solvent was evaporated under vacuum. The loaded Schlenk was purged by three vacuum/Ar cycles, and the solid dissolved under Ar pressure in 4 mL dist. DCM. 48 µL **TMSBr** (0.37 mmol, 6 equiv) were then added dropwise and the mixture was reacted under Ar for 36 h. The media was evaporated under vacuum, 4 mL MeOH were introduced and the mixture was stirred for 4 h, then evaporated to yield a green solid. The solid was washed with DCM and dried under vacuum to give the expected **Co$_{C8C12P}$** in mixture with undeprotected and mono-deprotected analogues (19 mg, 40 % yield).

Co$_{C8C12P}$

¹H NMR (CD$_3$OD, 300 MHz): δ (ppm) 6.13-5.85 (m, 1H, H$_g$), 5.15-4.80 (m, 2H, H$_h$) 4.70-4.42 (m, 2H, H$_{h'}$), 4.32-4.20 (m, 1H, H$_e$), 4.15-3.83 (m, 2H, H$_d$), 3.20-2.88 (m, 2H, H$_f$), 2.74-2.63 (m, 6H, H$_i$), 2.62-2.53 (m, 6H, H$_i$), 2.45-2.14 (m, 2H, H$_f$), 2.27-2.08 (m, 1H, H$_f$), 2.03-1.49 (m, 13H, H$_f$ + H$_b$) 1.47-1.16 (m, 14H, H$_b$).

Presence of signals of **Co$_{C8C12PEt}$**.

^{31}P NMR (CD$_3$OD, 121 MHz)**:** δ (ppm) 33.59

MS (ESI+): *m/z* calcd for C$_{33}$H$_{58}$BrCoN$_8$O$_7$P 847.3; found 847.2 [M–Br$^-$]$^+$.

Presence of signals of **Co$_{C8C12PEt}$** and of the mono-deprotected version.

Phosphonic acid derivative: Co$_{C11P}$

[Cu(DO)(DOH)pnN$_3$]ClO$_4$

To a solution of ligand (**DOH)$_2$pnN$_3$** (800 mg, 2.84 mmol, 1.5 equiv.) in tepid acetone (6 mL) at 50°C was added dropwise a solution of **Cu(ClO$_4$)$_2$·6H$_2$O** (702 mg, 1.90 mmol, 1 equiv.) in 4 mL acetone. The reaction mixture was stirred 5 min at room temperature and left to precipitate in the fridge overnight. The precipitate was filtered and washed with 3 portions of 10 mL of cold acetone and dried overnight in a dessicator. The red brownish powder obtained (466 mg, 55 % yield) was used without further purification for the next step.

[Cu(DO)(DOH)N$_3$pn]ClO$_4$
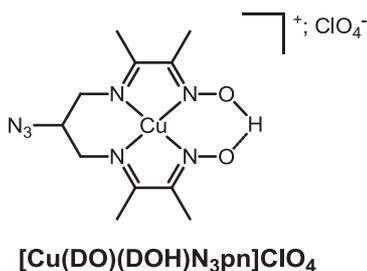
MS (ESI+): *m/z* calcd for C$_{11}$H$_{18}$CuN$_7$O$_2$ 343.1; found 343.1 [M–ClO$_4$$^-$]$^+$.

Cu$_{C11PEt}$

Complex **[Cu(DO)(DOH)pnN$_3$]ClO$_4$** (70 mg, 0.24 mmol, 1.0 equiv.) and **P$_{Et}$C$_9$CC** (108 mg, 0.24 mmol, 1.0 equiv.) were introduced in 6 mL of a methanol/water (2:1) mixture, without complete dissolution of the starting materials. The mixture was flushed with Ar and **sodium ascorbate** (43 mg, 0.22 mmol, 0.9 equiv.) and **CuSO$_4$·5H$_2$O** (18 mg, 0.07 mmol, 0.3 equiv.) were added. The mixture was stirred at room temperature for 2 days. The reaction mixture was evaporated. The crude was purified on SiO$_2$ flash chromatography eluting with a gradient of MeCN/aqueous KNO$_3$ solution at 10% of the saturating concentration (39:1 to 8:2). The purified fraction was dissolved in the minimum MeOH and precipitated with an aqueous KPF$_6$-saturated solution to yield the **Cu$_{C11PEtPF6}$** hexafluorophosphate salt of the expected product (86 mg, 48 % yield).

$Cu_{C11PEtPF6}$

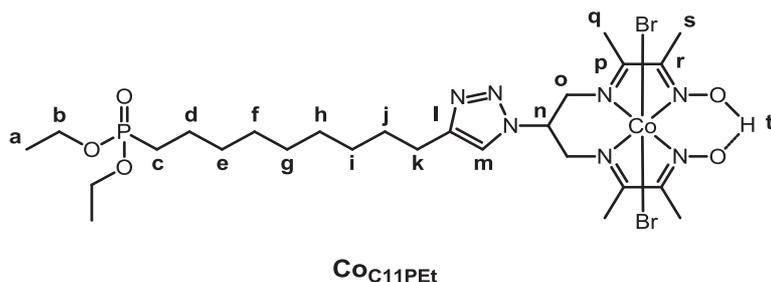**HR-MS** (ESI+): *m/z* calcd for $C_{26}H_{47}BrCuN_7O_5P$ 631.2667; found 631.2668 $[M-PF_6^-]^+$.

For further syntheses, the crude was alternatively used without purification under the form of the **Cu$_{C11PEt}$** perchlorate salt.

Cu_{C11PEt}

MS (ESI+): *m/z* calcd for $C_{26}H_{47}CuN_7O_5P$ 631.3; found 631.3 $[M-ClO_4^-]^+$.

Co$_{C11PEt}$

To a solution of **Cu$_{C11PEt}$** (218 mg, 0.29 mmol, 1 equiv.) in acetone (50 mL) were added 5 equiv. of **CoCl$_2$·6H$_2$O** (354 mg, 1.49 mmol, 5 equiv.). The mixture was stirred under vigorous air bubbling at R.T. for 2 hours, stirred an additional 16 hours and again under air bubbling for 4 hours. The solvent was evaporated and the solid kept in the fridge overnight. The crude was purified on SiO$_2$ flash chromatography and the elution gradient was MeCN/aqueous KNO$_3$ solution at 10% of the saturating concentration from 1:0 to 8:2. The selected fraction was evaporated. The solid obtained was dissolved in a minimal amount of MeOH and an aqueous NaBr saturated solution was added until a green compound precipitated. The solvent was evaporated to remove MeOH, the precipitate was filtered and washed by several fractions of water. The green solid was dissolved in MeOH, the solution evaporated and the solid dried under vacuum to yield the expected **Co$_{C11PEt}$** compound (42 mg, 18% yield).

Co_C11PEt

¹H NMR (CD₃CN, 300 MHz): δ (ppm) 19.28 (s, 1H, H_t), 7.85 (broad s, 1H, H_m), 5.76-5.50 (m, 1H, H_n), 4.67-4.31 (m, 4H, $H_{o,o'}$), 4.10-3.84 (m, 4H, H_b), 2.79-2.62 (m, 2H, H_k), 2.59 (s, 6H, H_q), 2.54 (s, 6H, H_s) 1.78-1.61 (m, 4H, $H_c + H_j$), 1.60-1.44 (m, 2H, H_d), 1.45-1.29 (m, 10H, H_{f-i}), 1.26 (t, 6H, J = 7.1 Hz, H_a).

¹³C NMR (CD₃CN, 75 MHz): δ (ppm) 177.9 ($C_{p/r}$), 157.9 ($C_{p/r}$), 148.8 (C_l), 122.4 (C_m), 62.1 (C_b), 62.0 ($C_{b'}$), 58.6 (C_n), 31.2 (C_{c-j}), 31.0 (C_{c-j}), 30.2 (C_{c-j}), 30.0 (C_{c-j}), 29.8 (C_{c-j}), 29.8 (C_{c-j}), 26.8 (C_{c-j}), 26.2 (C_k), 25.0 (C_{c-j}), 23.3 (C_{c-j}), 23.2 (C_{c-j}), 18.6 (C_q), 16.9 (C_a), 16.8 ($C_{a'}$), 14.1 (C_s).

³¹P NMR (CD₃CN, 121 MHz)**:** δ (ppm) 33.30

MS (ESI+): *m/z* calcd for $C_{26}H_{47}BrCoN_7O_5P$ 706.2; found 706.1 [M–Br⁻]⁺.
HR-MS (ESI+): *m/z* calcd for $C_{26}H_{47}BrCoN_7O_5P$ 706.1886; found 706.1887 [M–Br⁻]⁺.

Co_C11P

Co_C11PEt (42 mg, 0.05 mmol, 1 equiv.) was dissolved in 5 mL of dist. DCM under inert atmosphere. A solution of **TMSBr** (46 µL, 0.35 mmol, 6.5 equiv.) in 2 mL dist. DCM was added dropwise. The mixture was stirred under Ar for 42 hours at R.T. The solvent was removed under vacuum. 4 mL MeOH were added and the reaction was stirred for 3 hours at R.T. The solvent was removed under vacuum to give the expected **Co_C11P** as a green solid (37 mg, 94 % yield).

Co_C11P

^{1}H NMR (CD$_3$OD, 300 MHz): δ (ppm) 8.54 (broad s, 1H, H$_l$), 5.94 (m, 1H, H$_m$), 4.78 (s, 2H, H$_n$), 4.76 (s, 2H, H$_{n'}$), 2.86 (m, 2H, H$_j$), 2.71 (s, 6H, H$_p$), 2.58 (s, 6H, H$_r$), 1.83-1.52 (m, 6H, H$_i$, H$_{h-b}$), 1.50-1.31 (m, 10H, H$_{h-b}$).

H$_s$ observed in DSMO-d$_6$ at δ = 19.27 ppm.

^{13}C NMR (CD$_3$OD, 75 MHz): δ (ppm) 179.1 (C$_{o/q}$), 158.3 (C$_{o/q}$), 126.6 (C$_l$), 61.5 (C$_m$), 54.6 (C$_{n,n'}$), 31.7 (C$_{b-h}$), 31.5 (C$_{b-h}$), 30.3 (C$_{b-h}$), 30.2 (C$_{b-h}$), 30.2 (C$_{b-h}$), 30.1 (C$_{b-h}$), 29.7(C$_i$), 25.0 (C$_j$), 23.8 (C$_{b-h}$), 23.8 (C$_{b-h}$), 18.3 (C$_p$), 13.8 (C$_r$).

^{31}P NMR (CD$_3$OD, 121 MHz): δ (ppm) 31.69

MS (ESI+): *m/z* calcd for C$_{22}$H$_{39}$BrCoN$_7$O$_5$P 650.1; found 650.3 [M–Br$^-$]$^+$.

MS (ESI–): *m/z* calcd for C$_{22}$H$_{38}$Br$_2$CoN$_7$O$_5$P 730.0; found 729.8 [M–H$^+$]$^-$.

HR-MS (ESI+): *m/z* calcd for C$_{22}$H$_{39}$BrCoN$_7$O$_5$P 650.1266; found 650.1260 [M–Br$^-$]$^+$.

E.A.: calcd for C$_{22}$H$_{39}$Br$_2$CoN$_7$O$_5$P + 1.35 H$_2$O + 1.05 NaBr: C, 30.60; H, 4.87; N, 11.35; found: C, 30.74; H, 4.81; N, 11.20.

TCO sensitization

Materials

TiO$_2$ substrates were purchased from *Solaronix*, where they were prepared by screen-printing of a paste of preformed TiO$_2$ nanoparticles onto FTO conducting glass. Singly and doubly screen-printed electrodes were used.

NiO substrates were purchased from *Dyenamo*, where they were prepared by screen-printing of a paste of preformed NiO nanoparticles onto FTO conducting glass. Doubly screen-printed electrodes were used.

A *Harry Gestigkeit* flat furnace operated with a *Detflef Gestigkeit-Programmer PR5* control board was used to sinter the electrodes.

Procedures

Sequential functionalization

The FTO electrodes were washed with water and acetone, then dried. They were dipped in an aqueous solution 1 mM in **PCH$_2$NH$_2$** contained in PTFE boxes, which were closed to sensitize the

electrodes for 24 h at R.T. on orbital stirring. The electrodes were rinsed with water and acetone then dried at Ar. Some plates were kept apart for characterization after this first step. Then, under a flow or Ar, the plates were introduced in PTFE boxes containing 10 mL of dist. DCM in which is dissolved 10 μL of 2,6-lutidine. After 10 min, under a flow of Ar were dissolved 7.4 mg of **[Co^{III}(DO)(DOH)pnC$_8$PhtCl$_2$]** (10 μmol) to give a 1 mM solution. The boxes were sealed and the electrodes bathed for 24 h at R.T. on orbital stirring. The electrodes were rinsed with DCM, MeCN, water, acetone and dried under Ar.

Full entity functionalization

In a typical experiment, the FTO/TCO substrates were first cut at the desired dimensions and then sintered under atmospheric conditions with the following temperature program: R.T. to 450°C (30 min), 30 min at 450°C. The substrates were cooled to *ca* 90°C and introduced in PTFE boxes containing 10 mL of a methanolic solution 0.5 mM in the considered derivative (5 μmol). Between 3 and 6 electrodes were introduced in the same box. The boxes were closed and the electrodes sensitized for 24 h on orbital stirring. The electrodes were removed from the solution, washed by dipping them in pristine methanol for 10 min on orbital stirring and dried with N$_2$, to yield the decorated TCO electrodes.

Characterization of the TCO electrodes

SEM measurements

Scanning electron microscopy (SEM) images showing the morphologies at the edge of the TCO electrodes were recorded with a field emission gun-scanning electron microscope (FEG-SEM) *Zeis-Leo 1530* (gun *Brüker 127 eV*) operating at 5 kV.

The measurements were performed at the *Laboratoire d'Innovation pour les Technologies des Energies Nouvelles et les Nanomatériaux* at *CEA-Grenoble* (Grenoble, FRANCE).

XPS analysis

The analyses were performed with a *VersaProbe II* spectrometer from *Physical Electronics* using a high-resolution monochromatic Al-K$_\alpha$ line X-ray source at 1486.7 eV. A fixed analyzer pass energy of 23 eV was used for core level scans leading to an overall energy resolution of 0.6 eV. Survey spectra were captured at pass energy of 117 eV. The photoelectron take-off angle was 45°, which provided an integrated sampling depth of approximately 5 nm. All spectra were

referenced against an internal signature, typically by adjusting the C *1s* level peak at a binding energy of 284.8 eV.

The measurements were performed at the *Laboratoire d'Electronique et de Technologies de l'Information* at *CEA-Grenoble* (Grenoble, FRANCE).

ToF-SIMS analysis

Time of flight secondary ions mass spectroscopy (ToF-SIMS) were recorded on a *Physical Electronics TRIFT III* ToF-SIMS instrument operated with a pulsed 22 keV Au^+ ion gun (ion current of 2 nA) rastered over a 300 μm × 300 μm area.

The measurements were performed at the *Institut des Sciences Analytiques* (Villeurbanne, FRANCE).

Electrochemistry

Electrochemical data were acquired with a *Biologic VSP 300* or a *Princeton Applied Research Ametek PARSTAT 4000* potentiostat. Electrochemical measurements were conducted in a 3-electrode cell made of two compartments separated by a porous glass frit. The working and reference electrodes were placed in the same compartment and the counter electrode in the other one. The working electrodes were the decorated or pristine TCO electrodes. The electroactive area was determined by applying a galvanoplastic tape at the top of the mesoporous TCO part. The electrical contact was taken at the FTO part of the electrodes. The reference electrode was made of a Ag/AgCl wire dipped into a KCl 3 M solution, separated from the supporting electrolyte by a Vycor® frit, and denoted below as Ag/AgCl. The counter electrode was a titanium wire.

NaCl 0.1 M aqueous solutions (approx. pH 6.4) or 0.1 M *n*Bu$_4$NBF$_4$ dist. MeCN solutions were used as supporting electrolytes for the electrochemical characterization of the plates. The supporting electrolytes were degassed with a flow of N$_2$ saturated with the corresponding solvent at least for 5 min before the measurements. The N$_2$ flow was removed from the solution but left in the headspace of the cell for the duration of the experiment. Cyclic voltammograms were typically conducted at a scan rate of 10 mV·s^{-1}.

The potential of the reference electrode was calibrated before or after each experiment in an external electrochemical setup, using a glassy carbon electrode (S = 0.196 cm^2) and a platinum wire as working and auxiliary electrodes, respectively. In the case of measurements performed in aqueous electrolytes, the calibration was realized with [K$_4$Fe(CN)$_6$] in a 0.1 M potassium phosphate buffer at pH 7, by determination of the potential of the [Fe(CN)$_6$]$^{3-}$/[Fe(CN)$_6$]$^{4-}$ couple, denoted below as $E_{Fe(III)/Fe(II)}$. The conversion of potentials against the Normal Hydrogen

Electrode (NHE) and the Reversible Hydrogen Electrode (RHE) are thus obtained using the following equations, respectively:

$$E_{vs\ NHE} = E_{vs\ Ag/AgCl} - E_{Fe(III)/Fe(II)} - E_{Fe(III)/Fe(II)\ vs\ NHE} \qquad \textbf{Eqn. III.1}$$

$$E_{vs\ RHE} = E_{vs\ NHE} + 0.059 \cdot pH \qquad \textbf{Eqn. III.2}$$

where $E_{Fe(III)/Fe(II)\ vs\ NHE}$ refers to the tabulated value of $E_{Fe(III)/Fe(II)}$ against the Normal Hydrogen Electrode (under these conditions, $E_{Fe(III)/Fe(II)\ vs\ NHE} = -0.425$ V).[34]

In the case of measurements performed in organic electrolytes, the calibration was made with ferrocene (Fc) in a 0.1 M nBu$_4$NBF$_4$ MeCN solution, by determination of the potential of the Fc$^{+/0}$ couple, denoted below as $E_{Fc(I)/Fc(0)}$. Conversion of potentials against the Fc$^{+/0}$ couple are thus realized using the following equation:

$$E_{vs\ Fc(I)/Fc(0)} = E_{vs\ Ag/AgCl} - E_{Fc(I)/Fc(0)} \qquad \textbf{Eqn. III.3}$$

Spectroelectrochemistry

The measurements were performed in a 1 cm x 1 cm x 4 cm quartz cell as electrochemical cell, placed in the beam of an *Agilent Technologies Cary 60 UV-Vis* spectrometer. The working electrode was a pristine or a decorated NiO electrode and was set perpendicular to the analytic beam. A Pt wire and a Ag/AgCl electrodes served as counter and reference electrodes, respectively. The NaCl 0.1 M aqueous solution was degassed with Ar prior to the measurements and a constant flow of Ar was let in the headspace of the cell during the acquisition. Chronoamperometric measurements at different applied potentials were performed. UV-visible spectra were acquired after 30 s of equilibration at the considered potential.

Electrocatalytic behavior

The electrocatalytic tests were performed in the two-compartment cell described above, with a similar configuration of the electrodes.

The supporting electrolytes were degassed with a constant flux of N$_2$ monitored by a *Bronkhorst EL Flow Select* mass flowmeter at least for 5 min before the measurements. The N$_2$ flow was stopped and the cell closed just before the electrocatalytic measurements were started. The electrolyte in the cathodic part was vigorously stirred during the chronoamperometric experiments. The volumes of electrolyte in the cathodic and anodic parts were typically *ca* 16 mL and 4 mL, respectively.

The supporting electrolytes used were a NaCl 0.1 M aqueous solution at approx. pH 6.4, a TEOA 0.1 M aqueous buffer adjusted at pH 7 by adding a HCl 2 M aqueous solution and a CH_3COOH/CH_3COO^- 0.1 M aqueous buffer at pH 4.5.

Detection of dissolved hydrogen was performed through a *Unisense H2-N* in-needle Clark micro-sensor dipped in the electrolyte of the cathodic compartement. The sensor was driven by a 2-channel *Unisense micrometer monometer* unit and poised at a voltage of 1000 mV. The probe was calibrated prior to the electrocatalytic measurements by exposing it to saturating, half-saturating and nil concentrations of H_2 in the buffer in which measurements were run.

References

1. (a) Andreiadis, E. S.; Jacques, P. A.; Tran, P. D.; Leyris, A.; Chavarot-Kerlidou, M.; Jousselme, B.; Matheron, M.; Pecaut, J.; Palacin, S.; Fontecave, M.; Artero, V. *Nat. Chem.* **2013,** *5* (1), 48-53; (b) Kaeffer, N.; Morozan, A.; Artero, V. *J. Phys. Chem. B* **2015,** *119* (43), 13707-13713.

2. (a) Queyriaux, N.; Kaeffer, N.; Morozan, A.; Chavarot-Kerlidou, M.; Artero, V. *J. Photochem. Photobiol., C* **2015,** *25*, 90-105; (b) Yu, Z.; Li, F.; Sun, L. *Energy Environ. Sci.* **2015,** *8* (3), 760-775; (c) Swierk, J. R.; Mallouk, T. E. *Chem. Soc. Rev.* **2013,** *42* (6), 2357-87.

3. (a) Le Goff, A.; Artero, V.; Jousselme, B.; Tran, P. D.; Guillet, N.; Metaye, R.; Fihri, A.; Palacin, S.; Fontecave, M. *Science* **2009,** *326* (5958), 1384-7; (b) Seo, J.; Pekarek, R. T.; Rose, M. J. *Chem. Commun.* **2015,** *51* (68), 13264-7; (c) Rodriguez-Macia, P.; Dutta, A.; Lubitz, W.; Shaw, W. J.; Rudiger, O. *Angew. Chem. Int. Ed.* **2015**; (d) Das, A. K.; Engelhard, M. H.; Bullock, R. M.; Roberts, J. A. *Inorg. Chem.* **2014,** *53* (13), 6875-85.

4. Liu, H.; Avrutin, V.; Izyumskaya, N.; Özgür, Ü.; Morkoç, H. *Superlattices Microstruct.* **2010,** *48* (5), 458-484.

5. Bard, A. J.; Faulkner, L. R., *Electrochemical methods: fundamentals and applications.* Second ed.; Wiley: 2001.

6. Agard, N. J.; Baskin, J. M.; Prescher, J. A.; Lo, A.; Bertozzi, C. R. *ACS Chem. Biol.* **2006,** *1* (10), 644-648.

7. (a) Sletten, E. M.; Bertozzi, C. R. *Acc. Chem. Res.* **2011,** *44* (9), 666-676; (b) Jewett, J. C.; Bertozzi, C. R. *Chem. Soc. Rev.* **2010,** *39* (4), 1272.

8. Agard, N. J.; Prescher, J. A.; Bertozzi, C. R. *J. Am. Chem. Soc.* **2004,** *126* (46), 15046-15047.

9. (a) Spiteri, C.; Moses, J. E. *Angew. Chem. Int. Ed.* **2010,** *49* (1), 31-33; (b) Rostovtsev, V. V.; Green, L. G.; Fokin, V. V.; Sharpless, K. B. *Angew. Chem. Int. Ed.* **2002,** *41* (14), 2596-2599; (c) Tornøe, C. W.; Christensen, C.; Meldal, M. *J. Org. Chem.* **2002,** *67* (9), 3057-3064.

10. Jacques, P. A.; Artero, V.; Pecaut, J.; Fontecave, M. *Proc. Natl. Acad. Sci. USA* **2009,** *106* (49), 20627-32.

11. (a) Ardo, S.; Meyer, G. J. *Chem. Soc. Rev.* **2009,** *38* (1), 115-164; (b) Bisquert, J.; Fabregat-Santiago, F.; Mora-Seró, I.; Garcia-Belmonte, G.; Barea, E. M.; Palomares, E. *Inorg. Chim. Acta* **2008,** *361* (3), 684-698; (c) Berger, T.; Monllor-Satoca, D.; Jankulovska, M.; Lana-Villarreal, T.; Gomez, R. *ChemPhysChem* **2012,** *13* (12), 2824-75.

12. (a) Fabregat-Santiago, F.; Mora-Seró, I.; Garcia-Belmonte, G.; Bisquert, J. *J. Phys. Chem. B* **2003,** *107* (3), 758-768; (b) Rothenberger, G.; Fitzmaurice, D.; Graetzel, M. *J. Phys. Chem.* **1992,** *96* (14), 5983-5986; (c) Knauf, R. R.; Brennaman, M. K.; Alibabaei, L.; Norris, M. R.; Dempsey, J. L. *J. Phys. Chem. C* **2013,** *117* (48), 25259-25268.

13. (a) Renault, C.; Nicole, L.; Sanchez, C.; Costentin, C.; Balland, V.; Limoges, B. *PCCP* **2015,** *17* (16), 10592-10607; (b) Renault, C.; Balland, V.; Martinez-Ferrero, E.; Nicole, L.; Sanchez, C.; Limoges, B. *Chem. Commun.* **2009,** (48), 7494-7496; (c) Renault, C.; Balland, V.; Limoges, B.; Costentin, C. *J. Phys. Chem. C* **2015,** *119* (27), 14929-14937; (d) Bachmeier, A.; Hall, S.; Ragsdale, S. W.; Armstrong, F. A. *J. Am. Chem. Soc.* **2014,** *136* (39), 13518-21; (e) Bachmeier, A.; Wang, V. C.; Woolerton, T. W.; Bell, S.; Fontecilla-Camps, J. C.; Can, M.; Ragsdale, S. W.; Chaudhary, Y. S.; Armstrong, F. A. *J. Am. Chem. Soc.* **2013,** *135* (40), 15026-32; (f) Wang, Q.; Zakeeruddin, S. M.; Cremer, J.; Bäuerle, P.; Humphry-Baker, R.; Grätzel, M. *J. Am. Chem. Soc.* **2005,** *127* (15), 5706-5713.

14. Kaeffer, N.; Chavarot-Kerlidou, M.; Artero, V. *Acc. Chem. Res.* **2015,** *48* (5), 1286-95.

15. Westermark, K.; Henningsson, A.; Rensmo, H.; Södergren, S.; Siegbahn, H.; Hagfeldt, A. *Chem. Phys.* **2002,** *285* (1), 157-165.

16. Berger, T.; Lana-Villarreal, T.; Monllor-Satoca, D.; Gómez, R. *J. Phys. Chem. C* **2007,** *111* (27), 9936-9942.

17. (a) Pujari, S. P.; Scheres, L.; Marcelis, A. T.; Zuilhof, H. *Angew. Chem. Int. Ed.* **2014,** *53* (25), 6322-56; (b) Brennan, B. J.; Llansola Portoles, M. J.; Liddell, P. A.; Moore, T. A.; Moore, A. L.; Gust, D. *PCCP* **2013,** *15* (39), 16605-14; (c) Martini, L. A.; Moore, G. F.; Milot, R. L.; Cai, L. Z.; Sheehan, S. W.; Schmuttenmaer, C. A.; Brudvig, G. W.; Crabtree, R. H. *J. Phys. Chem. C* **2013,** *117* (28), 14526-14533.

18. Muresan, N. M.; Willkomm, J.; Mersch, D.; Vaynzof, Y.; Reisner, E. *Angew. Chem. Int. Ed.* **2012,** *51* (51), 12749-53.

19. Pellegrin, Y.; Le Pleux, L.; Blart, E.; Renaud, A.; Chavillon, B.; Szuwarski, N.; Boujtita, M.; Cario, L.; Jobic, S.; Jacquemin, D.; Odobel, F. *J. Photochem. Photobiol., A* **2011,** *219* (2-3), 235-242.

20. Li, F.; Fan, K.; Xu, B.; Gabrielsson, E.; Daniel, Q.; Li, L.; Sun, L. *J. Am. Chem. Soc.* **2015,** *137* (28), 9153-9.

21. (a) Dini, D.; Halpin, Y.; Vos, J. G.; Gibson, E. A. *Coord. Chem. Rev.* **2015,** *304-305*, 179-201; (b) Odobel, F.; Pellegrin, Y. *J. Phys. Chem. Lett.* **2013,** *4* (15), 2551-2564.

22. Kim, K. S.; Winograd, N. *Surf. Sci.* **1974,** *43* (2), 625-643.

23. Adden, N.; Gamble, L. J.; Castner, D. G.; Hoffmann, A.; Gross, G.; Menzel, H. *Langmuir* **2006,** *22* (19), 8197-8204.

24. Natu, G.; Hasin, P.; Huang, Z.; Ji, Z.; He, M.; Wu, Y. *ACS Appl. Mater. Interf.* **2012,** *4* (11), 5922-9.

25.   Zhang, P.; Jacques, P. A.; Chavarot-Kerlidou, M.; Wang, M.; Sun, L.; Fontecave, M.; Artero, V. *Inorg. Chem.* **2012,** *51* (4), 2115-20.

26.   (a) Bates, M. K.; Jia, Q.; Ramaswamy, N.; Allen, R. J.; Mukerjee, S. *J. Phys. Chem. C* **2015,** *119* (10), 5467-5477; (b) Xu, Y. F.; Gao, M. R.; Zheng, Y. R.; Jiang, J.; Yu, S. H. *Angew. Chem. Int. Ed.* **2013,** *52* (33), 8546-50.

27.   Saveant, J. M., *Elements of Molecular and Biomolecular Electrochemistry - An Electrochemical Approach to Electron Transfer Chemistry*. John Wiley & Sons, Inc.: 2006.

28.   Bonhôte, P.; Gogniat, E.; Tingry, S.; Barbé, C.; Vlachopoulos, N.; Lenzmann, F.; Comte, P.; Grätzel, M. *J. Phys. Chem. B* **1998,** *102* (9), 1498-1507.

29.   (a) Hod, I.; Sampson, M. D.; Deria, P.; Kubiak, C. P.; Farha, O. K.; Hupp, J. T. *ACS Cat.* **2015,** *5* (11), 6302-6309; (b) Kornienko, N.; Zhao, Y.; Kley, C. S.; Zhu, C.; Kim, D.; Lin, S.; Chang, C. J.; Yaghi, O. M.; Yang, P. *J. Am. Chem. Soc.* **2015,** *137* (44), 14129-35.

30.   (a) Natu, G.; Huang, Z.; Ji, Z.; Wu, Y. *Langmuir* **2012,** *28* (1), 950-6; (b) D'Amario, L.; Boschloo, G.; Hagfeldt, A.; Hammarström, L. *J. Phys. Chem. C* **2014,** *118* (34), 19556-19564.

31.   D'Amario, L.; Antila, L. J.; Pettersson Rimgard, B.; Boschloo, G.; Hammarstrom, L. *J. Phys. Chem. Lett.* **2015,** *6* (5), 779-83.

32.   Liu, Q.; Wei, L.; Yuan, S.; Ren, X.; Zhao, Y.; Wang, Z.; Zhang, M.; Shi, L.; Li, D.; Li, A. *RSC Adv.* **2015,** *5* (88), 71778-71784.

33.   Castillo, C. E.; Gennari, M.; Stoll, T.; Fortage, J.; Deronzier, A.; Collomb, M. N.; Sandroni, M.; Légalité, F.; Blart, E.; Pellegrin, Y.; Delacote, C.; Boujtita, M.; Odobel, F.; Rannou, P.; Sadki, S. *J. Phys. Chem. C* **2015,** *119* (11), 5806-5818.

34.   O'Reilly, J. E. *Biochim. Biophys. Acta* **1973,** *292*, 509-515.

Chapter IV

Construction of molecular photocathodes for hydrogen evolution

The final aim of this work is the construction of light-driven photocathodes for hydrogen evolution. In the previous chapter, we showed that the **[Co^{III}(DO)(DOH)pnL$_2$]** derivative **Co$_{C11P}$** can be attached onto NiO, a *p*-type TCO. We now seek to introduce light-harvesting moieties along with the catalyst.

We first briefly rationalize our choice of NiO substrate. This part is supported by some results of a benchmarking study of different NiO preparations, conducted in collaboration with other groups. Especially, we focused our interest on light-harvesting and photoelectrocatalytic properties of the material.

Then, the construction DS photocathodes for hydrogen evolution by the co-grafting strategy is developed. The materials used and the energetic considerations are presented. The construction of the photocathodes is described in a second time, with following structural characterizations. Photoelectrocatalytic experiments, joined with hydrogen detection, is finally shown.

Last, but not least, the building of a covalent dye-catalyst assembly for attachment onto surface is depicted. The first synthetic issues are shortly summarized, followed by a successful synthetic route. To end, some molecular characterizations are presented for the dye-catalyst dyad prepared.

1. Preamble: from DSSCs to DS PECs

Half part of the job of a HER photocathode is light harvesting and charge separation. Thus, a prior step was to identify good candidates in this regard. The NiO substrate plays a crucial role in the performance of the photocathode. At the start of our studies on *p*-type SC-based photocathodes we had two types of NiO electrodes at our disposal. One type was purchased from the *Dyenamo* company, one was obtained from the *Solaronix* one. But the performance of these NiO electrodes implemented in light-harvesting systems had not been assessed priorly.

Being part of a joint initiative in the frame of the *Perspect H₂O* COST network, we included these NiO substrates in a benchmarking study, led by the group of E. Gibson at the *University of Nottingham* (now at *Newcastle University*). This collaborative study aims at comparing different NiO preparations, with consideration of their performance for DSSC and DS PEC applications. This work has been recently published and the advance article is provided as an appendix of this manuscript (Paper IV).[1] The reader is invited to refer to this appendix in which more insightful discussions can be found regarding the benchmarking study. We will only reproduce in this part results related to the NiO substrates we had. Particularly, we will support our choice of the substrate used along our studies based on the behavior in light-harvesting photoelectrodes.

1.1. NiO samples and DSSC assembly

The electrodes provided by *Dyenamo* were generally described in the previous chapter. Here, we use singly or doubly screen-printed electrodes that are either sintered at 350°C or at 450°C. Such temperatures for sintering NiO preparations dedicated to *p*-DSSCs are consistent with the literature.[2] The electrodes from *Solaronix* are singly screen-printed and annealed at the same temperatures. The preparations are summarized in Table IV.1.

Table IV.1. Description of the NiO electrodes used.

Provider	Screen-printed layers	Sintering temperature (°C)	Symbol
Solaronix	1	350	**SL-350**
		450	**SL-450**
Dyenamo	1	350	**DL-350**
		450	**DL-450**
	2	350	**D2L-350**
		450	**D2L-450**

To assess their performance as *p*-type supports in light-harvesting electrodes, these NiO substrates were implemented in inverse DSSCs. For this, NiO electrodes were sensitized with the **P1** organic dye[3] by soaking into a 0.3 mM solution of the dye in MeCN for 12 hours. **P1** is actually a well-known organic photosensitizer, the integration of which gives top standard *p*-DSSCs.[4] In a classical manner the I_3^-/I^- couple was used as a redox mediator. The cells are mounted with a FTO conductive glass coated with Pt to act as the counter-electrode. The DSSCs obtained are schematically depicted in Figure IV.1, with the associated energy levels of the dye and redox shuttle.
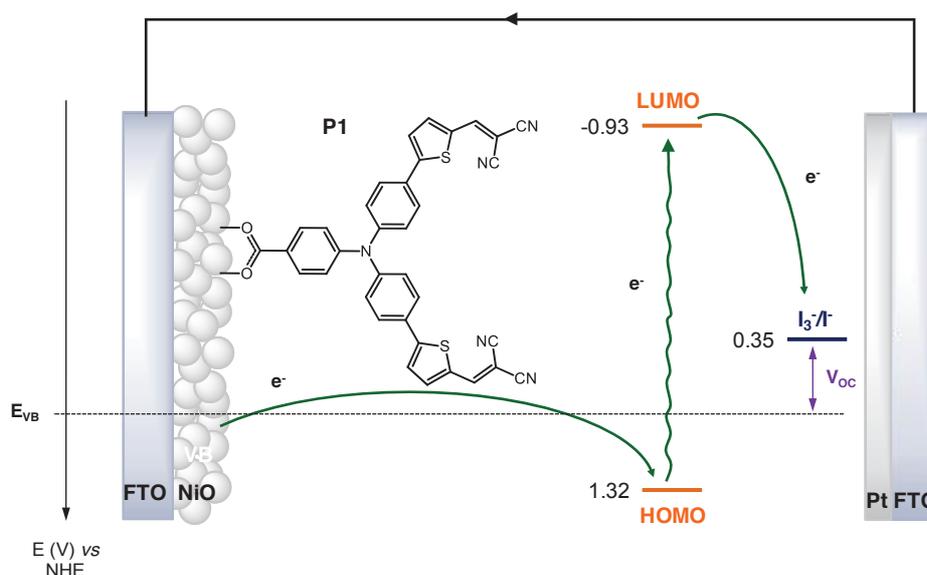
Figure IV.1. Schematic representation of the inverse DSSCs used in the study, with values of potentials in acetonitrile for the HOMO and LUMO levels of **P1**[5] and for the I^{3-}/I^- couple.[6]

1.2. Assessment of the photoelectrodes

1.2.1. Metrics examined

The *p*-type DS photocathode in such a DSSC can be assessed in terms of light-harvesting properties but also in regard to the flow or energy of the electrons it delivers. Here, we will mainly focus on metrics for the LH/CS properties (IPCE and ACPE) and for the electron delivery (short-circuit photocurrent density, J_{SC}).

We note that the open-circuit voltage of the DSSCs mainly depends on the difference in energy between the valence band of NiO and the thermodynamic potential of the redox shuttle (I_3^-/I^-).[7] The I_3^-/I^- coupled used here is broadly used in *n*-type DSSCs but is not optimized for *p*-type DSSCs since the relatively anodic potential of this couple actually limits the V_{OC}. An ideal redox shuttle should have a potential just positive of the LUMO of the PS utilized. Also, in the targeted H_2-evolving DS photocathode application, the electron acceptor species is not a redox shuttle but

the active state of the HER catalyst. For these reasons, we will not consider in this first approach the energetic issue *i.e*. the V_{OC} of the device.

1.2.2. Performances in DSSC

The performances of the DSSCs built with the different NiO preparations are summarized in Table IV.2. **P1** has an absorption maximum at 481 nm in solution (ε(481 nm) = 57 900 M$^{-1} \cdot$cm^{-1}).[5] Upon grafting, a bathochromic shift is observed and the maximum is displaced at around 500 nm. Thus, the absorbance, IPCE and APCE are given at 500 nm.

Table IV.2. Performances of the DSSCs built with the different NiO preparations.

Preparation	A$_{500\ nm}$ (a.u.)	IPCE$_{500nm}$ (%)	APCE$_{500nm}$ (%)	J$_{SC}$ (mA·cm^{-2})
SL-350	2.89	33	33	1.57
SL-450	3.23	26	26	1.15
DL-350	1.78	31	31	1.65
DL-450	1.05	29	32	1.85
D2L-350	3.33	37	37	2.49
D2L-450	1.98	40	41	2.40

The absorbance at 500 nm is comparatively high for the *Solaronix* samples. This point is explained by a quite high absorption of the NiO substrate itself, as exemplified in Figure IV.2 for the **SL-450** sample. Moreover, this high absorption does not secure improved IPCE$_{500nm}$, APCE$_{500nm}$ or photocurrent densities (Table IV.2).
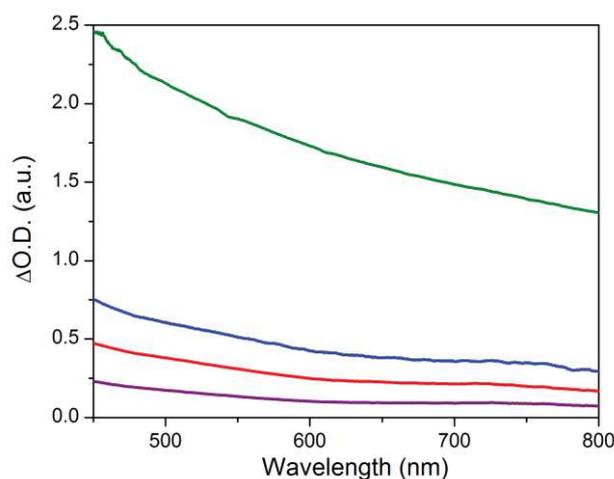
Figure IV.2. UV-visible absorbance spectra of the blank **SL-450** (green line), **DL-450** (purple line), **D2L-350** (blue line) and **D2L-450** (red line) samples, after subtraction of the signature of the corresponding supporting glass/FTO substrates.

These low performances are likely a consequence of the absorbance of the sensitized electrodes, which is not specific to the attached PS but mainly arises from the NiO substrate. Hence, the electrodes prepared by *Solaronix* will not be utilized for the construction of DS photocathodes in the current manuscript, although they represented interesting substrates for other works.

By contrast, NiO electrodes from *Dyenamo* display much lower intrinsic absorptions (Figure IV.2). As expected, the thicker films (2 layers) have background absorptions *ca* twice as the thinner ones (1 layer). This behavior is exemplified with **DL-450** and **D2L-450** substrates in Figure IV.2. A higher thickness of the film also translates in a higher absorbance of the **P1**-sensistized electrode at 500 nm (Table IV.2). This observation indicates that the loading of the dye is larger on doubly screen-printed samples, also in an approximate 2-fold increase. With the *Dyenamo* samples, thicker films yield improved $IPCE_{500nm}$, $APCE_{500nm}$ and J_{SC} values. This trend evidences that the LH/CS processes are enhanced with increased grafting densities of the dye. Such result demonstrates that these processes can mostly be attributed here to light absorption by the immobilized PS and not by the supporting NiO. Knowing that, we decided to select the doubly screen-printed *Dyenamo* NiO electrodes to conduct our studies on the construction of DS photocathodes. Given the very close performances between the substrates sintered at 350 °C and at 450°C (**D2L-350**, **D2L-450**, respectively; Table IV.2), we intentionally chose to work on the one sintered at 450°C, since its background absorbance is less marked over the UV-visible range (Figure IV.2). The spectra of the **P1-**sensitized **D2L-450** plate are depicted in Figure IV.3 with or without subtraction of the NiO background. The NiO background-subtracted spectrum evidences a clear feature, with a peak centered at 494 nm attributed to the attached **P1** dye.
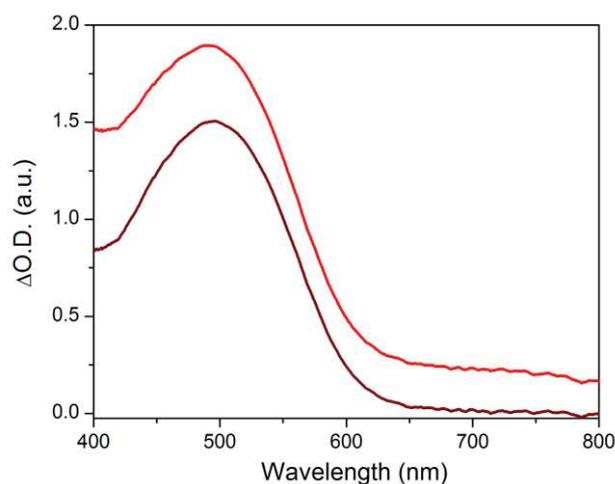
Figure IV.3. UV-visible absorbance spectra of the **P1**-sensitized **D2L-450** electrode, after subtraction of the signature of the supporting glass/FTO substrate (red line) and after subtraction of the signature of the **D2L-450** blank electrode (wine line).

Hence, we conclude that the **D2L-450** substrate can achieve substantial grafting densities of dye and/or catalyst on the surface, while correct UV-visible characterizations of the grafted species are enabled by the limited NiO background signature. These properties of the **D2L-450** substrate were already harnessed to characterize the Co^{I} state of the NiO-anchored **Co$_{C11P}$** in the Chapter III.

Overall, we believe that such a NiO preparation actually represents a fair compromise between important surface loadings, limited background absorbance and, hopefully, good performances of the photoelectrodes.

1.2.3. Photoelectrochemical experiment

To further assess the possibility to use the **D2L-450** NiO electrode for HER photoelectrocatalysis, a model experiment was conducted in water. This model experiment follows a procedure set by Sun and co-workers to prepare a **P1**-sensitized NiO electrode loaded with the **[Co(dmgBF$_2$)$_2$(H$_2$O)$_2$]** HEC.[8] As described in the introduction (Chapter I.2.2.3.1), this photocathode was shown to evolve hydrogen from a neutral aqueous media, although it experiences short-term stability.

Our photocathode was constructed in a similar manner. A solution of the **[Co(dmgBF$_2$)$_2$(H$_2$O)$_2$]** complex in acetonitrile (2 mM, 100 µL) was drop-cast onto the **P1**-sensitized **D2L-450** NiO electrode, which was further dried in air. The corresponding energy diagram is presented in Figure IV.4. In this configuration, the energy of the **P1** LUMO level is high enough to enable reduction of the catalyst from the Co^{II} to the Co^{I} state ($E_{Co^{II/I}}$ = −0.46 V *vs* NHE at pH 7)[9] and further from the subsequent Co^{III}-hydride intermediate to the active Co^{II}-hydride species.[10]
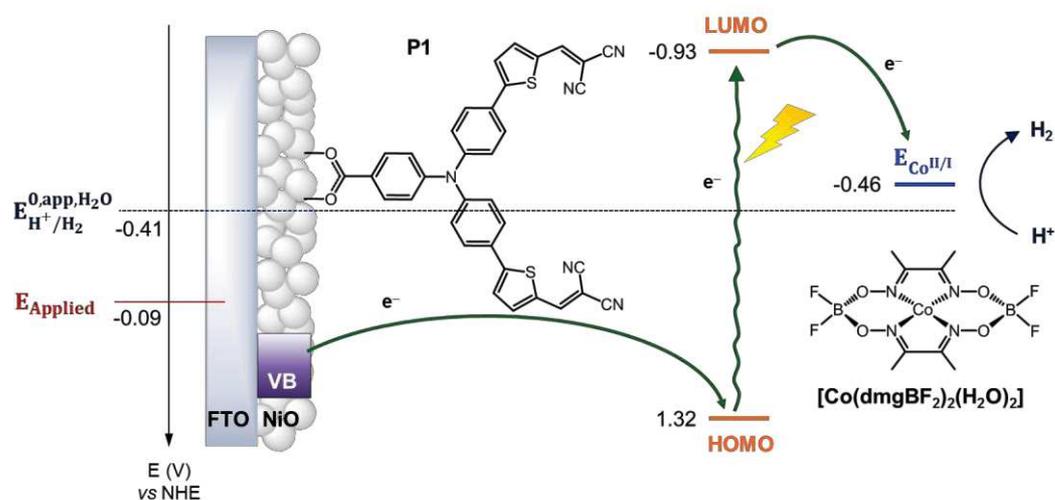
Figure IV.4. Schematic energy diagram of the **NiO-P1|[Co(dmgBF$_2$)$_2$(H$_2$O)$_2$]** photocathode. The aquo

ligands of **[Co(dmgBF₂)₂(H₂O)₂]** have been omitted for the sake of clarity. Potentials are considered *versus* NHE at pH 7.

To run the photoelectrocatalytic assays, the photocathode was poised at –0.09 V *vs* NHE. Under the neutral aqueous conditions used (KPi 50 mM; pH 7), this potential is positive compared to the thermodynamic equilibrium of proton interconversion ($E_{H^+/H_2}^{0,app,H_2O}$ = –0.41 V *vs* NHE at pH 7). The chronoamperometry at the photocathode is shown in Figure IV.5. At the start of the experiment, an intense transient reduction current is observed in the dark, which quickly decays to almost 0. Then, when light is shined on the electrode, a photocurrent establishes, which also undergoes a transient decay before the light is shut down and the current density comes back to background values. These transient behaviors might be attributed to a capacitive phenomenon occurring at the electrode or to the reduction of residual traces of O_2 trapped within the NiO film.

During next light irradiation periods, the photocurrent density is found around −5 to −10 µA·cm^{-2}, whereas the dark current density is about −2 to −3 µA·cm^{-2}. These values of photocurrent compare well with the one observed by Sun and co-workers.[8] Although it experiences an overall decay, the photocurrent is retained over the whole measurement time. For practical reasons, hydrogen detection could not be performed at the time of the workshop. Still, we note that the charge passed during the total 700 s of irradiation is –9.4 mC, which corresponds to a theoretical amount of 49 nmol of H_2 produced.
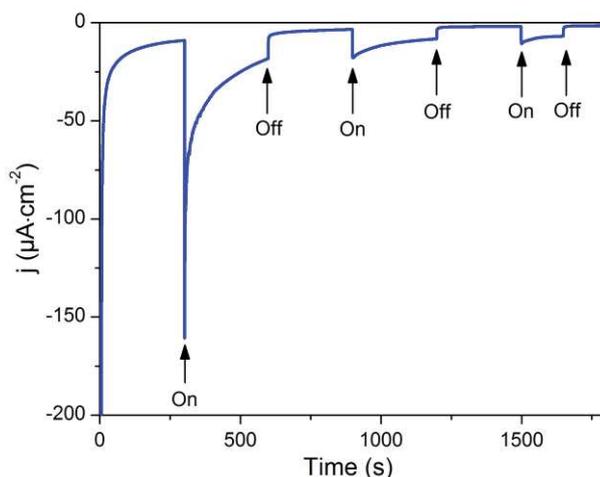
Figure IV.5. Chronoamperometric measurement at the **NiO-P1|[Co(dmgBF₂)₂(H₂O)₂]** electrode poised at –0.09 V *vs* NHE in a 50 mM potassium phosphate aqueous buffer at pH 7 under chopped light irradiation (1000 lm).

Anyway, the photocurrent proves that a light-driven electron transfer from the electrode to the solution takes place, possibly achieving hydrogen evolution. The photocathode based on the **D2L−450** NiO preparation is shown here to operate in aqueous media. This observation points out that this type of NiO electrode is a candidate suitable for the construction of DS photocathodes for

hydrogen evolution. Also of note, the **NiO-P1|[Co(dmgBF$_2$)$_2$(H$_2$O)$_2$]** photocathode used in this study is a non-optimized architecture since the catalyst is adsorbed on the electrode, thus not firmly attached to it. Such a weak immobilization was actually raised as the source of the limited stability over time of this architecture.[8] These points encouraged us to construct DS photocathodes relying on covalently bound dye and catalyst species at the NiO surface.

2. Co-grafted photocathodes for HER

In this part, we present the construction of co-grafted photocathodes for HER. First, the components involved will be briefly described or recalled. Particular attention will be drawn to the energetic matching between the different species implemented in the electrode.

Then, we will show the procedure we followed to prepare the photocathode. In line with the results presented in Chapter III, we will present a set of structural characterization data for the immobilized architectures.

Further, photoelectrocatalytic tests of hydrogen evolution with the assembled electrodes will be described. For these assays, the quantification of hydrogen production will be provided. These results will finally be discussed and perspectives to improve the co-grafted architectures will be proposed.

This work was conducted in collaboration with the team of B. Jousselme at the *Laboratory of Innovation in Surface Chemistry and Nanosciences* (*CEA-Saclay*, FRANCE) within the frame of the *ArtipHyction* European project.

2.1. Components

2.1.1. Overview

The architecture envisioned in this approach relies on the concomitant attachment of a PS and a catalyst onto a *p*-type NiO substrate.

Capitalizing on the works presented above in the manuscript, we will base our construction of the photocathodes on the immobilization of the **Co$_{C11P}$** derivative (see Chapter III) onto **D2L-450** NiO substrates (see Chapter IV.1). The **D2L-450** preparation will be used exclusively for the rest of this work.

The final component to create a light-harvesting electrode is a photosensitizer. Previous reports of performing NiO-based DS photocathodes mainly rely on organic dyes, as described in introduction (see Chapter I.2.2.3). Especially, push-pull dyes attached to NiO surfaces *via* carboxylate groups gave encouraging results in inverse DSSCs[7, 11] but also in DS photocathodes able to operate in fully aqueous media[12] and catalyze HER.[8, 13] Besides, Ru(bpy)$_3$-like complexes are benchmark PSs broadly implemented into DS photoelectrodes. More particularly, this type of dye has been shown to enable light-driven electron transfer at the surface of NiO for applications in hydrogen evolution catalysis.[14] We thus decided to create two DS photocathodes, one relying on an organic dye and one on a Ru(bpy)$_3$ prototype PS.

To ensure these light-harvesting units are suitable for the construction of NiO-based DS photocathodes for hydrogen evolution, energy considerations have to be examined. The orbitals corresponding to the HOMO and the LUMO levels of the photosensitizers should lay at energies suitable for hole injection into NiO and reduction of the catalytic active species, respectively. To verify this point, the energy levels were estimated through electrochemistry, UV-visible spectroscopy and with the income of computational simulations (not shown here), when available. The architectures proposed for the DS photocathodes, with the associated estimated energy levels of dyes and catalysts, are presented afterwards.

2.1.2. Organic dye: **TPAT$_2$NMI**

2.1.2.1. Description

The **TPAT$_2$NMI** organic dye used in our study is shown in Figure IV.6. The synthesis of the dye has been developed and performed by R. Brisse, a PhD student in the team of our collaborators at *CEA-Saclay*. This organic PS has a push-pull structure the properties of which will be more extensively described in the next section. Also, the molecule features two acid carboxylic moieties dedicated to the anchoring onto NiO surfaces. We note that a similar structure was proved quite efficient for the targeted application of H$_2$-evolving photocathodes.[13a]

R = *t*Bu   **TPA$_{tBu}$T$_2$NMI**
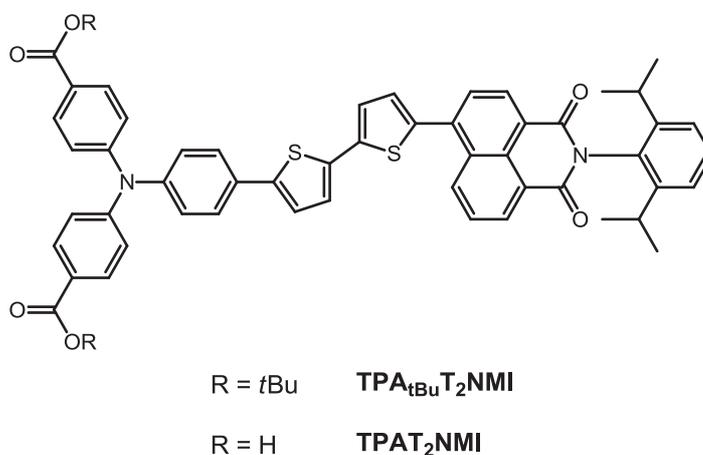
R = H   **TPAT$_2$NMI**

Figure IV.6. Protected *tert*-butyl ester **TPA$_{tBu}$T$_2$NMI** and deprotected acid carboxylic **TPAT$_2$NMI** versions of the organic dye used for the construction of DS photocathode.

The carboxylic acids are protected under the form of *tert*-butyl esters (compound **TPA$_{tBu}$T$_2$NMI**, Figure IV.6) until the last synthetic step. For solubility issues, this protected version is utilized to perform most of the characterization in solution.

2.1.2.2. Energetics

The characterization of the molecular homogeneous species have been provided by our collaborators at *CEA-Saclay*. The ones related to properties in DS photocathodes are briefly shown here with a draw of the subsequent consequences in terms of energetic levels.

The CV of **TPA$_{tBu}$T$_2$NMI** (Figure IV.7, left) in the cathodic region displays two reversible waves. By comparison to similar dye backbones, these waves are attributed to two successive oxidations of the donor part mixing the triphenylamine (**TPA$_{tBu}$**) and the bithiophene (**T$_2$**) moieties.[12, 15] The potential of the first wave is found at 1.20 V *vs* NHE. Associated with the first oxidation of the donor part, this potential indicates the energy of the HOMO level of the PS (E_{HOMO}).
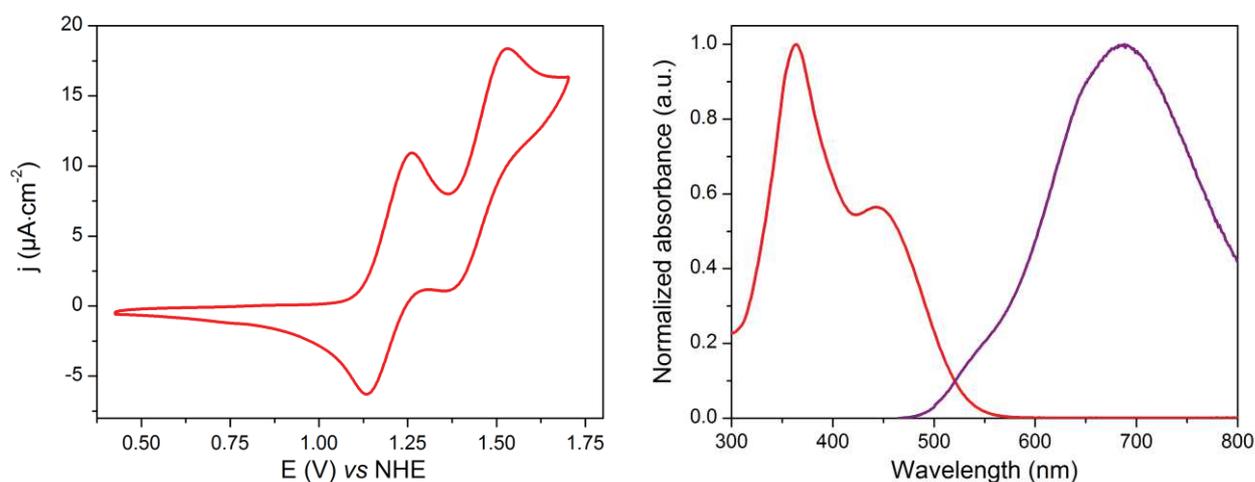
Figure IV.7. CV of **TPA$_{tBu}$T$_2$NMI** recorded at a Pt electrode in a 0.1 M nBu$_4$NPF$_6$ DCM electrolyte with a scan rate of 100 mV·s^{-1} (left) and normalized absorption (red line) and emission upon excitation at 450 nm (purple line) spectra of **TPA$_{tBu}$T$_2$NMI** in DCM at R.T. (right).

The **TPA$_{tBu}$T$_2$NMI** dye displays two bands in the UV-visible range (Figure IV.7, right). The two bands are partially merged with maxima at 364 nm and at 442 nm corresponding to molar absorptivities of 47 974 and 27 104 M^{-1}·cm^{-1}, respectively. From computational simulations, the first band centered at 442 nm can mainly be attributed to mixed HOMO to LUMO, HOMO–1 to LUMO and HOMO to LUMO+1 transitions. The HOMO-LUMO transition is a charge transfer process from the **TPA$_{tBu}$T$_2$** donor part to the naphthalene monoimide (**NMI**) acceptor moiety. Upon excitation on this transition (450 nm), the emission spectrum (Figure IV.7, right) features a broad band centered at 688 nm. From the intersection between normalized absorption and emission spectra (520 nm), the 0-0 transition energy (E_{0-0}) was estimated to be of 2.38 eV.

The subtraction of the E_{0-0} transition energy from the energy of the HOMO level permits us to estimate the energy of the LUMO level (E_{LUMO}) around −1.18 V *vs* NHE.

2.1.3. Ru(bpy)₃-like photosensitizer: **RuP₄**

2.1.3.1. Description

The Ru(bpy)₃-like photosensitizer utilized is the study, named as **RuP₄**, is presented in Figure IV.8. The synthesis of this complex has been performed by N. Queyriaux, a PhD candidate in the group, in the context of a broader study. In this work, a series of new bis-heteroleptic Ru(bpy)₃ PSs that feature two bipyridine ligands each decorated by two phosphonic acids and a third π-extended bipyridine-based ligand is developed. These new architectures aim to improve the attachment of Ru(bpy)₃-like PS at the surface of TCOs and fostering the charge separation upon light irradiation. This work is described in N. Queyriaux's PhD thesis.

R = Et, X⁻ = PF₆⁻   **RuPEt₄**

R = H, X⁻ = Cl⁻   **RuP₄**
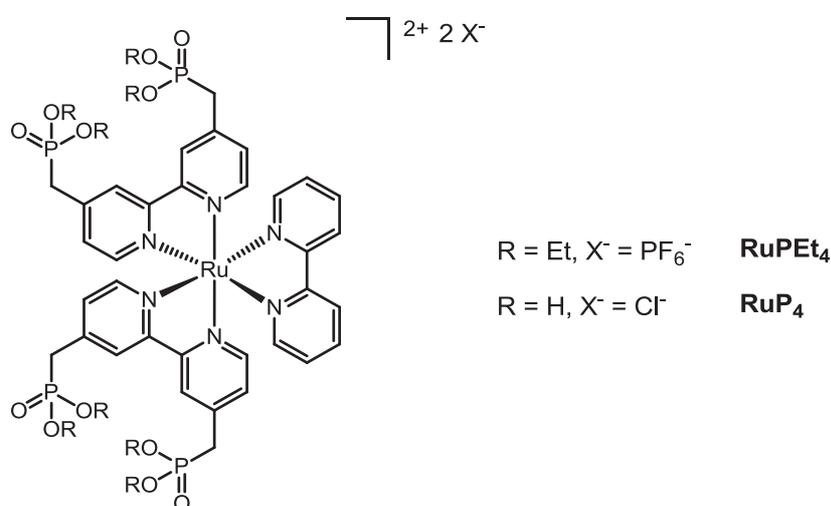
Figure IV.8. Protected diethyl ester phosphonate **RuPEt₄** and deprotected phosphonic acid **RuP₄** versions of the Ru-based PS used for the construction of DS photocathode.

Especially, the **RuP₄** complex used in the current work bears two bipyridine ligands functionalized by two methylenephosphonic acids in 4 and 4' positions. The presence of four phosphonic acid moieties is expected to increase the stability of the anchoring onto NiO surfaces. For questions of solubility, homogeneous characterization was performed with the **RuPEt₄** diethyl ester phosphonate protected version of the PS (Figure IV.8).

2.1.3.2. Energetics

The characterizations presented here were performed by N. Queyriaux. In the oxidative regime, the CV (Figure IV.9, left) of **RuPEt₄** depicts a reversible wave, which is ascribed to the $Ru^{III/II}$ couple. The potential of this wave, found at 1.39 V *vs* NHE (0.86 V *vs* $Fc^{+/0}$ converted to NHE by addition of 0.53 V),[16] gives the energy of the HOMO level. This HOMO level corresponds to an orbital mainly localized on the Ru metallic atom.[17]
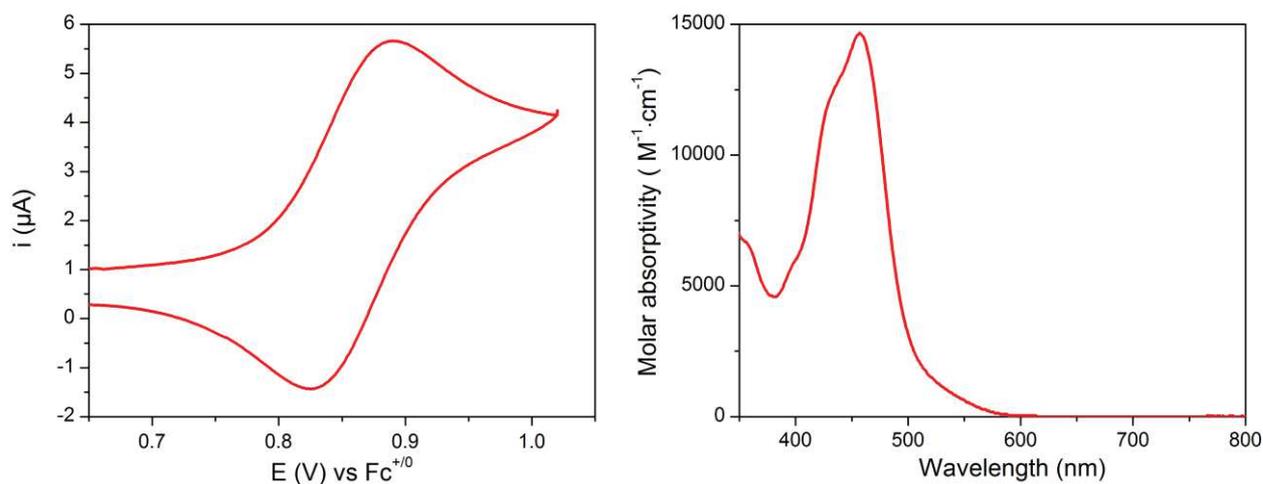
Figure IV.9. CV of **RuPEt$_4$** recorded at a Pt electrode in a 0.1 M nBu$_4$NBF$_4$ MeCN electrolyte with a scan rate of 100 mV·s^{-1} (left) and molar absorptivity of **RuPEt$_4$** in MeCN (right).

In the UV-visible region, the absorbance spectrum of the **RuPEt$_4$** complex (Figure IV.9, right) shows a broad band centered on a maxima at 457 nm with a corresponding molar absorptivity of 14 668 M^{-1}·cm^{-1}. This band is assigned to a spin allowed metal-to-ligand charge transfer (MLCT) transition, as extensively described for Ru(bpy)$_3$-type PSs.[17b] The first excited singlet state is expected to undergo an ultrafast intersystem crossing (ISC) to a triplet state, as observed for the [Ru(bpy)$_3$] prototype (subpicosecond time scale).[17b] This longer-lived triplet state is usually the one associated with the LUMO level, located on π^* orbitals of the bipyridine ligands. For instance, on a similar Ru complex having a single bi-phosphonic acid substituted bipyridine ligand (and two bipyridine ligands), the triplet LUMO level was shown to be delocalized over the π^* orbitals of the three ligands.[17a]

The transition between the primary excited singlet state and the reemitting triplet state generally implies that fluorescence should be performed at low temperature to correctly determine the E_{0-0} transition energy. While these experiments are still ongoing at the time this thesis is being written, we will in first approximation estimate the E_{0-0} energy with the foot of the UV band (*ca* 588 nm). The approximate value of E_{0-0} is thus found at 2.11 eV, which is likely an overestimation, given the explained above ISC phenomenon. Still, this value is in good line with the one reported for the analogous Ru complex bearing a single bi-phosphonic acid substituted bipyridine.[17a]

From the values of E_{HOMO} and E_{0-0}, the energy of the LUMO level for **RuPEt$_4$** was estimated at –0.72 V *vs* NHE.

2.2. Proposed architectures

We designed two prototype DS photocathodes. The first one contains the **TPAT$_2$NMI** dye and the **Co$_{C11P}$** catalyst derivative. This co-grafted electrode, named as **NiO-TPAT$_2$NMI-Co$_{C11P}$**, is shown in Figure IV.10. The second architecture unites the **RuP$_4$** PS with the **Co$_{C11P}$** moiety in the **NiO-RuP$_4$-Co$_{C11P}$** photocathode, as represented in Figure IV.11.
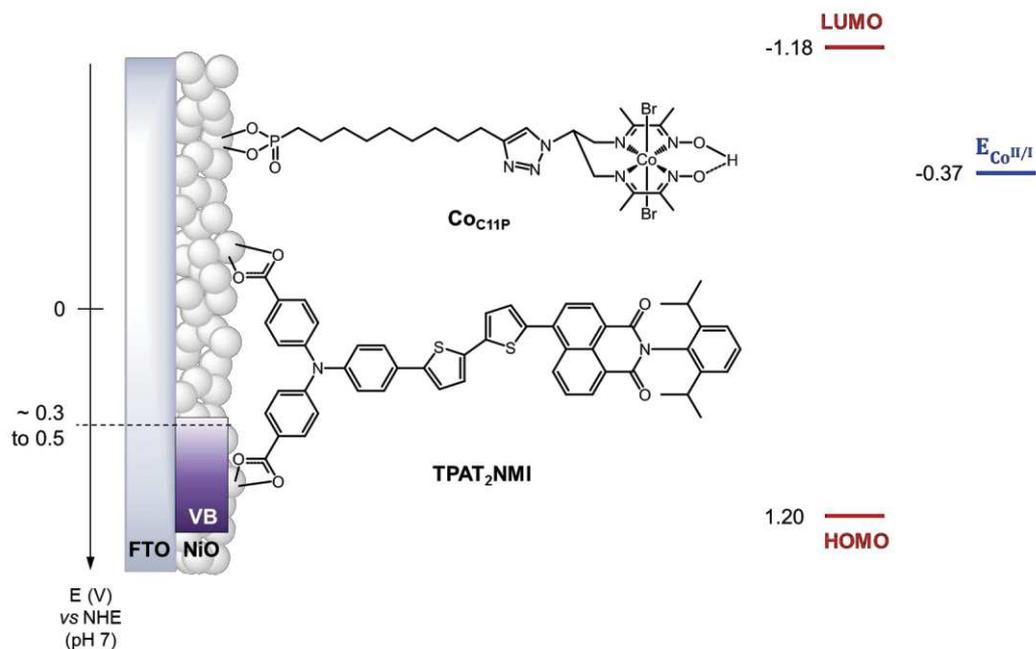

Figure IV.10. Schematic energy diagram of the **NiO-TPAT$_2$NMI-Co$_{C11P}$** photocathode. Energy levels estimated from the **TPA$_{tBu}$T$_2$NMI** protected analogue under homogeneous conditions (see Chapter IV.2.1.2.2) for **TPAT$_2$NMI**, from the Co$^{II/I}$ potential observed on **NiO-Co$_{C11P}$** electrodes (see Chapter III.3.2.1.3) for **Co$_{C11P}$** and from literature[18] for the edge of the NiO VB.

In both cases, the potential of the HOMO levels should allow the injection of a hole from the excited dye into the NiO VB. Also, the LUMO levels of the dyes are located higher than the Co$^{II/I}$ potential. This should permit the reduction to the Co^I state that gives access to the catalytic turnover for HER.[19]

The energy levels of the PSs are reported for the protected versions **TPA$_{tBu}$T$_2$NMI** and **RuPEt$_4$**. Upon deprotection and also upon grafting to the surface, slight shifts of these levels are possible. This point is particularly true for the **TPAT$_2$NMI** dye since the HOMO level is partially delocalized on the carboxylic anchors directly conjugated with the **TPAT$_2$** donor part. Thus, the modification of this group by deprotection or coordination to surface can influence the energy of the HOMO level. Yet, the HOMO level is much more negative than the top edge of the NiO VB (a difference of 0.7-0.9 eV) and a minute modification of this level is not expected to sharply impact the hole injection into the VB.

The LUMO level of the **TPAT$_2$NMI** dye, mainly centered on the **NMI** moiety, and thus less prone to energetic modifications upon grafting, has a large driving force (0.81 eV) for the reduction of the Co^{II} to Co^{I} state. For the **RuP$_4$** PS, the driving force (0.35 eV) is still large but less important compared to the organic dye.

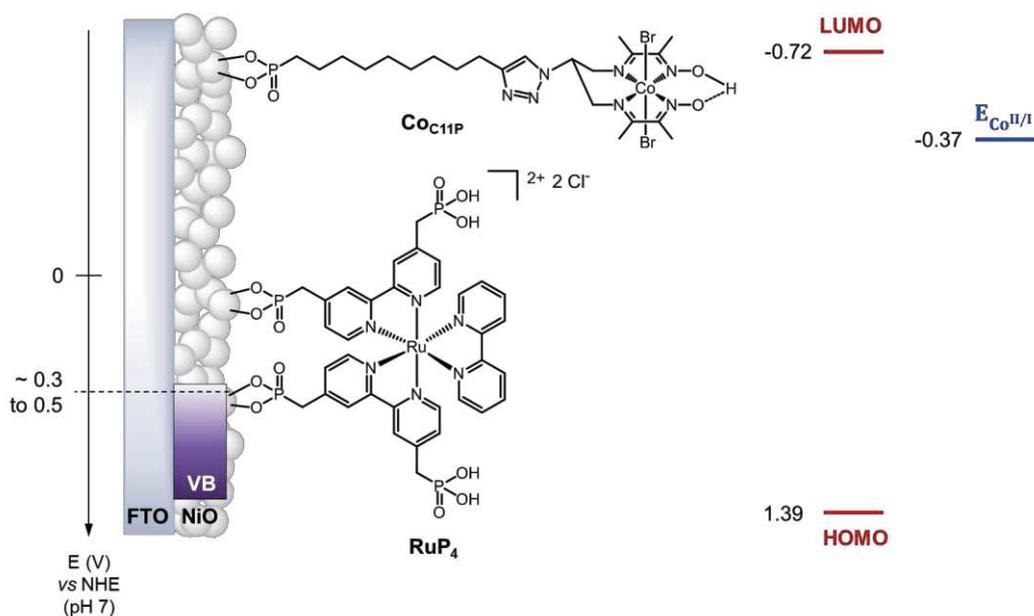Finally, to effectively assess the two architectures, we undertook their construction and characterization.

Figure IV.11. Schematic energy diagram of the **NiO-RuP$_4$-Co$_{C11P}$** photocathode. Energy levels estimated from the **RuPEt$_4$** protected analogue under homogeneous conditions (see Chapter IV.2.1.3.2) for **RuP$_4$**, from the Co$^{II/I}$ potential observed on **NiO-Co$_{C11P}$** electrodes (see Chapter III.3.2.1.3) for **Co$_{C11P}$** and from literature[18] for the edge of the NiO VB.

2.3. Preparation of the electrodes

As the immobilization was performed initially with a methanolic solution containing equimolar quantities of a dye and the catalyst (0.5 mM each). The obtained electrodes were analyzed by electrochemistry. The signal corresponding to the attached **Co$_{C11P}$** could not be detected at decent levels at these electrodes. We concluded that the loading of the catalyst derivative was not significant under such conditions. This observation suggests that the binding of dye *versus* the binding of catalyst are competitive processes at the surface. While the dyes feature multiple anchoring groups (two COOH for **TPAT$_2$NMI**, four PO$_3$H$_2$ for **RuP$_4$**), the catalyst only displays a single attachment moiety (one PO$_3$H$_2$). As a consequence, the binding equilibria can be displaced toward the attachment of the dyes rather than the attachment of **Co$_{C11P}$**.
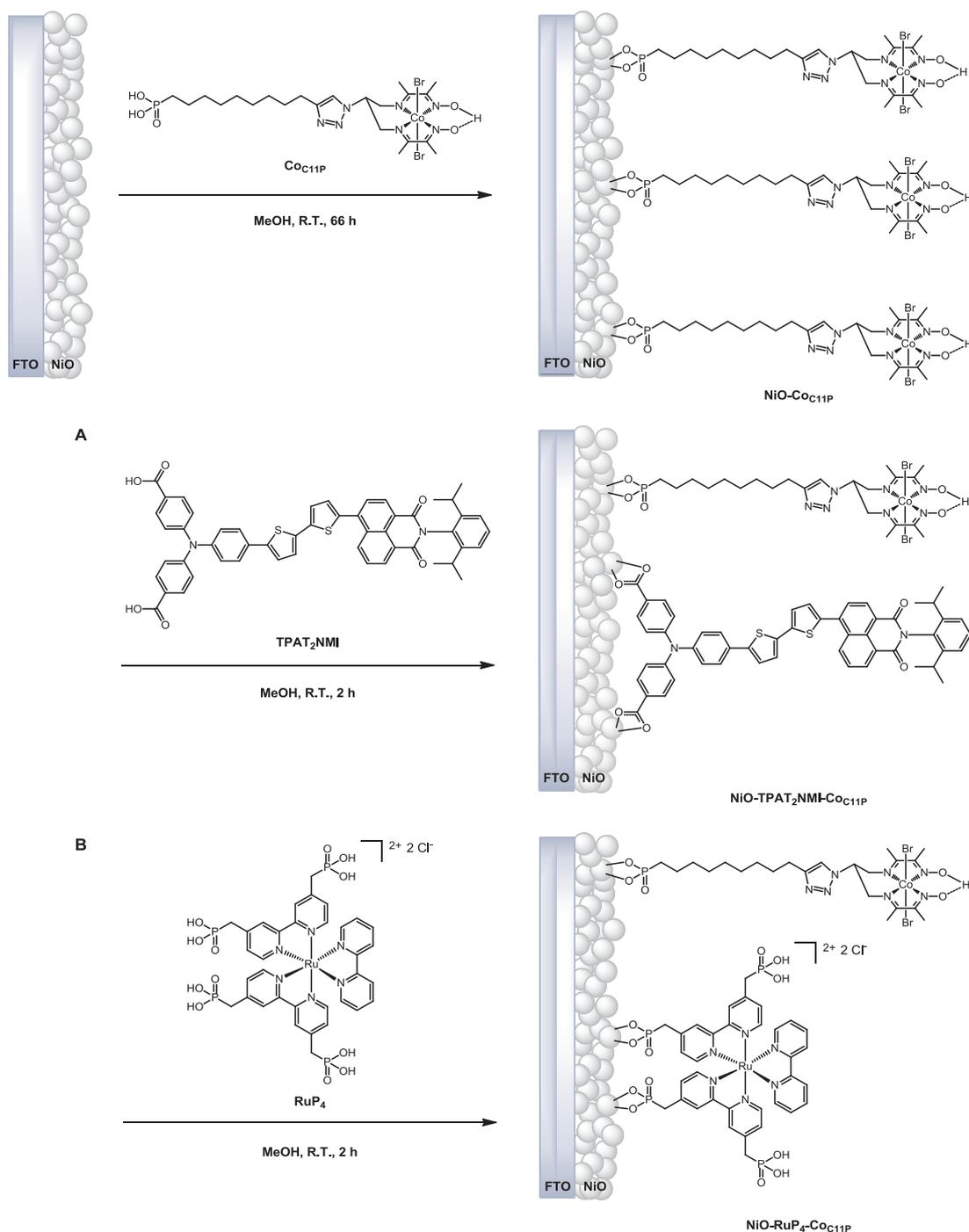
Figure IV.12. Sequential pathways for the preparation of (**A**) the **NiO-TPAT₂NMI-Co_C11P** and (**B**) the **NiO-RuP₄-Co_C11P** photocathodes.

To bypass this issue, we decided to exploit this equilibrium by preparing the electrodes in a sequential way (Figure IV.12). First the **Co_C11P** catalyst alone is grafted on the surface following the procedure used to construct **NiO-Co_C11P** electrodes (see Chapter III.3). The bathing time was intentionally kept longer (typically 66 h) to foster a larger loading of the catalyst derivative and, possibly, lead to full surface coverage. Then, the electrodes were rinsed with MeOH to remove weakly bound catalysts. In a second step, the electrodes were dipped in a 0.5 mM methanolic

solution of photosensitizer (**TPAT$_2$NMI** or **RuP$_4$**). During this second step, the photosensitizer is expected to attach to the surface by partially displacing the **Co$_{C11P}$** derivative. Hence, the immobilization was performed for only two hours to avoid the complete substitution of the catalyst for the dye. The electrodes should thus display a shared decoration of the surface by both entities. These electrodes were finally rinsed with MeOH to further eliminate the physisorbed molecules.

For the sake of comparison, control electrodes loaded only with the photosensitizers in a similar fashion (two hours of dying) were prepared. These electrodes are referred to as **NiO-TPAT$_2$NMI** and **NiO-RuP$_4$** and shown in Figure IV.13.
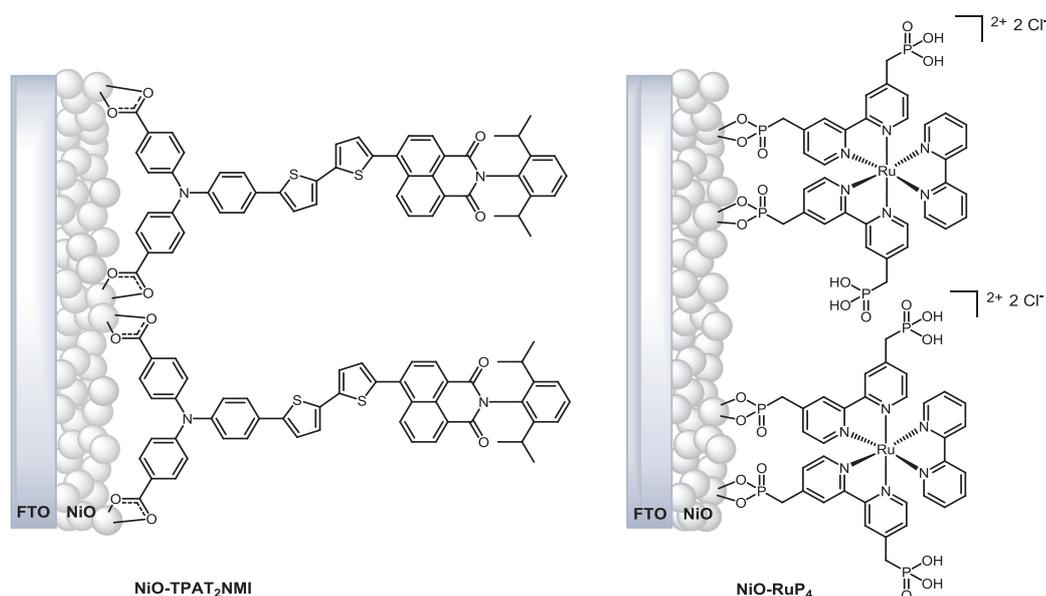
Figure IV.13. The **NiO-TPAT$_2$NMI** (left) and the **NiO-RuP$_4$** (right) control photocathodes.

2.4. Structural characterizations

The electrodes were characterized by UV-visible spectroscopy, electrochemistry, XPS and surface mass spectroscopy. Comparisons with the **NiO-Co$_{C11P}$** electrodes, *i.e.* at the first immobilization step, as well as with only dye-sensitized electrodes (**NiO-TPAT$_2$NMI** and **NiO-RuP$_4$**) are provided.

2.4.1. **NiO-TPAT$_2$NMI-Co$_{C11P}$** electrodes

2.4.1.1. Electrochemistry

The cyclic voltammograms in the cathodic regime of the **NiO-Co$_{C11P}$** and **NiO-TPAT$_2$NMI-Co$_{C11P}$** electrodes are shown in Figure IV.14. The CV of **NiO-Co$_{C11P}$** *i.e.* at the first step of the sequential immobilization (blue line) shows an ill-defined event with a reduction wave at *ca* −0.45 V *vs* NHE and a much less marked reoxidation wave at −0.28 V *vs* NHE.
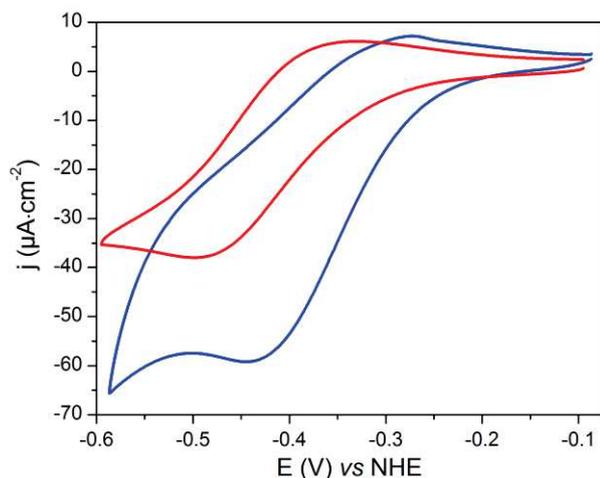
Figure IV.14. CVs at the **NiO-Co$_{C11P}$** (blue line) and the **NiO-TPAT$_2$NMI-Co$_{C11P}$** (red line) electrodes recorded in NaCl 0.1 M aqueous electrolyte at a scan rate of 10 mV·s^{-1}.

These potentials are in good agreement with the signature observed previously with **NiO-Co$_{C11P}$** electrodes (see Chapter III.3.2.1.3) and thus can be attributed to the Co$^{II/I}$ couple of the bound **Co$_{C11P}$** catalyst. However, the low resolution of this wave compared to our precedent assays on the **NiO-Co$_{C11P}$** electrodes (see Figure III.23 and Figure III.22) is quite questioning. We found that this difference was mainly due to the setup used for the characterization of the electrodes.
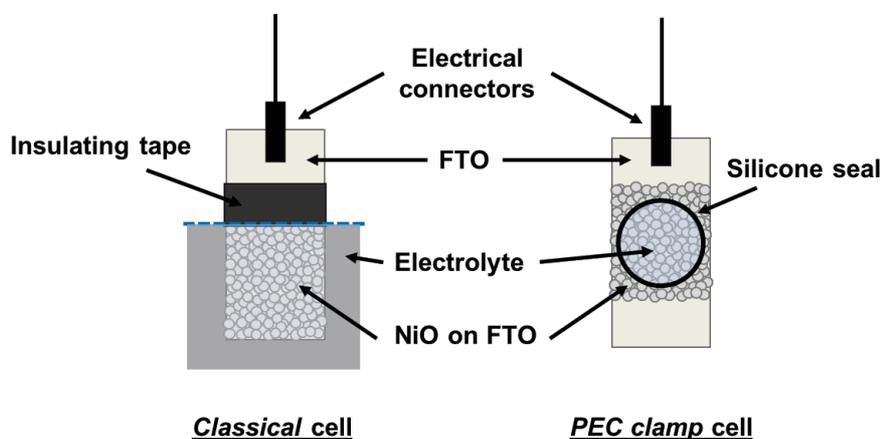
Figure IV.15. Electrochemical setup previously used for the characterization of hybrid electrodes (*classical* cell) compared to the one used for the characterization during the construction of co-grafted electrodes (*PEC clamp* cell).

Indeed, our previous electrochemical experiments with the **NiO-Co$_{C11P}$** electrodes were conducted in a *classical* 3-electrode electrochemical cell. In this configuration shown in Figure IV.15, left, the mesoporous NiO layer is dipped in the electrolyte and the FTO part insulated from it by a galvanoplastic tape. By contrast, for the experiments presented from now, we used another cell in which photoelectrochemistry can be performed. We intentionally utilized this cell, called

PEC clamp cell (Figure IV.15, right), to stay consistent with future studies that will require a controlled light irradiation of the photocathodes. In that configuration, the electrode is clamped to the electrochemical cell and constitutes a window of the cell. The NiO layer is in contact with the electrolyte and, to ensure the tightness at the NiO/cell interface, an O-ring seal is inserted in between.

We discovered that the definition of the $Co^{II/I}$ signal depends on the cell configuration. The waves are well defined in the *classical* cell, but have temperamental shapes in the *PEC clamp* cell. We could not give a clear explanation on the origin of this behavior. Yet, we postulate that the low definition observed in the *PEC clamp* cell is a result of handling and pressing the seal against the NiO layer, which might create micro-cracks into it. These cracks can possibly put the underlying FTO layer in direct contact with the electrolyte. In that way, the NiO network might be short-circuited, the electronic conduction being mainly ensured by the FTO layer. Thus, the signature of the Co_{C11P} species immobilized onto the NiO mesoporous layer would be lowered down. We could not completely exclude this undesired effect from our experiment, even by applying scotch tape at the contact between the seal and the NiO film, but the electrodes were clamped with extreme care to minimize it.

After the attachment of **TPAT$_2$NMI** onto the **NiO-Co$_{C11P}$** electrode, an electrochemical signature with well-defined waves is observed at *ca* −0.40 V *vs* NHE (Figure IV.14, red line). This signature is ascribed to the $Co^{II/I}$ couple of **Co$_{C11P}$**. Hence, the attached cobalt diimine-dioxime complex is still present after the dying with **TPAT$_2$NMI**. The grafting densities in Co centers at the **NiO-TPAT$_2$NMI-Co$_{C11P}$** electrode is estimated by integration of these waves about 1.5 to 2 nmol·cm^{-2}. This value is slightly inferior to the loading densities observed for the **NiO-Co$_{C11P}$** electrodes (2 to 4 nmol·cm^{-2}, see Chapter III.3.2.1.3). Such an observation would support a partial displacement of the **Co$_{C11P}$** complexes by the **TPAT$_2$NMI** PSs.

2.4.1.2. UV-visible spectroscopy

The loading of the **TPAT$_2$NMI** photosensitizers on the **NiO-Co$_{C11P}$** electrodes can also be assessed by UV-visible spectroscopy. First, the signature of the control **NiO-TPAT$_2$NMI** electrode was acquired. The differential spectrum of this electrode is displayed in Figure IV.16 (orange line). A broad band is observed, rising from *ca* 580 nm, with a marked shoulder about 460 nm and a maximum at 360 nm. The broadening of the UV-visible spectra upon grafting is commonly observed for TCO-anchored organic photosensitizers.[5, 15, 20] Thus, by comparison to the solution spectrum of **TPA$_{tBu}$T$_2$NMI,** this feature is assigned to the immobilized **TPAT$_2$NMI** dye at the surface of NiO.
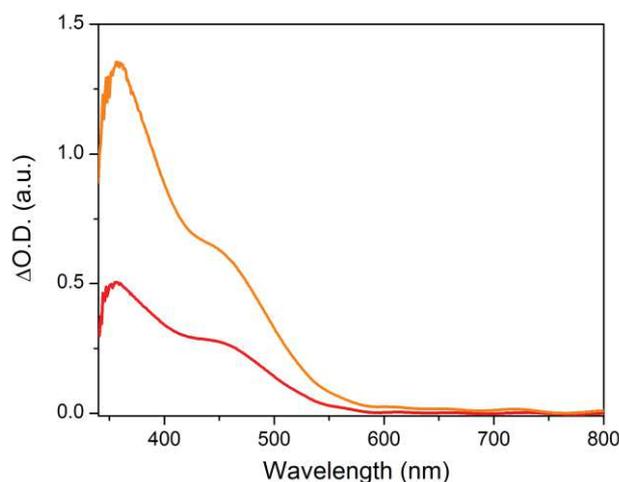
Figure IV.16. UV-visible spectra of the **NiO-TPAT₂NMI-Co$_{C11P}$** electrode after subtraction of the spectrum of the **NiO-Co$_{C11P}$** electrode (red line) and of the **NiO-TPAT₂NMI** electrode after subtraction of the spectrum of the pristine **NiO** electrode (orange line).

The surface loading in PS (Γ_{PS}) can be roughly estimated using the following equation:[21]

$$\Gamma_{PS} = \frac{A^{electrode}\left(\lambda(\varepsilon_{max}^{solution})\right)}{1000 \cdot \varepsilon_{max}^{solution}} \qquad \textbf{Eqn. IV.1}$$

where $\varepsilon_{max}^{solution}$ is the maximum absorptivity of the dye in solution and $A^{electrode}(\lambda)$ the absorbance of the electrode at the λ wavelength.

The substansial absorbance of the FTO|NiO layers under 400 nm does not permit to finely subtract the spectra in this region. Thus, we considered the second maximum of the spectrum in solution, at 442 nm ($\varepsilon^{solution} = 27\ 104\ \text{M}^{-1}\cdot\text{cm}^{-1}$). Due to the broadening upon attachment of the dye, the UV-visible spectrum of **NiO-TPAT₂NMI** does not display a local maximum at this wavelength, but only a shoulder. We took the absorbance at this shoulder $A^{electrode}$(442 nm) = 0.654 to estimate the grafting density of the PS, found at *ca* 24.1 nmol·cm^{-2}.

The UV-visible differential spectrum of **NiO-TPAT₂NMI-Co$_{C11P}$** is shown in Figure IV.16 (red line). This spectrum is a difference between the one after the first step (**NiO-Co$_{C11P}$**) and the one after the second step (**NiO-TPAT₂NMI-Co$_{C11P}$**). In that way, the contribution of **TPAT₂NMI** only is pictured. The spectrum displays a signature of similar shape compared to that of **NiO-TPAT₂NMI**, but with lower intensity. Especially, the absorbance at 442 nm is 0.282, which is *ca* 43 % of that of the **NiO-TPAT₂NMI** electrode. The related grafting density of the dye on **NiO-TPAT₂NMI-Co$_{C11P}$** is about Γ_{PS} = 10.4 nmol·cm^{-2}. This observation clearly demonstrates that a smaller amount of dye can be immobilized when **Co$_{C11P}$** is already present on the surface. Hence, the competition for binding onto NiO is further confirmed by the UV-visible spectroscopy.

2.4.1.3. XPS analysis

The XP spectra of the **NiO-Co_{C11P}**, **NiO-TPAT₂NMI** and **NiO-TPAT₂NMI-Co_{C11P}** electrodes at the N *1s*, S *2p* and P *2p* core levels are shown in Figure IV.17.

Data for the **NiO-Co_{C11P}** electrode, which have already been discussed (see Chapter III.3.2.1.1), are added here (Figure IV.17, top) as comparison. First, a quick introduction of the main features observed on **NiO-TPAT₂NMI** is made, that will facilitate the following description of the spectra of the **NiO-TPAT₂NMI-Co_{C11P}** co-grafted architecture.

The **NiO-TPAT₂NMI** electrode displays signatures at the N *1s* and S *2p* levels (the P *2p* levels were not scanned) as presented in Figure IV.17, middle row. At the N *1s* level (Figure IV.17, middle left), the signal shows a main contribution centered at 399.7 eV. This energy is in good correlation with that observed for the *1s* level of the nitrogen atom of the triphenylamine moiety in similar push-pull organic dyes, although attached at the surface of TiO₂.[22] This contribution is thus ascribed to the N *1s* level of the nitrogen atom in **TPAT₂NMI**. A smaller contribution at higher binding energies (401.4 eV) might be an indication of a different binding mode of the dye at the surface.[22a] Yet, the presence of small nitrogen-containing contaminations of the plates could not be completely excluded.

At the S *2p* core levels (Figure IV.17, center), two signals are seen, centered at 163.8 and 167.8 eV. The feature at 167.8 eV corresponds to a contaminant since it is already present on the control **NiO-Co_{C11P}** electrode (Figure IV.17, top middle). The peak at 163.8 eV can be deconvoluted into two contributions (163.8 and 165.0 eV) of area ratio 2:1 and energy split of 1.1 eV. This signature correlates quite well with the one evidenced for S *2p* levels of thiophene moieties in similar TiO₂-immobilized organic backbones.[22] This signal is hence undifferentially ascribed to the S *2p* core levels of the two sulfur atoms in **TPAT₂NMI,** which have nearly identical chemical environments.

The characterization of the final electrode was realized after immobilization of the **TPAT₂NMI** photosensitizer on the **NiO-Co_{C11P}** electrode. The XP spectrum at the Co *2p* core levels of the **NiO-TPAT₂NMI-Co_{C11P}** electrode is depicted in Figure IV.18, bottom. Two peaks are observed at 780.6 and 796.6 eV. By comparison with the corresponding spectrum at a **NiO-Co_{C11P}** electrode (Figure IV.18, top), these peaks are assigned to the *2p_{2/3}* and *2p_{1/2}* levels of the Co center in the **[Co^{III}(DO)(DOH)pnBr₂]** coordination sphere. As well, the signature of the phosphonic acid anchor of **Co_{C11P}** is observed (Figure IV.17, bottom right), with a peak centered at 131.9 eV and accounting for the P *2p* core levels.
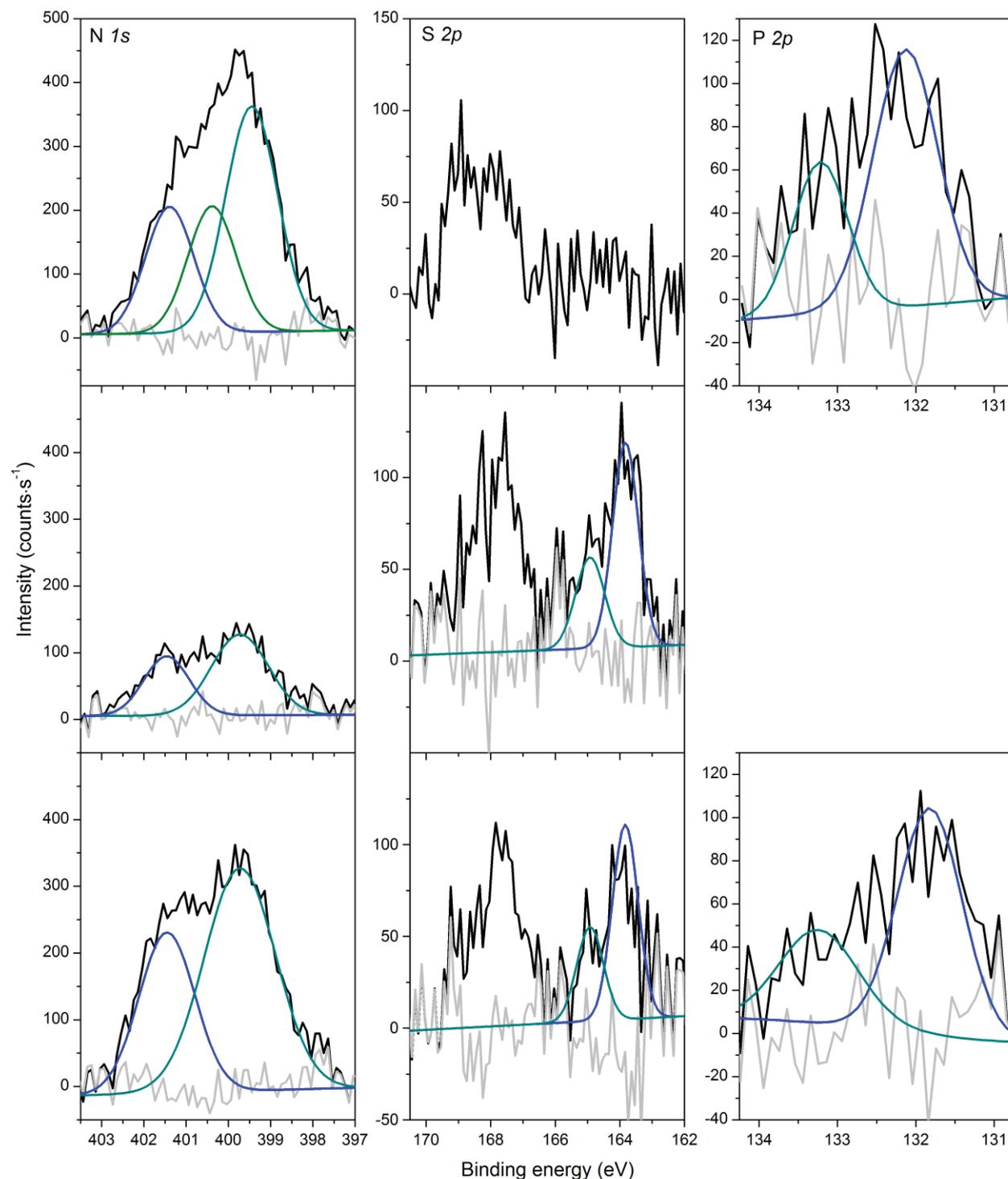
Figure IV.17. XPS analyses of the **NiO-Co$_{C11P}$** (top), **NiO-TPAT$_2$NMI** (middle) and **NiO-TPAT$_2$NMI-Co$_{C11P}$** (bottom) electrodes at the baseline-corrected N *1s* (left), S *2p* (middle) and P *2p* (right) core levels. Black lines: baseline corrected spectra; blue, cyan, olive and green lines: fitted deconvolutions; gray lines: residual backgrounds.

In general, the peaks attributed to **Co$_{C11P}$** are less intense at the **NiO-TPAT$_2$NMI-Co$_{C11P}$** electrode than at the **NiO-Co$_{C11P}$** electrode. This observation is consistent with a lower surface density of the cobalt complex at the co-grafted electrode. From the area of the Co *2p$_{3/2}$* peaks at

the **NiO-Co$_{C11P}$** electrode and the **NiO-TPAT$_2$NMI-Co$_{C11P}$** electrode, a relative Co loading ratio might be roughly estimated at 1.7:1. Such ratio is quite in line with the comparison obtained from electrochemistry, which also suggests that about half of the attached **Co$_{C11P}$** derivatives are displaced at the second step of the sequential immobilization.
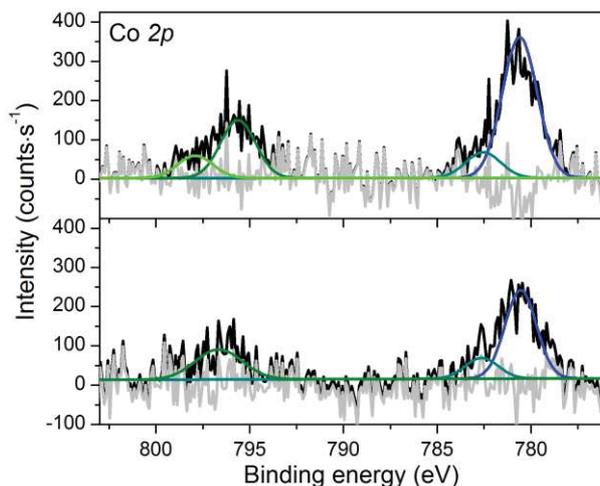
Figure IV.18. XPS analyses of the **NiO-Co$_{C11P}$** (top) and **NiO-TPAT$_2$NMI-Co$_{C11P}$** (bottom) electrodes at the baseline-corrected Co *2p* core levels. Black lines: baseline corrected spectra; blue, cyan, olive and green lines: fitted deconvolutions; gray lines: residual backgrounds.

Besides, the S *2p* signal assigned to the sulfur atoms of **TPAT$_2$NMI** is seen at the **NiO-TPAT$_2$NMI-Co$_{C11P}$** electrode (Figure IV.17, bottom middle). This feature indicates that the PS is present on the surface, as expected after the second step of the sequential immobilization. The intensity of this peak was decreased compared to that of the control **NiO-TPAT$_2$NMI** electrode (Figure IV.17, center). The integration of the peak does not evidence a noticeable difference in dye loading on **NiO-TPAT$_2$NMI-Co$_{C11P}$** compared to the control electrode. By contrast, UV-visible spectroscopy indicated that only 43% of the grafting density in PS observed at **NiO-TPAT$_2$NMI** was reached on the co-grafted electrode. Such ambiguity might originate from an inhomogeneous repartition of the PS within the NiO film, since XPS only probes the top layer (*ca* 5 nm here), whereas UV-visible spectroscopy scans the whole thickness of the film.

The analysis at the N *1s* core level for **NiO-TPAT$_2$NMI-Co$_{C11P}$** displays a large peak centered at 399.8 eV (Figure IV.17, bottom left). This peak is likely a shared signature of the N atoms in **Co$_{C11P}$** (Figure IV.17, top left) and in **TPAT$_2$NMI** (Figure IV.17, middle left).

To conclude, the XPS analysis shows that features accounting for both the **Co$_{C11P}$** complex and the **TPAT$_2$NMI** dye are present at the co-sensitized electrode. Interestingly, the signal corresponding to **Co$_{C11P}$** is less marked compared to the one observed on the **NiO-Co$_{C11P}$** control electrode, which also suggests a partial displacement of **Co$_{C11P}$** upon immobilization of **TPAT$_2$NMI**.

2.4.1.4. ToF-SIMS

ToF-SIMS characterizations were also realized for this series of electrodes.

The analysis was first performed at the **NiO-TPAT₂NMI** electrode. The spectrum in the positive mode displays noteworthy fragments at high molecular mass (Figure IV.19).
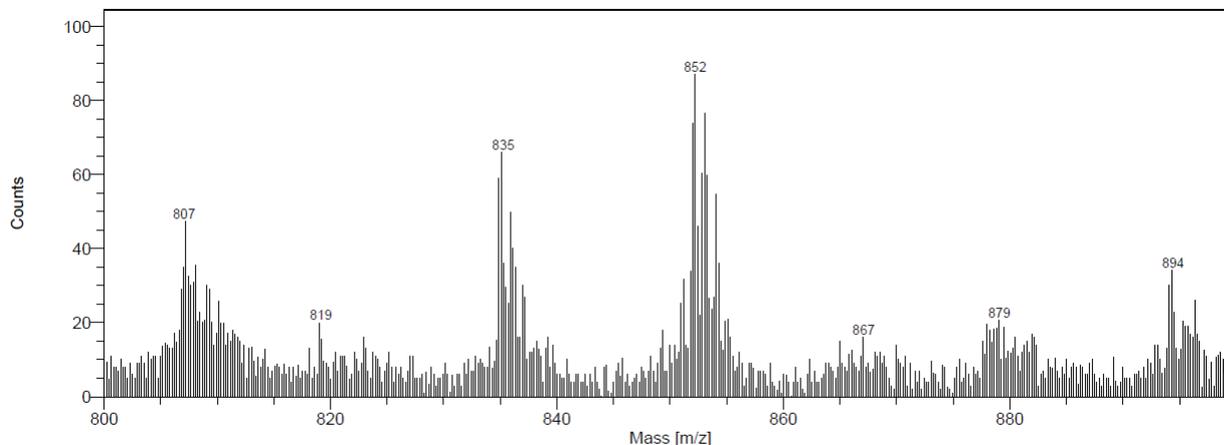

Figure IV.19. ToF-SIMS analysis at the surface of a **NiO-TPAT₂NMI** electrode, recorded in the positive mode at m/z between 800-900.

A broad pattern centered at m/z = 852 is a clear indication of the molecular ion **[TPAT₂NMI]⁺** of exact mass 852.23 g·mol⁻¹ (Figure IV.20, left). Additional features around m/z = 835 and 807 respectively correspond to the loss of an hydroxyl group from a carboxylic moiety yielding the **[TPAT₂NMI – OH⁻]⁺** fragment (835.23 g·mol⁻¹) and to a further decarbonylation giving the **[TPAT₂NMI – OH⁻ – CO]⁺** one (807.24 g·mol⁻¹), as shown in Figure IV.20, left.

The **[TPAT₂NMI]⁺** molecular ion monitored at m/z = 852 is protonated at the carboxylate ends. Although, a protonation in the source of the mass spectrometer cannot be ruled out, this observation might point that some of the dye units are physisorbed or binding *via* H-bonds to the NiO surface. But this signature also demonstrates that the molecular structure of the PS has been conserved during the process of grafting.

The **NiO-TPAT₂NMI-Co_C11P** co-grafted electrode displays a similar set of peaks at high m/z (around 852 and 835), as depicted in Figure IV.21, top, in line with the backbone of **TPAT₂NMI**. Interestingly, the massifs attributed to the **Co_C11P** complex (see Chapter III.3.2.1.2) are also present. The peaks at m/z around 650, 627 and 570 (Figure IV.21, middle and bottom) have been attributed to fragmentations of the immobilized **Co_C11P** complex, recalled in Figure IV.20, right. Thus, the sensitization with **TPAT₂NMI** is believed not to alter the attached **Co_C11P** catalysts on a structural point of view.

The detection of the preserved molecular backbones of both the dye and the catalyst at the co-grafted electrode indicates the successful co-immobilization process, which further supports the strategy followed.
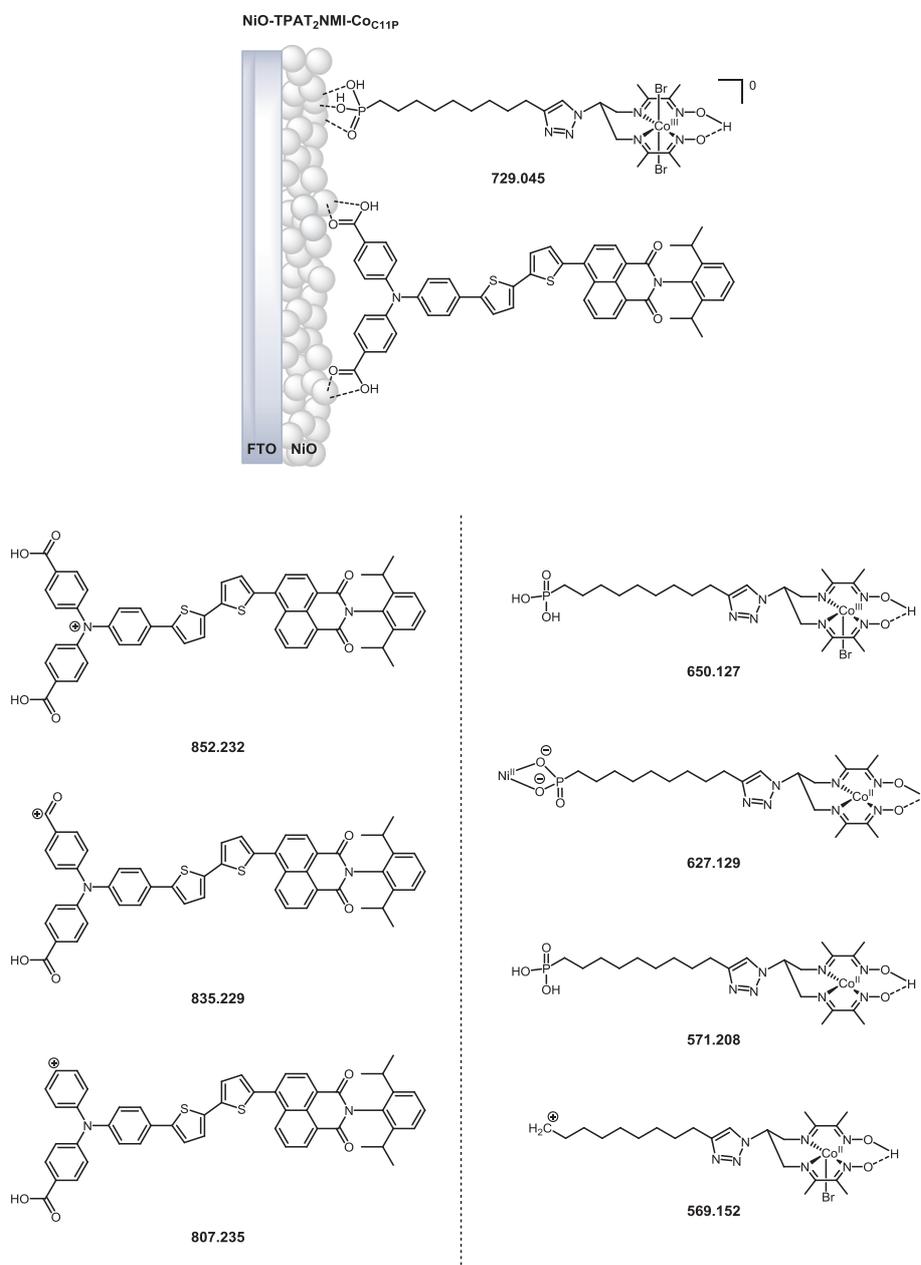

Figure IV.20. Proposed fragments for the attribution of peaks on the ToF-SIMS positive mode analysis at a **NiO-TPAT₂NMI** (bottom left) and a **NiO-TPAT₂NMI-Co_C11P** (top, bottom left and right) electrodes. Figures indicate the exact mass of considered compounds; for the sake of clarity the charges of the compounds have been omitted and, unless otherwise noted, are all equal to +1.
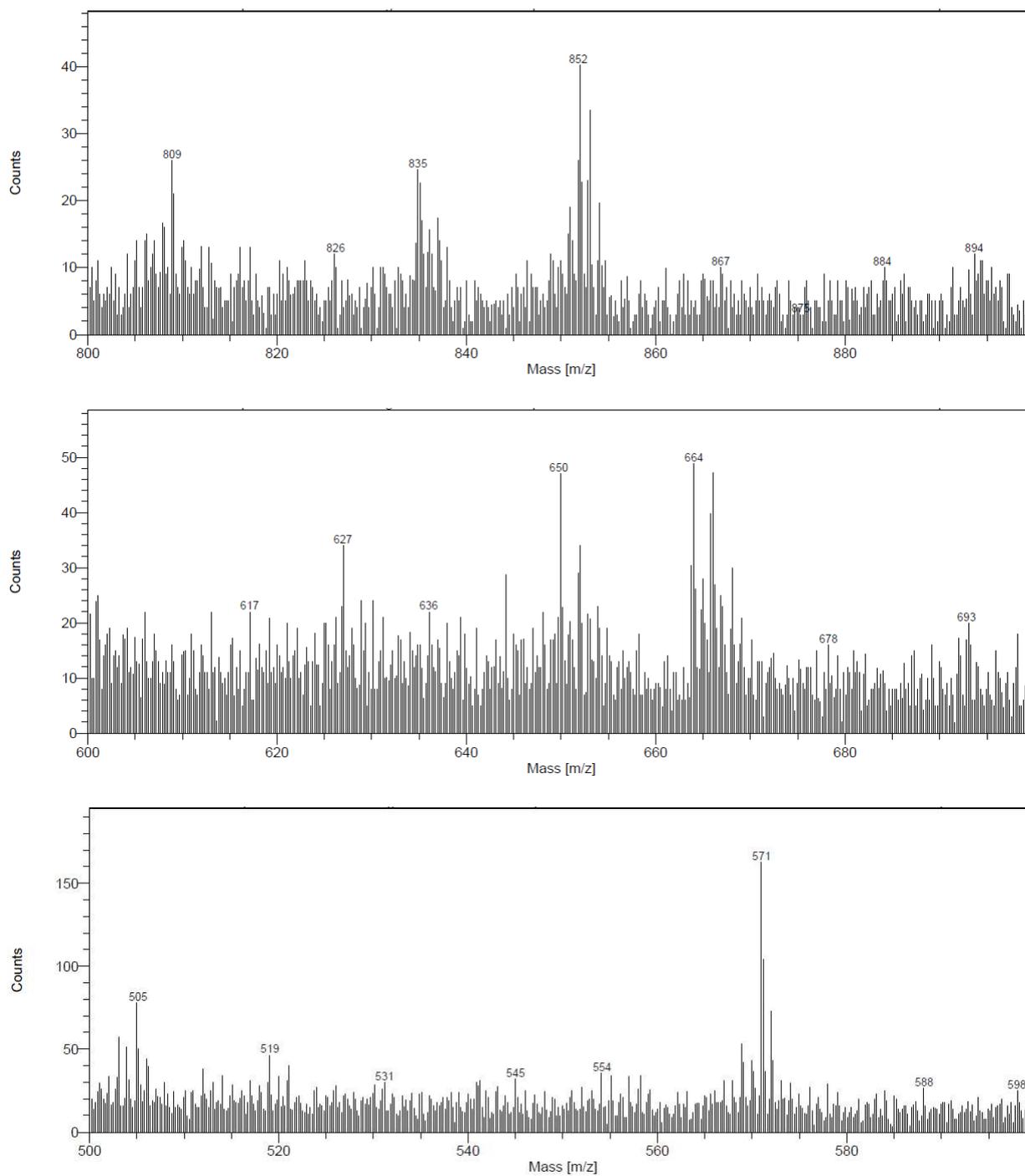
Figure IV.21. ToF-SIMS analysis at the surface of a **NiO-TPAT₂NMI-Co$_{C11P}$** electrode, recorded in the positive mode at m/z between 800-900 (top), 600-700 (middle) and 500-600 (bottom).

2.4.2. **NiO-RuP₄-Co_C11P** electrodes

A similar scheme of characterization was achieved during the construction of **NiO-RuP₄-Co_C11P** electrodes. As many features are redundant, the description will be conducted more briefly. We note that the surface mass spectroscopic analysis was also performed on this series of electrodes but will not be detailed here. Indeed, the processing of the results is still ongoing to find the correct fragmentation pathways, especially for the attached **RuP₄** moiety, although some of the fragments observed are in agreement with the intact molecular structures of both the dye and the catalyst.

2.4.2.1. Electrochemistry

The CV of the **NiO-RuP₄-Co_C11P** electrode in the cathodic region is shown in Figure IV.22, left (red line). The signature is ill-defined with a reduction event displaying a peak at *ca* −0.47 V *vs* NHE and a sluggish reoxidation around −0.22 V *vs* NHE. The origin of the low resolution has been explained above (see Chapter IV.2.4.1.1). This badly resolved event is ascribed to the Co$^{II/I}$ couple of the immobilized **Co_C11P**. A quite rough estimate of the loading in **Co_C11P** at the **NiO-RuP₄-Co_C11P** electrode gives a value of 1 nmol·cm^{-2}, consistent with that observed on the **NiO-TPAT₂NMI-Co_C11P** electrode and *ca* half of the density on **NiO-Co_C11P**.
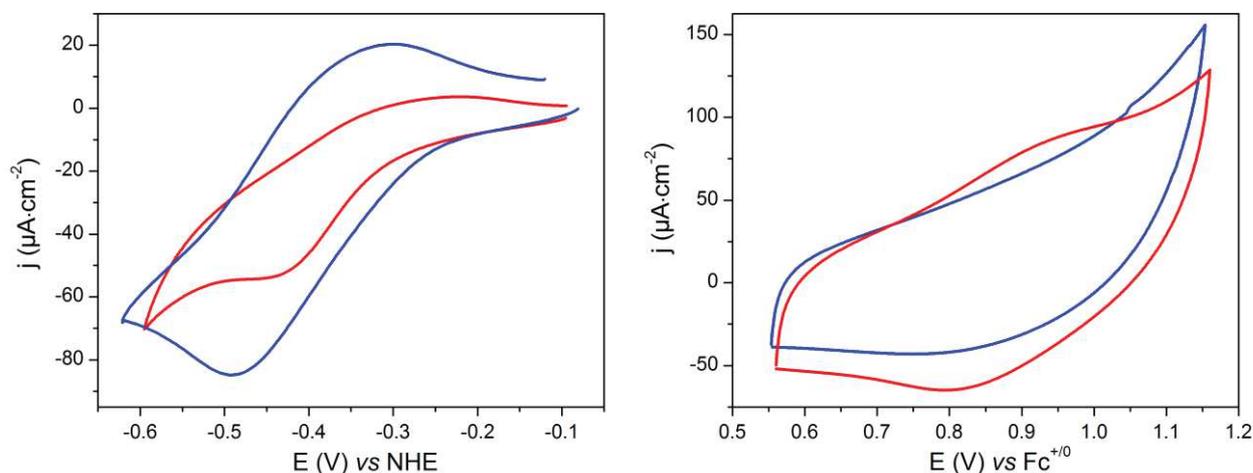

Figure IV.22. CVs at the **NiO-Co_C11P** (blue lines) and the **NiO-RuP₄-Co_C11P** (red lines) electrodes recorded in NaCl 0.1 M aqueous electrolyte (left) and in *n*Bu₄NBF₄ 0.1 M MeCN electrolyte (right) at a scan rate of 10 mV·s^{-1}.

Interestingly, after immobilization of the **RuP₄** PS, a redox wave is seen in the anodic regime at about 0.87 V *vs* Fc$^{+/0}$, when the electrochemistry is recorded in acetonitrile (Figure IV.22, right). By comparison with the signature at the control **NiO-RuP₄** electrode (not shown), this wave is attributed to the Ru$^{III/II}$ couple of the anchored **RuP₄** species. The potential of this wave is also in good agreement with the one of the **RuPEt₄** protected version in homogeneous solution

(0.86 V *vs* RHE, see Chapter IV.2.1.3.2). This point speaks in favor of a moderate impact of the deprotection and the surface anchoring of the phosphonic acid groups on the electronic levels of the Ru(bpy)$_3$ core. Such behavior might be explained by an electronic decoupling of the phosphonic acid from the bipyridine aromatic rings, provided by the interstitial CH$_2$ group. From this wave, the surface density in **RuP$_4$** at the **NiO-RuP$_4$-Co$_{C11P}$** electrode was approximatively determined as 3-3.5 nmol·cm^{-2}.

2.4.2.2. UV-visible spectroscopy

The differential UV-visible spectrum of **NiO-RuP$_4$** (Figure IV.23, orange line) displays a broad peak with a maximum centered at 460 nm ($A^{electrode}$(460 nm) = 0.457). This peak is attributed to the MLCT process at the immobilized **RuP$_4$** PS by comparison with the spectrum of **RuPEt$_4$** in solution (see Chapter IV.2.1.3.2). The maximum of this peak is barely shifted in regard to the one of the homogeneous system (457 nm). This observation corroborates the minute influence of the modifications on the phosphonic acid groups, *i.e.* deprotection and grafting, on the energetic levels at the Ru(bpy)$_3$ center.

The amount of PS loaded on the **NiO-RuP$_4$** electrode is estimated through Eqn. IV.1 to be of 28.0 nmol·cm^{-2}. This amount is quite close to the one in **TPAT$_2$NMI** at the **NiO-TPAT$_2$NMI** electrodes (24.1 nmol·cm^{-2}), although the two PSs feature different structures and binding groups.
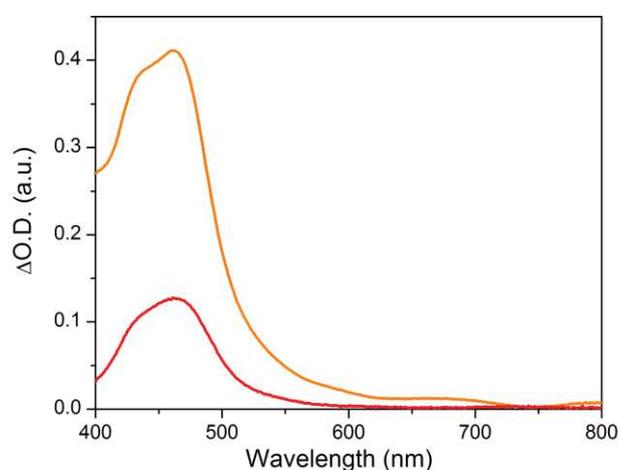

Figure IV.23. UV-visible spectra of the **NiO-RuP$_4$-Co$_{C11P}$** electrode after subtraction of the spectra of the **NiO-Co$_{C11P}$** electrode (red line) and of the **NiO-RuP$_4$** electrode after subtraction of the spectra of the pristine **NiO** electrode (orange line).

The spectrum recorded after the second step of the sequential immobilization at **NiO-RuP$_4$-Co$_{C11P}$** is shown in Figure IV.23 (red line). The band attributed to **RuP$_4$** also displays a maximum at 460 nm but in lower intensity ($A^{electrode}$(460 nm) = 0.127) compared to the **NiO-RuP$_4$** electrode. The grafting density estimated from the UV-visible spectrum of **NiO-RuP$_4$-Co$_{C11P}$** is in that case

about 8.7 nmol·cm^{-2}, which is only 28 % of that observed at the control **NiO-RuP$_4$** electrode. We notice that this value differs from the one reported by electrochemistry (3-3.5 nmol·cm^{-2}). The detection of smaller amounts of **RuP$_4$** by electrochemistry can be explained considering that not all the **RuP$_4$** units grafted on the mesoporous NiO layer are electrochemically addressable. Such statement was also made on other TCO surfaces decorated with coloured redox probes.[23]

Still, similarly to the behavior observed on **NiO-TPAT$_2$NMI-Co$_{C11P}$**, the data from electrochemistry and UV-visible spectroscopy collectively suggest that a competition for binding at the surface of NiO also occurs between **Co$_{C11P}$** and **RuP$_4$**.

2.4.2.3. XPS analysis

The XPS analysis includes the **NiO-RuP$_4$** and **NiO-RuP$_4$-Co$_{C11P}$** electrodes at the N *1s*, P *2p* and Ru *3d$_{5/2}$* regions (Figure IV.24).

In the N *1s* region, the **NiO-RuP$_4$** electrode displays a peak that can be split into two contributions, at 399.9 and 401.4 eV (Figure IV.24, middle left). The major feature at 399.9 eV is ascribed to the *1s* level of the N atoms on the bipyridine ligands.[24] The smaller contribution at 401.4 eV is possibly indicative of a different chemical environment or of an exogenous N contaminant.

The P *2p* core levels of **NiO-RuP$_4$** show a signature centered at 132.4 eV (Figure IV.24, centre). The deconvolution of this signal gives two peaks of energy 132.0 and 133.0 eV, separated from 1.0 eV and in a 2:1 ratio, thus accounting for the P *2p$_{3/2}$* and P *2p$_{1/2}$* levels. Such signal is then ascribed to the P atoms of the phosphonic acid moieties on **RuP$_4$**. We note that the binding energy of this signal is quite comparable to that observed for the phosphorous of the **Co$_{C11P}$** complex attached onto NiO (Figure IV.24, top middle). This point can suggest that the **RuP$_4$** is anchored to the NiO substrate in a similar fashion. Binding through the four phosphonic acid groups of **RuP$_4$** is, however, unlikely. Thus, at least two different contributions for P *2p* levels might be expected, mirroring chemically inequivalent phosphorous atoms of the NiO-linked phosphonates and the free phosphonic acids. Yet, at the resolution of the spectrum, we could not differentiate these two chemical environments.

The Ru *3d$_{5/2}$* region of **NiO-RuP$_4$** contains a peak at 280.8 eV (Figure IV.24, middle right). A similar signature has been observed for a related Ru(bpy)$_3$-like complex immobilized onto NiO and ascribed to the *3d$_{5/2}$* core level of the Ru^{II} metallic center.[14a] Thus, we attributed this signature to the Ru^{II} core of the attached **RuP$_4$**. We note that the signal of the Ru *3d$_{3/2}$* level could not be straightforwardly exploited since their contribution is hidden in the intense peak corresponding to

the C *1s* core levels at *ca* 285 eV. A peak at 462.2 eV was also analyzed (not shown) that matches with the Ru *3p3/2* core level.
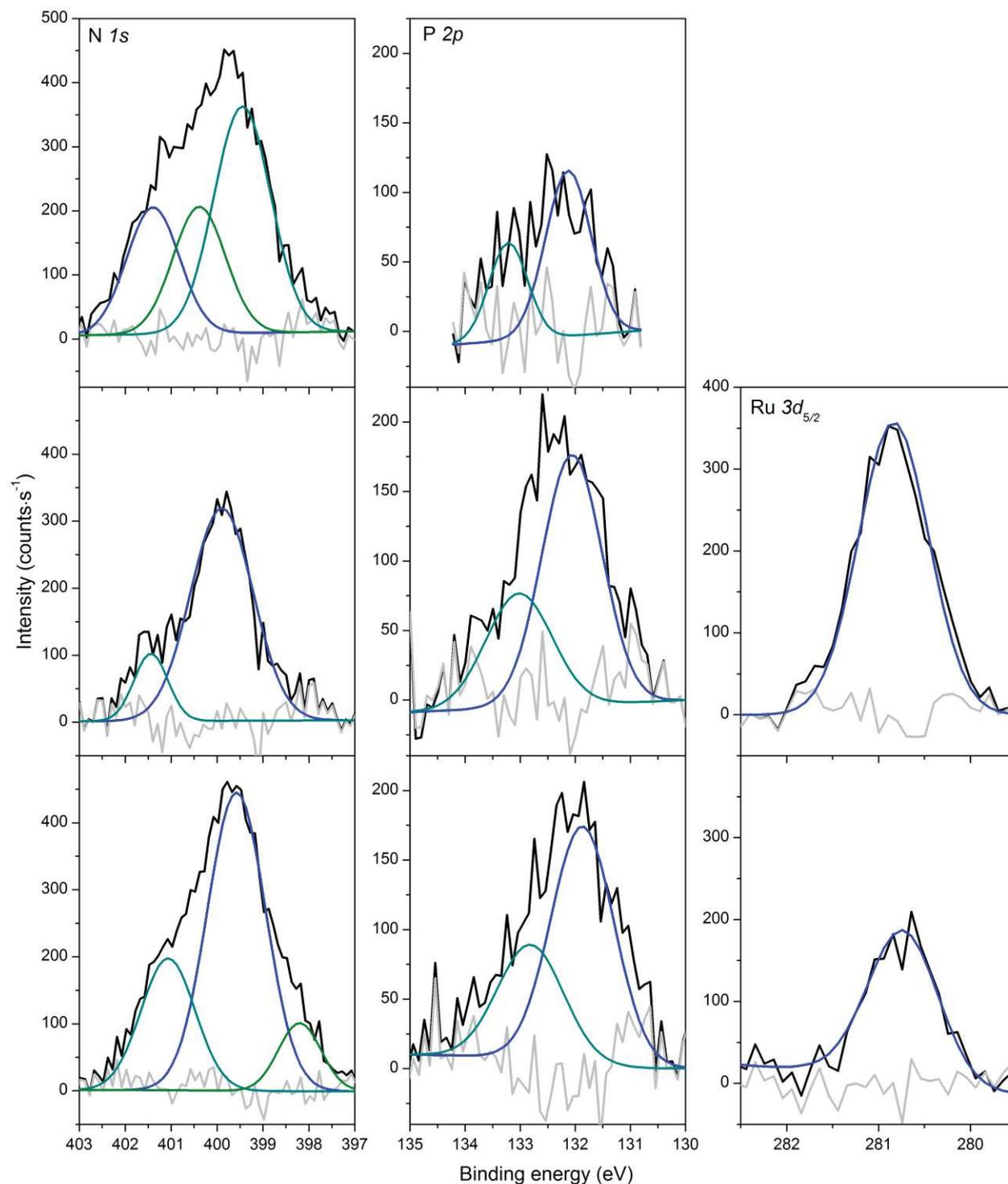

Figure IV.24. XPS analyses of the **NiO-Co$_{C11P}$** (top), **NiO-RuP$_4$** (middle) and **NiO-RuP$_4$-Co$_{C11P}$** (bottom) electrodes at the baseline-corrected N *1s* (left), P *2p* (middle) and Ru *3d$_{5/2}$* (right) core levels. Black lines: baseline corrected spectra; blue, cyan, olive and green lines: fitted deconvolutions; gray lines: residual backgrounds.

An atomic ratio of 1:3.6:6.9 for Ru/P/N could be estimated at the surface of the **NiO-RuP₄** electrode. This ratio is generally in agreement with the calculated one expected from the molecular structure (1:4:6), although this estimation is subject to caution.

At the **NiO-RuP₄-Co_{C11P}** electrode, the Co $2p_{3/2}$ and $2p_{1/2}$ levels (Figure IV.25, bottom) display a signature in consistent with the one observed at the **NiO-Co_{C11P}** electrode (Figure IV.25, top) and thus attributed to the grafted **Co_{C11P}** species. But again, the intensity is decreased upon immobilization of the PS (about 20 % less).
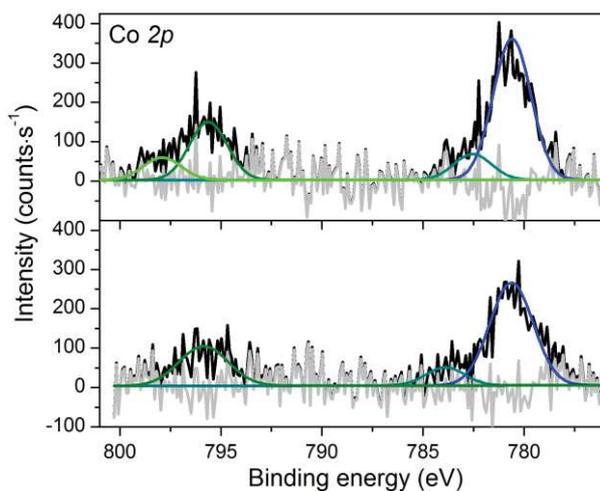
Figure IV.25. XPS analyses of the **NiO-Co_{C11P}** (top) and **NiO-RuP₄-Co_{C11P}** (bottom) electrodes at the baseline-corrected Co $2p$ core levels. Black lines: baseline corrected spectra; blue, cyan, olive and green lines: fitted deconvolutions; gray lines: residual backgrounds.

The signals for the N $1s$ and P $2p$ levels (Figure IV.24, bottom left and middle) show convoluted contributions from the P and N atoms of both **RuP₄** and **Co_{C11P}**. The respective contributions could not be differentiated within the accuracy of the measurement.

Finally, on the co-grafted electrode, the signature attributed to the Ru^{II} center in **RuP₄** is also observed (Figure IV.24, bottom right). The peak is although less intense than for the **NiO-RuP₄** control electrode. This observation once again indicates that the surface density of **RuP₄** at the NiO layer is less important at the **NiO-RuP₄-Co_{C11P}** electrode. However, the density in **RuP₄** is here found around 50% of that at **NiO-RuP₄** whereas the UV-visible spectroscopy gave 28 %. The divergence between the two techniques is similar as that seen on **NiO-TPAT₂NMI-Co_{C11P}**.

Still, the analyses perfomed at the **NiO-RuP₄-Co_{C11P}** electrode all together indicate the successful construction of a co-grafted structure.

2.5. Performance

The performances of the photocathodes were finally assessed through PEC measurements. We present here the main results obtained with the **NiO-TPAT$_2$NMI-Co$_{C11P}$** series of electrodes as well as some preliminary ones obtained with the **NiO-RuP$_4$-Co$_{C11P}$** series.

The functional characterizations were performed in a first step by potential sweep techniques. Then, chronoamperometric measurements coupled to H$_2$ detection are realized.

The attached **[Co^{III}(DO)(DOH)pnCl$_2$]** complex was proven to have enhanced activity for hydrogen evolution in an acetate buffer at pH 4.5.[25] Yet, we observed that the anchoring of **Co$_{C11P}$** was not stable enough at the surface of NiO in such acidic media (see Chapter III.3.2.2.2). At the same time, the immobilized catalyst does not turn over for proton reduction in neutral media, as demonstrated above (see Chapter III.3.2.2.1) and in previous work.[25-26]

To find a balance between these two counter-acting effects, we decided to work at an intermediate pH. Hence, all the photoelectrochemical experiments were recorded in a 2-(N-morpholino)ethanesulfonic acid (MES) 0.1 M / NaCl 0.1 M aqueous buffer at pH 5.5. We note that under aqueous homogeneous photocatalytic conditions, the cobalt diimine-dioxime catalyst was proven to turn over at pH 5-6.[26-27] Also, the use of an aqueous MES buffer (pH 6) for photoelectrocatalytic experiments at **P1**-sensitized NiO electrodes leads to the establishment of stable cathodic photocurrents.[28]

2.5.1. **NiO-TPAT$_2$NMI-Co$_{C11P}$** electrodes

As for the structural characterizations, the performances of the **NiO-TPAT$_2$NMI-Co$_{C11P}$** electrodes have been assessed along with the ones of the **NiO-TPAT$_2$NMI** electrodes.

2.5.1.1. Photoelectrochemistry

The **NiO-TPAT$_2$NMI** electrode was swept from anodic to cathodic potentials (0.70 to −0.19 V *vs* NHE *i.e.* 1.01 to 0.14 V *vs* RHE) in the dark or under irradiation (Figure IV.26, left). In the dark, cathodic background currents are observed with a large wave at *ca* 0.58 V *vs* NHE. For the same experiment but performed under light irradiation (Figure IV.26, left), a cathodic photocurrent develops on this wave from 0.60 V *vs* NHE. The onset potential of the photocurrent actually reflects the point from which light-driven hole injection in the NiO can occur. In particular, this potential is located slightly below the edge of the VB, estimated at 0.46 V *vs* NHE at pH 5.5 by a Nernstian correction in pH from ref[18a].
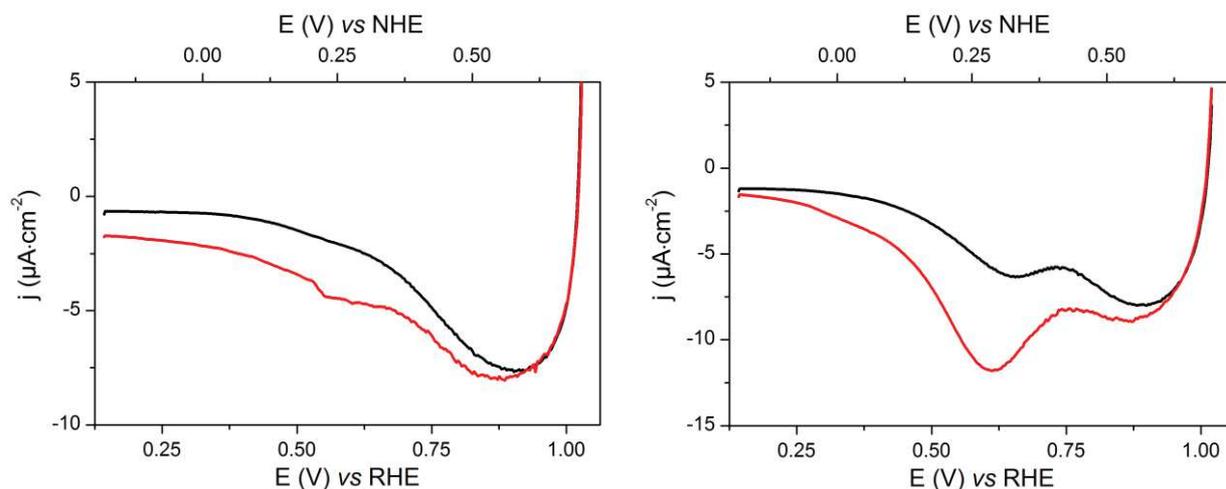
Figure IV.26. LSVs at the **NiO-TPAT₂NMI** (left) and **NiO-TPAT₂NMI-Co$_{C11P}$** (right) electrodes recorded in the dark (black lines) or under light irradiation (red lines) in a MES 0.1 M/NaCl 0.1 M aqueous buffer (pH 5.5) at a scan rate of 1 mV·s⁻¹.

By subtracting the dark current from the current under irradiation, the relative photocurrent density can be calculated. The values lay in the −0 to −2 µA·cm⁻² range over the scanned window of potentials (Figure IV.27).
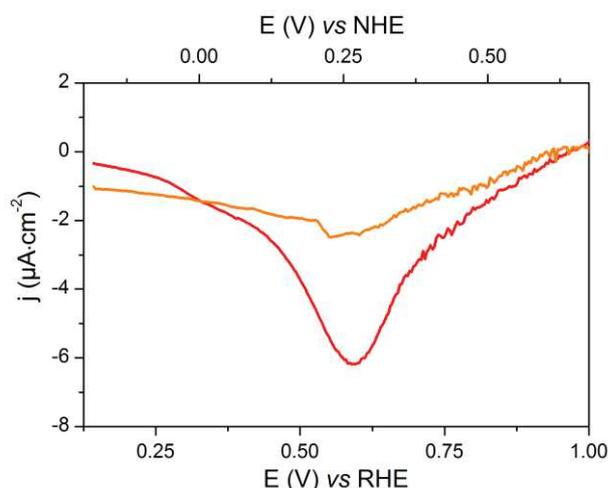
Figure IV.27. Relative photocurrent densities as a function of the potential at the **NiO-TPAT₂NMI** (orange line) and **NiO-TPAT₂NMI-Co$_{C11P}$** (red line) electrodes in a MES 0.1 M/NaCl 0.1 M aqueous buffer (pH 5.5) at a scan rate of 1 mV·s⁻¹.

The **NiO-TPAT₂NMI-Co$_{C11P}$** electrode was investigated in a similar fashion (Figure IV.26, right). In the absence of light, a large cathodic wave at ca 0.58 V *vs* NHE is observed, in a similar way to that monitored on **NiO-TPAT₂NMI**, and we have attributed that wave to the reduction of Ni^{III} surface sites (see Chapter I.2.2.2.1.2). A second, less marked wave is seen at 0.34 V *vs* NHE (0.66 V *vs* RHE), which is not present at the control electrode. This process is possibly ascribed to the Co^{III} to Co^{II} reduction of **Co$_{C11P}$** as also observed on **TiO₂-Co$_{C11P}$** (0.25 V *vs* NHE at pH ~ 6.4 *i.e.* 0.63 V *vs* RHE, see Chapter III.2.2.3.3).

Under irradiation, a cathodic photocurrent builds up when the electrode is irradiated. The onset is located at about 0.63 V *vs* NHE, slightly anodically moved (30 mV) from the one at the **NiO-TPAT₂NMI** electrode. A similar shift of the onset potential has been reported by Wu and co-workers upon bridging a cobaloxime catalyst to a surface-anchored Ru(bpy)₃-like PS (see Chapter I.2.2.3.2).[14a] These authors tentatively ascribed the shift of the onset photocurrent to the possible electron transfer from the PS to the catalyst at the co-sensitized electrode.

For **NiO-TPAT₂NMI-Co_{C11P}** the photocurrent features a sharp wave of maximal current density -11.8 µA·cm^{-2} at 0.29 V *vs* NHE. This wave is not displayed at the **NiO-TPAT₂NMI** electrode. As a result, we attribute this wave to the presence of **Co_{C11P}** at the surface of the **NiO-TPAT₂NMI-Co_{C11P}** electrode. The event translates in a maximal relative photocurrent density of -6.2 µA·cm^{-2} at 0.27 V *vs* NHE *i.e.* 0.59 V *vs* RHE (Figure IV.27).

Finally, when potentials are swept more cathodically, the photocurrent densities diminish and nearly reach dark current values (-1.2 µA·cm^{-2}) at -0.19 V *vs* NHE.

Collectively, the data from LSVs with or without light irradiation demonstrate that the presence of the co-grafted **Co_{C11P}** complex at the surface enhances the cathodic photocurrent at the electrode. This observation suggests that a light-driven electron transfer occurs between NiO and the catalyst, permitted through the photoexcitation of the dye. The process thus likely permits the reduction of the bound **Co_{C11P}** entity. The next step was to identify if such photoelectroreduction can lead to hydrogen evolution.

2.5.1.2. Chronoamperometric measurements

We conducted photoelectrocatalytic experiments in a closed electrochemical cell. The potential is set at a given value and light is shined on the **NiO-TPAT₂NMI-Co_{C11P}** sample. During this measurement, a Clark micro-electrode records the concentration of hydrogen in solution. As well, aliquots of the headspace of the electrochemical cell are analyzed by GC at the end of the chronoamperometry to check for hydrogen gas.

To optimize the photocurrent, we fixed the potential to values close to the maximum of the relative photocurrents curve (Figure IV.27). In a first attempt, such an experiment was realized at 0.49 V *vs* RHE and the results are shown in Figure IV.28.

At start, the electrode is left to equilibrate in the dark for 650 s, during which no hydrogen production is detected (Figure IV.28). This observation is however expected since in the absence of an external driving force, the electrode poised at a potential *more positive than RHE* cannot generate hydrogen.

Then, light is switched on and a cathodic photocurrent develops. This photocurrent spikes at $-7.4\ \mu A \cdot cm^{-2}$, then decays to reach about $-2\ \mu A \cdot cm^{-2}$ after 600 s (Figure IV.28, top left). This first period is likely attributed to capacitive phenomena at the NiO VB occurring upon irradiation. Accordingly, no hydrogen is observed during this period (Figure IV.28, top right). Following this first stage, the photocurrent slowly decreases until 22 000 s where it stabilizes around $-0.5\ \mu A \cdot cm^{-2}$ (Figure IV.28, bottom left).
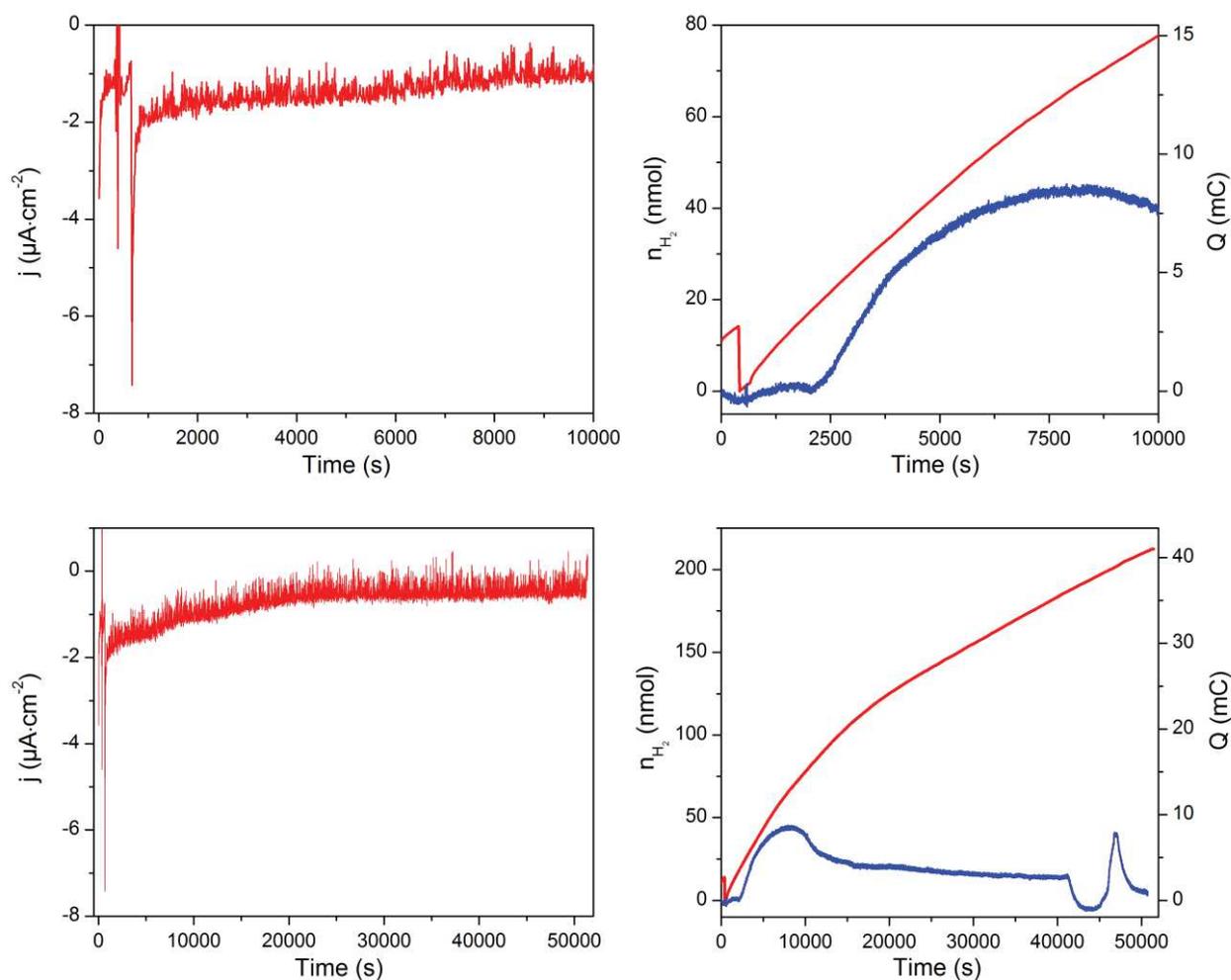
Figure IV.28. Current density (left), charge passed (right, red lines) and H_2 produced as monitored by the Clark microsensor (right, blue lines) during the first 10 000 s (top) and the whole measurement time (bottom) of an electrolysis at the **NiO-TPAT₂NMI-Co$_{C11P}$** electrode recorded under light irradiation at an applied potential of 0.49 V vs RHE, in a MES 0.1 M/NaCl 0.1 M aqueous buffer (pH 5.5). On the graphs on the right, scales are adjusted so that the superimposition of both curves would correspond to 100% faradaic efficiency. The sharp shift in the amount of charges passed observed at about 400 s (top right) is due to a brief adventitious issue in the electrical connection of the working electrode.

From ca 1 400 s after the irradiation has been started, the hydrogen concentration in solution starts to rise, as monitored by the Clark micro-probe (Figure IV.28, top right). The hydrogen produced for the first 5 000 s follows in a good fashion the theoretical amount deduced from the charge passed, indicating a satisfactory faradaic efficiency (ca 80%). This trend steps down

afterwards and the Clark micro-sensor indentified a decrease in dissolved hydrogen after about 8 000 s (Figure IV.28, top and bottom right). Until the end of the experiment, the hydrogen concentration values slowly decay to almost return to the background values. Although the probe showed an erratic (and not understood) fluctuation around 42 000-48 000 s, the decay in the concentration of dissolved hydrogen is likely ascribed to an equilibration in the gas phase of this species.

Before stopping the chronoamperometric measurement, light is switched off and a small positive shift in current is seen, showing that the current observed until there was still photoinduced.

At the end, a GC analysis of the headspace gave an estimated 49 nmol of hydrogen present in the gas phase. This quantity correlates with an overall 23 % faradaic efficiency, quite low in comparison to the one measured by the sensor at the beginning of the experiment. We note that such figures correspond to very low values of hydrogen generated and thus detected in our GC setup. Accordingly, any leak of H_2 from the cell might have a large impact on the faradaic efficiency.

To foster the generation of hydrogen, we reproduced the same experiment but at a potential exactly centered on the maximum relative photocurrent value (0.63 V *vs* RHE, Figure IV.27). The experiment was replicated at several occurrences and the corresponding chronoamperometric measurements are displayed in Figure IV.29. For all these experiments, the initial photocurrent reaches higher value than the one observed at 0.43 V *vs* RHE. Also, in all cases, a decay over several thousands of seconds is seen.
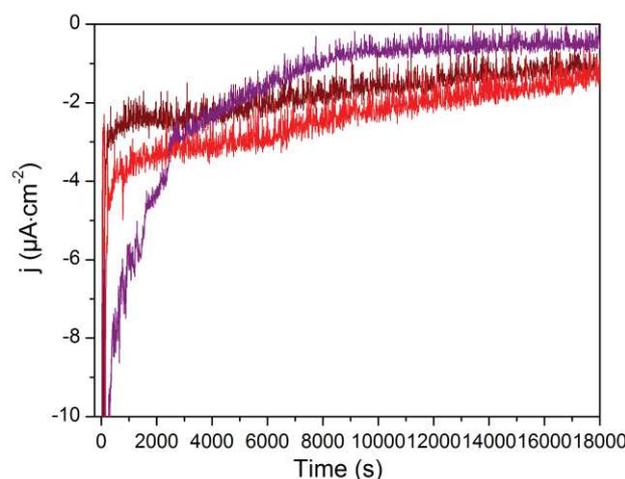

Figure IV.29. Current density *vs* time for electrolyses at different **NiO-TPAT$_2$NMI-Co$_{C11P}$** electrodes (red, purple and wine lines) recorded under light irradiation at an applied potential of 0.63 V *vs* RHE in a MES 0.1 M/NaCl 0.1 M aqueous buffer (pH 5.5). Faradaic efficiencies at the end of the irradiation by GC: 87% (purple line), 0% (wine line), not determined (red line).

Despite these common features, clear divergences appear along this series of identical experiments. Namely, the values of the photocurrents after 500 s of irradiation range between -7.3 and -2.2 $\mu A \cdot cm^{-2}$. Also, the decay period observed to reach a stable current is about 10 000 s for one sample, whereas this decay is still ongoing at the end of the experiment for the other two samples. Finally, the faradaic efficiencies measured by GC analysis at the end of the different chronoamperometric measurements are 0%, 87% and an aberrant figure (superior to 100 %). These values are indeed quite dispersed and the question of the poor reproducibility of these results in general will be discussed later. But the difference in faradaic efficiencies might tentatively be explained by an inhomogeneous distribution of the hydrogen gas in the headspace of the cell or a leak.

To gain insight in the origin of the divergence in monitored photocurrents and, possibly, hydrogen production, a control experiment was run with the **NiO-TPAT$_2$NMI** electrode that does not bear the **Co$_{C11P}$** catalyst. The photocurrent establishes at values similar to the one observed for **NiO-TPAT$_2$NMI-Co$_{C11P}$** (-3.0 $\mu A \cdot cm^{-2}$ after 500 s of irradiation) but undergoes a much faster decay (Figure IV.30) to almost reach 0 at the end of the chronoamperometry. Hydrogen evolution could be detected by GC and resulted in a 98 % faradaic yield. Hydrogen production by **NiO-TPAT$_2$NMI** is in line with a report by Mozer and co-workers, in which NiO sensitized with a similar push-pull organic dye evolves hydrogen from aqueous media under photoelectrochemical conditions (see Chapter I.2.2.3.3).[13a]
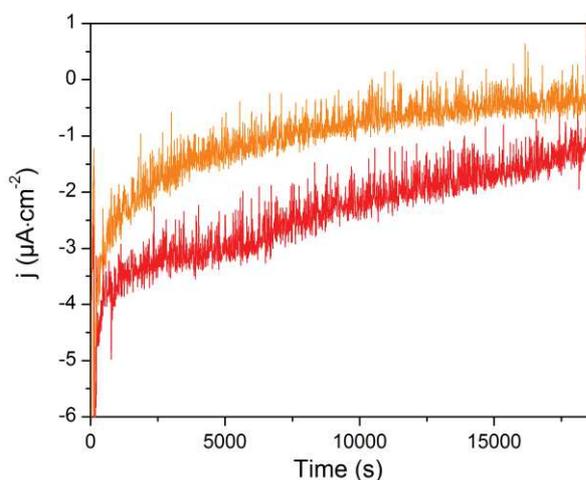

Figure IV.30. Current density *vs* time for electrolyses at the **NiO-TPAT$_2$NMI-Co$_{C11P}$** (red line) and **NiO-TPAT$_2$NMI** (orange line) electrodes recorded under light irradiation at an applied potential of 0.63 V *vs* RHE, in a MES 0.1 M/NaCl 0.1 M aqueous buffer (pH 5.5).

The faster decay in current observed on **NiO-TPAT$_2$NMI** is ascribed to a faster deactivation of the electrode. Likely, this deactivation is attributed to the light-induced degradation of the dye in the absence of a catalytic center able to rapidly extract photogenerated charges from the reduced

state of **TPAT$_2$NMI**. The deactivation process is longer on the co-sensitized electrode, which tends to demonstrate that **Co$_{C11P}$** stabilizes the electrode in acting as the catalytic entity. This point is also underlined by an improvement in relative photocurrents at the **NiO-TPAT$_2$NMI-Co$_{C11P}$** electrode compared to the **NiO-TPAT$_2$NMI** one (Figure IV.27). Thus, we postulate that the loss in photocurrent at the co-grafted electrode originates both from the degradation of the dye and a slow deactivation or leach off of **Co$_{C11P}$** from the NiO surface.

The question of the low photocurrent densities as well as the lack of reproducibility in currents and faradaic efficiencies will be further discussed at the end of this section. But overall, we could evidence here that a light-induced electron transfer from the NiO to the **Co$_{C11P}$** catalyst occurs at the irradiated **NiO-TPAT$_2$NMI-Co$_{C11P}$** electrode. Although the electrode intrinsic activity when sensitized by the dye only, the co-grafting of **Co$_{C11P}$** increases the photocurrent and its stability. Such a co-grafted architecture generates hydrogen at potentials positive to RHE under light irradiation.

2.5.2. **NiO-RuP$_4$-Co$_{C11P}$** electrodes

The electrodes sensitized with **RuP$_4$** were subjected to a preliminary series of experiments, but are still under investigation. First results are shown here.

2.5.2.1. Photoelectrochemistry

In the dark, the electrode decorated with **RuP$_4$** displays an identical electrochemical background to that observed with the electrodes dyed with **TPAT$_2$NMI**. Under irradiation, the onset photopotential of **NiO-RuP$_4$** is found at 0.47 V *vs* NHE and the relative photocurrent saturates about -2.5 μA$\cdot$cm^{-2} (Figure IV.31, left).
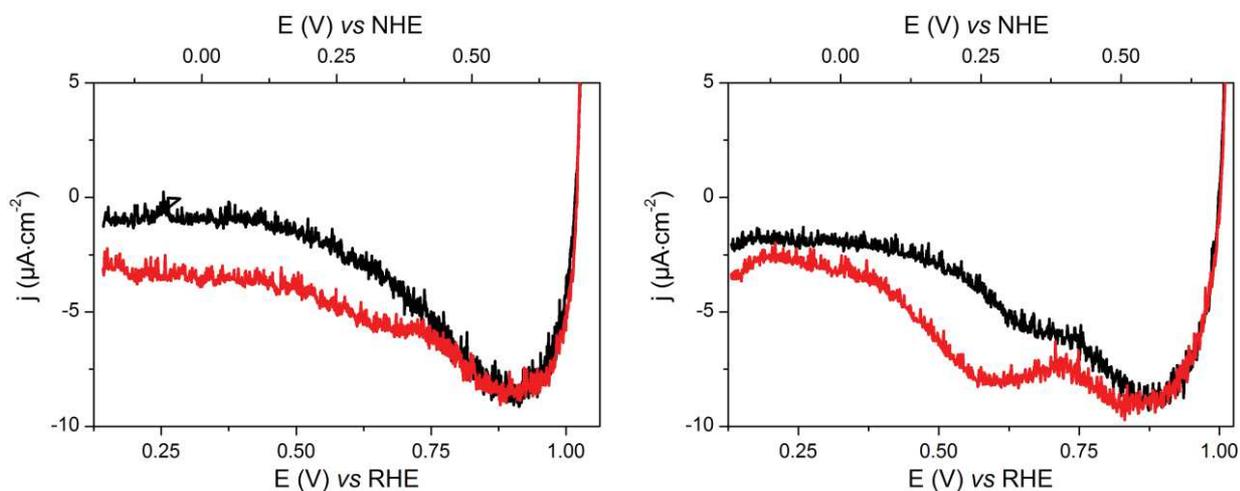

Figure IV.31. LSVs at the **NiO-RuP$_4$** (left) and **NiO-RuP$_4$-Co$_{C11P}$** (right) electrodes recorded in the dark (black lines) or under light irradiation (red lines) in a MES 0.1 M/NaCl 0.1 M aqueous buffer (pH 5.5) at a scan rate of 1 mV$\cdot$s^{-1}.

As observed for the **TPAT$_2$NMI**-decorated electrodes, the onset photopotential shifts anodically when **Co$_{C11P}$** is co-grafted on the electrode. The photocurrent starts from *ca* 0.52 V *vs* NHE and the relative photocurrent peaks at a maximal value of –4 µA·cm^{-2} at 0.23 V *vs* NHE (Figure IV.31, right), as determined by subtraction of the curve recorded in the dark from that recorded under irradiation.

Surprisingly, the onset photopotentials observed at the **RuP$_4$**-functionalized electrodes are more cathodic (110-130 mV) compared to their **TPAT$_2$NMI**-functionalized counterparts. On the basis of calculations, Pavone and co-workers recently proposed that the nature of the anchoring group (COOH or PO$_3$H$_2$) and the surface binding mode can influence the driving force of hole injection into the NiO VB. Such effects give some rationale to the observed difference in onset photopotential.[29]

2.5.2.2. *Chronoamperometric measurement*

The **NiO-RuP$_4$-Co$_{C11P}$** electrode was also submitted to a constant potential electrolysis at 0.58 V vs RHE, nearby the maximal relative photocurrent value (0.23 V *vs* NHE *i.e.* 0.55 V *vs* RHE). When light is shined, a photocurrent around −1.4 µA·cm^{-2} is established (Figure IV.32). This photocurrent is quite stable over the measurement time, still at −1.2 µA·cm^{-2} after 17 000 s.
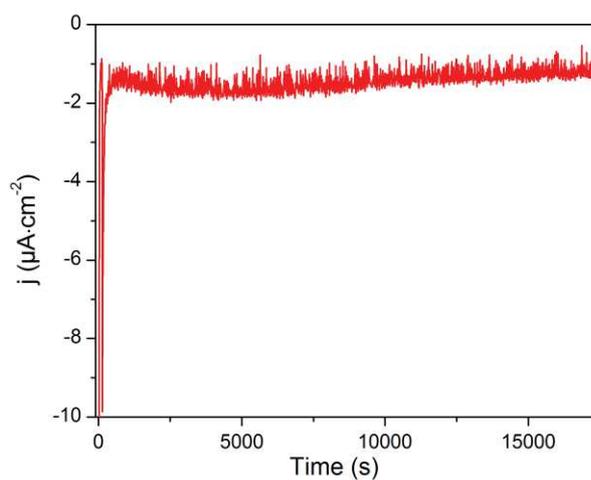

Figure IV.32. Current density *vs* time for electrolysis at the **NiO-RuP$_4$-Co$_{C11P}$** electrode recorded under light irradiation at an applied potential of 0.58 V *vs* RHE, in a MES 0.1 M/NaCl 0.1 M aqueous buffer (pH 5.5).

However, the GC analysis of the headspace did not reveal the presence of hydrogen at the end of the experiment, due to a leak observed at the cathodic part. We also note that the values of the photocurrents at **NiO-RuP$_4$-Co$_{C11P}$**, either from LSVs or from chronoamperometry, are slightly

inferior to that monitored at the **NiO-TPAT$_2$NMI-Co$_{C11P}$** electrode. These observations can indicate a less efficient photon-to-current conversion at the **NiO-RuP$_4$-Co$_{C11P}$** electrode. This phenomenon is consistent with a reduced molar absorptivity of **RuP$_4$** compared to **TPAT$_2$NMI** and the subsequent reduced absorbance of the sensitized electrode ($A^{electrode, \ max}$(**NiO-RuP$_4$-Co$_{C11P}$**) = 0.127 *vs* $A^{electrode, \ max}$(**NiO-TPAT$_2$NMI-Co$_{C11P}$**) = 0.282). Still, supplementary studies are required to better assess the activity of the **NiO-RuP$_4$-Co$_{C11P}$** electrode, especially regarding the detection of hydrogen and the comparison with the **NiO-RuP$_4$** control electrode.

2.6. Discussion and outlook

From the set of structural characterizations presented above, we could demonstrate that the attachment of a PS, **TPAT$_2$NMI** or **RuP$_4$**, along with **Co$_{C11P}$** at the surface of NiO is possible. The competition for binding at the surface leads to a shared decoration of the surface. Importantly, the molecular structures of both the dye and the catalyst are retained during the sequential immobilization pathway, as demonstrated by the XPS and ToF-SIMS (**TPAT$_2$NMI**) analyses at the co-grafted electrodes. Yet, the quantity of Co complexes grafted onto NiO is decreased roughly by a factor 2 upon sensitization of a PS and found in the 1-2 nmol·cm^{-2} range. At the same time, the surface concentration of dye reaches only between a third and a half of the value determined when the dye is attached alone on the mesoporous layer. Overall, the procedure used for co-sensitization yields higher loadings in PS than in catalyst, in a ratio found in the range 2-10. The exact balance of molecular species at the surface is still subject to caution, since the relative decrease in surface densities have been found to differ according to the analytic technique used (electrochemistry, UV-visible spectroscopy or XPS) for their estimations. Such differences might originate from the diverse properties of the attached molecules probed by these techniques. While CV can detect only electrochemically addressable moieties, the UV-visible spectroscopy pictures the whole pool of coloured units attached to the mesoporous film and XPS scans the very top surface of this film. An inhomogeneous decoration of the NiO surface could thus explain different surface coverage values found for the same immobilized molecule. Given that UV-visible spectroscopy and CV probe the whole thickness of the electrode, we believe that they lead to a more accurate estimate in surface concentrations of the bulk electrode

The position on the surface of **TPAT$_2$NMI** or **RuP$_4$** in regard to **Co$_{C11P}$** is not controlled here and has possibly a substantial influence on the electronic communication between the PS and the catalyst. But the final figure of merit for such architectures being the light-driven hydrogen evolution, they were further assessed on a functional point.

The control **NiO-TPAT$_2$NMI** and **NiO-RuP$_4$** electrodes both generate photocurrents starting from potentials nearby the edge of the NiO VB. In the case of **NiO-TPAT$_2$NMI** the photocurrent is related to the production of hydrogen in unity faradaic efficiency at 0.63 V *vs* RHE, likely occurring *via* the excited dye, and that was also observed on similar dye-sensitized NiO electrodes.[13a]

The presence of **Co$_{C11P}$** on the surface modifies the pattern of the photocurrent densities observed by LSV with the appearance of a cathodic event around 0.6 V *vs* RHE. This event might be correlated to the reduction of the catalyst at the Co^I state that is permitted at such oxidative potential through the photo-excited dye. Intriguingly, at potentials more cathodic, the relative photocurrent values nearly reach back 0 µA·cm^{-2}. This observation differs from other reported examples of NiO-based molecular photocathodes,[13-14] which usually sustain the photocurrent densities at negative potentials. As this feature is more marked on co-grafted electrodes, such behavior can tentatively be attributed to the **Co$_{C11P}$** derivative. We therefore postulate that this behavior pictures recombination processes fostered by the Co redox center, e.g. between an electron transferred from the excited dye to the catalyst and relaxed holes present at the top of the VB under the cathodic applied potential.

However, at potentials positive to RHE, the co-grafted **NiO-TPAT$_2$NMI-Co$_{C11P}$** electrode displays steady-state photocurrents that are catalytic for hydrogen evolution and enhanced compared to those observed at the control **NiO-TPAT$_2$NMI** electrode. This effect is noteworthy since **NiO-TPAT$_2$NMI-Co$_{C11P}$** is loaded with less than half of the dyes present on **NiO-TPAT$_2$NMI** (43 %). Such point further supports that the attached **Co$_{C11P}$** actually partakes in improving the photoelectrocatalytic currents for proton reduction.

Still, the poor reproducibility of photocurrents and faradaic efficiencies in such photoelectrocatalytic experiments is unclear and might originate from two aspects.

The first one is innate to the preparation of the electrodes. Among others, as said above, the procedure used to co-sensitize the electrodes does not permit to rule the respective placement between the catalyst and the dye at the surface. Especially, some preferential grafting sites can generate inhomogeneities in the surface coverage and create irregular dye and/or catalyst loadings that would differ from an electrode to another. A mapping of the surface, as performed *via* resonance Raman on model dye-sensitized NiO electrodes,[12] could give information in that regard.

The second set of causes arises from the setup of the experiments. Indeed, we have observed that the electrochemical signature of the attached **Co$_{C11P}$** complex is dependent on the cell utilized and that it gives temperamental features in the *PEC clamp* cell. Thus, we cannot exclude that the

same effect applies for the photoelectrocatalytic experiment and impart the current densities. Also, we showed in 0 that the **[Co^{III}(DO)(DOH)pnCl₂]** can reduce O_2. Especially, if the conditions are not forced toward hydrogen evolution by applying a negative external potential, the complex can turn over for ORR rather than HER. Such a poisoning effect has been monitored to a noticeable extent with **[Co^{III}(DO)(DOH)pnL₂]**-decorated electrodes (see Chapter II.3.2.2) operated at current densities similar to that of the **NiO-TPAT₂NMI-Co_{C11P}** photocathode (-1 to $-10\ \mu A\cdot cm^{-2}$). The possible presence of adventitious residual oxygen trapped within the NiO film can hence introduce an additional source perturbating the photoelectrocatalytic measurements.

These points should give a partial solution to the question of the low reproducibility during photoelectrocatalytic experiments.

On the other hand, we can remark generally that the steady-state photocurrents established at the **NiO-TPAT₂NMI-Co_{C11P}** electrode (between -7.3 and $-2.2\ \mu A\cdot cm^{-2}$ at 500 s) achieve H_2 evolution but are quite modest. Especially, a photocathode recently developed by L. Sun and co-workers and built on a similar co-grafting pattern (see Chapter I.2.2.3.3) gives current densities around $-30\ \mu A\cdot cm^{-2}$ at 500 s in a phosphate buffer at pH 7.[13b] Such a difference in the photoelectrocatalytic performance is thus intriguing and putative explanations are reviewed here.

First, in the study by Sun and co-workers, the electrode is constructed with the **P1** organic dye, which is attached first (for 5 min), and a cobaloxime bound to the surface *via* a phosphonate anchor, which is attached second (for 1 h), in a procedure reverse to ours. Although few characterizations are presented, the surface loading in **P1** can be estimated around 5 nmol·cm^{-2} from the UV-visible spectrum of the co-sensitized NiO films. As **TPAT₂NMI** is grafted onto **NiO-TPAT₂NMI-Co_{C11P}** with a surface density about 10 nmol·cm^{-2} and as it is assumed to display improved charge separation characteristics, we postulate that the LH/CS properties of the dye on the electrode is not the origin of the moderate performances.

A possible limitation of our photocathode could then arise from the catalyst, which has a long, flexible linker (9 aliphatic C atoms). Such feature is intended to position the catalyst at the top of the **TPAT₂NMI** layer, nearby the electron-acceptor part of the dye. But this linker may also favor the charge recombination by enabling the movement of the reduced **[Co(DO)(DOH)pnCl₂]** end to come in contact with the NiO surface. In contrast, in the photocathode by Sun and co-workers, the linker is smaller (4 aliphatic C atoms), but still flexible.

Additionally, Sun and co-workers used a phosphate buffer at pH 7 (0.05 M) in which the cobaloxime is active for HER. In our case, the experiments are conducted at pH 5.5 (MES 0.1 M/NaCl 0.1 M) since the **[Co^{III}(DO)(DOH)pnBr₂]** derivative we used has an increased activity in

mildly acidic media. Shifting from pH 7 to pH 5.5 has been observed to result in a drastic loss of the cathodic photocurrents for the reduction of a molecular HER pre-catalyst at a NiO electrode sensitized with a Ru(bpy)-like PS (see Chapter I.2.2.3.1).[30] The authors attribute the loss of the photocurrent upon acidification to a reduced driving force of hole injection between the HOMO of the excited PS and the NiO VB. Such phenomenon likely originates from a downward band bending at the NiO/electrolyte interface which occurs when the pH is decreased. A similar process might take place to a certain extent with the **NiO-TPAT$_2$NMI-Co$_{C11P}$** electrode operated in the MES buffer at pH 5.5, although photocurrents are still observed.

As well, an acidic electrolyte can facilitate the detachment of the dye or the catalyst by displacing the equilibrium towards the protonation of the anchoring groups. The slow desorption of the catalyst and/or the dye from the NiO surface would also explain the continuous decrease in photocurrents monitored during photoelectrocatalytic experiments at **NiO-TPAT$_2$NMI-Co$_{C11P}$**. However, the good stability in acidic media of related dye backbones attached to NiO was underlined elsewhere (see Chapter I.2.2.3.3).[13a]

Also, light-driven chronoamperometries are performed at an oxidative potential (0.63 *vs* RHE *i.e.* 0.31 *vs* NHE) at which electrochemical processes at the NiO surface coupled with hydroxyl or proton exchange are observed.[2, 31] Such surface processes might modify the binding of the anchoring groups linking the molecules onto NiO. By contrast, in the study by Sun and co-workers the electrolyses under irradiation are performed at more negative potentials (around 0 V *vs* NHE) in a region where the NiO is in theory electrochemically silent.[13b] Even if the expected energetic savings is higher at quite anodic operating potentials, performing photoelectrocatalytic experiments in a region where the NiO surface redox processes are absent would be an interesting option.

Overall, important points for enhancing the light-driven hydrogen evolution and the stability at the co-grafted **NiO-TPAT$_2$NMI-Co$_{C11P}$** and, likely, **the NiO-RuP$_4$-Co$_{C11P}$** electrodes have been identified. The mingling of analytic techniques presented here gives insightful information on the co-grafted electrodes at the molecular scale. Especially, these powerful tools can now be harnessed to realize post-*operando* analyses of the photocathodes and gain understanding in the origin of their deactivation. This step would then access the design of more stable DS photocathodes. In particular, the interaction between the NiO surface and the electrolyte or the anchoring groups is believed to play a major role on the efficiency and the robustness of the electrode. Thus, the deposition of a layer passivating the decorated surface, e.g. by ALD, could represent an interesting track to explore.[14a, 32] Besides, alternative molecular structures might also be envisioned. Such backbones will be the object of the final part of this manuscript.

3. *Dyecat*: a covalent dye-catalyst assembly

The last approach presented in this manuscript to create molecular photocathodes for HER consists in immobilizing a species that gathers a photosensitizing unit directly linked to a catalytic one. This approach was previously explored by the group to build an entity containing a pyridine-decorated Ru(bpy)$_2$(phen)-like photosensitizer bridged to a cobaloxime catalyst *via* a supramolecular Co-pyridine bond.[33] Under homogeneous conditions, such a system proved to be more efficient for hydrogen evolution than the bimolecular analogue. Recently, this approach was translated onto NiO surface by the group of Wu, which gave one of the first examples of NiO-based molecular photocathode catalyzing proton reduction (see Chapter I.2.2.3.2).[14a] However, the systems developed to date rely on a supramolecular link between both units, possibly labile during catalytic turnover. To improve stability, an option is to assemble the dye and the catalyst *via* a covalent bond. With the background we had from previous studies on **[Co^{III}(DO)(DOH)pnL$_2$]** catalysts and organic dyes, we attempted to create such a covalent bi-functional entity.

This project is lead in a shared income with J. Massin, post-doctoral fellow in the group. The synthesis of the photosensitizing unit was developed by J. Massin, partially described in a published work in *Focus: Interface* (appendix of this manuscript, Paper III),[12] and further adapted for the purpose of creating the dye-catalyst entity. The parts of synthesis related to the dye unit are not described in the current manuscript. The assays to couple the photosensitizing and catalytic parts together were realized in a common effort and will be shown here.

Due to challenges in organic synthesis, the route to create the desired dye-catalyst entity has been successfully achieved only very recently. As such, we will present here a brief overview of the results obtained.

3.1. Synthesis

The backbone of the photosensitizing part is adapted from the organic PS used in our previous publication,[12] which was inspired from the architecture of the **O2** dye (see Chapter I.2.2.2.2).[34] The dye has a push-pull structure that couples an electron-donating triphenylamine moiety with a thiophene unit. Two phenyl moieties bear *tert*-butyl carboxylic esters, the hydrolysis of which should yield two carboxylic acid groups for the attachment onto NiO. The terminal thiophene is functionalized for the purpose of coupling the catalytic part.

3.1.1. First attempts

The first attempts described were not successful but served us to gain a better design of the synthetic route. We give here only details of interest and do not report them in the experimental part.

3.1.1.1. Knoevenagel reaction

The strategy we investigated first consists in derivatizing the catalytic unit with another reactive moiety. In that aim, the **Co$_{CN}$** complex (Figure IV.33) was constructed *via* a pathway (not shown) involving a CuAAC step and a Co-Cu exchange, inspired from the synthesis of **Co$_{C11P}$** (Chapter III.2.1.2.2). This derivative displays a cyanoacetamide end with an activated CH$_2$ group. This methylene group can react with the aldehyde moiety present on the **TPA$_{tBu}$T$_1$CO** PS unit (Figure IV.33) in the Knoevenagel condensation.
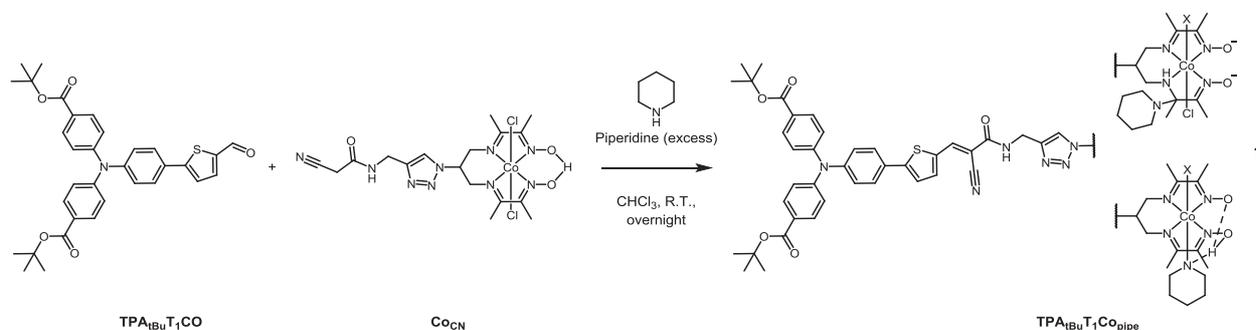
Figure IV.33. Attempt for the synthesis of the dye-catalyst entity yielding an undesired and partially identified **TPA$_{tBu}$T$_1$Co$_{pipe}$** product.

Such coupling was realized in the presence of piperidine as a catalytic base. At the end of the reaction, a product is precipitated by adding diethylether in the reaction mixture. The analysis of the crude product by mass spectroscopy reveals the presence of an entity gathering both the PS part and the Co complex one, but with a piperidine bound to the molecule. Also, the signal corresponding to the methyl groups on the imino positions is split into two distinct singlets. This observation tends to indicate an unsymmetrical modified diimine-dioxime ligand. Such point might be explained by the nucleophilic attack of the piperidine on one imine position, as proposed in Figure IV.33 (**TPA$_{tBu}$T$_1$Co$_{pipe}$**, top structure). We note that addition of water on this imine position has been recently reported on a similar diimine-dioxime cobalt complex. At the same time, the NMR spectra does not contain the unshielded signal around 19 ppm usually assigned to the proton of the O−H·O bridge in **[Co^{III}(DO)(DOH)pnL$_2$]**. This proton could not been recovered even under highly acidic conditions (TFA). Thus, we could not exclude an alternative structure in which the piperidine is directly coordinated to Co while the proton of the amine is

involved into H bonds with oximato oxygen atoms (Figure IV.33, **TPA$_{tBu}$T$_1$Co$_{pipe}$**, bottom structure). We were unable to exactly identify the structure of the obtained product but the use of a nucleophilic base was clearly demonstrated to alter the first coordination sphere of the Co complex. As the first coordination sphere is important for the activity of the catalyst, these conditions were not further explored. Since non-catalyzed conditions proved unfruitful to couple both parts, we switched to a different approach.

3.1.1.2. Click-chemistry: first assay

Here, we intended to directly join the catalyst *via* an azide-alkyne cycloaddition, also following the synthetic scheme of **Co$_{C11P}$** (Chapter III.2.1.2.2). The dye was decorated with a terminal alkyne on the thiophene end (**TPA$_{tBu}$T$_1$**, Figure IV.34). This alkyne-functionalized dye was then reacted with **[Cu^{II}(DO)(DOH)N$_3$pn]ClO$_4$**, the copper precursor of the **[Co^{III}(DO)(DOH)pnL$_2$]** coordination sphere.
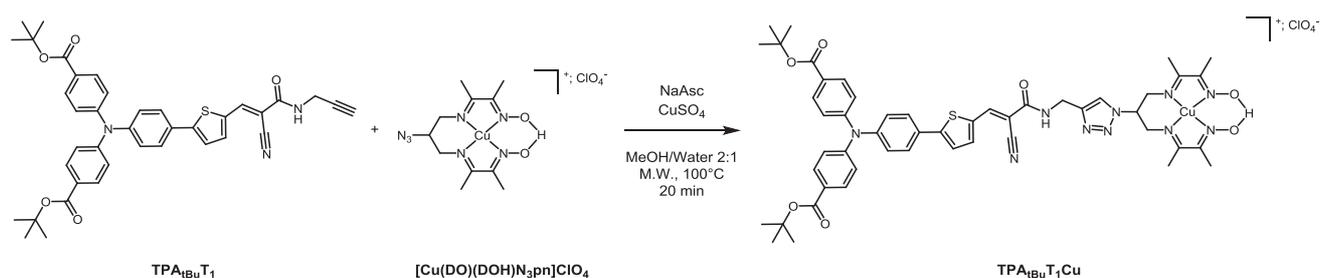

Figure IV.34. First synthesis of the **TPA$_{tBu}$T$_1$Cu** dye-complex intermediate. M.W.: micro-wave (oven).

This AAC was realized under copper-catalyzed conditions. The reaction mixture was reacted in a closed vessel inside a micro-wave oven, under elevated temperature (100°C) and pressure. While the starting materials are not completely soluble at R.T. in the mixture of solvents used (MeOH/water 2:1), the harsh micro-wave conditions likely favor their full solubilization. Washing the crude reaction mixture with DCM gave a dark red solid. An analysis in mass spectroscopy of this solid revealed the single presence of the expected **TPA$_{tBu}$T$_1$Cu** intermediate. These conditions thus prove quite effective to synthetize **TPA$_{tBu}$T$_1$Cu**.

However, this test was conducted on small quantities of starting materials and the amount of **TPA$_{tBu}$T$_1$Cu** was not sufficient enough to pursue the synthetic path. Hence, we decided to reproduce the synthetic step on larger amounts. But the scale up of the reaction proved unfruitful, likely due to solubility issues evoked above.

3.1.2. Final route

We utilized different conditions that have been set up in our laboratory to couple hydrophobic compounds with hydrophilic ones through CuAAC and successfully applied to related dyad structures. These conditions rely on a biphasic mixture of DCM and water, led to a single homogeneous phase by adding MeOH. Such a homogeneous mixture of solvents permits the complete dissolution of the reagents and catalysts. With that procedure, we realized the *click*-wise coupling of the **TPA_tBuT_1** with the **[Cu^II(DO)(DOH)N_3pn]PF_6** complex. This first step gave the **TPA_tBuT_1Cu** intermediate (Figure IV.35) that was used in one-pot for the next step. In this second step, the substitution of Co^III for Cu^II was made according to the procedure developed for the synthesis of **Co_C11P**, but with an extended reaction time. The purification of the crude mixture with chromatography over SiO_2 followed by a precipitation in NaBr-saturated solution afforded the protected **TPA_tBuT_1Co** dye-catalyst entity bearing Br^− axial ligands (Figure IV.35).
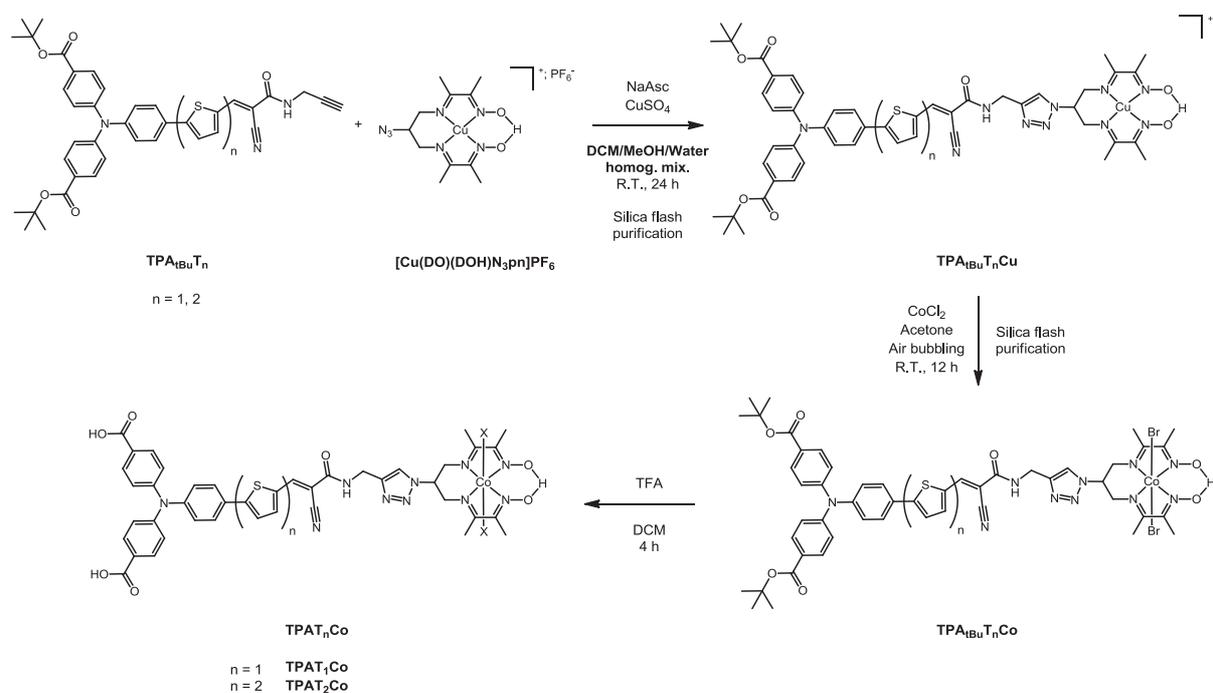

Figure IV.35. Synthetic route to the **TPAT_nCo** (n = 1 or 2) immobilizable dye-catalyst entities. homog. mix.: homogeneous mixture; TFA: trifluoroacetic acid.

Soaking the protected **TPA_tBuT_1Co** dyads in the presence of excess amounts of TFA for 4 hours resulted in the quantitative hydrolysis of *tert*-butyl carboxylic esters into carboxylic acids. This last step thus successfully yielded the expected **TPAT_1Co** dye-catalyst entity that displays carboxylic anchoring groups for the attachment onto NiO.

3.2. Characterization

Subsequently, we characterized the **TPA$_{tBu}$T$_1$Co** dyad, firstly using electrochemistry. The CV in DCM of **TPA$_{tBu}$T$_1$Co** displays four events (Figure IV.36, purple line). In the anodic regime, a reversible wave is observed at 0.68 V *vs* Fc$^{+/0}$. This wave is ascribed to the oxidation of the **TPA** donor part, by comparison with the electrochemical signature of the **TPA$_{tBu}$T$_1$** dye (Figure IV.36, red line) and is accordingly assigned to the HOMO level of the dye. In the cathodic window, the **TPA$_{tBu}$T$_1$Co** features a first wave at −0.61 V *vs* Fc$^{+/0}$ and a second reversible wave at −1.03 V *vs* Fc$^{+/0}$. Given the electrochemical signature of the **[Co^{III}(DO)(DOH)N$_3$pnCl$_2$]** control complex under identical conditions (Figure IV.36, blue line), these events are ascribed to the Co$^{III/II}$ and Co$^{II/I}$ couples at the **[Co(DO)(DOH)pnBr$_2$]** moiety, respectively.
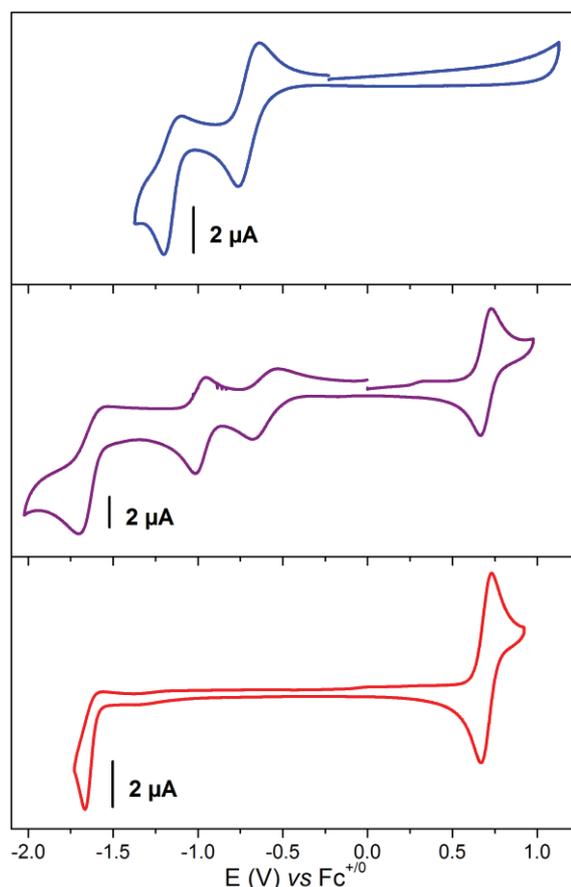

Figure IV.36. CVs of **[Co^{III}(DO)(DOH)N$_3$pnCl$_2$]** (blue line), **TPA$_{tBu}$T$_1$Co** (purple line) and **TPA$_{tBu}$T$_1$** (red line) in *n*BuNPF$_6$ 0.1 M DCM electrolyte recorded at a glassy carbon electrode with a scan rate of 100 mV·s^{-1}.

An irreversible cathodic wave monitored at $E_p = -1.70$ V *vs* Fc$^{+/0}$ (Figure IV.36, purple line) is assigned to a reduction on the PS unit, by comparison with the CV of **TPA$_{tBu}$T$_1$** (Figure IV.36, red line). A similar irreversible reduction has been observed on organic dyes with very close structures and attributed to the reduction of the electron accepting group. Although the

irreversibility of the process has not been explained to date, it denotes an intrinsic instability of the electrochemically-generated radical anion.

On the dyad, we note that the signatures of the PS part are slightly cathodically shifted (20-30 mV), whereas the events attributed to the **[Co^{III}(DO)(DOH)pnBr₂]** complex are moved anodically of 100-130 mV, compared to their respective monomolecular analogues. This observation would be consistent with an increase in the electronic density around the Co center upon coupling, and a corresponding small decrease on the dye. However, the electrochemistry is performed in poorly dissociating DCM. Thus we cannot rule out that the difference in ancillary ligands at **TPA_{tBu}T₁Co** and **[Co^{III}(DO)(DOH)pnCl₂]** (Br⁻ *vs* Cl⁻) might impact the potentials of the redox events at the Co diimine-dioxime complex. Further investigations are ongoing to tackle this point.
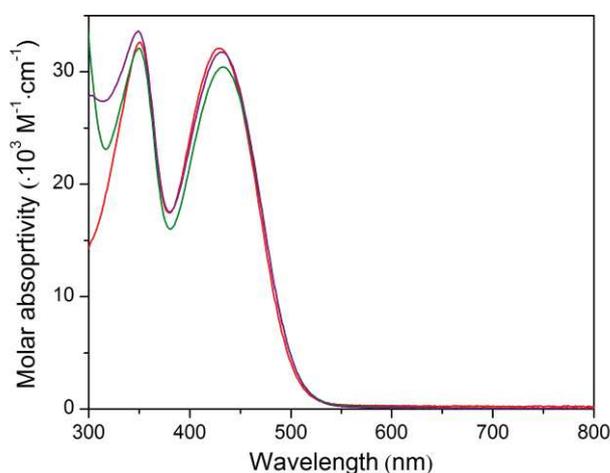

Figure IV.37. UV-visible spectra of **TPA_{tBu}T₁** (red line), **TPA_{tBu}T₁Cu** (green line) and **TPA_{tBu}T₁Co** (purple line) in MeCN.

The UV-visible spectrum of the **TPA_{tBu}T₁Co** dyad (Figure IV.37, purple line) displays two CT bands at 349 and 431 nm of molar absorptivities 33 630 and 31 757 $M^{-1}\cdot cm^{-1}$, respectively. This signature is nearly identical to that of the **TPA_{tBu}T₁** dye and the **TPA_{tBu}T₁Cu** analogue (Figure IV.37) that feature bands of similar intensity and centered at 429 nm (ε(429 nm) = 32 095 $M^{-1}\cdot cm^{-1}$) and 433 nm ((ε(433 nm) = 30 436 $M^{-1}\cdot cm^{-1}$), respectively. Such signal is characteristic of a HOMO-LUMO transition on the PS unit. Thus, the retainment of this band on the dyads indicates that the covalent linkage of the diimine-dioxime Cu or Co complexes does not mainly influence the LH ability of the PS part. This point also corroborates the minute shift in the redox signature of the PS part observed in CV.

From the foot of the HOMO-LUMO band of **TPA_{tBu}T₁Co** (550 nm), we could estimate an E_{0-0} value of *ca* 2.25 eV. This value permits to approximate the energy of the LUMO level at

−1.57 V *vs* Fc$^{+/0}$. The LUMO level is more than 500 mV negative than the Co$^{II/I}$ couple on **TPA$_{tBu}$T$_1$Co**, which should enable the reduction at the Co^I state by the excited PS part, as required for further HER catalysis.

Collectively, the data presented in this last part support that the LH properties are retained in the **TPA$_{tBu}$T$_1$Co** dyad and further demonstrate that a light-driven reduction *via* the excited dye moiety to the Co^I state is possible. In this architecture, the electron transfer from the PS part to the catalyst can only occur through non-conjugated bonds or through space. The global process of light-driven hydrogen evolution implying successive electron and proton transfers, the kinetic issues at such a dyad will be of major importance. Especially, the comparison between the kinetics of dye-to-catalyst electron transfers, of unproductive recombination pathways and of catalytic steps has to be investigated.

The synthetic pathway developed in this work further allowed us to prepare the bithiophene analogue dyad **TPAT$_2$Co** (Figure IV.35). This second dyad provides an interesting point of comparison for drawing structure-property relationships, since increasing the number of thiophene units on similar push-pull dyes proved to enhance charge separation.[11]

As well, these *dyecat* dyads contain carboxylic acid groups for the purpose of immobilization at the surface of TCOs. The assessment of NiO-immobilized dyads in photoelectrochemical experiments therefore constitutes the step further.

Conclusion

In this last chapter, we first selected the best NiO candidate for the assembly of a DS photocathode for proton reduction based on light-harvesting properties and performance in *p*-DSSC. The model photoelectrode constructed on the chosen NiO **D2L-450** substrate by sensitization with **P1** was further translated for application in DS PEC. Adsorbing the **[Co(dmgBF$_2$)$_2$(H$_2$O)$_2$]** catalyst at the surface of this electrode yields a DS photocathode that generates −5 to −10 μA·cm^{-2} of photocurrent in neutral aqueous media. Although hydrogen detection was not performed, such results proved encouraging for the creation of fully covalent molecular photocathodes.

We then built the **NiO-TPAT$_2$NMI-Co$_{C11P}$** and **NiO-RuP$_4$-Co$_{C11P}$** co-grafted photocathodes, following a stepwise immobilization procedure. The analyses by electrochemistry, UV-visible spectroscopy, XPS and ToF-SIMS demonstrated that both catalyst and dye were present under their intact molecular form at the surface. As well, we could estimate the surface coverage in each species. These investigations revealed that the surface concentrations of dyes lay in the 10 nmol·cm^{-2} range and are larger than that in catalyst by a factor 2 to 10.

The light-driven experiments led at the **NiO-TPAT$_2$NMI-Co$_{C11P}$** electrodes evidenced relative photocurrents starting from 0.63 V *vs* NHE and displaying a maximum around −6 μA·cm^{-2} at 0.27 V *vs* NHE. Long-term photoelectrocatalytic experiments around this potential, at values positive to RHE, gave steady-state photocurrents between −7 and −2 μA·cm^{-2}, associated with hydrogen evolution. Although the control **NiO-TPAT$_2$NMI** electrode has an intrinsic activity for light-driven HER, the presence of **Co$_{C11P}$** on the surface improves the activity and stability of the photocathode, demonstrating the noticeable role of the co-grafted catalyst.

While the photocurrents are still modest, the analytic techniques exploited here to scan the electrodes both from structural and functional perspective give us tools in hands to gain understanding and subsequent improvement of these co-grafted photocathodes.

In parallel, the construction of molecular dye-catalyst dyads potentially immobilizable onto surface can represent an alternative approach. This path was followed and the synthesis of **TPAT$_1$Co** was successfully achieved. First characterization indicates that the light harvesting ability is preserved in the dyad and that a light-driven electron injection into the **[Co^{III}(DO)(DOH)pnBr$_2$]** catalytic center is possible. The synthetic pathway also gave access to the **TPAT$_2$Co** analogue. These immobilizable *dyecat* entities open stimulating tracks for the assembly of new NiO-based molecular photocathodes.

Experimental part

The experimental part for Chapter IV.1 is described in the revised version of the manuscript accepted for publication in *Physical Chemistry Chemical Physics* and added as an appendix of this thesis (Paper IV)

Co-grafted photocathodes

Materials

Solvents, starting materials and supporting electrolyte salts were purchased from Sigma-Aldrich and used without further purification, unless otherwise stated.

TPA_{tBu}T_2NMI and **TPAT_2NMI** were synthetized and characterized by R. Brisse, PhD student in the team of B. Jousselme at the *Laboratory of Innovation in Surface Chemistry and Nanosciences* (*CEA-Saclay*, FRANCE).

RuPEt_4 and **RuP_4** were synthetized and characterized by N. Queyriaux, PhD student in our team (V. Artero's team, *Laboratory of Chemistry and Biology of Metals*, *CEA-Grenoble*, FRANCE).

NiO co-sensitization

The NiO substrates and the sintering procedure have been described in Chapter III. Alterations to the procedure of sensitization are given here.

After sintering at 450°C, the plates were let to cool to *ca* 90°C. A first UV-visible spectrum of the NiO electrodes was taken at this step. Then, the plates were put again in the still hot oven (about 90°C) for 5 min.

The electrodes were further introduced in PTFE boxes containing 10 mL of a methanolic solution 0.5 mM in the **Co_{C11P}** derivative (5 μmol). Between 3 and 6 plates were introduced in the same box. The boxes were closed and the plates let to sensitize for at least 66 h on orbital stirring. The plates were removed from the solution, washed by dipping them in pristine methanol for 10 min on orbital stirring and dried with N_2 to give the **NiO-Co_{C11P}** electrodes. A second UV-visible spectrum of the sensitized NiO electrodes was acquired at this stage.

The plates were further dipped in PTFE boxes containing a methanolic solution (10 mL) 0.5 mM in **TPAT_2NMI** or 0.5 mM in **RuP_4**. The boxes were closed and the electrodes let to sensitize for exactly 2 h on orbital stirring. The plates were removed from the solution, washed by dipping them in pristine methanol for 10 min on orbital stirring and dried with N_2 to yield the **NiO-**

TPAT₂NMI-Co_{C11P} and **NiO-RuP₄-Co_{C11P}** electrodes. A last UV-visible spectrum of the co-sensitized NiO electrodes was taken.

NiO-Co_{C11P} control electrodes are kept after the first sensitization stage.

NiO-TPAT₂NMI and **NiO-RuP₄** control electrodes were prepared from NiO plates sintered with the same temperature program as described above, but let to cool to R.T. A first UV-visible spectrum of the pristine NiO electrodes was acquired. Then, the plates were dipped into methanolic solutions (10 mL) 0.5 mM in **TPAT₂NMI** or 0.5 mM in **RuP₄**, contained in PTFE boxes. The boxes were closed and the electrodes let to sensitize for exactly 2 h on orbital stirring. The plates were removed from the solution, washed by dipping them in pristine methanol for 10 min on orbital stirring and dried with N₂ to yield the **NiO-TPAT₂NMI** and **NiO-RuP₄** control electrodes. Finally, UV-visible spectrum of the sensitized NiO electrodes was acquired.

Characterizations

ToF-SIMS and XPS analyses were carried out in the same manner as described in Chapter III.

UV-visible spectroscopy

UV-visible spectra of the plates were recorded with an *Agilent Technologies Cary 60 UV-Vis* spectrometer. Spectra were taken just after sintering of the plates, after sensitization by **Co_{C11P}** and/or after co-sensitization with **TPAT₂NMI** or **RuP₄**. For each spectrum, a baseline corresponding to the related underlying glass|FTO support was recorded and automatically subtracted from the spectrum of the electrode. Differential spectra were obtained by subtraction of spectra prior and after sensitization with **TPAT₂NMI** or **RuP₄**.

Electrochemistry

General electrochemical methods are identical to that described in Chapter III. Alterations to these methods are noted here.

Detection of grafted species

The electrochemical characterization of the plates was made in a three-electrode electrochemical cell setup for photoelectrochemistry. The working electrode was the NiO-sensitized substrate, priorly covered by a galvanoplastic scotch tape bearing a hole of 8 mm diameter to determine the electroactive area ($S = 0.5$ cm²). Using a clamp, the working electrode was pressed against a 9 mm diameter hole in the electrochemical cell, with an intercalary O-ring

seal to ensure tightness at the junction. The electrical contact was taken at the FTO part of the electrodes. The counter electrode was a titanium wire, separated from the working electrode compartment either by a Nafion® N-117 (180 µm, 0.90 meq/g exchanging capacity) membrane in the case of aqueous electrolytes or by a Vycor® frit in the case of organic electrolytes. The media was degassed with a stream of N_2 or Ar at least 10 min prior to the measurements and the stream was kept in the headspace during the measurement.

The electrolytes used were a NaCl 0.1 M aqueous solution and a nBu$_4$NBF$_4$ 0.1 M MeCN solution.

Photoelectrochemistry

Light source

The light beam was generated by a Newport ozone-free Xenon lamp operated at 280 W mounted with a water filled *Spectra-Physics 6123NS* liquid filter for elimination of IR radiation and a *Spectra-Physics 59472* UV cut-off filter ($\lambda > 400$nm). Incident light flux on the working electrode was calibrated at 50 mW·cm^{-2} (nearly equivalent to 1 sun) with a *Newport PM1918-R* power-meter coupled to a *Newport 919-020-12* photodiode or with a *Newport Control 91150V* photodiode/power-meter setup. A *Jeulin* frequency generator was used to drive an automatic shutter via a *Newport electronic shutter* controller in order to shine light at regular intervals in the case of chopped-light measurements.

Linear sweep experiments

The electrochemical cell used is described above. The working electrode substrates were back-irradiated. A stream of Ar or N_2 was bubbled in the electrolyte at least 10 min prior to the measurement. A slow bubbling rate was maintained during the linear sweep voltammetry and the electrolyte stirred. Linear sweep voltammograms were conducted at scan rate of 1 mV·s^{-1}, starting from anodic potentials to cathodic potentials.

Chronoamperometric measurements under light irradiation coupled with H_2 detection

A similar electrochemical cell was used. Additional necks on the cell permitted to introduce the sensor for hydrogen detection and to sample aliquots of the headspace with a syringe for GC analysis. The working electrode was the NiO-sensitized substrate joined to the cell in a similar fashion as described above but with an electroactive area of S = 1.15 cm^2. The media was degassed at least 10 min prior to the measurement by bubbling of N_2 or Ar. Before starting the experiment, the cathodic part of the electrochemical cell was tightly closed and the stream

stopped. The electrolyte in the cathodic part was vigorously stirred during the chronoamperometric experiment. A flux of N_2 or Ar was bubbled at the anodic part, separated from the cathode by a Nafion® membrane, during the whole measurement time. The volumes of electrolyte and headspace in the cathodic part were typically *ca* 10 mL and 8 mL, respectively. In a typical experiment, the electrode was poised at the desired potential in the dark for 120 s before light was shined on the sample.

The electrolyte used was a MES 0.1 M/NaCl 0.1 M aqueous buffer at pH 5.5.

Detection of dissolved hydrogen was performed through a *Unisense H2-N* in-needle Clark micro-sensor dipped in the cathodic compartment. The sensor was calibrated and operated as described in Chapter III.

GC analysis of the headspace was realized by sampling 50 µL of the headspace with a gas tight syringe through a silicone/PTFE stopper. The content of the syringe was introduced into the injection loop of a *Perkin-Elmer Clarus 500* gas chromatograph equipped with a porapack Q 80/100 column (6' 1/8") thermostated at 40 °C and a TCD detector thermostated at 100 °C. The area under the H_2 peak permitted to access the concentration of hydrogen in the headspace through a calibration curve plotted from known concentrations of H_2.
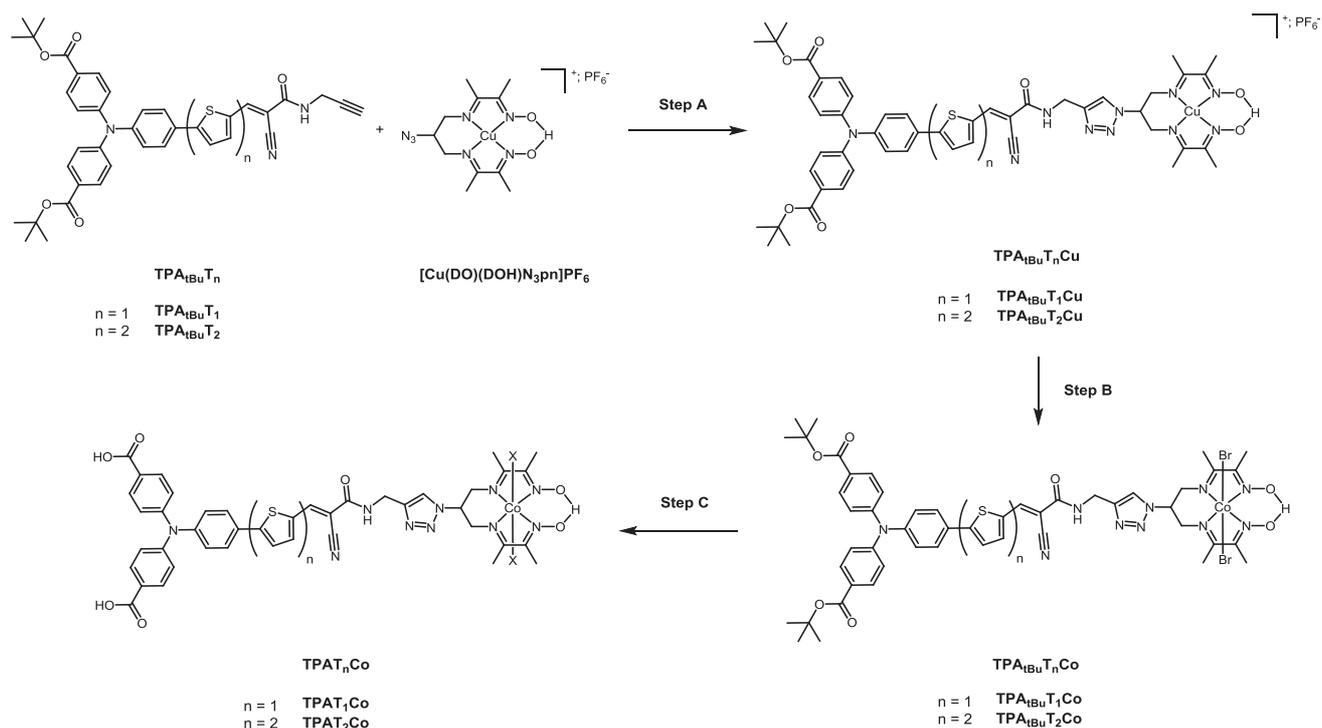
Dyecat

The synthetic routes for the construction of the **TPAT$_n$Co** dyads were imagined and developed during this work in an joint project with J. Massin. The synthetic steps described here have been optimized and scaled-up by J. Massin.

Synthesis

General synthetic methods and characterizations are identical to that described in Chapter III, unless otherwise stated.

NMR spectra were recorded at 298 K in 5 mm o.d. tubes on a *Bruker Avance III* spectrometer equipped with a *Prodigy* cryoprobe and operating at 500.0 MHz for ^{1}H and 126 MHz for ^{13}C. Chemical shifts reported in ppm are given relative to TMS. ^{1}H and ^{13}C NMR spectra were referenced internally to the residual solvent resonance.

Synthetic route to the **TPAT$_n$Co** (n = 1 or 2) immobilizable dye-catalyst entities. Step A: **CuSO$_4$·5H$_2$O** and **sodium ascorbate** in water/DCM/MeOH for 24 h at R.T.; Step B: **CoCl$_2$·6H$_2$O** in acetone under air bubbling for 12 h at R.T.; Step C: **TFA** in DCM for 4 h at R.T.

Step A: CuAAC

General procedure A

The **dye** and **[Cu(DO)(DOH)N$_3$pn]PF$_6$** were solubilized in DCM under Ar. A solution of **CuSO$_4$·5H$_2$O** and **sodium ascorbate** in dearated water was added. Then, Ar-degassed MeOH was added to the biphasic mixture until a single phase was obtained. The reaction mixture was stirred at R.T under Ar. After 24 h the solution was concentrated under vacuum yielding a precipitate, which was filtered and washed with water. The solid was purified by flash chromatography on silica gel using as eluent a mixture MeCN/aqueous KNO$_3$ solution at 10% of the saturating concentration. The pure product was obtained after evaporation of MeCN in the combined fractions and precipitation by addition of a KPF$_6$-saturated aqueous solution. The precipitate was filtered, washed with water and dried under vacuum to give a red brick solid, which was used one-pot for the next step.

TPA$_{tBu}$T$_1$Cu

The synthesis of **TPA$_{tBu}$T$_1$Cu** was made according to the general procedure A. Quantities: **TPA$_{tBu}$T$_1$** (1 equiv., 150 mg, 0.22 mmol), **[Cu(DO)(DOH)N$_3$pn]PF$_6$** (1 equiv., 100 mg, 0.22 mmol), DCM (7.3 mL), **CuSO$_4$·5H$_2$O** (0.3 equiv., 17 mg, 0.07 mmol), **sodium ascorbate** (0.9

equiv., 41 mg, 0.20 mmol), water (3.7 mL), MeOH (12.3 mL). 177 mg (68% yield) of the product were obtained as a red brick solid.

TPA$_{tBu}$T$_2$Cu

The synthesis of **TPA$_{tBu}$T$_2$Cu** was made according to the general procedure A. Quantities: **TPA$_{tBu}$T$_2$** (1 equiv., 150 mg, 0.22 mmol), **[Cu(DO)(DOH)N$_3$pn]PF$_6$** (1 equiv., 120 mg, 0.27 mmol), DCM (8.6 mL), **CuSO$_4$·5H$_2$O** (0.3 equiv., 26 mg, 0.10 mmol), **sodium ascorbate** (0.9 equiv., 48 mg, 0.24 mmol), water (4.3 mL), MeOH (16.6 mL). 196 mg (59% yield) of the product were obtained as a red brick solid.

Step B: Cu-Co exchange

General procedure B

TPA$_{tBu}$T$_n$Cu and **CoCl$_2$·6H$_2$O** were solubilized in acetone and stirred under air bubbling. After 12 h the solution was evaporated under vacuum and the solid was purified by flash chromatography on silica gel using as eluent a mixture of MeCN and aqueous KNO$_3$ solution at 10% of the saturating concentration, then a solution of acetone saturated in NaI was added to completely desorb the product from the silica gel. The desired fractions were combined and the organic solvents were evaporated under vacuum, yielding a precipitate that was filtered and washed with water. The solid was re-dissolved in acetone. To this solution a NaBr-saturated aqueous solution (a third of the final volume) was added. The mixture was stirred at R.T. over the week-end to allow the acetone to slowly evaporate, giving a precipitate. This precipitate was filtered, washed with water and dried under vacuum to obtain the expected product as a pure solid.

TPA$_{tBu}$T$_1$Co

The synthesis of **TPA$_{tBu}$T$_1$Co** was made according to the general procedure B. Quantities: **TPA$_{tBu}$T$_1$Cu** (1 equiv., 160 mg, 0.14 mmol), **CoCl$_2$·6H$_2$O** (7 equiv., 234 mg, 0.98 mmol), acetone (24.5 mL). 95 mg (59% yield) of the **TPA$_{tBu}$T$_1$Co** product were obtained as an orange solid.

^{1}H NMR (CD$_3$CN, 500 MHz): δ (ppm) 19.23 (s, 1H), 8.28 (s, 1H), 7.88 (s, 1H), 7.80 (d, J = 8.6 Hz, 4H), 7.68 (s, 1H), 7.60 (d, J = 8.3 Hz, 2H), 7.38 (s, 1H), 7.23 (s, 1H), 7.08 (d, J = 8.3 Hz, 2H), 7.03 (d, J = 8.6 Hz, 4H), 5.71 (t, J = 9.7 Hz, 1H), 4.68 – 4.37 (m, 6H), 2.52 (s, 6H), 2.48 (s, 6H), 1.49 (s, 18H).

^{13}**C NMR** (CD$_3$CN, 126 MHz): δ (ppm) 177.32, 165.60, 161.60, 157.39, 152.73, 150.88, 148.05, 145.29, 144.76, 139.99, 135.62, 131.38, 129.32, 128.24, 127.56, 126.11, 124.87, 123.92, 123.51, 100.42, 81.25, 58.46, 55.50, 36.25, 30.83, 28.25, 18.52, 14.00.

HR-MS (ESI+): *m/z* calcd for C$_{50}$H$_{55}$BrCoN$_{10}$O$_7$S 1077.2486; found 1077.2487 [M–Br$^-$]$^+$.

E.A.: calcd for C$_{50}$H$_{55}$Br$_2$CoN$_{10}$O$_7$S + 0.25 NaBr: C, 50.70; H, 4.68; N, 11.82; found: C, 50.91; H, 4.87; N, 11.53.

TPA$_{tBu}$T$_2$Co

The synthesis of **TPA$_{tBu}$T$_2$Co** was made according to the general procedure B. Quantities: **TPA$_{tBu}$T$_2$Cu** (1 equiv., 155 mg, 0.13 mmol), **CoCl$_2$·6H$_2$O** (7 equiv., 220 mg, 0.91 mmol), acetone (22 mL). 105 mg (67% yield) of the **TPA$_{tBu}$T$_1$Co** product were obtained as a red solid.

^{1}**H NMR** (CD$_3$CN, 500 MHz): δ (ppm) 19.23 (s, 1H), 8.27 (s, 1H), 7.88 (s, 1H), 7.78 (d, *J* = 8.6 Hz, 4H), 7.62 (s, 1H), 7.53 (d, *J* = 8.3 Hz, 2H), 7.34 (d, *J* = 3.4 Hz, 1H), 7.26 (m, 3H), 7.05 (d, *J* = 8.3 Hz, 2H), 7.02 (d, *J* = 8.6 Hz, 4H), 5.70 (t, *J* = 11.2 Hz, 1H), 4.60 – 4.40 (m, 6H), 2.52 (s, 6H), 2.47 (s, 6H), 1.48 (s, 18H).

^{13}**C NMR** (CD$_3$CN/CD$_2$Cl$_2$ 2:1, 126 MHz): δ (ppm) 176.82, 165.14, 161.08, 156.90, 150.52, 146.48, 145.61, 145.34, 144.77, 144.01, 139.47, 134.73, 130.83, 129.72, 127.71, 127.06, 126.75, 126.10, 124.66, 124.56, 123.07, 123.02, 99.88, 80.69, 57.95, 54.99, 35.74, 27.75, 18.02, 13.50.

HR-MS (ESI+): *m/z* calcd for C$_{54}$H$_{57}$BrCoN$_{10}$O$_7$S$_2$ 1159.2363; found 1159.2369 [M–Br$^-$]$^+$.

E.A.: calcd for C$_{54}$H$_{57}$Br$_2$CoN$_{10}$O$_7$S$_2$ + 2.35 NaBr: C, 43.74; H, 3.87; N, 9.45; found: C, 43.53; H, 4.22; N, 9.19.

Step C: carboxylic ester deprotection

General procedure C

TPA$_{tBu}$T$_n$Co was solubilized in DCM and **TFA** was slowly added to this solution. The mixture was stirred at R.T. for 4 hours and then evaporated to dryness. The solid was taken up in DCM, filtered, washed successively with DCM and MeCN and dried under vacuum to obtain the pure product.

TPAT₁Co

The synthesis of **TPAT₁Co** was made according to the general procedure C. Quantities: **TPAT₁Co** (1 equiv., 35 mg, 30 µmol), DCM (1.5 mL), **TFA** (30 equiv., 0.15 mL, 0.88 mmol). 28 mg (88% yield) of the **TPAT₁Co** product were obtained as an orange solid.

¹H NMR (acetone-d_6/DMSO-d_6 3:1, 500 MHz): δ (ppm) 19.40 (s, 1H), 12.64 (s, 2H), 8.47 (s, 1H), 8.40 (s, 1H), 7.96 (d, J = 8.7 Hz, 4H), 7.93 (d, J = 4.1 Hz, 1H), 7.84 (d, J = 8.7 Hz, 2H), 7.71 (d, J = 4.1 Hz, 1H), 7.25 (d, J = 8.7 Hz, 2H), 7.19 (d, J = 8.7 Hz, 4H), 5.85 – 5.77 (m, 1H), 4.77 – 4.49 (m, 6H), 2.74 (s, 6H), 2.57 (s, 6H).

¹³C NMR (acetone-d_6/DMSO-d_6 3:1, 126 MHz): δ (ppm) 177.18, 167.24, 161.52, 156.79, 151.76, 150.72, 147.66, 143.94, 140.08, 135.45, 131.59, 129.34, 128.18, 126.34, 126.26, 125.06, 123.66, 123.48, 117.15, 101.39, 58.29, 55.47, 55.07, 35.95, 18.05, 13.55.

HR-MS (ESI+): *m/z* calcd for $C_{42}H_{39}BrCoN_{10}O_7S$ 965.1234; found 965.1235 $[M–Br^-]^+$.

E.A.: calcd for $C_{42}H_{39}Br_2CoN_{10}O_7S$ + 0.8 NaBr: C, 44.68; H, 3.48; N, 12.41; found: C, 44.93; H, 3.78; N, 12.06.

TPAT₂Co

The synthesis of **TPAT₂Co** was made according to the general procedure C. Quantities: **TPAT₂Co** (1 equiv., 35 mg, 28 µmol), DCM (1.5 mL), **TFA** (31 equiv., 0.15 mL, 0.88 mmol). 29 mg (90% yield) of the **TPAT₂Co** product were obtained as an orange solid.

¹H NMR (acetone-d_6/DMSO-d_6 3:1, 500 MHz): δ (ppm) 12.60 (s, 2H), 8.78 (s, 1H), 8.46 (s, 1H), 8.40 (s, 1H), 7.95 (d, J = 8.5 Hz, 3H), 7.89 (d, J = 3.7 Hz, 1H), 7.78 (d, J = 8.5 Hz, 2H), 7.61 (d, J = 3.7 Hz, 1H), 7.58 (d, J = 3.8 Hz, 1H), 7.56 (d, J = 3.9 Hz, 1H), 7.23 (d, J = 8.5 Hz, 2H), 7.18 (d, J = 8.5 Hz, 4H), 5.81 (t, J = 11.8 Hz, 1H), 4.87 – 4.48 (m, 6H), 2.74 (s, 6H), 2.57 (s, 6H).

¹³C NMR (acetone-d_6/DMSO-d_6 3:1, 126 MHz): δ (ppm) 177.33, 167.46, 161.62, 157.00, 156.93, 151.01, 146.85, 145.41, 145.32, 143.92, 140.29, 135.23, 135.08, 131.72, 130.27, 128.44, 127.67, 126.78, 126.30, 125.64, 125.28, 123.65, 123.53, 117.31, 58.45, 55.64, 55.24, 36.12, 18.18, 13.76.

HR-MS (ESI+): *m/z* calcd for $C_{46}H_{41}BrCoN_{10}O_7S_2$ 1047.1111; found 1047.1114 $[M–Br^-]^+$.

E.A.: calcd for $C_{46}H_{41}Br_2CoN_{10}O_7S_2$ + 1.65 NaBr: C, 42.55; H, 3.18; N, 10.79; found: C, 42.91; H, 3.39; N, 10.34.

Electrochemistry

Electrochemical data were acquired with a *Biologic VSP 300* potentiostat. Electrochemical measurements were conducted in a 3-electrode cell. The working electrode was a glassy carbon electrode and the auxiliary electrode a Pt wire. A plain Ag wire dipped in the supporting electrolyte served as pseudo-reference electrode, denoted below as Ag(I)/Ag(0). The supporting electrolyte was 0.1 M nBu₄NPF₆ in DCM. The supporting electrolyte was degassed with a flow of N_2 saturated with DCM at least for 5 min before the measurements. The N_2 flow was removed from the solution but let in the headspace of the cell for the duration of the experiment. The concentration of the compound of interest was 1 mM. Cyclic voltammograms were typically conducted at a scan rate of 100 mV·s⁻¹.

The potential of the pseudo-reference electrode was calibrated after each experiment by adding in the supporting electrolyte ferrocene, whose potential was measured as $E_{Fc(I)/Fc(0)}$ against the Ag(I)/Ag(0) reference. Conversion of potentials against the Fc⁺/⁰ couple are thus realized using the following equation:

$$E_{vs\,Fc(I)/Fc(0)} = E_{vs\,Ag(I)/Ag(0)} - E_{Fc(I)/Fc(0)} \qquad\qquad \textbf{Eqn. IV.2}$$

UV-visible spectroscopy

UV spectra of compounds were recorded with an *Agilent Technologies Cary 60 UV-Vis* spectrometer in a 1 cm optical light path quartz cuvette. The compounds of interest were dissolved in MeCN at a concentration of 0.01 mM.

References

1. Wood, C. J.; Summers, G. H.; Clark, C. A.; Kaeffer, N.; Braeutigam, M.; Carbone, L. R.; D'Amario, L.; Fan, K.; Farre, Y.; Narbey, S.; Oswald, F.; Stevens, L. A.; Parmenter, C. D. J.; Fay, M. W.; La Torre, A.; Snape, C. E.; Dietzek, B.; Dini, D.; Hammarstrom, L.; Pellegrin, Y.; Odobel, F.; Sun, L.; Artero, V.; Gibson, E. A. *PCCP* **2016**, DOI: 10.1039/c5cp05326a.

2. Dini, D.; Halpin, Y.; Vos, J. G.; Gibson, E. A. *Coord. Chem. Rev.* **2015**, *304-305*, 179-201.

3. Qin, P.; Zhu, H.; Edvinsson, T.; Boschloo, G.; Hagfeldt, A.; Sun, L. *J. Am. Chem. Soc.* **2008**, *130* (27), 8570-8571.

4. Li, L.; Gibson, E. A.; Qin, P.; Boschloo, G.; Gorlov, M.; Hagfeldt, A.; Sun, L. *Adv. Mater.* **2010**, *22* (15), 1759-62.

5. Qin, P.; Wiberg, J.; Gibson, E. A.; Linder, M.; Li, L.; Brinck, T.; Hagfeldt, A.; Albinsson, B.; Sun, L. *J. Phys. Chem. C* **2010**, *114* (10), 4738-4748.

6. Boschloo, G.; Hagfeldt, A. *Acc. Chem. Res.* **2009**, *42* (11), 1819-1826.

7. Odobel, F.; Pellegrin, Y. *J. Phys. Chem. Lett.* **2013**, *4* (15), 2551-2564.

8. Li, L.; Duan, L.; Wen, F.; Li, C.; Wang, M.; Hagfeldt, A.; Sun, L. *Chem. Commun.* **2012**, *48* (7), 988-90.

9. Berben, L. A.; Peters, J. C. *Chem. Commun.* **2010**, *46* (3), 398-400.

10. (a) Muckerman, J. T.; Fujita, E. *Chem. Commun.* **2011**, *47* (46), 12456-8; (b) Solis, B. H.; Hammes-Schiffer, S. *J. Am. Chem. Soc.* **2011**, *133* (47), 19036-9; (c) Lazarides, T.; McCormick, T.; Du, P.; Luo, G.; Lindley, B.; Eisenberg, R. *J. Am. Chem. Soc.* **2009**, *131* (26), 9192-9194.

11. Nattestad, A.; Mozer, A. J.; Fischer, M. K.; Cheng, Y. B.; Mishra, A.; Bauerle, P.; Bach, U. *Nat. Mater.* **2010**, *9* (1), 31-5.

12. Massin, J.; Brautigam, M.; Kaeffer, N.; Queyriaux, N.; Field, M. J.; Schacher, F. H.; Popp, J.; Chavarot-Kerlidou, M.; Dietzek, B.; Artero, V. *Interface Focus* **2015**, *5* (3), 20140083.

13. (a) Tong, L.; Iwase, A.; Nattestad, A.; Bach, U.; Weidelener, M.; Götz, G.; Mishra, A.; Bäuerle, P.; Amal, R.; Wallace, G. G.; Mozer, A. J. *Energy Environ. Sci.* **2012**, *5* (11), 9472; (b) Li, F.; Fan, K.; Xu, B.; Gabrielsson, E.; Daniel, Q.; Li, L.; Sun, L. *J. Am. Chem. Soc.* **2015**, *137* (28), 9153-9.

14. (a) Ji, Z.; He, M.; Huang, Z.; Ozkan, U.; Wu, Y. *J. Am. Chem. Soc.* **2013**, *135* (32), 11696-9; (b) Gennari, M.; Legalite, F.; Zhang, L.; Pellegrin, Y.; Blart, E.; Fortage, J.; Brown, A. M.; Deronzier, A.; Collomb, M. N.; Boujtita, M.; Jacquemin, D.; Hammarstrom, L.; Odobel, F. *J. Phys. Chem. Lett.* **2014**, *5* (13), 2254-8.

15. Weidelener, M.; Mishra, A.; Nattestad, A.; Powar, S.; Mozer, A. J.; Mena-Osteritz, E.; Cheng, Y.-B.; Bach, U.; Bäuerle, P. *J. Mater. Chem.* **2012**, *22* (15), 7366.

16. Parker, V. D.; Handoo, K. L.; Roness, F.; Tilset, M. *J. Am. Chem. Soc.* **1991**, *113* (20), 7493-7498.

17. (a) Pellegrin, Y.; Le Pleux, L.; Blart, E.; Renaud, A.; Chavillon, B.; Szuwarski, N.; Boujtita, M.; Cario, L.; Jobic, S.; Jacquemin, D.; Odobel, F. *J. Photochem. Photobiol., A* **2011**, *219* (2-3), 235-242; (b) Campagna, S.; Puntoriero, F.; Nastasi, F.; Bergamini, G.; Balzani, V., Photochemistry and Photophysics of Coordination Compounds: Ruthenium. In *Photochemistry and Photophysics of Coordination Compounds I*, Balzani, V.; Campagna, S., Eds. Springer Berlin Heidelberg: 2007; Vol. 280, pp 117-214.

18. (a) Natu, G.; Hasin, P.; Huang, Z.; Ji, Z.; He, M.; Wu, Y. *ACS Appl. Mater. Interf.* **2012**, *4* (11), 5922-9; (b) He, J.; Lindström, H.; Hagfeldt, A.; Lindquist, S.-E. *J. Phys. Chem. B* **1999**, *103* (42), 8940-8943.

19. (a) Kaeffer, N.; Chavarot-Kerlidou, M.; Artero, V. *Acc. Chem. Res.* **2015**, *48* (5), 1286-95; (b) Bhattacharjee, A.; Andreiadis, E. S.; Chavarot-Kerlidou, M.; Fontecave, M.; Field, M. J.; Artero, V. *Chem. Eur. J.* **2013**, *19* (45), 15166-74.

20. Huang, S.-T.; Hsu, Y.-C.; Yen, Y.-S.; Chou, H. H.; Lin, J. T.; Chang, C.-W.; Hsu, C.-P.; Tsai, C.; Yin, D.-J. *J. Phys. Chem. C* **2008**, *112* (49), 19739-19747.

21. Gallagher, L. A.; Serron, S. A.; Wen, X.; Hornstein, B. J.; Dattelbaum, D. M.; Schoonover, J. R.; Meyer, T. J. *Inorg. Chem.* **2005**, *44* (6), 2089-2097.

22. (a) Hahlin, M.; Johansson, E. M. J.; Plogmaker, S.; Odelius, M.; Hagberg, D. P.; Sun, L.; Siegbahn, H.; Rensmo, H. *PCCP* **2010**, *12* (7), 1507; (b) Ellis, H.; Eriksson, S. K.; Feldt, S. M.; Gabrielsson, E.; Lohse, P. W.; Lindblad, R.; Sun, L.; Rensmo, H.; Boschloo, G.; Hagfeldt, A. *J. Phys. Chem. C* **2013**, *117* (41), 21029-21036.

23. (a) Schaming, D.; Renault, C.; Tucker, R. T.; Lau-Truong, S.; Aubard, J.; Brett, M. J.; Balland, V.; Limoges, B. *Langmuir* **2012**, *28* (39), 14065-72; (b) Hamd, W.; Chavarot-Kerlidou, M.; Fize, J.; Muller, G.; Leyris, A.; Matheron, M.; Courtin, E.; Fontecave, M.; Sanchez, C.; Artero, V.; Laberty-Robert, C. *J. Mater. Chem. A* **2013**, *1* (28); (c) Hoertz, P. G.; Chen, Z.; Kent, C. A.; Meyer, T. J. *Inorg. Chem.* **2010**, *49* (18), 8179-8181.

24. (a) Agnès, C.; Arnault, J.-C.; Omnès, F.; Jousselme, B.; Billon, M.; Bidan, G.; Mailley, P. *PCCP* **2009**, *11* (48), 11647; (b) Liu, G.; Klein, A.; Thissen, A.; Jaegermann, W. *Surf. Sci.* **2003**, *539* (1-3), 37-48.

25. Andreiadis, E. S.; Jacques, P. A.; Tran, P. D.; Leyris, A.; Chavarot-Kerlidou, M.; Jousselme, B.; Matheron, M.; Pecaut, J.; Palacin, S.; Fontecave, M.; Artero, V. *Nat. Chem.* **2013**, *5* (1), 48-53.

26. Roy, S.; Bacchi, M.; Berggren, G.; Artero, V. *ChemSusChem* **2015**, *8* (21), 3632-3638.

27.   Guttentag, M.; Rodenberg, A.; Kopelent, R.; Probst, B.; Buchwalder, C.; Brandstätter, M.; Hamm, P.; Alberto, R. *Eur. J. Inorg. Chem.* **2012,** *2012* (1), 59-64.

28.   Bachmeier, A.; Hall, S.; Ragsdale, S. W.; Armstrong, F. A. *J. Am. Chem. Soc.* **2014,** *136* (39), 13518-21.

29.   Munoz-Garcia, A. B.; Pavone, M. *PCCP* **2015,** *17* (18), 12238-46.

30.   Castillo, C. E.; Gennari, M.; Stoll, T.; Fortage, J.; Deronzier, A.; Collomb, M. N.; Sandroni, M.; Légalité, F.; Blart, E.; Pellegrin, Y.; Delacote, C.; Boujtita, M.; Odobel, F.; Rannou, P.; Sadki, S. *J. Phys. Chem. C* **2015,** *119* (11), 5806-5818.

31.   Boschloo, G.; Hagfeldt, A. *J. Phys. Chem. B* **2001,** *105* (15), 3039-3044.

32.   Gu, J.; Yan, Y.; Young, J. L.; Steirer, K. X.; Neale, N. R.; Turner, J. A. *Nat. Mater.* **2015**.

33.   (a) Fihri, A.; Artero, V.; Razavet, M.; Baffert, C.; Leibl, W.; Fontecave, M. *Angew. Chem. Int. Ed.* **2008,** *47* (3), 564-7; (b) Fihri, A.; Artero, V.; Pereira, A.; Fontecave, M. *Dalton Trans.* **2008,** (41), 5567-5569.

34.   Ji, Z.; Natu, G.; Huang, Z.; Wu, Y. *Energy Environ. Sci.* **2011,** *4* (8), 2818.

Conclusion and perspectives

This work is focused on the implementation of the **[Co^{III}(DO)(DOH)pnL₂]** complex into light-driven WS devices.

We knew from previous studies conducted in organic media that this complex is one of the most efficient molecular catalyst for hydrogen evolution. A previous report proposed the use of a quite acidic electrolyte (pH 2.2) for operation of this catalyst under fully aqueous conditions. We could demonstrate that at such a pH the molecular complex actually degrades and yields a Co-based nanoparticulate materials responsible for HER catalysis but the detection of which is tedious. Besides, in a former work of the group, the cobalt diimine-dioxime complex was covalently attached on a conducting substrate to create a highly active and stable **GDL/MWCNT-Co** cathode for hydrogen evolution from midly acidic aqueous media (pH 4.5).

We further explored the operation of such cathode under PEC relevant conditions. With oxygenic concentrations in the electrolyte, the reduction of oxygen is catalyzed by the supported complex. However, this side-reduction does not impact the proton reduction catalysis occurring at a more negative potential and the activity is retained under the conditions used that reflect the startup of a PEC device. The **GDL/MWCNT-Co** electrode was then implemented into a tandem device for overall water-splitting, along with a photoanode and DSSCs. While a model device achieves unassisted light-driven water oxidation, photocurrents are also observed in the unbiased final cell integrating **GDL/MWCNT-Co**.

These first studies served us as a starting point for the task of constructing photocathodes based on **[Co^{III}(DO)(DOH)pnL₂]**. At the beginning of this work, DS photocathodes for hydrogen evolution were almost absent from the literature. The proof of concept has now been made, in this work and by others, and some examples are reported. Yet, the efficient systems developed to date all rely on a catalyst bound to the supporting TCO by a coordination link, which is usually labile. In our studies, we sought to create derivatives of the cobalt diimine-dioxime complex for the covalent attachment onto TCO.

Several functionalized **[Co^{III}(DO)(DOH)pnL₂]** species have been synthetized, bearing carboxylic or phosphonic acids as grafting moieties. They were first assessed for attachment onto TiO₂, as a benchmark TCO. From this study, we focused our work on the **Co_{C11P}** derivative displaying a phosphonic acid anchoring group. With the income of the knowledge gained at **Co_{C11P}**-decorated TiO₂ electrodes, we could translate our investigations to the attachment of the catalyst onto *p*-type NiO substrate, relevant for the construction of photocathodes. A series of

analytical characterizations confirmed the attachement of **Co$_{C11P}$** at the surface of NiO that also displays a good stability in neutral aqueous media. Interestingly, we evidenced that the Co$^{II/I}$ process is electrochemically accessible on the **NiO-Co$_{C11P}$** hydrid electrode, although it is located in a potential window where NiO is usually assumed not to be conductive. We attributed this effect to electron-hopping between Co centers. To the best of our knowledge, this study constitutes the first occurrence of electrochemical probing at an immobilized complex in the band gap region of NiO. Besides, reaching the Co^I state, thought as being the active state, gives good hope to use **Co$_{C11P}$** into DS photocathodes.

Based on the best compromise in terms of NiO preparation, we thus explored co-grafted architectures for HER photocathodes. In that aim, we exploited an engineered push-pull organic dye (**TPAT$_2$NMI**), since this type of backbone was demonstrated as particularly efficient in *p*-type DS photocathodes for DSSCs. In parallel, an architecture relying on the **RuP$_4$** Ru(bpy)$_3$-like prototype photosensitizer was also constructed. The co-sensitization of NiO with **Co$_{C11P}$** and the dyes was performed in a sequential process. A set of surface characterizations permitted to validate the successful shared decoration of the NiO layer, with retainment of the molecular structures of both entities once grafted.

The DS photocathodes were further assessed in PEC experiments. The electrodes showed onset photocurrents at high anodic potentials. The presence of the co-grafted **Co$_{C11P}$** at the surface was demonstrated to foster the light-driven electron transfer compared to the catalyst-free electrodes. Poised at potentials around 0.5-0.6 V *vs* RHE the **NiO-TPAT$_2$NMI-Co$_{C11P}$** photocathode develops steady-state photocurrents in the -2 to -7 μA·cm^{-2} range that achieve catalytic hydrogen evolution.

While these photocurrents are modest, future works should be dedicated to improve the co-grafted architectures, for instance by varying the linker, the anchoring groups or the acidity of the electrolyte.

We proposed that phosphonate moieties are partially grafted through strong P-O-Ni bonds and we believe that key information are to be found in the binding modes of the anchors onto NiO, which might be further deciphered through IR spectroscopy or modelling. Another track to explore is the use of a passivating layer at the top of the NiO surface both to consolidate the attachment and to limit the charge recombination. In this regard, photophysical studies would also give insightful information concerning electron transfers at the surface.

Overall, the pattern of structural and functional characterizations developed in this work will provide a convenient guidance in the improvement of the DS photocathodes.

As an opening, the successful synthesis of a series of immobilizable dye-catalyst dyads was achieved. The first characterizations provided evidenced that the covalent link used to gather the dye and the **[Co^{III}(DO)(DOH)pnL$_2$]** complex does not modify the LH ability of the PS part, that should enable light-driven reduction of the catalytic part. This work opens immediate and exciting perspectives to generate new H$_2$-evolving DS photocathodes over the *dyecat* dyads.

Résumé en français des travaux

Chapitre I :   Introduction

A l'heure où nos ressources fossiles s'amenuisent et où les rejets carbonés anthoropogènes génèrent un réchauffement climatique aux conséquences non maîtrisées, la recherche de sources d'énergie renouvelables et un pas important vers une indépendance énergétique future. Parmi les choix qui s'offrent à nous, l'utilisation d'une source abondante et ubiquitaire comme le rayonnement solaire paraît judicieuse. Bien que dix-mille fois supérieure à la consommation humaine, cette source d'énergie connaît néanmoins un inconvénient majeur, celui de l'intermittence. Ainsi, pour une utilisation à grande échelle, le stockage de l'énergie solaire doit être considéré. Pour ce faire, produire *via* l'énergie solaire un carburant, c'est-à-dire une espèce chimique à haute valeur énergétique, est une option attractive. En effet, un tel carburant, permet non seulement de stocker l'énergie sur le long terme, mais également avec de bonnes densités de stockage. Ce carburant, auquel la communauté scientifique a donné le nom de *carburant solaire*, pourrait être l'hydrogène, obtenu par *photoélectrolyse de l'eau*. Dans ce processus, l'eau, autre ressource abondante de notre planète, est cassée en dihydrogène et dioxygène. L'hydrogène ainsi obtenu peut ensuite être recombiné avec l'oxygène au sein d'un dispositif appelé *pile à combustible*. Ce processus permet de restituer l'énergie stockée sous forme de courant électrique, tout en relarguant un seul et inoffensif gaz d'échappement, l'eau. Ce cercle vertueux s'incrit dans le champ de la *photosynthèse artificielle*, puisqu'il s'inspire de la photosynthèse naturelle qui transforme l'eau et le dioxyde de carbone atmosphérique en sucre et en dioxygène grâce à l'apport de l'énergie lumineuse du soleil. Néanmoins, ces réactions nécessitent un apport supplémentaire en énergie par rapport au strict minimum requis par la thermodynamique, nommé *surtension*. Ainsi, pour effectuer de telles réactions, les systèmes vivants sont dotés de machineries extrêmement efficaces qui permettent d'éliminer ces surtensions. Par exemple, la production d'hydrogène à partir de l'eau, où plus précisément des protons de l'eau, est catalysée par des enzymes appelées hydrogénases. Ces enzymes effectuent de manière réversible l'interconversion des protons en dihydrogène au potentiel de l'équilibre thermodynamique du couple H^+/H_2.[1] Pour contourner l'utilisation du platine, un métal rare et cher, comme catalyseur, certains chimistes ont développé selon une approche dite *bio-inspirée* des molécules incorporant des métaux abondants

et qui reproduisent certains aspects fonctionnels des hydrogénases. Ces catalyseurs permettent de réduire les protons en dihydrogène à de faibles surtensions.

Au sein de notre laboratoire a été mis au point un catalyseur constitué d'un centre métallique de cobalt chelaté par un ligand tétradente diimine-dioxime N₂,N₂-propanediylbis(2,3-butanedione 2-imine 3-oxime), abrégé **(DOH)₂pn,** et deux ligands axiaux L.[2] Ce complexe diimine-dioxime de cobalt, noté **[Co(DO)(DOH)pnL₂]** (L = Cl, Br) et représenté Figure R1, a été mis en évidence comme l'un des catalyseurs moléculaires les plus performants pour la réduction des protons.[2-3] De manière intéressante, il a pu être immobilisé par un lien covalent à la surface d'un matériau d'électrode fait d'une membrane à diffusion de gaz (GDL) sur laquelle est déposé un film de nanotubes de carbone multi-paroi (MWCNT) emprisonnés dans du Nafion®, un polymère conducteur de protons. La cathode **GDL/MWCNT-Co** (Figure R1) ainsi obtenue a démontré l'électroréduction des protons en hydrogène depuis un milieu totalement aqueux à un pH modérément acide (4.5), avec de très bonnes performances tant d'un point de vue de la rapidité des cycles catalytiques que de la stabilité.[4] Cette architecture au sein de laquelle le catalyseur est supporté présente un intérêt tout particulier pour l'intégration en cellule complète de photoélectrolyse de l'eau (PEC) effectuant d'un côté la production d'hydrogène et de l'autre la production d'oxygène.

A côté de cela, l'utilisation de la lumière comme unique source d'énergie pour réaliser la réduction des protons est possible moyennant l'ajout d'une entité photoactive à l'électrode. Pour ce faire et prenant appui sur les résultats précédents, le travail présenté ici s'intéresse à l'immobilisation du catalyseur **[Co(DO)(DOH)pnX₂]** à la surface d'un matériau transparent et conducteur, par exemple un oxyde métallique transparent conducteur (TCO), sur laquelle sera aussi introduit un photosensibilisateur. Cet objet porte le nom de photocathode sensibilisée par un colorant (DS photocathode) pour la production d'hydrogène.

Cette approche va donner le cadre des travaux de thèse développés ici, dont le but est de construire des cathodes et photocathodes moléculaires de production d'hyrogène à visée d'intégration dans des cellules complètes de photoélectrolyse de l'eau. Cette dissertation s'articulera autour de trois axes :

- Dans un premier temps, nous nous intéresserons aux conditions opératoires aqueuses (l'eau étant le solvant de choix) du catalyseur **[Co(DO)(DOH)pnL₂]**, qu'il soit en solution homogène ou supporté. Nous décrirons d'abord l'activité du catalyseur en présence d'oxygène dans l'électrolyte. D'autre part, nous discuterons la nature de l'espèce catalytique en milieu aqueux acide. Enfin, nous présenterons les premiers essais

d'intégration de la cathode **GDL/MWCNT-Co** en cellule tandem de photoélectrolyse de l'eau.

- Dans un second temps, nous décrirons nos travaux visant à créer des matériaux cathodiques en immobilisant le complexe **[Co^{III}(DO)(DOH)pnL₂]** sur TCO. Des dérivés nouveaux du catalyseur portant des fonctions dédiées à l'ancrage sur surface de TCO seront présentés. La caractérisation des électrodes ainsi préparées sera ensuite détaillée.

- Pour finir, la mise au point de photocathodes moléculaires sur surface d'oxyde de nickel (NiO), un TCO de type *p*, sera plus largement développée. Le choix du NiO utilisé sera d'abord rationnalisé. Puis, la construction de photocathodes par co-greffage d'un dérivé du catalyseur **[Co^{III}(DO)(DOH)pnL₂]** et d'un colorant sera présentée. Les caractérisations structurales et fonctionnelles de ces entités seront données. Enfin, la synthèse d'une espèce moléculaire associant de manière covalente un colorant et un catalyseur et qui peut être attachée sur surface sera décrite, avec les caractérisations moléculaires associées.
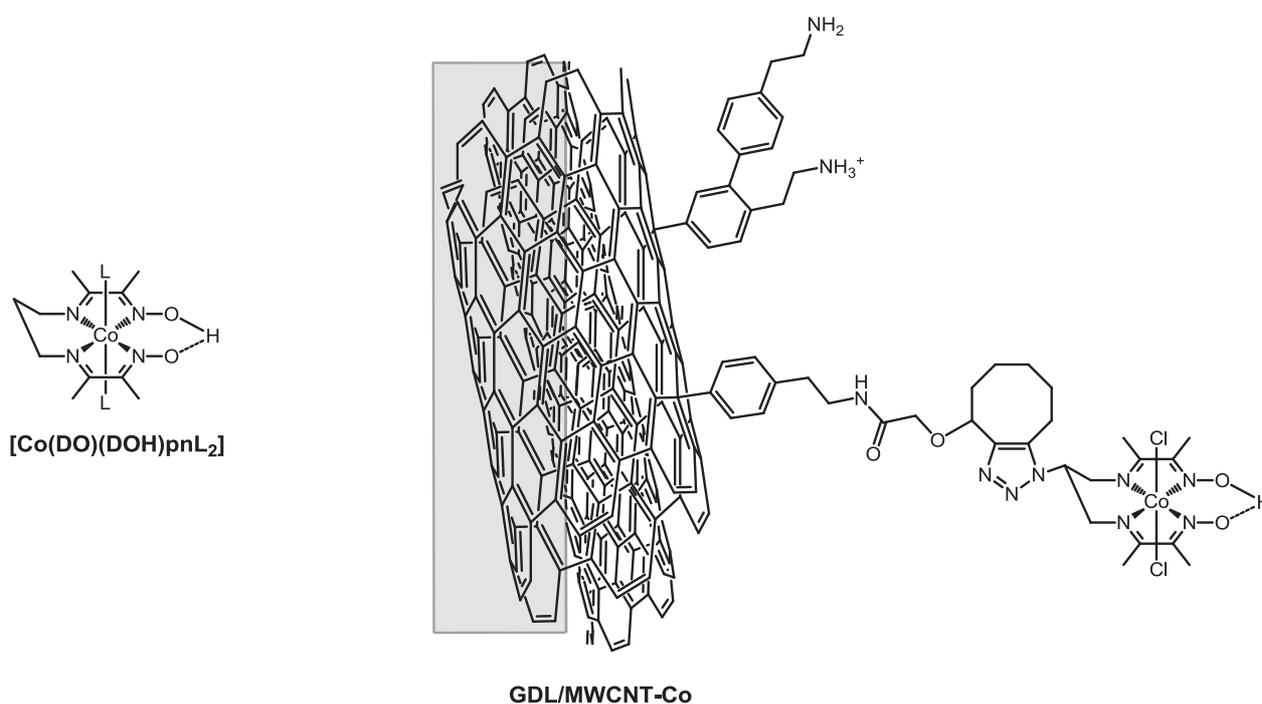
Figure R1. Représentations du complexe **[Co^{III}(DO)(DOH)pnL₂]** et de l'électrode hybride GDL/MWCNT-Co.

Chapitre II : De la catalyse en milieu aqueux à l'intégration en dispositif

Dans ce chapitre nous nous intéressons aux propriétés du catalyseur **[Co^{III}(DO)(DOH)pnL$_2$]** au regard de son intégration en dispositif.

Dans un premier temps, nous avons pu montrer que le catalyseur se dégrade, s'il est opéré à bas potentiels en conditions acides (pH 2.2) aqueuses homogènes. Cette dégradation forme des nanoparticules à base de cobalt (Figure R2, gauche) qui sont responsables de l'activité d'électroréduction des protons. Néanmoins, l'observation de ces nanoparticules demande des précautions particulières. Notamment, dans le cadre d'une procédure de test de rinçage, les nanoparticules se redissolvent (Figure R2, droite) et l'activité catalytique est perdue.
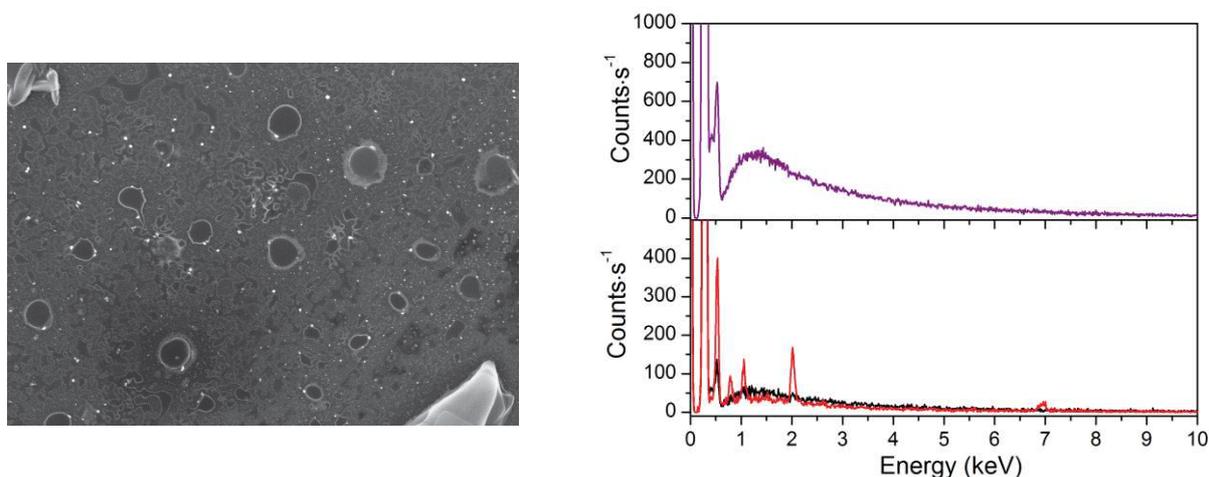
Figure R2. Image de microscopie électronique à balayage (SEM) du dépôt nanoparticulaire à base de cobalt (particules rondes) formé par équilibration d'une électrode de carbone vitreux (GCE) à –0,57 V vs RHE pour 1 heure en tampon phosphate 0,1 M à pH 2,2 et 0,3 mM en **[Co^{III}(DO)(DOH)pnCl$_2$]** (gauche) et spectres d'analyse dispersive en énergie à rayons X (EDX) des nanoparticules à base de cobalt (trait rouge) et du substrat (trait noir) enregistrés sur l'électrode de la figure de gauche et de la surface de l'électrode après rinçage dans l'eau distillée (trait violet) (droite).

Par contre, la structure du complexe moléculaire est conservée s'il est immobilisé sur un matériau d'électrode et son activité catalytique maintenue.[4] Cette observation est d'autant plus intéressante que le catalyseur supporté garde l'activité de réduction des protons même en présence d'oxygène dans le milieu d'électrolyse (Figure R3), comme cela pourrait être le cas dans une cellule PEC complète.
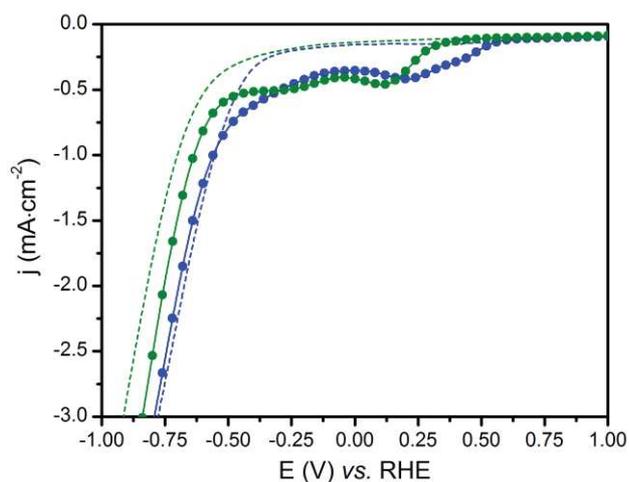
Figure R3. Voltampérogrammes à balayage linéaire (LSV) à une GCE décorée par des MWCNTs fonctionnalisés par le complexe **[Co^{III}(DO)(DOH)pnCl$_2$]** (traits bleus) ou sans le complexe (traits verts) enregistrés dans un électrolyte tampon acétate 0,1 M à pH 4,5 saturé en O$_2$ (traits pleins) ou en N$_2$ (traits pointillés) à une vitesse de balayage de 10 mV·s^{-1}.

Ainsi, nous avons été amenés à introduire notre électrode **GDL/MWCNT-Co** au sein d'une cellule tandem, dans le cadre d'une collaboration avec l'équipe de D. Gust à *Arizona State University*. Dans ce dispositif, la cathode a été associée avec des cellules solaires à colorant (DSSCs) de type **TMP** et une photoanode **ZnP/BIP/IrO$_x$** faite d'un photosensiblisateur moléculaire et de nanoparticules d'oxyde d'iridium comme catalyseur d'oxydation de l'eau (Figure R4).

Un système analogue modèle a démontré l'oxydation de l'eau avec de bons rendements faradiques. Néanmoins, la réduction des protons n'a pu être observée à la cathode **GDL/MWCNT-Co** intégrée dans le dispositif, du fait de la présence d'oxygène résiduel et des faibles courants générés sous irradiation.
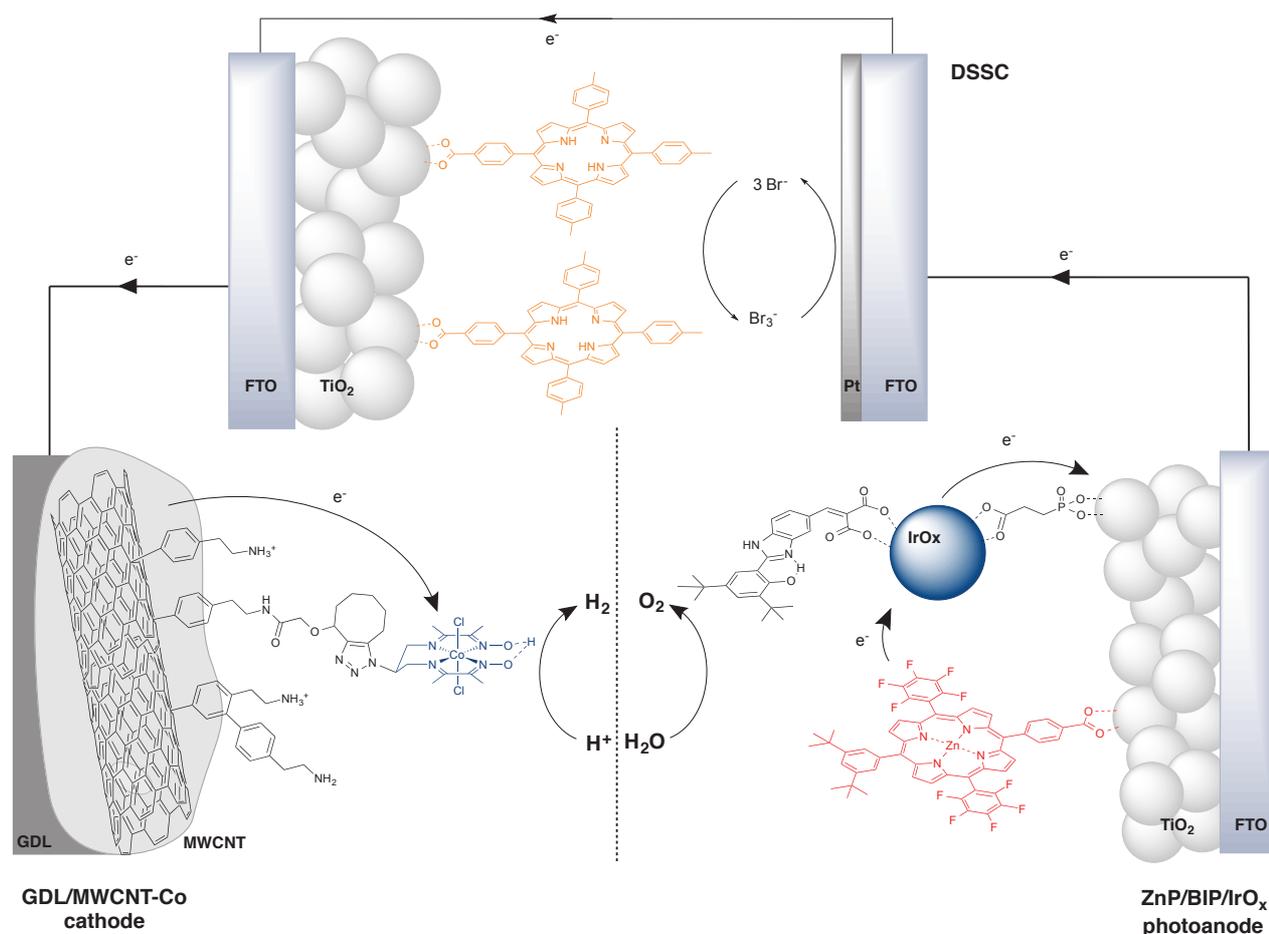
Figure R4. Schéma de la cellule tandem éaborée rassemblant la cathode **GDL/MWCNT-Co** de production d'hydrogène, une DSSC **TMP** et la photoanode **ZnP/BIP/IrO$_x$** de production d'oxygène.

Ces premiers essais d'uitlisation du catalyseur en dispositifs fonctionnels de photoélectrolyse de l'eau nous ont fait cheminer vers l'intégration directe d'une entité photoactive à la cathode.

Chapitre III : Vers l'ancrage de complexes diimine-dioxime de cobalt sur oxydes transparents conducteurs

Dans un premier temps, nous avons synthétisé une série de dérivés du complexe **[Co^{III}(DO)(DOH)pnL$_2$]** portant des groupements d'ancrage acide carboxylique ou phosphonique. Ces groupements ont été choisis car ils sont connus pour permettre l'attachement sur des surfaces d'oxydes métalliques transparents conducteurs.[5]

Parmi ces dérivés, la synthèse du complexe **Co$_{C11P}$** (Figure R5) a été effectuée, en mettant en œuvre un couplage par cycloaddition de Huisgen catalysé au cuivre, suivi de la substitution du cuivre par le cobalt dans la sphère de coordination du complexe.
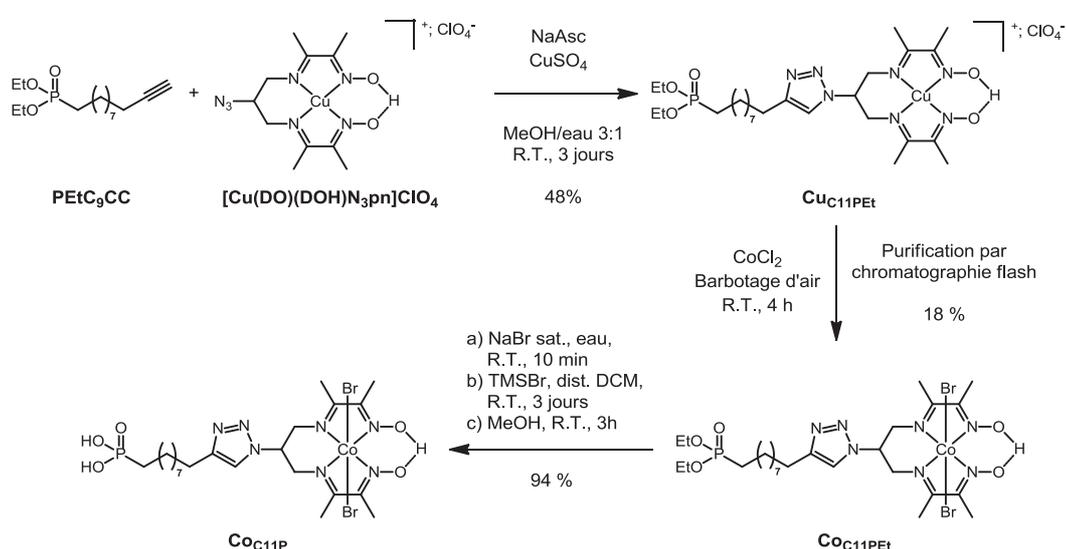
Figure R5. Schéma de synthèse du dérivé **Co$_{C11P}$** portant un acide phosphonique. R.T. : *room temperature* (température ambiante).

Ce dérivé a d'abord été immobilisé sur surface d'oxyde de titane (TiO$_2$) mésoporeuse, un TCO modèle. Cette électrode hybride a été caractérisée par électrochimie et spectroscopie à émission de photoélectrons à rayons X (XPS) et l'attachement du complexe moléculaire sur la surface a pu être validé.

Cette approche a ensuite été translatée au greffage du même dérivé sur surface mésoporeuse d'oxyde de nickel (NiO), un TCO de type *p*. Le complexe a été greffé selon la procédure décrite Figure R6. Identiquement, l'électrochimie, l'analyse spectrométrique de masse en surface (ToF-SIMS) et l'analyse XPS confirme la présence du dérivé ancré sur NiO.
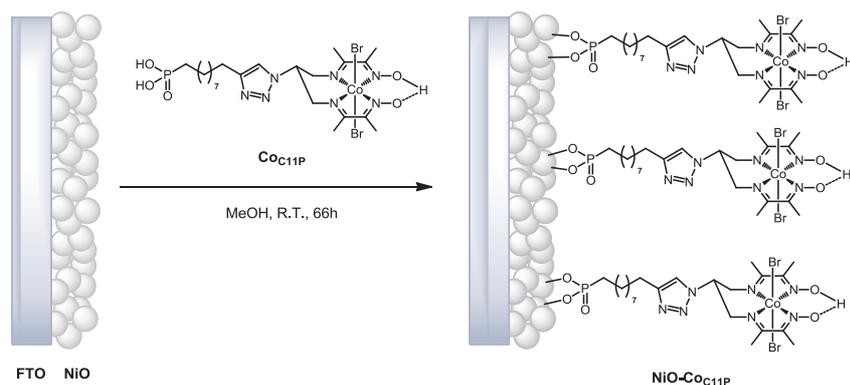
Figure R6. Préparation des électrodes **NiO-Co$_{C11P}$**.

Une vague électrochimique liée au dérivé immobilisé est observée aux potentiels négatifs sur la surface de NiO (Figure R7, gauche), alors même que la conduction électronique est interdite à ces potentiels à la surface d'un tel semi-conducteur de type *p*.
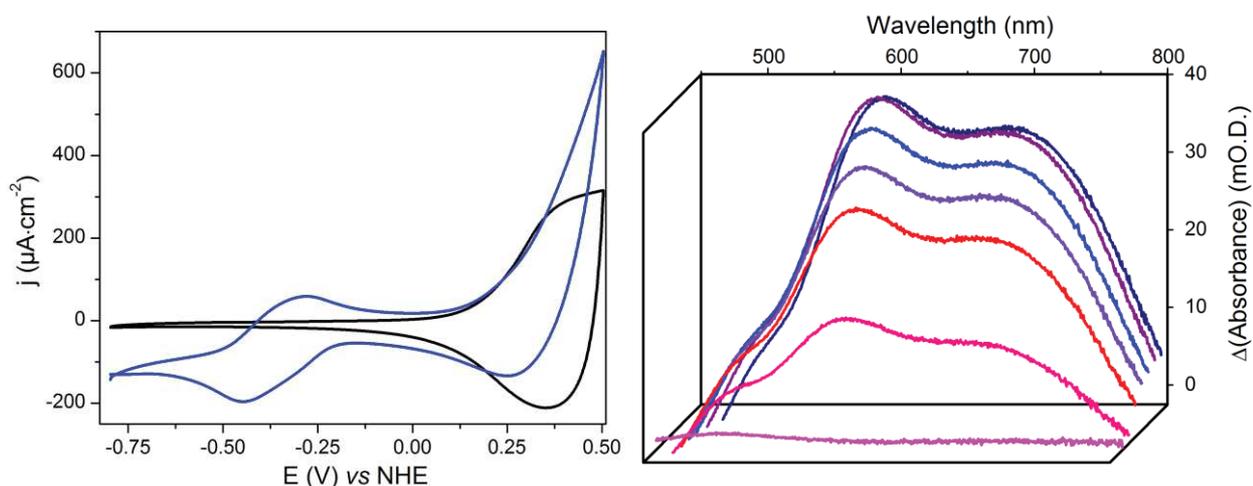

Figure R7. Voltampérogrammes cycliques (CV) d'une électrode NiO vierge (trait noir) et d'une électrode **NiO-Co$_{C11P}$** (trait bleu) à 100 mV·s^{-1} (gauche) et spectres UV-visible différentiels à l'électrode **NiO-Co$_{C11P}$** équilibrée à –0,44 (trait magenta), –0,54 (trait rose), –0,64 (trait rouge), –0,74 (trait mauve), –0,84 (trait bleu), –0,94 (trait violet) et –1,04 (trait bleu foncé) V *vs* NHE, après soustraction du spectre de l'électrode équilibrée à –0,34 V *vs* NHE dans les mêmes conditions (droite), enregistrés en électrolyte aqueux NaCl 0,1 M.

La spectroélectrochimie UV-visible d'une lame **NiO-Co$_{C11P}$** (Figure R7, droite) nous a permis de montrer que cette vague est celle du couple Co$^{II/I}$ du complexe ancré. Nous avons proposé que cet évènement chimique soit accessible *via* un phénomène de *saut d'électrons*.

En tout cas, l'observation du complexe greffé de manière stable sur la surface de NiO nous a encouragés à co-immobiliser un photosensibilisateur pour créer une photocathode moléculaire de production d'hydrogène.

Chapitre IV : Construction de photocathodes moléculaires de production d'hydrogène

Dans cette dernière partie, nous avons préparé des photocathodes moléculaires pour la réduction des protons.

D'abord, des architectures basées sur une approche de co-greffage séquentiel d'un catalyseur et d'un colorant ont été mises au point. Par exemple, le colorant organique **TPAT$_2$NMI** a été co-immobilisé sur NiO avec le dérivé **Co$_{C11P}$** (Figure R8). Le bon ajustement des niveaux d'énergie a pu être validé d'après les données obtenues sur les différentes entités (NiO, colorant, catalyseur) prises séparément.
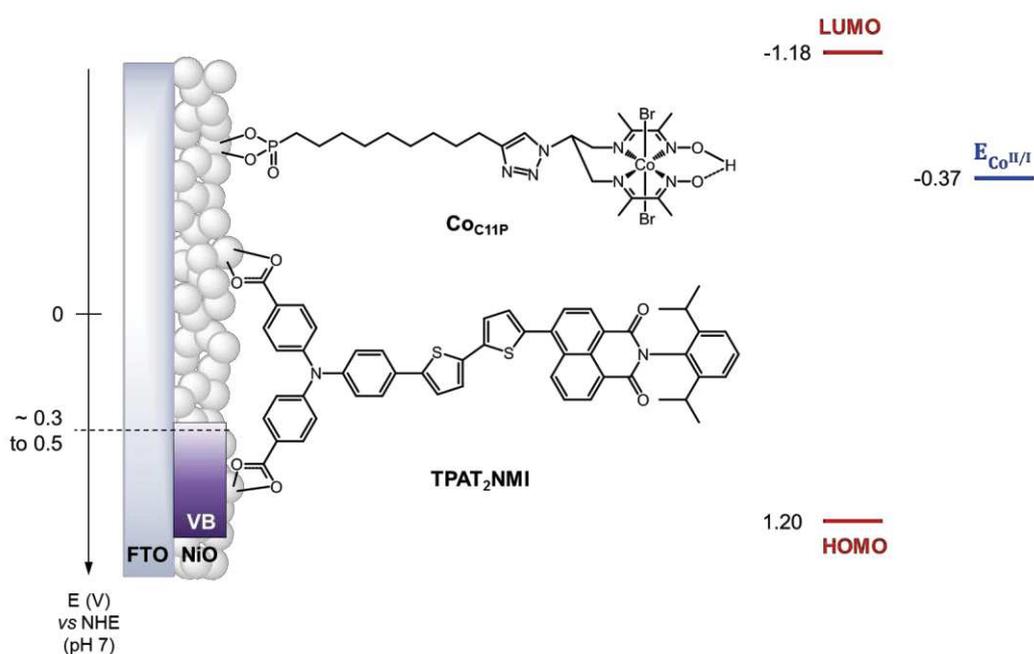
Figure R8. Diagramme schématique des niveaux d'énergie en jeu à la photocathode **NiO-TPAT$_2$NMI-Co$_{C11P}$**.

La présence des deux entités de manière concomitante sur la surface a pu être démontrée par différentes techniques d'analyse (électrochimie, spectroscopie UV-visible, XPS, ToF-SIMS). Notamment, l'électrochimie nous montre que le complexe de cobalt **Co$_{C11P}$** est bien observé sur l'électrode co-greffée (Figure R9, gauche). D'autre part, la spectroscopie UV-visible nous permet aussi de conclure que le colorant est également présent (Figure R9, droite) sur cette électrode.
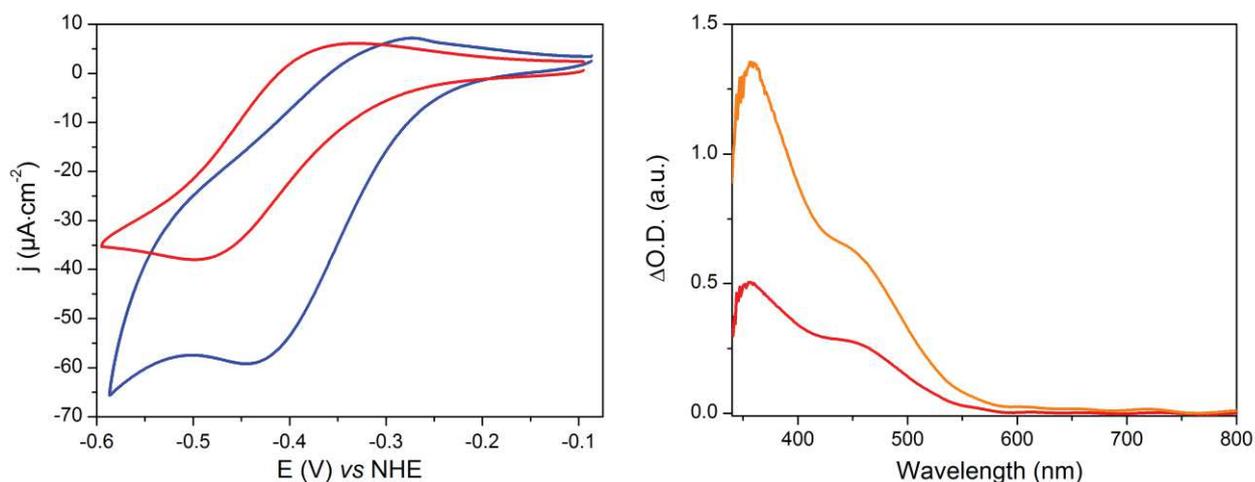
Figure R9. CV à l'électrode **NiO-Co_{C11P}** (trait bleu) et à l'électrode **NiO-TPAT₂NMI-Co_{C11P}** (trait rouge) enregistrées en électrolyte aqueux NaCl 0.1 M à 10 mV·s⁻¹ (gauche) et spectres UV-visible de l'électrode **NiO-TPAT₂NMI** (trait orange) et de l'électrode **NiO-TPAT₂NMI-Co_{C11P}** (trait rouge) (droite).

Cette électrode a ensuite été caractérisée de manière fonctionnelle. Sous irradiation lumineuse, un photocourant a pu être observé à partir de 0,60 V *vs* NHE (Figure R10, gauche). Ce photocourant est également observé si l'électrode est équilibrée pendant un temps long à un potentiel supérieur à l'équilibre thermodynamique H⁺/H₂ (Figure R10, droite). D'autre part, ce photocourant se trouve augmenté lorsque le catalyseur est co-greffé sur la surface. Bien que la valeur et la reproductiblité des photocourants soient encore à améliorer, la production photoélectrocatalytique d'hydrogène a pu être validée lors de telles expériences.
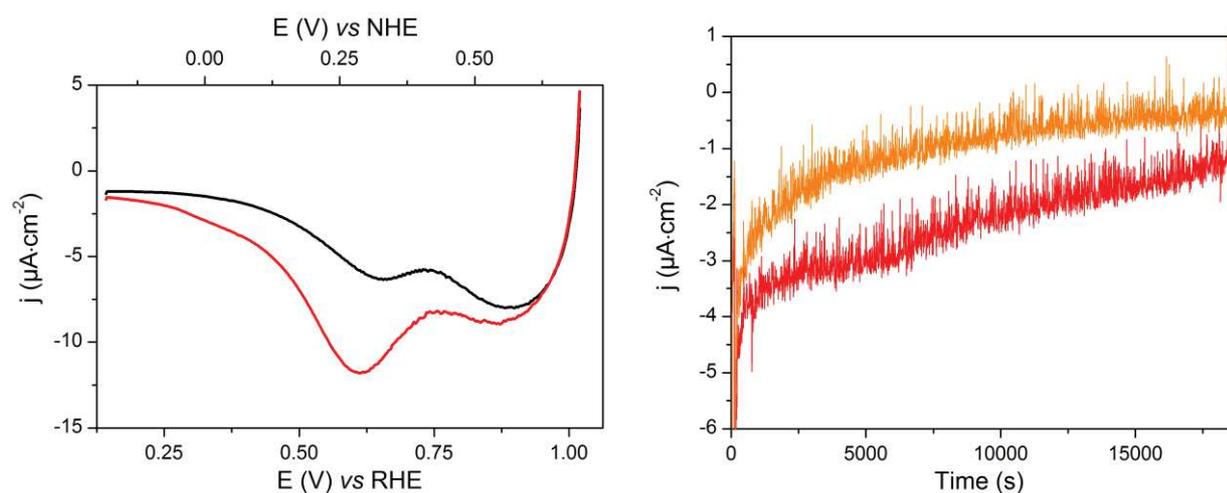

Figure R10. LSV à l'électrode **NiO-TPAT₂NMI-Co_{C11P}** dans le noir (trait noir) et sous irradiation lumineuse (trait rouge) à 1 mV·s⁻¹ (gauche) et chronoampérométries à 0,63 V vs RHE sous irradiation lumineuse à l'électrode **NiO-TPAT₂NMI-Co_{C11P}** (trait rouge) et à l'électrode **NiO-TPAT₂NMI** (trait orange) (droite) enregistrées dans un tampon aqueux MES 0.1 M/NaCl 0.1 M (pH 5.5).

L'approche consistant à directement unir le photosensibilisateur et le catalyseur au sein d'une même entité moléculaire greffable sur surface a été abordée en clôture de ces travaux. La synthèse des dyades *dyecat* **TPAT$_1$Co** et **TPAT$_2$Co** est présentée en Figure R11.
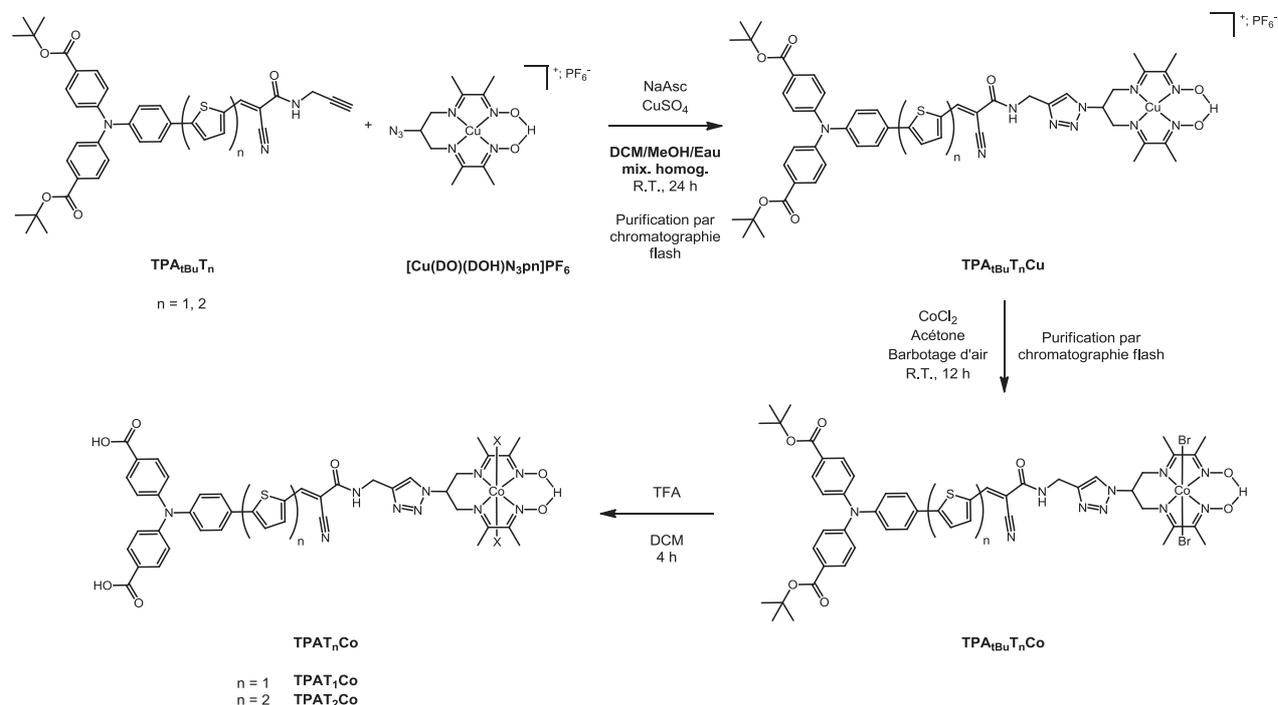

Figure R11. Synthèse de dyades colorant-catalyseur greffables sur surface.

Les caractérisations moléculaires (spectroscopie UV-visible, électrochimie) ont mis en évidence que les propriétés de capture de lumière n'étaient pas altérées dans la dyade **TPA$_{tBu}$T$_1$Co** par rapport au colorant **TPA$_{tBu}$T1** de départ. Egalement, les niveaux d'énergie électronique au sein de la dyade sont *a priori* favorables à l'injection d'électrons depuis l'état photoexcité de la partie photosensibilisatrice vers la partie catalytique.

Ces dyades pourront par la suite être greffées sur surface de NiO pour générer de nouvelles architectures de photocathodes moléculaires pour la production d'hydrogène.

Conclusion et perspectives

Ces travaux de thèse ont été articulés autour de l'intégration du complexe **[Co^{III}(DO)(DOH)pnL$_2$]** en architectures pour la production photoélectrocatalytique d'hydrogène.

Différentes conditions opératoires dans l'eau, solvant de choix, ont été examinées. En milieu acide aqueux, le complexe en solution homogène se dégrade pour donner des nanoparticules responsables de l'activité catalytique. A l'opposé, son activité est maintenue, même en présence d'oxygène, s'il est immobilisé sur électrode. Une telle électrode portant le catalyseur supporté a d'ailleurs été mise en jeu dans la construction d'une cellule tandem de photoélectrolyse complète de l'eau.

D'autre part, de nouveaux dérivés du complexe portant des groupements pour l'attachement sur oxydes transparents conducteurs ont été synthétisés. Le complexe fonctionnalisé **Co$_{C11P}$** a d'abord été greffé et caractérisé sur surface de TiO$_2$ mésoporeux, un TCO modèle. Puis, l'immobilisation du complexe sur NiO a été démontrée. Nous avons pu confirmer que le couple Co$^{II/I}$ du complexe greffé était électrochimiquement accessible sur l'électrode et nous avons proposé que cela soit dû à un phénomène de saut d'électron.

Dans une dernière partie, nous avons associé sur surface de NiO le complexe **Co$_{C11P}$** avec des photosensibilisateurs pour créer des architectures co-greffées. Nous avons mis en évidence que les deux espèces (catalyseur et colorant) étaient présentes de manière concomitante à la surface de ces électrodes. La photocathode **NiO-TPAT$_2$NMI-Co$_{C11P}$** développe des photocourants cathodiques depuis des potentiels supérieurs à l'équilibre thermodynamique H$^+$/H$_2$ et qui sont associés à la production d'hydrogène.

Enfin, des dyades regroupant de manière covalente un colorant et un catalyseur ont été synthétisées. Les caractérisations moléculaires montrent qu'un transfert photoinduit d'électrons vers le catalyseur est possible. Ces dyades portent des groupements d'attache sur surface et représentent donc une nouvelle opportunité de créer des photocathodes moléculaires originales.

Références

1. Lubitz, W.; Ogata, H.; Rudiger, O.; Reijerse, E. *Chem. Rev.* **2014,** *114* (8), 4081-148.
2. Jacques, P. A.; Artero, V.; Pecaut, J.; Fontecave, M. *Proc. Natl. Acad. Sci. USA* **2009,** *106* (49), 20627-32.
3. Fourmond, V.; Jacques, P. A.; Fontecave, M.; Artero, V. *Inorg. Chem.* **2010,** *49* (22), 10338-47.
4. Andreiadis, E. S.; Jacques, P. A.; Tran, P. D.; Leyris, A.; Chavarot-Kerlidou, M.; Jousselme, B.; Matheron, M.; Pecaut, J.; Palacin, S.; Fontecave, M.; Artero, V. *Nat. Chem.* **2013,** *5* (1), 48-53.
5. Pujari, S. P.; Scheres, L.; Marcelis, A. T.; Zuilhof, H. *Angew. Chem. Int. Ed.* **2014,** *53* (25), 6322-56.

Appendices

- **Addendum to Chapter III.3.2.1.**

- **Paper I:** Kaeffer, N.; Chavarot-Kerlidou, M.; Artero, V. *Acc. Chem. Res.* **2015**, *48* (5), 1286-95.

- **Paper II:** Queyriaux, N.; Kaeffer, N.; Morozan, A.; Chavarot-Kerlidou, M.; Artero, V. *J. Photochem. Photobiol., C* **2015**, *25*, 90-105.

- **Paper III:** Massin, J.; Brautigam, M.; Kaeffer, N.; Queyriaux, N.; Field, M. J.; Schacher, F. H.; Popp, J.; Chavarot-Kerlidou, M.; Dietzek, B.; Artero, V. *Interface Focus* **2015**, *5* (3), 20140083.

- **Paper IV:** Wood, C. J.; Summers, G. H.; Clark, C. A.; Kaeffer, N.; Braeutigam, M.; Carbone, L. R.; D'Amario, L.; Fan, K.; Farre, Y.; Narbey, S.; Oswald, F.; Stevens, L. A.; Parmenter, C. D. J.; Fay, M. W.; La Torre, A.; Snape, C. E.; Dietzek, B.; Dini, D.; Hammarstrom, L.; Pellegrin, Y.; Odobel, F.; Sun, L.; Artero, V.; Gibson, E. A. *PCCP* **2016**, *advance article*, DOI: 10.1039/c5cp05326a.

Addendum to Chapter III.3.2.1.

We demonstrated in Chapter III that **Co$_{C11P}$** is attached to the surface of NiO. In section 3.2.1.4., we attributed through UV-visible spectroelectrochemistry the redox event observed at −0.37 V *vs* NHE on the **NiO-Co$_{C11P}$** to the Co$^{II/I}$ event. We further proposed that the redox probing of the Co$^{II/I}$ wave was allowed in this insulating region of NiO through electron hopping between adjacent immobilized **Co$_{C11P}$**. The electron hopping mechanism is expected to infer a charge-diffusional behavior.[1] In this Addendum, we calculated the apparent diffusion coefficient D_{app} (given in section 3.2.1.3.) related to the overall charge-transfer processes at the interface and that includes the hypothetized electron hopping mechanism.

First, we will restrict here our investigations to the cathodic wave from Co^{II} to Co^{I}. We consider here the height of the wave, instead of the peak current, by subtracting the background current related to non-faradaic events.
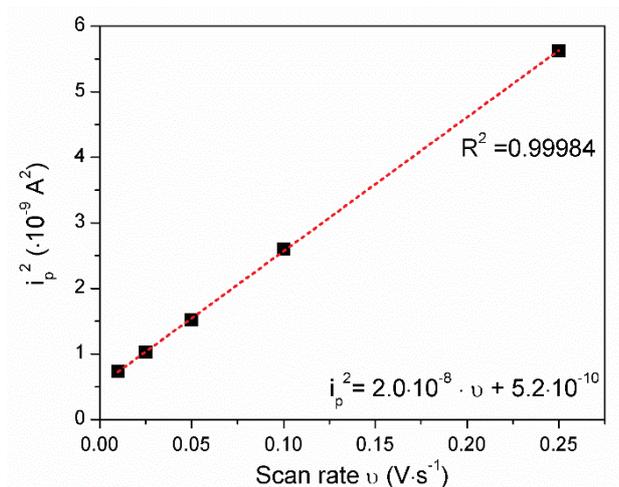

Figure III.23.bis. Square *baseline-corrected* peak current as a function of the scan rate (dots) with associated linear fit (dashed lines) for CVs recorded at a **NiO-Co$_{C11P}$** electrode in a NaCl 0.1 M aqueous electrolyte.

As shown in Figure III.23.bis, the square height of the cathodic wave displays a well linear dependence in scan rate over the whole range studied. This observation is indicative of a diffusion-limited process occurring at the interface. The experimental data are fitted with a linear function of slope: $a = 2.0 \times 10^{-8}$ A^2·s·V^{-1}.

---

[1] Savéant, J. M., *Elements of Molecular and Biomolecular Electrochemistry*, Wiley:2006, p. 284-287.

Modelling the process by a single electron transfer at the interface under diffusion-limited conditions, the peak current might be related to the scan rate through the following equation:[2]

$$i_p^2 = \frac{0.446^2 \cdot F^3 \cdot C_b^2 \cdot S^2}{R \cdot T} \cdot D_{app} \cdot v \qquad \text{Eqn.III.bis.1.}$$

where C_b is the concentration in redox species in the bulk of the solution (in mol·cm^{-3}), D_{app} the apparent diffusion coefficient of the redox species (in cm^2·s^{-1}) and S the surface of the electrode (in cm^2), others terms being defined in the parent manuscript.

The apparent diffusion coefficient may thus be recovered as such:

$$D = \frac{a \cdot R \cdot T}{0.446^2 \cdot F^3 \cdot C_b^2 \cdot S^2} \qquad \text{Eqn.III.bis.2.}$$

To obtain the apparent diffusion coefficient, we considered the electron hopping process starting from the FTO back-contact and diffusing within the mesoporous NiO film. Hence, the C_b concentration has been assumed in first approximation as the [**Co$_{C11P}$**]$_{NiO}$ concentration of grafted **Co$_{C11P}$** within the NiO layer. This concentration might be obtained knowing the surface coverage in **Co$_{C11P}$** (Γ_{CoC11P}) and the thickness l of the NiO film, through:

$$[Co_{C11P}]_{NiO} = \frac{\Gamma_{CoC11P}}{l} \qquad \text{Eqn.III.bis.3.}$$

Considering a diffusion-controlled process, the surface coverage cannot be directly obtained by integration of the Co$^{II/I}$ wave. Instead, we used UV-visible data obtained at the **NiO-Co$_{C11P}$** electrode after reduction of the immobilized catalyst to the Co^I state shown in Figure III.25, left. In that aim, we first estimated the molar absorptivity of the **[Co^I(DO)(DOH)pn]** model complex in solution by recording spectroelectrochemistry starting from the **[Co^{III}(DO)(DOH)pnBr$_2$]** one under homogeneous conditions (MeCN, TBAPF$_6$ 0.1 M). We could determine a molar absorptivity coefficient at maximal absorbance 601 nm of $\varepsilon_{601\ nm}^{Co(I)} \approx 8300$ L·mol^{-1}·cm^{-1}. Using equation Eqn. IV.1 (see main manuscript) and the UV-visible signature of the reduced **NiO-Co$_{C11P}$** electrode shown in Figure III.25, left (main manuscript) the surface loading in **Co$_{C11P}$** was

[2] Savéant, J. M., *Elements of Molecular and Biomolecular Electrochemistry*, Wiley: 2006, p. 7.
Bard, A. J.; Faulkner, L. R., *Electrochemical methods: fundamentals and applications*. Second ed.; Wiley: 2001, p. 231.

estimated at $\Gamma_{CoC11P} \approx 4.5$ nmol·cm^{-2}. The thickness of the NiO film is *ca* 1.75 μm, which yields a concentration in **Co$_{C11P}$** in the NiO film [**Co$_{C11P}$**]$_{NiO} \approx 2.5$ μmol·cm^{-3}.

The apparent diffusion coefficient was then calculated formally assuming the surface of the FTO back-contact as S = 1 cm^2 (geometric surface of the electrode studied). The experiment being conducted at room temperature, T was taken as 298 K.

We could thus obtain the value of the apparent diffusion coefficient:

$$D_{app} = 4.4 \cdot 10^{-8} \, cm^2 \cdot s^{-1}$$

Although the electron hopping process has not been reported to date at the surface of NiO, the value of the diffusion coefficient is in the same order of magnitude than values reported for charges hopping at the insulating region of electrodes, namely at the surface of mesoporous TCO.[3] This value is also orders of magnitude higher than that observed for species adsorbed within mesoporous semi-conducting films for which the charge transport is limited by the physical diffusion of the redox active species throughout the film to the conductive back-contact.[4]

Overall, this analysis comes as an addendum to Chapter III and clarifies the conclusions:

- **Co$_{C11P}$** is firmly bound to NiO surface, as shown by a stable electrochemical feature (Figure III.22) and a sustained UV-visible signature at the reduced Co^I state (Figure III.25) in neutral aqueous media, as well as by the suggestion of strong Ni-O-P bounds from the ToF-SIMS analysis (Figure III.20).
- The scan rate dependence at **NiO-Co$_{C11P}$** does include a diffusion-limited process namely attributed to the postulated electron hopping mechanism.
- The apparent diffusion coefficient is found at 4.4 10^{-8} cm^2·s^{-1}. This value is in good line with the one observed for other examples of charge hopping through mesoporous TCO films.

[3] Bonhote P. et al. *J. Phys. Chem. B* **1998**, *102*, 1498-1507.
[4] Renault C. et al. *PCCP* **2015**, *17*, 10592.

Hydrogen Evolution Catalyzed by Cobalt Diimine–Dioxime Complexes

Nicolas Kaeffer, Murielle Chavarot-Kerlidou, and Vincent Artero*

Laboratoire de Chimie Biologie des Métaux, Univ. Grenoble Alpes, CNRS, CEA Life Science Division, 17 rue des Martyrs, 38000 Grenoble, France

CONSPECTUS: Mimicking photosynthesis and producing solar fuels is an appealing way to store the huge amount of renewable energy from the sun in a durable and sustainable way. Hydrogen production through water splitting has been set as a first-ranking target for artificial photosynthesis. Pursuing that goal requires the development of efficient and stable catalytic systems, only based on earth abundant elements, for the reduction of protons from water to molecular hydrogen. Cobalt complexes based on glyoxime ligands, called cobaloximes, emerged 10 years ago as a first generation of such catalysts. They are now widely utilized for the construction of photocatalytic systems for hydrogen evolution.

In this Account, we describe our contribution to the development of a second generation of catalysts, cobalt diimine–dioxime complexes. While displaying similar catalytic activities as cobaloximes, these catalysts prove more stable against hydrolysis under strongly acidic conditions thanks to the tetradentate nature of the diimine–dioxime ligand. Importantly, H_2 evolution proceeds via proton-coupled electron transfer steps involving the oxime bridge as a protonation site, reproducing the mechanism at play in the active sites of hydrogenase enzymes. This feature allows H_2 to be evolved at modest overpotentials, that is, close to the thermodynamic equilibrium over a wide range of acid–base conditions in nonaqueous solutions.

Derivatization of the diimine–dioxime ligand at the hydrocarbon chain linking the two imine functions enables the covalent grafting of the complex onto electrode surfaces in a more convenient manner than for the parent bis-bidentate cobaloximes. Accordingly, we attached diimine–dioxime cobalt catalysts onto carbon nanotubes and demonstrated the catalytic activity of the resulting molecular-based electrode for hydrogen evolution from aqueous acetate buffer. The stability of immobilized catalysts was found to be orders of magnitude higher than that of catalysts in the bulk. It led us to evidence that these cobalt complexes, as cobaloximes and other cobalt salts do, decompose under turnover conditions where they are free in solution. Of note, this process generates in aqueous phosphate buffer a nanoparticulate film consisting of metallic cobalt coated with a cobalt-oxo/hydroxo-phosphate layer in contact with the electrolyte. This novel material, H_2–CoCat, mediates H_2 evolution from neutral aqueous buffer at low overpotentials.

Finally, the potential of diimine–dioxime cobalt complexes for light-driven H_2 generation has been attested both in water/acetonitrile mixtures and in fully aqueous solutions. All together, these studies hold promise for the construction of molecular-based photoelectrodes for H_2 evolution and further integration in dye-sensitized photoelectrochemical cells (DS-PECs) able to achieve overall water splitting.
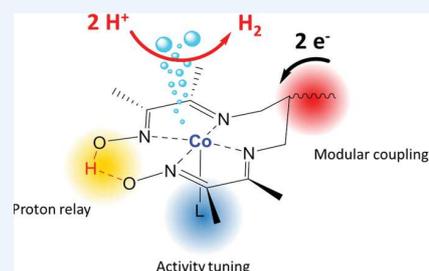
INTRODUCTION

The amount of solar energy reaching the Earth exceeds our societal needs by several orders of magnitude.[1] However, worldwide energy demand does not correlate with the availability of sunlight. Trapping energy in chemical bonds, by producing fuels, is the only way to storing at the terawatt scale. Such a solution has already been massively implemented by photosynthetic organisms which use sunlight to sustain their metabolism and produce biomass. Mimicking this natural process to produce solar fuels is the founding principle of a large field of research called "artificial photosynthesis".[2] Solar-driven water-splitting and production of molecular hydrogen has been set as a first target in this context, in line with the promises held by H_2 as an energy vector. A related key challenge is the finding of new efficient and robust catalysts based on earth abundant elements for the reduction of protons into H_2.[3] To design such catalysts, inspiration naturally arises

from the dinuclear FeFe and NiFe active sites of hydrogenases (Figure 1),[4] the metallo-enzymes achieving H^+/H_2 intercon-version both at fast rate and close to the thermodynamic equilibrium. A number of promising catalytic systems derived from this approach.[5] Actually, mimics of another important enzyme, the cobalt-containing vitamin B_{12} (Figure 1), also called cobalamin, proved among the most efficient molecular electrocatalysts for H_2 evolution. In its super-reduced state (B_{12sr}) featuring a Co^I center, cobalamin is the most powerful nucleophile in nature.[6] Accordingly, cobalt bis-glyoximato complexes, largely developed by Schrauzer as B_{12} mimics and known as cobaloximes (Figure 1),[6] can be protonated in their reduced form to yield hydridocobaloximes or tautomeric forms, the structure of which is still under investigation.[7] Such species
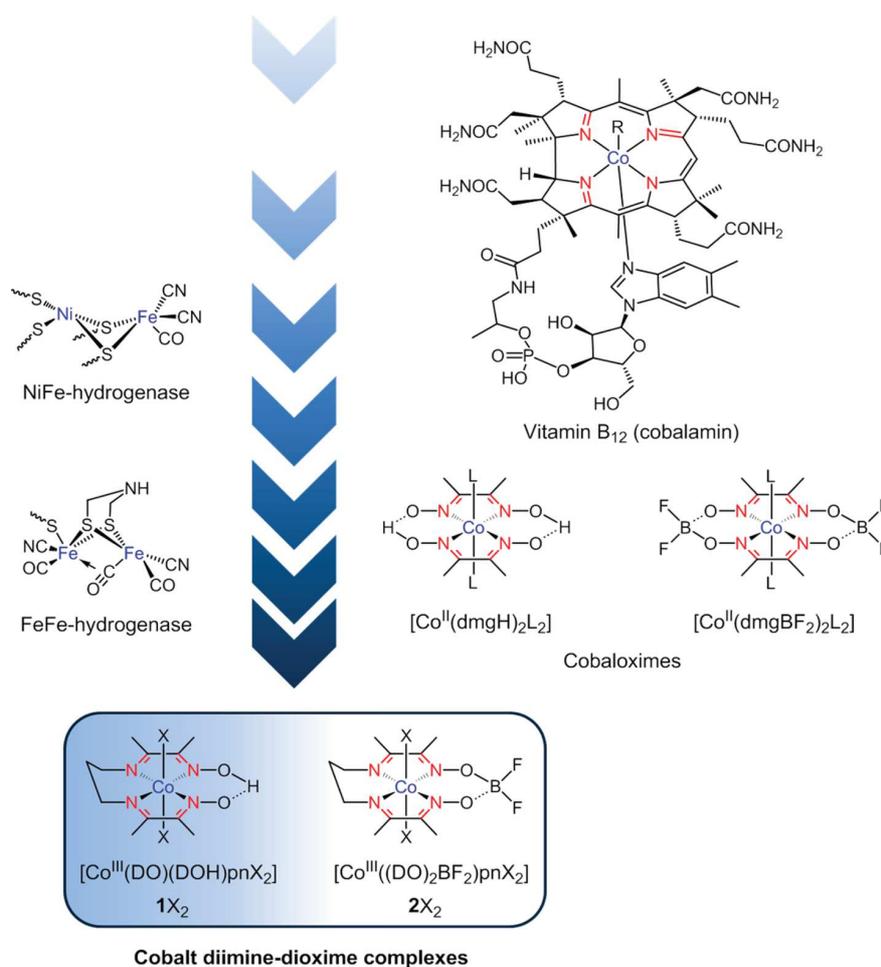
Figure 1. Structures of the active sites of NiFe and FeFe hydrogenases and of vitamin B_{12} (R = H_2O, CN^-, CH_3, adenosyl,...), proton-bridged and difluoroboryl-annulated cobaloximes (L = solvent (H_2O, CH_3CN, DMF)), and cobalt diimine−dioxime complexes $1X_2$ and $2X_2$ (X = Br, Cl,...).

actually turn to be the key intermediates in H_2 evolution catalyzed by this class of compounds.[8] Catalytic activity, initially reported in 1983 by Ziessel and co-workers in the context of light-driven H_2 evolution,[9] was confirmed from 2005 by two independent electrochemical studies carried out in our laboratory[10] and in the one of Peters at Caltech.[11] Further studies involved, among others, the groups of Gray[8b] and Eisenberg.[8c] For now, cobaloximes appear as one of the most active series of molecular catalysts when considering turnover frequencies and overpotential requirement, as evidenced by a recent benchmarking study in nonaqueous solutions.[12] However, these compounds suffer from degradation in acidic solutions, which limits their stability under turnover conditions. This prompted us to investigate the reactivity of another class of B_{12} mimics. Cobalt diimine−dioxime complexes (Figure 1), mainly developed by Marzilli and co-workers in the 1980s,[13] indeed contain single tetradentate equatorial ligands which are hardly displaced whereas hydrolysis of both oxime bridges in cobaloximes leads to the displacement (or exchange)[14] of both glyoxime ligands. In this Account, we highlight the potential of this second generation of cobalt catalysts for H_2 evolution as an opportunity to design molecular-engineered electrodes and light-driven systems working in aqueous media.

■ SYNTHESIS

Diimine−dioxime ligands are synthesized in one step through Schiff base condensation of butanedione-monoxime on diamine compounds. These ligands are abbreviated as $(DOH)_2xx$ where *xx* indicates the length of the hydrocarbon chain separating the two imine functions. Hence $(DOH)_2pn$ (Figure 1) corresponds to $N^2,N^{2'}$-propanediylbis-butan-2-imine-3-oxime. Metalation readily occurs when the ligand is reacted with a metallic salt.[15] Specifically, cobalt complexes rapidly react with oxygen from the air to yield octahedral Co^{III} derivatives such as $[Co(DO)(DOH)pnX_2]$ ($1X_2$, Figure 1), in which the diimine−dioxime ligand occupies all four equatorial positions. The oximato oxygen atoms are engaged in a hydrogen bond. The bridging proton can be replaced by a difluoroboryl group, as in $[Co((DO)_2BF_2)pnX_2]$ ($2X_2$, Figure 1), through reaction with $BF_3·Et_2O$.

■ ELECTROCATALYTIC ACTIVITY FOR H_2 EVOLUTION

Black traces in Figure 2 correspond to the cyclic voltammograms (CVs) of $1Br_2$ and $2Br_2$ recorded in acetonitrile at a glassy carbon electrode.[16] Two quasi-reversible monoelectronic processes are observed corresponding to the stepwise reduction of the Co^{III} complex to the Co^{II} and Co^I derivatives. X-ray
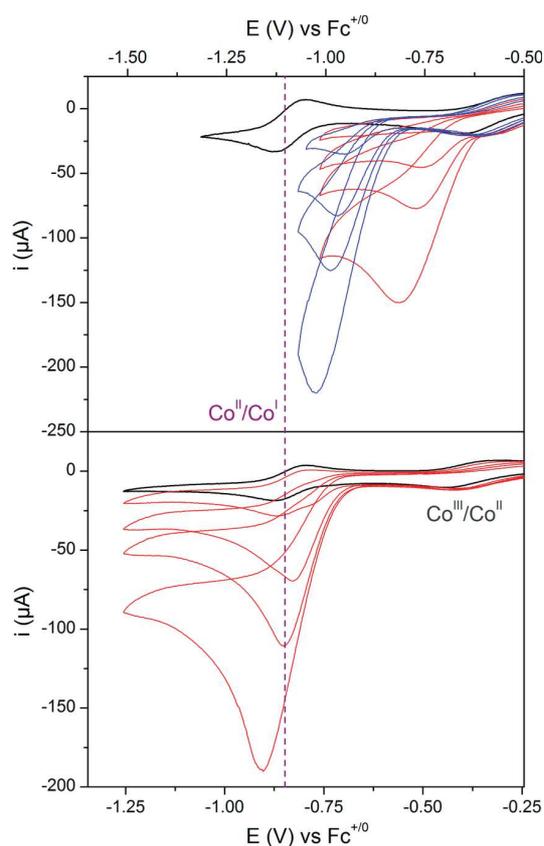
Figure 2. Cyclic voltammograms of $1Br_2$ (top) and $2Br_2$ (bottom) (1 mM, black traces) recorded in CH_3CN (0.1 M nBu_4NBF_4) at a glassy carbon electrode (100 mV·s^{-1}) in the presence of p-cyanoanilinium tetrafluoroborate (red traces; 1, 3, 5, and 10 equiv) and anilinium tetrafluoroborate (blue traces; 1, 3, 5, and 10 equiv).

absorption spectroscopies have shown that halide ligands are fully displaced by acetonitrile in the reduced Co^{II} and Co^{I} states.[17] Upon reduction, the coordination number also decreases from 6 in the Co^{III} state to 5 in both the Co^{II} and Co^{I} state, a feature supported by DFT calculations.[18]

Electrocatalytic hydrogen evolution is evidenced in the CVs of $1Br_2$ and $2Br_2$ by the appearance of an irreversible wave that raises in height with increasing concentrations of proton sources such as anilinium or $para$-cyanoanilinium. H_2 production was quantified by gas chromatography coupled to coulometric monitoring, during bulk electrolysis experiments carried out at constant potential values corresponding to those of the electrocatalytic waves. In the case of the BF_2-annulated complex $2Br_2$, this electrocatalytic wave develops at potentials corresponding to the Co^{II}/Co^{I} process, in line with the behavior of cobaloximes (Figure 2).[10,11] By contrast, in the case of the H-bridged complex $1Br_2$, electrocatalytic H_2 evolution occurs at potentials positively shifted with regard to the Co^{II}/Co^{I} couple. The extent of this shift depends on the strength of the acid used as proton source as shown in Figure 2. We hypothesized that proton transfer at the oxime bridge is involved in the rate-determining step of the catalytic reaction. To further support this hypothesis, we consequently carried out computational studies at the DFT level in collaboration with Field et al. at the Institute of Structural Biology in Grenoble.[18a] Figure 3 displays a part of the mechanistic scheme that resulted from calculations in good agreement, within methodological errors,[19] with electrochemically determined potentials of the redox processes (both measured and computed versus the Fc^+/Fc couple), and reproducing the electrocatalytic behavior of H-bridged diimine−dioxime complexes. The point of entry of the catalytic cycle is a Co^{II} derivative. A subsequent proton-coupled electron transfer process leads to a Co^{I} compound containing a protonated oxime bridge, which turns to be the initial active state, denoted as $Co^{I}LH$. Hammes-Schiffer and co-workers reached the same conclusion on the basis of similar DFT studies.[18b] The computed potential of the $Co^{II}/Co^{I}LH$ couple appears significantly more positive than that of the Co^{II}/Co^{I} couple, consistent with the observed positive shift of the electrocatalytic potential. A second PCET step is then required to form a Co^{II}-hydride species bearing a protonated ligand, $Co^{II}HLH$. Finally, H_2 is produced, either through external protonation or through an intramolecular mechanism that would reproduce the formation of a dihydrogen bond,[20] as suggested to occur at the active sites of hydrogenases.[5a] We have been able to locate a transition state for such an intramolecular process whose activation energy value is ∼90 kJ mol^{-1}, a value in agreement with other studies regarding H_2-evolving catalysts[21] or enzymes.[22] Formation of a H_2-bound species is suggested by theoretical computations. However,
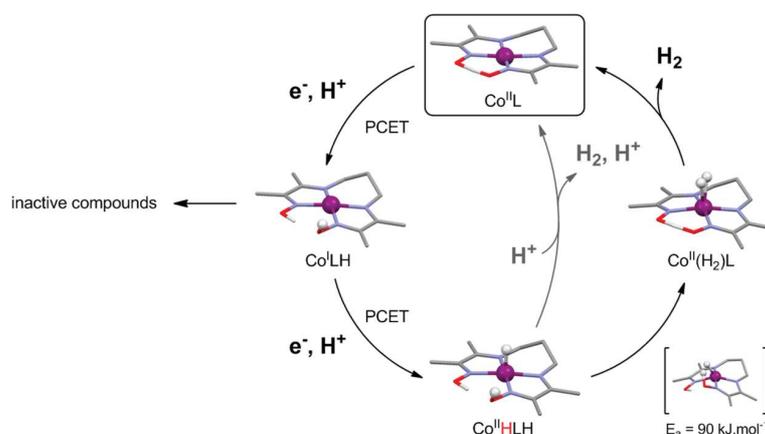

Figure 3. Possible pathways for catalytic hydrogen evolution, involving PCET processes, with DFT-optimized structures of the key intermediates. Axial ancillary ligands have been omitted for the sake of clarity.
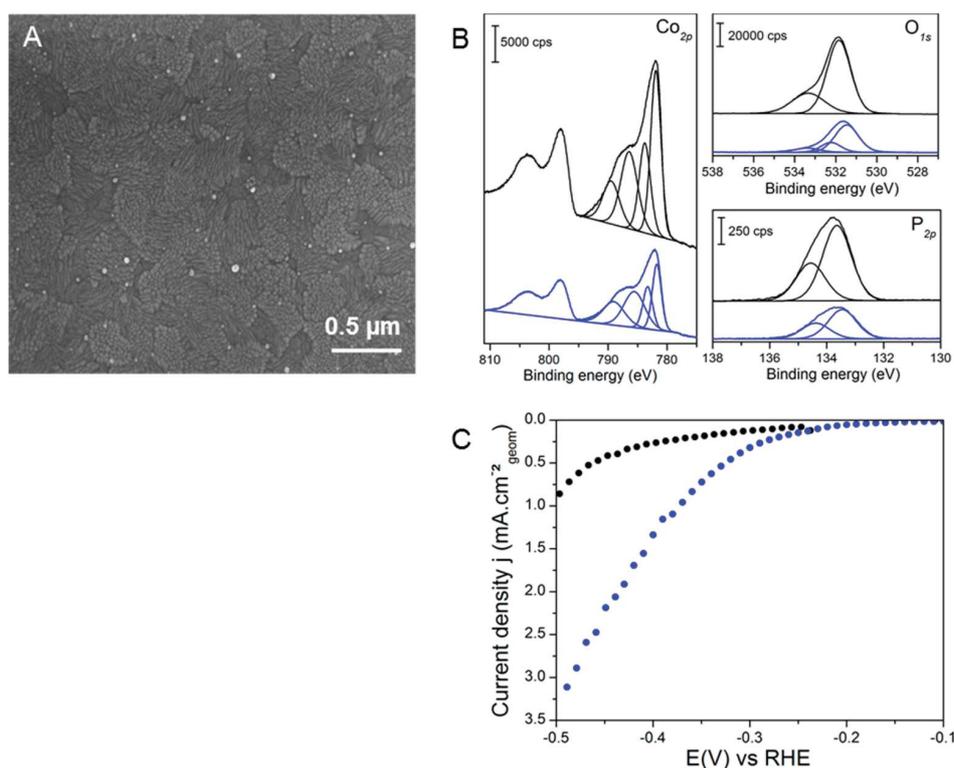
Figure 4. SEM image of an ITO electrode modified by electrolysis at -0.9 V vs Ag/AgCl of a solution containing $1Cl_2$ (0.5 mM) in aqueous phosphate buffer (0.5 M, pH 7) for 1 h (0.1 $C \cdot cm^{-2}_{geometric}$) (A), XPS data ($Co_{2p}$, O_{1s}, and P_{2p} cores) of a H_2–CoCat material deposited onto FTO substrate (blue traces) vs commercial $Co_3(PO_4)_2 \cdot xH_2O$ (black traces) (B), and polarization of a FTO electrode modified with H_2–CoCat (blue dots) compared with that of a Co foil electrode (black dots) in phosphate buffer (0.5 M, pH 7) at 0.05 $mV \cdot s^{-1}$ (C). Reproduced with permission from ref 27. Copyright 2012 Nature Publishing Group.

Table 1. pK_a's and Equilibrium Potentials of the H^+/H_2 Couple in CH_3CN for Various Acids (10 mM), Taking into Account Homoconjugation When Applicable,[26] Together with the Half-Wave Potentials of the Electrocatalytic Wave Corresponding to H_2 Evolution Mediated by $1Br_2$ (Data Reported in Refs 16 and 26)

	p-cyanoanilinium	tosic acid	anilinium	trifluoroacetic acid
pK_a	7.6	8.7	10.7	12.6
$E°$ (H^+/H_2)	-0.46 V vs $Fc^{+/0}$	-0.48 V vs $Fc^{+/0}$	-0.68 V vs $Fc^{+/0}$	-0.68 V vs $Fc^{+/0}$
$E^{cat}_{1/2}$	-0.68 V vs $Fc^{+/0}$	-0.73 V vs $Fc^{+/0}$	-0.92 V vs $Fc^{+/0}$	-0.96 V vs $Fc^{+/0}$

given the fact that H_2 elimination is entropically favored, it may not exist as a true intermediate in the catalytic mechanism.

Nonetheless, these calculations confirm that a Co(II)-hydride species is the active intermediate for H_2 evolution, in agreement with the mechanism initially proposed by Eisenberg et al.,[23] and further supported by DFT studies by Muckerman and Fujita,[24] and Hammes-Schiffer and Solis[25] for parent cobaloximes. They also support a bridge-protonation pathway. Proton relays have already been shown crucial for promoting heterolytic H^+/H_2 interconversion. The most popular examples are probably DuBois's nickel bisdiphosphine complexes containing basic amino sites in the second coordination sphere.[5c] Whether bridge protonation takes place in H_2 evolution mediated by cobaloximes is unclear and still under investigation.[7b,d,e] In the present case, protonation of the oxime bridge allows diimine–dioxime complexes to adapt their electrocatalytic potential to the acid–base conditions of the medium, as shown in Table 1. Table 1 compares the potentials measured at half the catalytic wave and the equilibrium potential of the H^+/H_2 couple in acetonitrile, computed from

tabulated values and taking into account the homoconjugation effect as previously reported.[26] From these data and in first approximation, it was possible to estimate the overpotential value at the middle of the catalytic wave (such an estimation is more accurate with S-shaped voltammograms recorded at rotating electrodes),[26] by subtracting the standard potential of the H^+/H_2 couple from the measured value. It follows that the overpotential requirement for H_2 evolution catalysis is kept within a 220–290 mV window over a wide range of acid–base conditions, that is, in the presence of acids with pK_a's ranging from 7.6 to 12.6. To the best of our knowledge, such a behavior reproducing that of hydrogenases and platinum surfaces has never been reported for synthetic catalysts. In addition, these values compare well with those previously obtained for cobaloximes.[10,11] Current work in progress in our laboratory is devoted to the accurate determination of turnover frequencies, with the aim to establish "catalytic Tafel plots", displaying the relationship between turnover frequency and overpotential, for a rational benchmarking of the catalytic activity.[12]
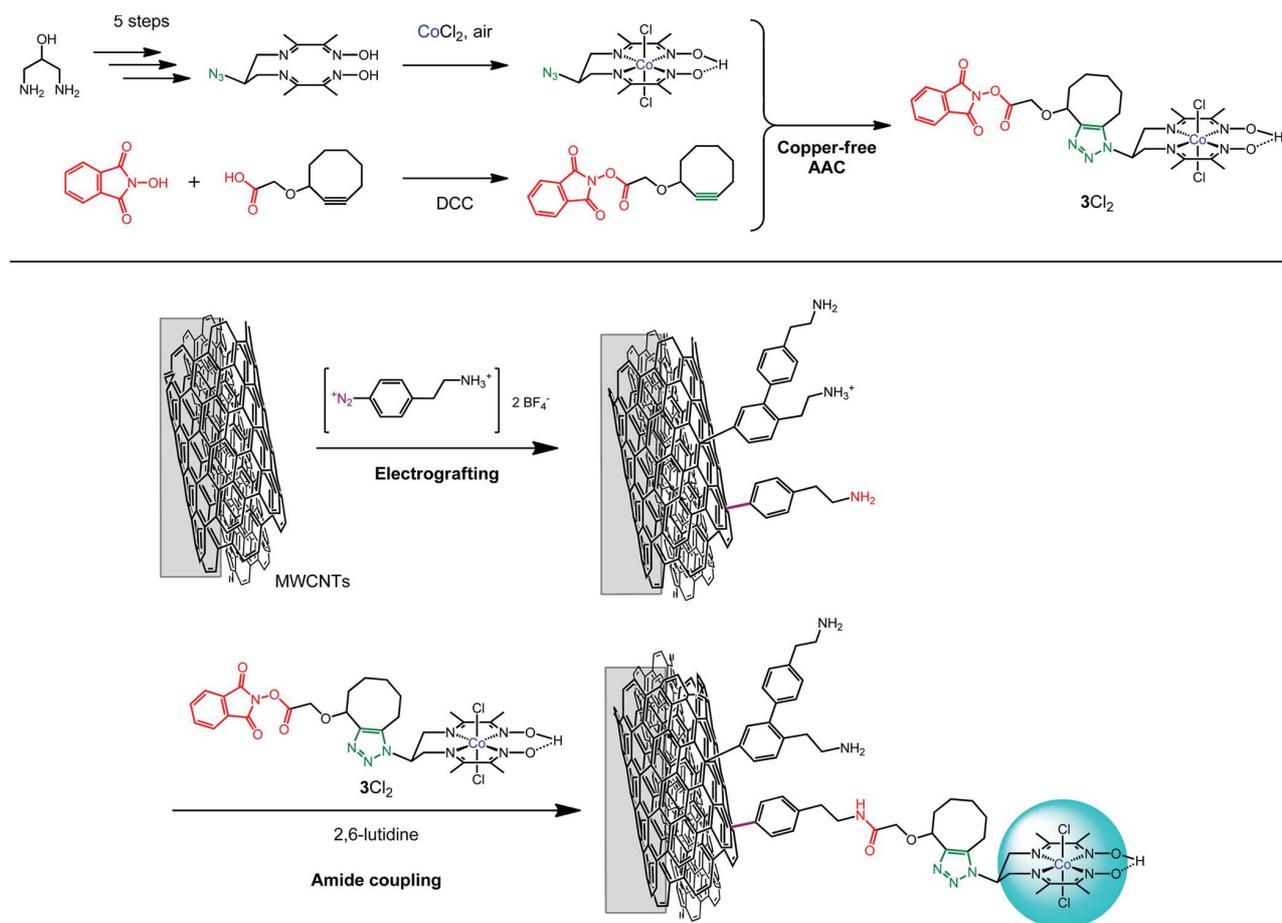
Figure 5. Synthetic strategy for the preparation of **3**Cl$_2$-functionalized MWCNTs electrodes (DCC = dicyclohexylcarbodiimide).

ASSESSMENT OF CATALYTIC ACTIVITY IN AQUEOUS MEDIA

We found that diimine–dioxime complexes decompose under aqueous catalytic conditions. Actually, in pH 7 aqueous phosphate buffer they experience an electroreductive transformation into a nanoparticulate material which is deposited on the electrode as confirmed by SEM analysis (Figure 4A).[27] Small nanoparticles with average diameter of 10 nm (Figure 4A) are initially formed. Upon prolonged deposition time or when reduction is carried out at a more negative potential, an ∼2 μm thick film made of larger particles (100 nm) is obtained. The same coating can be obtained starting from simple cobalt salts. On the basis of advanced spectroscopic measurements (XPS; Figure 4B, EDX, EXAFS, and XANES), we could show that this novel material, called H$_2$–CoCat, consists of metallic cobalt coated with a cobalt-oxo/hydroxo/phosphate layer in contact with the electrolyte. Interestingly, H$_2$–CoCat mediates H$_2$ evolution from neutral aqueous buffer with onset potential, that is, the potential at which we could analytically detect H$_2$ evolution using continuous-flow gas chromatography, of 50 mV vs RHE (Figure 4C). Remarkably, it can be converted upon anodic equilibration into the cobalt-oxide film catalyzing O$_2$ evolution described by Nocera et al.[28] The switch between the two catalytic forms is fully reversible and corresponds to a local interconversion between two morphologies and compositions at the surface of the electrode.

This raises the general and important question of distinguishing true homogeneous catalysis by metal complexes from heterogeneous catalysis by metal or metal-oxide particles derived from in situ transformations. This situation, much more prevalent than currently appreciated, sometimes hard to detect and quite ubiquitous in catalysis, has been recently reviewed in the context of electro- or photochemical processes.[29] As an example, H$_3$PO$_4$/H$_2$PO$_4^-$ aqueous solution (pH 2.2) was previously reported suitable for the benchmarking of the catalytic activity for H$_2$ evolution of molecular cobalt catalysts including **1**(H$_2$O)$^{2+}$.[30a] However, recent investigations in our laboratory evidenced that decomposition occurs under these conditions, accompanied by the deposition of an electrocatalytically active coating at the electrode.[30b] Similar observations have also been made for cobalt complexes in nonaqueous media in the presence of strong acids.[31]

MOLECULAR-BASED ELECTRODE MATERIALS

The results described above may seem disappointing, at least in the context of molecular chemistry. Ligand design allows for a fine-tuning of the catalytic properties, but the inherent fragility of the resulting catalysts, when exposed to reducing/oxidizing and/or hydrolytic conditions, may condemn such an approach in the context of photoelectrochemical water splitting. In other words, is it worth developing molecular catalysts if they transform under turnover conditions into catalytically active species that can alternatively be obtained from simple metal

salts? The answer is "yes", since we could evidence that immobilization onto electrode surface is a very efficient way to stabilize such molecular catalysts and avoid their degradation/transformation under catalytic conditions. To achieve this goal, we functionalized the hydrocarbon chain bridging the two imine functions to create a covalent link between these catalysts and multiwall carbon nanotubes (MWCNTs) used as electrode material. We first prepared an azido derivative starting from 2-hydroxy-1,3-diaminopropane (Figure 5).[32] Alternatively, malonic synthesis strategies proved fruitful to generate a series of ligands derivatized with different functional groups.[33] In our case, azide−alkyne coupling (AAC) allowed preparation of **3Cl₂** (Figure 5) containing a terminal activated ester group. For that purpose, we used a strained cyclooctyne precursor enabling the use of copper-free AAC conditions[34] and thus avoiding substitution of copper for cobalt in the complex. In parallel, MWCNTs, deposited as a mat, were decorated with amino functions through the electroreduction of 4-(2-aminoethyl)-benzene diazonium. This results in the coating of the electrode with a film of aminoethylphenylene oligomers as represented in Figure 5.[35] Finally **3Cl₂** was covalently, thus durably, anchored on MWCNTs through the formation of amide linkages, as confirmed by XPS.

Cyclic voltammograms measured on the modified electrode displayed two redox systems corresponding to the Co^{III}/Co^{II} and Co^{II}/Co^{I} couples (Figure 6) assigned by analogy with **3Cl₂**.

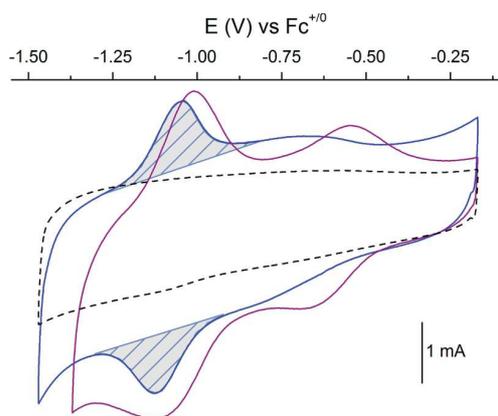**Figure 6.** Cyclic voltammogram of **3Cl₂** recorded in CH₃CN (0.1 M nBu₄NBF₄) at a MWCNT electrode (purple trace) and cyclic voltammogram of a **3Cl₂**-functionalized MWCNTs electrode (blue trace) recorded in CH₃CN (0.1 M Et₄NCl). The response of the unmodified MWCNTs electrode is represented with a dashed black trace. Scan rate: 100 mV·s⁻¹.

The first system is ill-defined, but the Co^{II}/Co^{I} wave is reversible with peak intensities directly proportional to scan rate, confirming covalent immobilization of the cobalt complexes on the electrode surface. Surface concentrations as high as 4.5 nmol·cm⁻² could be determined from the integration of this monoelectronic system.

The resulting material proved active for electrocatalytic H₂ generation at relatively low overpotentials from pure aqueous solutions ranging from pH 2.2 to 5, whereas no catalytic activity could be detected in pH 7 phosphate buffer solutions.[36] The onset potential for H₂ evolution was found to be 350 mV vs RHE in pH 4.5 acetate buffer (Figure 7).[32] This material is also remarkably stable, allowing extensive cycling without degradation. This is underlined by a 7 h electrolysis experiment, during
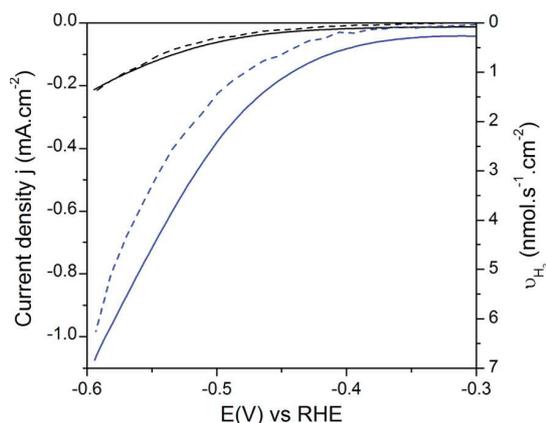
Figure 7. Linear sweep voltammograms (solid traces; left scale) of a **3Cl₂**-functionalized MWCNTs electrode (blue trace) compared to unmodified MWCNTs material (black trace) in a pH 4.5 acetate buffer (0.1 M) recorded at 0.1 mV·s⁻¹ with simultaneous monitoring of H₂ production rate (dashed traces; right scale) using constant-flow continuous GC measurements.

which each immobilized cobalt center achieves more than 50 000 turnovers without significant deactivation. Electrochemical and XPS measurements confirmed preservation of the molecular structure (except for axial ligands that are rapidly exchanged in reduced states)[17] of the grafted complex after catalytic turnover. SEM was also used to exclude the formation of any deposit, such as the H₂−CoCat material,[27] at the surface of MWCNTs.

Previous studies of **1Br₂** solubilized in nonaqueous media showed significant degradation after 50 turnovers.[16] This clearly indicates that grafting provides a largely increased protection of these cobalt catalysts against modification during extensive cycling. A similar example has been reported by our group with DuBois' nickel bisdiphosphine catalysts. Once immobilized on carbon nanotubes, they can turn over more than 100 000 times without loss of activity or formation of heterogeneous active metal species.[37a,b] Though no detailed "postmortem" analysis has been reported for cobaloxime or cobalt diimine−dioxime catalysts yet, a recent work on related diimine−dipyridine metal complexes[38] showed insightful details on possible deactivation pathways. Reduction at the metal site may generate transient carbon-based α-imino radical species subjected to reductive homocoupling, that finally yields dimeric complexes with new metal coordination spheres likely not suitable for catalysis. Our hypothesis is that once grafted onto electrode materials the molecular complexes are isolated one from each other and cannot react in such bimolecular manner. Another mechanism for deactivation includes ligand hydrogenation through hydride transfer from the $Co^{III}HL$ species, either directly formed from the Co^{I} state or through isomerism of the $Co^{I}LH$ species (Figure 3).[39] For complexes grafted onto electrodes, immediate reduction of this species is likely to compete with hydride transfer and to form the catalytically competent Co^{II}-hydride species, resulting in enhanced activity and stability.

We note however that covalent immobilization of a catalyst is not always as straightforward as a way to generate efficient electrocatalytic materials. This point arises from, at least, two reasons. First, the linker introduced between the catalytic moiety and the surface often acts as an insulator, which results in the requirement of increased overpotentials for catalysis to occur.[3,40] In the course of a long-standing and fruitful
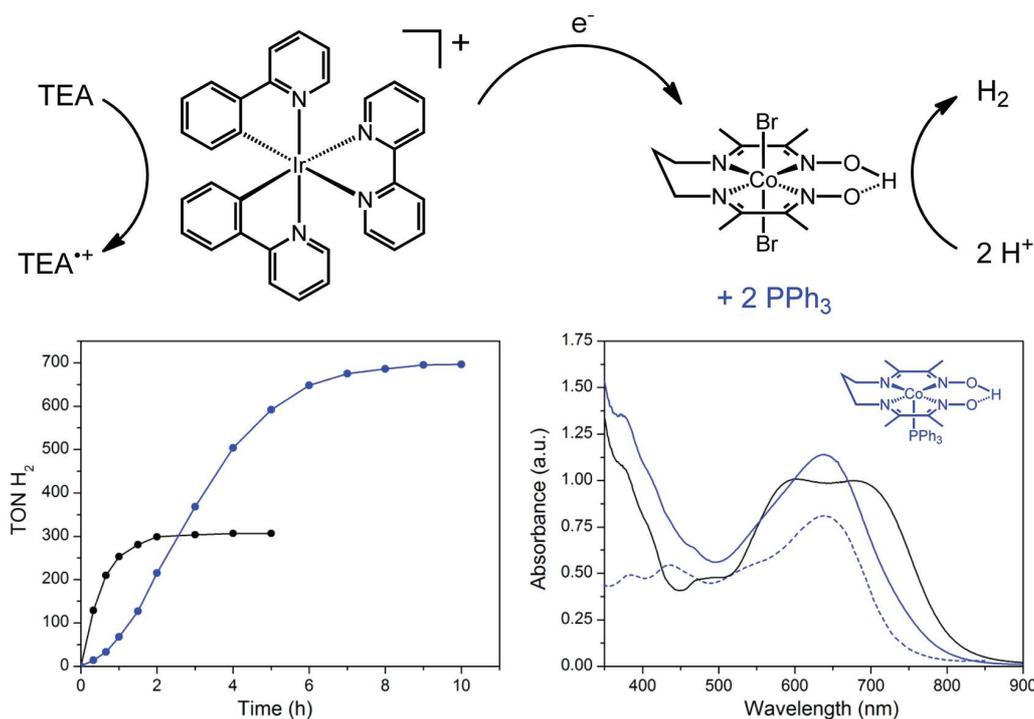
Figure 8. Photocatalytic system based on $1Br_2$ (top), H_2 evolution versus time (bottom left), and spectroscopic signature of the resting state (bottom right) during continuous irradiation in the absence (black traces) and the presence (blue traces) of 2 equiv of PPh_3. The dashed blue trace shows the spectrum of authentic $[Co(DO)(DOH)pn(PPh_3)]$.

collaboration with Jousselme, Palacin, and co-workers from the Matter Science Division of CEA (Saclay, France),[27,32,35,37] we could show that, when performed onto MWCNTs, the electroreduction of diazonium salts provides a quite unique way to graft a significant amount of redox probes on the electrode surface without introducing such electron transfer barrier.[35b] Second, the structure of a molecular catalyst is significantly reorganized on completion of the catalytic cycle. This statement is particularly true for redox catalysts transitioning through various oxidation states. The immobilization mode must thus enable easy conformational changes. Grafting of diimine–dioxime complexes onto oxide surfaces has been described by Peters and Berben,[41] and Reisner and co-workers.[33a,42] However, these immobilization modes, involving two anchoring groups, do not allow for H_2 evolution catalysis to occur at significant rate, which probably originates from constrains generated at the cobalt center upon grafting.

■ PHOTOCHEMICAL SYSTEMS

Cobalt diimine–dioxime catalysts also proved to be active for H_2 evolution under light-driven conditions through their association with molecular Ru-, Ir-, or Re-based photosensitizers. Such homogeneous systems rely on sacrificial electron donors such as triethanolamine, triethylamine (TEA), or ascorbic acid. In the context of a collaboration with the group of Wang and Sun at Dalian Institute of Technology (China), we assessed the photocatalytic activity of $1Br_2$ in mixed H_2O/CH_3CN conditions in the presence of TEA and a cyclometalated iridium-based photosensitizer.[43] Turnover numbers (TON) as high as 300 could be obtained after 4 h of visible light irradiation. Under the same conditions, the BF_2-annulated complex $2Br_2$ only led to 50 TON, consistent with the inability of this complex to be protonated at the oxime

bridge. The addition of triphenylphosphine resulted in a significant increase of the stability of the system with up to 700 TON achieved within 10 h (Figure 8). Phosphine ligands are known to stabilize low oxidation states of cobalt complexes that are the key intermediates in the H_2 evolution mechanism. Indeed, stabilization of the Co^I state of $1Br_2$ by coordination of PPh_3 has been confirmed by cyclic voltammetry measurements with a ~280 mV anodic shift of the electrochemical potential of the Co^{II}/Co^I couple. In order to get more information on the reduced species generated during photocatalysis, we monitored the reaction using UV–vis spectroscopy: starting from the Co^{III} complex, irradiation leads after 10–20 s to a first absorption band at 472 nm, characteristic of a Co^{II} species. When PPh_3 is present in solution, a second band at 638 nm then appears after 70 s, corresponding to the exact signature of the Co^I complex $[Co(DO)(DOH)pn(PPh_3)]$ (Figure 8). By contrast, in the absence of PPh_3, the resting state of the catalyst displayed another signature, characterized by two new bands centered at 602 and 678 nm. Similar spectroscopic signatures have been reported for reduced cobaloxime $[Co-(dmgBF_2)_2(H_2O)_2]^{7e,11b,23,44}$ and have been assigned to a spectroscopic Co^I state, a statement supported by ab initio calculations.[45] However, a similar spectrum has also been calculated for a Co^{II}–H intermediate.[24] While more studies are still needed to fully characterize these intermediates, it seems that coordination of the π-acceptor phosphine ligand stabilizes the system by preventing side reactions, such as the above-mentioned hydride transfer processes,[39b,c] to occur. Similarly, a derivative of $1Br_2$ containing a pendant methylpyridine ligand[33b] showed increased activity under photochemical conditions.[46] These results highlight the relevance of ligand tuning for the optimization of such systems.

Cobalt diimine–dioxime catalysts so far display lower activity under light driven conditions as compared to parent cobaloximes.[8a,c] They however prove quite versatile as H_2 evolution catalysts as far as the reaction conditions are concerned: they function in fully organic solutions[47] as well as in fully aqueous conditions.[46,48] Not surprisingly, the optimal acid/base conditions in terms of activity in water (up to 90 TON) correspond to a pH of 4,[48a] thus matching the optimal value determined for the molecular-based cathode material containing the same cobalt diimine–dioxime catalytic moiety.[32]

SUMMARY AND OUTLOOK

In the past 5 years, we have developed cobalt diimine–dioxime complexes as molecular catalysts for H_2 evolution. The tetradentate nature of the diimine–dioxime ligand warrants stability against hydrolysis, while letting an oxime bridge available to act as a proton relay. In addition, derivatization of this ligand at the hydrocarbon chain bridging the two imine functions enables its coupling with a surface, or possibly a photosensitizer, in a much more convenient manner than for the parent cobaloximes. Cobalt diimine–dioxime catalysts finally prove active for H_2 evolution in fully aqueous conditions both after immobilization onto electrode materials and in light-driven homogeneous conditions. These two properties hold promise for the construction of molecular-based photocathodes as key components of dye-sensitized photoelectrochemical cells.

AUTHOR INFORMATION

Corresponding Author

*E-mail: vincent.artero@cea.fr.

Notes

The authors declare no competing financial interest.

Biographies

Nicolas Kaeffer received both a Chimie ParisTech engineer diploma and a master level in molecular chemistry from the Université Pierre et Marie Curie (Paris) in 2012. Since there, he works as a graduate student in CEA-Grenoble on the construction of molecular cathodes and photocathodes for hydrogen evolution based on cobalt diimine–dioxime complexes, under the supervision of Dr. Vincent Artero.

Murielle Chavarot-Kerlidou studied organic chemistry at the University of Grenoble (Ph.D. 1998) and obtained a CNRS position (2002) to develop organometallic chemistry in Paris, from where she moved in 2009 to join CEA-Grenoble and work on hydrogen photoproduction.

Vincent Artero graduated from the Ecole Normale Supérieure (Ulm) and studied inorganic chemistry at the University Pierre et Marie Curie in Paris (Ph.D. 2000). He moved to the CEA center in Grenoble (Life Science Division) in 2001 to develop bioinspired chemistry related to hydrogen production and artificial photosynthesis. He received the "Grand Prix Mergier-Bourdeix de l'Académie des Sciences" (2011) and was granted in 2012 with a Starting Grant from the European Research Council (ERC).

ACKNOWLEDGMENTS

REFERENCES

(1) Sherman, B.; Vaughn, M.; Bergkamp, J.; Gust, D.; Moore, A.; Moore, T. Evolution of reaction center mimics to systems capable of generating solar fuel. *Photosynth. Res.* **2014**, *120*, 59−70.

(2) Andreiadis, E. S.; Chavarot-Kerlidou, M.; Fontecave, M.; Artero, V. Artificial Photosynthesis: From Molecular Catalysts for Light-driven Water Splitting to Photoelectrochemical Cells. *Photochem. Photobiol.* **2011**, *87*, 946−964.

(3) Artero, V.; Fontecave, M. Some general principles for designing electrocatalysts with hydrogenase activity. *Coord. Chem. Rev.* **2005**, *249*, 1518−1535.

(4) Lubitz, W.; Ogata, H.; Rüdiger, O.; Reijerse, E. Hydrogenases. *Chem. Rev.* **2014**, *114*, 4081−4148.

(5) (a) Simmons, T. R.; Berggren, G.; Bacchi, M.; Fontecave, M.; Artero, V. Mimicking hydrogenases: From biomimetics to artificial enzymes. *Coord. Chem. Rev.* **2014**, *270−271*, 127−150. (b) Canaguier, S.; Artero, V.; Fontecave, M. Modelling NiFe hydrogenases: nickel-based electrocatalysts for hydrogen production. *Dalton Trans.* **2008**, *39*, 315−325. (c) DuBois, D. L. Development of Molecular Electrocatalysts for Energy Storage. *Inorg. Chem.* **2014**, *53*, 3935−3960.

(6) Schrauzer, G. N. Organocobalt chemistry of vitamin B_{12} model compounds (cobaloximes). *Acc. Chem. Res.* **1968**, *1*, 97−103.

(7) (a) Schrauzer, G. N.; Holland, R. J. Hydridocobaloximes. *J. Am. Chem. Soc.* **1971**, *93*, 1505−1506. (b) Bhattacharjee, A.; Chavarot-Kerlidou, M.; Andreiadis, E. S.; Fontecave, M.; Field, M. J.; Artero, V. Combined Experimental-Theoretical Characterization of the Hydrido-Cobaloxime $[HCo(dmgH)_2(P^nBu_3)]$. *Inorg. Chem.* **2012**, *51*, 7087−7093. (c) Chao, T. H.; Espenson, J. H. Mechanism of Hydrogen Evolution from Hydridocobaloxime. *J. Am. Chem. Soc.* **1978**, *100*, 129−133. (d) Lacy, D. C.; Roberts, G. M.; Peters, J. C. The Cobalt Hydride that Never Was: Revisiting Schrauzer's "Hydridocobaloxime. *J. Am. Chem. Soc.* **2015**, *137*, 4860−4864. (e) Estes, D. P.; Grills, D. C.; Norton, J. R. The Reaction of Cobaloximes with Hydrogen: Products and Thermodynamics. *J. Am. Chem. Soc.* **2014**, *136*, 17362−17365.

(8) (a) Artero, V.; Chavarot-Kerlidou, M.; Fontecave, M. Splitting water with cobalt. *Angew. Chem., Int. Ed.* **2011**, *50*, 7238−7266. (b) Dempsey, J. L.; Brunschwig, B. S.; Winkler, J. R.; Gray, H. B. Hydrogen Evolution Catalyzed by Cobaloximes. *Acc. Chem. Res.* **2009**, *42*, 1995−2004. (c) Eckenhoff, W. T.; McNamara, W. R.; Du, P.; Eisenberg, R. Cobalt complexes as artificial hydrogenases for the reductive side of water splitting. *Biochim. Biophys. Acta* **2013**, *1827*, 958−973.

(9) Hawecker, J.; Lehn, J. M.; Ziessel, R. Efficient Homogeneous Photochemical Hydrogen Generation and Water Reduction Mediated by Cobaloxime or Macrocyclic Cobalt Complexes. *New J. Chem.* **1983**, *7*, 271−277.

(10) (a) Razavet, M.; Artero, V.; Fontecave, M. Proton electro-reduction catalyzed by cobaloximes: Functional models for hydrogenases. *Inorg. Chem.* **2005**, *44*, 4786−4795. (b) Baffert, C.; Artero, V.; Fontecave, M. Cobaloximes as functional models for hydrogenases. 2. proton electroreduction catalyzed by difluoroborylbis-(dimethylglyoximato)cobalt(II) complexes in organic media. *Inorg. Chem.* **2007**, *46*, 1817−1824.

(11) (a) Hu, X. L.; Cossairt, B. M.; Brunschwig, B. S.; Lewis, N. S.; Peters, J. C. Electrocatalytic hydrogen evolution by cobalt difluor-oboryl-diglyoximate complexes. *Chem. Commun.* **2005**, *45*, 4723−4725. (b) Hu, X.; Brunschwig, B. S.; Peters, J. C. Electrocatalytic hydrogen evolution at low overpotentials by cobalt macrocyclic glyoxime and tetraimine complexes. *J. Am. Chem. Soc.* **2007**, *129*, 8988−8998.

(12) Artero, V.; Saveant, J.-M. Toward the rational benchmarking of homogeneous H₂-evolving catalysts. *Energy Environ. Sci.* **2014**, *7*, 3808−3814.

(13) Seeber, R.; Parker, W. O.; Marzilli, P. A.; Marzilli, L. G. Electrochemical Synthesis of Costa-Type Cobalt Complexes. *Organometallics* **1989**, *8*, 2377−2381.

(14) McCormick, T. M.; Han, Z. J.; Weinberg, D. J.; Brennessel, W. W.; Holland, P. L.; Eisenberg, R. Impact of Ligand Exchange in Hydrogen Production from Cobaloxime-Containing Photocatalytic Systems. *Inorg. Chem.* **2011**, *50*, 10660−10666.

(15) Costa, G.; Mestroni, G.; de Savorgnani, E. *Inorg. Chim. Acta* **1969**, *3*, 323−328.

(16) Jacques, P.-A.; Artero, V.; Pécaut, J.; Fontecave, M. Cobalt and nickel diimine−dioxime complexes as molecular electrocatalysts for hydrogen evolution with low overvoltages. *Proc. Natl. Acad. Sci. U.S.A.* **2009**, *106*, 20627−20632.

(17) Giorgetti, M.; Berrettoni, M.; Ascone, I.; Zamponi, S.; Seeber, R.; Marassi, R. X-ray absorption spectroscopy study on the electrochemical reduction of Co((DO)(DOH)(pn))Br₂. *Electrochim. Acta* **2000**, *45*, 4475−4482.

(18) (a) Bhattacharjee, A.; Andreiadis, E. S.; Chavarot-Kerlidou, M.; Fontecave, M.; Field, M. J.; Artero, V. A Computational Study of the Mechanism of Hydrogen Evolution by Cobalt (Diimine-Dioxime) Catalysts. *Chem.—Eur. J.* **2013**, *19*, 15166−15174. (b) Solis, B. H.; Yu, Y.; Hammes-Schiffer, S. Effects of Ligand Modification and Protonation on Metal Oxime Hydrogen Evolution Electrocatalysts. *Inorg. Chem.* **2013**, *52*, 6994−6999.

(19) Roy, L. E.; Jakubikova, E.; Guthrie, M. G.; Batista, E. R. Calculation of One-Electron Redox Potentials Revisited. Is It Possible to Calculate Accurate Potentials with Density Functional Methods? *J. Phys. Chem. A* **2009**, *113*, 6745−6750.

(20) Niu, S.; Hall, N. B. Modeling the active sites in metalloenzymes 5. The heterolytic bond cleavage of H₂ in the [NiFe] hydrogenase of *Desulfovibrio gigas* by a nucleophilic addition mechanism. *Inorg. Chem.* **2001**, *40*, 6201−6203.

(21) Sundstrom, E. J.; Yang, X.; Thoi, V. S.; Karunadasa, H. I.; Chang, C. J.; Long, J. R.; Head-Gordon, M. Computational and Experimental Study of the Mechanism of Hydrogen Generation from Water by a Molecular Molybdenum-Oxo Electrocatalyst. *J. Am. Chem. Soc.* **2012**, *134*, 5233−5242.

(22) Ridder, L.; Mulholland, A. J.; Vervoort, J.; Rietjens, I. M. C. M. Correlation of Calculated Activation Energies with Experimental Rate Constants for an Enzyme Catalyzed Aromatic Hydroxylation. *J. Am. Chem. Soc.* **1998**, *120*, 7641−7642.

(23) Du, P. W.; Schneider, J.; Luo, G. G.; Brennessel, W. W.; Eisenberg, R. Visible Light-Driven Hydrogen Production from Aqueous Protons Catalyzed by Molecular Cobaloxime Catalysts. *Inorg. Chem.* **2009**, *48*, 4952−4962.

(24) Muckerman, J. T.; Fujita, E. Theoretical Studies of the Mechanism of Catalytic Hydrogen Production by a Cobaloxime. *Chem. Commun.* **2011**, *47*, 12456−12458.

(25) Solis, B. H.; Hammes-Schiffer, S. Theoretical Analysis of Mechanistic Pathways for Hydrogen Evolution Catalyzed by Cobaloximes. *Inorg. Chem.* **2011**, *50*, 11252−11262.

(26) Fourmond, V.; Jacques, P. A.; Fontecave, M.; Artero, V. H₂ Evolution and Molecular Electrocatalysts: Determination of Overpotentials and Effect of Homoconjugation. *Inorg. Chem.* **2010**, *49*, 10338−10347.

(27) Cobo, S.; Heidkamp, J.; Jacques, P.-A.; Fize, J.; Fourmond, V.; Guetaz, L.; Jousselme, B.; Ivanova, V.; Dau, H.; Palacin, S.; Fontecave, M.; Artero, V. A Janus cobalt-based catalytic material for electrosplitting of water. *Nat. Mater.* **2012**, *11*, 802−807.

(28) Kanan, M. W.; Surendranath, Y.; Nocera, D. G. Cobalt-phosphate oxygen-evolving compound. *Chem. Soc. Rev.* **2009**, *38*, 109−114.

(29) Artero, V.; Fontecave, M. Solar fuels generation and molecular systems: is it homogeneous or heterogeneous catalysis? *Chem. Soc. Rev.* **2013**, *42*, 2338−2356.

(30) (a) McCrory, C. C. L.; Uyeda, C.; Peters, J. C. Electrocatalytic Hydrogen Evolution in Acidic Water with Molecular Cobalt Tetraazamacrocycles. *J. Am. Chem. Soc.* **2012**, *134*, 3164−3170. (b) Kaeffer, N.; Morozan, A.; Artero, V. *Unpublished data.*

(31) (a) Anxolabéhère-Mallart, E.; Costentin, C.; Fournier, M.; Nowak, S.; Robert, M.; Savéant, J. M. Boron-Capped Tris(glyoximato) Cobalt Clathrochelate as a Precursor for the Electrodeposition of Nanoparticles Catalyzing H₂ Evolution in Water. *J. Am. Chem. Soc.* **2012**, *134*, 6104−6107. (b) Anxolabéhère-Mallart, E.; Costentin, C.; Fournier, M.; Robert, M. Cobalt-Bisglyoximato Diphenyl Complex as a Precatalyst for Electrocatalytic H₂ Evolution. *J. Phys. Chem. C* **2014**, *118*, 13377−13381.

(32) Andreiadis, E. S.; Jacques, P.-A.; Tran, P. D.; Leyris, A.; Chavarot-Kerlidou, M.; Jousselme, B.; Matheron, M.; Pécaut, J.; Palacin, S.; Fontecave, M.; Artero, V. Molecular Engineering of a Cobalt-based Electrocatalytic Nano-Material for H₂ Evolution under Fully Aqueous Conditions. *Nat. Chem.* **2013**, *5*, 48−53.

(33) (a) Muresan, N. M.; Willkomm, J.; Mersch, D.; Vaynzof, Y.; Reisner, E. Immobilization of a Molecular Cobaloxime Catalyst for Hydrogen Evolution on a Mesoporous Metal Oxide Electrode. *Angew. Chem., Int. Ed.* **2012**, *51*, 12749−12753. (b) Gerli, A.; Sabat, M.; Marzilli, L. G. Lariat-Type-B₁₂ Model Complexes 0.1. New Pendant Methylpyridyl Costa-Type Organocobalt Complexes Provide Insight into the Role of the Axial Ligand in Butterfly Bending and Redox Properties. *J. Am. Chem. Soc.* **1992**, *114*, 6711−6718. (c) Reynal, A.; Willkomm, J.; Muresan, N. M.; Lakadamyali, F.; Planells, M.; Reisner, E.; Durrant, J. R. Distance dependent charge separation and recombination in semiconductor/molecular catalyst systems for water splitting. *Chem. Commun.* **2014**, *50*, 12768−12771.

(34) Sletten, E. M.; Bertozzi, C. R. From Mechanism to Mouse: A Tale of Two Bioorthogonal Reactions. *Acc. Chem. Res.* **2011**, *44*, 666−676.

(35) (a) Le Goff, A.; Artero, V.; Metayé, R.; Moggia, F.; Jousselme, B.; Razavet, M.; Tran, P. D.; Palacin, S.; Fontecave, M. Immobilization of FeFe hydrogenase mimics onto carbon and gold electrodes by controlled aryldiazonium salt reduction: An electrochemical, XPS and ATR-IR study. *Int. J. Hydrogen Energy* **2010**, *35*, 10719−10724. (b) Le Goff, A.; Moggia, F.; Debou, N.; Jegou, P.; Artero, V.; Fontecave, M.; Jousselme, B.; Palacin, S. Facile and tunable functionalization of carbon nanotube electrodes with ferrocene by covalent coupling and pi-stacking interactions and their relevance to glucose bio-sensing. *J. Electroanal. Chem.* **2010**, *641*, 57−63.

(36) Thus excluding the formation of the catalytically active H₂-CoCat under turnover conditions.

(37) (a) Le Goff, A.; Artero, V.; Jousselme, B.; Tran, P. D.; Guillet, N.; Metaye, R.; Fihri, A.; Palacin, S.; Fontecave, M. From Hydrogenases to Noble Metal-Free Catalytic Nanomaterials for H₂ Production and Uptake. *Science* **2009**, *326*, 1384−1387. (b) Tran, P. D.; Le Goff, A.; Heidkamp, J.; Jousselme, B.; Guillet, N.; Palacin, S.; Dau, H.; Fontecave, M.; Artero, V. Noncovalent Modification of Carbon Nanotubes with Pyrene-Functionalized Nickel Complexes: Carbon Monoxide Tolerant Catalysts for Hydrogen Evolution and Uptake. *Angew. Chem., Int. Ed.* **2011**, *50*, 1371−1374.

(38) Hulley, E. B.; Wolczanski, P. T.; Lobkovsky, E. B. Carbon−Carbon Bond Formation from Azaallyl and Imine Couplings about Metal−Metal Bonds. *J. Am. Chem. Soc.* **2011**, *133*, 18058−18061.

(39) (a) Shi, S.; Bakac, A.; Espenson, J. H. Reduction-Induced Cleavage of the Cobalt Carbon Bond in Macrocyclic Organocobalt Complexes. *Inorg. Chem.* **1991**, *30*, 3410−3414. (b) Simandi, L. I.; Budo-Zahonyi, E.; Szeverenyi, Z. Effect of Strong Base on the Activation of Molecular Hydrogen by Pyridinebis-(dimethylglyoximato)cobalt(II). *Inorg. Nucl. Chem. Lett.* **1976**, *12*, 237−241. (c) Simandi, L. I.; Szeverenyi, Z.; Budozahonyi, E. Activation of Molecular-Hydrogen by Cobaloxime(II) Derivatives. *Inorg. Nucl. Chem. Lett.* **1975**, *11*, 773−777.

(40) Tran, P. D.; Artero, V.; Fontecave, M. Water electrolysis and photoelectrolysis on electrodes engineered using biological and bio-inspired molecular systems. *Energy Environ. Sci.* **2010**, *3*, 727−747.

(41) Berben, L. A.; Peters, J. C. Hydrogen evolution by cobalt tetraimine catalysts adsorbed on electrode surfaces. *Chem. Commun.* **2010**, *46*, 398−400.

(42) Scherer, M. R. J.; Muresan, N. M.; Steiner, U.; Reisner, E. RYB tri-colour electrochromism based on a molecular cobaloxime. *Chem. Commun.* **2013**, *49*, 10453−10455.

(43) Zhang, P.; Jacques, P.-A.; Chavarot-Kerlidou, M.; Wang, M.; Sun, L.; Fontecave, M.; Artero, V. Phosphine Coordination to a Cobalt Diimine−Dioxime Catalyst Increases Stability during Light-Driven H$_2$ Production. *Inorg. Chem.* **2012**, *51*, 2115−2120.

(44) Dempsey, J. L.; Winkler, J. R.; Gray, H. B. Mechanism of H$_2$ Evolution by a Photogenerated Hydridocobaloxime. *J. Am. Chem. Soc.* **2010**, *132*, 16774−16776.

(45) Bhattacharjee, A.; Chavarot-Kerlidou, M.; Dempsey, J. L.; Gray, H. B.; Fujita, E.; Muckerman, J. T.; Fontecave, M.; Artero, V.; Arantes, G. M.; Field, M. J. Theoretical Modeling of Low-Energy Electronic Absorption Bands in Reduced Cobaloximes. *ChemPhysChem* **2014**, *15*, 2951−2958.

(46) Probst, B.; Guttentag, M.; Rodenberg, A.; Hamm, P.; Alberto, R. Photocatalytic H$_2$ Production from Water with Rhenium and Cobalt Complexes. *Inorg. Chem.* **2011**, *50*, 3404−3412.

(47) Oberholzer, M.; Probst, B.; Bernasconi, D.; Spingler, B.; Alberto, R. Photosensitizing Properties of Alkynylrhenium(I) Complexes [Re(−C≡C−R)(CO)$_3$(N∩N)] (N∩N = 2,2′-bipy, phen) for H$_2$ Production. *Eur. J. Inorg. Chem.* **2014**, *2014*, 3002−3009.

(48) (a) Guttentag, M.; Rodenberg, A.; Kopelent, R.; Probst, B.; Buchwalder, C.; Brandstatter, M.; Hamm, P.; Alberto, R. Photocatalytic H$_2$ Production with a Rhenium/Cobalt System in Water under Acidic Conditions. *Eur. J. Inorg. Chem.* **2012**, *2012*, 59−64. (b) Varma, S.; Castillo, C. E.; Stoll, T.; Fortage, J.; Blackman, A. G.; Molton, F.; Deronzier, A.; Collomb, M. N. Efficient photocatalytic hydrogen production in water using a cobalt(III) tetraaza-macrocyclic catalyst: electrochemical generation of the low-valent Co(I) species and its reactivity toward proton reduction. *Phys. Chem. Chem. Phys.* **2013**, *15*, 17544−17552.
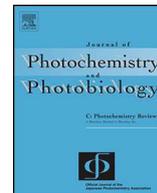
Invited Review

Molecular cathode and photocathode materials for hydrogen evolution in photoelectrochemical devices

Nicolas Queyriaux[1], Nicolas Kaeffer[1], Adina Morozan[1], Murielle Chavarot-Kerlidou, Vincent Artero*

Laboratoire de Chimie et Biologie des Métaux, Université Grenoble Alpes, CNRS, CEA, Life Science Division, 17 rue des Martyrs, 38000 Grenoble, France

ARTICLE INFO

ABSTRACT

Storage of solar energy in the form of readily available easy-to-handle fuels is the main bottleneck toward the development of a carbon-neutral alternative energy. Taking inspiration from natural systems, artificial photosynthesis is a technology to be for efficiently converting the tremendous solar energy received every day on Earth into chemical energy, *i.e.* fuels. In particular, hydrogen production through light-driven water splitting is the subject of numerous investigations. We focus here on the construction of electrodes and photoelectrodes achieving H_2 evolution, as components of photoelectrochemical (PEC) cells. In such devices, H_2 evolution at the cathode or photocathode is combined with water oxidation to oxygen at the photoanode or anode. We review here the various molecular-based materials developed in this context with emphasis on those specifically exploiting the properties of Earth-abundant elements.

© 2015 Elsevier Ireland Ltd. All rights reserved.

Contents

* Corresponding author.
  E-mail address: vincent.artero@cea.fr (V. Artero).
[1] These authors equally contributed to the paper.

Nicolas Queyriaux is a graduate of the Ecole Normale Supérieure (Ulm) and of the University Pierre et Marie Curie (Paris 6). He joined in 2012 the Life Science Division of CEA as a graduate student in the group of Dr Vincent Artero with a project related to the design of new photo- and electro-catalysts for hydrogen production and their subsequent grafting onto conducting surfaces.

Nicolas Kaeffer received both a Chimie ParisTech engineer diploma and a master level in molecular chemistry from the Université Pierre et Marie Curie (Paris 6) in 2012. Since there, he works as a graduate student in CEA-Grenoble, on the construction of molecular cathodes and photocathodes for hydrogen evolution based on cobalt diimine–dioxime complexes, under the supervision of Dr Vincent Artero.

Adina Morozan received her PhD from the University of Bucharest in 2007. From 2009 to 2013 her research activity at CEA Saclay and ICGM in Montpellier has been focused on non-precious metal catalysts for the oxygen reduction reaction in fuel cell. She joined in 2014 the group of Dr. Vincent Artero to work on the development of photocathodes for hydrogen production and to study electrocatalytic processes.

Murielle Chavarot-Kerlidou studied organic chemistry at the University of Grenoble (PhD 1998) and obtained a CNRS position (2002) to develop organometallic chemistry in Paris, from where she moved in 2009 to join CEA-Grenoble and work on hydrogen photoproduction.

Vincent Artero studied at the Ecole Normale Supérieure (Ulm) and graduated in inorganic chemistry at the University Pierre et Marie Curie in Paris (PhD 2000). After a post-doctoral stay in RWTH Aachen in the group of Prof. U. Kölle, he moved to the CEA center in Grenoble (Life Science Division) in 2001 to develop bioinspired chemistry related to hydrogen production and artificial photosynthesis. He received the "Grand Prix Mergier-Bourdeix de l'Académie des Sciences" (2011) and was granted in 2012 with a Starting Grant from the European Research Council (ERC).

1. Introduction

There is now a consensus on the urgency to diversify the energetic mix of our societies by the introduction of a growing amount of renewables. Because of the availability of sunlight at the surface of Earth, solar energy research is the spearhead of these new non-carbon based energy technologies. It has recently been shown that, among all other renewable energy sources, only solar energy would be able to provide the additional >14 terawatts required by our societal needs by 2050 [1,2]. However, this additional energy input must be stored in a durable way because of the mismatch between solar energy intermittence and economic/domestic demand. In that prospect, producing fuels from readily available resources such as water is probably the only sustainable way to go. Hydrogen

production through water splitting thus appears as an attractive solution to store the abundant flow of sunlight falling on Earth. This clean energy carrier can then be used to produce electricity on-demand in fuel cells with very high energy conversion efficiencies [3]. A close-to-market way to convert solar energy into hydrogen is to interface photovoltaic technologies with water electrolysis. However, such a solution remains expensive and still needs further technological developments. Alternatively, direct utilization of sunlight, *i.e.* without intermediate production of electricity, to split water into oxygen and hydrogen in a single device would be a major breakthrough in hydrogen production, as far as mass production costs are concerned [4–6]. A recent life-cycle net energy assessment has shown that such devices can be economically viable when developed at large scale if they exhibit a solar-to-hydrogen yield superior to 5% and a stability over 10 years [7]. Anticipated costs for H_2 production are in the range of $2–4 per kg H_2 [8].

A major issue related to both reductive and oxidative processes involved in water splitting, *i.e.* the hydrogen evolution reaction (HER) and the oxygen evolution reaction (OER), resides in their multielectronic nature, resulting in strong kinetic limitations. This bottleneck requires the development of efficient electrocatalysts proceeding at high rates and low driving force, called overpotential. So far, the most efficient electrocatalysts are based on noble metals, in particular platinum for both HER and OER and iridium or ruthenium oxide for OER. However, the utilization of Pt and Ir-/Ru-based catalysts in technological devices for worldwide energy supply is not sustainable because of their scarcity in Earth crust's and their related high costs [1,9,10]. Intense research activity in this field during the last two decades has led to the development of new electrocatalytic materials based on non-noble metals [11–13] including both solid state materials and molecular catalysts. In this review we almost exclusively focus on the later series and limit our scope to hydrogen evolution. Similar approaches that include biomolecules such as enzymes and photosystems will not be discussed here [14–17]. After a general introduction on photoelectrochemical devices, we describe how catalysts can be immobilized onto cheap carbon-based materials so as to prepare active cathodes for HER. We then consider their integration into photocathode materials, where the photoactive component can be solid-state inorganic semiconductors, organic semiconductors or molecular photosensitizers. As a final step, we point out few recent attempts toward the build-up of overall water-splitting cells which include such molecular-based photocathodes.

2. Overview on photoelectrochemical devices for water splitting

Building photoelectrochemical cells (PECs) is not a straightforward procedure. Several architectures have been identified, each of them presenting its own advantages and drawbacks. We present below an overview of these possible architectures.

The simplest configuration involves a single photoactive component, usually coupled to the OER catalyst as described in Fig. 1a. The resulting photoanode, reproducing the function of Photosystem II during biological light-driven water-splitting processes in photosynthetic microorganisms, uses solar energy to extract electrons from water which is oxidized to O_2. Then, the electrons generated at the photoanode are collected at the cathode where a catalyst evolves H_2. Proton transfer through the electrolyte and possibly through a membrane ensuring the separation of H_2 and O_2 gases allows for the mass balance in the whole device. There is no fundamental reason why a similar architecture with the light-harvesting unit connected to the HER catalyst could not be considered [18]. The resulting system (Fig. 1b) then combines an anode with a photocathode. Nevertheless, in most cases, the use
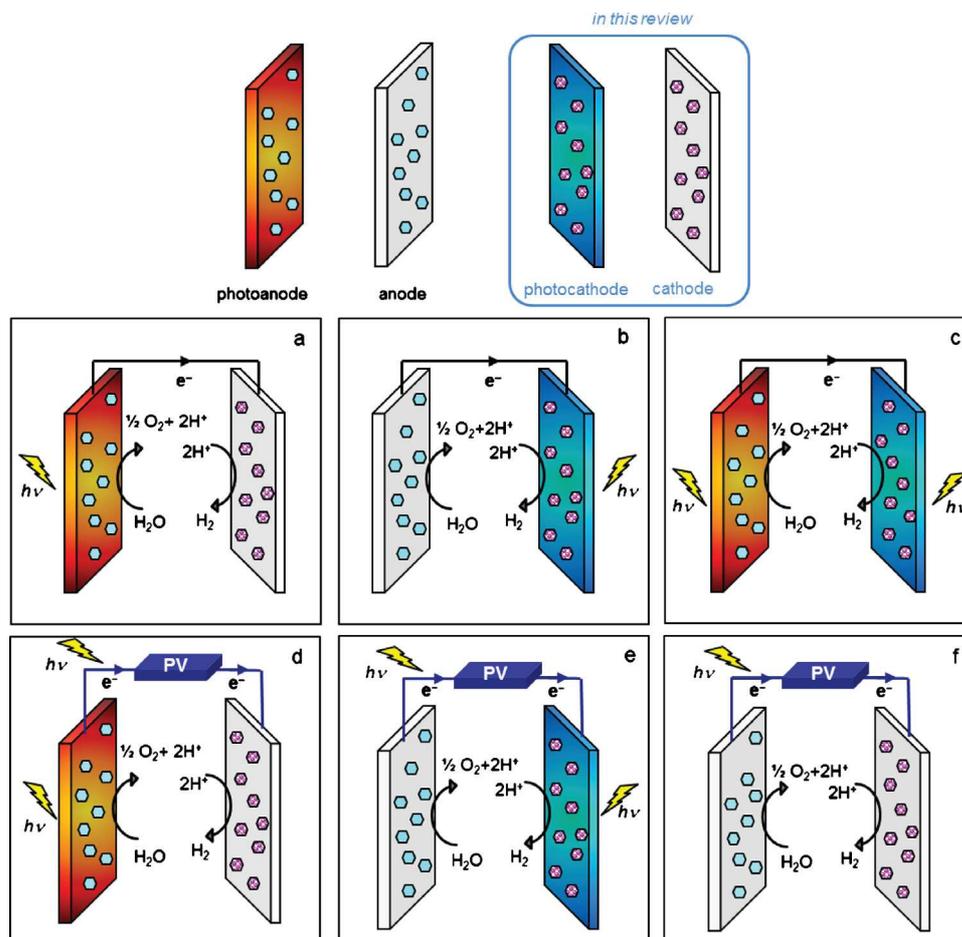
Fig. 1. Schematic representations of photoelectrochemical cell (PEC) architectures for water splitting: self-sufficient PEC cells based on one (a, b) and two (c) photoelectrodes or PV-biased PEC (d, e) and electrochemical (f) cells. The catalysts for water oxidation and reduction are depicted by blue and pink hexagons, respectively. PV indicates a photovoltaic component containing at least one buried p/n junction (*i.e.* shielded from contact with any electrolyte) in a wireless mode (monolithic cells) or wired to the PEC or electrochemical cell.

of a single photoactive component does not allow to reach the required photovoltage to drive water splitting. To overcome this problem, it is possible to couple two photoelectrodes, *i.e.* a photocathode for H_2 evolution and a photoanode for O_2 evolution (Fig. 1c). This configuration mimics the situation found in the Z-scheme of the photosynthetic chain of microorganisms which have evolved two photosystems (Photosystems I and II) for that purpose [19]. A technologically relevant alternative finally consists in providing a part (Fig. 1d and e) or the whole (Fig. 1f) of the energy required for water splitting by a photovoltaic module, which includes p/n junctions made of inorganic semiconductors, organic photovoltaic (OPV) cells, perovskite solar cells or dye-sensitized solar cells (DSSCs). This photovoltaic module may be integrated within the device, in a so-called non-wired configuration. In this case the junction is buried in the architecture and protected from any contact with the electrolyte. Acknowledging the diversity of possible architectures, a full taxonomy for solar fuel generator has been recently proposed [20].

A comprehensive survey of the self-sufficient photoelectrochemical operational devices reported so far recently appeared [21]. The seminal work on that topic was reported by Fujishima and Honda in 1972 with a water splitting cell made from a TiO_2 photoanode and a Pt cathode [22,23], thus with an architecture similar to that shown in Fig. 1a. To the best of our knowledge, no PEC cell with the architecture shown in Fig. 1b has been described so far. Reisner and coworkers reported the first $Cu_2O/NiO - WO_3$ PEC cell (Fig. 2a) corresponding to the architecture shown in

Fig. 1c [24]. Sivula and coworkers designed a similar cell based on a $Cu_2O/Al:ZnO/TiO_2/RuO_x$ photocathode and a $BiVO_4/CoPi$ photoanode with 0.5% solar-to-hydrogen (STH) conversion efficiency [25]. The nanodevice developed by Yang and coworkers based on platinum nanoparticles decorated Si nanowires grown on TiO_2 nanorods loaded with iridium oxide nanoparticles (Fig. 2b) has a similar working principle [26]. A similar combination but with a hematite photoanode has been used by Wang and coworkers [27]. The most efficient operating cells known in the literature however integrate a photovoltaic module. The monolithic photovoltaic–photoelectrochemical device reported by Turner combines a $GaInP_2/Pt$ photocathode, two p/n junctions and a Pt anode (Fig. 2c) [28]. Rocheleau and coworkers designed a similar hybrid-junction photoelectrode configuration, incorporating cheap, environmentally benign and highly stable photoanode materials. Deposited on top of a solid-state multijunction (double and triple junctions based on a-Si and a-Si:Ge), α-Fe_2O_3, WO_3 were used to oxidize water while enhancing the electrochemical bias for water reduction at a platinum electrode [29–32]. More recently, van de Krol and coworkers reported on a similar device combining a $BiVO_4/CoPi$ photoanode (Fig. 2d) [33]. Another example is the so-called tandem-cell that consists of a WO_3/Pt or a Fe_2O_3/Pt photoelectrochemical cell biased with a dye-sensitized solar cell (DSSC, Fig. 2f) and that achieves an overall yield up to 3.1% [34–36]. These first examples display quite good efficiencies for energetic conversion (12.4% for the cell reported by Turner) but are very expensive owing to the fabrication of the photovoltaic assembly
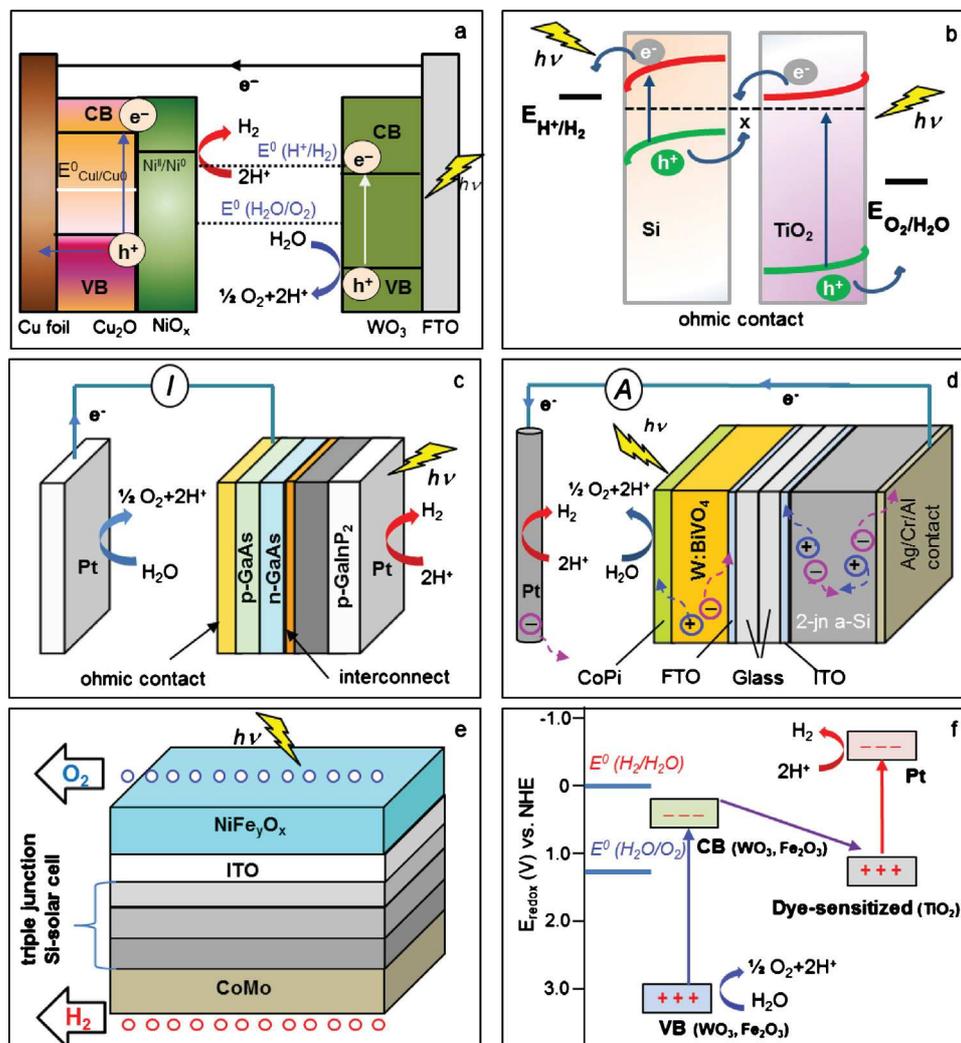
Fig. 2. Selected devices for photocatalytic water splitting: (a) the two-electrode PEC system reported by Reisner and coworkers [24], (b) semiconductor nanowire-based PEC design from Yang and coworkers [27], (c) monolithic PV-biased PEC cell from Turner and coworkers [28], (d) non-wired PV-biased PEC cell from van de Kroll and coworkers [33], (e) non-wired PV-biased electrochemical cell [32,38,39], (f) principle of the tandem PEC cell including a DSSC [34–36].

and the presence of Pt as a catalyst. Of note, Licht and coworkers reported on very efficient cells with STH efficiency over 18% but based on quite expensive multi-junction composite materials using III–V semiconductors and noble metal-based catalysts (Pt and RuO₂) [37]. Platinum-free PV-biased electrochemical cells have also been developed combining either a multi-junction photovoltaic device (triple junction a-Si/a-Si:Ge/a-Si:Ge) or three copper–indium–gallium-sulfide (CGIS) cells connected in series and nickel–molybdenum (NiMo) or cobalt–molybdenum (CoMo) (HER)/NiFe$_y$O$_x$ (OER) electrocatalytic layers (Fig. 2e); these devices are able to operate under basic conditions, though with associated corrosion issues [32,38,39]. The artificial leaf developed by Nocera and coworkers has a similar structure but integrates NiMo (HER) and CoPi (OER) catalysts allowing it to function in near-neutral conditions [40,41].

Current research targets the use of low-cost materials absorbing in the visible spectrum and possessing valence band and conduction band energies competent for OER and HER, respectively [42]. Nevertheless, many of these systems rely on rare and/or scarce elements. By reducing the amount of material used and providing high modularity, the construction of earth-abundant element based molecular electrode and photoelectrode materials constitutes an interesting alternative to the use of bulk solid-state materials. In

the following, we describe how such molecular approaches have led to the design of cathodes and photocathodes for H₂ evolution. Of note similar approaches have been developed for the construction of molecular anode [43–45] and photoanode [46–53] materials.

3. Molecular H₂-evolving cathodes

The recent years have seen the rise of a number of novel solid-state inorganic materials based on earth-abundant elements and able to catalyze hydrogen evolution often over a large pH range in aqueous solutions [54]. Novel formulations include, among others, sulfides [55–58], phosphides [59–61], nitrides [62,63] and carbides [62–64] compounds. Some of these catalytic materials have been combined with carbon nanomaterials to enhance both the conductivity and the active surface of the electrode [54]. With the same objective of designing cheap carbon-based electrodes for H₂ production, a number of groups have extended the studies of H₂-evolving molecular catalysts to their immobilization onto carbon-based materials. Such projects require the development of relevant methods to achieve efficient and stable grafting of the molecular catalyst onto the electrode surface. In that purpose, different strategies have been applied so far and reported in the

literature concerning both standard carbon surfaces and carbon nanotubes (CNTs).

3.1. Entrapment of the catalyst within a polymeric material

First achievements have been described by Kellet and Spiro in the 1980s. They reported that stable catalytic materials can be simply obtained by incorporating positively charged cobalt porphyrin complexes into a Nafion film cast onto a glassy carbon electrode. However, the inherent poor electron-transfer characteristics of these films only allowed low electroactivity [65]. Similarly, the coating of a bare pyrolytic graphite electrode with the neutral cobalt porphyrin [Co(TPP)] (**1**, Fig. 3) incorporated in a Nafion film can reduce protons. Nonetheless, a large overpotential (450 mV, pH = 1) and a quite low turnover frequency value of $70\,h^{-1}$ are observed [66]. Better turnover frequency (TOF = $2 \times 10^5\,h^{-1}$) could be achieved with an applied potential of -0.90 vs Ag/AgCl and at pH = 1 for a the cobalt phthalocyanine **2** (Fig. 3) incorporated in a poly(4-vinylpyridine-co-styrene) film deposited on a graphite electrode [67]. Here again HER was limited by the electron transfer within the matrix.

3.2. Covalent attachment of the catalyst within an oligomeric or polymeric material

Carbon-based electrodes can also be easily coated with conducting polymers obtained via electropolymerization processes. Indeed, electropolymerization of [Cp*Rh(L)Cl](BF$_4$) (L = bis-4,4′-(bis(pyrrol-1-ylmethyl)methoxycarbonyl)-2,2′-bipyridyl) (**3**) (Fig. 3) leads to a stable film capable of proton electroreduction at -0.31 V vs NHE at pH values lower than 4. Quantitative current efficiency corresponding to 353 turnovers was observed during a 14 h electrolysis experiment at pH 1 using a carbon-felt electrode coated with the electropolymerized rhodium complex [68]. Sequential strategies were also employed, relying on the electrode coating with conducting polymers obtained via an electropolymerization process in a first step and the functionalization of this polymer with the catalyst in a second step. Such an electropolymeric material incorporating a hydrogenase model compound was provided by Pickett and coworkers [70]. Mimicking the active site of [FeFe]-hydrogenases [71,72], the dinuclear Fe complex **5** (Fig. 4) was reacted with a glassy carbon (GC) electrode coated with a functionalized polypyrrole film. This material has been shown to evolve hydrogen at potentials slightly more positive than those measured in the case of the complex-free polymer, thus with overpotential requirement remaining too large for any practical applications. A similar strategy has been developed by DuBois and coworkers with the mononuclear Ni complex **6a** (Fig. 5) carrying electropolymerizable thiophene groups [73]. While the molecular complex displays interesting electrocatalytic properties when assayed in solution (limited overpotential requirement of 280 mV at the middle of the electrocatalytic wave and TOF of $56\,s^{-1}$ at the catalytic plateau), the related **6a**-decorated polythiophene film is not electrocatalytically active for still unknown reasons.

Electroreduction of diazonium salts (Fig. 6) also proves to be an efficient alternative method to form covalent linkages between a catalyst and a carbon electrode [74]. The electrode surface is first covered with a polyphenylene film bearing amine moieties through electrochemical polymerization and further chemical modification (Fig. 6). The catalyst is then covalently immobilized by amide-coupling with the amino groups of the film. This methodology was applied by Darensbourg's group (Fig. 7a) [75], Gloaguen and coworkers [76] (Fig. 7b) and ourselves [77] (Fig. 7c) to dinuclear Fe complexes **7a–c** modeling [FeFe]-hydrogenase active sites. The grafting of dithiolate-bridged diiron complexes, **7b** and **7c**, with activated succinimide ester groups has been achieved

on glassy carbon electrodes modified with either p-aminophenyl or p-(2-aminoethyl)phenyl groups. Unfortunately, these materials displayed very weak electrocatalytic responses because of a great instability, due to the loss of CO ligands in the reduced state of the catalyst as shown by X-ray photoelectron spectroscopy (XPS) and attenuated-total-reflectance infrared spectroscopy (ATR-IR) studies [77].

A major breakthrough was reported in our laboratory in 2009, thanks to a fruitful collaboration with Jousselme and Palacin in CEA Saclay (France), regarding novel Ni-based CNT-coated electrodes with remarkable electrocatalytic activities both for H$_2$ evolution and oxidation [78]. Among hydrogenase bioinspired catalysts, DuBois' nickel-bis(diphosphine) complexes are probably the ones with the most outstanding catalytic properties, as recently shown by a benchmark study in non-aqueous solutions [79]. Such catalysts can function in both directions (proton reduction and H$_2$ oxidation) depending on the operating conditions [80]. In addition, their synthetic versatility allowed us to prepare the analog **6b** (Fig. 5), in which activated ester functionalities were introduced. An amidation reaction then afforded covalent attachment of the catalyst to CNTs previously decorated with amine groups at their surface through electrochemical reduction of the 4-(2-aminoethyl)phenyldiazonium salt (Figs. 8 and 9, left) [78]. Later on, Roberts and coworkers reported on a similar grafting of **6b** onto 1,2,3-triazolyllithium-terminated planar glassy carbon surfaces [81].

These electroactive Ni-functionalized CNTs were then deposited onto a gas diffusion layer (GDL) and coated with a Nafion membrane. GDLs are carbon clothes coated with a gas-permeable water-tight conductive membrane and have been specifically developed for proton exchange membrane (PEM)-based technologies. This architecture led to a cheap, stable, air-resistant membrane-electrode assembly (MEA, Fig. 9, right) with unique performances, especially under the strongly acidic conditions required in the expanding PEM-based technology. Hydrogen indeed evolves from aqueous sulphuric acid solution at the thermodynamic equilibrium (no overpotential requirement) and the material proved remarkably stable: up to 100 000 turnovers could be measured during a 10 h experiment without loss of activity. Interestingly, this Pt-free catalyst is also very efficient for hydrogen oxidation under the same conditions with current densities similar to those observed for hydrogenase-based materials ($1–2\,mA\,cm^{-2}$) under mass-transport limitation. The maximum current density that can be measured in the absence of such limitation (i.e. using a rotating disk electrode on which the catalytic material has been deposited) reaches $40\,mA\,cm^{-2}$. Bidirectional catalysis was completely unexpected from solution studies. This behavior shows how modification of the distant environment of a metal complex, in other words its third coordination sphere, may also allow to tune its catalytic properties. Later on, colleagues from DuBois' group modified the nature of the substituents at the P$_2$N$_2$ ligand [82–84] and obtained catalysts showing similar bidirectional catalytic activity but in the homogeneous bulk phase. To the best of our knowledge, the Ni-functionalized CNTs are the first molecular-engineered and noble-metal free electrode materials capable of hydrogen evolution/oxidation at the thermodynamic equilibrium.

The same methodology was used to immobilize the diimine–dioxime cobalt catalyst **8** [85–87] at the surface of a similar CNT-based electrode (Fig. 10) [88]. Again, this yielded a very active electrocatalytic cathode material, mediating H$_2$ generation with a turnover number of 55.000 ton in 7 h from fully aqueous solutions at mild pH (acetate buffer pH 4.5) and modest overpotentials (onset potential for H$_2$ evolution is -350 mV vs RHE) [88]. Scanning electron microscopy (SEM) was used to exclude the formation of any particle at the surface of CNTs and XPS confirmed the preservation of the molecular structure of
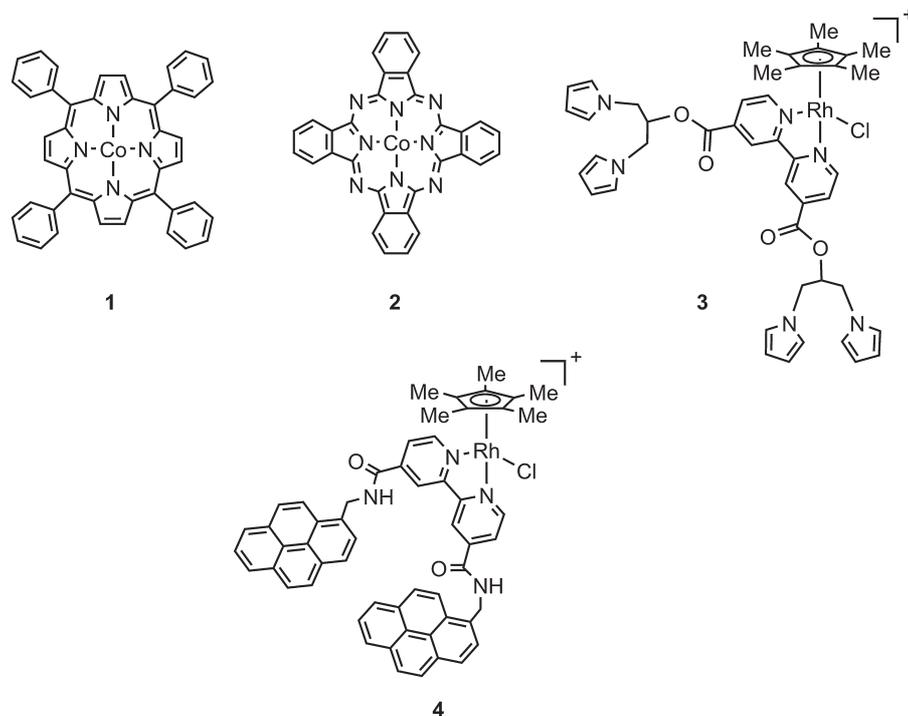
Fig. 3. Selected cobalt [65–67] and rhodium-based [68,69] H$_2$-evolving catalysts that have been immobilized though entrapment or π staking onto electrode surfaces.
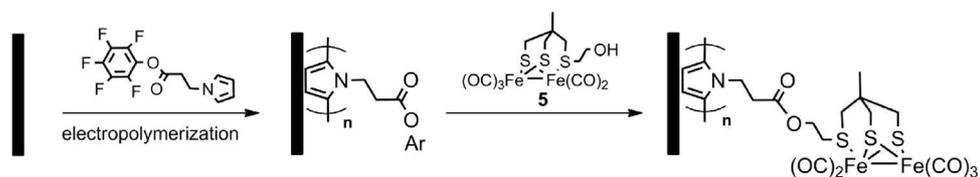

Fig. 4. Immobilization of the biomimetic complex **5** by covalent attachment to a polypyrrole film electrodeposited onto a GC electrode [70].
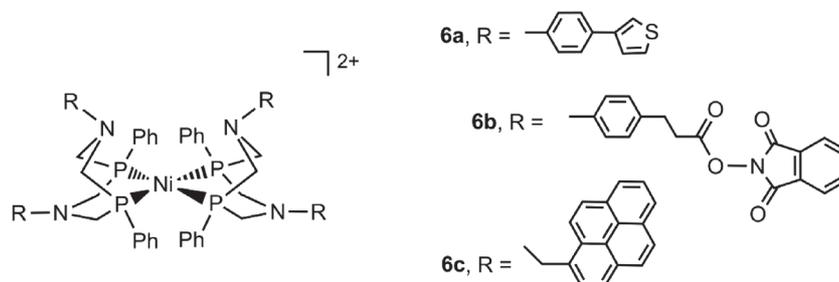

Fig. 5. Structure of DuBois' nickel-bis(diphosphine) catalysts **6a–c** modified for their immobilization onto electrode surfaces.
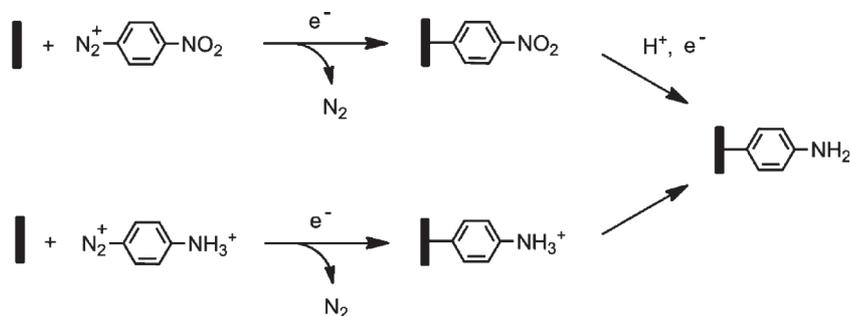

Fig. 6. Functionalization of conductive surfaces by an amino-polyphenylene layer *via* diazonium salt reduction [74].
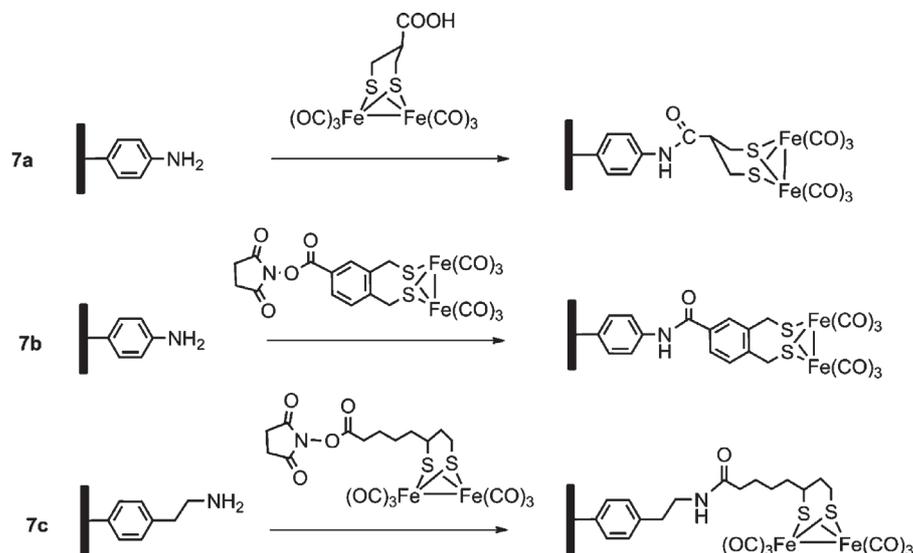
Fig. 7. Covalent immobilization of [FeFe]-hydrogenase mimics *via* amide coupling.
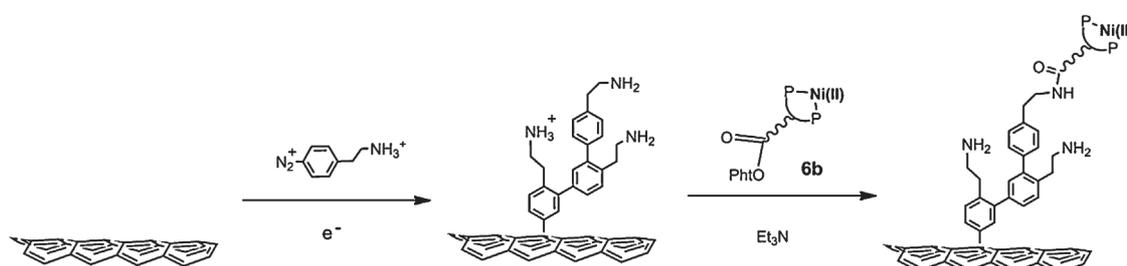

Fig. 8. Electrografting of amine groups multiwalled carbon nanotubes (MWCNTs) and post-functionalization with complex **6b** through amide coupling [78]. This is a simplified representation of the structure of the material for sake of clarity: the number of phenylene residues is indeed arbitrary and attachment of the nickel complex to two or more surface amine groups not excluded.
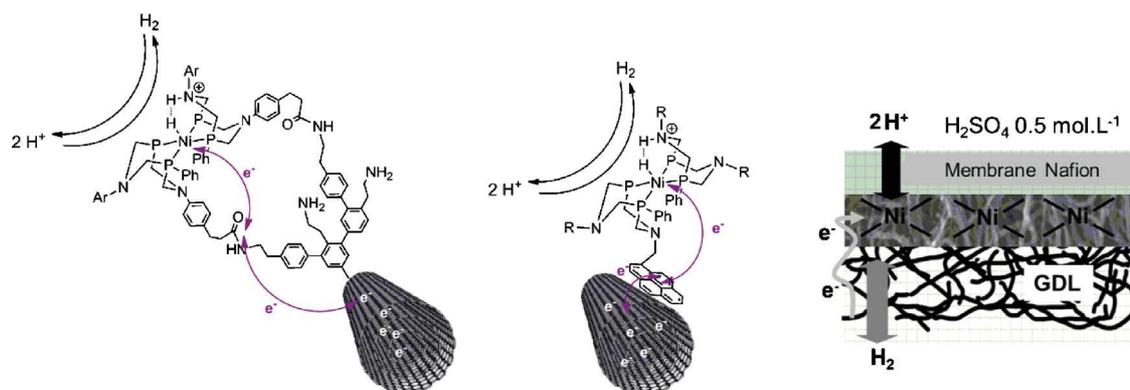

Fig. 9. Left: schematic representation of the structure and reactivity of the bioinspired H_2-evolving nickel catalyst **6b** covalently grafted onto CNTs [78]. Electrons are exchanged between the CNTs and the metallic centers where H^+ is reduced to H_2 or H_2 oxidized to H^+. Middle: schematic representation of the structure and reactivity of catalyst **6c** immobilized onto CNTs by π stacking. Right: structure of the membrane-electrode assembly used for the electrocatalytic characterization of the Ni-functionalized CNTs under conditions relevant for PEM-based technologies.

the grafted complex after extensive catalytic turnover. The good stability of this material upon cycling contrasts with the limited stability of the same molecular catalyst under bulk electrolysis conditions. This point clearly indicates that grafting provides a largely increased protection of these cobalt catalysts against decomposition and allows preserving their molecular structure and the related activity. We recently demonstrated that this material proves O_2-tolerant [89], *i.e.* it can evolve H_2 even in the presence of a significant amount of dissolved O_2.

A last example implementing electroreduction of diazonium salts for catalyst immobilization has been recently described by the groups of Fontecave and Bedioui. In that case a diazotized terpyridine ligand was first electrodeposited onto a GC electrode. Further treatment with cobalt salt yielded an Co-terpyridine modified electrode material, the structure of which is shown in Fig. 10 (right) [90]. This material proves active for H_2 evolution from pH 7 aqueous solutions, although with the requirement of a quite high overpotential.
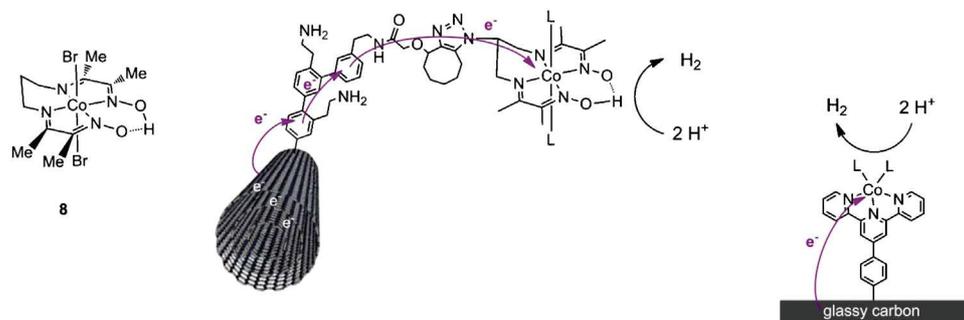
Fig. 10. Schematic representation of the structure and reactivity of bioinspired H$_2$-evolving cobalt catalysts grafted onto CNTs [88] or GC [90].

3.3. Non-covalent attachment of the catalyst via π stacking interactions

Among the available CNTs functionalization approaches, non-covalent π stacking of conjugated molecules on the nanotube surface is also quite attractive. Especially, pyrene derivatives are well-known for their ability to adsorb onto graphite via π–π interactions. We successfully used this strategy for the immobilization of DuBois' nickel-bis(diphosphine) catalysts onto CNTs. Pyrene derivatives of nickel complexes such as **6c** (Fig. 5) can be easily immobilized onto CNTs, prior to their deposition onto a GDL substrate. This one-step process is practically a much easier method than the covalent grafting as described above that necessitates three steps: (i) deposition of CNTs onto the electrode support; (ii) modification of the CNTs with the electrografting process and (iii) post-functionalization reaction. In addition, using the π stacking method surface catalyst loading can be easily tailored by varying the amount of CNTs deposited on the electrode. For example, a catalyst surface concentration as high as 8×10^{-9} mol cm^{-2} was obtained with a functionalized CNTs deposit of 0.2 mg cm^{-2}. For comparison, the covalent method relying on diazonium electroreduction followed by an amidation post-functionalization step affords a limited surface coverage of 1.5×10^{-9} mol cm^{-2}, regardless of the amount of CNTs deposited on the GDL [91]. Finally, when stacked onto CNTs, the nickel bis(diphosphine) complexes show catalytic performances comparable with those displayed by the complexes covalently attached to CNTs. We thus believe that this methodology will be useful to design more efficient electrocatalytic materials.

Recently Blakemore, Brunschwig, Gray and coworkers used the π stacking method to revisit electrode functionalization with the [Cp*Rh(bipy)Cl]$^+$ catalyst [69]. They prepared the pyrene-appended complex **4** (Fig. 3) and immobilized it onto a high surface area carbon black material, used as electrode substrate to afford conductive surfaces with a high microscopic area that support high electrocatalytic current densities. The surface-anchored complex proved active for proton reduction from p-toluenesulfonic acid solubilized in CH$_3$CN with a TOF of $\sim$1 s^{-1} at 14 mM acid concentration. The activity proved stable with 206 turnovers achieved over 1.25 h during controlled potential electrolysis carried out with 5 mM acid initially introduced. Such performances measured in CH$_3$CN are thus comparable to those reported in 1989 with a polypyrrole-based electrode-containing catalyst **3** (Fig. 3) and assayed in aqueous electrolyte [68].

The π stacking methodology was also used to immobilize cobalt dithiolene complexes. Lehnert and coworkers showed that a cobalt-bis(arenedithiolate) complex spontaneously adsorbs at a graphene surface deposited onto a fluorine-doped tin oxide (FTO) electrode. The resulting electrode is active for H$_2$ evolution from weakly acidic aqueous solutions (pH > 3) with polarization curves cathodically shifted by 370 mV with regards to platinum.
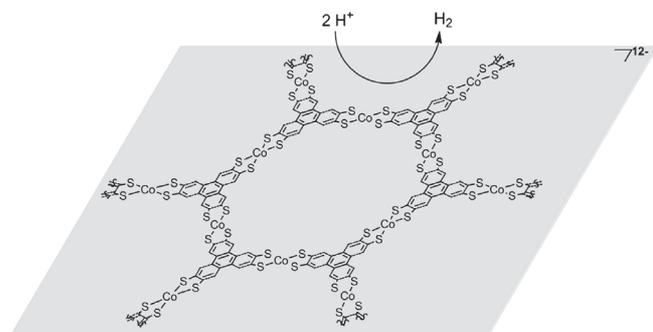

Fig. 11. Self-assembled 2D coordination polymer based on cobalt-bis(arenedithiolate) moieties deposited onto glassy carbon or highly oriented pyrolytic graphite (HOPG) electrodes.

A TOF > 1000 s^{-1} has been announced, together with O$_2$ tolerance [92]. The same methodology has been used by Marinescu and coworkers to deposit a self-assembled 2D coordination polymer based on cobalt-bis(arenedithiolate) moieties (Fig. 11) onto glassy carbon or highly oriented pyrolytic graphite (HOPG) electrodes [93]. H$_2$ evolution activity was attested from pH 1 to 2.6 aqueous solutions. A relatively low overpotential of 340 mV is required to reach 10 mA cm^{-2} current density at pH 1.3 and the electrode material is stable over hours under these conditions. Progressive peeling-off of the deposited layered coordination polymer though occurs after extensive use.

4. Molecular H$_2$-evolving photocathodes based on solid-state semiconductors

The development of methodologies to anchor molecular HER catalysts onto electrodes has led chemists to envision the integration of such catalysts in photocathodes (Fig. 1), which are able to perform both light-harvesting and hydrogen evolution. A possible architecture for such electrodes couples a light-harvesting semiconductor (SC) with a molecular catalyst directly grafted onto its surface. In this section, we will focus on the use of inorganic solid-state SCs. A common feature to all these electrodes is the utilization of a low band gap SC (Si, GaP, InP, Cu$_2$O, etc.) to perform light-harvesting in the visible region. The potential of their conduction band should be located downward from the thermodynamic equilibrium potential of the H$^+$/H$_2$ couple so as to enable photodriven proton reduction. Doped p-type materials are typically used for the construction of photocathodes: the SC-electrolyte junction formed upon equilibration is indeed suitable for the injection of photogenerated electrons toward electron acceptors located at the surface of the electrode or in the electrolyte. Such SC are either in the form of bulk material exposing a specific crystallographic plan [94–98] or made of a nanoparticulate network or film deposited onto a
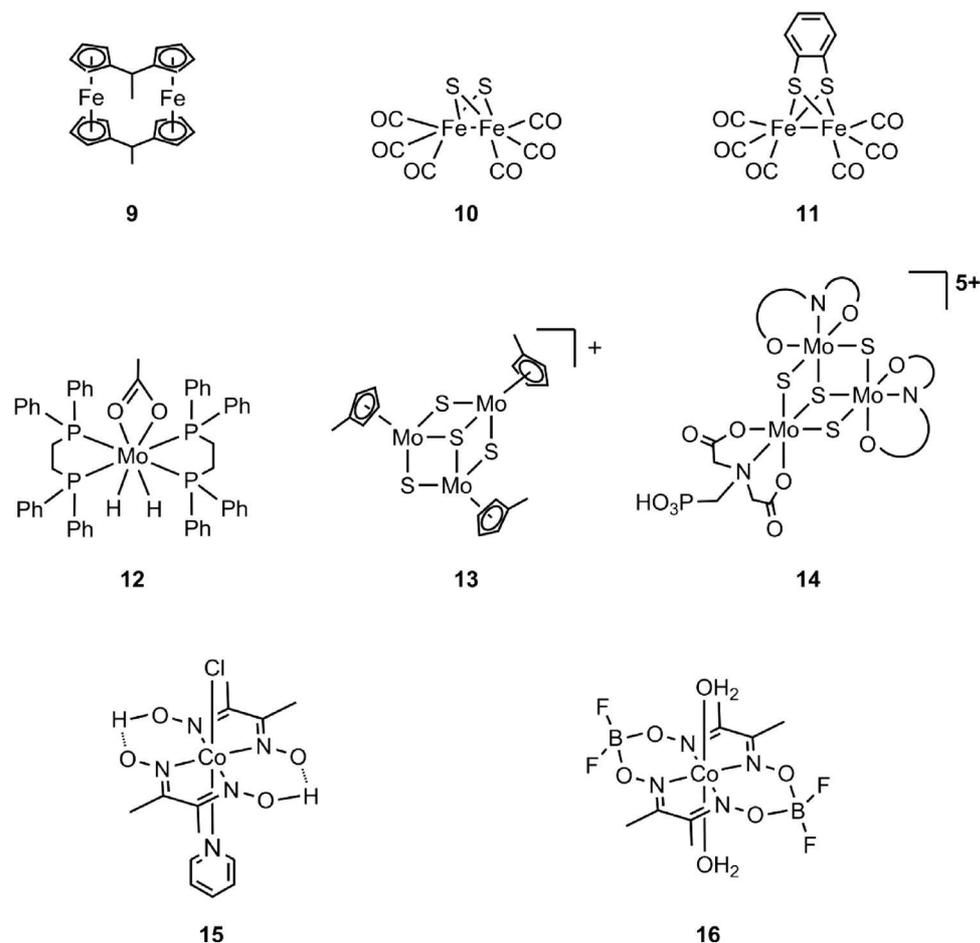
Fig. 12. Structures of the iron-based, molybdene-based and cobaloxime H_2-evolving catalysts that have been integrated into various interfacial photocatalytic systems.

conductive electrode [99]. If the latter architecture could ensure high catalyst loading thanks to its large surface area, the same could be achieved with planar substrates through coating with thick polymeric films embedding catalysts as explained in part 3. Under irradiation, pristine SC materials generally exhibit large photocurrents. However in many cases a (so-called native) oxide layer readily forms at the surface/electrolyte junction if the electrode is exposed to air. The insulating properties of this oxide layer modify the band-bending and hinders electronic injection at the interface. Such surface passivation issue is well known in Si-based photoelectrodes [100,101] and different strategies have been developed to overcome it. Protection of the surface can be achieved by deposition of thin metal–oxide layer(s) tolerant to aqueous media onto a freshly etched SC surface [100,101]. Depending on the nature of the protective layer (TiO_2, Al_2O_3, etc.) and its thickness, photogenerated electrons in the SC may reach the electrolyte through the conduction band [100] of the protective oxide or by tunneling [102]. Of note, functionalization of SC surface by organic groups is an interesting way to form a molecular protective layer [102]. Yet, due to the difficulty to achieve complete SC surface coverage, punctual surfaces sites are often still present and constitute entry points for passivation, thus limiting such an approach [96].

Inorganic solid-state SCs have been intensively used for developing photocathodes based on solid-state HER catalysts [100,103–115]. Organic functionalization has also been developed to attach a catalyst onto the SC surface. The first example of such a photocathode integrating a molecular HER catalyst dates back from 1984. The electrode was made of *p*-Si onto which a polystyrene

film functionalized with 1-methyl-[1.1]ferrocenophane **9** (Fig. 12) was immobilized [94]. In this study, hydrogen evolution from neat boron trifluoride hydrate (HBF_3OH) used as the electrolyte occurred at potential shifted 300 mV more negative than at a Pt electrode in the dark. Although no gas quantification was provided, saturating currents of $230\,mA\,cm^{-2}$ under nine suns as well as extended activity over 5 days proved the good stability of such electrodes. The unusual nature of the neat HBF_3OH electrolyte used here might also contribute to such performances, possibly by preventing surface oxide passivation, even if the photocathode was also shown to operate in aqueous $HClO_4$ electrolyte.

Another example has been reported by Nann, Pickett and coworkers [99]. Using a layer-by-layer procedure, they first crosslinked InP nanocrystals through 1,4-benzenedithiolate bridges onto a gold electrode. The molecular $[Fe_2(\mu-S)_2(CO)_6]$ complex **10** (Fig. 12), whose structure partly mimics the active site of [FeFe]-hydrogenases, was then simply adsorbed on this material, as evidenced by FTIR spectroscopy. Under irradiation at 395 nm using a light-emitting diode (LED) array, photocurrents of $\sim250\,nA\,cm^{-2}$ at $-0.4\,V$ *vs* Ag/AgCl could be observed in $NaBF_4$ aqueous electrolyte. This photocurrent was correlated to hydrogen evolution through quantification by gas chromatography after 1 h of electrolysis.

In a more recent attempt, Ott, Kubiak and coworkers were able to prove quantitative faradaic efficiency using a (1 1 1) *p*-Si electrode poised at $-900\,mV$ *vs* $Fc^{+/0}$ and a similar $[Fe_2(\mu-bdt)CO_6]$ (bdt^{2-} = benzenedithiolate) catalyst, **11** (Fig. 12), here dissolved in a dry organic electrolyte and not immobilized onto the surface of the
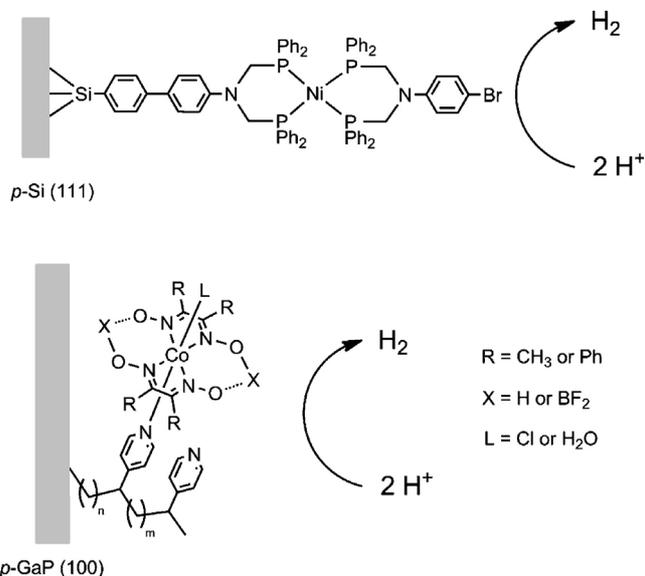
Fig. 13. Structure of molecular-based photoelectrodes based on p-Si or p-GaP SC materials.

SC [98]. Interestingly, using $HClO_4$ as a proton source, the 661 nm illuminated *p*-Si electrode evolves hydrogen at potentials 500 mV higher than those required in the dark at a GC electrode. Yet, the relatively high intrinsic overpotential for HER of **11** does not allow this irradiated system to reduce protons at potentials upward from the thermodynamic equilibrium potential of the H^+/H_2 couple. Similarly, a robust molybdenum hydride complex, **12** (Fig. 12), was shown by Pickett and coworkers [116] to sustain hydrogen evolution photoelectrocatalysis at boron-doped, hydrogen-terminated, *p*-type silicon. With 37 mW cm^{-2} illumination in the 600–700 nm range, the light-to-electrochemical energy conversion was estimated to be 2.8%.

The use of catalysts displaying lower overpotential and operating in aqueous media is then highly desirable. In this frame, Sharp and Moore exploited the phthalimide-functionalized nickel bis(diphosphine) catalyst **6b** (Fig. 5), initially developed for a covalent attachment onto CNTs [78]. (1 1 1) *p*-Si and (1 0 0) *p*-GaP substrates were etched with buffered hydrofluoric acid and then decorated by protected pendant amino groups using UV-induced covalent grafting of *N*-allyl-2,2,2-trifluoro-acetamide [96]. Further deprotection of the amino groups followed by amide coupling with **6b** gave SC substrates bearing the nickel complex at the surface as shown by grazing angle attenuated total reflectance (GATR) FTIR and XPS spectroscopies. GATR-FTIR spectra of the functionalized substrates also display a vibrational band characteristic of surface oxide layers likely formed during surface functionalization. No photoelectrochemical activity is reported for this construct. However, poor performances would be expected because of the presence of this passivating layer.

Rose and coworkers constructed a related nickel bis(diphosphine) complex (Fig. 13) onto a methyl protected (1 1 1) *p*-Si wafer by a stepwise surface modification procedure exploiting palladium-catalyzed coupling chemistry [117]. XPS and electrochemical characterizations allowed a *ca* 2.5×10^{-10} mol cm^{-2} coverage of the Ni catalyst to be estimated. The surface protective methyl layer provides a good stability upon cycling in the presence of trifluoroacetic acid (TFA) in CH_3CN under a LED 33 mW cm^{-2} irradiation. The onset HER potential under light irradiation is of −0.06 V *vs* NHE, only 40 mV more negative than a control Pt-coated *p*-Si electrode. The covalently assembled SC-molecular catalyst construct proved more active than a solution of the same catalyst

in contact with a methylated *p*-Si photoelectrode (the onset potential for light driven HER is shifted 200 mV more positive). The photoelectrocatalytic activity for proton reduction is confirmed by controlled potential electrolysis, although no faradaic efficiency nor control electrolysis experiment at a non-decorated substrate are reported.

Moore and coworkers used a similar strategy to immobilize a distinct molecular HER catalysts and reported stable activity in aqueous media. In this case, they successfully decorated etched (1 0 0) *p*-GaP by UV-induced grafting and polymerization of 4-vinylpyridine [95]. The functionalization results in a polyvinylpyridine (PVP) film coating the GaP substrate and featuring pendant pyridine sites, used to bind the cobaloxime $[Co(dmgH)(dmgH_2)Cl_2]$ (Fig. 13). Coordination of the cobalt catalyst to the pyridine sites was confirmed by XPS and XANES analysis, with a maximum surface loading estimated around 1.3×10^{-8} mol cm^{-2}. The polymeric PVP coverage of the GaP surface likely provides protection against oxide layer passivation by restricting access to surface GaP sites. The authors could thus operate the photoelectrode in neutral aqueous media with onset potential at +0.76 V *vs* RHE and saturating currents close to 3 mA cm^{-2}. Performance of the electrode is further assessed by 30 min electrolysis at +0.17 V *vs* RHE under simulated solar irradiation (AM 1.5 illumination) with hydrogen evolution as detected by GC analysis of the headspace of the cell. The modest decrease of the current (20%) after 30 min is attributed to the leaching of coordinated catalysts, as supported by XPS data, rather than surface passivation. This observation further demonstrates the interest of such polymeric functionalization strategy to develop stable SC-based photoelectrodes. The relatively good stability of the catalyst-polymer assembly overlayed onto GaP allows the authors to analyze the performances of the electrode depending on light intensity and pH of the electrolyte [118,119] and to screen alternative cobaloximes as catalysts [119]. Of note, they observe a linear dependence of current density with light intensity, which is a good indication that such a photocathode is limited by the light flux and not by the amount or activity of the grafted catalyst [118]. A controlled potential electrolysis carried out at +0.17 V *vs* RHE under AM 1.5 gives an external quantum efficiency of 1.5% and a faradaic efficiency >88%, further confirming the high performance of this construction [118].

Alternatively very efficient photocathodes were reported by Chorkendorff and coworkers based on the drop casting of a solution of trinuclear molybdenum cluster salts such as $[(Cp')_3Mo_3S_4](OTs)$ (**13**, Cp' = methylcyclopentadienyl, Fig. 12) or $Na_5[Mo_3S_4(Hpmida)_3]$ (**14**, Hpmida = N-(phosphonomethyl)iminodiacetate, Fig. 12) onto p-type planar and/or pillared Si electrodes [101,120]. The resulting electrode displayed impressive properties for H_2 evolution under red-light illumination. In particular, the stability of the light-driven HER activity was found excellent with only 5% decay in the first 30 min. The exact nature of the active species responsible for HER was however not clarified, with the possibility for a transformation of the incomplete $[Mo_3S_4]$ cubane clusters into amorphous molybdenum sulphide [55] during catalysis.

In conclusion, architectures assembling a molecular catalyst at the surface of a light-harvesting semiconductor seem promising, especially when coupled with technologies able to overcome surface passivation issues. Yet, it should be noted that such photoelectrodes often rely on materials incorporating rare elements such as In, Ga or Ge and that fabrication of single crystalline wafers is highly demanding in terms of energy cost. While nanosciences may help to identify cheaper and more durable SC candidates, the recent development of organic photovoltaic solar cells has made room to substitute crystalline SC for cheaper materials in identical architectures.
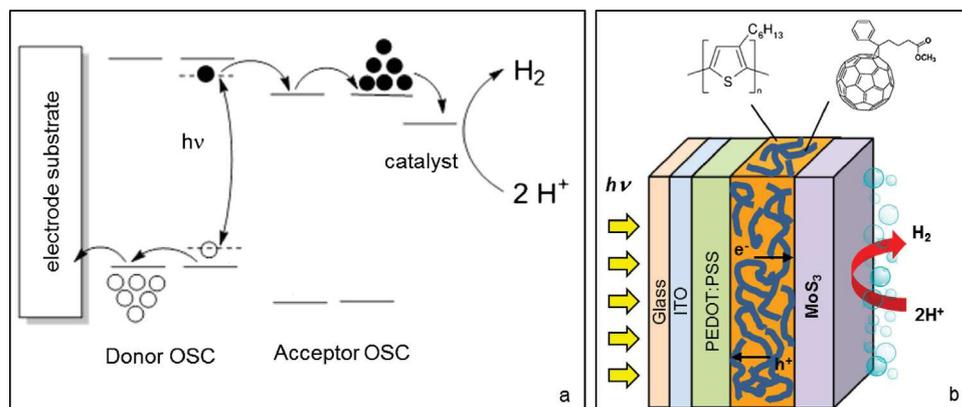
Fig. 14. (a) Schematic for H$_2$-evolving photocathode architecture based on OSCs. (b) Architecture of the P3HT:PCBM/MoS$_3$ H$_2$-evolving photocathode [119].

5. H$_2$-evolving photocathodes based on organic semiconductors

Organic semiconductor materials (OSCs) made of conducting polymers, oligomers or self-assembled discrete molecules allowed to develop organic photovoltaics (OPV), with solar cells reaching 10% of power conversion efficiency (PCE) [121] using abundant materials and low-cost solution-based processes. Additional advantages of using OSCs in the perspective of the construction of PEC devices are linked to their high optical absorption in the visible region of the solar spectrum. They generally possess much more reducing excited states than inorganic semiconductors and their electronic properties can be easily tuned through structural modifications [122]. Thus, a wide variety of materials can be obtained with different energy levels which can be tuned to the redox potentials of both reductive and oxidative half-reactions in water splitting. Organic photovoltaic cells are obtained from the combination and structuration of two OSCs. Light-induced charge separation is achieved at the interface between the two OSCs. Upon absorption of a photon in one of the OSCs, an exciton (*i.e.* a pair of electrostatically bound electron and hole) forms and then migrates to the junction with the other OSC. Here the exciton dissociates, resulting in the appearance of a hole in one OSC called the donor and an electron in the other OSC called the acceptor. In photovoltaic cells, electrons and holes then migrate to the electrodes where charges are collected. A key issue is the structuration of the two materials since excitons can only diffuse over a few nm during their lifetime, *i.e.* before spontaneous recombination takes place. Therefore the two OSC must be either deposited as two very thin layers, possibly with an interlayer containing both compounds, yielding a mixed interlayer junction, or as a blend of the two materials forming molecular p-n junctions all over the bulk layer (bulk heterojunction, BHJ). In general, BHJ are formed between a polymer or an array of small molecules, acting as the light absorber, and a fullerene derivative [123].

Organic photovoltaic cells in triple-junction configuration, allowing to reach an open-circuit voltage of $V_{OC} = 2.33$ V, have been employed in a PV-electrolyzer configuration operated at $V \approx 1.70$ V [124] with a lower estimate of the STH efficiency of 3.1%. If now organic junctions are to be used in the context of direct photoelectrochemical water splitting, different conditions should be met: (i) the organic layer in contact with a liquid electrolyte must maintain the capacity of light absorption and generating charges as well as the internal charge separation and transport to the active surface; (ii) an appropriate photovoltage must be reached to allow charge transfer between the organic layer and an acceptor located in the electrolyte or at the surface of the photoelectrode and (iii) the electrochemical reaction at the organic semiconductor/liquid electrolyte interface must be facilitated by an appropriate catalyst. Early reports described photocathodes made of conducting polymers, such as polyacetylene, (CH)$_x$ [125], poly(p-phenylene) [126], polypyrrole [127], polyaniline [128], poly(3-methylthiophene) [129] or poly(3-hexylthiophene), P3HT [130,131]. However, these photoelectrodes did not contain any junction between OSCs nor HER catalysts. Hence only low photocurrents (few to tens of μA cm^{-2}) were obtained in aqueous electrolytes, depending on the solution pH, irradiation intensity, excitation wavelength and film thickness. Another step in the photoactive cathode design was to blend the p-type P3HT conjugated polymer as the light-harvesting unit and a fullerene derivative as electron acceptor in a BHJ structure in order to promote electron transfer. Substituted polythiophenes exhibit interesting properties as semiconducting photoactive materials. In particular, P3HT combines commercial availability, sufficient solubility, low band gap and a high degree of intermolecular order leading to high-charge carrier mobility [132]. A BHJ of n-type fullerene derivative, phenyl-C$_{61}$-butyric-acid methyl ester (PCBM) and p-type P3HT conjugated polymer was prepared and used as photocathode in aqueous saline solution [133]. Again, in the absence of any catalyst, very low photocurrents are observed and the faradaic yield for H$_2$ evolution was determined to be 0.3% [133].

Implementation of HER catalysts was found to be key to reach higher efficiencies. With Pt nanoparticles loaded onto the top of an organic p/n bilayer film of small molecules (metal-free phtalocyanine, H$_2$Pc/fullerene, C$_{60}$), photocurrent values reached several cents of μA cm^{-2} and the faradaic efficiency for hydrogen production in aqueous media approached unity [134]. H$_2$ production at Pt-coated C$_{60}$/water interface uses electrons from the conduction band of the C$_{60}$ layer. The formation of the two-electron reduced C$_{60}^{2-}$ species was evidenced spectroscopically [134].

More recently, our group collaborated with Jousselme, Geffroy and coworkers in Saclay to develop a series of photocathodes based on the same P3HT/PCBM BHJ but using amorphous molybdenum sulfide (MoS$_3$) as an earth-abundant HER catalyst instead of Pt [135]. Photocathodes prepared by the direct spray deposition of MoS$_3$ on the organic BHJ active layer (Fig. 14) deliver a photocurrent of 200 μA cm^{-2} at 0 V vs RHE and up to 300 μA cm^{-2} at -0.4 V vs RHE with a 0.6 V anodic shift of the H$_2$ evolution reaction onset potential, a value close to the open-circuit potential of the P3HT:PCBM solar cell. Catalysis in this design was promoted by the addition of TiO$_2$ nanoparticles in the MoS$_3$ film, which optimizes both electron extraction at the PCBM interface and electron transport within the catalytic layer [135]. Similar effects were observed by other authors with a compact TiO$_x$ layer separating the P3HT:PCBM BHJ layer and the catalytic film [136]. Different interfacial layers were investigated
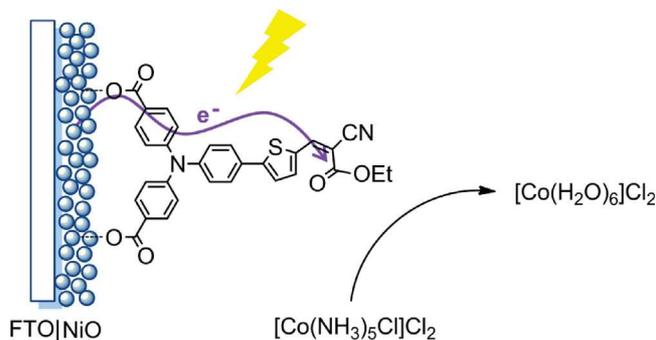
Fig. 15. Structure of the NiO-based photocathode sensitized with a push–pull organic dye designed in our group.

to improve the charge transfer between P3HT:PCBM and MoS$_3$. Metallic Al/Ti interfacial layers led to an increase of the photocurrent by up to 8 mA cm^{-2} at 0 V *vs* RHE. A 50-nm-thick C$_{60}$ layer also works as an interfacial layer, with a current density reaching 1 mA cm^{-2} at 0 V *vs* RHE [137]. A P3HT:PCBM BHJ photocathode was also recently reported to produce hydrogen from HCl-containing acetonitrile in the presence of the cobaloxime [Co(dmgH)$_2$pyCl] (**15**, dmgH$_2$ = dimethylglyoxime, Fig. 15) used as a homogeneous catalyst. A maximum photocurrent value of 1.15 mA cm^{-2} at −0.97 V *vs* Fc$^+$/Fc was obtained with almost quantitative faradaic yield [138]. A common issue is the long term stability of the light-driven activity under operation. Use of an insoluble cross-linked PEDOT:PSS hole selective underlayer between the transparent conducting oxide substrate and the P3HT:PCBM BHJ layer proved to be quite efficient to avoid delamination of the organic layer and to allow sustained PEC activity for more than 3 h with faradaic efficiency of 100% in pH 2 aqueous media [136].

6. Dye-sensitized molecular H$_2$-evolving photocathodes

The development of dye-sensitized photocathodes for hydrogen evolution is a relatively recent research area taking most of its inspiration from the *p*-type dye-sensitized solar cells (p-DSSCs) [139]. Indeed, both systems strongly rely on similar requirements: (i) a *p*-type semiconductor fulfilling precise specifications (transparency in the visible-light domain, high electronic conductivity, low-cost material and suitability of the valence band potential for electron transfer to a molecular photosensitizer), (ii) the robust grafting of a photosensitizing unit onto the surface of the semiconductor and (iii) the choice of an efficient electron acceptor in order to avoid the detrimental recombination of the photoreduced dye with the holes generated in the semiconductor. However, two main differences also arise for the construction of dye-sensitized photocathodes for hydrogen evolution: firstly, the final electron acceptor is the HER catalyst instead of a soluble electron mediator (electrolyte); as a consequence, the efficiency of the process does not rely anymore on a single electron transfer but on multielectronic catalysis, thus introducing kinetic limitations. Secondly, the system should operate in aqueous electrolytes, which introduces new constrains both regarding stability and electronics because of the pH dependence of the surface state of the semiconductor. Such additional complexity makes the development of efficient dye-sensitized H$_2$-evolving photocathodes highly challenging.

Hence many model studies are limited to the characterization of dye-sensitized electrodes assessed in aqueous solutions but in the presence of homogeneous electron acceptors. Transparent conducting oxides (TCO) with high surface area are typically used. Our group, in collaboration with Laberty-Robert and Sanchez, described the sensitization of new nanostructured mesoporous tin-doped indium oxide (ITO) films prepared by a polymer-templated

sol–gel technique with a ruthenium-based redox-active dye [140]. Thanks to a large surface area and good electrical conductivity, cathodic photocurrents as high as 50 μA cm^{-2} were recorded in the presence of [Co(NH$_3$)$_5$Cl]Cl$_2$ used as an irreversible electron acceptor at an applied potential of 0 V *vs* Ag/AgCl (phosphate buffer 0.1 M, pH 7). A 150-fold lower photocurrent was measured under the same conditions on planar ITO, demonstrating the critical role of the nanostructured pattern on the performances of the electrode material. Further improvements were recently demonstrated on similar nanostructured ITO surfaces thanks to smart optimization of the photosensitizer, now based on a triarylamine-cyclometalated ruthenium dyad. Thanks to energy level alignment between the excited states orbitals of the chromophore and the conduction band of ITO, dramatic photocurrents enhancements were observed [141]. Current density as high as 6 mA cm^{-2} could be reached in the presence of the LiI/I$_2$ electrolyte in acetonitrile. Whether such high current may be reachable in aqueous electrolytes remains to be proven since band bending may occur at a different extent in acetonitrile relative to water.

However, ITO is a degenerate *n*-type semiconductor, thus presenting a quasi-metallic character. To gain a better control on the directionality of the electron transfer from the electrode to the photosensitizer, the ideal candidate is a *p*-type semiconductor, specifically suitable for hole injection from the ground state of the excited photosensitizer. In this context, nickel oxide (NiO), successfully used for the construction of *p*-type and tandem DSSCs, is a promising electrode substrate for H$_2$-evolving photocathode applications. In collaboration with the groups of Schacher and Dietzek (Jena, Germany), we recently described how the grafting of a push–pull organic dye onto polymer-templated *p*-type NiO could generate stable cathodic photocurrents (up to 180 μA cm^{-2}) in the presence of [Co(NH$_3$)$_5$Cl]Cl$_2$ used as an irreversible electron acceptor with an applied potential of 0 V *vs* Ag/AgCl (Fig. 15) [142]. These results were obtained in aqueous acetate buffer (0.1 M, pH 4.5) conditions where cobalt-based catalysts are stable and active for H$_2$ evolution [87,88,143].

A step further consists in the replacement of the sacrificial electron acceptor by well-known HER catalysts. In this context, Odobel, Collomb and coworkers have measured the photocurrent generated by a [Ru(bipy)$_3$]-sensitized NiO photoelectrode in the presence of different cobalt- and rhodium-based complexes in acetonitrile [144]. Photoaccumulation of a square planar Rh(I) complex, irreversibly formed from octahedral [Rh(bipy)$_2$Cl$_2$]$^+$ was established and the corresponding Rh(III)-hydride could be formed in the presence of formic acid. However, no photoelectrocatalytic H$_2$ evolution has been evidenced for this system, as the Rh(II)-hydride derivative, key intermediate in the H$_2$-evolving catalytic cycle, could not be generated under these light-driven conditions.

The group of Sun designed a first proof-of-concept for a fully molecular H$_2$-evolving photocathode [145]. The construction relies on the covalent anchoring of a push–pull organic chromophore onto a nanostructured NiO electrode followed by physisorption of the H$_2$-evolving cobaloxime catalyst **16** (Fig. 12) using a simple drop-casting method. Upon irradiation the resulting photocathode was able to generate modest photocurrents (5–15 μA cm^{-2}) associated with H$_2$ evolution, that vanished within minutes due to the leaching of the catalyst out of the surface. Even though both the photocurrent value and the stability are low, this was the first demonstration that hydrogen production from sunlight and water could be achieved in a noble metal-free PEC device.

It rapidly appeared that stable photosensitizer-catalyst assemblies onto the electrode surface are required to warrant a sustained activity and also for a better control of the electron transfer cascade from the NiO to the catalyst. A wide variety of molecular strategies have already been evaluated to assemble a photosensitizer and a water oxidation catalyst for the construction of
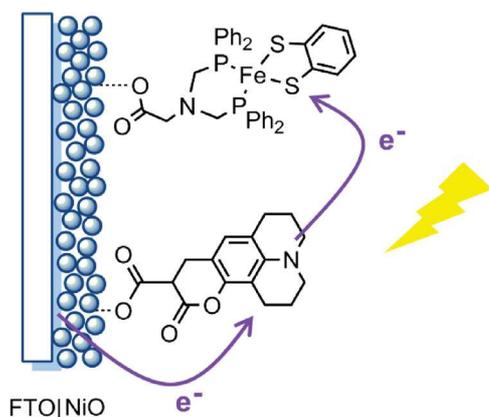
Fig. 16. Structure of the fully molecular photocathode designed by Ott and coworkers [155].

Fig. 17. Structure of the molecular H_2-evolving photocathode designed by Wu and coworkers.

dye-sensitized photoanodes. These approaches, mostly developed by the group of Meyer, take advantage of the covalent grafting of phosphonic acid groups onto transparent conductive oxide surfaces and rely either on covalent photocatalyst assemblies [52,146], self-assembled bilayers of photosensitizer and catalyst [147,148], co-immobilization of photosensitizer and catalysts on a peptide chain [149,150] and also electropolymerization of catalysts and photosensitizer films [51,151]. Co-grafting of ruthenium dyes with water-oxidizing catalysts on TiO_2 has also resulted in efficient molecular-based O_2-evolving photoanodes with photocurrents in the $100\,\mu A\,cm^{-2}$ to few $mA\,cm^{-2}$ range [48,52,148,152–154]. By contrast, molecular design for the construction of dye-sensitized H_2-evolving photocathodes is still at its early stage and only a couple of examples have been reported so far.

The relevance of the co-grafting strategy for the construction of H_2-evolving dye-sensitized photocathodes has been first established by Hammarström and Ott. Co-sensitization of a nanostructured NiO film by a mononuclear iron-dithiolate H_2-evolving catalyst and a Coumarin-343 organic dye (Fig. 16) allowed them to spectroscopically characterize electron transfer from light-driven reduced dye to the catalyst [155]. Although the photoelectrode has not been assessed for hydrogen production under photoelectrochemical conditions, the co-grafting strategy presents the advantage of the assessment of various photosensitizer/catalyst combinations without requiring difficult synthesis of photosensitizer-catalyst assemblies. In this perspective, alternative catalysts ready to be grafted on transparent conductive oxide substrates have been described in the recent years [156–158].

A more elaborated strategy relies on the grafting of supramolecular or covalent photocatalyst assemblies [14] onto the TCO surface. Although this approach is more costly from the synthetic point of view, it fully benefits from molecular photocatalyst studies under homogeneous conditions, which have been at the core of the field of light-driven hydrogen production for many years. Rau recently described the synthesis of a Ru-Pt heterobimetallic complex bearing four phosphonic acids, together with its grafting onto NiO electrode [159]. However, although spectroscopic characterization is reported, photoelectrochemical properties of the resulting photoelectrode have not been evaluated yet.

More conveniently, Wu and coworkers described the stepwise surface assembly of a supramolecular Ru-Co photocatalyst (Fig. 17) by binding of the classical cobaloxime catalyst **16** (Fig. 12) on a pyridine-substituted cyclometalated ruthenium dye anchored onto NiO [160]. This design is directly inspired by early work from our group on supramolecular photocatalysts [161,162]. This approach does not require the preliminary demanding synthesis of covalently linked photocatalyst. The resultant photoelectrode exhibits stable
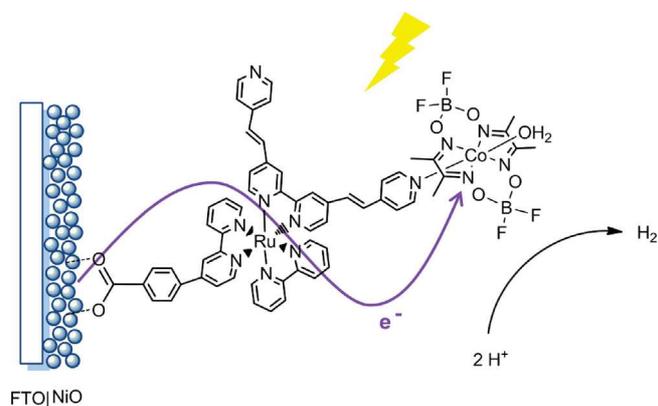
photocurrents of $10\,\mu A\,cm^{-2}$ in aqueous phosphate buffer (0.1 M, pH 7) at an applied potential of 0.1 V *vs* NHE, associated to hydrogen production (measured by gas chromatography). A preliminary Al_2O_3 coating of the NiO surface using atomic layer deposition (ALD) proved to be crucial to enhance the activity. This insulating layer is proposed to slow down electron–hole recombination between photosensitizer and NiO surface.

As an alternative to the covalent anchoring of phosphonate or carboxylate-functionalized ruthenium photosensitizers onto TCO, Moutet, Deronzier and coworkers have recently described the construction of a composite photocathode by electropolymerisation of a pyrrole-functionalized $[Ru(bipy)_3]^{2+}$ precursor, followed by electrosynthesis of nanoparticles of MoS_x, a highly efficient HER catalyst, within the resulting poly(tris(bipyridyl))ruthenium film [163]. These particles were electrogenerated from $[MoS_4]^{2-}$ anions incorporated as counterions in a polypyrrolic ruthenium-based film. Steady-state illumination of the resulting electrode material under acidic conditions (0.5 M H_2SO_4, −0.1 V *vs* Ag/AgCl applied potential) yielded stable photocurrents of $15\,\mu A\,cm^{-2}$, associated to H_2 production with faradaic yield close to unity.

Finally, the overall Z-scheme of photosynthesis could be reproduced by combining such dye-sensitized H_2-evolving photocathode with O_2-evolving photoanode in a dye-sensitized PEC cell (Fig. 1c). Such overall light-driven water splitting has been achieved by two different teams in the last years. First, Mozer and coworkers described the use of a NiO-based photocathode, sensitized by an organic push–pull dye. The reduction potential of the reduced dye generated upon steady-state illumination is proposed to be low enough to allow direct proton reduction, in the absence of any catalyst. When used in combination with a solid-state $BiVO_4$-based photoanode in a two-electrode tandem cell, such a system gave rise to a stable photocurrent of $2.7\,\mu A\,cm^{-2}$ in aqueous solution (Na_2SO_4, pH 7) without any external bias [164]. Hydrogen production was confirmed by gas chromatography measurements, allowing the determination of a faradic yield of ~80–90%. The low activity probably originates from the absence of any H_2-evolving catalyst in the design. Moreover, the authors were unable to measure O_2 production at the anodic compartment.

More recently, the group of Sun described a fully molecular PEC cell (Fig. 18, top) [153]. Co-adsorption of a ruthenium-based light-harvesting unit with a cobaloxime catalyst derived from **15** (Fig. 12) onto NiO allowed the preparation of the molecular photocathode. The anodic counterpart of the system was based on a dye-sensitized TiO_2 photoelectrode on which a ruthenium catalyst was co-grafted, adapted from previous studies reported by the same group [148,152–154]. The PEC device obtained by the association of these two photoelectrodes was able to generate a photocurrent of $25\,\mu A\,cm^{-2}$ under visible-light illumination
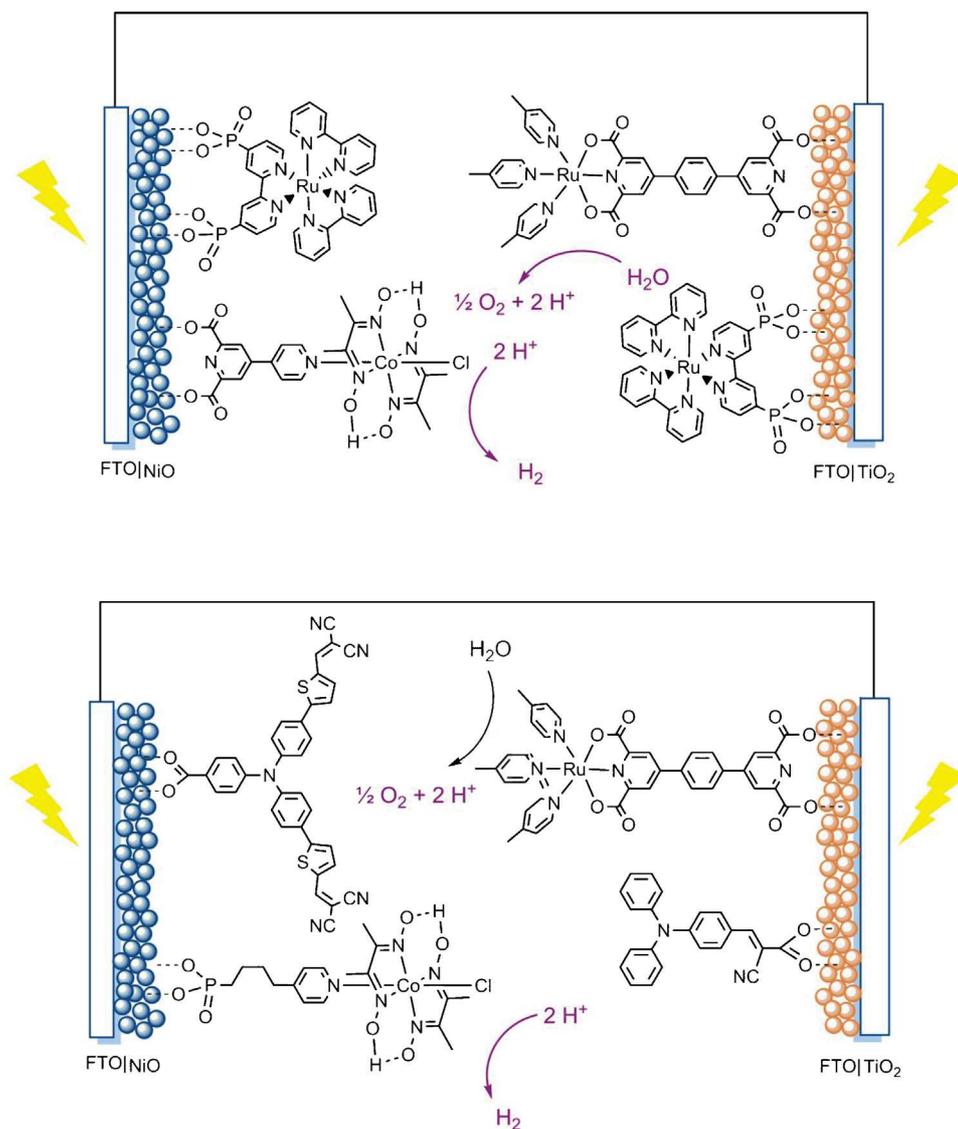
Fig. 18. Structure of the fully molecular PEC cells designed in the group of Sun [155,165].

(300 mW cm^{-2}). However, it showed to be relatively unstable over time, only 70% of the photocurrent remaining after 200 s of irradiation. The same group recently reported an improved fully molecular tandem cell, relying on the co-grafting of organic dyes with the same Ru-based water oxidation catalyst at the photoanode and a slightly modified cobaloxime catalyst at the cathode (Fig. 18, bottom) [165]. Water splitting activity has been established under neutral aqueous conditions, with a photocurrent density of 70 µA cm^{-2} that slowly decays (40% loss within 10 min) and a faradic yield of 55% measured over 100 min of operation. The STH yield of this device was estimated to be 0.05%.

7. Conclusion

As exemplified in this review, significant progresses have been made in the last decade regarding the immobilization of molecular catalysts for H$_2$ evolution onto surfaces. This encompasses the production of dark cathodes, for which highly conductive and cheap nanocarbon materials are the best choice as electrode materials, and first attempts toward the construction of molecular photocathodes. The target here is both to increase the onset potential for light-driven H$_2$ evolution and to reach high photocurrent

density values, with 20 mA cm^{-2} corresponding to a proper use of each photon provided by the sun [21]. To date the use of bulk semiconductors, both solid-state inorganic and organic materials provide the highest photocurrent values but suffer from low stability when in contact with aqueous electrolytes. Alternatively all molecular assemblies exploiting part of the DSSC technology seems promising, but this approach is hampered by the lack of a transparent p-type semi-conducting photocathode material which could equal the properties of TiO$_2$ as a photoanode substrate.

Acknowledgements

References

[1] P.C.K. Vesborg, T.F. Jaramillo, RSC Adv. 2 (2012) 7933.
[2] N.S. Lewis, D.G. Nocera, Proc. Natl. Acad. Sci. U. S. A. 104 (2007) 20142.

[3] N. Armaroli, V. Balzani, ChemSusChem 4 (2011) 21.
[4] T. Faunce, S. Styring, M.R. Wasielewski, G.W. Brudvig, A.W. Rutherford, J. Messinger, A.F. Lee, C.L. Hill, H. deGroot, M. Fontecave, D.R. MacFarlane, B. Hankamer, D.G. Nocera, D.M. Tiede, H. Dau, W. Hillier, L. Wang, R. Amal, Energy Environ. Sci. 6 (2013) 1074.
[5] T.A. Faunce, W. Lubitz, A.W. Rutherford, D. MacFarlane, G.F. Moore, P. Yang, D.G. Nocera, T.A. Moore, D.H. Gregory, S. Fukuzumi, K.B. Yoon, F.A. Armstrong, M.R. Wasielewski, S. Styring, Energy Environ. Sci. 6 (2013) 695.
[6] A. Thapper, S. Styring, G. Saracco, A.W. Rutherford, B. Robert, A. Magnuson, W. Lubitz, A. Llobet, P. Kurz, A. Holzwarth, S. Fiechter, H. de Groot, S. Campagna, A. Braun, H. Bercegol, V. Artero, Green 3 (2013) 43.
[7] R. Sathre, C.D. Scown, W.R. Morrow, J.C. Stevens, I.D. Sharp, J.W. Ager, K. Walczak, F.A. Houle, J.B. Greenblatt, Energy Environ. Sci. 7 (2014) 3264.
[8] B.A. Pinaud, J.D. Benck, L.C. Seitz, A.J. Forman, Z. Chen, T.G. Deutsch, B.D. James, K.N. Baum, G.N. Baum, S. Ardo, H. Wang, E. Miller, T.F. Jaramillo, Energy Environ. Sci. 6 (2013) 1983.
[9] R.B. Gordon, M. Bertram, T.E. Graedel, Proc. Natl. Acad. Sci. U. S. A. 103 (2006) 1209.
[10] T.E. Graedel, E.M. Harper, N.T. Nassar, B.K. Reck, Proc. Natl. Acad. Sci. U. S. A. 112 (2013) 6295–6300.
[11] P.W. Du, R. Eisenberg, Energy Environ. Sci. 5 (2012) 6012.
[12] V.S. Thoi, Y.J. Sun, J.R. Long, C.J. Chang, Chem. Soc. Rev. 42 (2013) 2388.
[13] J.R. McKone, S.C. Marinescu, B.S. Brunschwig, J.R. Winkler, H.B. Gray, Chem. Sci. 5 (2014) 865.
[14] E.S. Andreiadis, M. Chavarot-Kerlidou, M. Fontecave, V. Artero, Photochem. Photobiol. 87 (2011) 946.
[15] P.D. Tran, V. Artero, M. Fontecave, Energy Environ. Sci. 3 (2010) 727.
[16] A. Bachmeier, F. Armstrong, Curr. Opin. Chem. Biol. 25 (2015) 141.
[17] T.W. Woolerton, S. Sheard, Y.S. Chaudhary, F.A. Armstrong, Energy Environ. Sci. 5 (2012) 7470.
[18] B. Seger, I.E. Castelli, P.C.K. Vesborg, K.W. Jacobsen, O. Hansen, I. Chorkendorff, Energy Environ. Sci. 7 (2014) 2397.
[19] N. Nelson, A. Ben-Shem, Nat. Rev. Mol. Cell Biol. 5 (2004) 971.
[20] A.C. Nielander, M.R. Shaner, K.M. Papadantonakis, S.A. Francis, N.S. Lewis, Energy Environ. Sci. 8 (2015) 16.
[21] J.W. Ager III, M. Shaner, K. Walczak, I.D. Sharp, S. Ardo, Energy Environ. Sci. (2015), http://dx.doi.org/10.1039/C5EE00457H.
[22] A. Fujishima, K. Honda, Nature 238 (1972) 37.
[23] A. Fujishima, K. Kohayakawa, K. Honda, J. Electrochem. Soc. 122 (1975) 1487.
[24] C.Y. Lin, Y.H. Lai, D. Mersch, E. Reisner, Chem. Sci. 3 (2012) 3482.
[25] P. Bornoz, F.F. Abdi, S.D. Tilley, B. Dam, R. van de Krol, M. Graetzel, K. Sivula, J. Phys. Chem. C 118 (2014) 16959.
[26] C. Liu, J. Tang, H.M. Chen, B. Liu, P. Yang, Nano Lett. 13 (2013) 2989.
[27] J.-W. Jang, C. Du, Y. Ye, Y. Lin, X. Yao, J. Thorne, E. Liu, G. McMahon, J. Zhu, A. Javey, J. Guo, D. Wang, Nat. Commun. 6 (2015).
[28] O. Khaselev, J.A. Turner, Science 280 (1998) 425.
[29] E.L. Miller, B. Marsen, D. Paluselli, R. Rocheleau, Electrochem. Solid State Lett. 8 (2005) A247.
[30] E.L. Miller, D. Paluselli, B. Marsen, R.E. Rocheleau, Sol. Energy Mater. Sol. Cells 88 (2005) 131.
[31] E.L. Miller, R.E. Rocheleau, S. Khan, Int. J. Hydrogen Energy 29 (2004) 907.
[32] E.L. Miller, R.E. Rocheleau, X.M. Deng, Int. J. Hydrogen Energy 28 (2003) 615.
[33] F.F. Abdi, L.H. Han, A.H.M. Smets, M. Zeman, B. Dam, R. van de Krol, Nat. Commun. 4 (2013).
[34] J. Brillet, J.-H. Yum, M. Cornuz, T. Hisatomi, R. Solarska, J. Augustynski, M. Graetzel, K. Sivula, Nat. Photon. 6 (2012) 824.
[35] M. Gratzel, Nature 414 (2001) 338.
[36] J.H. Park, A.J. Bard, Electrochem. Solid-State Lett. 9 (2006) E5.
[37] S. Licht, B. Wang, S. Mukerji, T. Soga, M. Umeno, H. Tributsch, Int. J. Hydrogen Energy 26 (2001) 653.
[38] R.E. Rocheleau, E.L. Miller, A. Misra, Energy Fuels 12 (1998) 3.
[39] Y. Yamada, N. Matsuki, T. Ohmori, H. Mametsuka, M. Kondo, A. Matsuda, E. Suzuki, Int. J. Hydrogen Energy 28 (2003) 1167.
[40] D.G. Nocera, Acc. Chem. Res. 45 (2012) 767.
[41] S.Y. Reece, J.A. Hamel, K. Sung, T.D. Jarvi, A.J. Esswein, J.J.H. Pijpers, D.G. Nocera, Science 334 (2011) 645.
[42] M.D. Hernandez-Alonso, F. Fresno, S. Suarez, J.M. Coronado, Energy Environ. Sci. 2 (2009) 1231.
[43] S.W. Sheehan, J.M. Thomsen, U. Hintermair, R.H. Crabtree, G.W. Brudvig, C.A. Schmuttenmaer, Nat. Commun. 6 (2015).
[44] K.S. Joya, N.K. Subbaiyan, F. D'Souza, H.J.M. de Groot, Angew. Chem. Int. Ed. 51 (2012) 9601.
[45] Z. Chen, J.J. Concepcion, J.W. Jurss, T.J. Meyer, J. Am. Chem. Soc. 131 (2009) 15580.
[46] W.J. Youngblood, S.-H.A. Lee, K. Maeda, T.E. Mallouk, Acc. Chem. Res. 42 (2009) 1966.
[47] R.K. Hocking, R. Brimblecombe, L.-Y. Chang, A. Singh, M.H. Cheah, C. Glover, W.H. Casey, L. Spiccia, Nat. Chem. 3 (2011) 461.
[48] Y.X. Zhao, J.R. Swierk, J.D. Megiatto, B. Sherman, W.J. Youngblood, D.D. Qin, D.M. Lentz, A.L. Moore, T.A. Moore, D. Gust, T.E. Mallouk, Proc. Natl. Acad. Sci. U. S. A. 109 (2012) 15612.
[49] L. Li, L.L. Duan, Y.H. Xu, M. Gorlov, A. Hagfeldt, L.C. Sun, Chem. Commun. 46 (2010) 7307.
[50] Z. Yu, F. Li, L. Sun, Energy Environ. Sci. 8 (2015) 760.
[51] D.L. Ashford, B.D. Sherman, R.A. Binstead, J.L. Templeton, T.J. Meyer, Angew. Chem. Int. Ed. 54 (2015) 4778.
[52] L. Alibabaei, M.K. Brennaman, M.R. Norris, B. Kalanyan, W. Song, M.D. Losego, J.J. Concepcion, R.A. Binstead, G.N. Parsons, T.J. Meyer, Proc. Natl. Acad. Sci. U. S. A. 110 (2013) 20008.
[53] L. Alibabaei, H. Luo, R.L. House, P.G. Hoertz, R. Lopez, T.J. Meyer, J. Mater. Chem. A 1 (2013) 4133.
[54] M.S. Faber, S. Jin, Energy Environ. Sci. 7 (2014) 3519.
[55] C.G. Morales-Guio, X. Hu, Acc. Chem. Res. 47 (2014) 2671.
[56] P.D. Tran, S.Y. Chiam, P.P. Boix, Y. Ren, S.S. Pramana, J. Fize, V. Artero, J. Barber, Energy Environ. Sci. 6 (2013) 2452.
[57] P.D. Tran, M. Nguyen, S.S. Pramana, A. Bhattacharjee, S.Y. Chiam, J. Fize, M.J. Field, V. Artero, L.H. Wong, J. Loo, J. Barber, Energy Environ. Sci. 5 (2012) 8912.
[58] D.-Y. Wang, M. Gong, H.-L. Chou, C.-J. Pan, H.-A. Chen, Y. Wu, M.-C. Lin, M. Guan, J. Yang, C.-W. Chen, Y.-L. Wang, B.-J. Hwang, C.-C. Chen, H. Dai, J. Am. Chem. Soc. 137 (2015) 1587.
[59] E.J. Popczun, J.R. McKone, C.G. Read, A.J. Biacchi, A.M. Wiltrout, N.S. Lewis, R.E. Schaak, J. Am. Chem. Soc. 135 (2013) 9267.
[60] A.B. Laursen, K.R. Patraju, M.J. Whitaker, M. Retuerto, T. Sarkar, N. Yao, K.V. Ramanujachary, M. Greenblatt, G.C. Dismukes, Energy Environ. Sci. 8 (2015) 1027.
[61] P. Jiang, Q. Liu, C. Ge, W. Cui, Z. Pu, A.M. Asiri, X. Sun, J. Mater. Chem. A 2 (2014) 14634.
[62] W.-F. Chen, J.M. Schneider, K. Sasaki, C.-H. Wang, J. Schneider, S. Iyer, S. Iyer, Y. Zhu, J.T. Muckerman, E. Fujita, ChemSusChem 7 (2014) 2414.
[63] W.F. Chen, J.T. Muckerman, E. Fujita, Chem. Commun. 49 (2013) 8896.
[64] H. Vrubel, X.L. Hu, Angew. Chem. Int. Ed. 51 (2012) 12703.
[65] R.M. Kellett, T.G. Spiro, Inorg. Chem. 24 (1985) 2378.
[66] T. Abe, F. Taguchi, H. Imaya, F. Zhao, J. Zhang, M. Kaneko, Polym. Adv. Technol. 9 (1998) 559.
[67] F. Zhao, J. Zhang, T. Abe, D. Wohrle, M. Kaneko, J. Mol. Catal. A 145 (1999) 245.
[68] S. Cosnier, A. Deronzier, N. Vlachopoulos, J. Chem. Soc. Chem. Commun. (1989) 1259.
[69] J.D. Blakemore, A. Gupta, J.J. Warren, B.S. Brunschwig, H.B. Gray, J. Am. Chem. Soc. 135 (2013) 18288.
[70] S.K. Ibrahim, X.M. Liu, C. Tard, C.J. Pickett, Chem. Commun. (2007) 1535.
[71] W. Lubitz, H. Ogata, O. Rüdiger, E. Reijerse, Chem. Rev. 114 (2014) 4081.
[72] P. Chenevier, L. Mugherli, S. Darbe, L. Darchy, S. DiManno, P.D. Tran, F. Valentino, M. Iannello, A. Volbeda, C. Cavazza, V. Artero, C.R. Chim. 16 (2013) 491.
[73] D.H. Pool, D.L. DuBois, J. Organomet. Chem. 694 (2009) 2858.
[74] J. Pinson, F. Podvorica, Chem. Soc. Rev. 34 (2005) 429.
[75] C.M. Thomas, O. Rudiger, T. Liu, C.E. Carson, M.B. Hall, M.Y. Darensbourg, Organometallics 26 (2007) 3976.
[76] V. Vijaikanth, J.F. Capon, F. Gloaguen, P. Schollhammer, J. Talarmin, Electrochem. Commun. 7 (2005) 427.
[77] A. Le Goff, V. Artero, R. Metayé, F. Moggia, B. Jousselme, M. Razavet, P.D. Tran, S. Palacin, M. Fontecave, Int. J. Hydrogen Energy 35 (2010) 10719.
[78] A. Le Goff, V. Artero, B. Jousselme, P.D. Tran, N. Guillet, R. Metaye, A. Fihri, S. Palacin, M. Fontecave, Science 326 (2009) 1384.
[79] V. Artero, J.-M. Saveant, Energy Environ. Sci. 7 (2014) 3808.
[80] D.L. DuBois, Inorg. Chem. 53 (2014) 3935.
[81] A.K. Das, M.H. Engelhard, R.M. Bullock, J.A.S. Roberts, Inorg. Chem. 53 (2014) 6875.
[82] S.E. Smith, J.Y. Yang, D.L. DuBois, R.M. Bullock, Angew. Chem. Int. Ed. 51 (2012) 3152.
[83] A. Dutta, D.L. DuBois, J.A.S. Roberts, W.J. Shaw, Proc. Natl. Acad. Sci. U. S. A. 111 (2014) 16286.
[84] A. Dutta, S. Lense, J. Hou, M.H. Engelhard, J.A.S. Roberts, W.J. Shaw, J. Am. Chem. Soc. 135 (2013) 18490.
[85] P.-A. Jacques, V. Artero, J. Pécaut, M. Fontecave, Proc. Natl. Acad. Sci. U. S. A. 106 (2009) 20627.
[86] A. Bhattacharjee, E.S. Andreiadis, M. Chavarot-Kerlidou, M. Fontecave, M.J. Field, V. Artero, Chem. Eur. J. 19 (2013) 15166.
[87] N. Kaeffer, M. Chavarot-Kerlidou, V. Artero, Acc. Chem. Res. 48 (2015) 1286–1295.
[88] E.S. Andreiadis, P.-A. Jacques, P.D. Tran, A. Leyris, M. Chavarot-Kerlidou, B. Jousselme, M. Matheron, J. Pécaut, S. Palacin, M. Fontecave, V. Artero, Nat. Chem. 5 (2013) 48.
[89] N. Kaeffer, A. Morozan, V. Artero, J. Phys. Chem. B (2015), http://dx.doi.org/10.1021/acs.jpcb.5b03136.
[90] N. Elgrishi, S. Griveau, M.B. Chambers, F. Bedioui, M. Fontecave, Chem. Commun. 51 (2015) 2995.
[91] P.D. Tran, A. Le Goff, J. Heidkamp, B. Jousselme, N. Guillet, S. Palacin, H. Dau, M. Fontecave, V. Artero, Angew. Chem. Int. Ed. 50 (2011) 1371.
[92] S.C. Eady, S.L. Peczonczyk, S. Maldonado, N. Lehnert, Chem. Commun. 50 (2014) 8065.
[93] A.J. Clough, J.W. Yoo, M.H. Mecklenburg, S.C. Marinescu, J. Am. Chem. Soc. 137 (2015) 118.
[94] U.T. Muellerwesterhoff, A. Nazzal, J. Am. Chem. Soc. 106 (1984) 5381.
[95] A. Krawicz, J. Yang, E. Anzenberg, J. Yano, I.D. Sharp, G.F. Moore, J. Am. Chem. Soc. 135 (2013) 11861.
[96] G.F. Moore, I.D. Sharp, J. Phys. Chem. Lett. 4 (2013) 568.
[97] D. Cedeno, A. Krawicz, G.F. Moore, Interface Focus 5 (2015) 20140085.
[98] B. Kumar, M. Beyler, C.P. Kubiak, S. Ott, Chem. Eur. J. 18 (2012) 1295.
[99] T. Nann, S.K. Ibrahim, P.-M. Woi, S. Xu, J. Ziegler, C.J. Pickett, Angew. Chem. Int. Ed. 49 (2010) 1574.

[100] B. Seger, T. Pedersen, A.B. Laursen, P.C.K. Vesborg, O. Hansen, I. Chorkendorff, J. Am. Chem. Soc. 135 (2013) 1057.

[101] Y.D. Hou, B.L. Abrams, P.C.K. Vesborg, M.E. Bjorketun, K. Herbst, L. Bech, A.M. Setti, C.D. Damsgaard, T. Pedersen, O. Hansen, J. Rossmeisl, S. Dahl, J.K. Norskov, I. Chorkendorff, Nat. Mater. 10 (2011) 434.

[102] J. Seo, H.J. Kim, R.T. Pekarek, M.J. Rose, J. Am. Chem. Soc. 137 (2015) 3173.

[103] C.G. Morales-Guio, L. Liardet, M.T. Mayer, S.D. Tilley, M. Gratzel, X. Hu, Angew. Chem. Int. Ed. 54 (2015) 664.

[104] C.G. Morales-Guio, S.D. Tilley, H. Vrubel, M. Gratzel, X.L. Hu, Nat. Commun. 5 (2014) 3059.

[105] A. Paracchino, V. Laporte, K. Sivula, M. Gratzel, E. Thimsen, Nat. Mater. 10 (2011) 456.

[106] D. Barreca, P. Fornasiero, A. Gasparotto, V. Gombac, C. Maccato, T. Montini, E. Tondello, ChemSusChem 2 (2009) 230.

[107] P.D. Tran, S.S. Pramana, V.S. Kale, M. Nguyen, S.Y. Chiam, S.K. Batabyal, L.H. Wong, J. Barber, J. Loo, J. Chem. Eur. J. 18 (2012) 13994.

[108] C. Yang, P.D. Tran, P.P. Boix, P.S. Bassi, N. Yantara, L.H. Wong, J. Barber, Nanoscale 6 (2014) 6506.

[109] Y.J. Sun, C. Liu, D.C. Grauer, J.K. Yano, J.R. Long, P.D. Yang, C.J. Chang, J. Am. Chem. Soc. 135 (2013) 17699.

[110] J.R. McKone, A.P. Pieterick, H.B. Gray, N.S. Lewis, J. Am. Chem. Soc. 135 (2012) 223.

[111] J.R. McKone, E.L. Warren, M.J. Bierman, S.W. Boettcher, B.S. Brunschwig, N.S. Lewis, H.B. Gray, Energy Environ. Sci. 4 (2011) 3573.

[112] S.W. Boettcher, E.L. Warren, M.C. Putnam, E.A. Santori, D. Turner-Evans, M.D. Kelzenberg, M.G. Walter, J.R. McKone, B.S. Brunschwig, H.A. Atwater, N.S. Lewis, J. Am. Chem. Soc. 133 (2011) 1216.

[113] L. Gao, Y.C. Cui, J. Wang, A. Cavalli, A. Standing, T.T.T. Vu, M.A. Verheijen, J.E.M. Haverkort, E.P.A.M. Bakkers, P.H.L. Notten, Nano Lett. 14 (2014) 3715.

[114] Y.-H. Lai, H.S. Park, J.Z. Zhang, P.D. Matthews, D.S. Wright, E. Reisner, Chem. Eur. J. 21 (2015) 3919.

[115] B. Seger, A.B. Laursen, P.C.K. Vesborg, T. Pedersen, O. Hansen, S. Dahl, I. Chorkendorff, Angew. Chem. Int. Ed. 51 (2012) 9128.

[116] L.R. Webster, S.K. Ibrahim, J.A. Wright, C.J. Pickett, Chem. Eur. J. 18 (2012) 11798.

[117] J. Seo, R.T. Pekarek, M.J. Rose, Chem. Commun. (2015), http://dx.doi.org/10.1039/c5cc02802g.

[118] A. Krawicz, D. Cedeno, G.F. Moore, Phys. Chem. Chem. Phys. 16 (2014) 15818.

[119] D. Cedeno, A. Krawicz, P. Doak, M. Yu, J.B. Neaton, G.F. Moore, J. Phys. Chem. Lett. 5 (2014) 3222.

[120] B. Seger, K. Herbst, T. Pedersen, B. Abrams, P.C.K. Vesborg, O. Hansen, I. Chorkendorff, J. Electrochem. Soc. 161 (2014) H722.

[121] M.A. Green, K. Emery, Y. Hishikawa, W. Warta, E.D. Dunlop, Prog. Photovolt. Res. Appl. 23 (2015) 1.

[122] B.C. Thompson, J.M.J. Frechet, Angew. Chem. Int. Ed. 47 (2008) 58.

[123] N.S. Sariciftci, L. Smilowitz, A.J. Heeger, F. Wudl, Science 258 (1992) 1474.

[124] S. Esiner, H. van Eersel, M.M. Wienk, R.A.J. Janssen, Adv. Mater. 25 (2013) 2932.

[125] S.N. Chen, A.J. Heeger, Z. Kiss, A.G. MacDiarmid, S.C. Gau, D.L. Peebles, Appl. Phys. Lett. 36 (1980) 96.

[126] S. Yanagida, A. Kabumoto, K. Mizumoto, C. Pac, K. Yoshino, J. Chem. Soc. Chem. Commun. (1985) 474.

[127] M. Kaneko, K. Okuzumi, A. Yamada, J. Electroanal. Chem. 183 (1985) 407.

[128] E.M. Genies, M. Lapkowski, Synth. Met. 24 (1988) 69.

[129] S. Glenis, G. Tourillon, F. Garnier, Thin Solid Films 122 (1984) 9.

[130] O.A. El-Rashiedy, S. Holdcroft, J. Phys. Chem. 100 (1996) 5481.

[131] G. Suppes, E. Ballard, S. Holdcroft, Polym. Chem. 4 (2013) 5345.

[132] C. Li, M. Liu, N.G. Pschirer, M. Baumgarten, K. Müllen, Chem. Rev. 110 (2010) 6817.

[133] E. Lanzarini, M.R. Antognazza, M. Biso, A. Ansaldo, L. Laudato, P. Bruno, P. Metrangolo, G. Resnati, D. Ricci, G. Lanzani, J. Phys. Chem. C 116 (2012) 10944.

[134] T. Abe, S. Tobinai, N. Taira, J. Chiba, T. Itoh, K. Nagai, J. Phys. Chem. C 115 (2011) 7701.

[135] T. Bourgeteau, D. Tondelier, B. Geffroy, R. Brisse, C. Laberty-Robert, S. Campidelli, R. de Bettignies, V. Artero, S. Palacin, B. Jousselme, Energy Environ. Sci. 6 (2013) 2706.

[136] M. Haro, C. Solis, G. Molina, L. Otero, J. Bisquert, S. Gimenez, A. Guerrero, J. Phys. Chem. C 119 (2015) 6488.

[137] T. Bourgeteau, D. Tondelier, B. Geffroy, R. Brisse, R. Cornut, V. Artero, B. Jousselme, ACS Appl. Mater. Interfaces (2015), http://dx.doi.org/10.1021/acsami.5b03532.

[138] A. Guerrero, M. Haro, S. Bellani, M.R. Antognazza, L. Meda, S. Gimenez, J. Bisquert, Energy Environ. Sci. 7 (2014) 3666.

[139] F. Odobel, Y. Pellegrin, J. Phys. Chem. Lett. 4 (2013) 2551.

[140] W. Hamd, M. Chavarot-Kerlidou, J. Fize, G. Muller, A. Leyris, M. Matheron, E. Courtin, M. Fontecave, C. Sanchez, V. Artero, C. Laberty-Robert, J. Mater. Chem. A 1 (2013) 8217.

[141] Z. Huang, M. He, M. Yu, K. Click, D. Beauchamp, Y. Wu, Angew. Chem. Int. Ed. 54 (2015) 6857.

[142] J. Massin, M. Bräutigam, N. Kaeffer, N. Queyriaux, M.J. Field, F.H. Schacher, J. Popp, M. Chavarot-Kerlidou, B. Dietzek, V. Artero, Interface Focus 5 (2015) 20140083.

[143] S. Varma, C.E. Castillo, T. Stoll, J. Fortage, A.G. Blackman, F. Molton, A. Deronzier, M.N. Collomb, Phys. Chem. Chem. Phys. 15 (2013) 17544.

[144] C.E. Castillo, M. Gennari, T. Stoll, J. Fortage, A. Deronzier, M.N. Collomb, M. Sandroni, F. Légalité, E. Blart, Y. Pellegrin, C. Delacote, M. Boujtita, F. Odobel, P. Rannou, S. Sadki, J. Phys. Chem. C 119 (2015) 5806.

[145] L. Li, L.L. Duan, F.Y. Wen, C. Li, M. Wang, A. Hagfeld, L.C. Sun, Chem. Commun. 48 (2012) 988.

[146] D.L. Ashford, W. Song, J.J. Concepcion, C.R.K. Glasson, M.K. Brennaman, M.R. Norris, Z. Fang, J.L. Templeton, T.J. Meyer, J. Am. Chem. Soc. 134 (2012) 19189.

[147] C.R.K. Glasson, W. Song, D.L. Ashford, A. Vannucci, Z. Chen, J.J. Concepcion, P.L. Holland, T.J. Meyer, Inorg. Chem. 51 (2012) 8637.

[148] X. Ding, Y. Gao, L. Zhang, Z. Yu, J. Liu, L. Sun, ACS Catal. 4 (2014) 2347.

[149] D. Ma, S.E. Bettis, K. Hanson, M. Minakova, L. Alibabaei, W. Fondrie, D.M. Ryan, G.A. Papoian, T.J. Meyer, M.L. Waters, J.M. Papanikolas, J. Am. Chem. Soc. 135 (2013) 5250.

[150] D.M. Ryan, M.K. Coggins, J.J. Concepcion, D.L. Ashford, Z. Fang, L. Alibabaei, D. Ma, T.J. Meyer, M.L. Waters, Inorg. Chem. 53 (2014) 8120.

[151] D.L. Ashford, A.M. Lapides, A.K. Vannucci, K. Hanson, D.A. Torelli, D.P. Harrison, J.L. Templeton, T.J. Meyer, J. Am. Chem. Soc. 136 (2014) 6578.

[152] Y. Gao, X. Ding, J.H. Liu, L. Wang, Z.K. Lu, L. Li, L.C. Sun, J. Am. Chem. Soc. 135 (2013) 4219.

[153] K. Fan, F. Li, L. Wang, Q. Daniel, E. Gabrielsson, L. Sun, Phys. Chem. Chem. Phys. 16 (2014) 25234.

[154] L. Zhang, Y. Gao, X. Ding, Z. Yu, L. Sun, ChemSusChem 7 (2014) 2801.

[155] J.M. Gardner, M. Beyler, M. Karnahl, S. Tschierlei, S. Ott, L. Hammarstrom, J. Am. Chem. Soc. 134 (2012) 19322.

[156] L.A. Berben, J.C. Peters, Chem. Commun. 46 (2010) 398.

[157] M.R.J. Scherer, N.M. Muresan, U. Steiner, E. Reisner, Chem. Commun. 49 (2013) 10453.

[158] N.M. Muresan, J. Willkomm, D. Mersch, Y. Vaynzof, E. Reisner, Angew. Chem. Int. Ed. 51 (2012) 12749.

[159] M. Braumuller, M. Schulz, D. Sorsche, M. Pfeffer, M. Schaub, J. Popp, B.-W. Park, A. Hagfeldt, B. Dietzek, S. Rau, Dalton Trans. 44 (2015) 5577.

[160] Z. Ji, M. He, Z. Huang, U. Ozkan, Y. Wu, J. Am. Chem. Soc. 135 (2013) 11696.

[161] A. Fihri, V. Artero, M. Razavet, C. Baffert, W. Leibl, M. Fontecave, Angew. Chem. Int. Ed. 47 (2008) 564.

[162] A. Fihri, V. Artero, A. Pereira, M. Fontecave, Dalton Trans. (2008) 5567.

[163] Y. Lattach, J. Fortage, A. Deronzier, J.-C. Moutet, ACS Appl. Mater. Interfaces 7 (2015) 4476.

[164] L. Tong, A. Iwase, A. Nattestad, U. Bach, M. Weidelener, G. Gotz, A. Mishra, P. Bauerle, R. Amal, G.G. Wallace, A.J. Mozer, Energy Environ. Sci. 5 (2012) 9472.

[165] F. Li, K. Fan, B. Xu, E. Gabrielsson, Q. Daniel, L. Li, L. Sun, J. Am. Chem. Soc. 137 (2015) 9153.

THE ROYAL SOCIETY PUBLISHING

Dye-sensitized PS-*b*-P2VP-templated nickel oxide films for photoelectrochemical applications

Julien Massin[1], Maximilian Bräutigam[2,3], Nicolas Kaeffer[1], Nicolas Queyriaux[1], Martin J. Field[4], Felix H. Schacher[5], Jürgen Popp[2,3], Murielle Chavarot-Kerlidou[1], Benjamin Dietzek[2,3] and Vincent Artero[1]

[1]Laboratoire de Chimie et Biologie des Métaux, University Grenoble Alpes, CNRS, CEA, 17 rue des martyrs, 38000 Grenoble, France
[2]Leibniz Institute of Photonic Technology (IPHT) Jena e. V., Albert-Einstein-Strasse 9, Jena 07745, Germany
[3]Institute for Physical Chemistry and Abbe Center of Photonics, Friedrich Schiller University Jena, Helmholtzweg 4, Jena 07743, Germany
[4]Institut de Biologie Structurale Jean-Pierre Ebel, University Grenoble Alpes, CNRS, CEA, 71 rue des martyrs, 38000 Grenoble, France
[5]Institute of Organic Chemistry and Macromolecular Chemistry and Jena Center for Soft Matter (JCSM), Friedrich-Schiller-University Jena, Lessingstrasse 8, Jena 07743, Germany

Moving from homogeneous water-splitting photocatalytic systems to photoelectrochemical devices requires the preparation and evaluation of novel *p*-type transparent conductive photoelectrode substrates. We report here on the sensitization of polystyrene-*block*-poly-(2-vinylpyridine) (PS-*b*-P2VP) diblock copolymer-templated NiO films with an organic push–pull dye. The potential of these new templated NiO film preparations for photoelectrochemical applications is compared with NiO material templated by F108 triblock copolymers. We conclude that NiO films are promising materials for the construction of dye-sensitized photocathodes to be inserted into photoelectrochemical (PEC) cells. However, a combined effort at the interface between materials science and molecular chemistry, ideally funded within a Global Artificial Photosynthesis Project, is still needed to improve the overall performance of the photoelectrodes and progress towards economically viable PEC devices.

1. Introduction

The production of fuels through light-driven processes is a promising solution for the durable storage of solar energy [1–3]. For example, molecular hydrogen can be produced from water splitting with O_2 being generated as a side product. Alternatively, coupling photocatalytic water oxidation with the reduction of CO_2 produces carbon-based fuels, with a net zero-carbon footprint. A number of molecular and supramolecular photocatalytic systems for H_2 evolution, CO_2 reduction or water oxidation have been reported during the last decade [4–20]. These systems however only achieve one-half of the targeted process and require the use of sacrificial components to furnish or accept the electrons required or produced by the catalytic reaction, respectively. Most attempts to couple light-driven oxidative and reductive processes in homogeneous phase have not been successful so far. A solution to this issue consists of separating these processes into two compartments of a photoelectrochemical (PEC) cell [21]. This approach has the obvious advantage of avoiding the production of potentially exploding mixtures. It, however, requires a fine regulation of photon, electron and proton management between both photocatalytic systems, which can be achieved through the grafting of the active components at the surface of transparent conductive electrode substrates [22]. Extending the *n*-type dye-sensitized solar cell (DSSC) technology, significant achievements in this direction have been reported recently regarding the
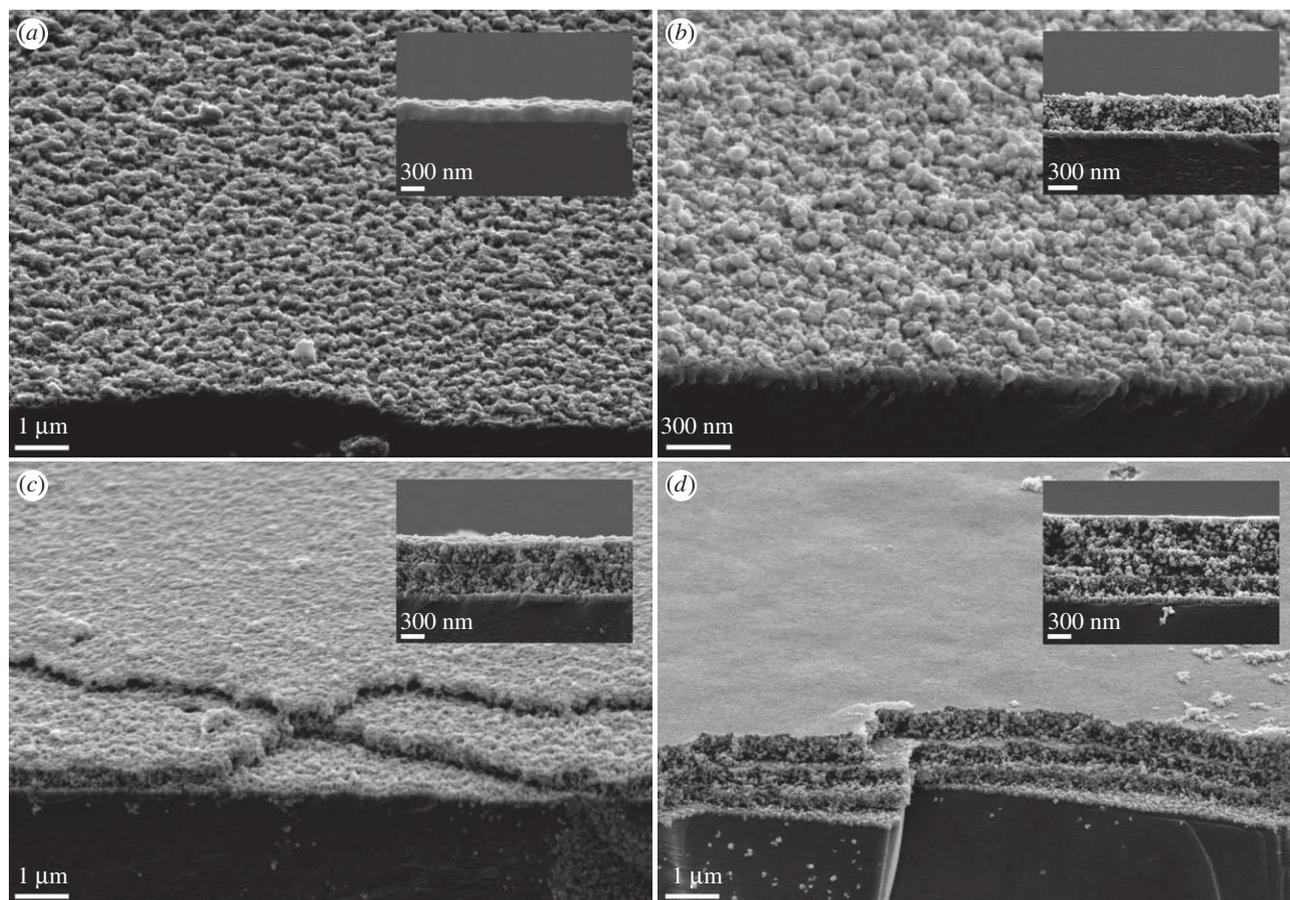
Figure 1. Scanning electron micrographs from secondary electrons (SEI) (top view and inset: cross-section) of NiO films. (*a*) A triple layer of NiO synthesized with PS-*b*-P2VP as template; (*b*–*d*) F108-templated NiO with increasing number of layers from 1 to 3.

preparation of molecular-based photoanodes for water oxidation [23–29]. Co-grafting of a water-oxidizing catalyst with a molecular dye on mesoscopic TiO$_2$ substrates yielded electrodes able to deliver up to 2 mA cm^{-2} photocurrent corresponding to O$_2$ evolution under visible irradiation [27]. Of note, such a current density corresponds to approximately 20% of the targeted performance for implementation in a PEC device with 10% solar to fuel efficiency [30]. By contrast, the preparation of molecular photocathodes with similar architectures is strongly hampered by the lack of a suitable *p*-type transparent electrode substrate [31]. Despite its inherently low electronic conductivity, nickel oxide (NiO) currently stands as the benchmark of such materials. Efforts have targeted the preparation of nanostructured NiO films to increase the active surface area of the electrode, and thus to optimize the loading in photocatalytic units [32–37]. A facile synthetic route to nanostructured NiO films with a Brunauer–Emmett–Teller (BET) area of about 50 m^2 g^{-1} has been recently described based on the use of amphiphilic polystyrene-*block*-poly-(2-vinylpyridine) (PS-*b*-P2VP) diblock copolymers as templates [38]. We report here on the sensitization of such a material with an organic push–pull dye and demonstrate the potential of templated NiO film preparation for photoelectrochemical applications.

2. Results and discussion

2.1. NiO film preparation

Porous nanostructured NiO films were deposited onto fluorine-doped tin oxide (FTO)-coated glass substrates

according to a procedure previously described for deposition on glass substrates using amphiphilic polystyrene-*block*-poly-(2-vinylpyridine) (PS$_{75}$-*b*-P2VP$_{25}$) diblock copolymers—the subscripts denote the weight fraction of the corresponding block [38]. The procedure was repeated three times to obtain three-layer films with homogeneous film thicknesses of 150–200 nm as measured by scanning electron microscopy (figure 1). These films are almost transparent in the visible region (400–800 nm; see below). In this study, we compared PS-*b*-P2VP-templated films with previously reported F108-templated films [35,39]. These films (figure 1) have thicknesses ranging from 300–400 nm for mono-layered substrates to 900–1000 nm for three-layer films.

2.2. Synthesis and characterization of a push–pull organic dye

Donor-π-acceptor (push–pull) organic dyes have shown relatively high performances in NiO-based *p*-type DSSCs because of their large molar extinction coefficients [40]. Compound **1** (figure 2 and table 1), containing a triarylamine electron-donor part and an ethyl cyanoacetate electron-acceptor part separated by a thiophene unit, has been prepared in two steps from previously described di-tert-butyl 4,4′-((4-(5-formylthiophen-2-yl)phenyl)azanediyl)dibenzoate [41]. The UV–visible absorption spectrum of **1** in CH$_3$CN solution displays a typical charge-transfer (CT) band centred at 436 nm (29 300 M^{-1} cm^{-1}). Upon excitation at 420 nm, emission of **1** is observed with maximum intensity at 572 nm. The cyclic voltammogram of **1** in CH$_3$CN displays a reversible
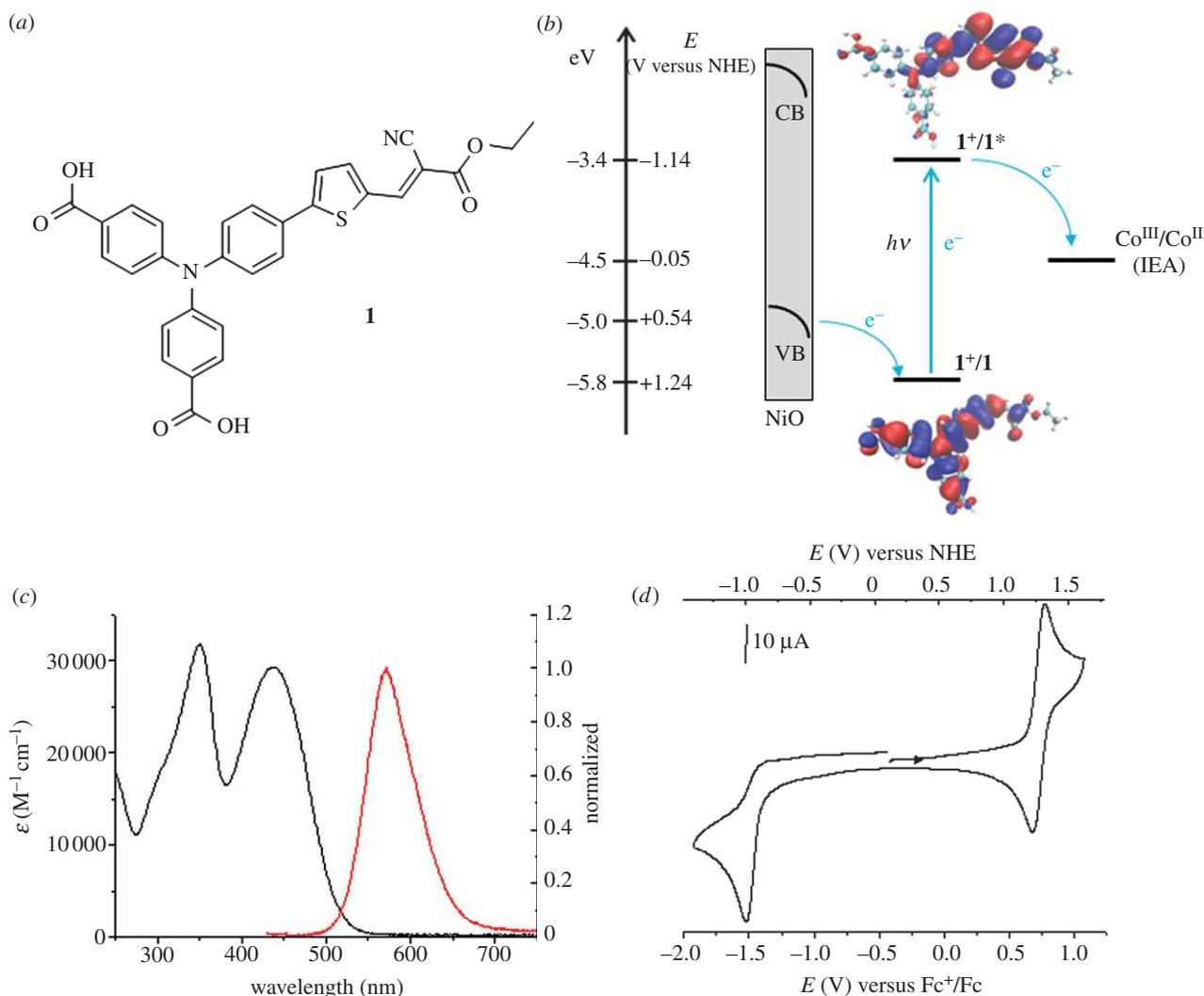
Figure 2. (*a*) Structure of **1**. (*b*) Energy-level diagram of a *p*-type NiO photocathode sensitized with **1**, in the presence of $[Co(NH_3)_5Cl]Cl_2$ as the irreversible electron acceptor (IEA) in solution. (*c*) UV–vis (black line) and normalized fluorescence (red line, excitation at 420 nm) spectra of **1** measured in CH_3CN at a concentration of 5 μM. (*d*) Cyclic voltammogram of compound **1** (1 mM) recorded at a scan rate of 100 mV s^{-1} on a glassy carbon electrode in CH_3CN containing 0.1 M *n*-Bu_4NPF_6 as supporting electrolyte. (Online version in colour.)
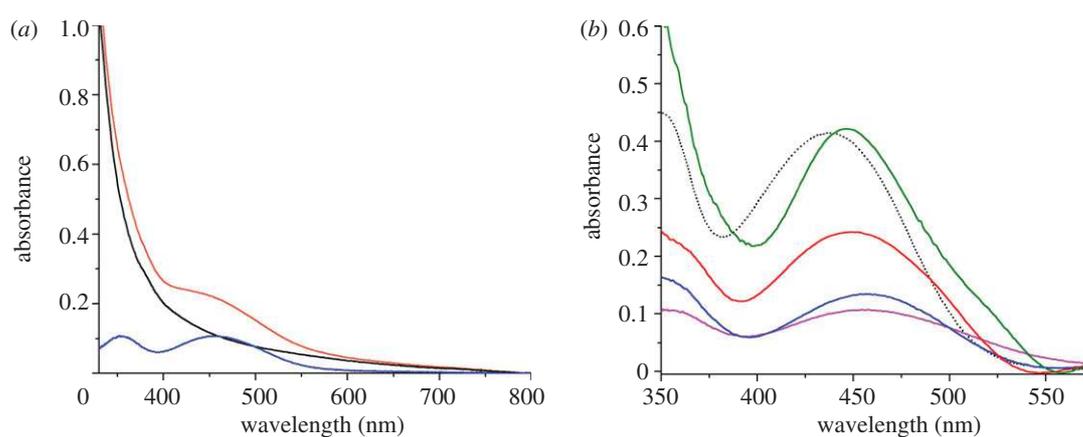
Figure 3. (*a*) Absorption spectra of a blank PS-*b*-P2VP-templated three-layer NiO electrode (black line) and of the same electrode after sensitization with **1** (orange line). The difference between these two spectra is shown as a blue line. (*b*) Comparison of corrected spectra recorded on a dye-sensitized PS-*b*-P2VP-templated three-layer NiO film (blue line), dye-sensitized F108-templated NiO films (one layer: fuchsia line; two layers: red line; three layers: green line) and CH_3CN (5 μM) solution spectrum of **1** (dotted line).

oxidation signal at +0.72 V versus Fc$^+$/Fc and an irreversible reduction wave at $E_{pc} = -1.57$ V versus Fc$^+$/Fc (figure 2). From these values, we could determine potential values of

+1.24 V versus the normal hydrogen electrode (NHE) and −1.14 V versus NHE for the **1/1**$^+$ and **1***/1$^+$ couples, respectively, **1*** representing the excited state of **1** (table 1). These

Table 1. Spectroscopic and energetic data for compound **1**.

λ_{max}(Abs)[a]	λ_{max}(Em)[a]	ε[a]	E_{0-0}[b]	E_{HOMO}		E_{LUMO}	
nm	nm	$M^{-1}\,cm^{-1}$	eV	(V versus NHE)[c]	eV[d]	(V versus NHE)[e]	eV[e]
436	572	29 300	2.39	+1.24	−5.82	−1.14	−3.43

[a]Spectra measured at 5 μM in CH_3CN.
[b]0−0 transition energy, E_{0-0}, estimated from the intercept of the normalized absorption and emission spectra in CH_3CN.
[c]Estimated HOMO energy, E_{HOMO}, obtained from the ground state oxidation potential.
[d]HOMO energy in eV obtained from the redox potential related to Fc^+/Fc with a calculated absolute energy of −0.51 eV [44].
[e]Estimated LUMO energy, E_{LUMO}, obtained from the estimated HOMO energy by adding the 0−0 transition energy, E_{0-0}.

Table 2. Surface and volume concentrations of **1** grafted on different substrates.

substrate	thickness (nm)	dye surface conc. (mol cm^{-2})	dye volume conc. (mol cm^{-3})
PS-*b*-P2VP-templated three-layer films	150−200	3×10^{-9}−5×10^{-9}	14×10^{-5}
F108-templated one-layer films	300−400	4×10^{-9}−5×10^{-9}	12×10^{-5}
F108-templated two-layer films	500−600	7×10^{-9}−9×10^{-9}	13×10^{-5}
F108-templated three-layer films	900−1000	9×10^{-9}−1.5×10^{-8}	14×10^{-5}

potentials can be approximated to the highest occupied molecular orbital (HOMO) and lowest unoccupied molecular orbital (LUMO) energy levels, respectively (figure 2*b*), calculated using quantum chemistry (density functional theory (DFT)) to be separated by 2.1 eV. This value was determined as the lowest energy from the UV–vis spectrum evaluated using a time-dependent DFT method [42]. Plots of the HOMO and LUMO are shown in figure 2*b*, whereas the calculated spectrum is shown in the electronic supplementary material. The distributions of HOMO and LUMO of **1** evidence another advantage of push–pull dyes achieving spatial charge separation in the excited state. Indeed, the donor part, where the HOMO is centred and a hole located in the excited state, was designed to support the anchor groups. It is thus connected to the electrode which optimizes hole injection. By contrast, the acceptor moiety, where the LUMO is centred and an electron is located in the excited state, is located away from the electrode surface, which both limits recombination with the *p*-type semi-conductor material and fosters electron transfer towards an electron acceptor in solution. The HOMO energy level in **1** is lower than the top of the valence band (VB) in NiO (0.54 V versus NHE at pH 7) [43] (table 1), in good agreement with hole injection from photo-excited **1** to the NiO VB (figure 2*b*). In that context, the presence of two anchoring carboxylate groups attached on the triarylamine moiety favours both strong binding of **1** to NiO and electronic coupling optimization between the HOMO in **1** and the NiO VB orbitals.

2.3. NiO film sensitization and characterization

The different NiO substrates were sensitized through soaking in a CH_3CN solution of dye **1** for 24 h. The samples were rinsed with CH_3CN and dried in air before characterization. Figure 3 displays typical absorption spectra of the dye-sensitized electrodes showing new features as compared with the spectra of pure NiO samples. Subtraction of the absorption of the blank NiO substrate (blanks were measured on the same sample before sensitization) reveals the absorption spectrum of dye **1** grafted onto the NiO surface. For all samples, a spectral broadening associated with a small red shift (*ca* 10 nm) of the absorption band is observed. These modifications could result from interactions of the dye molecules with the NiO substrate through grafting and possibly from intermolecular interactions between adjacent grafted dyes. Assuming that these interactions do not significantly modify the molar absorption coefficient ε_{max} of the dye, we estimated the surface concentration of **1** using equation (2.1). We give in table 2 the ranges of dye surface and volume concentrations obtained for the various substrates using equations (2.1) and (2.2),

$$\text{surf. conc. (mol cm}^{-2}) = \frac{\text{max} \times \text{absorbance}}{1000 \times \varepsilon_{max}\,(M^{-1}\,cm^{-1})} \quad (2.1)$$

and

$$\text{vol. conc. (mol cm}^{-3}) = \frac{\text{surf. conc.}}{\text{thickness}}. \quad (2.2)$$

As expected, the surface concentration of the F108-templated substrates varies almost linearly with the thickness of the films. The surface concentration of PS-*b*-P2VP-templated three-layer films is slightly lower than the one obtained for the mono-layer F108-templated films, in good agreement with the reduced thickness of these films. Accordingly, the calculated dye volume concentration is almost identical in all dye-sensitized films.

In order to detail the electron-density changes within the dye on the NiO surface, which are associated with photo-absorption, resonance Raman (rR) measurements have been carried out. Furthermore, rR mapping allows for visualizing the distribution of the dye on the NiO surface. The rR spectra in solution (figure 4*a*) and on NiO (figure 4*b,c*) are identical except for the fluorescence background (see below) and the Raman bands of the solvent. All of them are in good agreement with the DFT-calculated Raman spectra after application of a 0.98 scaling factor (figure 4*d*). This means that binding to the surface does not influence the nature of the initial photoexcitation in **1**. Upon changing the excitation
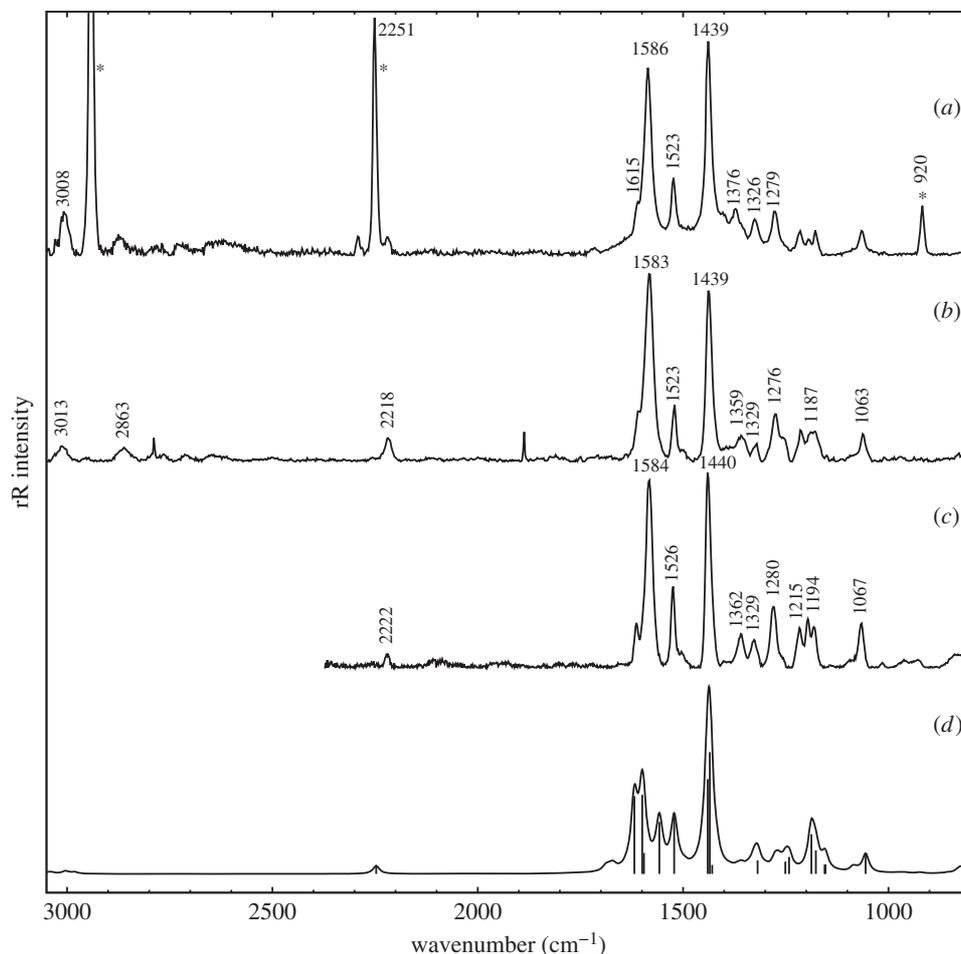
Figure 4. Resonance Raman spectra of **1** in CH_3CN at an excitation wavelength of 413 nm (*a*); **1** on PS-*b*-P2VP-templated three-layer NiO film at 413 nm (*b*) and 476 nm (*c*) excitation wavelengths; DFT-calculated Raman spectrum of **1** after application of a 0.98 scaling factor (*d*).

wavelength from 413 to 476 nm the overall pattern of the rR spectrum of **1** is preserved except for slight alterations of band intensities: bands at 1440, 1526 and the three bands at about 1200 cm^{-1} gain intensity, while the band at 1584 cm^{-1} drops in intensity. The rR map (figure 5) shows a homogeneous distribution of the dye on the surface since most pixels of the map exhibit integrals of the band at 1440 cm^{-1}, which correlates with the dye concentrations between 3500 and 4500 counts cm^{-1}. Nonetheless, some regions of higher dye concentration (up to *ca* 6500 counts cm^{-1}) on the surface are observed. These might originate from inhomogeneities in the NiO surface introduced upon the deposition of the copolymer–Ni reaction mixture during the doctor blading.

2.4. Photoelectrochemical properties of dye-sensitized NiO films

We then investigated the PEC properties of these dye-sensitized NiO films. The substrates were used as the working electrode in a three-electrode configuration purpose-designed cell. Aqueous sodium acetate buffer (pH 4.5; 0.1 M) was first chosen as the electrolyte and the current was recorded under chopped irradiation conditions (400–800 nm filtered Xe lamp light; 100 mW cm^{-2}; two suns) at various potentials applied to the working electrode in the presence of $[Co(NH_3)_5Cl]Cl_2$ as an irreversible electron acceptor (IEA in figure 2*b*) in the solution. The linear sweep voltammogram recorded under chopped light (figure 6) shows the establishment of a photocurrent with onset at

+0.61 V versus NHE, in good agreement with the potential of the VB edge of NiO (figure 2), and maximum photocurrent densities at +0.20 V versus NHE (0 V versus Ag/AgCl). We therefore used this potential for the whole series of experiments described below. In the absence of any electron acceptor in solution, small cathodic photocurrents (*ca* 10 μA cm^{-2}) were recorded. This phenomenon has been previously observed and assigned to H_2 evolution [45] although we could not detect any hydrogen in the headspace of the cell after 12 h of continuous photoelectrolysis. We thus believe that a significant part of this photocurrent is due to the reduction of residual traces of O_2 present in the electrolyte or trapped within the nickel oxide films. Nevertheless, such a behaviour is directly related to the presence of **1** at the surface of the films since non-sensitized NiO films do not show any photocurrent under the same conditions.

Photocurrent enhancement observed in the presence of IEA (figure 6) is attributed to the establishment of photo-induced electron transfers from NiO to IEA, mediated by the excited dye. Two mechanisms are possible: in the oxidative quenching process, a photo-induced electron transfer occurs from photo-excited **1** to the Co(III) acceptor in solution, the ground state of **1** being subsequently regenerated through hole transfer to the conducting band of NiO. In the alternative reductive quenching process, hole injection from the excited state of **1** to NiO occurs first, producing surface immobilized **1**$^-$, which in turns reduces the Co(III) complex and regenerates the ground state of **1**. The latter mechanism is supported by the strongly reduced fluorescent background
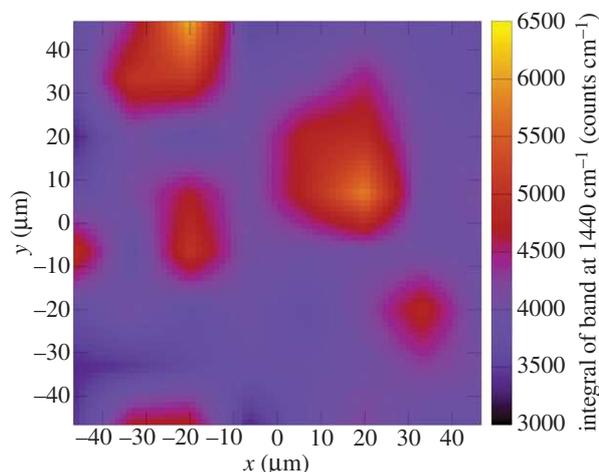
Figure 5. Resonance Raman map of **1** on a PS-*b*-P2VP-templated three-layer NiO film. (Online version in colour.)
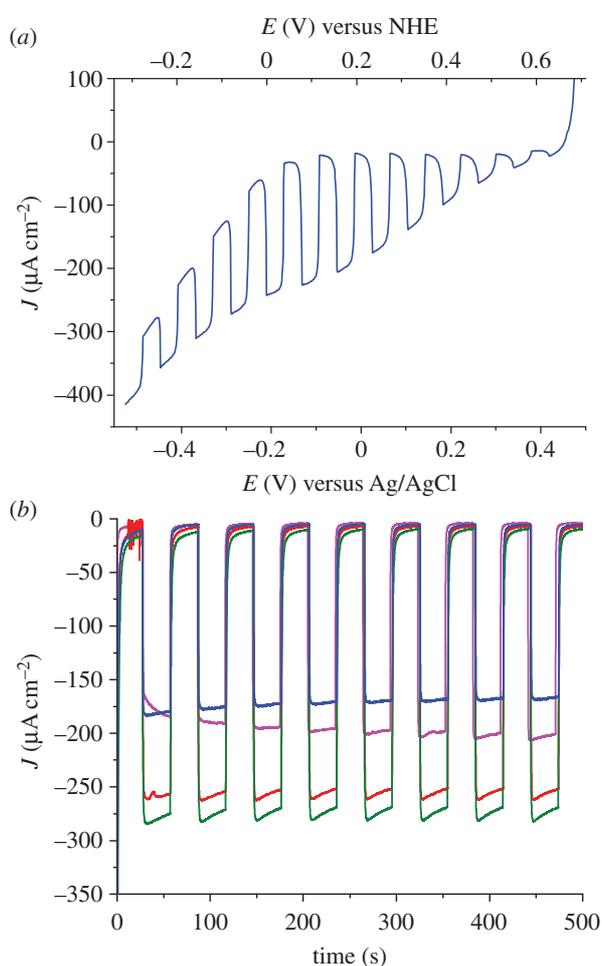

Figure 6. (*a*) Linear sweep voltammogram (10 mV s^{-1}) recorded under chopped light on a PS-*b*-P2VP-templated three-layer NiO film sensitized with **1** in [Co(NH$_3$)$_5$Cl]Cl$_2$ (10 mM)/acetate buffer (pH 4.5; 0.1 M). (*b*) Cathodic photocurrent measurements recorded on NiO electrodes sensitized with **1** in [Co(NH$_3$)$_5$Cl]Cl$_2$ (10 mM)/acetate buffer (pH 4.5; 0.1 M) with 0 V versus Ag/AgCl applied potential: PS-*b*-P2VP-templated three-layer NiO film (blue trace) and F108-templated NiO films (one layer: fuchsia trace; two layers: red trace; three layers: green trace).

observed during rR spectra of **1** when shifting from solution onto NiO (see electronic supplementary material). We have studied the variation of the photocurrent value with the concentration of the Co(III) electron acceptor in solution. Figure 7
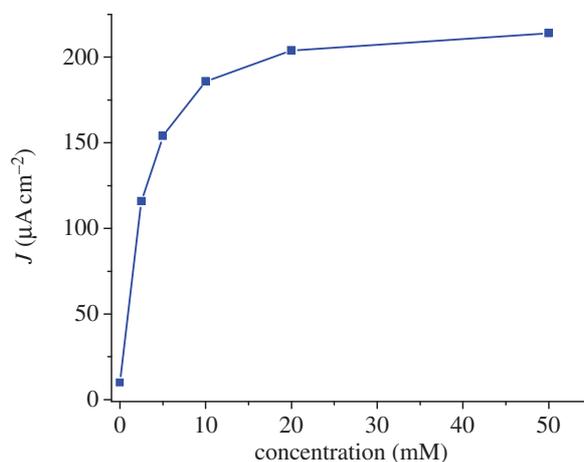

Figure 7. Variation of the stabilized photocurrent with the concentration of [Co(NH$_3$)$_5$Cl]Cl$_2$, measured on a PS-*b*-P2VP-templated three-layer film sensitized with **1**, in acetate buffer (0.1 M, pH 4.5) at an applied potential of 0 V versus Ag/AgCl. (Online version in colour.)
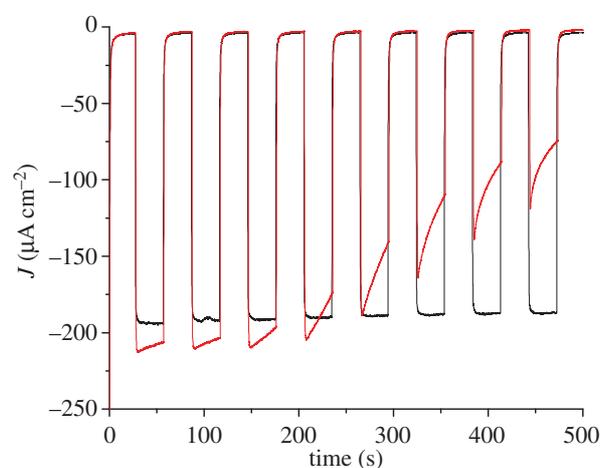
Figure 8. Cathodic photocurrent measurements recorded on PS-*b*-P2VP-templated three-layer NiO electrodes sensitized with **1** in [Co(NH$_3$)$_5$Cl]Cl$_2$ (10 mM) with 0 V versus Ag/AgCl applied potential. The measurement was first carried out in acetate buffer pH 4.5 (black trace). Then the electrolyte was changed for phosphate buffer pH 7 and a new measurement was performed (red trace).

shows that the photocurrent value does not vary much for cobalt concentrations superior to 10 mM. There are two possibilities for the rate-determining step in this experiment. First, diffusion of the Co(III) electron acceptor within the porous film can limit the reaction. Second, under the assumption that diffusion does not influence photocurrents, hole injection can be rate-determining. The probability that diffusion is dominating this process is higher as hole injection is generally reported to be very fast with time constants of hundreds of femto-seconds to a few pico-seconds for organic dyes [46–50]. Photocurrent densities as high as 270 µA cm^{-2} are obtained for F108-templated three-layer NiO films (figure 6). Interestingly, **1**-sensitized PS-*b*-P2VP-templated three-layer films display photocurrent values as high as those obtained for thicker F108-templated one-layer films. This indicates that the PS-*b*-P2VP-templated formulation proves superior to the thicker F108-templated one for such PEC applications. For thicker films, however, the photocurrent density does not linearly vary with the film thickness or the surface concentration of the dye. Such a current

plateauing may come from limited diffusion of the Co(III) complex within the films.

Nevertheless, in all cases, the photocurrents proved very stable with time. We thus decided to compare the aqueous acetate buffer conditions examined here with phosphate buffer conditions more typically used in the literature [27,51,52]. Figure 8 compares the PEC performance of the same electrode recorded first in acetate buffer (pH 4.5, black trace) and then in phosphate buffer (pH 7, red trace). Photocurrents measured in phosphate buffer are clearly less stable with time than those measured in the presence of acetate buffer as the electrolyte. After 10 min, they usually stabilize to values between 40 and 60 μA cm^{-2}. This is likely to be due to the fact that phosphate ions interact more strongly with the NiO surface than the carboxylate anchors in **1**, so that some dye leaches from the surface. We observe a lag phase to this phenomenon which may correspond to the time required to displace surface-anchored acetate anions which are more tightly bound than dye **1**.

We finally compared the push–pull dye **1** with the Ru-based dye [Ru(bpy)$_2$(4,4′-(CH$_2$PO$_3$H$_2$)$_2$-bpy)]Cl$_2$ (**2**) containing two phosphonic acid functions as anchoring groups. This dye also absorbs visible light around 450 nm but with a lower molar absorptivity ($\varepsilon = 11\,000$ M^{-1} cm^{-1}) than **1**. PS-*b*-P2VP-templated NiO films sensitized with **2** display similar surface concentrations in the 1.5–2.8 nmol cm^{-2} range. A maximum photocurrent density value of 15 μA cm^{-2} could be measured at 0 V versus Ag/AgCl for 20 mM concentrations of [Co(NH$_3$)$_5$Cl]Cl$_2$ in either acetate or phosphate buffer. This value is 10-fold lower than those obtained with **1**-sensitized films under similar conditions. This value is also lower than that (50 μA cm^{-2}) measured for a 500-nm-thick polymer-templated nano-ITO film sensitized with the same ruthenium-based dye **2** and a similar surface concentration (4.4 nmol cm^{-2}) [51]. This comparison supports the combination of a *p*-type NiO electrode substrate with push–pull organic dyes with enhanced light absorptivity as optimal architecture for the design of molecular-based photoelectrodes.

3. Conclusion

This study shows that state-of-the-art NiO films are suitable materials for the construction of dye-sensitized photocathodes with current densities up to 300 μA cm^{-2}. Such photocurrent densities can be achieved with simple and easily accessible push–pull organic dyes displaying high molar absorptivities in the visible region. Further developments in materials chemistry are needed to increase these values to a few mA cm^{-2} and to comply with the requirement of economically viable PEC devices [30]. Nevertheless, state-of-the-art H$_2$-evolving molecular photocathodes still exhibit 10-fold lower photocurrents, indicating that efforts should now be directed towards the optimization of directional electron transfer from the grafted dye (either in the photoexcited or reduced state) to the catalytic unit and/or the development and integration of faster multi-electron reduction catalysts. The stable photocurrents obtained in pH 4.5 acetate buffer electrolyte, i.e. conditions where cobalt-based catalysts have proved to be stable and active for H$_2$ evolution [53,54], hold promise for the development of functional photoelectrodes. This study resulting from the combined efforts of four

distinct groups from France and Germany demonstrates the relevance of a Global Artificial Photosynthesis Project promoting interactions at the interface between various fields such as materials science, molecular chemistry, theoretical chemistry and physical chemistry. Such a global enterprise must not only be continued, but also supported and funded, at the international level.

3.1. Experimental section

All chemical reagents were purchased from Sigma sources and used as received. Di-tert-butyl-4,4′-((4-(5-formylthiophen-2-yl)phenyl)azanediyl)dibenzoate was synthesized as previously described [41]. FTO-coated glass substrates (1.1 mm thickness; 80 $\Omega\square^{-1}$) were purchased from SOLEMS S.A., Palaiseau, France. ^{1}H and ^{13}C NMR analyses were performed on a Bruker Avance III 300 spectrometer. Chemical shift values are given in ppm with reference to solvent residual signals [55]. Fourier transform infrared spectra were recorded on a Perkin-Elmer Spectrum 100 spectrometer using a Pike Miracle single reflection attenuated total reflectance (ATR) sampling accessory equipped with a Ge crystal. UV–visible absorption and emission spectra were recorded on an Agilent Cary 60 UV–Vis spectrometer and a Jasco FP-8500 fluorimeter, respectively. Cyclic voltammograms were recorded with a Bio-logic SP300 potentiostat under nitrogen at room temperature. A standard three-electrode configuration was used consisting of a glassy carbon working electrode, an auxiliary platinum wire and an Ag/AgCl/aqueous AgCl$_{sat}$ + KCl 3 mol l^{-1} (denoted as Ag/AgCl throughout this text) reference electrode closed by a Vycor frit and dipped directly into the solution. The [Fe(CN)$_6$]$^{3-}$/[Fe(CN)$_6$]$^{4-}$ couple ($E^0 = +0.215$ V versus Ag/AgCl; referred at $+0.425$ V versus NHE in 0.1 M potassium phosphate buffer at pH $= 7$) [56] was then used for the standardization of the measurements in aqueous solution [56]. The Fc$^+$/Fc couple (measured at $E^0 = +0.43$ V versus Ag/AgCl) was used as a reference for CV measurements in acetonitrile (potentials measured versus Fc$^+$/Fc and converted to NHE by addition of $+0.53$ V [57]).

The ORCA program [58] (v. 3.0.2) was employed for all DFT calculations. Geometry optimizations were performed using the B3LYP functional [59,60] and the Ahlrichs TZVP basis set, which is of triple-zeta quality [61], augmented by extra polarization and diffuse functions (ORCA keyword ACCOPT). Calculations were done both in vacuum and with an implicit solvent model of acetonitrile, using ORCA's version of the COSMO method [62]. After geometry optimization, time-dependent DFT calculations were carried out to determine the UV–vis spectra and the HOMO–LUMO gap [42], together with harmonic frequency calculations to evaluate the IR and Raman spectra. The plots of the HOMO and LUMO orbitals were made with the VMD program [63].

Scanning electron microscopy was performed on a JSM-6300F (JEOL, Tokyo, Japan) field-emission microscope (FE-SEM). The lateral resolving power of the system is specified to be approximately 3 nm at 15 keV. An Everhardt–Thornley-type detector was used for imaging for secondary electrons (SEI). If needed the specimen stage was tilted (up to 60°) to enhance the topographic visibility. The Ni^{2+}-loaded material was deposited onto glass substrates. In order to avoid charging effects all samples were coated

with approximately 20 nm carbon. Cross-sectional preparations were performed after short-term LN$_2$-cooling in order to reduce the degree of ductility and to achieve plain true-edge fracture patterns.

For the rR microspectroscopy measurements a conventional micro-Raman set-up (Labram HR, Horiba Jobin Yvon) was used. The spectrometer was equipped with a 600 line mm^{-1} grating and combined with an Olympus inverse microscope IX71. The excitation wavelengths were delivered by a krypton-ion laser (Model Coherent Innova 301C; $\lambda = 413$ and 476 nm). For the measurements, the laser was focused onto the dye-sensitized NiO surface using an Olympus 20× UPlan FLN microscope objective. The incident laser power was 1 mW at the sample, the spot diameter was 1 μm. The spectra were recorded with an integration time of 2 s per spectrum. All spectra presented in this paper are mean spectra of a quadratic map (60 μm edge length, 10 × 10 spectra), which builds a profound and statistically reliable basis for the comparison of rR intensities. The mean spectra were processed by the statistics-sensitive nonlinear iterative peak-clipping (SNIP) algorithm for background correction using Gnu R [64] and the library 'Peaks' with 20 iterations [65].

The synthetic procedure for the preparation of templated NiO films followed that described in the literature [38]. Polystyrene-*block*-poly(2-vinylpyridine) (PS-*b*-P2VP) was synthesized via sequential anionic polymerization using a procedure adopted from the literature [66]. The mixture of block copolymer and Ni was deposited through doctor blading for three times on FTO-coated glass substrates with 5 min in a furnace at 450°C after deposition of the first and second layer and 25 min in the furnace after the third deposition step.

3.1.1. Di-tert-butyl-(E)-4,4'-((4-(5-(2-cyano-3-ethoxy-3-oxoprop-1-en-1-yl)thiophen-2-yl)phenyl)azanediyl)dibenzoate

To a solution of di-tert-butyl-4,4'-((4-(5-formylthiophen-2-yl)phenyl)azanediyl)dibenzoate (1 eq, 0.2 mmol, 110 mg) and ethyl cyanoacetate (95 eq, 19 mmol, 2 ml) in 5 ml of dry CHCl$_3$ was added piperidine (25 eq, 5 mmol, 0.5 ml). The reaction mixture was stirred at room temperature for 12 h under argon and protected from sunlight. The mixture was diluted with CHCl$_3$ and washed with 1 M aqueous HCl then water. After removal of the solvent, the crude product was purified on a silica gel column using pentane/ethyl acetate (8/2) as eluent to give the di-tert-butylester as an orange solid (88 mg; 68%). ^{1}H NMR (CDCl$_3$, 300 MHz): δ (ppm) 8.27 (s, 1H), 7.90 (d, $J = 8.6$ Hz, 4H), 7.73 (d, $J = 4$ Hz, 2H), 7.60 (d, $J = 8.5$ Hz, 2H), 7.35 (d, $J = 4$ Hz, 1H), 7.11 (m, 6H), 4.35 (q, $J = 7.1$ Hz, 2H), 1.58 (s, 18H), 1.38 (t, $J = 7.1$ Hz, 3H). ^{13}C NMR (CDCl$_3$, 75 MHz): δ (ppm) 165.3, 163.1, 154, 150.2, 147.8, 146.5, 139.3, 134.8, 131.1, 128.6, 127.8, 127.2, 125.3, 124.1, 123.5, 116.2, 97.9, 81, 62.5, 28.3, 14.3. HR-MS (ESI$^+$): m/z calcd for C$_{38}$H$_{39}$N$_2$O$_6$S 651.2523; found 651.2517 [M + H]$^+$.

3.1.2. (E)-4,4'-((4-(5-(2-cyano-3-ethoxy-3-oxoprop-1-en-1-yl)thiophen-2-yl)phenyl)azanediyl)dibenzoic acid (1)

To a solution of di-tert-butylester (1 eq, 35 mg. 53.8 μmol) in 3.5 ml of CH$_2$Cl$_2$ was added trifluoroacetic acid (10 eq, 0.4 ml, 0.52 mmol). The reaction mixture was stirred for 5 h at room temperature. After removal of the solvent, the crude product was purified by precipitation from a CH$_2$Cl$_2$/cyclohexane mixture. The resulting orange powder was filtered, washed with pentane and dried under a vacuum to afford pure 1 (28 mg; 97%). ^{1}H NMR (CDCl$_3$ + 10% MeOD, 300 MHz): δ 8.28 (s, 1H), 7.97 (d, $J = 8.1$ Hz, 4H), 7.74 (d, $J = 3.3$ Hz, 2H), 7.63 (d, $J = 8.1$ Hz, 2H), 7.36 (d, $J = 3.3$ Hz, 1H), 7.15 (m, 6H), 4.35 (q, $J = 7$ Hz, 2H), 1.38 (t, $J = 7$ Hz, 3H). ^{13}C NMR (CDCl$_3$ + 10% MeOD, 75 MHz): δ 168.4, 163.2, 154, 150.6, 147.5, 146.7, 139.5, 134.7, 131.6, 128.9, 127.9, 125.7, 125.3, 124.2, 123.3, 116.1, 97.7, 62.6, 14.2. HR-MS (ESI$^+$): m/z calcd for C$_{30}$H$_{23}$N$_2$O$_6$S 539.1271; found 539.1268 [M + H]$^+$.

3.2. Film sensitization

The variously prepared NiO electrodes were soaked in a 0.5 mM solution of 1 in CH$_3$CN for 24 h on an orbital stirring table. The electrodes were rinsed with CH$_3$CN and dried in air.

3.3. Photoelectrochemical measurements

Photocurrent measurements were performed in a specific cell in a three-electrode configuration. The FTO-coated glass substrate (onto which the NiO film had been deposited) was clamped on the cell, serving as both working electrode and window. The surface of the working electrode in contact with the electrolyte was 0.42 cm^2. Ti wire and Ag/AgCl have been used as counter and reference electrodes, respectively. We used sodium acetate buffer (0.1 M, pH = 4.5) and potassium phosphate buffer (0.1 M, pH = 7) as electrolytes and [Co(NH$_3$)$_5$Cl]Cl$_2$ (10 mM) as the electron acceptor in solution.

Photoelectrodes were back-illuminated with a 300 W ozone-free xenon lamp (Newport) operated at 280 W coupled to a water-filled Spectra-Physics 6123NS liquid filter for elimination of IR radiation and a Spectra-Physics 59472 UV cut-off filter ($\lambda > 400$ nm). Irradiance at the substrate surface was measured to 100 mW cm^{-2} (*ca* two suns) using the Newport PM1918-R power-meter.

References

1. Faunce TA *et al*. 2013 Energy and environment policy case for a global project on artificial photosynthesis. *Energy Environ. Sci.* **6**, 695–698. (doi:10.1039/c3ee00063j)

2. Faunce T *et al*. 2013 Artificial photosynthesis as a frontier technology for energy sustainability. *Energy Environ. Sci.* **6**, 1074–1076. (doi:10.1039/c3ee40534f)

3. Thapper A *et al*. 2013 Artificial photosynthesis for solar fuels—an evolving research field within AMPEA, a Joint Programme of the European Energy Research Alliance. *Green* **3**, 43–57. (doi:10.1515/green-2013-0007)

4. Artero V, Chavarot-Kerlidou M, Fontecave M. 2011 Splitting water with cobalt. *Angew. Chem. Int. Ed.* **50**, 7238–7266. (doi:10.1002/anie.201007987)

5. Andreiadis ES, Chavarot-Kerlidou M, Fontecave M, Artero V. 2011 Artificial photosynthesis: from molecular catalysts for light-driven water splitting to photoelectrochemical cells. *Photochem. Photobiol.* **87**, 946–964. (doi:10.1111/j.1751-1097.2011.00966.x)

6. Eckenhoff WT, Eisenberg R. 2012 Molecular systems for light driven hydrogen production. *Dalton Trans.* **41**, 13 004–13 021. (doi:10.1039/c2dt30823a)

7. Krassen H, Ott S, Heberle J. 2011 *In vitro* hydrogen production—using energy from the sun. *Phys. Chem. Chem. Phys.* **13**, 47–57. (doi:10.1039/C0CP01163K)

8. Schulz M, Karnahl M, Schwalbe M, Vos JG. 2012 The role of the bridging ligand in photocatalytic supramolecular assemblies for the reduction of protons and carbon dioxide. *Coord. Chem. Rev.* **256**, 1682–1705. (doi:10.1016/j.ccr.2012.02.016)

9. Thoi VS, Sun Y, Long JR, Chang CJ. 2013 Complexes of earth-abundant metals for catalytic electrochemical hydrogen generation under aqueous conditions. *Chem. Soc. Rev.* **42**, 2388–2400. (doi:10.1039/C2CS35272A)

10. Halpin Y, Pryce MT, Rau S, Dini D, Vos JG. 2013 Recent progress in the development of bimetallic photocatalysts for hydrogen generation. *Dalton Trans.* **42**, 16 243–16 254. (doi:10.1039/c3dt52319e)

11. McKone JR, Marinescu SC, Brunschwig BS, Winkler JR, Gray HB. 2014 Earth-abundant hydrogen evolution electrocatalysts. *Chem. Sci.* **5**, 865–878. (doi:10.1039/C3SC51711J)

12. Appel AM *et al*. 2013 Frontiers, opportunities, and challenges in biochemical and chemical catalysis of CO2 fixation. *Chem. Rev.* **113**, 6621–6658. (doi:10.1021/cr300463y)

13. Morris AJ, Meyer GJ, Fujita E. 2009 Molecular approaches to the photocatalytic reduction of carbon dioxide for solar fuels. *Acc. Chem. Res.* **42**, 1983–1994. (doi:10.1021/ar9001679)

14. Reithmeier R, Bruckmeier C, Rieger B. 2012 Conversion of CO_2 via visible light promoted homogeneous redox catalysis. *Catalysts* **2**, 544–571. (doi:10.3390/catal2040544)

15. Finn C, Schnittger S, Yellowlees LJ, Love JB. 2012 Molecular approaches to the electrochemical reduction of carbon dioxide. *Chem. Commun.* **48**, 1392–1399. (doi:10.1039/C1CC15393E)

16. Kondratenko EV, Mul G, Baltrusaitis J, Larrazabal GO, Perez-Ramirez J. 2013 Status and perspectives of CO2 conversion into fuels and chemicals by catalytic, photocatalytic and electrocatalytic processes. *Energy Environ. Sci.* **6**, 3112–3135. (doi:10.1039/c3ee41272e)

17. Qiao JL, Liu YY, Hong F, Zhang JJ. 2014 A review of catalysts for the electroreduction of carbon dioxide to produce low-carbon fuels. *Chem. Soc. Rev.* **43**, 631–675. (doi:10.1039/C3CS60323G)

18. Romain S, Vigara L, Llobet A. 2009 Oxygen—oxygen bond formation pathways promoted by ruthenium complexes. *Acc. Chem. Res.* **42**, 1944–1953. (doi:10.1021/ar900240w)

19. Sala X, Romero I, Rodriguez M, Escriche L, Llobet A. 2009 Molecular catalysts that oxidize water to dioxygen. *Angew. Chem. Int. Ed.* **48**, 2842–2852. (doi:10.1002/anie.200802659)

20. Herrero C, Quaranta A, Leibl W, Rutherford AW, Aukauloo A. 2011 Artificial photosynthetic systems. Using light and water to provide electrons and protons for the synthesis of a fuel. *Energy Environ. Sci.* **4**, 2353–2365. (doi:10.1039/c0ee00645a)

21. Meyer TJ. 2011 Catalysis: oxidizing water two ways. *Nat. Chem.* **3**, 757–758. (doi:10.1038/nchem.1161)

22. Artero V, Fontecave M. 2011 Light-driven bioinspired water splitting: recent developments in photoelectrode materials. *C. R. Chim.* **14**, 799–810. (doi:10.1016/j.crci.2011.06.004)

23. Hocking RK, Brimblecombe R, Chang L-Y, Singh A, Cheah MH, Glover C, Casey WH, Spiccia L. 2011 Water-oxidation catalysis by manganese in a geochemical-like cycle. *Nat. Chem.* **3**, 461–466.

24. Brimblecombe R, Koo A, Dismukes GC, Swiegers GF, Spiccia L. 2010 Solar driven water oxidation by a bioinspired manganese molecular catalyst. *J. Am. Chem. Soc.* **132**, 2892–2894. (doi:10.1021/ja910055a)

25. Youngblood WJ, Lee SHA, Kobayashi Y, Hernandez-Pagan EA, Hoertz PG, Moore TA, Moore AL, Gust D, Mallouk TE. 2009 Photoassisted overall water splitting in a visible light-absorbing dye-sensitized photoelectrochemical cell. *J. Am. Chem. Soc.* **131**, 926–927. (doi:10.1021/ja809108y)

26. Zhao YX *et al*. 2012 Improving the efficiency of water splitting in dye-sensitized solar cells by using a biomimetic electron transfer mediator. *Proc. Natl Acad. Sci. USA* **109**, 15 612–15 616. (doi:10.1073/pnas.1118339109)

27. Gao Y, Ding X, Liu JH, Wang L, Lu ZK, Li L, Sun LC. 2013 Visible light driven water splitting in a molecular device with unprecedentedly high photocurrent density.. *J. Am. Chem. Soc.* **135**, 4219–4222. (doi:10.1021/ja400402d)

28. Alibabaei L *et al*. 2013 Solar water splitting in a molecular photoelectrochemical cell. *Proc. Natl Acad. Sci. USA* **110**, 20 008–20 013. (doi:10.1073/pnas.1319628110)

29. Ding X, Gao Y, Zhang L, Yu Z, Liu J, Sun L. 2014 Visible light-driven water splitting in photoelectrochemical cells with supramolecular catalysts on photoanodes. *ACS Catalysis* **4**, 2347–2350. (doi:10.1021/cs500518k)

30. Walter MG, Warren EL, McKone JR, Boettcher SW, Mi Q, Santori EA, Lewis NS. 2010 Solar water splitting cells. *Chem. Rev.* **110**, 6446–6473. (doi:10.1021/cr1002326)

31. Odobel F, Pellegrin Y. 2013 Advances in the sensitization of wide-band-gap nanostructured p-type semiconductors. Photovoltaic and photocatalytic applications. *J. Phys. Chem. Lett.* **4**, 2551–2564. (doi:10.1021/jz400861v)

32. He JJ, Lindstrom H, Hagfeldt A, Lindquist SE. 1999 Dye-sensitized nanostructured p-type nickel oxide film as a photocathode for a solar cell. *J. Phys. Chem. B* **103**, 8940–8943. (doi:10.1021/jp991681r)

33. Li L, Gibson EA, Qin P, Boschloo G, Gorlov M, Hagfeldt A, Sun LC. 2010 Double-layered NiO photocathodes for p-type DSSCs with record IPCE. *Adv. Mater.* **22**, 1759–1762. (doi:10.1002/adma.200903151)

34. Nattestad A, Ferguson M, Kerr R, Cheng YB, Bach U. 2008 Dye-sensitized nickel(II)oxide photocathodes for tandem solar cell applications. *Nanotechnology* **19**, 295304. (doi:10.1088/0957-4484/19/29/295304)

35. Sumikura S, Mori S, Shimizu S, Usami H, Suzuki E. 2008 Syntheses of NiO nanoporous films using nonionic triblock co-polymer templates and their application to photo-cathodes of p-type dye-sensitized solar cells. *J. Photochem. Photobiol. A* **199**, 1–7. (doi:10.1016/j.jphotochem.2008.04.007)

36. Awais M, Gibson E, Vos JG, Dowling DP, Hagfeldt A, Dini D. 2014 Fabrication of efficient NiO photocathodes prepared via RDS with novel routes of substrate processing for p-type dye-sensitized solar cells. *Chemelectrochem* **1**, 384–391. (doi:10.1002/celc.201300178)

37. Gibson EA, Awais M, Dini D, Dowling DP, Pryce MT, Vos JG, Boschloo G, Hagfeldt A. 2013 Dye sensitised solar cells with nickel oxide photocathodes prepared via scalable microwave sintering. *Phys. Chem. Chem. Phys.* **15**, 2411–2420. (doi:10.1039/c2cp43592f)

38. Bräutigam M, Weyell P, Rudolph T, Dellith J, Krieck S, Schmalz H, Schacher FH, Dietzek B. 2014 Porous NiOx nanostructures templated by polystyreneblock-poly(2-vinylpyridine) diblock copolymer micelles. *J. Mater. Chem. A* **2**, 6158–6166. (doi:10.1039/c3ta14890d)

39. Ji Z, He M, Huang Z, Ozkan U, Wu Y. 2013 Photostable p-type dye-sensitized photoelectrochemical cells for water reduction. *J. Am. Chem. Soc.* **135**, 11 696–11 699. (doi:10.1021/ja404525e)

40. Mishra A, Fischer MKR, Bauerle P. 2009 Metal-free organic dyes for dye-sensitized solar cells: from structure: property relationships to design rules. *Angew. Chem. Int. Ed.* **48**, 2474–2499. (doi:10.1002/anie.200804709)

41. Ji Z, Natu G, Huang Z, Wu Y. 2011 Linker effect in organic donor-acceptor dyes for p-type NiO dye sensitized solar cells. *Energy Environ. Sci.* **4**, 2818–2821. (doi:10.1039/c1ee01527c)

42. Zhang G, Musgrave CB. 2007 Comparison of DFT methods for molecular orbital eigenvalue calculations. *J. Phys. Chem. A* **111**, 1554–1561. (doi:10.1021/jp061633o)

43. Boschloo G, Hagfeldt A. 2001 Spectroelectrochemistry of nanostructured NiO. *J. Phys. Chem. B* **105**, 3039–3044. (doi:10.1021/jp003499s)

44. Weidelener M *et al*. 2014 Synthesis and characterization of organic dyes with various electron-accepting substituents for p-type dye-sensitized solar cells. *Chem. Asian J.* **9**, 3251–3263.

45. Tong L *et al*. 2012 Sustained solar hydrogen generation using a dye-sensitised NiO photocathode/BiVO4 tandem photo-electrochemical

device. *Energy Environ. Sci.* **5**, 9472–9475. (doi:10.1039/c2ee22866a)

46. Qin P, Wiberg J, Gibson EA, Linder M, Li L, Brinck T, Hagfeldt A, Albinsson B, Sun L. 2010 Synthesis and mechanistic studies of organic chromophores with different energy levels for p-type dye-sensitized solar cells. *J. Phys. Chem. C* **114**, 4738–4748. (doi:10.1021/jp911091n)

47. Gibson EA *et al*. 2009 A p-type NiO-based dye-sensitized solar cell with an open-circuit voltage of 0.35 V. *Angew. Chem. Int. Ed.* **48**, 4402–4405. (doi:10.1002/anie.200900423)

48. Morandeira A, Boschloo G, Hagfeldt A, Hammarström L. 2005 Photoinduced ultrafast dynamics of coumarin 343 sensitized p-type-nanostructured NiO films. *J. Phys. Chem. B* **109**, 19 403–19 410. (doi:10.1021/jp053230e)

49. Le Pleux L, Smeigh AL, Gibson E, Pellegrin Y, Blart E, Boschloo G, Hagfeldt A, Hammarstrom L, Odobel F. 2011 Synthesis, photophysical and photovoltaic investigations of acceptor-functionalized perylene monoimide dyes for nickel oxide p-type dye-sensitized solar cells. *Energy Environ. Sci.* **4**, 2075–2084. (doi:10.1039/c1ee01148k)

50. Morandeira A, Boschloo G, Hagfeldt A, Hammarström L. 2008 Coumarin 343–NiO films as nanostructured photocathodes in dye-sensitized solar cells: ultrafast electron transfer, effect of the I 3–/I– redox couple and mechanism of photocurrent generation. *J. Phys. Chem. C* **112**, 9530–9537. (doi:10.1021/jp800760q)

51. Hamd W *et al*. 2013 Dye-sensitized nanostructured crystalline mesoporous tin-doped indium oxide films with tunable thickness for photoelectrochemical applications. *J. Mater. Chem. A* **1**, 8217–8225. (doi:10.1039/c3ta10728k)

52. Li L, Duan LL, Wen FY, Li C, Wang M, Hagfeld A, Sun LC. 2012 Visible light driven hydrogen production from a photo-active cathode based on a molecular catalyst and organic dye-sensitized p-type nanostructured NiO. *Chem. Commun.* **48**, 988–990. (doi:10.1039/C2CC16101J)

53. Varma S, Castillo CE, Stoll T, Fortage J, Blackman AG, Molton F, Deronzier A, Collomb MN. 2013 Efficient photocatalytic hydrogen production in water using a cobalt(III) tetraaza-macrocyclic catalyst: electrochemical generation of the low-valent Co(I) species and its reactivity toward proton reduction. *Phys. Chem. Chem. Phys.* **15**, 17 544–17 552. (doi:10.1039/c3cp52641k)

54. Andreiadis ES *et al*. 2013 Molecular engineering of a cobalt-based electrocatalytic nanomaterial for H_2 evolution under fully aqueous conditions. *Nat. Chem.* **5**, 48–53. (doi:10.1038/nchem.1481)

55. Gottlieb HE, Kotlyar V, Nudelman A. 1997 NMR chemical shifts of common laboratory solvents as trace impurities. *J. Org. Chem.* **62**, 7512–7515. (doi:10.1021/jo971176v)

56. O'Reilly JE. 1973 Oxidation-reduction potential of the ferro-ferricyanide system in buffer solutions. *Biochim. Biophys. Acta* **292**, 509–515. (doi:10.1016/0005-2728(73)90001-7)

57. Parker VD, Handoo KL, Roness F, Tilset M. 1991 Electrode potentials and the thermodynamics of isodesmic reactions. *J. Am. Chem. Soc.* **113**, 7493–7498. (doi:10.1021/ja00020a007)

58. Neese F. 2012 The ORCA program system. *WIREs Comput. Mol. Sci.* **2**, 73–78. (doi:10.1002/wcms.81)

59. Becke AD. 1988 Density-functional exchange-energy approximation with correct asymptotic behavior. *Phys. Rev. A* **38**, 3098–3100. (doi:10.1103/PhysRevA.38.3098)

60. Lee C, Yang W, Parr RG. 1988 Development of the Colle-Salvetti correlation-energy formula into a functional of the electron density. *Phys. Rev. B* **37**, 785–789. (doi:10.1103/PhysRevB.37.785)

61. Weigend F, Ahlrichs R. 2005 Balanced basis sets of split valence, triple zeta valence and quadruple zeta valence quality for H to Rn: design and assessment of accuracy. *Phys. Chem. Chem. Phys.* **7**, 3297–3305. (doi:10.1039/b508541a)

62. Sinnecker S, Rajendran A, Klamt A, Diedenhofen M, Neese F. 2006 Calculation of solvent shifts on electronic g-tensors with the conductor-like screening model (COSMO) and its self-consistent generalization to real solvents (direct COSMO-RS). *J. Phys. Chem. A* **110**, 2235–2245. (doi:10.1021/jp056016z)

63. Humphrey W, Dalke A, Schulten K. 1996 VMD: visual molecular dynamics. *J. Mol. Graphics* **14**, 33–38. (doi:10.1016/0263-7855(96)00018-5)

64. R Core Team. 2015 *R: a language and environment for statistical computing*. Vienna, Austria: R Foundation for Statistical Computing. See http://www.R-project.org/.

65. Bräutigam M, Schulz M, Inglis J, Popp J, Vos JG, Dietzek B. 2012 Resonance-Raman microspectroscopy for quality assurance of dye-sensitized NiOx films with respect to dye desorption kinetics in water. *Phys. Chem. Chem. Phys.* **14**, 15 185–15 190. (doi:10.1039/c2cp42938a)

66. Giebeler E, Stadler R. 1997 ABC triblock polyampholytes containing a neutral hydrophobic block, a polyacid and a polybase. *Macromol. Chem. Phys.* **198**, 3815–3825. (doi:10.1002/macp.1997.021981204)

PAPER

CrossMark
click for updates

A comprehensive comparison of dye-sensitized NiO photocathodes for solar energy conversion†

Christopher J. Wood,‡[a] Gareth H. Summers,‡[a] Charlotte A. Clark,[a] Nicolas Kaeffer,[b] Maximilian Braeutigam,[cd] Lea Roberta Carbone,[e] Luca D'Amario,[f] Ke Fan,[g] Yoann Farré,[h] Stéphanie Narbey,[i] Frédéric Oswald,[i] Lee A. Stevens,[j] Christopher D. J. Parmenter,[k] Michael W. Fay,[k] Alessandro La Torre,[k] Colin E. Snape,[l] Benjamin Dietzek,[cd] Danilo Dini,[e] Leif Hammarström,[f] Yann Pellegrin,[h] Fabrice Odobel,[h] Licheng Sun,[g] Vincent Artero[b] and Elizabeth A. Gibson‡*[a]

We investigated a range of different mesoporous NiO electrodes prepared by different research groups and private firms in Europe to determine the parameters which influence good quality photoelectrochemical devices. This benchmarking study aims to solve some of the discrepancies in the literature regarding the performance of p-DSCs due to differences in the quality of the device fabrication. The information obtained will lay the foundation for future photocatalytic systems based on sensitized NiO so that new dyes and catalysts can be tested with a standardized material. The textural and electrochemical properties of the semiconducting material are key to the performance of photocathodes. We found that both commercial and non-commercial NiO gave promising solar cell and water-splitting devices. The NiO samples which had the two highest solar cell efficiency (0.145% and 0.089%) also gave the best overall theoretical H_2 conversion.

[a] School of Chemistry, The University of Nottingham, University Park, Nottingham, NG7 2RD, UK

[b] Laboratoire de Chimie et Biologie des Métaux, Université Grenoble Alpes, CEA, CNRS, 17 rue des Martyrs, 38000 Grenoble, France

[c] Institute of Photonic Technology (IPHT) Jena e. V., Albert-Einstein-Straße 9, D-07745 Jena, Germany

[d] Institute for Physical Chemistry and Abbe Center of Photonics, Friedrich-Schiller University Jena, Helmholtzweg 4, D-07743 Jena, Germany

[e] Department of Chemistry, University of Rome "La Sapienza", Rome, Italy

[f] Department of Chemistry-Ångström, Uppsala University, Box 259, SE-751 05 Uppsala, Sweden

[g] School of Chemical Science and Engineering, Royal Institute of Technology (KTH), 100 44 Stockholm, Sweden

[h] CEISAM, Chimie et Interdisciplinarité, Synthèse, Analyse, Modélisation, CNRS, UMR 6230, Faculté des Sciences et des Techniques Université de Nantes, 2, rue de la Houssinière, BP 92208, 44322 NANTES Cedex 3, France

[i] Solaronix, rue de l'Ouriette 129, CH-1170 Aubonne, Switzerland

[j] Division of Materials, Mechanics and Structures, Faculty of Engineering, University of Nottingham, University Park, Nottingham, NG7 2RD, UK

[k] Nottingham Nanotechnology and Nanoscience Centre, University of Nottingham, University Park, Nottingham, NG7 2RD, UK

[l] Department of Chemical and Environmental Engineering, Faculty of Engineering, University of Nottingham, University Park, Nottingham, NG7 2RD, UK

† Electronic supplementary information (ESI) available. See DOI: 10.1039/c5cp05326a

‡ Present address: School of Chemistry, Newcastle University, Newcastle upon Tyne, NE1 7RU, UK. E-mail: Elizabeth.gibson@ncl.ac.uk

Introduction

Since He *et al.* reported the first dye-sensitized NiO photocathode and assembled it in a tandem dye-sensitized solar cell, an opportunity to increase the efficiency of solar energy conversion in photoelectrochemical devices has been recognised.[1,2] Firstly, the theoretical maximum efficiency of dye-sensitized solar cells (DSCs) is increased from 33% to 43% by replacing the platinized counter electrode in conventional DSC with a photocathode such as dye-sensitized NiO (Fig. 1a). Secondly, the redox electrolyte which completes the circuit in a photoelectrochemical solar cell (*i.e.* a DSC) can be replaced with water so that hydrogen can be generated at the photocathode and oxygen can be formed at the photoanode (Fig. 1b). This dye-sensitized photoelectrosynthetic cell (DPEC)[3] can produce hydrogen as a solar fuel while avoiding the requirement for sacrificial agents which are usually required in photocatalytic approaches.[3–5] In such architectures, catalysts, either molecular or materials, are usually required to facilitate water splitting into hydrogen and oxygen. Both types of device are relatively new concepts and the efficiency of the devices that have been reported is very low (2.42% efficiency for a tandem DSC[6] compared to 13% efficiency for the state of the art TiO_2-based DSCs;[7] maximum incident photon-to-current efficiencies up to 15% in TiO_2-based DPECs[8] compared to 0.6% for NiO-based DPECs[9]). Therefore the
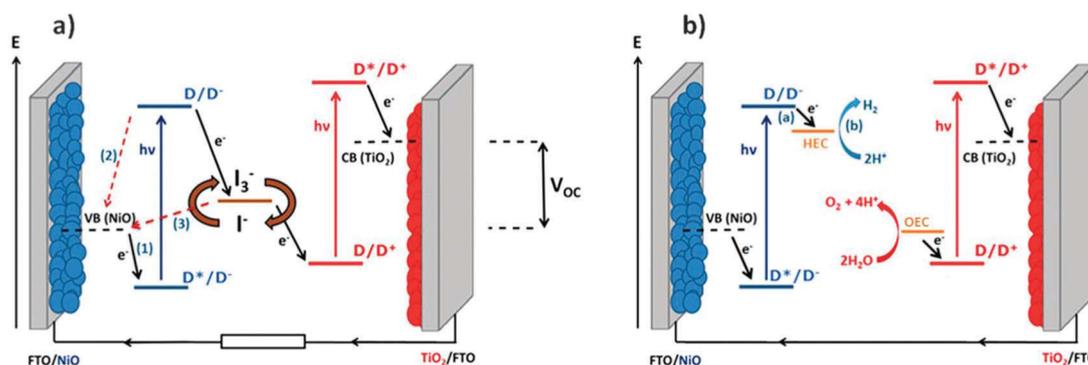
Fig. 1 Schematic illustration of (a) a tandem dye-sensitized solar cell and (b) a dye-sensitized photoelectrosynthetic cell. (VB: valence band; CB: conduction band; HEC: hydrogen evolution catalyst; OEC: oxygen evolution catalyst).

efficiency of tandem photoelectrochemical devices is limited by the performance of the photocathode. A breakthrough in this area is anticipated if highly efficient p-type photocathodes can be realised.[10]

Recently, the performance of NiO-based DSCs were reviewed in the context of the preparation method used for the mesoporous electrode.[11] It was observed that surface morphology is of primary importance to control the oxidation properties of NiO. The presence of defects is important to the performance of the device, especially the recombination reactions (2) and (3) in Fig. 1(a). The most efficient devices that have been reported were prepared from pre-formed NiO nanoparticles and companies such as Solaronix and Dyenamo are now selling screen-printable pastes. However, it is difficult to assess from the literature whether the source of NiO is important compared to other factors such as the device assembly method, choice of dye and sensitization conditions *etc.* we took the opportunity of the COST Action CM1202 on Supramolecular water splitting to organise a workshop for the benchmarking of different NiO electrodes, prepared in different research groups in Europe from

lab-made or commercial sources, in DSCs and DPECs under the same conditions. This was designed to answer questions such as whether the control over the purity and crystallinity achieved by preparing the particles in house is preferential to purchasing NiO nanoparticles or commercial paste; whether the trends observed in DSCs can be translated directly to the performance of water-splitting DPECs.

The experiments were chosen so that the chemical-physical properties such as crystal size, BET surface area and electrochemical properties could be compared to the DSC and DPEC device performance. The dye **P1** (Fig. 2) was chosen because it has been used in both p-type DSCs and DPECs.[12,13] The I_3^-/I^- electrolyte for the DSCs was chosen because this redox couple is known to be optimised for this dye.[14] The $[Co(dmgBF_2)_2(H_2O)_2]$ (dmg^{2-}: dimethylglyoximato dianion) hydrogen evolving catalyst was chosen for the DPEC because it has been extensively characterised elsewhere and because Li *et al.* demonstrated that it can be incorporated into a **P1**-sensitized NiO DPEC to reduce protons.[8,15] In the devices, absorption of visible light by **P1** leads to electron transfer from NiO to the dye. The potential of
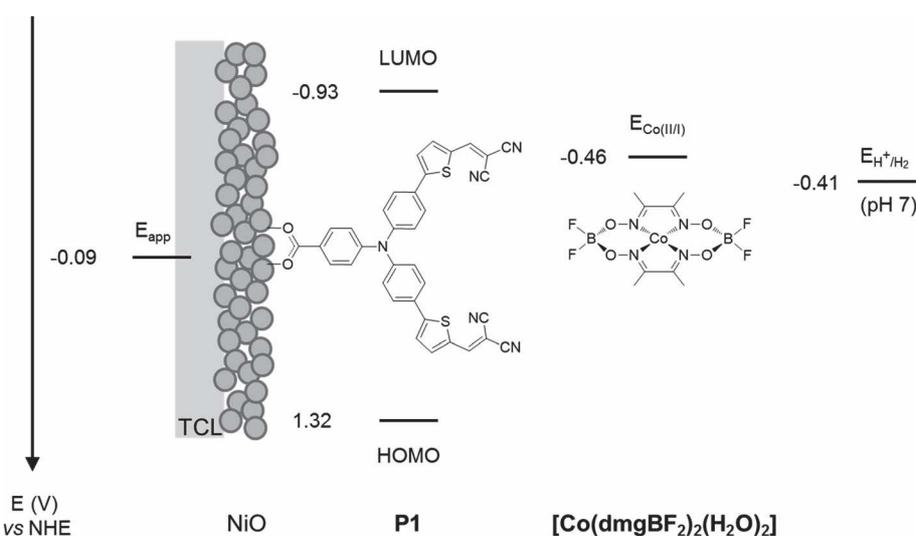

Fig. 2 Energy diagram of NiO-**P1**-[Co(dmgBF$_2$)$_2$(H$_2$O)$_2$] electrodes (note: potentials of **P1** in MeCN from Qin *et al.*[16] and for [Co(dmgBF$_2$)$_2$(H$_2$O)$_2$] in pH 7 phosphate buffer corrected *vs.* NHE from Berben *et al.*[20]). TCL: transparent conducting layer.

the reduced dye (-0.93 V *vs.* NHE)[16] is sufficient to reduce I_3^- to I^- or $[Co(dmgBF_2)_2(H_2O)_2]$ both from the Co(II) to the Co(I) state, the entry point of the catalytic proton reduction cycle, and further from the Co(III)–H to form the active Co(II)–H species.[17–19]

Experimental

Sample preparation

Sample **1a**/**1b** was prepared by following the method according to Grätzel for TiO_2.[21]

Sample **2** was prepared by grinding 3 g of NiO ground in planetary mill (500 rpm) for 24 h with EtOH. 10 mL of ethyl cellulose 10% in EtOH, 20 mL terpineol were added and the EtOH was removed under vacuum. The paste was deposited onto FTO glass by screen printing. The electrodes were sintered according to the following program:

Sample **3** was prepared according to Bräutigam *et al.*[22] Minor alterations included the deposition by doctor blading and the 3-fold repetition of this to yield thicker NiO surfaces.

Sample **4** conducting glass substrates were cut to size and then cleaned in an ultrasonic bath for 15 minutes, first in soapy water, second in propan-2-ol and finally in acetone. The NiO precursor solution was prepared by dissolving anhydrous $NiCl_2$ (1 g) and the tri-block co-polymer F108 (poly(ethylene glycol)-*block*-poly(propylene glycol)-*block*-poly(ethylene glycol)) (1 g) in ethanol (6 g) and ultrapure Milli-Q water (5 g).[23] NiO electrodes were made by applying the precursor solution onto conducting glass substrates (Pilkington TEC15, sheet resistance 15 Ω sq^{-1}) by doctor blade using Scotch tape as a spacer (0.2 cm^2 active area), followed by sintering in a Nabertherm B150 oven at 450 °C for 30 min.

Samples **5a–d** were purchased from Dyenamo, where they are prepared by screen printing (one layer for sample **a** and **b** and two layers for samples **c** and **d**). The as-received plates were sintered in a flat oven (PZ28-3TD, Harry Gestigkeit) monitored by a controller (Programmer PR5, Detlef Gestigkeit) applying the following temperature gradients:

– For samples **a** and **c**: from r.t. to 350 °C in 30 min; 30 min at 350 °C; gently back to r.t.

– For samples **b** and **d**: from r.t. to 450 °C in 30 min; 30 min at 450 °C; gently back to r.t.

Samples **5e,f** were prepared by Solaronix by screen printing of a NiO paste (Ni-Noxide N/SP). The as-received plates were sintered in a flat oven (PZ28-3TD, Harry Gestigkeit) monitored by a controller (Programmer PR5, Detlef Gestigkeit) applying the following temperature gradients:

– For samples **e**: from r.t. to 350 °C in 30 min; 30 min at 350 °C; gently back to r.t.

– For samples **f**: from r.t. to 450 °C in 30 min; 30 min at 450 °C; gently back to r.t.

Samples **6a–c** were prepared according to D'Amario *et al.*[24] 3 g of anhydrous $NiCl_2$ and 3 g of F108 polymer were dissolved in a mixture of deionized water (9 g) and 99.5% ethanol (18 g). The resulting green viscous solution was sonicated overnight. The mixture was centrifuged for 15 min to sediment out

Table 1 Sintering gradient used for preparation of sample 2

	Start temperature (°C)	End temperature (°C)	Ramp	Time at fixed temperature
1	RT	110	30 min	30 min
2	110	250	1 h	30 min
3	250	340	15 min	5 min
4	340	400	30 min	30 min

undissolved $NiCl_2$ and amorphous NiO. After centrifugation, the supernatant was collected as four separate batches for use as doctor-blading paste. The Li-doping was carried out by adding 0, 0.1 and 0.5 mol% of LiCl to the $NiCl_2$ sol–gel. The LiCl was added by water solution using less than 1% of the final batch volume. Then, the mixture was stirred for 1 day. Mesoporous NiO electrodes were prepared by spreading the doctor-blading paste onto FTO glass masked with adhesive tape and sintered in a furnace at 450 °C for 30 min.

Sample **7** commercial NiO nanoparticles (1.0 g, 20 nm Inframat Advanced Materials) were mixed with of ethanol (8.0 mL), acetic acid (0.2 mL), terpinol (3.0 g) and ethyl cellulose (0.5 g) by ball-milling for 2 h. The obtained paste was screen-printed on clean FTO glass, followed by sintering at 450 °C in air for 30 min (Table 2).

Electron microscopy

SEM micrographs for **5e** and **f** were recorded using a FEI Quanta200 3D DualBeam FIB/SEM. High resolution TEM was recorded using the JEOL 2100F TEM equipped with a JEOL digital STEM system and a Gatan Tridiem spectrometer at the Nottingham Nanoscience and Nanotechnology Centre. The NiO was removed from the FTO glass and loaded onto a carbon coated copper TEM grid (Agar Scientific).

Powder X-ray diffraction (PXRD)

PXRD patterns were collected at room temperature in the $10°$–$80°$ range on a PANanalytical Multi-purpose Diffractometer operated at 40 kV and 40 mA (Cu Kα1, $\lambda = 1.5406$ Å). Powder samples were deposited from a slurry in ethanol onto a silicon zero diffraction plate and NiO films on FTO were prepared as described above. The data was analysed using PANanalytical X'Pert Highscore.

Kr gas adsorption isotherms

Adsorption isotherms were carried out by using a Micromeritics ASAP 2420 (Micromeritics, Norcross, GA, USA) using krypton as the adsorbate. NiO samples were prepared as described above onto *ca.* 0.5 cm × 1 cm FTO glass substrates. Three replicates of each sample were inserted into glass sample tubes with a sealed frit. The samples were degassed under vacuum at 25 °C for 3 hours to remove moisture and other adsorbed gases. Krypton isotherms were acquired from 0.07–0.25 relative pressure (p/p_0) at -195.85 °C in liquid nitrogen (N_2). The glass samples were then weighed and reweighed following the removal of the NiO in order to give an accurate sample weight. The BET model for specific surface area was fitted to the Kr isotherms using Microactive V3.0 software (Micrometrics Instrument Corporation).

Table 2 A summary of the samples used in this study

| Sample | Deposition | Area (cm^2) | Type | Sintering | | Thickness (µm) |
				Ramp	Final	
1a	Screen print	0.25	Aldrich nanoparticles (around 20 nm)	40 min ramp r.t. to 550 °C	30 min@550 °C	2[b]
1b		0.25	Aldrich nanoparticles (around 20 nm)	40 min ramp r.t. to 550 °C	30 min@550 °C	5[b]
2	Screen print	0.36	Inframat nanoparticles (around 20 nm)	(See Table 1)		1.4[a]
3	Doctor blade 3 layers	0.36	Copolymer PS-b-P2VP		30 min@450 °C	0.2[a]
4	Doctor blade	0.20	F108	30 min ramp r.t. to 450 °C	30 min@450 °C	0.83[b]
5a	Screen print 1 layer	0.46	Dyenamo	30 min ramp r.t. to 350 °C	30 min@350 °C	0.74[a]
5b		0.44		30 min ramp r.t. to 450 °C	30 min@450 °C	
5c	Screen print 2 layers	0.37		30 min ramp r.t. to 350 °C	30 min@350 °C	1.75[a]
5d		0.26		30 min ramp r.t. to 450 °C	30 min@450 °C	
5e	Screen print 1 layer	0.41	Solaronix	30 min ramp r.t. to 350 °C	30 min@350 °C	
5f		0.37		30 min ramp r.t. to 450 °C	30 min@450 °C	
6a	Doctor blade	0.25	0% Li-doped F108		30 min@450 °C	0.70 ± 0.05[b]
6b			0.1% Li-doped F108			
6c			0.5% Li-doped F108			
7	Screen print 1 layer		Inframat nanoparticles (around 20 nm)		30 min@450 °C	

[a] Measured from SEM cross sectional images. [b] Measured using a Dektak Profilometer.

Electrochemistry

Cyclic voltammetry was carried out using a Palmsens Emstat potentiostat. A three electrode system was used with the NiO film working electrode, a Ag/Ag$^+$ (Sat. AgCl in 3 M NaCl$_{(aq)}$) reference electrode and a Pt wire counter electrode immersed in pH 7 buffer solution.

Solar cells

The NiO electrodes were soaked in an acetonitrile solution of **P1** (0.3 mM) for 16 h at room temperature. The dyed NiO electrode was assembled face-to-face with a platinized counter electrode (Pilkington TEC8, sheet resistance 8 Ω sq^{-1}) using a 30 µm thick thermoplastic frame (Surlyn 1702). Then the electrolyte, containing LiI (1.0 M) and I$_2$ (0.1 M) in acetonitrile, was introduced through the pre-drilled hole in the counter electrode, which was sealed afterwards. The UV-visible absorption spectra of the dyes adsorbed on NiO films were recorded using an Ocean Optics USB2000 + VIS-NIR fibre-optic spectrophotometer. Current–voltage measurements were measured using an Ivium CompactStat potentiostat under AM1.5 simulated sunlight from an Oriel 150 W solar simulator, giving light with an intensity of 100 mW cm^{-2}. Incident photon-to-current conversion efficiency curves (IPCE) were recorded by passing the light from the solar simulator through an Oriel Cornerstone 130 1/8m monochromator and recording the current from the solar cell with an Ivium CompactStat potentiostat which was calibrated against a Si photodiode.

Small amplitude square wave modulated (SSWM) photovoltage and photocurrent experiments were performed on the same p-DSCs used for the *J*–*V* and IPCE measurements at open circuit and short circuit, respectively. SSWM experiments were carried out over a range of light intensities, using an Ivium Modulight as a modulated light source with a 10% modulation of light intensity. The photovoltage and photocurrent rise and decays were recorded using an Ivium CompactStat potentiostat, the lifetimes were fitted to a 1st order exponential decay using Origin Pro 8. Charge extraction was performed using the same equipment, the cell was illuminated at open-circuit until a constant V_{OC} was reached, the light source was then switched off allowing for a decay in photovoltage, over a range of time intervals. Following this the cell was switched to short-circuit conditions and the current decay over 10 seconds was integrated to give the charge at varying photovoltages.

Photoelectrochemical measurements

For the electrochemical measurements a custom-built three compartment cell was used. A Pt wire (0.5 mm) counter electrode and a Ag/AgCl reference electrode were employed. The working electrode for each experiment were typically prepared on TEC 15 FTO glass with areas ranging between 0.636–0.25 cm^2. The sample preparation for each electrode was identical: (1) the NiO films were soaked in a CH$_3$CN dye bath containing **P1** (0.3 mM) for a period of 12 h. (2) The films were rinsed in CH$_3$CN to remove unadsorbed dye. (3) Finally, the co-catalyst [Co^{II}(dmg-BF$_2$)$_2$(OH)$_2$] was introduced by slow drop-casting 100 µL of a 2 mM solution in CH$_3$CN and the sample was dried in air.

The electrolyte used in all experiments was an aqueous solution containing 50 mM phosphate at pH 7. All solutions were degassed by bubbling with Ar for a minimum of 5 minutes prior to commencing of the experiment and Ar was continually bubbled through the solution using a Bronkhorst flow-controller (flow rate = 10 mL min^{-1}) throughout the measurement. A 200 µL sample of the Ar flowing out from the cell was analyzed automatically every 3 min using a gas chromatograph (Shimadzu 2014) with a thermal conductivity detector operating at 50 °C. There was insufficient H$_2$ produced in the cell to quantify it accurately using this method. The visible LED used for photolysis is an OSRAM® OSTAR® white LED with an output of 1000 lm. Care was taken to place the LED in an identical position for

each measurement. A constant potential of -0.4 V *vs.* Ag/AgCl was applied during each experiment and the current measured using an EmStat potentiostat.

Results and discussion

Film morphology

All the NiO samples were based on nanoparticles prepared either *in situ* or pre formed and applied as a paste using a combination of organic surfactants and binders. Full details are given in the Experimental section and the corresponding references. In general the particle shape and film morphology was similar for each sample. SEM for **1** can be found in ref. 34. SEM images for samples **2** and **5b** and **d** are provided in Fig. 3. High resolution TEM for **5e–f** are shown in Fig. 4. SEM images for the sol–gel prepared films **3**, **4** and **6** have previously been reported in ref. 12, 20 and 22 respectively and high resolution TEM images for **4** are provided in Fig. 4.

Powder X-ray diffraction (PXRD)

The undyed NiO films were characterised using powder X-ray diffraction both for the samples on FTO and for the nano-particles removed from the glass substrate. A representative X-ray diffraction pattern for the film on FTO (Fig. 5a) and the powder removed from the film (Fig. 5b) are given below.

The results of the XRD analysis are summarised in Table 3 for the film and powder respectively. The mean crystallite size estimated from the major diffractions ranged from 10 to 20 nm. Generally as the sintering temperature increases the mean crystallite size also increases, with the smallest being 10 nm for **5e** corresponding to a sintering temperature of 350 °C while the larger samples of 16 (**1a**) and 21 nm (**4**) were sintered at 550 and 450 °C respectively. For the screen printed pastes (**7**, **5d**, **1a**) sintered at 450 °C the mean crystallite sizes were fairly consistent and within the range of 13–16 nm while generally the NiO films made *via* a sol–gel process (**6**, **3**) were within the range of 12–14 nm which is smaller than for the screen printed pastes. The difference in crystallite size for the two films made *via* a sol–gel process using F108 (21 nm for the undoped film, **4**, to 12 nm with 0.5% Li, **6**) are attributed to the different solvent ratio in the precursor solution. The crystallite size in the Li-doped film **6** is in agreement with previously reported results by Sumikura *et al.* (12 nm with F108) and a slightly larger crystallite size was reported by Li *et al.* (16 nm).[12,23] Differences of around 1 nm were observed when comparing the mean crystallite size of the NiO films on FTO and the nanoparticles removed from the glass substrate. However, rather than a change in morphology this has been attributed to improved resolution for the measurement on the silicon zero diffraction plate (Fig. 5b) compared to the NiO on FTO (Fig. 5a) where there is a significant overlap of the diffractions from NiO and SnO$_2$.

This is most apparent for the thinner films (see ESI†) where the NiO diffractions were very low in intensity compared to those from SnO$_2$. Interestingly the crystallite size for samples **1**, **2** and **7** prepared from commercial NiO was less than the advertised
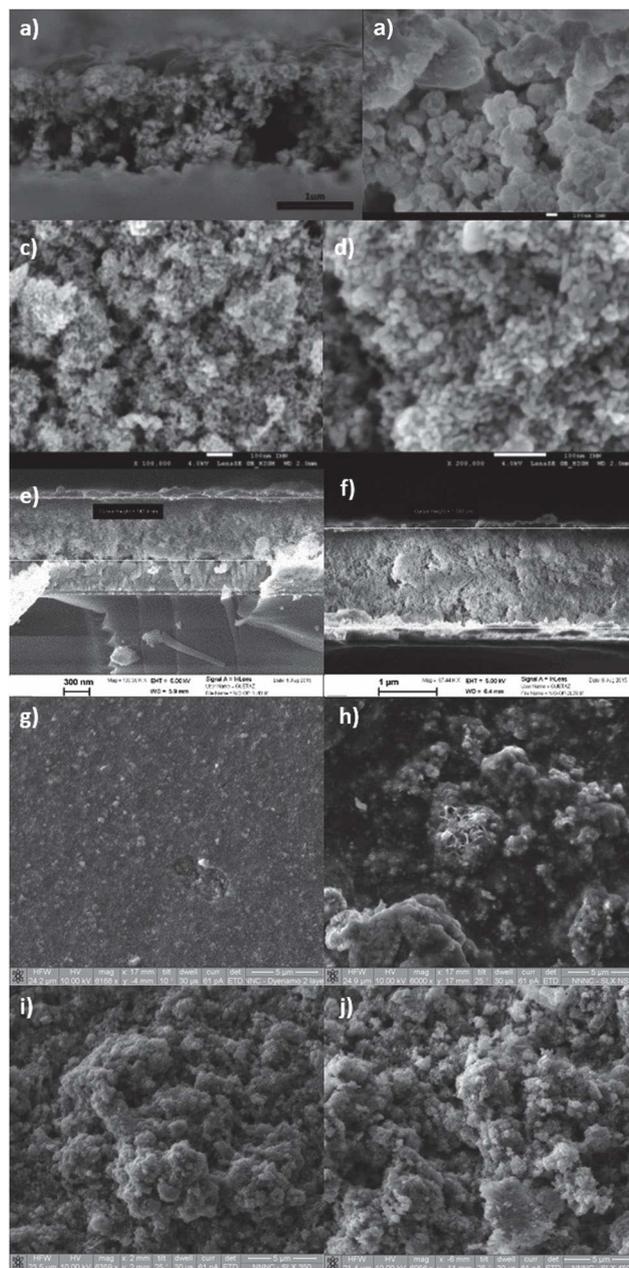

Fig. 3 SEM micrographs of (a), (b) the cross-section of **2** (50 000× magnification); (c) the surface morphology of **2** (100 000×), (d) the surface morphology of **2** (200 000×), (e) the cross section of **5b** (100 000×); (f) the cross section of **5d** (67 000×); (g) the surface of **5b** (6000×); (h) the surface of a film made from the Solaronix paste before sintering (6000×); (i) the surface of **5e** (6000×); (j) the surface of **5f** (7000×). HV = 5 kV (for sample **2**), 4 kV (**5b**, **5d**) 10 kV (**5e**, **5f**). WD = 2–5 mm.

average particle size of 20 nm. Samples **2** and **7**, which both contain Inframant NiO, agreed within 1 nm.

Kr gas adsorption

A summary of the surface areas obtained from Kr adsorption isotherms is given in Table 3 and examples of adsorption isotherms for samples **5c** and **5d**, as well as **3** and **4**, respectively, are given in Fig. 6. All samples gave BET surfaces areas within
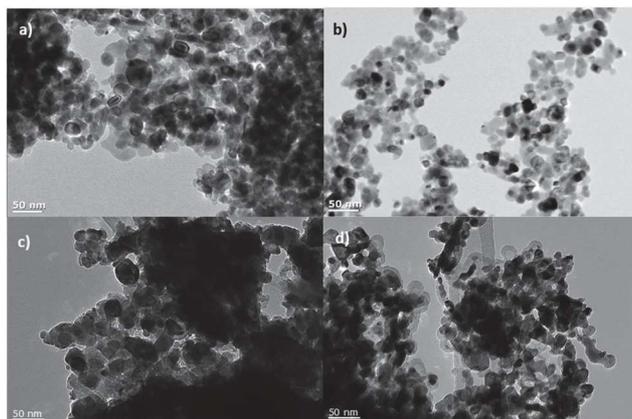
Paper

Fig. 4 High resolution TEM micrographs of (a) **1**, (b) 4, (c) **5e** and (d) **5f** at 50 000× magnification.

Table 3 Summary of the textural characterisation for NiO samples **1–7**

Sample	BET surface area[a] ($m^2\ g^{-1}$)	Mean crystallite size[b,c] (nm)
1	21.46 ± 0.07	16.1
2	—	(14.0)
3	7.71 ± 0.45	13
4	40.56 ± 0.19	20.6 (19.7)
5a	41.79 ± 0.71	(17)
5c	39.36 ± 0.77	—
5d	70.92 ± 0.58	15.4
5e	63.15 ± 0.46	9.9
6a	24.46 ± 0.70	—
6b	31.28 ± 0.44	—
6c	22.17 ± 0.54	11.5
7	60.48 ± 0.17	13.7 (14.8)

[a] BET specific surface areas obtained from Krypton adsorption isotherms. [b] Average mean crystallite size for NiO films on FTO, calculated using the Scherrer equation. [c] In parentheses, average mean crystallite size for NiO nanoparticles.
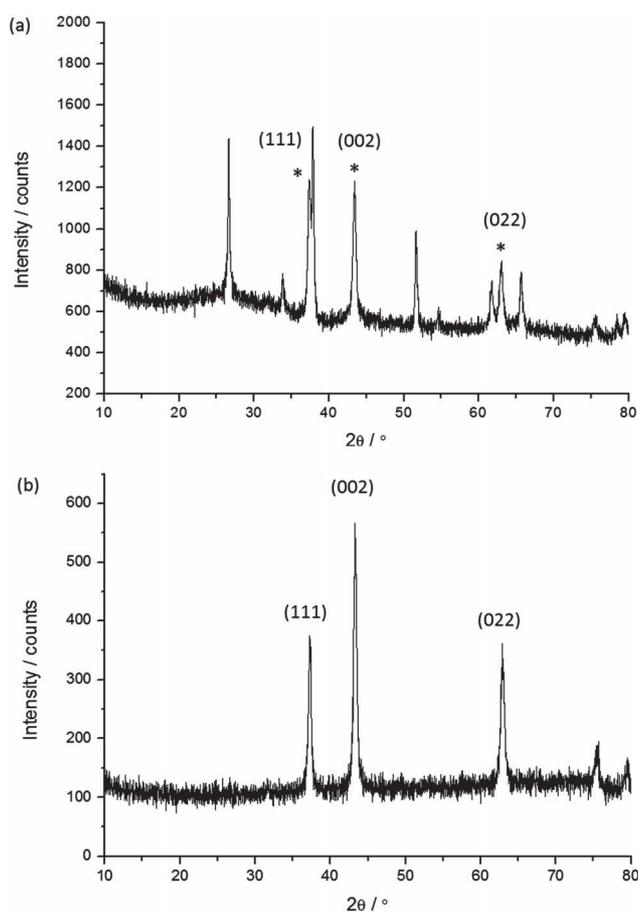

Fig. 5 Representative X-ray diffraction patterns for sample **4**: (a) the NiO film on FTO; (b) the NiO nanoparticles removed from the film. The diffraction peaks indexed with the (*hkl*) notation correspond to the main NiO phase.[25] * Denotes the peaks corresponding to NiO.
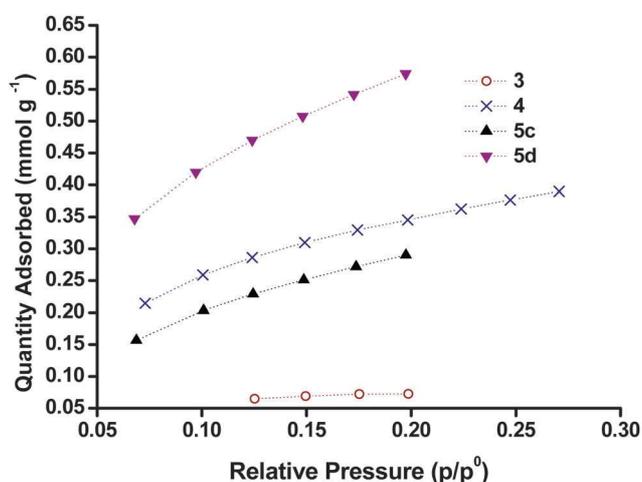

Fig. 6 Kr gas adsorption for NiO films made from NiO films made from sol–gel methods with different block copolymers, **4** (blue) and **3** (brown) and Dyenamo NiO paste and sintered at 350 °C (**5c**, black) and 450 °C (**5d**, purple).

an order of magnitude (7–70 m^2 g^{-1}). NiO screen printing pastes Dyenamo (**5d**), Solaronix (**5e**), typically had the highest surface areas (60–70 m^2 g^{-1}). There was a significant difference in the surface areas obtained from the NiO films with commercial NiO nanoparticles, **1b** (Sigma Aldrich) and **7** (Inframat).

The highest surface area was obtained with **5d** which was prepared from the Dyenamo NiO paste and sintered at 450 °C (71 m^2 g^{-1}). As shown in Fig. 6, this was significantly higher than the surface area obtained for **5c** sintered at 350 °C (39 m^2 g^{-1}) and it demonstrates the importance of temperature on the formation of NiO films. Here we attribute the lower surface area for the film sintered at lower temperature to incomplete combustion of the organic binders. However, sample **5e** made from the Solaronix screen printing paste and sintered 350 °C had a comparatively high surface area (63 m^2 g^{-1}). Unfortunately it was not possible to acquire gas adsorption for this paste sintered at 450 °C. In sol–gel NiO films, higher temperature are required to ensure the all the polymer template has been removed.[23] A study by Bach *et al.* demonstrated that sintering at higher temperatures (550 °C) improves the crystallinity but can lead to a large drop in the surface area (122 m^2 g^{-1} for unsintered NiO, 56 m^2 g^{-1} for 10 minutes at 550 °C and 12 m^2 g^{-1} for 200 minutes at 550 °C).[26] This may

explain the difference between samples **1b** and **7** made from commercial nanoparticles.

Also shown in Fig. 6 is the Kr adsorption for samples **3** and **4** which were prepared by sol–gel routes. The surface areas for the samples prepared from sol–gel methods were generally lower than those obtained from pre-formed NiO nanoparticles. The BET surface area of **4** was in agreement with the N_2 BET for NiO prepared by the same method reported by Sumikura *et al.*[23] However, the sample **6a**, which was prepared from the same method had a significantly lower surface area (24 m^2 g^{-1}). The sol–gel samples prepared using a polystyrene-*block*-poly(2-vinyl-pyridine) diblock copolymer template (**3**) gave the lowest surface area (7.7 m^2 g^{-1}). This value was significantly lower than the values for this sample using N_2 as the adsorbate as reported previously by Bräutigam *et al.* (*ca.* 50 m^2 g^{-1}).[22] Yet, we note that the preparation method for these samples has been slightly altered from the literature (*cf.* experimental part).

Cyclic voltammetry

Cyclic voltammetry (CV) was performed in a 50 mM phosphate buffer electrolyte at pH 7 with a scan rate of 20 mV s^{-1}. Two characteristic broad but distinct peaks can be observed in the anodic and cathodic scans for all the NiO electrodes including the Li-doped NiO sample **6b**. The peak current density and peak area in the voltammograms of the six NiO films shown in Fig. 7 differed greatly. The peak current density for both processes (and area under the peaks) was highest for the screen-printed NiO films **5d** and **7** (150–200 µA cm^{-2}), while **1b** and **3** exhibited very low redox peaks (less than 50 µA cm^{-2}). As a higher specific surface area leads to more active sites exposed to the electrolyte where electron transfer can take place, the magnitude of the peak area should be related to the specific surface area of the film. The results from the cyclic voltammetry were in agreement with the BET surface area (*vide supra*), for example, **5a** and **7** have the highest BET surface, while the surface area of **1b** and **3** were much lower. The matching trend in increasing peak area with increasing surface area is consistent with redox chemistry occurring at the surface of the electrodes.[27]
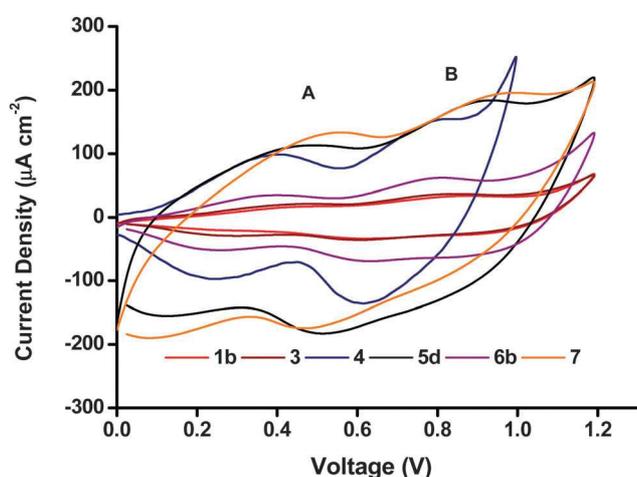
The two peaks have previously been attributed to Ni^{2+}/Ni^{3+} (peak A) and Ni^{3+}/Ni^{4+} (peak B), respectively.[11] However, if all the Ni atoms were first oxidized to Ni^{3+}, and then to Ni^{4+}, peak A and peak B should have a similar area.[27] In Fig. 7, the area of peak B seems to be consistently larger than the area of peak A. It could suggest that remaining Ni^{2+} might be directly oxidized to Ni^{4+} in peak B. Yet, we note the comparison of peak area for A and B is challenging due to the capacitive underlying currents. The overall attribution of the electrochemical processes is thus more complicated and probably does not involve the complete oxidation of all surface sites of NiO. This discussion falls out of the scope of the current manuscript but an analysis is available in ref. 11 and 28.

Dye-sensitized solar cells

IPCE, and APCE measurements. The NiO electrodes were sensitized with the **P1** dye, first reported by Qin *et al.* which produces one of the highest reported IPCE in NiO dye-sensitized solar cells.[12,29] The UV-visible absorption spectra of the sensitized films in addition to the IPCE and Absorbed Photon-to-Current Efficiency (APCE) p-type DSCs assembled with **5d** are summarized in Fig. S2 (ESI†) as an example. The data for all films are provided in Fig. 8 and Table 4.

There was a large difference in the optical density of the non-dyed NiO samples, which ranged between 0.16 (**6a**, **1a**) to 2.9 (**7**) at 500 nm. The films with the highest optical density were opaque and appear almost black. The optical density of all films increased upon sensitization with **P1**. This additional increase in optical density was most pronounced at 500 nm, *i.e.* at the maximum of the dye absorption.

Difference absorption spectra of the dye on the NiO surface were obtained *via* subtraction of the absorption spectra of the non-dyed NiO films from the spectra of the dye-sensitized NiO. We attribute the brown color of the films to the presence of Ni^{3+}

Fig. 7 Cyclic voltammograms of the different NiO preparations, recorded in phosphate buffer (0.05 M pH 7) at a scan rate of 20 mV s^{-1}.
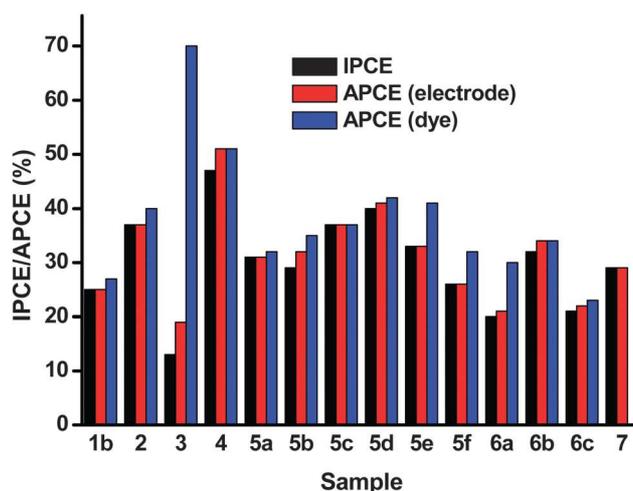

Fig. 8 Summary of all IPCE measurements and the derived APCE at 500 nm. The filled (first) bar indicates the IPCE value, the red bar (second) indicates the APCE calculated from the absorption spectrum of the complete electrode, and the blue (third) shows the APCE calculated from the difference dye spectrum of the surface.

Table 4 Summary of the IPCE values, APCE values relative to the absorption of the dye-sensitized NiO electrode, and APCE values relative to the difference absorption of the dye on the NiO films at 500 nm

Sample	IPCE (%)	APCE, electrode (%)	APCE, dye (%)	Absorbance at 500 nm (a.u.)
1b	25	25	27	3.17
2	37	37	40	2.33
3	13	19	70	0.51
4	47	51	51	1.12
5a	31	31	32	1.78
5b	29	32	35	1.05
5c	37	37	37	3.33
5d	40	41	42	1.98
5e	33	33	41	2.89
5f	26	26	32	3.23
6a	20	21	30	1.23
6b	32	34	34	1.64
6c	21	22	23	1.37
7	29	29	—	1.94

rather than Ni^0 since no Ni^0 was observed in the XRD patterns.[25,27] APCE spectra were calculated with respect to the absorption spectra of the dye-sensitized NiO surfaces and the difference absorption spectra. These two quantities should allow for the differentiation of photons absorbed by the electrode and photons absorbed only by the dye on the surface. The APCE is related to the dye on the NiO surface and reduces the wavelength dependency of the efficiency. However, for the samples in which the NiO itself absorbed strongly, the APCE values were disproportionately high (Table 4). This was particularly evident for sample **7** which had the highest absorption of all the NiO films tested making the calculation of an APCE from the dye on the surface inaccurate. Likewise sample **3** had the highest APCE using this method but the lowest IPCE because it had the smallest absorption from the dye. Some of the color from the NiO is bleached on dye adsorption which can introduce an error. Also some samples scatter light more than others. We obtained the most consistent results by calculating the APCE from the total absorbance of the film, without subtracting the spectrum for the non-sensitized NiO.

The results of the IPCE and APCE measurements are provided in Fig. 8 and Table 4. The lowest IPCE values were obtained for the polystyrene-*block*-poly-(2-vinylpyridine)-templated NiO films, **3**, while highest IPCEs were attained using the F108 templated NiO, **4**. The IPCEs for the PS-*b*-P2VP templated NiO films (**3**) were low due to the relatively small NiO thickness of about 200 nm compared to about 1.2 μm for **4**. This translates into a lower absorbance of the film (0.5 for **3** compared to 1.12 for **4**) which limits the light harvesting efficiency (LHE)§ to 69% for **3** compared to 92% for **4**. Sample **3** also had the lowest specific surface area which would lead to lower dye-loading compared to the other samples.

In general, the highest IPCE was observed for samples **7**, **5c–e**, **2** and **4**, which were prepared by screen printing a paste containing pre-formed NiO nanoparticles except for **4** which was prepared using the sol–gel method. These samples had the

§ LHE = 1–10^{-A} where A = absorbance.

highest specific surface area measured using BET and the highest current density in the cyclic voltammetry experiment. The NiO crystallite sizes ranged between 14–20 nm and samples **7**, **5e** and **2** were prepared from commercial NiO with an average particle size of 20 nm. Therefore it appears that 20 nm is the preferred size of the NiO nanoparticles in the case of our cohort of samples. However, since we did not have a sample with a higher crystallite size, we do not know if this is optimum. Smaller particles may lead to more dense packing in the film, lowering the amount of surface exposed to the electrolyte or dye solution. It is anticipated that on increasing the crystallite size the surface area should decrease. This in turn would result in lower dye loading, a lower light harvesting efficiency and a lower photocurrent. It is interesting to note that 20 nm anatase particles are used in state-of-the-art TiO$_2$-based dye-sensitized solar cells with iodine electrolyte.[21,30] **1b**, **5f** and **5b** which were also prepared by screen printing a paste containing pre-formed NiO nanoparticles gave a lower IPCE than similar screen-printed materials, which was consistent with the lower specific surface area. This was possibly because the sintering temperature was higher (550 °C for **1**, 450 °C for **5f** compared with 350 °C for **5e**). In general the lower sintering temperature gave better results for one-layer films.

Current–voltage measurements. The current–voltage measurements for p-type DSCs assembled with each electrode are given in Fig. 9(a) and are summarized in Table 5.

Most devices exhibited a V_{OC} between 95 and 115 mV which is typical for p-type DSCs with I$_3^-$/I$^-$ electrolyte. In general, devices obtained with pre made NiO nanoparticles have a higher V_{OC}, which is consistent with results in the literature and agrees with the trend in the charge lifetime studies (*vide infra*).[11] For example, sample **7** shows the highest measured open-circuit voltage (143 mV) in the series. Lithium doping also had a clear effect on the device photovoltaic performance. The 0.5% lithium doped NiO had a V_{OC} of 129 mV (**6c**) compared to 110 mV for the undoped sample (**6a**), this difference stems from the modification of the flat-band potential of the NiO following Li-doping.[27] For samples **5a–d** increasing the sintering temperature from 350 °C to 450 °C resulted in a lower V_{OC} whereas there was little difference in V_{OC} with sintering temperature between samples **5e,f**.

In general the trends in short-circuit photocurrent density (J_{SC}) followed the same trend at the IPCE. Lithium loading had a large effect on the photocurrent density. The current density rose from 1.67 mA cm^{-2} without lithium (**6a**) to 2.56 mA cm^{-2} (**6b**) with 0.1% lithium which is consistent with an increase in LHE from 94% for **6a** to 98% for **6b**. For commercially available Solaronix NiO paste (**5e** and **f**), the effect of sintering temperature on short circuit current density was clearly demonstrated: lower sintering temperature gives higher current density: 1.57 mA cm^{-2} for the sample annealed at 350 °C and 1.15 mA cm^{-2} with annealing at 450 °C. This is also true for the Dyenamo samples (**5c** and **d**), though to a lesser extent, despite the lower specific surface area of the film **5c**. It has been widely reported that the crystallite size of NiO nanoparticles increases when the sintering temperature is increased, subsequently leading to
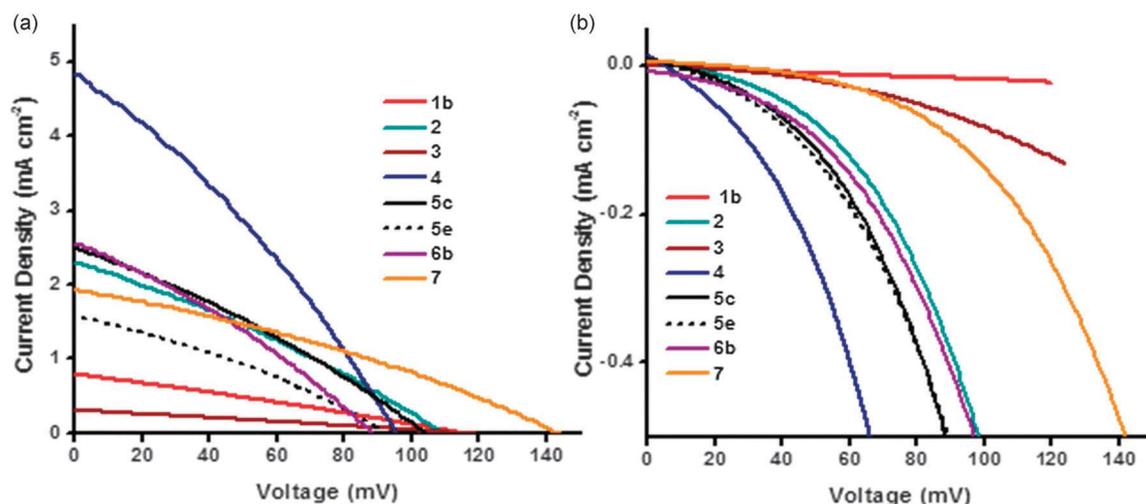
(a)

(b)

Fig. 9 Plot of current density vs. voltage curves (a) under AM1.5 illumination and (b) in the dark for the NiO DSCs.

Table 5 Photoelectrochemical characteristics of the p-DSCs with **P1** sensitizers employing the iodide/triiodide electrolyte recorded under AM1.5 G simulated sunlight (100 mW cm^{-2})

Sample	V_{OC} (mV)	J_{SC} (mA cm^{-2})	FF (%)	PCE (%)
1a	115	1.00	35	0.040
1b	114	0.79	28	0.025
2	110	2.31	30	0.075
3	115	0.31	26	0.009
4	96	4.83	31	0.145
5a	100	1.65	33	0.053
5b	80	1.85	29	0.042
5c	104	2.49	30	0.078
5d	98	2.40	29	0.069
5e	93	1.57	32	0.047
5f	97	1.15	32	0.035
6a	110	1.67	34	0.062
6b	88	2.56	31	0.070
6c	129	1.16	35	0.053
7	143	1.93	32	0.089

pore collapsing and a decrease in the amount of adsorbed dye and LHE.[11,31,32] Our BET measurements were inconsistent with this; **5c** had a specific surface area of 39 m^2 g^{-1} compared to 71 m^2 g^{-1} for **5d**, which suggests that 30 minutes at 350 °C is insufficient to remove all the organic material in the commercial paste. Yet, surprisingly, **5c** generated a better J_{SC}. The thickness of the films has an equally crucial effect. Following the same sintering conditions, the dye loading was greater for thicker NiO films (*e.g.* **5b** and **5d**), which is consistent with results in the literature.[12]

PS-*b*-P2VP templated sol–gel NiO films **3** suffer from very low thicknesses (around 200 nm). In this case, the dye loading and therefore the absorbance of photo-electrode was too low to afford a high photocurrent density. However, thicker films do not necessarily result in an improvement in J_{SC}. A 5 μm thick film (**1b**) produced a lower J_{SC} (J_{SC} = 0.79 mA cm^{-2}) but similar V_{OC} to a 2 μm thick film (**1a**, J_{SC} = 1.00 mA cm^{-2}). Since the specific surface area was low it is possible that dye was not adsorbed throughout the electrode or light absorption by the

NiO competes with absorption from the dye.[33] Fig. 9(b) shows the dark current curves for **1–7**. Samples **1** and **3** (the thickest and thinnest samples) displayed the lowest dark currents. The low dark current density for **1b** and **3** in the presence of the (I_3^-/I^-) redox electrolyte (Fig. 9(b)) is consistent with the low current density of **1b** and **3** in the presence of the aqueous electrolyte (Fig. 7), which suggests that the conductivity of the material is low. These observations could result from slow charge-recombination at the NiO/electrolyte interface or slow charge diffusion though the NiO, possibly as a consequence of poor connectivity in the mesoporous structure, and also may explain the low J_{SC} and IPCE. The optimum film thickness appears to be in the range of 1–2 μm which maximizes the LHE and charge-diffusion through the NiO films. The highest J_{SC} (4.83 mA cm^{-2}) was obtained with sample **4** which generated the highest photoconversion efficiency (PCE) of 0.145%. This sample appears to have the optimal surface area and thickness (1.2 μm). These results were consistent with a **4** having the best charge collection efficiency. This was deduced from the charge-lifetimes and transport times which were determined using small amplitude modulated photovoltage and photocurrent decay techniques.

Charge lifetime and charge extraction studies

Charge lifetimes (τ_h) and extracted charge densities were measured by small square modulated photovoltage and charge extraction measurements. τ_h vs. open-circuit photovoltage (V_{OC}) and open-circuit extracted charge density (Q_{OC}) are given in Fig. 10. Q_{OC} as a function of V_{OC} is displayed in Fig. 11. When τ_h was plotted as a function of V_{OC}, sample **3** has a similar value as *e.g.* sample **1** and **2**, but when plotted against Q_{OC}, τ_h for **3** is shifted relative to the other samples. This is possibly a consequence of the very thin films. With the exception of **3**, τ_h appears to be longer for the samples made from preformed NiO compared to those prepared from sol–gel methods. This fits with the higher V_{OC} obtained by these devices as discussed earlier. Fig. S3 in the ESI† compares the effect sintering temperature has on τ_h for
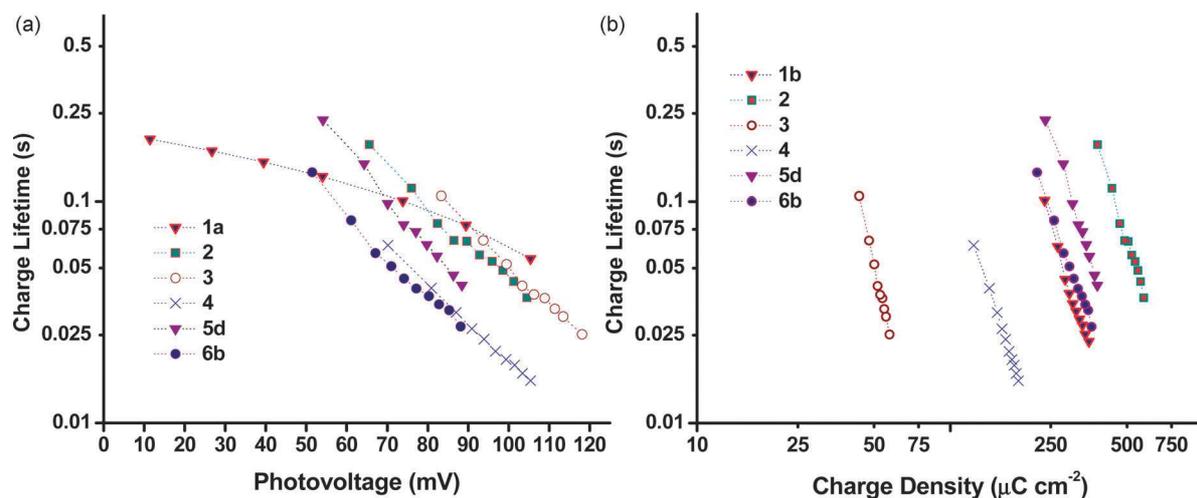
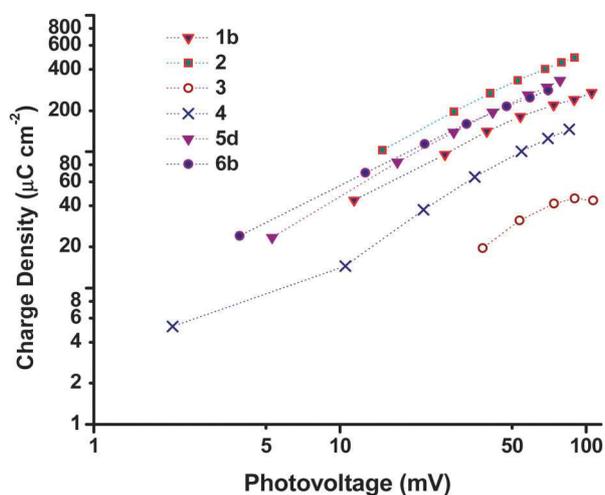Fig. 10 Plots of charge lifetime *vs.* (a) photovoltage and (b) charge density.

Fig. 11 Plot of extracted charge density *vs.* photovoltage.

the Dyenamo (**5c,d**) and Solaronix (**5e,f**) samples. At both sintering temperatures τ_h was longer for samples prepared from the Dyenamo NiO paste. In both cases τ_h decreased with increased sintering temperature, which is consistent with the decrease in V_{OC}. Also in both cases there seems to be a drop in Q_{OC} as a function of V_{OC} with increased sintering temperature. This implies a shift in the valence band edge which explains the higher V_{OC} obtained by sample **5f** compared to sample **5e** despite the notably shorter τ_h. Of the samples prepared from preformed NiO, **1b** had the shortest τ_h. **1b** was sintered at 550 °C, notably higher than any other samples in this study. This is somewhat unexpected as higher sintering temperatures have been used to obtain highly crystalline NiO or to post-treat samples, and has previously led to improved V_{OC}.[31,32]

τ_h and Q_{OC} for the Li doped samples **6a–c** as well as sample **4** are given in Fig. S4 (ESI†). The level of Li doping appears to have a notable effect on both τ_h and the potential of the valence band edge resulting in a significant improvement of 19 mV passing from undoped **6a** to 0.5% doped **6c**. Interestingly

sample **4** which was prepared using the same F108 block copolymer as **6a** had different τ_h and Q_{OC} at similar values of V_{OC} whereas the p-DSC containing **4** had a lower overall V_{OC} at 1 sun compared to **6a**. As discussed above, we attribute the different properties to the different solvent ratio in the sol–gel precursor.

Photoelectrochemical experiments

The NiO samples were used as photocathodes in water-splitting DSPEC cells as described in the study by Li *et al.* and the photoelectrocatalytic proton reduction properties were compared.[13] As for the DSCs, the sintered NiO electrodes were first sensitized with the organic dye **P1** (Fig. 2). After rinsing the electrodes to remove unabsorbed dye, the [Co(dmgBF$_2$)$_2$(H$_2$O)$_2$] H$_2$-evolving catalyst solution was drop-cast onto the surface of these electrodes to give a total loading of *ca.* 200 nmol cm^{-2}.¶ The catalyst-**P1** co-sensitized electrodes were then allowed to dry in air before they were assembled in the cell and immersed in aqueous pH 7 phosphate buffer. The photocurrent was recorded at an applied potential of −0.4 V *vs.* Ag/AgCl (*i.e.* −0.19 V *vs.* NHE, +0.22 *vs.* RHE) under chopped white LED illumination. The results are shown in Fig. 12. The stabilized photocurrents in the range of 5–25 μA cm^{-2} indicate electron-transfer from the photosensitized electrodes to the bound catalyst. All electrodes display an initially high transient current, rapidly decreasing to steady values. This phenomenon is particularly true for the first two irradiation periods (2 × 5 min), and tends to disappear for the last ones. This transient current may be attributed to capacitive charging of the NiO substrates or to the reduction of residual oxygen in the media. It was not observed during the whole measurement time and no anodic transient current, accounting for a back-electron-transfer, was observed when the light was switched off.

The photocurrent generated by each sample was similar in magnitude (*ca.* 10 μA cm^{-2}). The three NiO samples which produced the highest performances were **4**, **5d** and **7**, within the

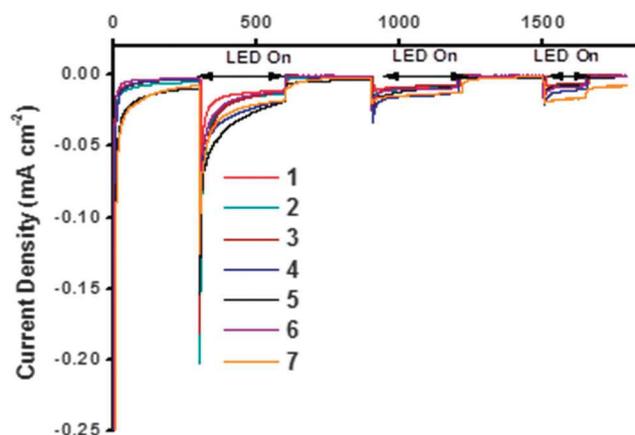¶ Accounting for the area of the substrate not the specific surface area of the sample.

Fig. 12 Summary of water-splitting data. The maximum photocurrent reported by Li et al. = 5.5 μA cm^{-2}.[13]

Table 6 Summary of water-splitting data

Sample	Area (cm^2)	Total charge LED on[a] (mC)	Theoretical H$_2$[a] (nmol)
1b	0.25	1.97	10.2
2	0.30	3.35	17.4
3	0.36	6.56	34.0
4	0.36	9.57	49.6
5d	0.36	9.42	48.8
6b	0.36	6.7	34.7
7	0.36	9.71	50.3
Li et al.[13]	1.0		93 nmol after 30 min

[a] After 800 seconds.

accuracy of the measurements. These electrodes had the highest specific surface area according to the BET experiments and cyclic voltammetry (*vide supra*). **4** (purple line) generated a photocurrent starting from 25 μA cm^{-2} and slowly decreasing to 12 μA cm^{-2} after 20 minutes. The total charge under irradiation corresponds to a theoretical amount of 49.6 nmol of H$_2$ after 800 seconds. A similar behavior was observed on electrode **5d**, which generated the highest initial photocurrent but this decayed more steeply than the other samples to values below 10 μA cm^{-2}. Sample **7** generated the steadiest current under irradiation, stabilizing at around 20 μA cm^{-2}. This corresponded to the highest theoretical amount of evolved hydrogen (50.3 nmol). It was noted that the expected H$_2$ production performances of these three samples were within a very close range and exceeded that reported by Li et al. after correction for surface area (Table 6).[13]

Conclusions

From these studies it appears that a crystallite size of at least 20 nm, a film thickness of 1–2 μm and a specific surface area above 40 m^2 g^{-1} is most appropriate for photoelectrochemical devices using NiO. For thinner films, a lower sintering temperature (350 °C) gave better results than a higher sintering temperature (450 °C and 500 °C). Both commercial and non-commercial NiO gave promising solar cell and water-splitting devices. There was a generally higher specific surface area for

preformed NiO nanoparticles compared to NiO formed *in situ* which was consistent with the trends in current density and charge in the cyclic voltammetry experiments. All the NiO films from different preparation methods showed typical electrochemical behaviour in redox electrolyte and phosphate buffer, but the differences in charge transferred varied consistently in agreement with the specific surface area of the electrode. This is a consequence of the surface confinement of the oxidation process in NiO thin film electrodes.

Samples **4** and **7** which had the two highest PCEs (0.145% and 0.089%) in the p-DSCs also gave the best overall theoretical H$_2$ conversion. However, the current voltage data for these two samples differed; sample **4** generated the highest photocurrent; sample **7** generated a relatively poor current but the V_{OC} for the DSC was the highest in this study. It appears that taking measures to improve both the current generated (surface area, hole mobility) and voltage across the device (surface passivation, tuned valence band energy) in a p-DSC are both key-approaches to improve dye sensitized photocathodes for hydrogen photoelectrochemical production.

Acknowledgements

References

1 J. He, H. Lindström, A. Hagfeldt and S. Lindquist, *J. Phys. Chem. B*, 1999, **103**, 8940–8943.

2 J. He, H. Lindström, A. Hagfeldt and S. Lindquist, *Sol. Energy Mater. Sol. Cells*, 2000, **62**, 265–273.

3 W. Song, Z. Chen, C. R. K. Glasson, K. Hanson, H. Luo, M. R. Norris, D. L. Ashford, J. J. Concepcion, M. K. Brennaman and T. J. Meyer, *ChemPhysChem*, 2012, **13**, 2882–2890.

4 E. S. Andreiadis, M. Chavarot-Kerlidou, M. Fontecave and V. Artero, *Photochem. Photobiol.*, 2011, 946–964.

5 N. Queyriaux, R. T. Jane, J. Massin, V. Artero and M. Chavarot-Kerlidou, *Coord. Chem. Rev.*, 2015, **304–305**, 3–19.

6 A. Nattestad, A. J. Mozer, M. K. R. Fischer, Y.-B. Cheng, A. Mishra, P. Bäuerle and U. Bach, *Nat. Mater.*, 2010, **9**, 31–35.

7 S. Mathew, A. Yella, P. Gao, R. Humphry-Baker, B. F. E. Curchod, N. Ashari-Astani, I. Tavernelli, U. Rothlisberger, M. K. Nazeeruddin and M. Grätzel, *Nat. Chem.*, 2014, **6**, 242–247.

8 Y. Gao, X. Ding, J. Liu, L. Wang, Z. Lu, L. Li and L. Sun, *J. Am. Chem. Soc.*, 2013, **135**, 4219–4222.

9 L. Tong, A. Iwase, A. Nattestad, U. Bach, M. Weidelener, G. Götz, A. Mishra, P. Bäuerle, R. Amal, G. G. Wallace and A. J. Mozer, *Energy Environ. Sci.*, 2012, **5**, 9472.

10 Z. Li, W. Luo, M. Zhang, J. Feng and Z. Zou, *Energy Environ. Sci.*, 2013, **6**, 347–370.

11 D. Dini, Y. Halpin, J. G. Vos and E. A. Gibson, *Coord. Chem. Rev.*, 2015, **304–305**, 179–201.

12 L. Li, E. A. Gibson, P. Qin, G. Boschloo, M. Gorlov, A. Hagfeldt and L. Sun, *Adv. Mater.*, 2010, **22**, 1759–1762.

13 L. Li, L. Duan, F. Wen, C. Li, M. Wang, A. Hagfeldt and L. Sun, *Chem. Commun.*, 2012, **48**, 988–990.

14 C. J. Wood, G. H. Summers and E. A. Gibson, *Chem. Commun.*, 2015, **51**, 3915–3918.

15 C. Baffert, V. Artero and M. Fontecave, *Inorg. Chem.*, 2007, **46**, 1817–1824.

16 P. Qin, J. Wiberg, E. A. Gibson, M. Linder, L. Li, T. Brinck, A. Hagfeldt, B. Albinsson and L. Sun, *J. Phys. Chem. C*, 2010, **114**, 4738–4748.

17 J. T. Muckerman and E. Fujita, *Chem. Commun.*, 2011, **47**, 12456.

18 B. H. Solis and S. Hammes-Schiffer, *J. Am. Chem. Soc.*, 2011, **133**, 19036–19039.

19 T. Lazarides, T. McCormick, P. Du, G. Luo, B. Lindley and R. Eisenberg, *J. Am. Chem. Soc.*, 2009, **131**, 9192–9194.

20 L. A. Berben and J. C. Peters, *Chem. Commun.*, 2010, **46**, 398–400.

21 S. Ito, P. Chen, P. Comte, M. K. Nazeeruddin, P. Liska, P. Péchy and M. Grätzel, *Prog. Photovoltaics Res. Appl.*, 2007, **15**, 603–612.

22 M. Bräutigam, P. Weyell, T. Rudolph, J. Dellith, S. Krieck, H. Schmalz, F. H. Schacher and B. Dietzek, *J. Mater. Chem. A*, 2014, **2**, 6158.

23 S. Sumikura, S. Mori, S. Shimizu, H. Usami and E. Suzuki, *J. Photochem. Photobiol., A*, 2008, **199**, 1–7.

24 L. D. Amario, G. Boschloo, A. Hagfeldt and L. Hammarström, *J. Phys. Chem. C*, 2014, **118**, 19556–19564.

25 A. Renaud, B. Chavillon, L. Cario, L. Le Pleux, N. Szuwarski, Y. Pellegrin, E. Blart, E. Gautron, F. Odobel and S. Jobic, *J. Phys. Chem. C*, 2013, **117**, 22478–22483.

26 A. Nattestad, M. Ferguson, R. Kerr, Y.-B. Cheng and U. Bach, *Nanotechnology*, 2008, **19**, 295304.

27 G. Boschloo and A. Hagfeldt, *J. Phys. Chem. B*, 2001, **105**, 3039–3044.

28 A. G. Marrani, V. Novelli, S. Sheehan, D. P. Dowling and D. Dini, *ACS Appl. Mater. Interfaces*, 2014, **6**, 143–152.

29 P. Qin, H. Zhu, T. Edvinsson, G. Boschloo, A. Hagfeldt and L. Sun, *J. Am. Chem. Soc.*, 2008, **130**, 8570–8571.

30 A. Hagfeldt, G. Boschloo, L. Sun, L. Kloo and H. Pettersson, *Chem. Rev.*, 2010, **110**, 6595–6663.

31 X. L. Zhang, F. Huang, A. Nattestad, K. Wang, D. Fu, A. Mishra, P. Bäuerle, U. Bach and Y.-B. Cheng, *Chem. Commun.*, 2011, **47**, 4808–4810.

32 X. L. Zhang, Z. Zhang, D. Chen, P. Bäuerle, U. Bach and Y.-B. Cheng, *Chem. Commun.*, 2012, **48**, 9885.

33 E. A. Gibson, M. Awais, D. Dini, D. P. Dowling, M. T. Pryce, J. G. Vos, G. Boschloo and A. Hagfeldt, *Phys. Chem. Chem. Phys.*, 2013, **15**, 2411–2420.

34 G. Naponiello, I. Venditti, V. Zardetto, D. Saccone, A. Di Carlo, I. Fratoddi, C. Barolo and D. Dini, *Appl. Surf. Sci.*, 2015, **356**, 911–920.

Abstract

Solar fuels generated from the light-induced splitting of water into H_2 and O_2 is an appealing strategy for securing future energy. The use of platinum for catalyzing hydrogen evolution may be bypassed with earth-abundant catalysts. In a previous study, our lab realized the immobilization of a proton reduction catalyst, the cobalt diimine-dioxime molecular complex, within a cathode material steadily evolving H_2 from fully aqueous media. In this work, we report on the implementation of this catalyst into light-driven devices. Operating conditions in the solvent of interest, water, were screened. The molecular catalyst degrades when free in solution, but retains activity when supported on an electrode, even in the presence of O_2, and could thus be integrated into a tandem cell. Further on, new derivatives of the catalyst were developed for the attachment onto transparent conducting oxides. Co-grafted photocathodes were constructed by anchoring a functionalized catalyst along with photosensitizers onto *p*-type NiO. These architectures were checked by a whole set of analytical techniques and light-driven catalytic hydrogen evolution was achieved by photocathodes assessed under device-related photoelectrochemical conditions. Immobilizable dye-catalyst dyads were also successfully synthetized as alternative derivatives and open up new possibilities to develop molecular photocathodes.

Résumé

Générer des carburants solaires, comme l'hydrogène *via* la photoélectrolyse de l'eau, est une stratégie à explorer pour notre futur énergétique. Pour éviter l'emploi du platine en tant que catalyseur de production d'hydrogène, des métaux abondants peuvent être utilisés. Au laboratoire, le complexe diimine-dioxime de cobalt, catalyseur moléculaire de réduction des protons, a pu être immobilisé pour créer une cathode produisant de manière stable de l'hydrogène en milieu aqueux. Dans ces travaux, nous avons étudié l'introduction du catalyseur dans des dispositifs photoélectrocatalytiques. Différentes conditions opératoires dans l'eau, solvant de choix, ont été examinées. Le complexe se dégrade s'il est en solution mais son activité est maintenue, même en présence d'oxygène, s'il est supporté sur électrode. Cette électrode a ainsi pu être intégrée en cellule tandem. De nouveaux dérivés du complexe ont aussi été développés pour l'attachement sur oxydes transparents conducteurs. Un dérivé a été co-immobilisé avec des photosensibilisateurs sur une surface de NiO, oxyde de type *p*. Les photocathodes co-greffées obtenues ont été caractérisées par un ensemble de techniques analytiques et ont démontré la production d'hydrogène en conditions photoélectrocatalytiques. Des entités colorant-catalyseur pouvant s'ancrer sur surface ont également été synthétisées et ouvrent de nouvelles voies pour élaborer des photocathodes moléculaires.